FEASIBILITY STUDY-II OF A MUON-BASED NEUTRINO SOURCE

Executive Editors
S. Ozaki*, R.B. Palmer*, M.S. Zisman#
*BNL, Upton, NY 11973, USA
#LBNL, Berkeley, CA 94720, USA
Editor
J.C. Gallardo*

June 14, 2001

Members of the Collaboration and Non-Member Participants of the Study

Maury Goodman, Ahmed Hassanein, James H. Norem, Claude B. Reed, Dale Smith, Lee C. Teng, Chun-xi Wang

Argonne National Laboratory, Argonne, IL 60439

Michael Anerella†, J. Scott Berg, Joseph M. Brennan†, Richard C. Fernow, Juan C. Gallardo, Ramesh Gupta, Michael Harrison†, Michael Hemmer†, Hsiao-C. Hseuh†, Michael A. Iarocci†, Stephen A. Kahn, Bruce J. King, Harold G. Kirk, David Lissauer, Laurence S. Littenberg, Alfredo Luccio†, Hans Ludewig†, Ioannis M. Marneris†, James Mills†, William A. Morse, Stephen V. Musolino†, Edward O'Brien†, Wonho Oh†, Satoshi Ozaki, Robert B. Palmer, Brett Parker†, Zohreh Parsa, Charles Pearson†, Ralf Prigl†, Pavel Rehak, Thomas Roser, Alessandro Ruggiero†, Roman Samulyak†, Jesse D. Schmalzle†, Nick Simos, Iuliu Stumer, Mariola Sullivan†, Valeri Tcherniatine, Peter Thieberger, Dejan Trbojevic, Robert Weggel, Erich H. Willen, Shuo-Yuan Zhang†, Yongxiang Zhao

Brookhaven National Laboratory, Upton, NY 11973

Gregory I. Silvestrov, Alexandr N. Skrinsky, Tatiana A. Vsevolozhskaya

Budker Institute of Nuclear Physics, 630090 Novosibirsk, Russia

Gregory Penn, Jonathan S. Wurtele*

University of California-Berkeley, Physics Department, Berkeley, CA 94720

John F. Gunion

University of California-Davis, Physics Department, CA 95616

David B. Cline, Yasuo Fukui, Alper A. Garren, Kevin Lee, Yuriy Pischalnikov

University of California-Los Angeles, Los Angeles, CA 90095

Bruno Autin, Roland Garoby, Helmut Haseroth, Colin Johnson, Helge Ravn, Edmund J. N. Wilson

CERN, 1211 Geneva 23, Switzerland

Kara Hoffman, Kwang-Je Kim, Mark Oreglia, Yau Wah

The University of Chicago, Chicago, IL 60637

Vincent Wu

University of Cincinnati, Cincinnati, OH 45221

Allen C. Caldwell, Janet M. Conrad, Jocelyn Monroe, Frank Sciulli, Michael H. Shaevitz, William J. Willis

Columbia University, Nevis Laboratory, Irvington, NY 10533

Rongli Geng†, Hasan Padamsee, Valery Shemelin†, Maury Tigner

Cornell University, Newman Laboratory for Nuclear Studies, Ithaca, NY

14853
Peter Hwang[†], Gregory Naumovich[†]
Everson Electric Company, Bethlehem, PA 18017
David R. Winn
Fairfield University, Fairfield, CT 06430
Charles M. Ankenbrandt, Muzaffer Atac, Valeri I. Balbekov, Elizabeth J. Buckley-Geer, David C. Carey, Sam Childress, Weiren Chou, Fritz DeJongh, H. Thomas Diehl, Alexandr Drozhdin, Daniel Elvira, David A. Finley, Stephen H. Geer, Krishnaswamy Gounder, Carol Johnstone, Paul Lebrun, Valeri Lebedev, Joseph D. Lykken, Frederick E. Mills, Nikolai V. Mokhov, Alfred Moretti, David V. Neuffer, King-Yuen Ng, Milorad Popovic, Zubao Qian, Rajendran Raja, John S. Reid, Panagiotis Spentzouris, Ray Stefanski, Sergei Striganov, Alvin V. Tollestrup, Andreas Van Ginneken, Steve Vejcik
Fermi National Accelerator Laboratory, P. O. Box 500, Batavia, IL 60510
Alain Blondel
University of Geneva, Switzerland
John G. Learned, Sandip Pakvasa
University of Hawaii, Department of Physics, Honolulu, HI 96822
Massimo Ferrario
INFN-LNF, via E-Fermi 40, Frascati (Roma), Italy
S. Alex Bogacz, Swapan Chattopadhyay, Haipeng Wang
Jefferson Laboratory, 12000 Jefferson Ave., Newport News, VA 23606
T. Bolton
Kansas State University, Manhattan, KS 66502-2601
Yoshitaka Kuno, Yoshiharu Mori, Takeichiro Yokoi
KEK High Energy Accelerator Research Organization, 1-1 Oho, Tsukuba 305, Japan
Edgar L. Black, Rolland Johnson[†], Daniel M. Kaplan, Nickolas Solomey, Yağmur Torun
Illinois Institute of Technology, Physics Div., Chicago IL 60616
Deborah Errede, Kyoko Makino
Illinois University, at Urbana, Urbana-Champaing, IL 61801
Michael S. Berger, Gail G. Hanson, Peter Schwandt
Indiana University, Physics Department, Bloomington, IN 47405
Ilya F. Ginzburg
Institute of Mathematics, Prosp. ac. Koptyug 4, 630090 Novosibirsk, Russia
Yasar Onel
University of Iowa, Physics Department, Van Allen Hall, Iowa City, IA

52242
Shlomo Caspi, John Corlett, Miguel A. Furman, Michael A. Green, Neal Hartman†,
Anthony S. Ladran†, Derun Li, Robert A. Macgill†, Alfred D. McInturff,
Louis L. Reginato, Robert Rimmer, Ronald M. Scanlan, Andrew M. Sessler,
Brad Shadwick, William C. Turner, David Vanecek†, Simon Yu, Michael S. Zisman,
Max Zolotorev
Lawrence Berkeley National Laboratory, 1 Cyclotron Rd., Berkeley, CA 94720
Joe Minervini†, Joel Schultz†
M.I.T., Plasma Science and Fusion Center, Cambridge, MA 02139
Martin Berz, Bela Erdelyi†, Richard York, Al Zeller
Michigan State University, East Lansing, MI 48824
Stephen B. Bracker, Lucien Cremaldi, Don Summers
University of Mississippi, Oxford, MS 38677
John R. Miller, Soren Prestemon
National High Magnetic Field Laboratory, Magnet Science & Technology, FL 32310
Gerald C. Blazey, Mary Anne Cummings, David Hedin
Northern Illinois University, DeKalb, IL 60115
Heidi M. Schellman
Northwestern University, Department of Physics and Astronomy, Evanston, IL 60208
J. B. Chesser†, David L. Conner†, Tony A. Gabriel, F. X. Gallmeier†, John R. Haines†,
Norbert Holtkamp, T. J. McManamy†, Philip T. Spampinato
Oak Ridge National Laboratory, Oak Ridge, TN 37831
Eun-San Kim, Moohyun Yoon
Pohang University of Science and Technology, POSTECH, Sam 31, Hyoja dong, Pohang, Kyungbuk, 790-784, Korea
Changguo Lu, Kirk T. McDonald, Eric J. Prebys
Princeton University, Joseph Henry Laboratories, Princeton, NJ 08544
Robert Rossmanith
Research Center Karlsruhe, D-76021 Karlsruhe, Germany
J. Roger J. Bennett
Rutherford Appleton Laboratory, Chilton, Didcot, Oxon OX11 0QX, UK
Peter Titus†
Stone and Webster Corp. (under contract to PSFC, MIT) Boston, MA
Robert Shrock

Department of Physics and Astronomy, SUNY, Stony Brook, NY 11790
Odette Benary
Tel-Aviv University, Ramat-Aviv, Tel-Aviv 69978, Israel
Vernon D. Barger, Tao Han
Department of Physics, University of Wisconsin, Madison, WI 53706

† Participant of the Study Group and non-member of the Muon Collider and Neutrino Factory Collaboration.

* also at Lawrence Berkeley National Laboratory.

Preface

Executive Summary

The concept of using a muon storage ring to provide a well characterized beam of muon and electron neutrinos (a Neutrino Factory) has been under study for a number of years now at various laboratories throughout the world. The physics program of a Neutrino Factory is focused on the relatively unexplored neutrino sector. In conjunction with a detector located a suitable distance from the neutrino source, the facility would make valuable contributions to the study of neutrino masses and lepton mixing. A Neutrino Factory is expected to improve the measurement accuracy of $\sin^2(2\theta_{23})$ and Δm^2_{32} and provide measurements of $\sin^2(2\theta_{13})$ and the sign of Δm^2_{32}. It may also be able to measure CP violation in the lepton sector.

In the U.S., a formal collaboration of some 140 scientists, the Neutrino Factory and Muon Collider Collaboration (MC), has undertaken the study of how to design such a machine. The MC has three "sponsoring" national laboratories, Brookhaven National Laboratory (BNL), Fermi National Accelerator Laboratory (FNAL or Fermilab), and Lawrence Berkeley National Laboratory (LBNL), and receives funding primarily from the U.S. Department of Energy (DOE).

Recently, the MC has gained from the addition of NSF-sponsored university groups, coordinated by Cornell University, and of various universities in Illinois sponsored by the Illinois Consortium for Accelerator Research (ICAR), coordinated by Illinois Institute of Technology.

In 1999, the MC aimed to define the scope of a Neutrino Factory facility by doing an end-to-end study of the entire complex. This led, in late 1999, to a request from the Fermilab Director, Michael Witherell, to carry out a Feasibility Study, in cooperation with the MC, of a Neutrino Factory sited at Fermilab. That initial Study (denoted here as "Study-I"), organized by Norbert Holtkamp and David Finley (Fermilab), demonstrated the feasibility of an entry-level machine, and outlined the features of the various systems needed to build it. However, the performance reached in that effort, characterized in terms of the number of muon decays aimed at a detector located 3000 km away from the muon storage ring, $N = 2 \times 10^{19}$ decays per "Snowmass year" ($\equiv 10^7$ s) per MW of protons on target, was lower than anticipated.

In June 2000, a request was made by the BNL Director, John Marburger, for the MC to participate in a second Neutrino Factory Feasibility Study (denoted here as "Study-II"), this time focused on a machine sited at BNL. Study-II was to aim at a high-performance machine, with an intensity an order of magnitude higher than achieved in Study-I. Study-II was co-organized by the MC and BNL. The Study Leaders (see below for the organization of the work) were Satoshi Ozaki and Robert Palmer (BNL) and Michael Zisman (LBNL). This document contains the results of Study-II.

In this report we first describe the exciting physics program that can be carried out at a Neutrino Factory. The context of the experimental program is defined in terms of the enhanced knowledge we expect to have at the time such a facility is anticipated to come on line, roughly 2013. Then we describe the Neutrino Factory facility, which comprises the following systems:

- Proton Driver (providing 1 MW of protons on target from an upgraded AGS)
- Target and Capture (a mercury-jet target immersed in a 20-T superconducting solenoidal field to capture pions, product of the proton-nucleus interactions)
- Decay and Phase Rotation (three induction linacs, with internal superconducting solenoidal focusing, to contain the muons from pion decays and provide nearly non-distorting phase rotation; a minicooling absorber section is included after the first induction linac)
- Bunching and Cooling (a solenoidal focusing channel with high-gradient rf cavities and liquid-hydrogen absorbers that bunches the 247 MeV/c muons into 201.25-MHz rf buckets and cools their transverse normalized emittance from 12 mm·rad to 2 mm·rad)
- Acceleration (a superconducting linac with solenoidal focusing to raise the muon beam energy to 2.48 GeV, followed by a four-pass superconducting recirculating linear accelerator to provide a 20 GeV muon beam)
- Storage Ring (a compact racetrack-shaped superconducting storage ring in which 35% of the stored 20 GeV muons decay toward a detector located 2900 km from the ring)

In addition to the Neutrino Factory facility, we describe the features of a possible neutrino detector that could carry out the appropriate physics program.

Performance estimates for the facility show that an intensity of $N = 1.2 \times 10^{20}$ decays per "Snowmass year" per MW of protons on target is feasible—a factor of 6 improvement over the Study-I result, though somewhat less than the original Study-II goal. Upgrade plans that increase the proton driver power from 1 to 4 MW would permit a corresponding increase in the overall intensity per year to $N = 4.8 \times 10^{20}$ decays. R&D to develop a target capable of handling this beam power would be needed. Taking the two Feasibility

Studies together, we conclude that a high-performance Neutrino Factory could easily be sited at either BNL or Fermilab.

Reaching the facility performance estimated here will require an intensive R&D program; an outline of the needed activities is included in this report. To assess the cost range of a Neutrino Factory, a top-down cost estimate has been carried out for the major components. This estimate represents an initial look at what is needed, and should not be construed as the kind of detailed estimate that would result from a Conceptual Design Report. With that caveat, we find that the cost of such a facility is about \$1.9 B in today's dollars. This value represents only direct costs, not including overhead or contingency allowances. Lastly, we describe a phased approach to arriving at the complete facility. At each step, we outline the capabilities of the facility and the corresponding scientific program that can be pursued. We also comment on the time scales and costs that would be implied by this approach. Such an "evolutionary" approach to the facility may represent the most effective way to achieve the ultimate goal of a high-performance Neutrino Factory, even if it stretches out the overall time line.

It is worth noting that the Neutrino Factory facility described here can be viewed as a first critical step on the path toward an eventual Muon Collider. Such a collider offers the potential of bringing the energy frontier in high energy physics within reach of a moderate sized machine. The very fortuitous situation of having an intermediate step along this path that offers a powerful and exciting physics program in its own right presents an ideal opportunity, and it is hoped that the high energy physics community will have the resources and foresight to take advantage of it.

Acknowledgment

We would like to thank the management of the Brookhaven National Laboratory, Dr. John Marburger and Dr. Peter Paul, for their support, interest and foremost for the commissioning of the Study. We would like also to express our gratitude to Dr. A. Sessler, spokesperson for the Neutrino Factory and Muon Collider Collaboration, for his continuous encouragement and technical guidance. Finally, our most sincere thanks to all the contributors, especially those who were not members of the Collaboration. Their technical expertise was crucial for the completion of this report.

Charge to the Study Group

Office of the Director

Upton, NY 11973-5000
Phone 516 344-2772
Fax 516 344-5803
marburge@bnl.gov

Memo

managed by Brookhaven Science Associates for the U.S. Department of Energy

BROOKHAVEN NATIONAL LABORATORY

Building 460
P.O. Box 5000

DATE: June 13, 2000
TO: Robert Palmer, Satoshi Ozaki
CC: Thomas Kirk, Peter Paul, Andrew Sessler
FROM: John Marburger
SUBJECT: Muon device studies

I am writing to request that you organize, in cooperation with the Muon Collider Collaboration, a BNL site-specific study on the feasibility of a 'high performance' muon storage ring neutrino source.

The study would complement the recently completed 'entry level' study commissioned by the Fermilab director and carried out together with the Muon Collider Collaboration.

The scope and parameters for this study have been developed and approved by the Muon Collider Collaboration Spokesperson, Andy Sessler, and Project Manager, Mike Zisman. The Muon Collaboration will participate in the study.

The study will also complement the AGS Targetry Experiment, E951, that will study two crucial components of the high performance version of the muon storage ring.

The study should consist of two components:

A. A BNL site specific part, led by S. Ozaki and including:

1. a technical description of upgrades to the AGS to reach an average beam power of 1 MW (e.g. 10^{14} pps at 24 GeV at 2.5 Hz), together with a preliminary cost estimate for this upgrade;

2. a design, layout and preliminary cost estimate for a muon storage ring with the requirement that it be sufficiently above the water table to minimize environmental impacts;

3. magnet studies for the above ring.

B. A generic part, led by the collaboration management, funded by DOE MCC Collaboration funds, and including:

1. the design and technical description of the non-AGS components of a high performance muon storage ring neutrino source, including liquid metal target, muon capture, cooling, acceleration and storage;

2. determination of cost drivers in these systems where not already covered in the Fermilab study;

3. areas for potential cost reduction;

4. continued physics and detector studies as needed.

The study should consider a facility with the following characteristics:

1. a muon storage ring energy of approximately 20 GeV;

2. a neutrino beam aimed at an optimized 50 kT detector located approximately 1800 km from BNL;

3. $2\ 10^{20}$ muons per (10^7 sec) year decaying in the detector direction; this is approximately one order of magnitude higher than the 'entry level' machine.

The written report on this new study should be submitted to me by April 30, 2001.

Organization of the Study

The organization chart of the Study is shown in the figure

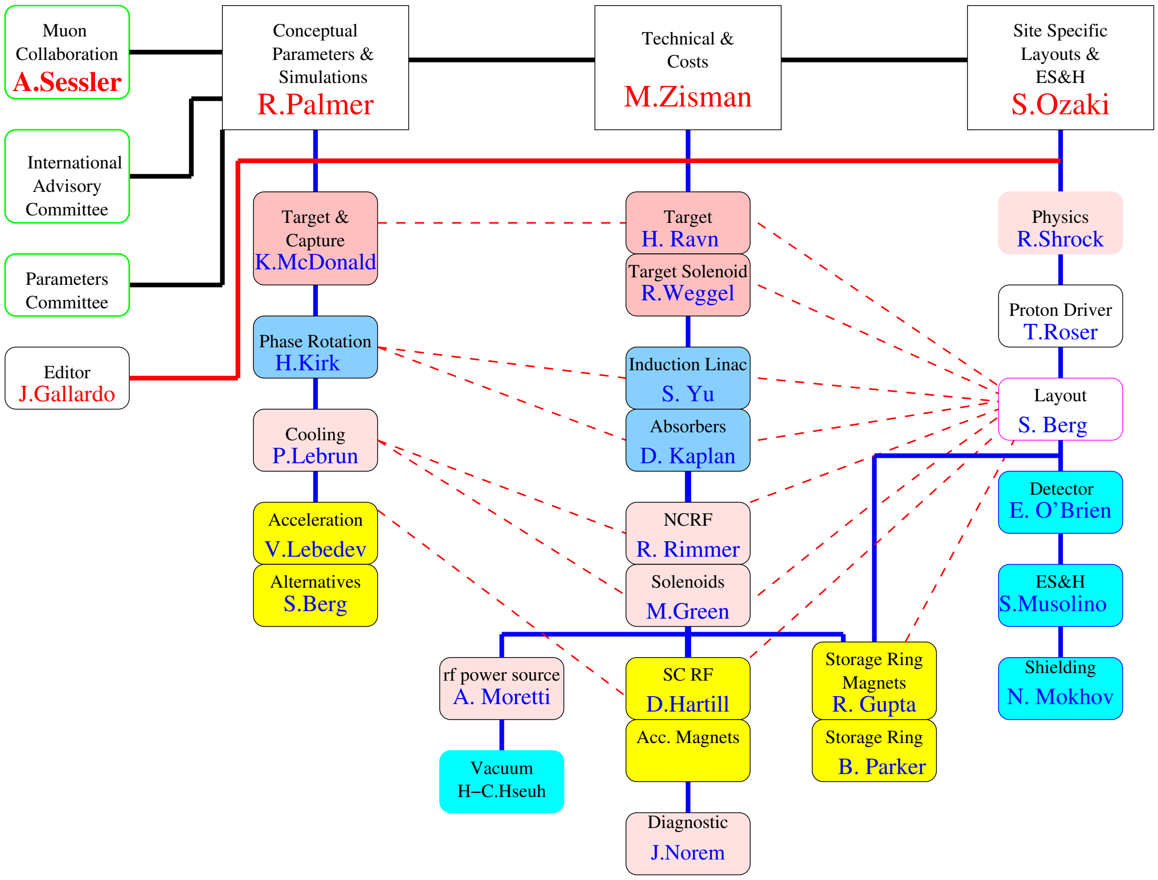

Figure 1: Organization chart for Study-II.

Summary of Parameters and Performance

In this section, we briefly summarize the overall parameters and predicted performance of the Neutrino Factory concept developed for Study-II and described in this document. The majority of the concepts developed here are generic, in the sense that they do not depend upon specifics of the BNL site. A few details, of course, do depend on the particular site chosen for this Study.

The proton driver on which this Study is based is the BNL Alternating Gradient Synchrotron (AGS). This machine delivers 24 GeV protons and presently holds the world's intensity record for proton accelerators. To create a 1 MW proton beam, the properties of the AGS dictate a ramp cycle of 150 ms up, 100 ms flat-top, and 150 ms down, with six proton bunches extracted sequentially at 20-ms intervals during the 100-ms flat-top. This cycle is repeated at 2.5 Hz, leading to an average pulse rate of 15 Hz, that is, 6 bunches per cycle at 2.5 Hz. Note that the instantaneous repetition rate is 50 Hz (20 ms bunch separation) even though the average rate is lower. Individual proton bunches have an rms length of 3 ns.

The other site-specific aspect of the Study-II design concerns the elevation of the facility. Local policy requires that no part of the Neutrino Factory complex that produces radiation lie below the local BNL water table elevation. This is not an issue for most of the facility, but it does constrain the location of the storage ring. Because the ring must be tilted vertically by 13.1° to aim at the Waste Isolation Pilot Plant (WIPP) site in Carlsbad, NM, some 2900 km distant, this vertical location requirement placed a premium on having a compact storage ring, and dictated using an above-ground berm to shield the ring.

The general design approach we follow is an outgrowth of the previous Feasibility Study ("Study-I"). However, we have made many technical changes from the previous design—in some cases simply to explore alternative design options, and in other cases to specifically enhance performance. As in the previous Study, we have chosen not to consider muon beam polarization as a design criterion. This avoids the need to place high-gradient rf cavities in the high-radiation environment very close to the target. The overall layout of the facility is presented in Fig. 2. Lengths of the various systems that comprise the facility are summarized in Table 1.

The specific changes made in Study-II to enhance facility performance include:

- Use of a liquid mercury target
- Use of three induction linac units, separated by suitable drift lengths, to achieve nearly non-distorting phase rotation

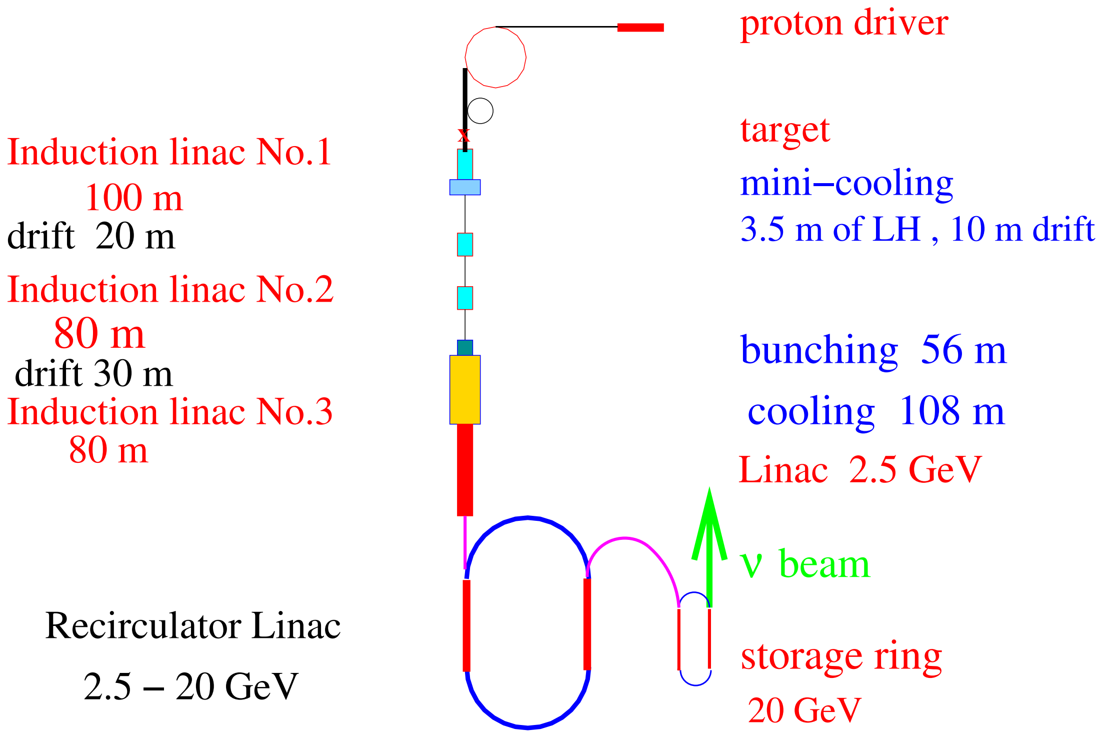

Figure 2: Schematic of the Neutrino Factory facility

Table 1: Length of the main components of a Neutrino Factory.

Component	Length (m)	Total (m)
Target	0.45	0.45
Taper	17.6	17.6
Drift	18	35.6
Induction 1	100	135.6
Drift	3.3	138.9
Mini-Cool	13.5	152.4
Drift	23.2	175.6
Induction 2	80	255.6
Drift	30	285.6
Induction 3	80	365.6
Match to Super FOFO	12	377.6
Buncher	$20 \times 2.75 = 55$	432.6
Cooling part 1	$16 \times 2.75 = 44$	476.6
Match	4.4	481.0
Cooling part 2	$36 \times 1.65 = 59.4$	540.4
Match	22.04	562.4
Linac	433	
RLA arcs min.	2×310	
RLA linacs	2×363.5	
Storage ring arcs	2×53	
Storage ring straights	2×126	

- Use of a graded focusing strength along the cooling channel to keep the beam angular spread nearly constant as the emittance decreases

As will be seen later, taken together these changes improved the overall performance of Study-II by a factor of 6 compared with Study-I.

Other changes in the present Study that differ from Study-I include:

- Use of a hollow-conductor resistive magnet insert at the target, in place of a Bitter magnet insert

- Use of a Super-FOFO ("SFOFO") cooling channel, in place of a FOFO channel

- Use of a large-acceptance superconducting linac for the initial acceleration after the cooling channel, in place of a conventional linac

- Use of a combined-function compact storage ring, in place of a conventional separated-function ring

These changes, as noted above, enhance our knowledge base by giving an expanded understanding of the parameter space available to the designers of a Neutrino Factory.

Key parameters for the overall facility are summarized in Table 2.

Table 2: Muon beam parameters along the length of the facility.

Location (end of)	σ_r (cm)	$\sigma_{r'}$ (mrad)	σ_p (MeV/c)	σ_t (ns)	$\langle p \rangle$ (GeV/c)
IL3	8.6	95	118		0.237
Matching	5.8	114	115		0.247
Buncher	5.7	134	110	0.84	0.247
2.75 m cooling lattice	3.0	87	72	0.55	0.222
1.65 m cooling lattice	2.4	109	32	0.51	0.204
Matching	10	29	27	0.97	0.270
Pre-accelerator			81	0.26	2.583
RLA			134	0.27	20.105
Storage Ring			134	0.27	20.105

Based on simulation results, we expect that the facility described herein will provide 1.2×10^{20} muons decays, per "Snowmass year" ($10^7 s$) and per MW of proton beam incident on the target, aimed at a detector some 3000 km distant from the storage ring. This value corresponds to our baseline case of a 1-MW proton driver.

For the enhanced case of a 4-MW proton driver, discussed in Section B.1, the muon decay rate would increase to 4.8×10^{20} muons decays, per "Snowmass year".

Contents

List of Figures

List of Tables

Chapter 1

Introduction and Overview

1.1 Context of the Present Study

Feasibility Study-II, described here, is a follow-on to Feasibility Study-I [1]. To put our work in context, it is important here to view the effort in a historical perspective, and to give proper credit to our predecessors.

The concept of a Muon Collider was first proposed by Budker [2], and by Skrinsky [3] in the 60s and early 70s. However, there was little substance to the concept until the idea of ionization cooling was developed by Skrinsky and Parkhomchuk [4]. The ionization cooling approach was expanded by Neuffer [5] and then by Palmer [6], whose work led to the formation of the Neutrino Factory and Muon Collider Collaboration (MC) [7] in 1995. A good summary of the Muon Collider concept can be found in the Status Report of 1999 [8]; an earlier document [9], prepared for Snowmass-1996, is also useful reading.

The concept of a Neutrino Factory based on a muon storage ring was suggested by Koshkarev [10], but there was likewise little to the concept until it was combined with the advanced thinking precipitated by the effort toward a Muon Collider. This gap was finally bridged by Geer in 1998 [11].

As a result of this work, the MC realized that a Neutrino Factory could be an important first step toward a Muon Collider. Furthermore, the physics that could be addressed by a Neutrino Factory was interesting in its own right. With this in mind, the MC has recently shifted its primary emphasis toward the issues of relevance to a Neutrino Factory. MUCOOL Notes prepared by the MC are available on the web [12]; these can be used to learn about the technical issues involved. Complementing the Feasibility Studies, the MC carries on an experimental and theoretical R&D program, including work on targetry, cooling, rf hardware (both normal conducting and superconducting), high-field solenoids, LH_2 absorber design, theory, simulations, parameter studies, and emittance exchange [13]. There is also considerable international activity on Neutrino Factories, with international conferences held at Lyon in 1999, Monterey in 2000, Tsukuba in 2001, and another planned for London in 2002 [14], [15].

In the fall of 1999, Fermilab—with significant contributions from the MC—undertook a Feasibility Study ("Study-I") of an entry-level Neutrino Factory [1]. Simultaneously, Fermilab launched a study of the physics that might be addressed by such a facility [16]. More recently, Fermilab initiated a study to compare the physics reach of a Neutrino Factory with that of conventional neutrino beams [17]; this activity is still in progress. The approach is to examine the physics that can be addressed with a conventional beam, but using an intense proton driver of the type envisioned for the Neutrino Factory, with that physics addressable *only* with a Neutrino Factory. Suffice it to say, there are good physics opportunities in both categories.

It is with this background that the BNL Director, John Marburger, decided in June 2000 to have a follow-on Study on a high-performance Neutrino Factory sited at BNL. Study-II was to be completed by April 2001. Clearly, an important goal of Study-II was to evaluate whether BNL was a suitable site for a Neutrino Factory. Based on the work contained in this report, that question can now be answered affirmatively.

1.2 Expected Performance and Parameters of Major Components

This second Feasibility Study, ("Study II"), commissioned by BNL Director John Marburger, uses BNL site-specific proton driver specifications and a BNL-specific layout of the storage ring, in particular, the pointing angle of the straight sections. It is a follow-up to the FNAL specific ("Study I") study commissioned by the Fermilab Director, that was completed in April 2000 [1] and is site specific in the same spirit, that is, in each study there are a few site-dependent parts; otherwise, the studies are generic. The primary difference is that this study is aimed at a lower muon energy (20 GeV), but higher intensity (for physics reach). Figure 1.1 has been adapted from a figure in the physics study [16]. Both studies were carried out jointly with the Neutrino Factory and Muon Collider Collaboration [18] which has over 140 members from many institutions in the U.S. and abroad.

The design and simulated performance are summarized here; specific details can be found in the chapters that follow.

The efficiency of producing muons at the end of the cooling channel is $\approx 0.17\ \mu/\mathrm{p}$

with 24 GeV protons. This higher efficiency translates, per MW of proton beam power, into about 6× that found in Feasibility Study I [1].

The higher efficiency is achieved by:

1. using a liquid mercury target

2. using three induction linacs to achieve nearly non-distorting phase rotation into a longer bunch train with less momentum spread

3. tapering the focusing strength in the cooling system so that the angular spread of the muons being cooled is maintained at a near-constant value

4. increasing the transverse acceptance of the muon acceleration and storage ring.

The components of the system are shown schematically in Fig. 2 (in the Preface).

1.2.1 Components

1.2.1.1 Proton Driver

The proton driver is an upgrade of the Brookhaven Alternating Gradient Synchrotron (AGS) and uses most of the existing components and facilities. The existing booster is replaced by a 1.2 GeV superconducting proton linac. The AGS repetition rate is increased from 0.5 Hz to 2.5 Hz. The total proton charge (10^{14} ppp) is only 40% higher than the current performance of the AGS. The six bunches are extracted separately, spaced by 20 ms, so that the target, induction linacs and rf systems that follow, need only be designed to deal with single bunches at an average repetition rate of 15 Hz, instantaneous rate of 50 Hz. The average power would be 1 MW. A possible future upgrade to 2×10^{14} ppp and 5 Hz could give an average beam power of 4 MW (see, Section B.1). In that scenario, a 1/4 circumference, fixed-field, superconducting bunch compressor ring would be added to reduce the rms bunch length, at the higher intensity, to 3 ns.

1.2.1.2 Target & Capture

A high Z, (mercury) jet target is chosen to give a high yield of pions per incident proton power ($\approx$ 1.9 × that for carbon, which was the choice in Study I).

The jet is continuous, is 1 cm diameter, and enters the target enclosure at a vertical angle of 100 mrad with respect to the magnetic axis. The proton beam intersects the jet at an angle of 33 mrad (*i.e.*, its trajectory is 67 mrad to the magnetic axis). The

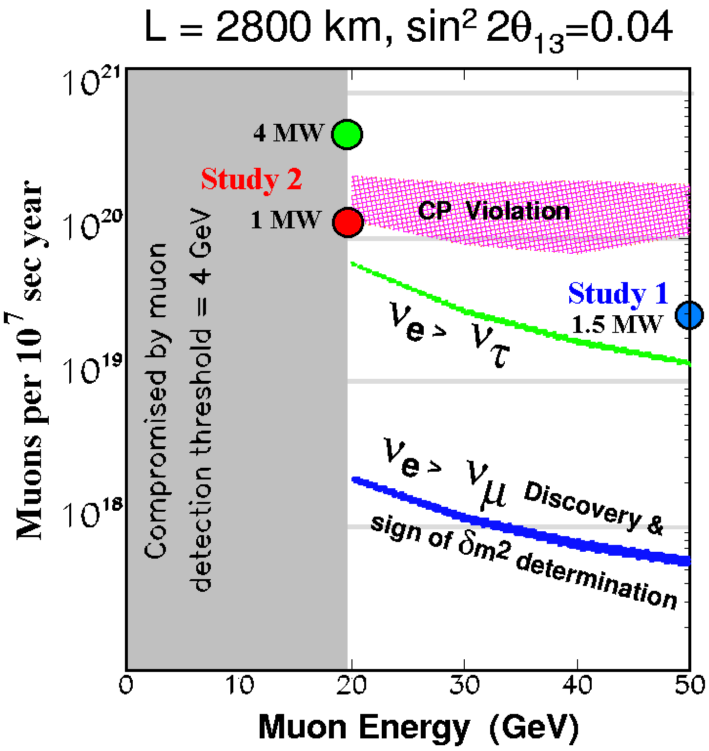

Figure 1.1: Muon decays in a straight section per 10^7 s *vs.* muon energy, with fluxes required for different physics searches assuming a 50 kT detector. Simulated performance of the two studies is indicated.

geometry is shown in Fig. 1.2. It is assumed that the thermal shock from the interacting proton bunch fully disperses the mercury. In this case, the jet must have a velocity of 30 m/s to be replaced before the next bunch. Perturbations to the jet by the capture magnetic field are controlled by placing the jet nozzle inside the field, so that the jet only sees 1 T field changes before it has passed beyond the production region.

Pions emerging from the target are captured and focused down the decay channel by a solenoidal field that is 20 T at the target center, and tapers down, over 18 m, to a periodic (50 cm) superconducting solenoid channel ($< B_z > \approx 1.25$ T) that continues through the phase rotation to the start of bunching.

Figure 1.3 shows a section of the 20 T hybrid magnet, the front end of the taper, the mercury containment, and the mercury pool proton beam dump. The 20 T solenoid,

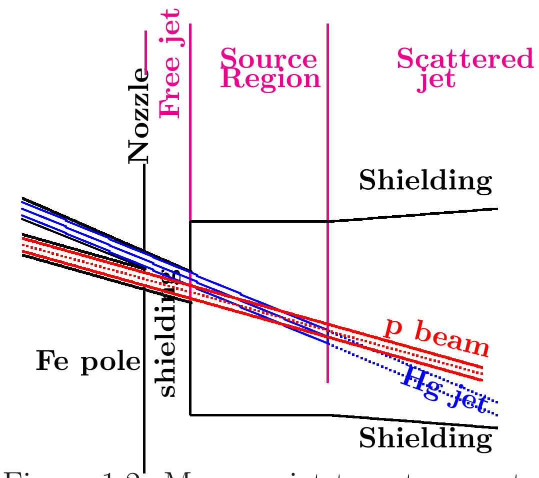

Figure 1.2: Mercury jet target geometry.

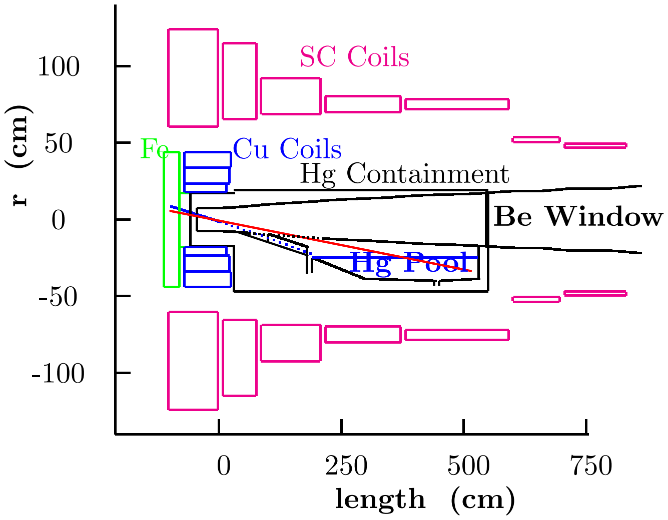

Figure 1.3: Mercury enclosure, mercury-pool beam dump, and solenoid capture magnets.

with a hollow copper conductor magnet insert and superconducting outer coil, is not different in character from the higher field (up to 45 T), but smaller bore, magnets at several existing laboratories. However, the magnet insert in this design is made with hollow copper conductor and ceramic insulation to withstand radiation. MARS [19] simulations of radiation levels show that, with the shielding provided, both copper and superconducting magnets could have a lifetime greater than 20 years, even at 4 MW.

1.2.1.3 Phase Rotation

Pions, and the muons into which they decay, are generated in the target over a very wide range of energies, but in a short time pulse (3 ns rms). This large energy is phase rotated using drifts and induction linacs into a pulse with a longer time duration and a lower energy spread. The muons first drift to spread out their time, the induction linacs then decelerate the early ones and accelerate those later. Three induction linacs (with lengths 100, 80, and 80 m) are used in a system that reduces distortion in the phase-rotated bunch, and allows all induction units to operate with unipolar pulses [20]. The 1.25-T beam transport solenoids are placed inside the induction cores to avoid saturating the core material. The induction units are similar to those being built for DARHT[22].

Between the first and second induction linacs, two hydrogen absorbers (each 1.7 m long and 30 cm radius), with a magnetic field reversal between them, are introduced to reduce the transverse emittance ("minicooling").

1.2.1.4 Buncher

The long bunch (400 ns) after the phase rotation is bunched at 201.25 MHz prior to cooling and acceleration at that frequency. The bunching is done in a lattice identical to that at the start of cooling, and is preceded by a matching section from the 1.25 T solenoids into this lattice. The bunching has three stages, each consisting of rf (with increasing acceleration) followed by drifts with decreasing length (27.5 m, 11 m, 5.5 m). In the first two rf sections, second harmonic rf is used together with the 201.25 MHz to improve the capture efficiency.

1.2.1.5 Cooling

Transverse emittance cooling is achieved by lowering the beam energy in hydrogen absorbers, interspersed with rf acceleration to keep the average energy constant. Transverse and longitudinal momenta are lowered in the absorbers, but only the longitudinal momentum is restored by the rf. The emittance increase from Coulomb scattering is minimized

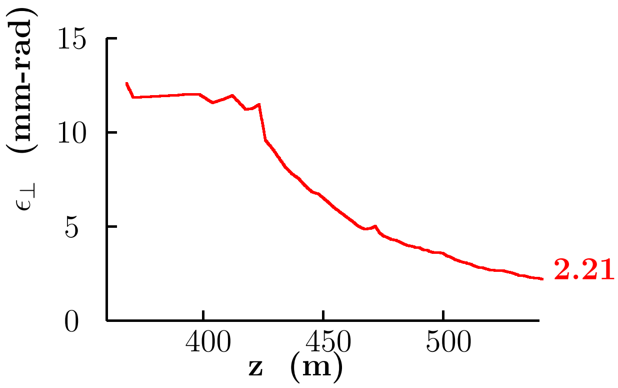

Figure 1.4: Transverse emittance along the cooling channel.

by maintaining the focusing strength so that the angular spread of the beam at the absorber locations is large. This is achieved by keeping the focusing strength inversely proportional to the emittance; *i.e.*, increasing as the emittance is cooled. This could be achieved by a simple solenoid, but such a field also must be reversed periodically to avoid a growth of angular momentum. For this study, a modified Focus-Focus (SFOFO) [21] lattice is employed. The solenoidal fields in each cell alternate in sign and the field shape is chosen to maximize the momentum acceptance ($\pm 22\%$).

Figure 1.4 shows a simulation of cooling, the emittance falls along the length of the channel.

1.2.1.6 Acceleration

A 20 m SFOFO matching section, using normal conducting rf systems, matches the beam optics to the requirements of a 2.5 GeV superconducting rf linac with solenoidal focusing. The linac is in three parts. The first part has a single 2 cavity unit per cell. The second, as a longer period becomes possible, has two 2 cavity units per cell. The last section, with still longer period, accommodates four 2 cavity units per cell.

This linac is followed by a single, recirculating linear accelerator (RLA) that raises the energy from 2.5 GeV to 20 GeV, in 4 passes. This RLA uses the same 4 cavity superconducting structures. The arcs have an average radius of 62 m. The final arc has a dipole field of 2 T.

1.2.1.7 Storage Ring

After acceleration in the RLA, the muons are injected into the upward straight of a racetrack shaped storage ring with a circumference of $\approx$ 358m. High field superconducting arc magnets are used to minimize the arc length and maximize the fraction (35%) of muons that decay in the downward straight and generate neutrinos headed towards the detector at the WIPP facility in Carlsbad, 2903 km away. All muons are allowed to decay; the total heating from the decay electrons is 42 kW (126 W/m). This load is too high to be dissipated in the superconducting coils. A magnet design has been chosen [23] that allows the majority of these electrons to pass out between separate upper and lower cryostats, and be dissipated in a dump at room temperature. To maintain the vertical cryostat separation in focusing elements, skew quadrupoles are employed in place of standard quadrupoles.

In order to maximize the average bending field, Nb_3Sn pancake coils are employed. One coil of the bending magnet is extended and used as one half of the previous or following skew quadrupole, (see Chapter 7).

Figure 1.5 shows a cross section of the ring, which is kept above the water table and is placed on a roughly 30 m high berm. The 110 m high BNL stack is also shown for scale.

1.2.2 Performance

Complete simulations up to the start of acceleration have been performed using the code MARS [19] (for pion production) followed by ICOOL [24] (for transport, phase rotation and cooling). These results have been confirmed by GEANT4 [25]. They show an average of 0.17 final muons per initial proton on the target, *i.e.*, 0.0071μ/p/GeV, (considering the energy of the initial beam). This can be compared with a value of 0.0011μ/p/GeV produced in Study I [1]. The gain ($6\times$) comes from:

- use of mercury, instead of carbon as a target (1.9 $\times$)
- use of three, instead of only one, phase rotation induction linacs (2 $\times$)
- use of a more efficient, tapered cooling channel design (1.4 $\times$)
- use of a larger accelerator acceptance (1.2 $\times$)

The muons delivered to the ring with a 1 MW (4 MW) proton driver would be:

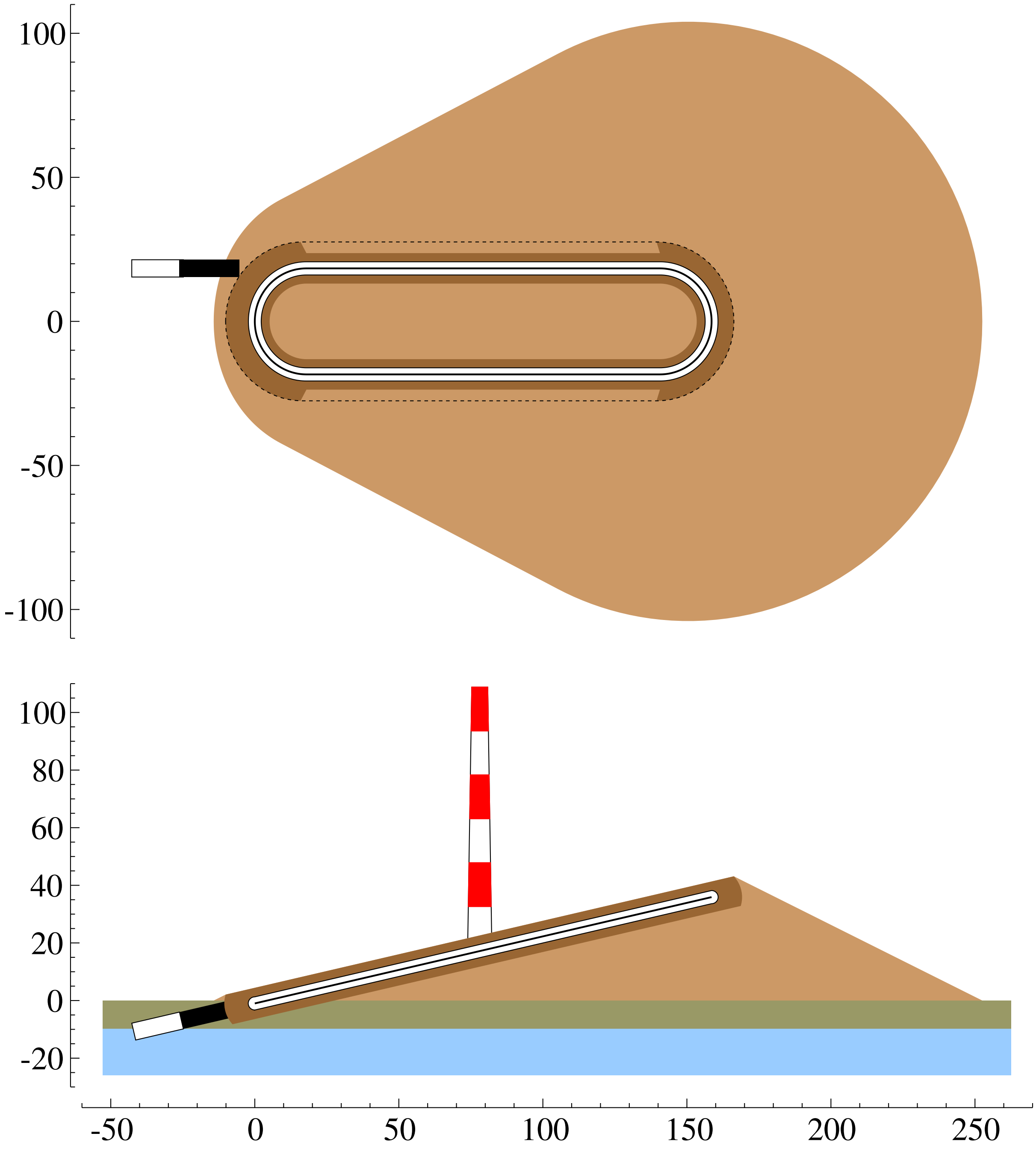

Figure 1.5: Top view and cross section through ring and berm. The 110 m tall tower, drawn to scale, gives a sense of the height of the ring on the BNL landscape.

$$\begin{aligned}\mu/\text{year} \; &= 10^{14}(\text{ppp}) \times 2.5 \text{ (Hz)} \times 10^{7} \text{ (s)} \times 0.17 \ (\mu/p) \times 0.81 \text{ (acc. efficiency)} \\ &= 3.4 \times 10^{20} \ (= 13.6 \times 10^{20}) \end{aligned} \quad (1.1)$$

and the number of muons decaying in the production straight section would be

$$1.2 \times 10^{20} \quad (= \ 4.8 \times 10^{20})$$

.

1.2.3 Conclusions

This Study II shows significant improvements (6×) over Study-I, yet there remains the possibility of further gains. Cooling of the longitudinal emittance [26] and the capture of both signs [27] appear possible and, together might improve overall performance by a factor between 2 and 4.

1.3 Physics Motivation

Here we discuss the current evidence for neutrino oscillations, and hence neutrino masses and lepton mixing, from solar and atmospheric data. A review is given of some theoretical background including models for neutrino masses and relevant formulas for neutrino oscillation transitions. We next mention the near-term and mid-term experiments in this area and comment on what they hope to measure. We then discuss the physics potential of a muon storage ring as a Neutrino Factory in the long term.

1.3.1 Evidence for Neutrino Oscillations

In a modern theoretical context, one generally expects nonzero neutrino masses and associated lepton mixing. Experimentally, there has been accumulating evidence for such masses and mixing. All solar neutrino experiments (Homestake, Kamiokande, SuperKamiokande (SuperK), SAGE, and GALLEX) show a significant deficit in the neutrino fluxes coming from the Sun [28]. This deficit can be explained by oscillations of the ν_e's into other weak eigenstate(s), with Δm^2_{sol} of the order 10^{-5} eV^2 for solutions involving the Mikheev-Smirnov-Wolfenstein (MSW) resonant matter oscillations [31, 32] or of the order of 10^{-10} eV^2 for vacuum oscillations. Accounting for the data with vacuum oscillations (VO) requires almost maximal mixing. The MSW solutions include one for small mixing angle (SMA) and one with large mixing angle (LMA).

Another piece of evidence for neutrino oscillations is the atmospheric neutrino anomaly, observed by Kamiokande [33], IMB [34], SuperKamiokande [35] with the highest statistics, and also by Soudan [36] and MACRO [37]. These data can be fit by the inference of $\nu_\mu \to \nu_x$ oscillations with $\Delta m^2_{atm} \sim 3.5 \times 10^{-3}$ eV^2 [35] and maximal mixing, *i.e.*, $\sin^2 2\theta_{atm} = 1$. The identification $\nu_x = \nu_\tau$ is preferred over $\nu_x = \nu_{sterile}$, and the identification $\nu_x = \nu_e$ is excluded by both the SuperKamiokande data and the Chooz experiment [39].

In addition to the above results, the LSND experiment [40] has reported observing $\bar{\nu}_\mu \to \bar{\nu}_e$ and $\nu_\mu \to \nu_e$ oscillations with $\Delta m^2_{LSND} \sim 0.1 - 1$ eV^2 and a range of possible mixing angles, depending on Δm^2_{LSND}. This result is not confirmed, but also not completely ruled out, by a similar experiment, KARMEN [41]. The miniBOONE experiment at Fermilab is designed to resolve this issue, as discussed below.

With only three neutrino species, it is not possible to fit all of these experiments. They involve three quite different values of $\Delta m^2_{ij} = m(\nu_i)^2 - m(\nu_j)^2$ which could not satisfy the identity for only three neutrino species that

$$\Delta m^2_{32} + \Delta m^2_{21} + \Delta m^2_{13} = 0. \tag{1.2}$$

It would follow then, that one would have to introduce further neutrino(s). As we know that there are only three leptonic weak doublets, and associated light neutrinos, with weak isospin $T = 1/2$ and $T_3 = 1/2$ from the measurement of the Z width, it follows that additional neutrino weak eigenstates would have to be electroweak singlets (that is, "sterile" neutrinos). Because the LSND experiment has not been confirmed by the KARMEN experiment, we choose here to use only the (confirmed) solar and atmospheric neutrino data in our analysis, and hence to work in the context of three active neutrino weak eigenstates.

1.3.2 Neutrino Oscillation Formalism

In this simplest theoretical context, there are three electroweak-doublet neutrinos. Although electroweak-singlet neutrinos may be present in the theory, one expects that, since their bare mass terms are electroweak-singlet operators, the associated masses should not have any close relation with the electroweak symmetry breaking scale. Indeed, from a top-down point of view, such as a grand unified theory, the masses should be much larger than this scale. If this is the case, then the neutrino mixing can be described by the matrix

$$U = \begin{pmatrix} c_{12}c_{13} & c_{13}s_{12} & s_{13}e^{-i\delta} \\ -c_{23}s_{12} - s_{13}s_{23}c_{12}e^{i\delta} & c_{12}c_{23} - s_{12}s_{13}s_{23}e^{i\delta} & c_{13}s_{23} \\ s_{12}s_{23} - s_{13}c_{12}c_{23}e^{i\delta} & -s_{23}c_{12} - s_{12}c_{23}s_{13}e^{i\delta} & c_{13}c_{23} \end{pmatrix} K' \tag{1.3}$$

where $c_{ij} = \cos\theta_{ij}$, $s_{ij} = \sin\theta_{ij}$, K' is a diagonal matrix with elements $diag(1, e^{i\phi_1}, e^{i\phi_2})$. The phases ϕ_1 and ϕ_2 do not affect neutrino oscillation. Thus, in this framework, the neutrino mixing depends on the four angles θ_{12}, θ_{13}, θ_{23}, and δ, and on two independent differences of squared masses, Δm^2_{atm}, which is $\Delta m^2_{32} = m(\nu_3)^2 - m(\nu_2)^2$ in the favored fit, and Δm^2_{sol}, which may be taken to be $\Delta m^2_{21} = m(\nu_2)^2 - m(\nu_1)^2$. Note that these quantities involve both magnitude and sign; although in a two-species neutrino oscillation in vacuum the sign does not enter, in the three species oscillations relevant here, and including both matter effects and CP violation, the signs of the Δm^2 quantities do enter and can, in principle, be measured.

For our later discussion it will be useful to record the formulas for the various relevant neutrino oscillation transitions. In the absence of any matter effect, the probability that a (relativistic) weak neutrino eigenstate ν_a becomes ν_b after propagating a distance L is

$$\begin{aligned} P(\nu_a \to \nu_b) &= \delta_{ab} - 4 \sum_{i>j=1}^{3} Re(K_{ab,ij}) \sin^2\Big(\frac{\Delta m^2_{ij} L}{4E}\Big) \\ &+ 4 \sum_{i>j=1}^{3} Im(K_{ab,ij}) \sin\Big(\frac{\Delta m^2_{ij} L}{4E}\Big) \cos\Big(\frac{\Delta m^2_{ij} L}{4E}\Big) \end{aligned} \tag{1.4}$$

where

$$K_{ab,ij} = U_{ai} U^*_{bi} U^*_{aj} U_{bj} \tag{1.5}$$

Note that, in vacuum, CPT invariance implies $P(\bar\nu_b \to \bar\nu_a) = P(\nu_a \to \nu_b)$ and hence, for $b = a$, $P(\bar\nu_a \to \bar\nu_a) = P(\nu_a \to \nu_a)$. For the CP-transformed reaction $\bar\nu_a \to \bar\nu_b$ and the T-reversed reaction $\nu_b \to \nu_a$, the transition probabilities are given by the right-hand side of (1.4) with the sign of the imaginary term reversed. (Below, we shall assume CPT invariance, so that CP violation is equivalent to T violation.)

In most cases there is only one mass scale relevant for long baseline neutrino oscillations, $\Delta m^2_{atm} \sim$ few $\times 10^{-3}$ eV^2 and one possible neutrino mass spectrum is the hierarchical one

$$\Delta m^2_{21} = \Delta m^2_{sol} \ll \Delta m^2_{31} \approx \Delta m^2_{32} = \Delta m^2_{atm} \tag{1.6}$$

In this case, CP (T) violation effects are negligibly small, so that in vacuum

$$P(\bar\nu_a \to \bar\nu_b) = P(\nu_a \to \nu_b) \tag{1.7}$$

$$P(\nu_b \to \nu_a) = P(\nu_a \to \nu_b) \tag{1.8}$$

In the absence of T violation, the second equality Eq. (1.8) would still hold in matter, but even in the absence of CP violation, the first equality Eq. (1.7) would not hold. With the hierarchy (1.6), the expressions for the specific oscillation transitions are

$$\begin{aligned} P(\nu_\mu \to \nu_\tau) &= 4|U_{33}|^2|U_{23}|^2 \sin^2\Big(\frac{\Delta m^2_{atm} L}{4E}\Big) \\ &= \sin^2(2\theta_{23})\cos^4(\theta_{13})\sin^2\Big(\frac{\Delta m^2_{atm} L}{4E}\Big) \end{aligned} \tag{1.9}$$

$$\begin{aligned} P(\nu_e \to \nu_\mu) &= 4|U_{13}|^2|U_{23}|^2 \sin^2\Big(\frac{\Delta m^2_{atm} L}{4E}\Big) \\ &= \sin^2(2\theta_{13})\sin^2(\theta_{23})\sin^2\Big(\frac{\Delta m^2_{atm} L}{4E}\Big) \end{aligned} \tag{1.10}$$

$$\begin{aligned} P(\nu_e \to \nu_\tau) &= 4|U_{33}|^2|U_{13}|^2 \sin^2\Big(\frac{\Delta m^2_{atm} L}{4E}\Big) \\ &= \sin^2(2\theta_{13})\cos^2(\theta_{23})\sin^2\Big(\frac{\Delta m^2_{atm} L}{4E}\Big) \end{aligned} \tag{1.11}$$

In neutrino oscillation searches using reactor antineutrinos, *i.e.*, tests of $\bar{\nu}_e \to \bar{\nu}_e$, the two-species mixing hypothesis used to fit the data is

$$\begin{aligned} P(\nu_e \to \nu_e) &= 1 - \sum_x P(\nu_e \to \nu_x) \\ &= 1 - \sin^2(2\theta_{reactor})\sin^2\Big(\frac{\Delta m^2_{reactor} L}{4E}\Big) \end{aligned} \tag{1.12}$$

where $\Delta m^2_{reactor}$ is the squared mass difference relevant for $\bar{\nu}_e \to \bar{\nu}_x$. In particular, in the upper range of values of Δm^2_{atm}, since the transitions $\bar{\nu}_e \to \bar{\nu}_\mu$ and $\bar{\nu}_e \to \bar{\nu}_\tau$ contribute to $\bar{\nu}_e$ disappearance, one has

$$P(\nu_e \to \nu_e) = 1 - \sin^2(2\theta_{13})\sin^2\Big(\frac{\Delta m^2_{atm} L}{4E}\Big) \tag{1.13}$$

i.e., $\theta_{reactor} = \theta_{13}$, and for the value $|\Delta m^2_{atm}| = 3 \times 10^{-3}\mathrm{eV}^2$ from SuperK, the Chooz reactor experiment yields the bound [39]

$$\sin^2(2\theta_{13}) < 0.1 \tag{1.14}$$

which is also consistent with conclusions from the SuperK data analysis [35].

Further, in the three-generation case, the quantity "$\sin^2(2\theta_{atm})$" often used to fit the data on atmospheric neutrinos with a simplified two-species mixing hypothesis, is,

$$\sin^2(2\theta_{atm}) \equiv \sin^2(2\theta_{23})\cos^4(\theta_{13}) \tag{1.15}$$

The SuperK experiment finds that the best fit to their data is to infer $\nu_\mu \to \nu_\tau$ oscillations with maximal mixing, and hence $\sin^2(2\theta_{23}) = 1$ and $|\theta_{13}| << 1$. The various solutions of the solar neutrino problem involve quite different values of Δm^2_{21} and $\sin^2(2\theta_{21})$: (i) large mixing angle solution, LMA: $\Delta m^2_{21} \simeq$ few $\times\ 10^{-5}$ eV^2 and $\sin^2(2\theta_{21}) \simeq 0.8$; (ii) small mixing angle solution, SMA: $\Delta m^2_{21} \sim 10^{-5}$ and $\sin^2(2\theta_{21}) \sim 10^{-2}$, (iii) LOW: $\Delta m^2_{21} \sim 10^{-7}$, $\sin^2(2\theta_{21}) \sim 1$, and (iv) "just-so": $\Delta m^2_{21} \sim 10^{-10}$, $\sin^2(2\theta_{21}) \sim 1$. The SuperK experiment favors the LMA solution [28]; for other global fits, see, *e.g.*, Gonzalez-Garcia *et al.* in [28].

1.3.3 Types of Neutrino Masses, Seesaw Mechanism

We review here the theoretical background concerning neutrino masses and mixing. In the standard SU(3) $\times$ SU(2)$_L\times$ U(1)$_Y$ model (SM), neutrinos occur in SU(2)$_L$ doublets with $Y = -1$:

$$\mathcal{L}_{L\ell} = \begin{pmatrix} \nu_\ell \\ \ell \end{pmatrix}, \quad \ell = e,\ \mu,\ \tau \tag{1.16}$$

There are no electroweak-singlet neutrinos (often called right-handed neutrinos) $\chi_{R,j}$, $j = 1, ..., n_s$. Equivalently, these could be written as $\overline{\chi^c}_{L,j}$. There are three types of possible Lorentz-invariant bilinear operator products that can be formed from two Weyl fermions ψ_L and χ_R:

- Dirac: $m_D\bar{\psi}_L\chi_R + h.c.$ This connects opposite-chirality fields and conserves fermion number.
- Left-handed Majorana: $m_L\psi_L^T C\psi_L + h.c.$ where $C = i\gamma_2\gamma_0$ is the charge conjugation matrix.
- Right-handed Majorana: $m_R\chi_R^T C\chi_R + h.c.$

The Majorana mass terms connect fermion fields of the same chirality and violate fermion number (by two units). Using the anticommutativity of fermion fields and the property $C^T = -C$, it follows that a Majorana mass matrix appearing as

$$\psi_i^T C(M_{maj})_{ij}\psi_j \tag{1.17}$$

is symmetric in flavor indices:

$$M_{maj}^T = M_{maj} \tag{1.18}$$

Thus, in the Standard Model (SM), there is no Dirac neutrino mass term because: i) it is forbidden as a bare mass term by the gauge invariance; ii) it cannot occur, as do the quark and charged-lepton mass terms, via spontaneous symmetry breaking (SSB) of the electroweak (EW) symmetry starting from a Yukawa term, as there are no EW-singlet neutrinos $\chi_{R,j}$. There is also no left-handed Majorana mass term because: i) it is forbidden as a bare mass term and ii) it would require a Higgs field with $T = 1$, $Y = 2$, but the SM has no such Higgs field. Finally, there is no right-handed Majorana mass term because there is no $\chi_{R,j}$. The same holds for the minimal supersymmetric standard model (MSSM) and the minimal SU(5) grand unified theory (GUT), both for the original and supersymmetric versions.

However, it is easy to add EW-singlet neutrinos χ_R to the SM, MSSM, or SU(5) GUT; these are gauge-singlets under the SM gauge group and SU(5), respectively. Denote these theories as the extended SM, etc. The extended theories give rise to both Dirac and Majorana mass terms, the former via Yukawa terms and the latter as bare mass terms. In the extended SM:

$$-\mathcal{L}_{Yuk} = \sum_{i=1}^{3}\sum_{j=1}^{n_s} h_{ij}^{(D)} \bar{\mathcal{L}}_{L,i}\chi_{R,j}\phi + h.c. \tag{1.19}$$

The electroweak symmetry breaking (EWSB), with

$$\langle\phi\rangle_0 = \begin{pmatrix} 0 \\ v/\sqrt{2} \end{pmatrix} \tag{1.20}$$

where $v = 2^{-1/4}G_F^{-1/2} \simeq 250$ GeV, yields the Dirac mass term

$$\sum_{i=1}^{3}\sum_{j=1}^{n_s} \bar{\nu}_{L,i}(M_D)_{ij}\chi_{Rj} + h.c. \tag{1.21}$$

with

$$(M_D)_{ij} = h_{ij}^{(D)}\frac{v}{\sqrt{2}} \tag{1.22}$$

The Majorana bare mass terms are

$$\sum_{i,j=1}^{n_s} \chi_{Ri}^T C (M_R)_{ij}\chi_{Rj} + h.c. \tag{1.23}$$

For compact notation, define the flavor vectors $\nu = (\nu_e, \nu_\mu, \nu_\tau)$ and $\chi = (\chi_1, .., \chi_{n_s})$ and observe that one can equivalently write ν_L or ν_R^c and χ_R or χ_L^c, where $\psi^c = C\overline{\psi}^T$, $\overline{\psi} = \psi^\dagger\gamma^0$. The full set of Dirac and Majorana mass terms can then be written in the compact matrix form

$$-\mathcal{L}_m = \frac{1}{2}(\bar{\nu}_L\ \overline{\chi^c}_L)\begin{pmatrix} M_L & M_D \\ (M_D)^T & M_R \end{pmatrix}\begin{pmatrix} \nu_R^c \\ \chi_R \end{pmatrix} + h.c. \tag{1.24}$$

where M_L is the 3×3 left-handed Majorana mass matrix, M_R is an $n_s \times n_s$ right-handed Majorana mass matrix, and M_D is the 3-row by n_s-column Dirac mass matrix. In general, all of these are complex, and $(M_L)^T = M_L$,$(M_R)^T = M_R$. Because the extension of the SM to include χ_R does not include a Higgs field with $T = 1$, $Y = 2$, allowing a renormalizable, dimension-4 Yukawa term that would yield a left-handed Majorana mass, one may take $M_L = 0$ at this level (but see below for dimension-5 contributions). The diagonalization of this mass matrix yields the neutrino masses and the corresponding transformation relating the neutrino weak eigenstates to the mass eigenstates.

The same comments apply to the extended MSSM and SU(5) GUT. In the extended SU(5) GUT, the Dirac neutrino mass term arises most simply from the Yukawa couplings of the 5_R with a 5-dimensional Higgs representation H^α (in terms of component fields):

$$\bar{\psi}_{R\alpha} M_D \chi_L^c H^\alpha + h.c. \tag{1.25}$$

and the bare Majorana mass term $\chi_R^T M_R \chi_R + h.c.$.

In the extended SM, MSSM, or SU(5) GUT, one could consider the addition of the χ_R fields as *ad hoc*. However, a more complete grand unification is achieved with the (SUSY) SO(10) GUT, since all of the fermions of a given generation fit into a single representation of SO(10), namely, the 16-dimensional spinor representation ψ_L. In this theory the states χ_R are not *ad hoc* additions, but are guaranteed to exist. In terms of SU(5) representations (recall, SO(10) $\supset$ SU(5) $\times$ U(1))

$$16_L = 10_L + \bar{5}_L + 1_L \tag{1.26}$$

so for each generation, in addition to the usual 15 Weyl fermions comprising the 10_L and 5_R, (equivalently $\bar{5}_L$) of SU(5), there is also an SU(5)-singlet, χ_L^c (equivalently, χ_R). So in SO(10) GUT, electroweak-singlet neutrinos are guaranteed to occur, with number equal to the number of SM generations, inferred to be $n_s = 3$. Furthermore, the generic scale for the coefficients in M_R is expected to be the GUT scale, $M_{GUT} \sim 10^{16}$ GeV.

There is an important mechanism, which originally arose in the context of GUT's, but is more general, that naturally predicts light neutrinos. This is the seesaw mechanism [42].

The basic point is that because the Majorana mass term $\chi_R^T C M_R \chi_R$ is an electroweak singlet, the associated Majorana mass matrix M_R should not be related to the electroweak mass scale v, and from a top-down point of view, it should be much larger than this scale. Denote this generically as m_R. This has the very important consequence that when we diagonalize the joint Dirac-Majorana mass matrix above, the eigenvalues (masses) will be comprised of two different sets: n_s heavy masses, of order m_R, and 3 light masses. We illustrate this in the simplest case of a single generation and $n_s = 1$. Then the mass matrix is simply

$$-\mathcal{L}_m = \frac{1}{2}(\bar{\nu}_L \ \bar{\chi^c}_L) \begin{pmatrix} 0 & m_D \\ m_D & m_R \end{pmatrix} \begin{pmatrix} \nu_R^c \\ \chi_R \end{pmatrix} + h.c. \tag{1.27}$$

The diagonalization yields the eigenvalues

$$\lambda = \frac{1}{2}\left[m_R \pm \sqrt{m_R^2 + 4m_D^2} \right] \tag{1.28}$$

Since $m_D \sim h^{(D)} v$ while m_R is naturally $>> v$ and hence $m_R >> m_D$, we can expand to get

$$\lambda_> \simeq m_R \tag{1.29}$$

and

$$\lambda_< \simeq -\frac{m_D^2}{m_R}\left[1 + O\Big(\frac{m_D^2}{m_R^2}\Big) \right]. \tag{1.30}$$

(The minus sign is not physically important.) The largeness of m_R then naturally explains the smallness of the masses of the known neutrinos. This appealing mechanism also applies in the physical case of three generations and for $n_s \geq 2$.

However, at a phenomenological level, without further theoretical assumptions, there is a large range of values for the light m_ν, since i) the actual scale of m_R is theory-dependent, and ii) it is, *a priori*, not clear what to take for m_D since the known (Dirac) masses range over 5 orders of magnitude, from $m_e, m_u \sim$ MeV to $m_t = 174$ GeV, and this uncertainty gets squared.

For the full case with three generations and $n_s > 1$, and assuming, as is generic, that $det(M_R) \neq 0$ so that M_R^{-1} exists, the set of three light neutrino mass eigenstates is determined by the matrix analogue of eq. (1.30):

$$M_\nu = -M_D M_R^{-1} M_D^T \tag{1.31}$$

A different way to get neutrino masses is to interpret the SM as a low-energy effective field theory, as is common in modern quantum field theory. Provided that their coefficients, of dimension $4 - d_{\mathcal{O}}$ in mass units, are sufficiently small, (nonrenormalizable) operators $\mathcal{O}$ in the Lagrangian of mass dimension $d_{\mathcal{O}} > 4$, are then allowed. In this case, the dimension-5 operator [43]

$$\mathcal{O} = \frac{1}{M_X} \sum_{a,b} h_{L,ab}(\epsilon_{ik}\epsilon_{jm} + \epsilon_{im}\epsilon_{jk}) \left[\mathcal{L}^{Ti}_{aL} C \mathcal{L}^{j}_{bL} \right] \phi^k \phi^m + h.c. \tag{1.32}$$

(where a, b are flavor indices, i, j, k, m are SU(2) indices) is an electroweak singlet. Upon electroweak symmetry breaking (EWSB), this operator yields a left-handed Majorana mass term

$$\sum_{a,b=1}^{3} \nu^T_{L,a} C (M_L)_{ab} \nu_{L,j} + h.c. \tag{1.33}$$

with

$$(M_L)_{ab} = \frac{(h_L)_{ab}(v/\sqrt{2})^2}{M_X} \tag{1.34}$$

Since the SM is phenomenologically very successful, one should have $M_X >> v$, so again these dimension-5 operators lead naturally to light neutrinos. The diagonalization of the above operator determines the unitary transformation relating the mass eigenstates to the weak eigenstates,

$$\nu_{\ell_a} = \sum_{i=1}^{3} U_{ai} \nu_i \ , \quad \ell_1 = e, \ \ell_2 = \mu, \ \ell_3 = \tau \tag{1.35}$$

i.e.,

$$\begin{pmatrix} \nu_e \\ \nu_\mu \\ \nu_\tau \end{pmatrix} = \begin{pmatrix} U_{e1} & U_{e2} & U_{e3} \\ U_{\mu 1} & U_{\mu 2} & U_{\mu 3} \\ U_{\tau 1} & U_{\tau 2} & U_{\tau 3} \end{pmatrix} \begin{pmatrix} \nu_1 \\ \nu_2 \\ \nu_3 \end{pmatrix} \tag{1.36}$$

For the case of electroweak-singlet neutrinos and the resultant seesaw, because of the splitting of the masses into a light set and a heavy set, the observed weak eigenstates of neutrinos are again, to a very good approximation, linear combinations of the three light mass eigenstates, so that the full $(3+n_s)\times(3+n_s)$ mixing matrix breaks into block diagonal form involving the 3×3 U matrix and an analogous $n_s \times n_s$ matrix for the heavy sector. In terms of the flavor vectors, this is

$$\begin{pmatrix} \nu_\ell \\ \chi^c \end{pmatrix} = \begin{pmatrix} U & 0 \\ 0 & U_{heavy} \end{pmatrix} \begin{pmatrix} \nu_i \\ \chi^c_{i,m} \end{pmatrix} \tag{1.37}$$

If all of the data indicating neutrino masses is accepted, including the solar neutrino deficiency, atmospheric neutrinos, and LSND experiments, then light sterile (electroweak-singlet) neutrinos with masses of $\sim$ eV or smaller are needed. These are usually considered unnatural, because electroweak-singlet neutrinos naturally have masses $\sim m_R >> M_{ew} = v$.

1.3.4 Tests for Neutrino Masses in Decays

Given the focus of this report, we shall not review the well-known kinematic tests for neutrino masses except to mention that these are of three main types. First there are direct tests, which search for the masses of the dominantly coupled neutrino mass eigenstates emitted in particle and nuclear decays; these yield the current upper bounds on these eigenstates for the three dominantly coupled mass components in ν_e, ν_μ, and ν_τ. Second, there are tests for rather massive neutrinos emitted, via lepton mixing, in particle and nuclear decays. Third, there are searches for neutrinoless double beta decay, which would occur if there are massive Majorana neutrinos. The quantity on which limits are put in searches for neutrinoless double beta decay is $\langle m_\nu \rangle = |U_{ei}^2 m(\nu_i)|$ provided that their coefficients, are sufficiently small. Note that since U_{ei} is complex, destructive interference can occur in this sum. At present, the upper limit on this quantity is $\langle m_\nu \rangle \sim 0.4$ eV [44]. A number of new proposals for more sensitive experiments have been put forward, including GENIUS, EXO, MOON, and MAJORANA, among others, which hope to reach a sensitivity below 0.01 eV in $\langle m_\nu \rangle$ [45].

1.3.5 Models for Neutrino Masses and Mixing

We discuss the seesaw mechanism in further detail here. In the SM, a single Higgs field ϕ breaks the gauge symmetry and gives masses to the fermions. In the MSSM, it requires two $T = 1/2$ Higgs fields, H_1 and H_2 with opposite hypercharges $Y = 1$ and $Y = -1$ to do this. GUT theories may have more complicated Higgs sectors; typically different Higgs are used to break the gauge symmetry and give masses to fermions. For the Clebsch-Gordan decomposition of the representations in the fermion mass term we have

$$16 \times 16 = 10_s + 120_a + 126_s \tag{1.38}$$

Hence, *a priori*, one considers using Higgs of dimension 10, 120, and 126. The coupling to the 10-dimensional Higgs fields yields Yukawa terms of the following form (suppressing generation indices).

$$\psi_L^T C \psi_L \bar{\phi}_{10} = (\bar{d}_R d_L + \bar{e}_R e_L)\phi_{10}(\bar{5}) + (\bar{u}_R u_L + \bar{\nu}_R \nu_L)\phi_{10}(5) \tag{1.39}$$

The coupling to the 126-dimensional Higgs yields a term

$$\chi_R^T C \chi_R \phi_{126}(1) \tag{1.40}$$

together with other linear combinations of $\bar{u}_R u_L$, $\bar{\nu}_R \nu_L$, $\bar{d}_R d_L$, and $\bar{e}_R e_L$ times appropriate SU(5)-Higgs; these four types of terms are also produced by the coupling to a 120-dimensional Higgs. Hence, in this approach, one expects some similarity in Yukawa matrices, and thus Dirac mass matrices, for $T_3 = +1/2$ fermions, *i.e.*, the up-type quarks u, c, t and the neutrinos:

$$M^{(u)} \sim M_D^{(\nu)} \ , \quad M^{(d)} \sim M_D^{(\ell)} \tag{1.41}$$

However, in many string-inspired models, high-dimension Higgs representations such as the 120- and 126-dimensional representations in SO(10), are avoided. Instead, one constructs the neutrino mass terms from nonrenormalizable higher-dimension operators. Some reviews of models are in Ref. [46].

To get a rough idea of the predictions, suppose that M_D and M_R are diagonal and let m_R denote a typical entry in M_R. Denote $m_{u,1} = m_u$, $m_{u,2} = m_c$, $m_{u,3} = m_t$. Then, (neglecting physically irrelevant minus signs)

$$m(\nu_i) \simeq \frac{m_{u,i}^2}{m_R} \tag{1.42}$$

This is the quadratic seesaw. For $m(\nu_3)$, one gets

$$m(\nu_3) \sim \frac{m_t^2}{m_R} \simeq \left(\frac{175 \text{ GeV}}{10^{16} \text{ GeV}}\right)(1.75 \times 10^{11} \text{ eV}) \sim 10^{-3} \text{ eV} \tag{1.43}$$

which, given the uncertainties in the inputs, is comparable to the value

$$m(\nu_3) \simeq \sqrt{\Delta m_{32}^2} =\simeq 0.05 \text{ eV} \tag{1.44}$$

inferred from the SuperK data with the assumption $\nu_\mu \to \nu_\tau$ and $m(\nu_2) << m(\nu_3)$. This gives an idea of how the seesaw mechanism could provide a neutrino mass in a region relevant to the SuperKamiokande data.

In passing, we note that string theories allow a low string scale, perhaps as low as 100 TeV. These models have somewhat different phenomenological implications for neutrinos than conventional models with a string scale comparable to the Planck mass.

1.3.6 Lepton Mixing

We proceed to consider off-diagonal structure in M_R, as part of the more general topic of lepton mixing. Neutrino mass terms naturally couple different generations and hence violate lepton family number; the Majorana mass terms also violate total lepton number. Lepton mixing angles are determined by diagonalizing the charged lepton and neutrino mass matrices, just as the quark mixing angles in the CKM (Cabibbo-Kobayashi-Maskawa) matrix are determined by diagonalizing the up-type and down-type quark mass matrices. Before the atmospheric neutrino anomaly was reported, a common expectation was that lepton mixing angles would be small, like the known quark mixing angles. This was one reason why theorists favored the MSW mechanism over vacuum oscillations as an explanation of the solar neutrino deficiency – MSW could produce the deficiency with small lepton mixing angles, whereas vacuum oscillations needed nearly maximal mixing. It was long recognized that an explanation of the atmospheric neutrino anomaly requires maximal mixing, and while neutrino masses are not surprising or unnatural to most theorists, the maximal mixing has been something of a challenge for theoretical models to explain.

Denoting the lepton flavor vectors as $\ell = (e, \mu, \tau)$ and $\nu = (\nu_e, \nu_\mu, \nu_\tau)$, we have, for the leptonic weak charged current,

$$J^\lambda = \bar{\ell}_L \gamma^\lambda \nu_L \tag{1.45}$$

The mass terms are

$$\bar{\ell}_L M_\ell \ell_R + \bar{\nu}_L M_\nu \nu_R^c + h.c. \tag{1.46}$$

where, as above, $M_\nu = -M_D M_R^{-1} M_D^T$ and we have used the splitting of the neutrino eigenvalues into a light sector and a very heavy sector. We diagonalize these so that, in terms of the associated unitary transformations, with the notation $\ell_m = (e_m, \mu_m, \tau_m)$ and $\nu_m = (\nu_1, \nu_2, \nu_3)$, for charged lepton and neutrino mass eigenstates, the the charged current is

$$J^\lambda = \bar{\nu}_{mL} U_L^{(\nu)} \gamma^\lambda U_L^{(\ell)\dagger} \ell_{mL} = \bar{\nu}_{mL} U \gamma^\lambda \ell_{mL} \tag{1.47}$$

where the lepton mixing matrix is

$$U = U_L^{(\nu)} U_L^{(\ell)\dagger} \tag{1.48}$$

Although many theorists expected before the SuperK results indicating that $\sin^2(2\theta_{23}) = 1$ that leptonic mixing angles would be small, like the quark mixing angles, after being confronted with the SuperK results, they have constructed models that can accommodate large mixing angles. Of course, θ_{13} must be small to fit experiment. Models are able to yield either $\sin^2(2\theta_{12}) \sim 1$ for the LMA, LOW, and just-so solutions, or $\sin^2(2\theta_{12}) << 1$ for the SMA solution.

1.3.7 Relevant Near- and Mid-Term Experiments

There are currently intense efforts to confirm and extend the evidence for neutrino oscillations in all of the various sectors - solar, atmospheric, and accelerator. Some of these experiments are now running. In addition to SuperKamiokande and Soudan-2, these include the Sudbury Neutrino Observatory, SNO, and the K2K long baseline experiment between KEK and Kamioka. Others are in the development and testing phases, such as BOONE, MINOS, the CERN-Gran Sasso (GNGS) program, KAMLAND, and Borexino [47]. Among the long baseline neutrino oscillation experiments, the approximate distances are $L \simeq 250$ km for K2K, 730 km for both MINOS, from Fermilab to Soudan, and the proposed CNGS experiments. K2K is a ν_μ disappearance experiment with a conventional neutrino beam having a mean energy of about 1.4 GeV, going from KEK to the SuperK detector; it has a near detector for beam calibration. It has obtained results consistent with the SuperK experiment, and has reported that its data disagree by 2σ with the no-oscillation hypothesis [38]. MINOS is another conventional neutrino beam experiment that takes a beam from Fermilab to a detector in the Soudan mine in Minnesota. It too uses a near detector for beam flux measurements and has opted for a low-energy configuration, with the flux peaking at about 3 GeV. This experiment expects to start taking data in early 2004 and, after some years of running, to obtain higher statistics than the K2K experiment and to achieve a sensitivity down to roughly the level $\Delta m^2_{32} \sim 10^{-3}\text{eV}^2$. The CNGS program will come on later, around 2005. It will involve taking a higher energy neutrino beam from CERN to the Gran Sasso deep underground laboratory in Italy. This program will emphasize detection of the τ's produced by the ν_τ's that result from the inferred neutrino oscillation transition $\nu_\mu \to \nu_\tau$. The OPERA experiment will do this using emulsions [50], while the ICARUS proposal uses a liquid argon chamber [51]. Moreover, at Fermilab, the MiniBOONE experiment plans to run in the next few years and to confirm or refute the LSND claim after a few years of running.

There are also several relevant solar neutrino experiments. The SNO experiment is currently running and should report their first results in spring 2001. These will involve measurement of the solar neutrino flux and energy distribution using the charged current reaction on heavy water, $\nu_e + d \to e + p + p$. Subsequently, they will measure the neutral current reaction $\nu_e + d \to \nu_e + n + p$. The KamLAND experiment in Japan expects to begin taking data in late 2001. This is a reactor antineutrino experiment using baselines of order 100-250 km and will search for $\bar{\nu}_e$ disappearance. On a similar time scale, the Borexino experiment in Gran Sasso expects to turn on and hopes to measure the ^{7}Be neutrinos from the sun. These experiments should help to decide which of the various solutions to the solar neutrino problem is preferred, and hence the corresponding values of Δm^2_{21} and $\sin^2(2\theta_{12})$.

This, then, is the program of relevant experiments during the period 2001-2010. By the end of this period, we may expect that much will have been learned about neutrino masses and mixing. However, there will remain several important quantities that will not be well measured and which can be measured by a Neutrino Factory.

1.3.8 Oscillation Experiments at a Neutrino Factory

Although a Neutrino Factory based on a muon storage ring will turn on several years after this near-term period in which K2K, MINOS, and the CNGS experiments will run, it has a valuable role to play, given the very high-intensity neutrino beams of fixed flavor-pure content, including, in particular, ν_e and $\bar{\nu}_e$ beams as well as the conventional ν_μ and $\bar{\nu}_\mu$ beams. The potential of the neutrino beams from a muon storage ring is that, in contrast to a conventional neutrino beam, which, say, from π^+ decay, is primarily ν_μ with some admixture of ν_e's and other flavors from K decays, the neutrino beams from the muon storage ring would be extremely high purity: μ^- beams would yield 50 % ν_μ and 50 % $\bar{\nu}_e$, and viceversa for the charge conjugate case of μ^+ beams. Furthermore, these could be produced with extremely high intensities; we shall take the BNL design value of $\approx 10^{20}\mu$ decays per Snowmass year, 10^7 s.

The types of neutrino oscillations that can be explored with the neutrino factory based on a muon storage ring are listed below for the case of μ^- decaying into $\nu_\mu e^- \bar{\nu}_e$:

1. $\nu_\mu \to \nu_\mu$, $\nu_\mu \to \mu^-$ (survival)
2. $\nu_\mu \to \nu_e$, $\nu_e \to e^-$ (appearance)
3. $\nu_\mu \to \nu_\tau$, $\nu_\tau \to \tau^-$; $\tau^- \to (e^-, \mu^-)$... (appearance*)
4. $\bar{\nu}_e \to \bar{\nu}_e$, $\bar{\nu}_e \to e^-$ (survival)
5. $\bar{\nu}_e \to \bar{\nu}_\mu$, $\bar{\nu}_\mu \to \mu^+$ (appearance)
6. $\bar{\nu}_e \to \bar{\nu}_\tau$, $\bar{\nu}_\tau \to \tau^+$; $\tau^+ \to (e^+, \mu^+)$... (appearance*)

where the $*$ on the term appearance refers to the greater difficulty in experimentally inferring the production of the τ particle. It is clear from the list of processes above that, since the beam contains both neutrinos and antineutrinos, the only way to determine the identity of the parent neutrino is to determine the identity of the final-state charged lepton and measure its sign. One aspect of the experiments will involve the measurement of $\nu_\mu \to \nu_\mu$ as a disappearance experiment. A unique aspect for the Neutrino Factory will be the measurement of the oscillation $\bar{\nu}_e \to \bar{\nu}_\mu$, giving a wrong-sign μ^+. Of greater difficulty would be the measurement of the transition $\bar{\nu}_e \to \bar{\nu}_\tau$, giving a τ^+ which will decay part of the time to μ^+. These physics goals mean that a detector must have excellent capability to identify muons and measure their charge sign. The oscillation $\nu_\mu \to \nu_e$ would be difficult to observe, since it would be difficult to identify an electron shower from a hadron shower. From the above formulas for oscillations, we can see that, given the knowledge of $|\Delta m^2_{32}|$ and $\sin^2(2\theta_{23})$ available by the time a Neutrino Factory is built, the measurement of the $\bar{\nu}_e \to \bar{\nu}_\mu$ transition yields the value of θ_{13}.

To get a rough idea of how the sensitivity of an oscillation experiment would scale with energy and baseline length, recall that the event rate in the absence of oscillations is simply the neutrino flux times the cross section. First of all, neutrino cross sections in the region above about 10 GeV (and slightly higher for τ production) grow linearly with the neutrino energy. Secondly, the beam divergence is a function of the initial muon storage ring energy; this divergence yields a flux, as a function of θ_d, the angle of deviation from the forward direction, that goes like $1/\theta_d^2 \sim E^2$. Combining this with the linear E dependence of the neutrino cross section and the overall $1/L^2$ dependence of the flux far from the production region, one finds that the event rate goes like

$$\frac{dN}{dt} \sim \frac{E^3}{L^2} \tag{1.49}$$

Estimated event rates have been given in the Fermilab Neutrino Factory Working Group Report [16], [17]. For a stored muon energy of 20 GeV, as considered in this report, and a distance of $L = 2900$ to the WIPP Carlsbad site in New Mexico, these event rates amount to several thousand events per kton of detector per year, *i.e.*, they are satisfactory for the physics program. This is also true for the other pathlengths under consideration, namely $L = 2500$ km from BNL to Homestake and $L = 1700$ km to Soudan. A usual racetrack design would only allow a single pathlength L, but a bowtie design could allow two different pathlengths (*e.g.*, [29]).

One could estimate that at a time when the neutrino factory turns on, $|\Delta m^2_{32}|$ and $\sin^2(2\theta_{23})$ would be known at perhaps the 10% level (1 σ) from MINOS [30] (we emphasize that future projections such as this are obviously uncertain and note that JHF anticipates better accuracy; see below). The Neutrino Factory should improve the precision on those two parameters, and can contribute to three important measurements:

- measurement of θ_{13}, as discussed above
- measurement of the sign of Δm^2_{32} using matter effects
- possibly a measurement of CP violation in the leptonic sector, if $\sin^2(2\theta_{13})$, $\sin^2(2\theta_{21})$, and Δm^2_{21} are sufficiently large

It is estimated that a Neutrino Factory with the BNL design parameters could achieve a sensitivity down to $\sin^2 2\theta_{13}) \sim 3 \times 10^{-4}$ or better, assuming a 50 kton water Cherenkov detector at $L = 2900$ km, after three years of running [17, 30]. To measure the sign of Δm^2_{32}, one uses the fact that matter effects reverse sign when one switches from neutrinos to antineutrinos, and carries out this switch in the charges of the stored $\mu^{\pm}$. We elaborate on this next.

1.3.9 Matter Effects

With the advent of the muon storage ring, the distances at which detectors can be placed are large enough that, for the first time, matter effects can be exploited in accelerator-based oscillation experiments. Simply put, matter effects are the matter-induced oscillations that neutrinos undergo along their flight path through the Earth from the source to the detector. Given the typical density of the earth, matter effects are important for the neutrino energy range $E \sim O(10\text{GeV})$ and $\Delta m^2_{32} \sim 10^{-3}$ eV^2, values relevant for the long baseline experiments. After the initial discussion of matter-induced resonant neutrino oscillations in [31], an early study of these effects, including three generations, was carried out in [54]. The sensitivity of an atmospheric neutrino experiment to small Δm^2 due to the long baselines, and the necessity of taking into account matter effects, was discussed *e.g.*, in [55]. After Ref. [32], many analyses were performed in the 1980s of the effects of resonant neutrino oscillations on the solar neutrino flux. Matter effects in the Earth were studied, *e.g.*, [56] and [57], which also discussed the effect on atmospheric neutrinos. Recent papers on matter effects relevant to atmospheric neutrinos include [58, 59]. Early studies of matter effects on long baseline neutrino oscillation experiments were carried out in [60]. More recent analyses relevant to neutrino factories include [52, 53], [61]-[67]. In recent papers [63], calculations were presented of the matter effect for parameters relevant to possible long baseline neutrino experiments envisioned for the Neutrino Factory. In particular, these authors compared the results obtained with constant density along the neutrino path with results obtained by incorporating the actual density profiles. They studied the dependence of the oscillation signal on both $\frac{E}{\Delta m^2_{32}}$ and on the angles in the leptonic mixing matrix, and commented on the influence of Δm^2_{21}.

In the constant-density approximation, one has

$$P(\nu_\mu \to \nu_e) = \sin^2(2\theta^m_{13}) \sin^2\theta_{23} \sin^2(\omega_{32} L) \tag{1.50}$$

where

$$\sin^2(2\theta^m_{13}) = \frac{\sin^2(2\theta_{13})}{\sin^2(2\theta_{13}) + \left[\cos(2\theta_{13}) - \frac{2\sqrt{2}G_F N_e E}{\Delta m^2_{32}}\right]^2} \tag{1.51}$$

and

$$\omega_{32}^2 = \left[\frac{\Delta m_{32}^2}{4E}\sin(2\theta_{13})\right]^2 + \left[\frac{\Delta m_{32}^2}{4E}\cos(2\theta_{13}) - \frac{G_F N_e}{\sqrt{2}}\right]^2 \tag{1.52}$$

where N_e is the electron number density in the medium. For antineutrinos, one reverses the sign of the matter term $\propto G_F N_e$. The resonance condition is that

$$\frac{\Delta m_{32}^2}{2E}\cos(2\theta_{13}) = \sqrt{2}G_F N_e \tag{1.53}$$

i.e., $E \simeq 15$ GeV for $\Delta m_{32}^2 = 3 \times 10^{-3}$ eV^2, $\rho = 3$ g/cm^2, and $Z/A \simeq 0.5$. Thus, if $\Delta m_{32}^2 > 0$, this resonance enhances the $\nu_e \to \nu_\mu$ transition, whereas if $\Delta m_{32}^2 < 0$, it enhances the $\bar{\nu}_e \to \bar{\nu}_\mu$ transition. By comparing these (using first a stored μ^+ beam and then a stored μ^- beam) one can thus determine the sign of Δm_{32}^2 as well as the value of $\sin^2(2\theta_{13})$. A rough estimate is that this could be done to the level $\sin^2(2\theta_{13}) \sim 10^{-3}$.

1.4 CP Violation

CP violation is measured by the (rephasing-invariant) Jarlskog product

$$\begin{aligned} J &= Im(U_{ai}U_{bi}^* U_{aj}^* U_{bj}) \\ &= 2^{-3}\sin(2\theta_{12})\sin(2\theta_{13})\cos(\theta_{13})\sin(2\theta_{23})\sin\delta \end{aligned} \tag{1.54}$$

Leptonic CP violation also requires that each of the leptons in each charge sector be nondegenerate with any other leptons in this sector; this is, course, true of the charged lepton sector and, for the neutrinos, this requires $\Delta m_{ij}^2 \neq 0$ for each such pair ij. In the quark sector, J is known to be small; $J_{CKM} \sim O(10^{-5})$. A promising asymmetry to measure is $P(\nu_e \to \nu_\mu) - P(\bar{\nu}_e - \bar{\nu}_\mu)$. As an illustration, in the absence of matter effects,

$$\begin{aligned} P(\nu_e \to \nu_\mu) - P(\bar{\nu}_e \to \bar{\nu}_\mu) &= -4J(\sin 2\phi_{32} + \sin 2\phi_{21} + \sin 2\phi_{13}) \\ &= -16J\sin\phi_{32}\sin\phi_{31}\sin\phi_{21} \end{aligned} \tag{1.55}$$

where

$$\frac{P(\nu_e \to \nu_\mu) - P(\bar{\nu}_e \to \bar{\nu}_\mu)}{P(\nu_e \to \nu_\mu) + P(\bar{\nu}_e \to \bar{\nu}_\mu)} = -\frac{\sin(2\theta_{12})\cot(\theta_{23})\sin\delta\sin\phi_{21}}{\sin\theta_{13}} \tag{1.56}$$

In order for the CP violation in Eq. 1.55 to be large enough to measure, it is necessary that θ_{12}, θ_{13}, and $\Delta m_{sol}^2 = \Delta m_{21}^2$ not be too small. From atmospheric neutrino data, we have

$\theta_{23} \simeq \pi/4$ and $\theta_{13} << 1$. If LMA describes solar neutrino data, then $\sin^2(2\theta_{12}) \simeq 0.8$, so $J \simeq 0.1 \sin(2\theta_{13}) \sin\delta$. Say $\sin^2(2\theta_{13}) = 0.04$; then J could be $>> J_{CKM}$. Furthermore, for the upper part of the LMA, $\Delta m^2_{sol} \sim 4 \times 10^{-5}$ eV^2, so the CP violating effects might be observable. In the absence of matter, one would measure the asymmetry

$$\frac{P(\nu_e \to \nu_\mu) - P(\bar{\nu}_e \to \bar{\nu}_\mu)}{P(\nu_e \to \nu_\mu) + P(\bar{\nu}_e \to \bar{\nu}_\mu)} = -\frac{\sin(2\theta_{12})\cot(\theta_{23})\sin\delta\sin(2\phi_{21})}{4\sin(\theta_{13})\sin^2(\phi_{32})} \tag{1.57}$$

However, in order to optimize this, because of the smallness of Δm^2_{21} even for the LMA, one must go to large pathlengths L, and here matter effects are important. These make leptonic CP violation challenging to measure, because, even in the absence of any intrinsic CP violation, these matter effects render the rates for $\nu_e \to \nu_\mu$ and $\bar{\nu}_e \to \bar{\nu}_\mu$ unequal since the matter interaction is opposite in sign for ν and $\bar{\nu}$. One must therefore subtract out the matter effects in order to try to isolate the intrinsic CP violation. Alternatively, one might think of comparing $\nu_e \to \nu_\mu$ with the time-reversed reaction $\nu_\mu \to \nu_e$. Although this would be equivalent if CPT is valid, as we assume, and although uniform matter effects are the same here, the detector response is quite different and, in particular, it is quite difficult to identify $e^\pm$. Results from SNO and KamLAND testing the LMA will help further planning.

1.4.1 Detector Considerations

We have commented on the requisite properties of detectors. These should be quite massive, O(10-100) kton. Possibilities include magnetized steel calorimetors, water Cherenkov detectors, and liquid-argon chambers. A description of the type of detector presently envisioned for the Neutrino Factory is given in Chapter 15.

1.4.2 Experiments with a High-Intensity Conventional Neutrino Beam

One possibility for the staging of the construction of the neutrino factory is to start with an intense, ~ 1 MW proton driver with an associated program of neutrino physics using a conventional ν_μ neutrino beam from pion decays. Comparisons of the capabilities of a neutrino factory with those of neutrino oscillation experiments with a very high luminosity conventional neutrino beam are discussed in [68]-[69]. The JHF proposal estimates that its planned long baseline $\nu_\mu \to \nu_e$ oscillation experiment to SuperK could reach a level of $\sin^2(2\theta_{13})$ of roughly 10^{-2} [70], and perhaps somewhat better, depending on the type of beam, the running time, and the value of $|\Delta m^2_{32}|$. The recent Fermilab study reached similar conclusions [30]. The JHF plans also consider the possibility of an upgrade to 4 MW and the construction of a much larger far detector, namely a 1 Mton water Cherenkov detector called HyperKamiokande. Long baseline experiments of this type also intend to carry out $\nu_\mu \to \nu_\mu$ disappearance measurements that will yield much more precise determinations of $\sin^2 2\theta_{23}$ and $|\Delta m^2_{32}|$ than are currently available from the atmospheric data. At Fermilab these plans are being considered in conjunction with plans to construct a more intense proton source [71]. Recently also there have been studies of a number of possible future options, including a 2100 km long baseline experiment using a conventional neutrino beam from JHF to a detector located in the Beijing area [72], an experiment taking a very low energy neutrino beam from CERN to a detector in Frejus [73], and long baseline experiments with a 600 kton water Cherenkov detector called UNO (Ultra Underground Nucleon Decay and Neutrino Detector) [74].

1.4.3 Uses of Intense Low-Energy Muon Beams

The front end of a neutrino factory would be a source of intense low-energy $\mu^\pm$ beams. There is a rich program of physics that could be explored with these beams. Plans are already underway to do this at JHF, using their 3 GeV proton source [75], and at CERN [76], [77]. One of the main areas would be searches for lepton family number violating (LFV) decays, such as $\mu \to e\gamma$ and $\mu \to ee\bar{e}$. A review of the current status of experimental searches for such decays is [78]. The generalization of the standard model to include massive neutrinos and lepton mixing does give rise to these decays, but with branching ratios many orders of magnitude below feasible levels of observation [79]. Models of dynamical electroweak symmetry breaking such as technicolor generically predict large flavor-changing neutral current processes, including these LFV decays. This statement also applies to many types of supersymmetric models [80]. Let us comment on the possible improvements for various decays:

- $\mu \to e\gamma$. A series of experiments of progressively better sensitivity at SIN, TRIUMF, and LASL have been performed to search for this decay. In 1988, the Crystal Box experiment at LASL achieved the limit $B(\mu^+ \to e^+\gamma) < 4.9 \times 10^{-11}$ [81]. This was improved by a factor of 4 by the MEGA experiment at LASL, to $B(\mu^+ \to e^+\gamma) < 1.2 \times 10^{-11}$ [82]. The MEGA experiment took advantage of a stopping μ^+ rate of about 10^8 μ/sec. A proposal has been approved [83] for a $\mu \to e\gamma$ search at PSI with a single event sensitivity of about 10^{-14}. With the increase in the stopping μ decay rate to 10^{13} or more that would be achieved at a low-energy muon facility as part of the neutrino factory, one might envision that it could be possible, if requisite improvements in background suppression and detector technology could be made, to get to a single event sensitivity of 10^{-15} or better.

- $\mu^+ \to e^+e^+e^-$. The current upper limit on this decay was set by the SINDRUM experiment in 1988 [84]: $B(\mu^+ \to e^+e^+e^-) < 1.0 \times 10^{-12}$. As is the case with $\mu \to e\gamma$, if the necessary background reduction can be achieved and detectors can be designed to take the much greater rates, then with the much higher stopping muon rates at the front end of a neutrino factory, one might be able to reach a sensitivity of 10^{-15} or better in this search.

- $\mu N \to eN$. The current upper limit on muon to electron conversion in the field of a nucleus was set by a PSI experiment [85]: $\sigma(\mu^- + Ti \to e^+ + Ca)/\sigma(\mu^- + Ti \to \nu_\mu + Sc) < 1.7 \times 10^{-12}$. Upgrades of this experiment at PSI hope to reach a sensitivity of $\sim 10^{-13}$. The MECO [86] experiment at Brookhaven plans to search for $\mu + Al \to e + Al$ conversion down to a sensitivity of order $10^{-16} - 10^{-17}$. This is predicated upon obtaining a stopped muon rate of 10^{11} per sec. With the increase in this rate at a neutrino factory to $10^{13} - 10^{14}$ per sec, again if backgrounds can be controlled, one might envision an improvement in the sensitivity of a muon to electron conversion experiment down to the level of perhaps 10^{-18}.

There are also many other interesting experiments that could be pursued. The Brookhaven muon $g-2$ experiment has reported a 2.6 σ discrepancy between the measured value of the anomalous magnetic moment of μ^+ and the theoretical prediction [87, 88]. Further μ^+ data and, in addition, μ^- data, will be analyzed in the near future. The projected sensitivity of this experiment in a_μ is about 0.4×10^{-9}. The current rate of stopping μ's at BNL is about 10^8 per sec. With the increase rate at a neutrino factory, one could perform a higher-statistics version of this experiment. This is particular interest in view of the discrepancy that has been reported between the measured value of the anomalous magnetic moment and the theoretical prediction.

At Brookhaven, a proposal [89] has been submitted for an experiment making use of the existing muon storage ring to search for a muon electric dipole moment (EDM) down to the level of 10^{-22} e-cm in a first stage, with an upgrade having a sensitivity of 10^{-24} e-cm. A more intense source of $\mu^\pm$ would also enable one to push this sensitivity down, perhaps to 10^{-25} e-cm or better.

1.4.4 Conclusions

Neutrino masses and mixing are generic theoretical expectations. The seesaw mechanism naturally yields light neutrinos, although its detailed predictions are model-dependent and may require a lower mass scale than the GUT mass scale. One of the most interesting findings from the atmospheric data has been the maximal mixing in the relevant channel, which at present is favored to be $\nu_\mu \rightarrow \nu_\tau$. Even after the near-term program of experiments by K2K, MINOS, CNGS, and MiniBOONE, a high-intensity Neutrino Factory at BNL with 10^{20} μ decays per Snowmass year and a stored $\mu^\pm$ energy of 20 GeV, coupled with a long-baseline neutrino oscillation experiment, say with $L = 2900$ km to the WIPP facility in Carlsbad, would make a valuable contribution to the physics of neutrino masses and lepton mixing. In particular, the Neutrino Factory should be able to improve the accuracy of the measurement of $\sin^2(2\theta_{23})$ and Δm^2_{32} and to measure $\sin^2(2\theta_{13})$ and the sign of Δm^2_{32}. It might also be able to measure leptonic CP violation.

Bibliography

[1] N. Holtkamp and D. Finley, eds., *A Feasibility Study of a Neutrino Source Based on a Muon Storage Ring*, Fermilab-Pub-00/108-E (2000), http://www.fnal.gov/projects/muon_collider/nu-factory/nu-factory.html

[2] G.I. Budker, in *Proceedings of the 7th International Conf. on High Energy Accelerators*, Yerevan, 1969, p.33; extract in *Physics Potential and Development of $\mu^+\mu^-$ Colliderss: Second Workshop*, Ed. D. Cline, AIP Conf. Proc. **352** (AIP, New York, 1996), p.4.

[3] A.N Skrinsky, *Proceedings of the International Seminar on Prospects of High-Energy Physics*, Morges, 1971 (unpublished);extract in *Physics Potential and Development of $\mu^+\mu^-$ Colliderss: Second Workshop*, Ed. D. Cline, AIP Conf. Proc. **352** (AIP, New York, 1996), p.6.

[4] A.N. Skrinsky and V.V. Parkhomchuk, Sov. J. of Nuclear Physics, 12, 3 (1981).

[5] D. Neuffer, Particle Accelerators, 14, 75 (1983).

[6] R.B. Palmer, D. Neuffer and J. Gallardo, *A practical High-Energy High-Luminosity $\mu^+\mu^-$ Collider*, Advanced Accelerator Concepts: 6th Annual Conference, ed. P. Schoessow, AIP Conf. Proc. **335** (AIP, New York, 1995), p.635; D. Neuffer and R.B. Palmer, *Progress Toward a High-Energy, High-Luminosity $\mu^+\mu^-$ Collider*, The Future of Accelerator Physics: The Tamura Symposium, ed. T. Tajima, AIP Conf. Proc. **356** (AIP, New York, 1996), p.344.

[7] Muon Collaboration Home Page: http://www.cap.bnl.gov/mumu/mu_home_page.html

[8] Charles M. Ankenbrandt *et al.* (Muon Collider Collaboration) Phys. Rev. ST Accel. Beams 2, 081001 (1999) (73 pages), http://publish.aps.org/ejnls/przfetch/abstract/PRZ/V2/E081001/

[9] *Muon-Muon Collider: A Feasibility Study*, BNL-52503, Fermilab Conf-96/092, LBNL-38946 (1996).

[10] D. Koshkarev, CERN/ ISRDI/7462 (1974).

[11] S. Geer, Phys. Rev. D 57, 6989 (1998).

[12] MUCOOL Notes http://wwwmucool.fnal.gov/notes/notes.html.

[13] MUCOOL home page http://www.fnal.gov/projects/muon_collider/cool/cool.html; Emittance exchange home page http://needmore.physics.indiana.edu/~gail/emittance_exchange.html; Targetry home page http://www.hep.princeton.edu/mumu/target/.

[14] NuFact99, Lyon, http://lyopsr.in2p3.fr/nufact99/.

[15] NuFact00, Monterey, http://www.lbl.gov/Conferences/nufact00/.

[16] C. Albright *et al.*, *Physics at a Neutrino Factory*, Fermilab FN692 (2000) http://www.fnal.gov/projects/muon_collider/nu/study/study.html.

[17] *The Potential for Neutrino Physics at Muon Colliders and Dedicated High Current Muon Storage Rings*, Fermilab (in progress).

[18] J. Gallardo, http://www.cap.bnl.gov/mumu/.

[19] N. Mokhov, http://www-ap.fnal.gov/mars/

[20] R.B. Palmer *Non-Distorting Phase Rotation*, MUC Note 0114, April 2000, (http://www-mucool.fnal.gov/notes/).

[21] Eun-San Kim *et al.*, *LBNL Report on Simulation and Theoretical Studies of Muon Ionization Cooling*, MUC Note 0036, July 1999; Eun-San Kim, M. Yoon, *Super FOFO cooling channel for a Neutrino Factory*, MUC Note 0191, Feb. 2001 (http://www-mucool.fnal.gov/notes/).

[22] M. J. Burns, *et al.*, *DARHT Accelerators Update and Plans for Initial Operation*, Proc. 1999 Acc. Conf., p. 617.

[23] A. Skrinsky, *Towards Ultimate Polarized Muon Collider*, AIP Conf. Proc. 441, 1997, p. 249.

[24] R. Fernow, http://pubweb.bnl.gov/people/fernow/icool/.

[25] The GEANT4 Tool Kit is available at http://wwwinfo.cern.ch/asd/geant4/geant4.html.

[26] G. Hanson, (http://needmore.physics.indiana.edu /g̃ail/emittance_exchange.html).

[27] D. Neuffer, *High Frequency Buncher and $\phi - \delta E$ Rotation for the $\mu^+ - \mu^-$ Source*, MUCOOL Note 0181, Oct. 2000, (http://www-mucool.fnal.gov/notes/).

[28] Fits and references to the Homestake, Kamiokande, GALLEX, SAGE, and Super Kamiokande data include N. Hata and P. Langacker, Phys. Rev. **D56** 6107 (1997); J. Bahcall, P. Krastev, and A. Smirnov, Phys. Rev. **D58**, 096016 (1998); J. Bahcall and P. Krastev, Phys. Lett. **B436**, 243 (1998); J. Bahcall, P. Krastev, and A. Smirnov, Phys. Rev. **D60**, 093001 (1999); J. Bahcall, P. Krastev, and A. Smirnov, hep-ph/0103179; M. Gonzalez-Garcia, C. Peña-Garay, and J. W. F. Valle, Phys. Rev. **D63**, 013007; M. Gonzalez-Garcia, M. Maltoni, C. Pena-Garay, and J. W. F. Valle, Phys. Rev. **D63**, 033005 (2001). Recent discussions of flux calculations are in J. Bahcall, Phys. Rept. **333**, 47 (2000), talk at Neutrino-2000, and http://www.sns.ias.edu/ jnb/. Super Kamiokande data is reported and analyzed in Super Y. Fukuda *et al.* (SuperKamiokande Collab.), Phys. Rev. Lett. **82**, 1810, 243 (1999); S. Fukuda *et al.* (SuperKamiokande Collab.), hep-ex/0103032, hep-ex/0103033. For recent reviews, see e.g., Y. Suzuki, talk at Neutrino-2000, Int'l Conf. on Neutrino Physics and Astrophysics, http://www.nrc.ca/confserv/nu2000/, Y. Takeuchi at ICHEP-2000, Int'l Conf. on High Energy Physics, Osaka, http://ichep2000.hep.sci.osaka-u.ac.jp; and talks at the Fifth Topical Workshop at the Gran Sasso National Laboratory: Solar Neutrinos, Mar., 2001.

[29] Z. Parsa, in Proceedings of NNN99, A.I.P. Conf. Proc. 533, pp. 181-195 (A.I.P., New York, 1999).

[30] V. Barger, R. Bernstein, A. Bueno, M. Campanelli, D. Casper, F. DeJohgh, S. Geer, M. Goodman, D.A. Harris, K.S. McFarland, N. Mokhov, J. Morfin, J. Nelson, F. Peitropaolo, R. Raja, J. Rico, A. Rubbia, H. Schellman, R. Shrock, P. Spentzouris, R. Stefanski, L. Wai, K. Whisnant, FERMILAB-FN-703, hep-ph/0103052.

[31] L. Wolfenstein, Phys. Rev. **D17**, 2369 (1978).

[32] S. P. Mikheyev and A. Smirnov, Yad. Fiz. **42**, 1441 (1985) [Sov.J. Nucl. Phys. **42**, 913 (1986)], Nuovo Cim., **C9**, 17 (1986).

[33] Kamiokande Collab., K. S. Hirata, Phys. Lett. **B205**, 416; *ibid.* **280**, 146 (1992); Y. Fukuda *et al.*, Phys. Lett. **B335**, 237 (1994); S. Hatakeyama *et al.* Phys. Rev. Lett. **81**, 2016 (1998).

[34] IMB Collab., D. Casper *et al.*, Phys. Rev. Lett. **66**, 2561 (1991); R.Becker-Szendy *et al.*, Phys. Rev. **D46**, 3720 (1992); Phys. Rev. Lett. **69**, 1010 (1992).

[35] Y. Fukuda *et al.*, Phys. Lett. **B433**, 9 (1998); Phys. Rev. Lett. **81**,1562 (1998); *ibid.*, **82**, 2644 (1999); Phys. Lett. **B467**, 185 (1999); H. Sobel, in Neutrino-2000, T. Toshito, in ICHEP-2000. Recent discussions of flux calculations are T. Gaisser, Nucl. Phys. (Proc. Suppl.) **87**, 145 (2000); P. Lipari, Astropart. Phys. **14**, 153 (2000); G. Battistoni, hep-ph/0012268; G. Fiorentini, V. Naumov, and F. Villante, hep-ph/0103322.

[36] W. Allison *et al.*, Phys. Lett. **B449**, 137 (1999), A. Mann, talk at Neutrino-2000, hep-ex/0007031.

[37] M. Ambrosio *et al.*, Phys. Lett. **B478**, 5 (2000); B. Barish, talk at Neutrino-2000.

[38] M. Sakuda and K. Nishikawa, talks at ICHEP-2000, Osaka; S. H. Ahn *et al.*, hep-ex/0103001.

[39] M. Apollonio *et al.*, Phys. Lett. **B420**, 397 (1998); Phys. Lett. **B466**, 415 (1999).

[40] LSND Collab., C. Athanassopoulous *et al.*, Phys. Rev. Lett. **77**, 3082 (1996), LSND Collab., C. Athanassopoulous *et al.*, Phys. Rev. Lett. **81**, 1774 (1998); K. Eitel, in Neutrino-2000.

[41] KARMEN Collab., K. Eitel, in Proceedings of Neutrino-2000, Nucl. Phys. (Proc. Suppl.) **91**, 191 (2000).

[42] M. Gell-Mann, P. Ramond, R. Slansky, in *Supergravity*, edited by P. van Nieuwenhuizen and D. Freedman (North Holland, Amsterdam, 1979), p. 315; T. Yanagida in proceedings of *Workshop on Unified Theory and Baryon Number in the Universe*, KEK, 1979.

[43] See, e.g., eq. (1) in R. Shrock, “Neutrinos”, in R. Barnett *et al.*, Review of Particle Physics, Phys. Rev. **D54**, 275 (1996).

[44] L. Baudis *et al.*, Phys. Rev. Lett. **83**, 41 (1999); H. Ejiri, in Proceedings of Neutrino 2000, Nucl. Phys. (Proc. Suppl.) **91**, 255 (2000).

[45] E. Fiorini, in in Proceedings of Neutrino 2000, Nucl. Phys. (Proc. Suppl.) **91**, 262 (2000).

[46] There are many reviews of the large number of theoretical models. A few of the recent ones are G. Altarelli and F. Feruglio, hep-ph/9905536, S. Bilenkii, C. Giunti, and W. Grimus, Prog. Part. Nucl. Phys. **43**, 1 (1999); E. Akhmedov, hep-ph/0001264 (ICTP Summer School Lectures, 1999); B. Kayser, A. Smirnov, and R. Mohapatra, in Proc. of Neutrino-2000, Nucl. Phys. B (Proc. Suppl.) **91**, 299, 313 (2000); S. M. Barr, and I. Dorsner, Nucl. Phys. **B585**, 79 (2000); C. H. Albright, hep-ph/0010268; K. Babu, J. Pati, F. Wilczek, Nucl. Phys. **B566**, 33 (2000); P. Ramond, in Proc. of TAUP-99, Nucl. Phys. Proc. Suppl. **87**, 259 (2000), J. Ellis, op cit.

[47] References and websites for these experiments and future projects can be found, e.g., at http://www.hep.anl.gov/ndk/hypertext/nu_industry.html.

[48] Some relevant websites at BNL, FNAL, and CERN containing further information are
http://www.cap.bnl.gov/mumu/
http://www.fnal.gov/projects/muon_collider/nu/study/study.html
http://www.cern.ch/~ autin/nufact99/whitepap.ps
See, in particular, the report of the Fermilab Working Group, C. Albright *et al.*, "FNAL Feasibility Study on a Neutrino Source Based on a Neutrino Storage Ring" (March 30, 2000), available at the above FNAL web site.

[49] Neutrino Factory and Muon Collider Collaboration, Expression of Interest for R+D towards a Neutrino Factory Based on a Storage Ring and Muon Collider, physics/9911009, http://puhep1.princeton.edu/mumu/NSFLetter/nsfmain.ps. This site also contains further references to the relevant literature.

[50] OPERA Collab., CERN-SPSC-97-24, hep-ex/9812015.

[51] ICANOE Collab. F. Cavanna *et al.*, LNGS-P21-99-ADD-1,2, Nov 1999; A. Rubbia, hep-ex/0001052.

[52] S. Geer, Phys. Rev. **D57**, 6989 (1998).

[53] De Rujula, M. B. Gavela, and P. Hernandez, Nucl. Phys. **B547**, 21 (1999).

[54] V. Barger, K. Whisnant, S. Pakvasa, and R. J. N. Phillips, Phys. Rev. **D22**, 2718 (1980); V. Barger, K. Whisnant, and R. J. N. Phillips, Rev. Rev. Lett. **45**, 2084 (1980).

[55] D. Ayres, T. Gaisser, A. K. Mann, and R. Shrock, in *Proceedings of the 1982 DPF Summer Study on Elementary Particles and Future Facilities*, Snowmass, p. 590; D. Ayres, B. Cortez, T. Gaisser, A. K. Mann, R. Shrock, and L. Sulak, Phys. Rev. **D29**, 902 (1984).

[56] P. Krastev, S. Petcov, Phys. Lett. **B205**, 8 (1988).

[57] A. J. Baltz, J. Weneser, Phys. Rev. **D37**, 3364 (1988).

[58] S. Petcov, Phys. Lett. **B434**, 321 (1998). M. Chizhov, M. Maris, S. Petcov, hep-ph/9810501; M. Chizhov, S. Petcov, Phys. Rev. **D63**, 073003 (2001); M.Chizhov, S.Petcov, Phys. Rev. Lett. **83**, 1096 (1999).

[59] E. Akhmedov, A. Dighe, P. Lipari, A. Smirnov, Nucl. Phys. **B542**, 3 (1999); E. Akhmedov, Nucl.Phys. **B538**, 25 (1999); hep-ph/0001264.

[60] P. Krastev, Nuovo Cimento **103A**, 361 (1990); R. H. Bernstein and S. J. Parke, Phys. Rev. **D44**, 2069 (1991).

[61] V. Barger, S. Geer, K. Whisnant, Phys.Rev. **D61**, 053004 (2000).

[62] M. Campanelli, A. Bueno, A. Rubbia, hep-ph/9905240; P. Lipari, Phys. Rev. D61, 113004; D. Dooling, C. Giunti, K. Kang, C. W. Kim, Phys. Rev. **D61** (2000) 073011.

[63] I. Mocioiu, R. Shrock, Phys. Rev. **D62**, 053017 (2000); Proceedings of NNN99, A.I.P. Conf. Proc. 533, pp. 74-79 (A.I.P., New York, 1999).

[64] V. Barger, S. Geer, R. Raja, K. Whisnant, Phys. Rev. **D62**, 013004, *ibid.* **D62**, 073002 (2000); Phys. Lett. —bf B485, 379 (2000); Phys. Rev. **63**, 033002 (2001).

[65] A. Cervera, A. Donini, M.B. Gavela, J. Gomez Cadenas, P. Hernandez, O. Mena, and S. Rigolin, Nucl. Phys. **B579**, 17 (2000), Erratum-ibid. **B593**, 731 (2001).

[66] M. Freund, T. Ohlsson, Mod. Phys. Lett. **15**, 867 (2000); T. Ohlsson, H. Snellman, J. Math. Phys. **41**, 2768 (2000); Phys. Rev. **D60** 093007 (1999); Phys. Lett. **B474**, 153 (2000); M. Freund, M. Lindner, S.T. Petcov, A. Romanino, Nucl. Phys. **B578**, 27 (2000); M. Freund, P. Huber, M. Lindner, Nucl. Phys. **B585**, 105 (2000); M. Freund, M. Lindner, and S. Petcov. Nucl. Instrum. Meth. **A451**, 18 (2000); K. Dick, M. Freund, P. Huber, and M. Lindner, Nucl. Phys. **B588**, 101; Nucl. Phys. —bf B598, 543 (2001).

[67] S.M. Bilenky, C. Giunti, W.Grimus, Phys.Rev.**D58**, 033001 (1998); K. Dick, M. Freund, M. Lindner, A. Romanino, Nucl. Phys. **B562**, 29 (1999); M. Tanimoto, Phys. Lett. **B462**, 115 (1999); A. Donini, M.B. Gavela, P. Hernandez, Nucl. Phys. **B574**, 23 (2000); M. Koike and J. Sato, Phys. Rev. **D61** 073012 (2000); Erratum-ibid. **D62**, 079903 (2000); M. Koike and J. Sato, Phys. Rev. **D62**, 073006 (2000); M. Koike, T. Ota, and J. Sato, hep-ph/0011387; F. Harrison, W.G. Scott, hep-ph/9912435.

[68] B. Richter, hep-ph/0008222.

[69] V. Barger, S. Geer, R. Raja, K. Whisnant, Phys. Rev. **D63**, 113011 (2001) (hep-ph/0012017).

[70] Y. Itoh *et al.* JHF Neutrino Working Group), Letter of Intent: a Long Baseline Neutrino Oscillation Experiment using the JHF 50 GeV Proton Synchroton and the Super-Kamiokande Detector (Feb. 2000); Y. Itoh *et al.*, The JHF-SuperKamiokande Neutrino Project, at http://neutrino.kek.jp/jhfnu.

[71] See http://www-bd.final.gov/pdriver.

[72] N. Okamura *et al.*, hep-ph/0104220; H. Chen *et al.*, hep-ph/0104266.

[73] J. Cadenas *et al.* (CERN Superbeam Working Group), hep-ph/0105297.

[74] See, *e.g.*, D. Harris, talk at UNO workshop (Aug. 2000), R. Shrock, talks at UNO workshop, June, 2001; http://superk.physics.sunysb.edu/uno/.

[75] See working group 2 in in NuFact2001, http://psux1.kek.jp/ nufact01/.

[76] For a recent general review, see J. Ellis, in Neutrino-2000.

[77] J. Ellis, hep-ph/0105265.

[78] Y. Kuno and Y. Okada, Rev. Mod. Phys. **73**, 151 (2001).

[79] S. Petcov, Yad. Fiz. **25**, 641 (1977) [Sov. J. Nucl. Phys. **25**, 340 (1977)]; W. Marciano and A. Sanda, Phys. Lett. **B67**, 303 (1977); B. W. Lee, S. Pakvasa, R. Shrock, and H. Sugawara, Phys. Rev. Lett. **38**, 937 (1977). These decays have also been studied in models with right-handed charged weak currents in T. P. Cheng and L. F. Li, Phys. Rev. Lett. **38**, 381 (1977).

[80] Some early work is L. Hall and M. Suzuki, Nucl. Phys. **B231**, 419 (1984); I-H. Lee, Phys. Lett. **138B**, 121 (1984); Nucl. Phys. **B246**, 120 (1984); recent calculations include R. Barbieri, L. Hall, and A. Strumia, Nucl. Phys. **B449**, 437 (1995); J. Hisano, D. Nomura, Y. Okada, Y. Shimizu, and M. Tanaka, Phys. Rev. **D58**, 116010 (1998).

[81] R. Bolton *et al.*, (Crystal Box Collab.), Phys. Rev. **D38**, 2077 (1988).

[82] M. Brooks *et al.*, (MEGA Collab.), Phys. Rev. Lett. **83**, 1521 (1999).

[83] Barkov *et al.*, PSI Proposal (1999).

[84] U. Bellgardt *et al.*, Nucl. Phys. **B229**, 1 (1988).

[85] J. Kaulard *et al.*, Phys. Lett. **B422** (1998) 334.

[86] MECO Collab., BNL.

[87] H. Brown *et al.* (Muon $g-2$ Collab.), Phys. Rev. Lett. **86**, 2227 (2001).

[88] For recent discussions, see, e.g., A. Czarnecki and W. Marciano, hep-ph/0102122, F. Jegerlehner, hep-ph/0104304; W. Marciano and B. L. Roberts, hep-ph/0105056 and references therein.

[89] Y. Semertzidis *et al.*, BNL Proposal; see also the proceedings of the BNL EDM Workshop (May, 2001), http://www.edm.bnl.gov/Workshop.

Chapter 2

Proton Driver

2.1 The AGS as a Proton Driver

After more than 40 years of operation, the AGS is still at the heart of the Brookhaven hadron accelerator complex. This system of accelerators presently comprises a 200 MeV linac for the pre-acceleration of high intensity and polarized protons, two Tandem Van de Graaff for the pre-acceleration of heavy ion beams, a versatile Booster that allows for efficient injection of all three types of beams into the AGS and, most recently, the two RHIC collider rings that produce high luminosity heavy ion and polarized proton collisions. For several years now, the AGS has held the world intensity record with more than 7×10^{13} protons accelerated in a single pulse.

We describe here possible upgrades to the AGS complex that would meet the requirements for the proton beam driver for Neutrino Factory operation. Those requirements are summarized in Table 2.1 and a layout of the upgraded AGS is shown in Fig. 2.1. Since the present number of protons per fill is already close to the required number, the upgrade focuses on increasing the repetition rate and reducing beam losses (to avoid excessive shielding requirements and to maintain the ability to service machine components by hand). It is also important to preserve all the present capabilities of the AGS, in particular its role as injector to RHIC.

The AGS Booster was built not only to allow the injection of any species of heavy ion into the AGS, but to allow a fourfold increase of the AGS intensity. It is one-quarter the circumference of the AGS with the same aperture. However, the accumulation of four Booster loads in the AGS takes time, and is therefore not well suited for high average beam power operation. We are proposing here to build a superconducting upgrade to the existing 200 MeV linac to reach an energy of 1.2 GeV for direct H^- injection into the AGS. This will be discussed in Section 2.2. The minimum ramp time to full energy is presently 0.5 s; this must be upgraded to reach the required repetition rate of 2.5 Hz. Since the six bunches are extracted one bunch at a time, as is presently done for the operation of the g-2 experiment, a 100 ms flattop is included, which leaves only 150 ms for the ramp up or ramp down cycle. The required upgrade of the AGS power supply will be described in Section 2.3. Finally, the increased ramp rate and the final bunch compression require a substantial upgrade to the AGS rf system and improvements in the vacuum chamber as well. The rf upgrade will be discussed in Section 2.4.

Table 2.1: AGS proton driver parameters.

Total beam power (MW)	1
Beam energy (GeV)	24
Average beam current (μA)	42
Cycle time (ms)	400
Number of protons per fill	1×10^{14}
Average circulating current (A)	6
No. of bunches per fill	6
No. of protons per bunch	1.7×10^{13}
Time between extracted bunches (ms)	20
Bunch length at extraction, rms (ns)	3
Peak bunch current (A)	400
Total bunch area (eVs)	5
Bunch emittance, rms (eV-s)	0.3
Momentum spread, rms	0.005

The front end consists of a high intensity negative ion source, followed by a 750 keV RFQ, and the first five tanks of the existing room temperature Drift Tube Linac (DTL). The superconducting linac (SCL) is made of three sections, each with its own energy range and cavity cryostat arrangement.

The front end ion source operates with a 1% duty cycle at the repetition rate of 2.5 Hz. The beam current within a pulse is 37.5 mA of H^-. The ion source sits on a platform at 35 kV. The beam is prechopped by a chopper located between the ion source and the RFQ. The chopping extends over 65% of the beam length, at a frequency matching the accelerating rf at injection into the AGS. Transmission efficiency through the RFQ is taken conservatively to be 80%, so that the average current of the beam pulse in the linac, where we assume no further beam loss, is 20 mA, with a peak value of 30 mA. The

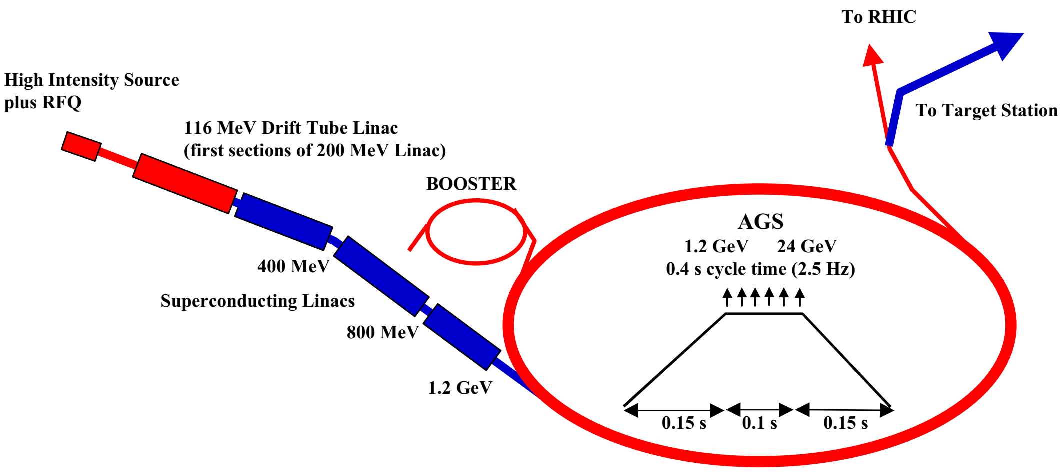

Figure 2.1: AGS proton driver layout.

combination of the chopper and the RFQ prebunches the beam with a sufficiently small bunch length that each beam bunch fits into an accelerating rf bucket of the downstream DTL, which operates at 201.25 MHz. The DTL is a room-temperature conventional linac that accelerates to 116 MeV.

The proposed new injector for the AGS adds a 1.2 GeV SCL with an average output beam power of about 50 kW. The injection energy is still low enough to control beam losses due to stripping of the negative ions that are used for multiturn injection into the the AGS. The duty cycle is about 0.5%. Injection into the AGS is modeled after the SNS scheme [1]. However, the repetition rate, and consequently the average beam power, is much lower here. The larger circumference of the AGS also reduces the number of foil traversals. Beam losses at injection into the AGS are estimated to be about 3% controlled losses and 0.3% uncontrolled losses. This is based on a comparison with the actual experience in the AGS Booster and the LANL PSR and the predicted losses at the SNS, using the quantity $\mathrm{N_P}\ /\beta^2\gamma^3$ A), which is proportional to the Laslett tune shift, as a scaling factor. This is summarized in Table 2.2. As can be seen, the predicted 3% beam loss is consistent with the AGS Booster and the PSR experience and also with the SNS prediction.

With the AGS rf harmonic number of 24, the Linac beam will be injected into 18 buckets, as discussed in Section 2.4. A bunch merge of 3 to 1 will take place later in the cycle to produce 6 bunches in the AGS.

The AGS injection parameters are summarized in Table 2.3. A relatively low rf voltage

Table 2.2: Comparison of H^- injection parameters.

	AGS Booster	SNS	PSR	1 MW AGS
Beam power, linac exit (kW)	3	1000	80	54
Kinetic energy (MeV)	200	1000	800	1200
No. of protons N_{P} (10^{12})	15	100	31	100
Vertical acceptance, A (π mm mrad)	89	480	140	55
$\beta^2\gamma^3$	0.57	6.75	4.50	9.56
$N_P/(\beta^2\gamma^3 A)$ ($10^{12}/\pi$ mm mrad)	0.296	0.031	0.049	0.190
Total beam losses (%)	5	0.1	0.3	3
Total lost beam power (W)	150	1000	240	1440
Circumference (m)	202	248	90	807
Lost beam power per meter (W/m)	0.8	4.0	2.7	1.8

of 450 kV at injection energy is necessary to limit the beam momentum spread during the multi-turn injection process to about 0.48%, and the longitudinal emittance to be about 1.2 eV-s per bunch. Such a small emittance is important to limit beam losses during transition crossing and to allow for effective bunch compression before extraction from the AGS.

A preliminary simulation of the 360-turn injection process is shown in Fig. 2.2. Without the second harmonic rf, some dilution in phase space of the injected particles is inevitable. The bunch shape is similar to that at the PSR in Los Alamos, with a noticeable sharp peak. A possible Linac beam momentum ramping could improve this if necessary.

Beam instability consideration are focused on two aspects. These are, for the AGS, the longitudinal instability around transition energy, and the transverse instability above transition, at high energy.

The fractional beam momentum spread at transition must be less than 0.0075 because of the limited momentum aperture during the transition-energy jump. With the transition jump, the slippage factor can be controlled to be greater than 0.002. With a bunch rms length of 4.25 ns and a peak current of 85 A at transition, the longitudinal impedance must be less than 11 Ω to avoid longitudinal microwave instability. An upgraded vacuum chamber to accomplish this is included in the baseline design.

The measured AGS broadband impedance is about 30 Ω. The broadband impedance mainly comes from the unshielded bellows, the vacuum chamber connections and steps, and cavities, and also has possible contributions from the BPMs and ferrite kickers. With

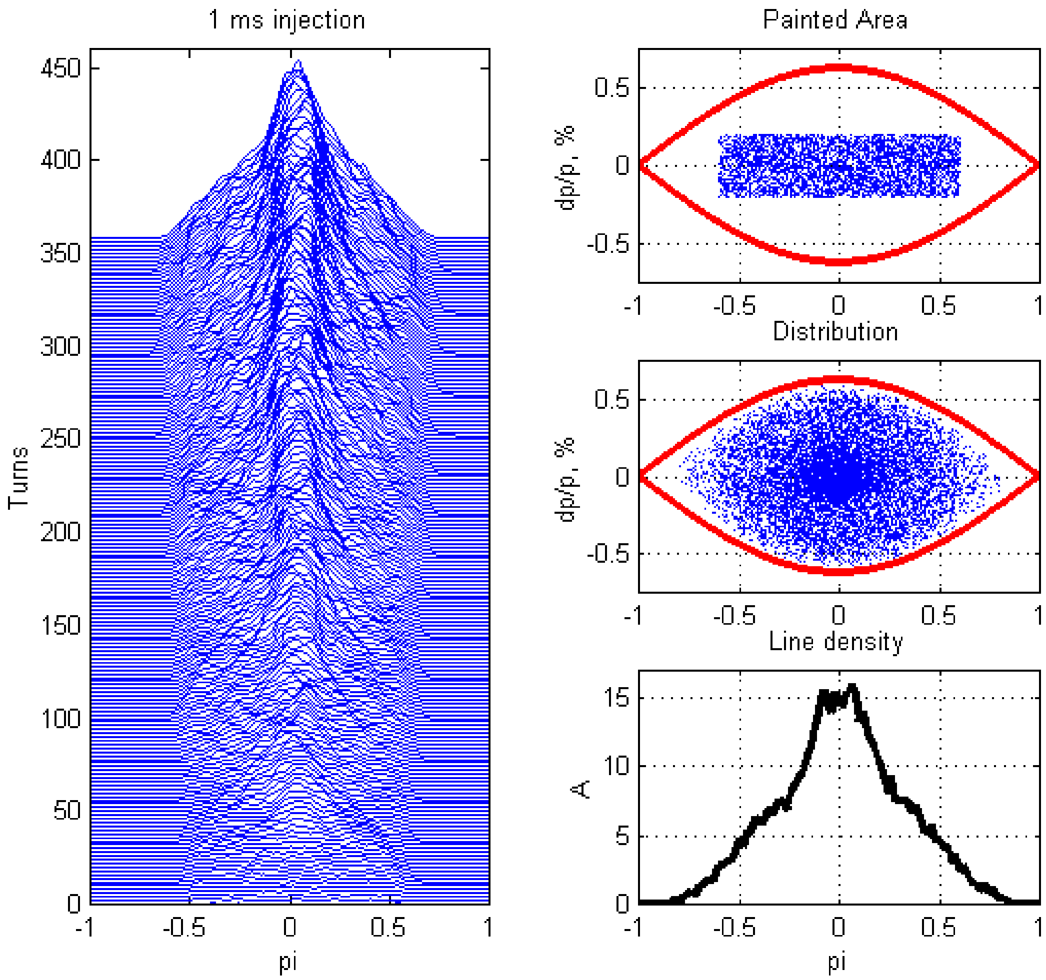

Figure 2.2: AGS injection simulation. The abscissa is phase.

Table 2.3: AGS injection parameters.

Injection turns	360
Repetition rate (Hz)	2.5
Pulse length (ms)	1.08
Chopping rate (%)	65
Linac average/peak current (mA)	20/30
Momentum spread	± 0.0015
Norm. 95% emittance ($\pi\mu$m $\cdot$ rad)	12
RF voltage (kV)	450
Bunch length (ns)	85
Longitudinal emittance (eV-s)	1.2
Momentum spread	± 0.0048
Norm. 95% emittance ($\pi\mu$m $\cdot$ rad)	100

a modest effort, this impedance can be reduced to be less than 10 Ω, which is consistent with newly designed proton machines.

In fact, if only the longitudinal microwave instability were of concern, a larger broadband impedance could be tolerated, since the longitudinal space-charge impedance of about 10 Ω at transition, which is capacitive, has the effect of canceling the inductive broadband impedance. However, the transverse instability at high energy is more serious, even with a broadband impedance of 10 Ω.

At 24 GeV, and with bunches compressed to 3 ns rms, each with an intensity of 1.7×10^{13} protons, the beam peak current reaches almost 400 A, which is about 7 times higher than the present running condition. With a transverse broadband impedance of 2.1 MΩ/m, scaled from the longitudinal impedance of 10 Ω, the coherent tune shift is then about 0.04, which implies an instability growth rate of 10 μs.

The space-charge incoherent tune spread, which is the main transverse microwave instability damping force at low energy, is reduced at high energy to a value comparable to 0.04. This is not sufficient to stabilize the beam. Other possible damping forces are discussed as follows. The slippage factor $\eta = 0.013$ at 24 GeV, together with the beam momentum spread of 0.01 for a bunch with 3 ns rms length, gives rise to a tune spread of 0.001, which is negligible. The chromatic tune spread with the chromaticity of 0.25 is 0.02, contributing only marginally to beam stability. Possibly the tune spread from octupoles or rf quadrupoles could stabilize the beam, but the choice of an improved vacuum chamber seems prudent.

Other issues are not as significant. For example, the space charge is not significant

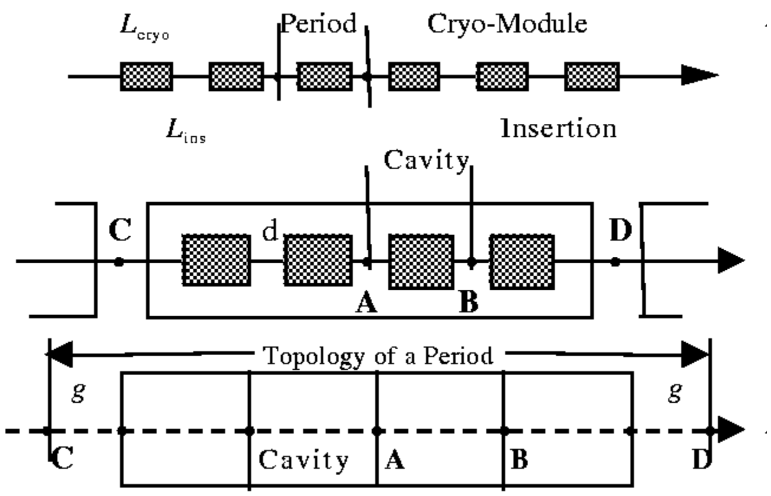

Figure 2.3: Configuration of the cavities within the cryo-modules (cryostats).

even for the compressed bunches and the beam momentum spread of ± 0.01 is well within the AGS momentum aperture at high energy.

In summary, since the intensity of 1×10^{14} is only marginally higher than the present intensity of 7×10^{13}, the beam instability during acceleration and transition crossing can be avoided. Transverse instability is likely to be the most dangerous during the bunch compression in the AGS ring, even with a reduced broadband impedance.

2.2 Superconducting Linac (SCL)

The SCLs accelerate the proton beam from 116 MeV to 1.2 GeV. The configuration we use follows a design similar to that described in Ref. [2]. All three linacs are built up from a sequence of identical periods, as shown in Fig. 2.2. Each period comprises a cryomodule and a room-temperature insertion that is needed for the placement of focusing quadrupoles, vacuum pumps, steering magnets, beam diagnostic devices, bellows and flanges. Each cryomodule includes four identical cavities, each with four or eight identical cells.

The choice of cryomodules with identical geometry, and with the same cavity/cell configuration, is economical and convenient for construction. Still, there is a penalty due to the reduced transit–time factors when a particle crosses cavity cells with lengths adjusted to a common central value β_o that does not correspond to the particle's in-

Table 2.4: Parameters of the superconducting linacs.

	Low energy	Medium energy	High
Beam power, linac exit (kW)	16	32	48
Kinetic energy range (MeV)	116 - 400	400 - 800	800 - 1200
Velocity range, β	0.4560 - 0.7131	0.7131 - 0.8418	0.8418 - 0.8986
Frequency (MHz)	805	1610	1610
Protons per bunch (10^8)	9.32	9.32	9.32
Temperature (K)	2.0	2.0	2.0
Cells per cavity	4	8	8
Cavities per cryo-module	4	4	4
Cell length (cm)	9.68	6.98	8.05
Cell reference velocity, β_o	0.520	0.750	0.865
Cavity internal diameter (cm)	10	5	5
Cavity separation (cm)	32	16	16
Cold-to-warm transition (cm)	30	30	30
Accelerating gradient (MV/m)	11.9	22.0	21.5
Cavities per klystron	4	4	4
No. of klystrons (or periods)	18	10	9
Klystron power (kW)	720	1920	2160
Energy gain per period (MeV)	16.0	42.7	48.0
Length of period (m)	4.2	4.4	4.7
Total length (m)	75.4	43.9	42.6

stantaneous velocity. This is the main reason to divide the superconducting linac into three sections, each designed around a different central value β_o, and, therefore, having different cavity/cell configurations. The cell length in a section is fixed to be $l\frac{\beta_o}{2}$ where l is the rf wavelength.

The major parameters of the three sections of the SCL are given in Table 2.4. The low-energy section operates at 805 MHz and accelerates from 116 to 400 MeV. The following two sections, accelerating to 800 MeV and 1.2 GeV, respectively, operate at 1.62 GHz. A higher frequency is desirable for obtaining a larger accelerating gradient with a more compact structure and reduced cost. Transverse focusing is done with a sequence of FODO cells with halflength equal to that of a period. The phase advance per cell is 90°. The rms normalized betatron emittance is $\approx 0.3\ \pi$ mm mrad. The rms bunch area is 0.5π MeV-deg. The rf phase angle is 30°. The length of the linac depends on the average accelerating gradient, which has a maximum value that is limited by three causes:

1. The surface-field limit at the frequency of 805 MHz, taken to be 26 MV/m. For a realistic cavity shape, we set a limit of 13 MV/m on the axial electric field. For the following two sections, the surface-field limit at 1.61 GHz is 40 MV/m and, correspondingly, we adopt a limit of 20 MV/m on the axial electric field.

2. The rf coupler power limit, which we take here not to exceed 400 kW (including a contingency of 50% to avoid saturation effects).

3. The need to make the longitudinal motion stable, which limits the energy gain per cryomodule to a small fraction of the beam energy [2].

The proposed mode of operation is to run each section of the SCL with the same rf input power per cryomodule. This will result in some variation of the actual axial field from one cryomodule to the next. A constant value of the axial field, if needed, could be obtained by locally adjusting the value of the rf phase.

For a pulsed mode of operation of the superconducting cavities, the Lorentz forces could deform the cavity cells enough to tune them off resonance. This is controlled with a thick cavity wall and additional supports. Also, a significant time to fill the cavities with rf power is required before the maximum gradient is reached and beam can be injected. The expected filling time is short compared with the beam pulse length of 1 ms.

2.3 AGS Main Power Supply Upgrade

2.3.1 Present Mode of Operation

The present AGS Main Magnet Power Supply (MMPS) is a fully programmable 6000 A, ±9000 V SCR power supply. A 9 MW Motor Generator (MG), made by Siemens, is a part of the main magnet power supply of the accelerator. The MG permits pulsing the main magnets up to 50 MW peak power, while the input power of the MG itself remains constant. The highest power into the MG ever utilized is 7 MW, that is, the maximum average power dissipated in the AGS magnets has never exceeded 5 MW.

The AGS ring comprises 240 magnets connected in series. The total resistance, R, is 0.27 Ω and the total inductance, L, is 0.75 H. There are 12 superperiods, designated A through L, of 20 magnets each, divided in two identical sets of 10 magnets per superperiod.

Two stations of power supplies are each capable of delivering up to 4500 V and 6000 A. Every station consists of two power supplies connected in parallel. One power supply is a 12-pulse SCR unit (P type) rated at ±5000 V, 6000 A, that is typically used for fast ramping during acceleration and energy recovery. The other is a lower voltage 24 pulse unit (F type), rated at ±1000 V, 6000 A, that is used for flattop or slow ramping operation. The two stations are connected in series, with the magnet coils arranged to have a total resistance $R/2$ and a total inductance of $L/2$. The grounding of the power supply is done only in one place, in the middle of station 1 or 2, through a resistive network. With this grounding configuration, the maximum voltage to ground in the magnets does not exceed 2500 V. The magnets are tested at 3 kV to ground prior to each startup of the AGS MMPS after long maintenance periods.

2.3.2 Neutrino Factory Mode of Operation

To cycle the AGS ring to 24 GeV at 2.5 Hz and with a ramp time of 150 ms, the magnet peak current is 4300 A and the peak voltage is 25 kV. Figure 2.4 displays the magnet current and voltage of a 2.5 Hz cycle. The cycle includes a 100 ms flat-top for the six single-bunch extractions. The total average power dissipated in the AGS magnets is estimated to be 3.7 MW. To limit the AGS coil voltage to ground to 2.5 kV, the AGS magnets must be divided into three identical sections, each powered similarly to the present AGS except that now the magnet loads represent only 1/6 of the total resistance and inductance. Every section will be powered separately with its own feed to the ring magnets and an identical system of power supplies, as shown in Fig. 2.5. Bypass SCRs will be used across the four new P-type stations, to bypass these units during the flat-top, and ensure minimum ripple. Note that only station 1 will be grounded, as done presently. Although the average power will not be higher than now, the peak power required is approximately 110 MW, exceeding the 50 MW rating of the existing MG. A new MG, capable of providing 100 MW, would operate with 12 phases to limit, or even eliminate, the need for phase-shifting transformers, so that every power supply system would generate 24 pulses. The generator voltage will be about 15 kV line-to-line, to limit the generator current to less than 6000 A during pulsing. The generator will be rated at a slip frequency of 2.5 Hz.

Running the AGS at 2.5 Hz requires that the acceleration ramp period decreases from 0.5 s to 0.15 s. That is, the magnet current variation dI/dt is about 3.3 times larger than at present. Eddy current losses in the vacuum chamber are proportional to the square of (dI/dt), that is, they are 10 times larger. However, this is still significantly below the present ramp rate of the AGS Booster which does not require active cooling. The increased eddy currents give rise to increased sextupole fields during the ramp, and will add about 20 units of chromaticity. The present chromaticity sextupoles will be upgraded to correct this and the upgraded vacuum chamber will also mitigate the effects of the faster cycle.

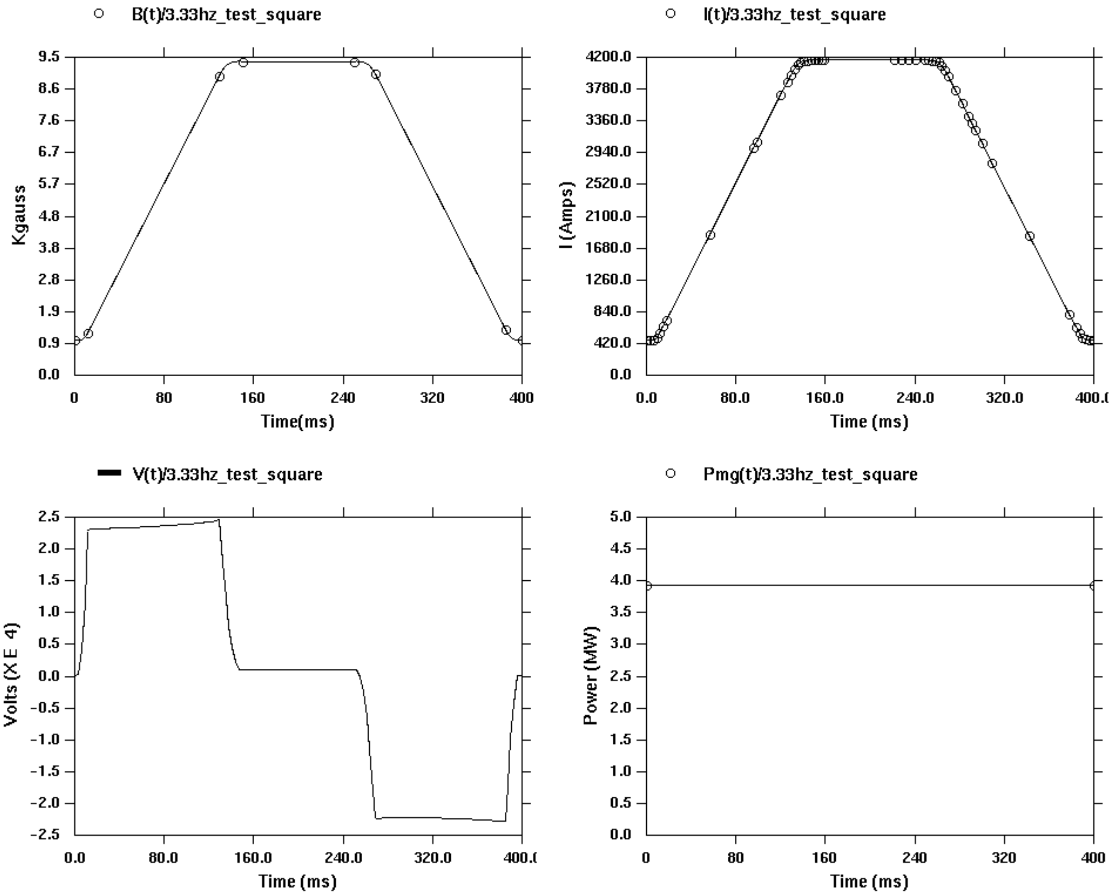

Figure 2.4: Current and voltage cycle for 2.5 Hz operation. Also shown are the AGS dipole field and average power.

2.4 AGS rf System Upgrade

At 2.5 Hz, the peak acceleration rate is three times the present value for the AGS. With 10 accelerating stations, each station will need to supply 270 kW peak power to the beam. The present power amplifier design, employing a 300 kW power tetrode will be suitable to drive the cavities and supply power to the beam. The number of power amplifiers will be doubled, so that each station will be driven by two amplifiers of the present design. This follows not so much from power considerations but from the necessity to supply 2.5 times the rf voltage.

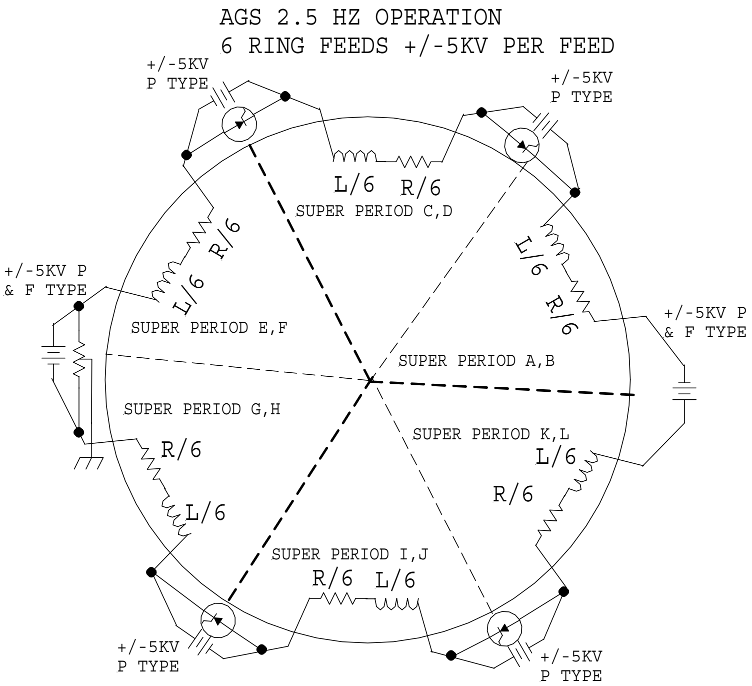

Figure 2.5: Schematic of power supply connections to the AGS magnets for 2.5-Hz operation.

An AGS rf station comprises four acceleration gaps surrounded by 0.35 m of ferrite stacks. The maximum voltage capability of a gap is not limited by the sparking threshold of the gap, but by the ability of the ferrite to supply the magnetic induction. When the AGS operates at 0.5 Hz, the gap voltage is 10 kV. At 2.5 Hz, we will need up to 25 kV per gap (roughly equal to the voltage from the same gap design used at the Booster, 22.5 kV) and this taxes the properties of the ferrite. Above a certain threshold value of B_{rf} (20 mT for AGS ferrite 4L2) a ferrite becomes unstable and excessively lossy. The gap voltage at this $B_{rf,max}$ is simply given by

$$V = -\frac{d}{dt} \int \omega B_{rf} dA = \omega a l B_{rf,max} \ln \frac{b}{a} \tag{2.1}$$

where ω is the rf angular frequency and the variables a, b, and l are the inner and outer radius and length of the ferrite stack, respectively.

The only free variable is ω. If we operate the rf system at the 24th harmonic of the revolution frequency (9 MHz) then the required voltage of 25 kV can be achieved with a safe value for $B_{rf,max}$ of 18 mT.

The next issue is the power dissipation in the ferrite and the thermal stress that is created by differential heating due to rf losses in the bulk of the material. We know from experience that below 300 mW/cm^3 the ferrites can be adequately cooled. The power density is also proportional to B_{rf}^2 and is given by

$$\frac{P}{V} = \frac{\omega B_{rf}^2}{2\mu_0(\mu Q)} \tag{2.2}$$

where μQ is the quality factor of the ferrite.

The μQ product is a characteristic of the ferrite material and depends on frequency and B_{rf}. We have data on ferrite 4M2 (used in the Booster and SNS) at 9 MHz and 20 mT where the power dissipation is 900 mW/cm^3. The details of the acceleration cycle determine the rf voltage program that is needed. For the cycle shown in Fig. 2.4, a peak voltage of 1 MV (40 gaps each with 25 kV) is needed but for only 20 ms during acceleration. An additional 100 ms operation at 1 MV is required for the bunch compression. Together, this is a duty factor of less than 0.3, giving an average power dissipation below our limit. We do not yet have data on the present AGS ferrite, 4L2 at 9 MHz. Characterizing 4L2 in this parameter regime is identified as an R&D issue, but we know that retrofitting the AGS cavities with 4M2 is a viable fallback option.

With the rf system operating on harmonic 24, there will be 24 rf buckets. However, we need all the beam in 6 bunches to extract to the production target. This can be arranged by filling 18 of the 24 buckets with 6 triplets of bunches, as shown in Fig. 2.6. The fast chopper in front of the linac can prepare this bunch pattern during the multi-turn injection as described in Section 2.1. The fast chopper fills the buckets to a longitudinal emittance of 1.2 eV-s which can be accelerated with 1 MV/turn of rf voltage, allowing some blowup during the acceleration cycle. At the end of the acceleration cycle, the triplets will be merged adiabatically into 6 single bunches [3] using separate 100 kV/turn harmonic 6 rf cavities. The final bunch emittance would be at least 5 eV-s per bunch after the 3:1 bunch merge.

With 100 kV/turn of the harmonic 6 rf system, the total bunch length will be 80 ns for a 5 eV-s bunch. The rf system will then be switched back to harmonic 24 and 1 MV/turn, where the bunch is now mismatched. By strongly modulating the rf voltage with a frequency close to twice the synchrotron frequency of 512 Hz, the tumbling bunch can be kept from decohering. Also, the quadrupole oscillation frequency of the bunch can be controlled so that the bunch length is minimal at the times of the 6 bunch extractions [4]. The minimal total bunch length is about 15 ns, or 3 ns rms. This is about half of the

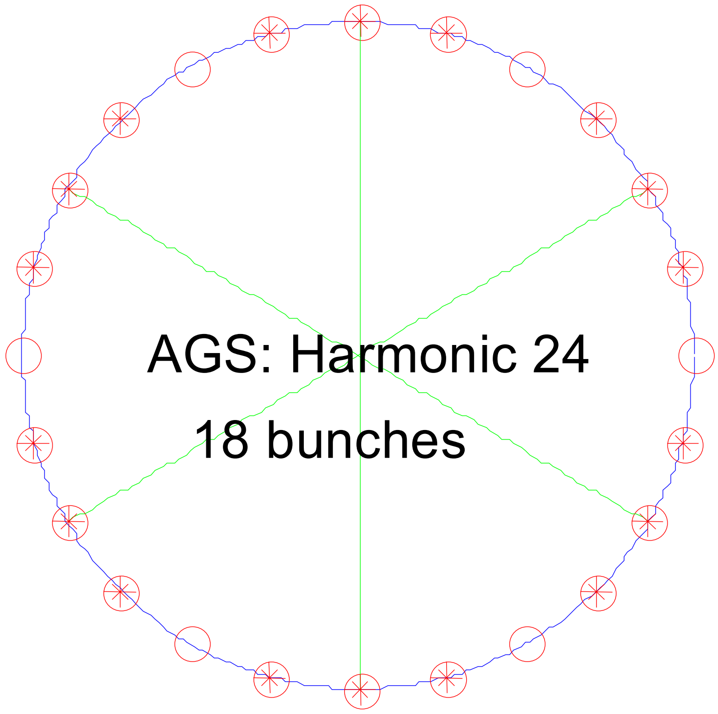

Figure 2.6: Bunch pattern for using harmonic 24 to create 6 bunches.

matched total bunch length of 32 ns.

2.5 Conclusions

The scheme for a 1-MW proton driver based on the AGS with upgraded injection is feasible. Indeed, the AGS beam intensity is only modestly higher than during the present high-intensity proton operation and, therefore, beam instability is not expected to be a problem during acceleration. Beam stability during the bunch compression is marginal, and requires some care to reach the 3 ns bunch length specification.

Bibliography

[1] J. Wei *et al.*, *Low-loss design for the high-intensity accumulator ring of the Spallation Neutron Source*, Phys. Rev. ST Accel. Beams 3, 080101 (2000).

[2] A. Ruggiero, *Design Considerations on a Proton Superconducting Linac*, BNL Internal Report 62312, 1995.

[3] R. Garoby, *Bunch Merging and Splitting Techniques in the Injectors for High Energy Hadron Colliders*, CERN/PS 98-048.

[4] M. Bai *et al.*, *Adiabatic excitation of longitudinal bunch shape oscillations*, Phys. Rev. ST Accel. Beams 3, 064001, 2000.

Chapter 3

Target System and Support Facility

3.1 Introduction

3.1.1 Overview

The role of the target system at a Neutrino Factory is to generate a maximal number of pions with an intense proton beam and then capture and guide them into a channel where the decay muons can be bunched, cooled, accelerated and stored in a ring from which the neutrinos emanate upon decay of the muons.

In this Study, the proton beam energy is 24 GeV, and the baseline beam power is 1 MW, upgradable to 4 MW.

The spectrum of pions from GeV protons interacting with a target peaks at a total momentum near 250 MeV/c, as shown in Fig. 3.1 [1], and has an average transverse momentum $\langle p_\perp \rangle = 150$ MeV/c. Thus, the majority of pions are produced at relatively large angles to the proton beam, and are not efficiently captured by devices placed downstream of the target. For maximal efficiency, the pion capture system must surround the target.

The capture mechanism considered here is a solenoidal magnetic field channel starting at 20 T near the target, then falling adiabatically to 1.25 T downstream (≈ 18 m) from the target. This configuration creates a kind of magnetic bottle whose mouth is the muon phase rotation system considered in Chapter 4. In a solenoidal field the pion (and muon) trajectories are helices, with adiabatic invariants BR^2 and $p_\perp^2/B$. We propose to capture pions with $p_\perp \leq 225$ MeV/c, for which an aperture of 7.5 cm is required at 20 T. After the adiabatic reduction of the solenoid field by a factor of 16, to 1.25 T, the captured pions are contained within an aperture of 30 cm and have a maximum $p_\perp$ of 67.5 MeV/c.

For proton beam energies above about 8 GeV, the pion yield per proton increases

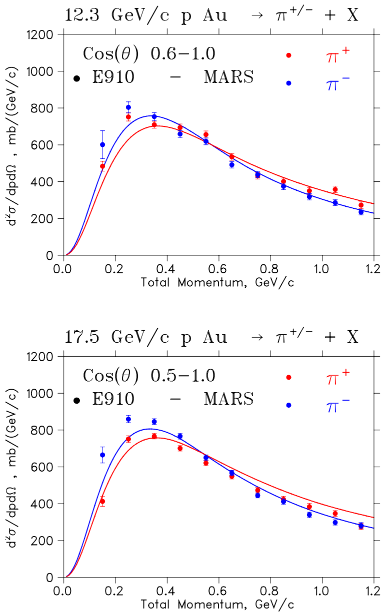

Figure 3.1: Momentum spectra for pion production by 12.3 and 17.5 GeV protons on a gold target, from BNL E910 and from MARS calculations.

with the atomic number of the target, as shown in Fig. 3.2 from a MARS calculation [2]. For 24 GeV protons, a high-Z target is distinctly superior in yield [3].

As the pions to be captured emerge from the target at large angles to the beam, and follow helical paths that may intersect the target at more than one point, it is advantageous for the target to be in the form of a narrow rod, tilted at a small angle to the magnetic axis. As shown in Fig. 3.3, suitable parameters for a mercury target in a 20 T solenoid are a tilt angle of 100 mrad and a target radius of 5 mm.

In a 1 MW beam with 15 pulses per second, each pulse contains 60 kJ energy, of which about 10% is deposited in a two-interaction-length high-Z target. The energy deposited in the target will heat the target to a temperature of several hundred °C and generate substantial shock pressures. A low-Z target, as proposed in Study-I [4], is expected to survive these shocks for a significant time with a 1.5 MW beam, but is predicted to have a pion production yield only half that of high-Z targets, such as Inconel, or mercury. It would also be expected to get too hot with a 4 MW beam, which we consider to be a likely upgrade. A liquid-mercury-jet target, too, will be disrupted by the heating from the beam, but such disruption is not expected to have significant adverse consequences,

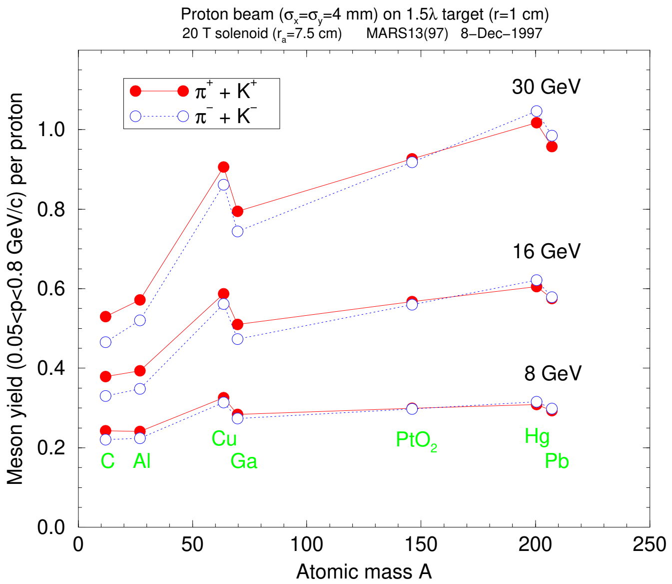

Figure 3.2: Pion yield *vs.* atomic mass number of the target at three proton beam energies.

even at 4 MW. For this reason, a mercury-jet target has been selected as the baseline for this study. If there were advantages to doing so, liquids such as a molten lead/tin eutectic, or other alloys, could be used. A graphite target (as considered in Study-I) would be available as a backup, though it would reduce the neutrino intensity by a factor of 1.9 (see [4], Section 3.5).

In this Study, the beam with rms radius σ_r, at a vertical angle θ_p, intersects the mercury jet of radius r_o and vertical angle θ_{Hg} at an angle $\theta_{\mathrm{crossing}}$. The forward velocity of the jet is v_o.The nozzle is at z_{nozzle} with respect to the intersection of the beam and jet center lines. The interval between pulses is t. The Study-II baseline values of these parameters are given in Table 3.1.

An alternative target concept based on a rotating Inconel band is discussed in [5].

3.1.2 Target System Layout

The target system consists of the following components:

- Target enclosure vessel

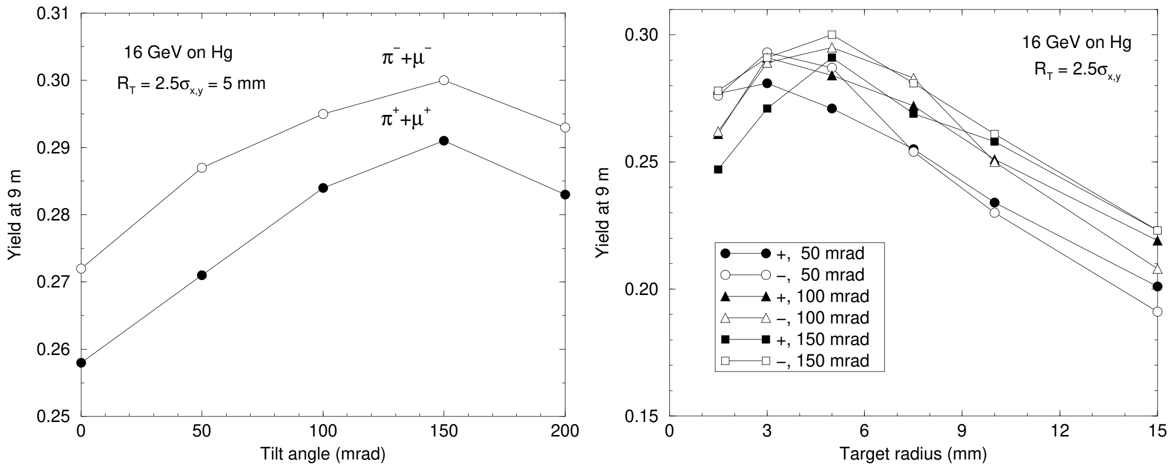

Figure 3.3: Pion yield from Hg targets *vs.* tilt angle angle between the target/beam axis and the solenoid axis (left) and *vs.* the radius of the target (right).

- Proton beam window
- Mercury jet, including its supply line within the enclosure vessel and the jet nozzle
- Magnet coils
- Internal shielding
- Mercury collection pool/dump and entrance baffle
- Downstream window

The overall layout of the target area is sketched in Fig. 3.4, with a detail of the target region shown at the bottom of Fig. 3.5. The intersection of the beam and jet is set at 45 cm from the nozzle. The distribution of the resulting interactions as a function of z, shown at the top of Fig. 3.5, starts about 15 cm from the nozzle.

It will be assumed here that, after a pulse, all the mercury outside of the nozzle is dispersed. This is predicted using the finite element analysis code FronTier [6], as illustrated in Fig. 3.6. At the arrival time of a subsequent bunch, the newly established jet will extend a distance $\Delta z = v_o\, t = 0.6$ m from the nozzle. Only 2.5% of the interactions occur beyond this location, so the disposition of the disturbed jet beyond this point has little effect on production.

Table 3.1: Proton beam and mercury jet geometric parameters.

Beam σ_r (mm)	1.5
Beam angle to magnet axis θ_p (mrad)	-67
Jet material	mercury
Velocity v_o (m/s)	30
Jet radius r_o (mm)	5
Jet angle to magnet axis θ_{Hg} (mrad)	-100
Crossing angle $\theta_{\mathrm{crossing}}$ (mrad)	33
t between bunches (ms)	20
z_{nozzle} (cm)	-60

The distance over which the jet must propagate without serious magnetic disruption is from the nozzle to a point 0.6 m downstream, defined as $z = 0$ in the coordinate system used here. In order to minimize the field nonuniformity over this length, the magnetic center (approximately the point of maximum B_z) is placed at the center of this length. *i.e.*, the magnetic center is at $z_o = -30$ cm. The intersection of the jet and beam is then at $z_{\mathrm{intersection}} = -15$ cm, and the nozzle is at $z_{\mathrm{nozzle}} = -60$ cm.

3.1.3 Capture and Matching Solenoids

The target is located in a 20 T solenoid to contain transverse momenta of outcoming pions up to 225 MeV/c, a large fraction of all pions produced. The central region of high field is designed to be uniform, drooping only 5% at its end, to limit the magnetic field gradients that might disrupt the mercury jet. The solenoid is a hybrid, with copper inner coils and superconducting outer coils. It is similar to that discussed in Feasibility Study-I [4]. However, here we use hollow copper conductor for the inner coils, rather than a Bitter-style magnet. This choice is aimed at achieving a magnet life over 40 years (compared with 6 months in Study-I), and avoiding possible corrosion problems with the highly irradiated wet insulation in a Bitter magnet. The main disadvantage of this choice is that it consumes more power and requires a greater field contribution from the SC coils..

Downstream of the 20 T magnet, additional superconducting coils taper the axial field down smoothly to 1.25 T over a distance of approximately 18 m, according to the form,

$$B(z) \approx \frac{B(0)\ \mathrm{T}}{1 + k\ z}. \tag{3.1}$$

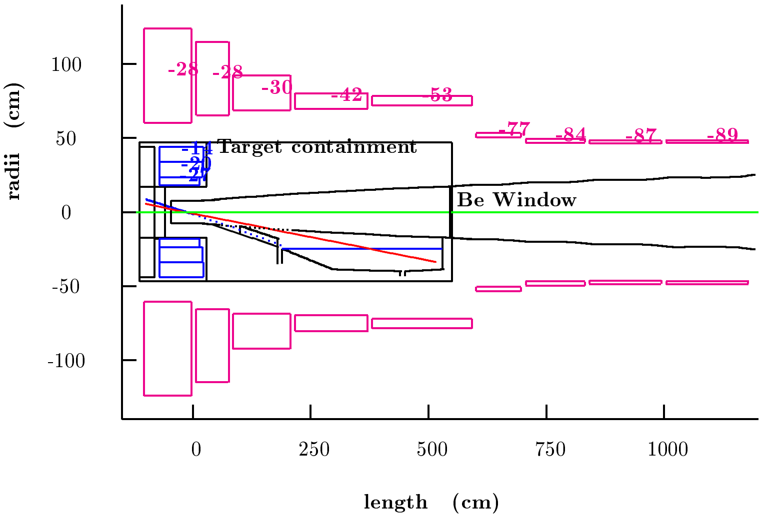

Figure 3.4: Target, capture solenoids and mercury containment.

Dimensions of the coils and the upstream iron pole are given in Table 3.2. The coils are shown in Fig. 3.4, and axial field profiles, over two scales of z, are shown in Fig. 3.8.

3.1.4 Magnetic Disruption of the Mercury Jet

As the jet moves through the magnet, eddy currents are induced in the mercury, and the resulting $\mathbf{J} \times \mathbf{B}$ force distorts the jet in various ways [7, 8]. Assuming a Gaussian distribution of B_z' *vs.* z' with a maximum value of B_o, where the z' axis is along the jet, jet conductivity κ, density ρ, and surface tension T_{surface} as given in Table 3.3, perturbation calculations [7] show that, over the extent of the jet from -0.6 to 0.0 m,

- The maximum axial field deviations are ± 1.1 T, *i.e.*, $\pm 5\%$.

- The axial pressure difference has a minimum of -0.25 atm. Thus, if the jet is operating in a gas (He or Ar) at a pressure greater than or equal to 0.25 atm, negative pressures will be avoided, and there will be no tendency to cavitate prior to the arrival of the beam.

- The maximum axial velocity change of the jet, 0.06 m/s, is very small compared with the average jet velocity, 30 m/s.

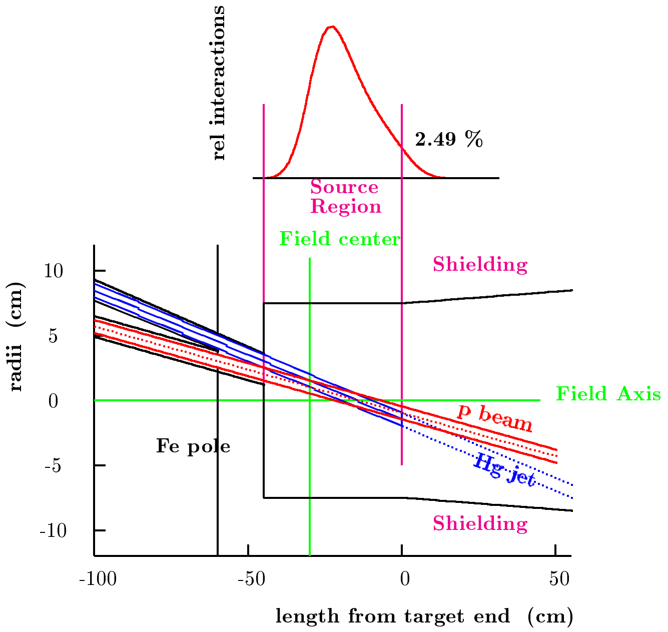

Figure 3.5: Top: Distribution of beam-target interactions as a function of z. Bottom: Layout of the target area.

- The maximum transverse velocity, 0.4 m/s, induced by shear forces is also small compared with the average jet velocity: $0.4/30 \approx 1.3\%$.
- The deflection of the jet, 5 μm, is very small.
- The transverse distortion of the jet (change in width relative to average width) is approximately 0.4% ignoring surface tension, and less than 0.2% when surface tension is included.

These disruptions are all relatively small, and should cause no problems for the beam-jet interaction.

Beyond the target region ($z > 0$), the magnetic effects are larger, but still not sufficient to break up the jet. Here, the maximum shear is about 5 m/s, and the transverse distortion 20%. However, since the beam-jet interaction will disperse the jet, a more significant effect thereafter is magnetic damping of the dispersal.

More detailed magnetohydrodynamic calculations are under way [6] using the FronTier 3-D finite element analysis code that includes liquid-gas boundaries and phase tran-

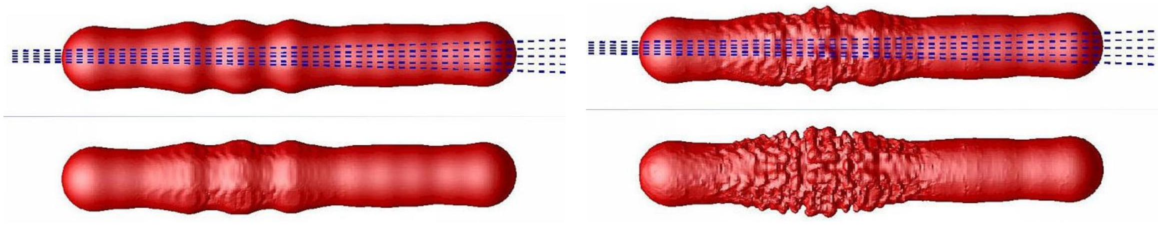

Figure 3.6: Beam-induced breakup of a mercury jet, as simulated by the FronTier code. The images are for 10 μs time steps.

sitions. Preliminary results are shown in Fig. 3.9.

A magnetic field also provides a desirable damping of oscillations of a mercury jet, with a time constant of roughly 100 μs. Figure 3.10 shows this effect in a recent study by a CERN/Grenoble collaboration as part of their Neutrino Factory R&D program.

3.1.5 Mercury Containment

Figure 3.4 also shows the concepts for the mercury containment vessel and the mercury pool beam dump, and Fig. 3.11 shows more detail. The containment vessel and dump are to be replacable, for which the hollow conductor coils must also be removed.

The mercury jet, or what remains of it, falls under gravity, and thus further separates from the beam axis. A system of grids or baffles slows the mercury spray before it joins the beam dump mercury pool. The outflow pipe is 10 cm in diameter to accommodate the considerable rate of filling from the jet. The drain would be opened only when emptying the containment vessel for its removal.

3.1.6 Target System Support Facility

The Target Support Facility consists of the target region and decay channel, a crane hall over the length of the facility, a maintenance cell at the ground floor elevation for handling magnet components, a hot cell at the tunnel level for mercury target system components, and various remote-handling equipment used for maintenance tasks. The facility is bounded by the proton beam window at the upstream end and the first induction linear accelerator at the downstream end. It contains the equipment for the mercury-jet target, high-field resistive and superconducting solenoids, low-field superconducting solenoids, water-cooled shielding to limit radiation dose and neutron heating to the coils, shielding to protect personnel and the environment, and a 50-ton crane that

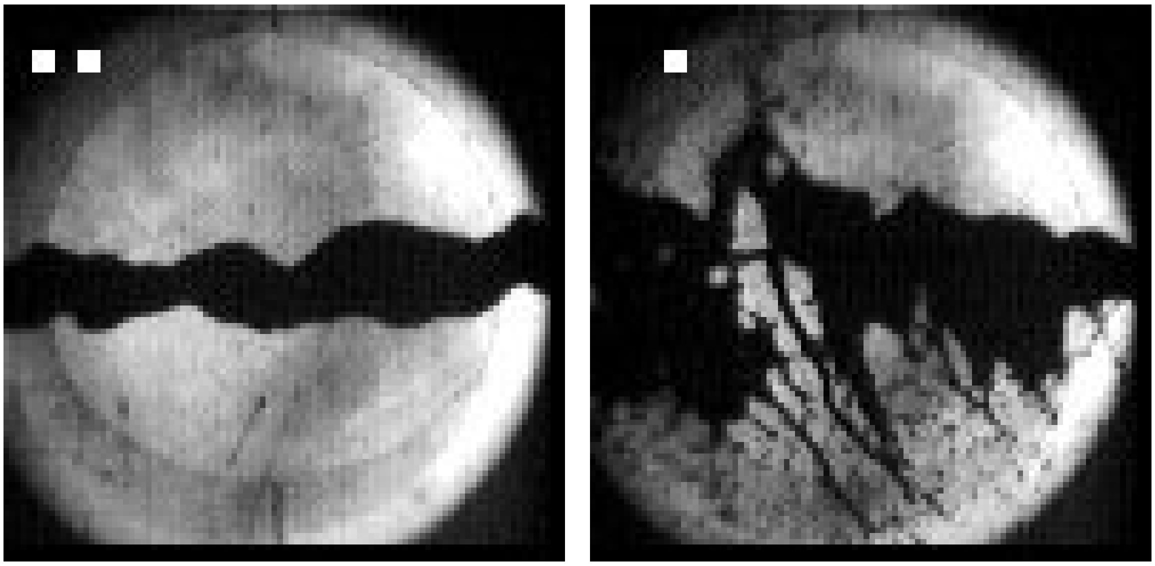

Figure 3.7: Breakup of a 1-cm-diameter mercury jet in a 24-GeV proton beam (BNL E951).

is used for the initial assembly and installation of major components and for subsequent maintenance activities. The target support facility is 12 m wide, and approximately 50 m long. Figure 3.12 is a view of the overall facility looking downstream.

The remainder of this section presents a conceptual design for the target caputure magnet, the mercury-jet target system, the proton-beam absorber, and the facility for the target/capture region.

3.2 Calculations of Pion Yield and Radiation Dose Using MARS

Detailed MARS14(2000) [9, 10] simulations have been performed for the optimized Study-II target-capture system configuration. A 24-GeV kinetic energy proton beam ($\sigma_x = \sigma_y =$ 1.5 mm, $\sigma_z = 3$ ns, 67 mrad) interacts with a 5 mm radius mercury jet tilted by 100 mrad, which is ejected from the nozzle at $z = -60$ cm, crosses the z-axis at $z = 0$ cm, and hits a mercury pool at $z = 220$ cm, $x = -25$ cm.

Results [11] are based on two runs of 400,000 protons on target each, including energy

Table 3.2: Solenoid coil geometric parameters.

	z (m)	Gap (m)	Δz (m)	R_i (m)	ΔR (m)	I/A (A/mm^2)	nI (A)	nIl (A-m)
Fe	0.980	0.980	0.108	0.000	0.313	0.00	0.00	0.00
	1.088	0.000	0.312	0.000	0.168	0.00	0.00	0.00
Cu coils	1.288	−0.112	0.749	0.178	0.054	24.37	0.98	1.26
	1.288	−0.749	0.877	0.231	0.122	19.07	2.04	3.74
	1.288	−0.877	1.073	0.353	0.137	14.87	2.18	5.78
SC coils	0.747	−1.614	1.781	0.636	0.642	23.39	26.77	160.95
	2.628	0.100	0.729	0.686	0.325	25.48	6.04	32.23
	3.457	0.100	0.999	0.776	0.212	29.73	6.29	34.86
	4.556	0.100	1.550	0.776	0.107	38.26	6.36	33.15
	6.206	0.100	1.859	0.776	0.066	49.39	6.02	30.59
	8.000	−0.065	0.103	0.416	0.051	68.32	0.36	1.00
	8.275	0.172	2.728	0.422	0.029	69.27	5.42	14.88
	11.053	0.050	1.749	0.422	0.023	75.62	3.00	8.18
	12.852	0.050	1.750	0.422	0.019	77.37	2.61	7.09
	14.652	0.050	1.749	0.422	0.017	78.78	2.30	6.22
	16.451	0.050	1.750	0.422	0.015	79.90	2.07	5.59
	18.251	0.050	2.366	0.422	0.013	-0.85	2.53	6.80

deposition in the mercury jet, the yield of captured pions, fluxes of charged and neutral particles and the consequent radiation dose in the materials of the target system. For example, the total power dissipation in the jet at $-60 < z < 0$ cm is 100 kW for 6 bunches at 2.5 Hz and 1.7×10^{13} protons per bunch. Preliminary results were given in Refs. [4, 3].

As noted earlier, to be conservative, we estimate radiation effects based on 2×10^7 s per operating year, though we estimate physics production based on a standard 1×10^7 s year.

3.2.1 Captured π/μ Beam *vs.* Target and Beam Parameters

Realistic 3-D geometry based on Fig. 3.4, together with material and magnetic field distributions based on the solenoid magnet design optimization, have been implemented into MARS. The level of detail in the model is illustrated by Fig. 3.13, which shows a

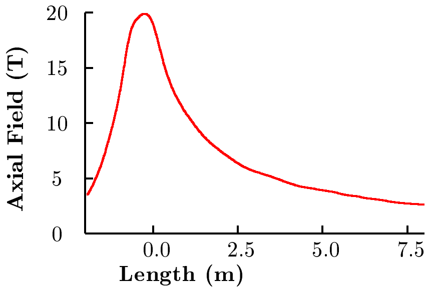

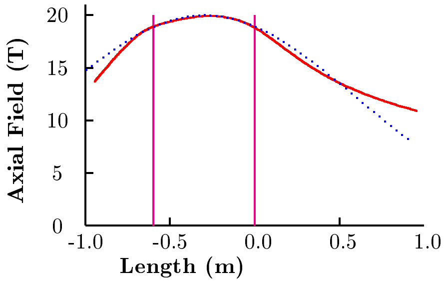

Figure 3.8: The axial magnetic field (solid lines) *vs.* length along the axis, on two scales. The dotted line is a Gaussian fit, with $\sigma_z = 0.8$ m, to the field in the jet region.

Table 3.3: Relevant properties of the mercury jet.

B_o (T)	20
σ_z' (m)	0.8
κ (Ω-m)	10^6
ρ (kg/m^3)	1.35×10^5
T_{surface} (N/m)	0.456

transverse section at $z = 5.2$ m that includes the mercury pool that serves as the proton beam absorber.

The use of a 3-D magnetic field map results in the reduction of the π/μ-yield in the decay channel by about 7% for C and by 10-14% for Hg targets, compared with the assumption that $B_z(r, z)$ obeys Eq. (3.1).

Both graphite (C) and mercury (Hg) tilted targets were studied. A two-interaction-length target (80 cm for C of radius $R_T = 7.5$ mm, and 30 cm for Hg of $R_T = 5$ mm) is found to be optimal in most cases, and we keep $R_T \geq 2.5\ \sigma_{x,y}$, where $\sigma_{x,y}$ are the beam rms spot sizes.

Results of a detailed optimization of the particle yield Y are presented below, in most cases for a sum of the numbers of π and μ of a given sign and energy interval at a fixed distance $z = 9$ m from the target. For proton energies E_p from a few GeV to about 30 GeV, the shape of the low-momentum spectrum of such a sum is energy-independent and peaks around 250 MeV/c momentum (145 MeV kinetic energy), as illustrated in Fig. 3.1. Moreover, the sum is practically independent of z at $z \geq 9$ m–confirming

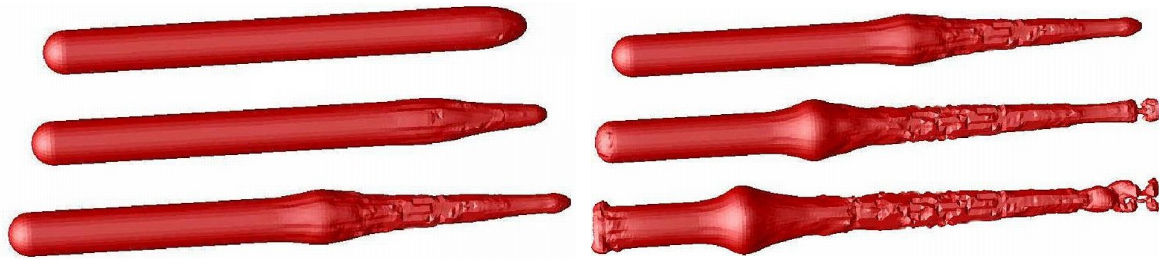

Figure 3.9: Disruption of a mercury jet on entering and exiting a solenoid magnet, as simulated by the FronTier code.

a good matching and capturing–with a growing number of muons and proportionately decreasing number of pions along the decay channel. For the given parameters, the π/μ kinetic energy interval of 30 MeV $\leq E \leq$ 230 MeV, around the spectrum maximum is considered as the one to be captured by the downstream phase rotation system.

The yield Y grows with the proton energy E_p, is almost material-independent at low energies and grows with target A at high energies, being almost a factor of two higher for Hg than for C at E_p=16-30 GeV (Fig. 3.2). To avoid absorption of spiraling pions by target material, the target and beam are tilted by an angle α with respect to the solenoid axis. The yield is higher by 10-30% for the tilted target. For a short Hg target, α=150 mrad seems to be the optimum, as shown in Fig. 3.3 (left). The maximum yield occurs at target radius $R_T = 5$ mm for Hg with $R_T = 2.5\sigma_{x,y}$ (R_T=7.5 mm and $R_T = 3.5\sigma_{x,y}$ for C), as shown in Figs. 3.3 (right) and 3.14 (left). The yield with mercury could be further increased by increasing the target radius to gain secondary pion production, but the target heating would also be increased significantly, as shown in Fig. 3.14 (right).

Figure 3.15 shows longitudinal profiles of the energy density deposited in the mercury jet target in three radial regions. The center of the proton beam enters the jet at $z = -45$ cm, and the energy deposition peaks about 12 cm downstream of this point, at $z = -33$ cm.

3.2.2 Particle Fluxes, Power Density and Radiation Dose

Figure 3.16 shows the radiation per 2×10^7 s in the vicinity of the target. Table 3.4 gives the maximum doses per year and expected lifetime for various components (Note that for assessing radiation effects we take a larger operating year to be conservative).

Figures 3.17 and 3.18 illustrate charged and neutral particle fluxes, and the resulting

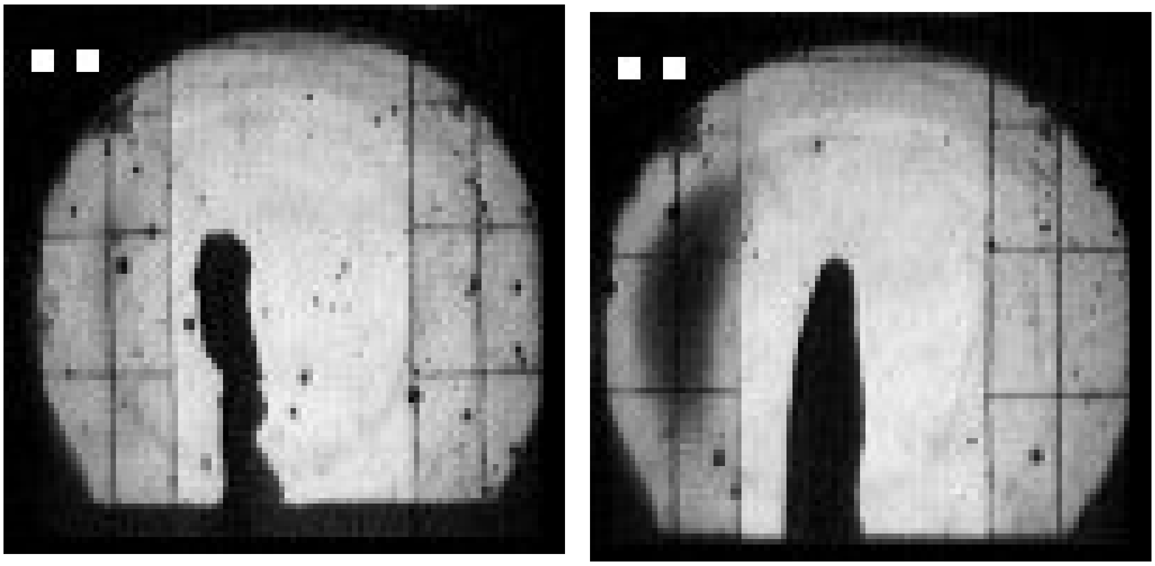

Figure 3.10: Magnetic damping of oscillations of a 1-cm-diameter, 4-m/s mercury jet in a 13-T solenoid magnet. Left: field off; right: field on.

power deposition and radiation dose, as a function of radius at the downstream end of the target. Figure 3.19 shows the power density and radiation dose in the beryllium window at $z = 6.1$ m.

The neutron flux in the target system is shown in Fig. 3.20, and the absorber radiation dose is shown in Figs. 3.16 and 3.21. Even at the end of the decay channel, at $z = 36$ m, the radiation levels remain high.

3.3 Calculations of Energy Deposition and Activation Using MCNPX

The energy deposition in, activation of, and radiation leakage from the target module have been estimated using the Monte Carlo code MCNPX [12]. This is a combination of the particle transport code MCNP-4B [13] and the high-energy transport code LAHET-2.8 [14]. This code employs a combinatorial surface/cell specification of the geometry, which permits modeling of the problem configuration with minimal approximations.

The MCNPX code has similar capabilities to those of the MARS code, although

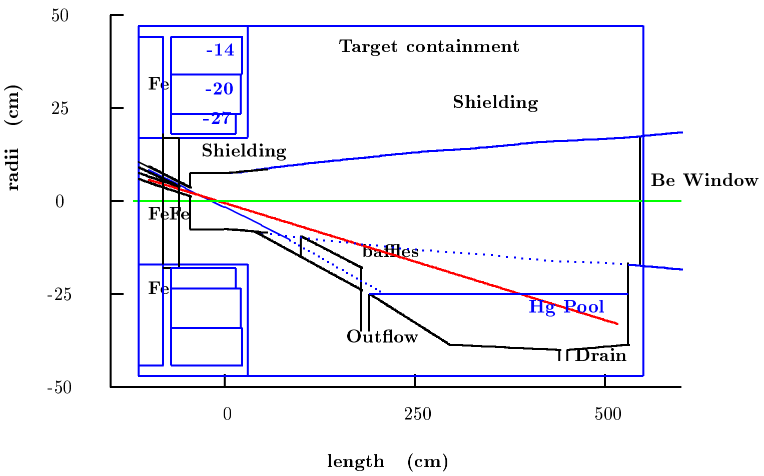

Figure 3.11: Beam dump, shielding and mercury containment detail.

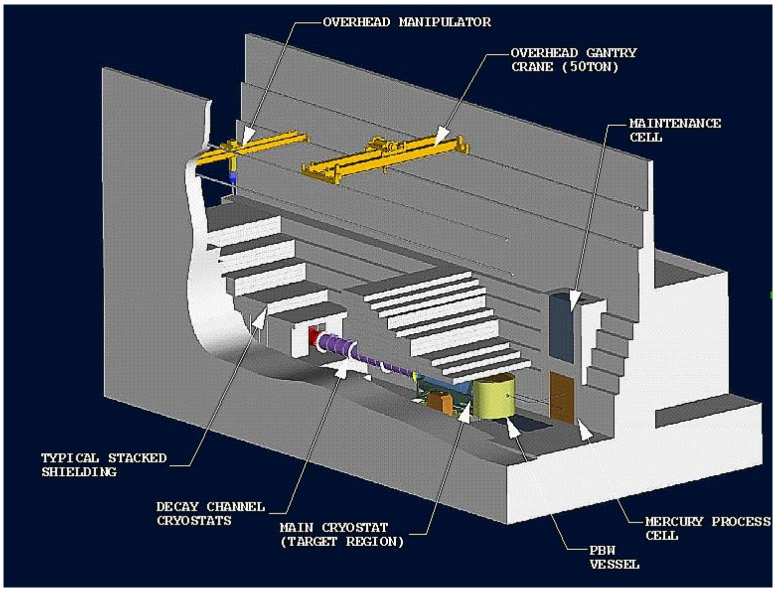

Figure 3.12: The overall target support facility.

MARS describes in great details the effects of magnetic field, capability that MCNPX is lacking. In addition, there are subtle differences in the way the geometry is represented

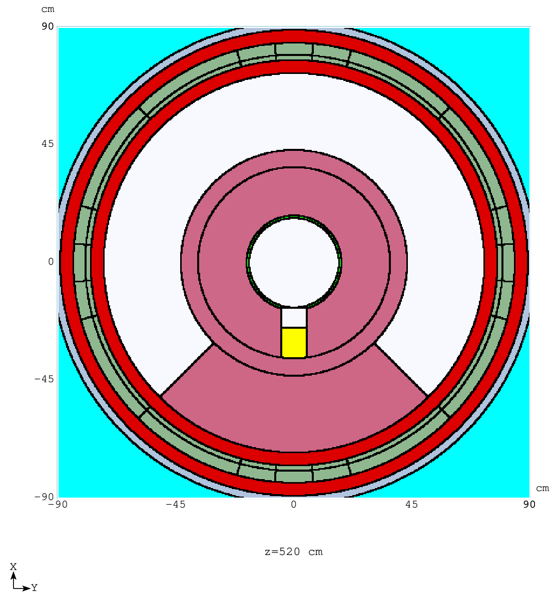

Figure 3.13: Transverse section of the target system at $z = 5.2$ m, showing the mercury pool that serves as the proton beam absorber.

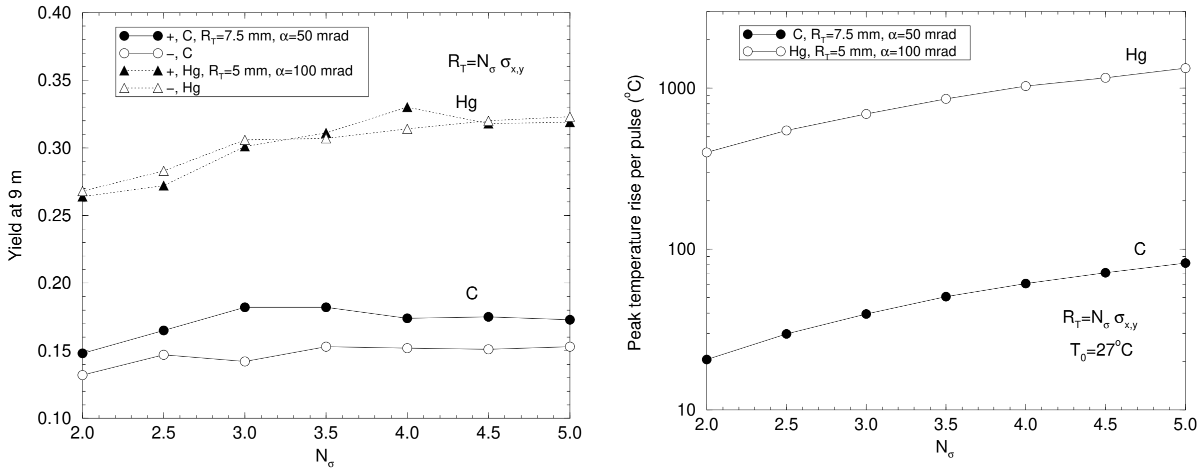

Figure 3.14: Pion yield (left) and maximum instantaneous temperature rise (right) as a function of the ratio of target radius to RMS beam spot size.

and nuclear data models are linked together, and the manner in which the activation

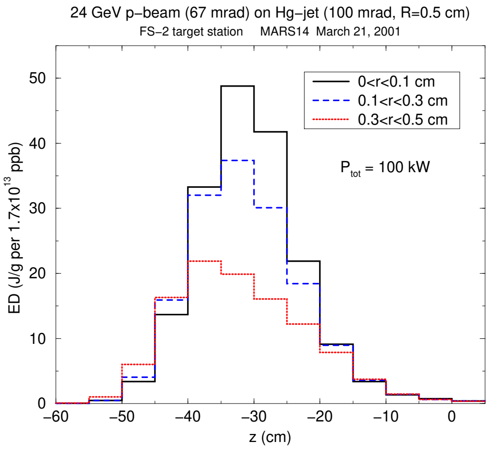

Figure 3.15: Longitudinal profiles of the energy density deposited in the mercury jet target in three radial regions.

and energy deposition analyses are carried out. Thus, the use of both codes provides important cross checks.

An appropriate model of the target module was created that includes the primary mercury jet, three surrounding magnets, the downstream shield structure, and a mercury beam stop. Two representative longitudinal and transverse sections through this model are shown in Figs. 3.22 and 3.23.

3.3.1 Energy Deposition

The energy deposition resulting from protons, neutrons, and photons is summarized in Table 3.5 in terms of MeV/gm-proton, as well as power density (W/cm^3) and total power per cell, assuming a 1-MW, 24-GeV proton beam.

The bulk of the beam power is deposited in the surrounding coaxial shield, the mercury jet target, and the coaxial shield surrounding the primary target (683 kW out of 1 MW). The total power deposited in the target module cells is 715 kW. The remaining 285 kW largely appears as radiation leakage out of the target system.

The two shield volumes are actively cooled by flowing water, and the above heat input sets the flow rate and the size of the heat exchanger. The iron plug immediately upstream of the primary target also requires active cooling, since it has a relatively high heat input. The magnets, of course, will be cooled actively. Finally, the mercury will be a flowing

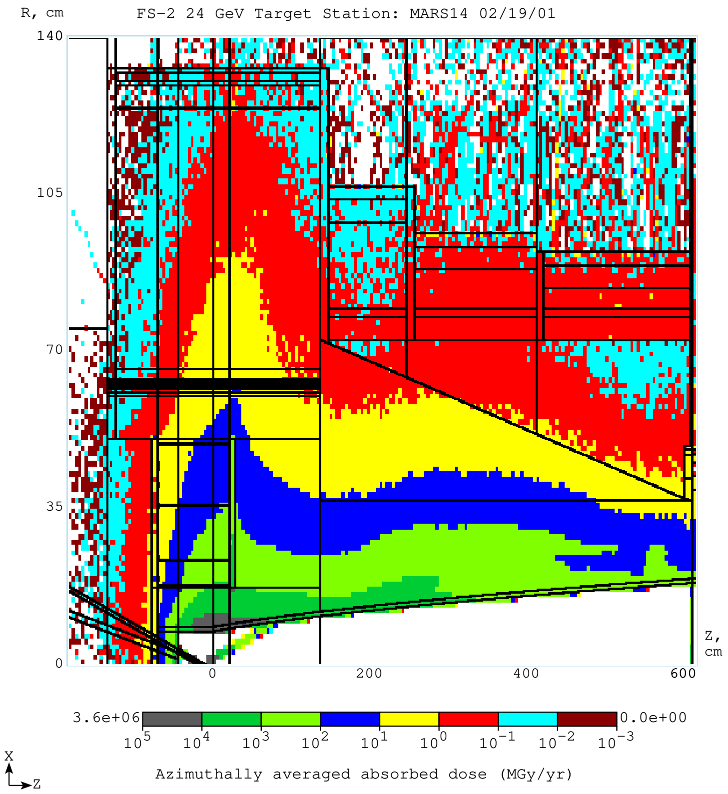

Figure 3.16: Absorbed radiation dose per year of 2×10^7 s and a 1 MW proton beam in the target system for $-2 < z < 6$ m and $r < 1.4$ m.

system, and the heat input determines the required capacity of the heat exchanger.

3.3.2 Activation Analysis

The activation analysis is based on the MCNPX estimates of neutron fluxes and spallation product masses. The neutron fluxes are used to determine cell-dependent activation cross sections, and the spallation mass distributions are used to determine the distribution of possible isotopes produced during the spallation reactions. The mass distributions are a function of cell type and position within the target module, since cells with the same composition in different positions are subject to different particle fluxes.

The time-dependent buildup of activation is based on the assumption of 100 days of

Table 3.4: Radiation doses and lifetimes of some components of the target system.

Component	Radius (cm)	Dose/yr (Grays/2×10^7 s)	Max allowed Dose (Grays)	1 MW Life (years)	4 MW life (years)
Inner shielding	7.5	2×10^{11}	10^{12}	5	1.25
Hg containment	18	2×10^9	10^{11}	50	12
Hollow conductor	18	1×10^9	10^{11}	100	25
Superconducting coil	65	6×10^6	10^8	16	4

Table 3.5: Energy deposition by cell in the target system. (x) stands for $\times 10^x$.

Cell Number	Description	Energy Deposition (Mev/gm-p)	(W/cm^3)	(kW)
8	Surrounding shield	3.11(-4)	0.16	589
12	Primary mercury target	2.62	1.48(3)	53.1
2	Coaxial shield around target	1.55(-3)	0.82	40.4
3	Iron plug behind target	1.21(-3)	0.39	0.99
81	First coaxial magnet	2.61(-4)	0.08	3.54
82	Second coaxial magnet	1.04(-4)	0.03	4.43
83	Third coaxial magnet	2.38(-5)	0.01	1.70
91	Mercury beam stop	6.04(-4)	0.34	1.07
92	Mercury beam stop	8.64(-4)	0.49	2.55
93	Mercury beam stop	1.13(-3)	0.64	4.01
94	Mercury beam stop	4.80(-4)	0.27	1.20
95	Mercury beam stop	4.42(-4)	0.25	1.57
96	Mercury beam stop	4.89(-4)	0.28	1.74
97	Mercury beam stop	5.34(-4)	0.30	1.89
98	Mercury beam stop	6.87(-4)	0.39	2.44
99	Mercury beam stop	6.61(-4)	0.37	2.35
100	Mercury beam stop	4.86(-4)	0.27	1.73
101	Mercury beam stop	3.65(-4)	0.21	0.93

operation at 1 MW with 24 GeV protons. To estimate the activation under different conditions, the results can be scaled by the number of MW-days.

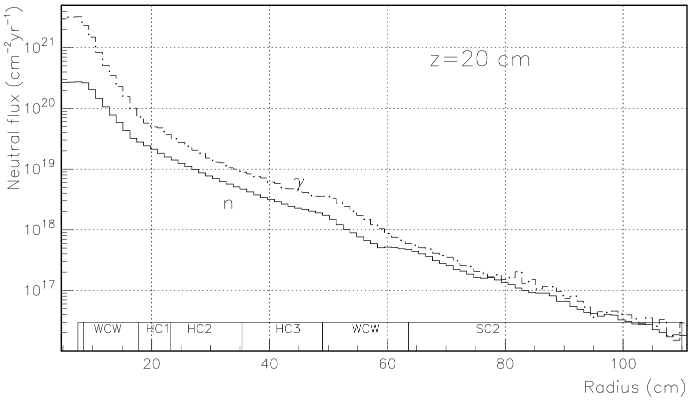

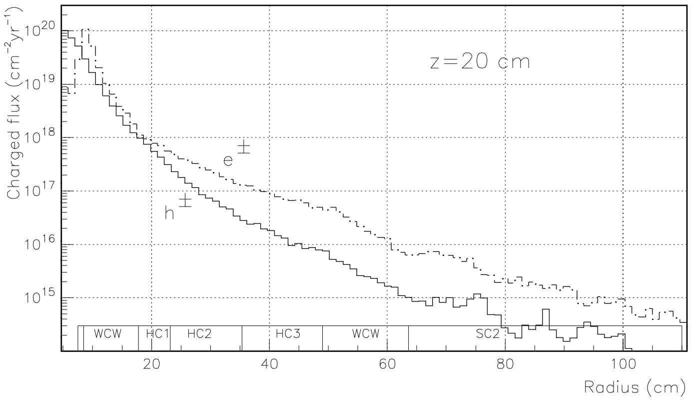

Figure 3.17: Flux of neutral (top) and charged (bottom) particles as a function of radius at the downstream end of the target.

Following operation of the machine for 100 days, the activity after 4 hrs, 1 day, 7 days, and 30 days of cooling has also been estimated. In addition, the total gamma-ray activity in each cell has been calculated, and used as input to a secondary calculation that determined the leakage of photons, and thus dose outside of the target module.

Tables 3.6-3.10 list the total neutron flux, activation, and gamma-ray intensity in various cells.

The values in Table 3.6 are the volume-averaged total neutron fluxes. The actual

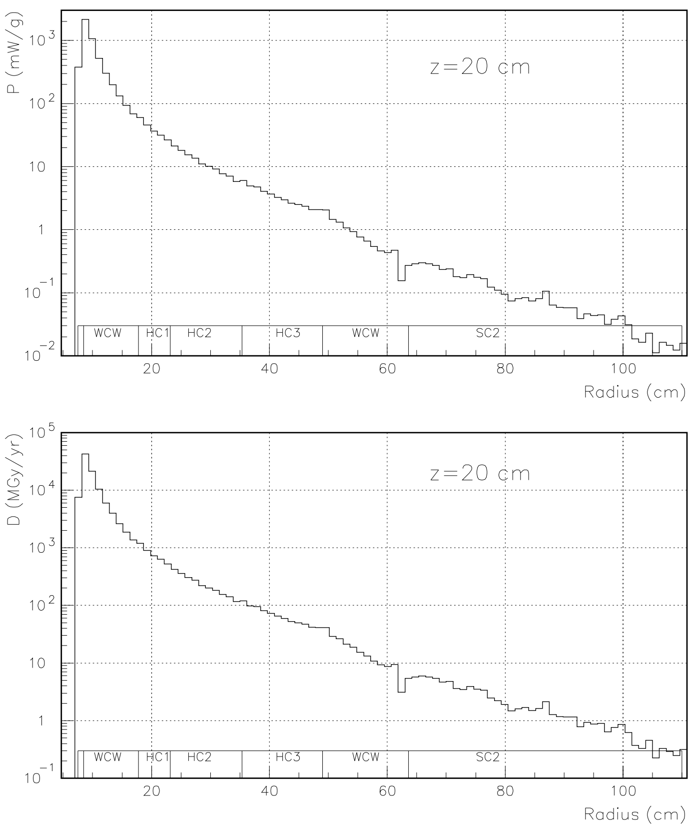

Figure 3.18: Power density (top) and total radiation dose (bottom) due to secondary particles as a function of radius at the downstream end of the target.

energy spectrum for each volume was used to determine the activation cross sections. Table 3.7 shows the resulting activation following 100 days of operation, and for selected time frames following machine shutdown.

The results in Table 3.7 are integral activation values for each of the cells. Each value is composed of contributions from hundreds of radioactive isotopes, which decay at different rates. Immediately following shutdown, the number of contributing isotopes is

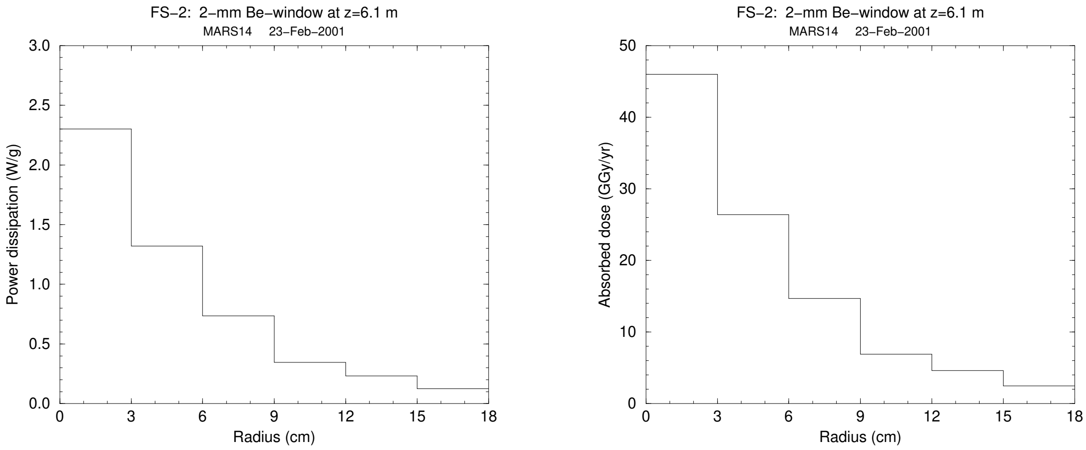

Figure 3.19: Power density (left) and absorbed radiation dose (right) in the beryllium window at $z = 6.1$ m.

extremely large. However, following 30 days of decay time, only the longest lived isotopes contribute, and generally there are only a limited number of isotopes at that stage. Two examples are presented in Tables 3.8 and 3.9, which list the major contributors to the activity after 30 days of decay time in a mercury pool cell (number 92), and a shield cell (number 8).

The major contributions to the activation of a mercury cell come from the isotopes closest to the target nucleus (mercury). The dominant contributor is an isotope of mercury, but there are significant contributions from lighter isotopes. Of particular interest are those that are, or could potentially be, volatile under operating conditions (Xe, Cs, Rb, *etc.*). Attention must also be paid to those elements that could pose material compatibility concerns when they come in contact with the structural materials of the cooling loop.

In the shield, the major contribution to the activation again comes from isotopes closest in mass to the target nucleus (primarily tungsten in this case). The distribution of major radioactive isotopes is different from the first case, although the tungsten and mercury nuclei are relatively close in mass. The reason for this difference is primarily due to the difference in proton energy of the spallating projectile particle and the fact that in the tungsten shield there is a significant amount of water present that softens the neutron spectrum. Finally, it should be noted that a significant amount of Be-7 (^{7}Be) is generated in this cell (all cells containing water will have Be-7 as part of their radioactive

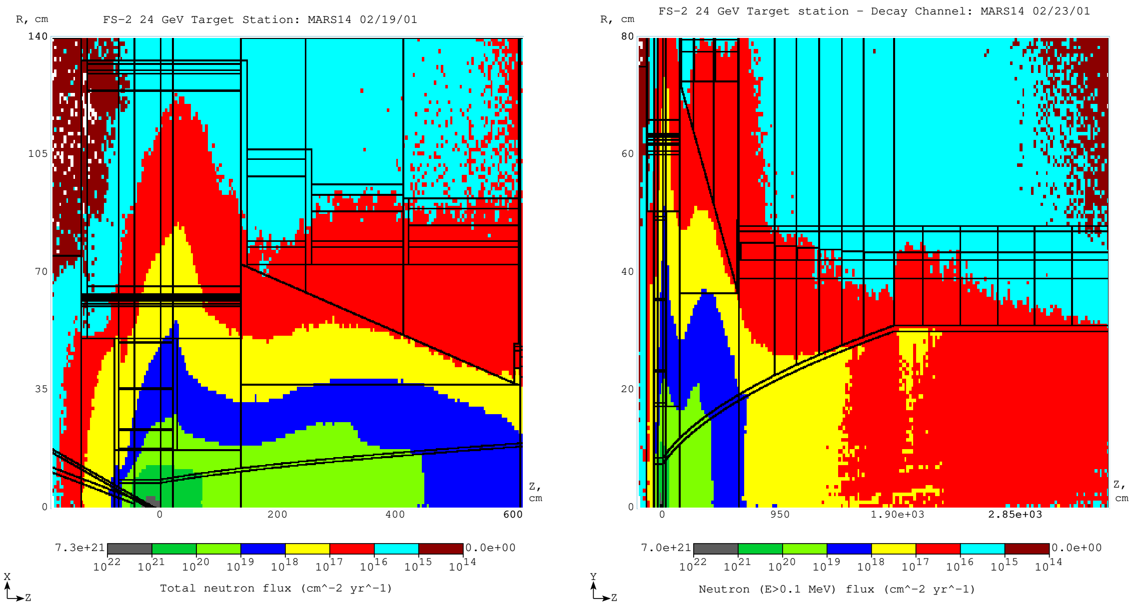

Figure 3.20: Flux of neutrons with $E > 100$ keV in the target system and decay channel for $-2 < z < 6$ m and $r < 1.4$ m (left) and $-2 < z < 36$ m (right) and $r < 0.8$ m.

inventory). This could be significant for operating the machine and maintaining the coolant loop. Tritium is also generated, and although it is not a major contributor to the overall inventory, its presence needs to be noted.

The radioactive nuclei considered here decay primarily by emitting a beta or gamma ray. These nuclides are generally not a personnel problem (unless they are ingested), since they are essentially totally self shielded by a component. However, the presence of gamma rays poses a personnel problem, and thus it is necessary to determine the gamma ray source strength associated with each of the above cells. This strength (as a function of gamma ray energy) can then be used in a separate calculation to determine the flux of gamma-rays leaving the target module, and the directional variation of the emitted radiation. The integrated source strength in photons per second for each volume as a function of time following shutdown is given in the Table 3.10.

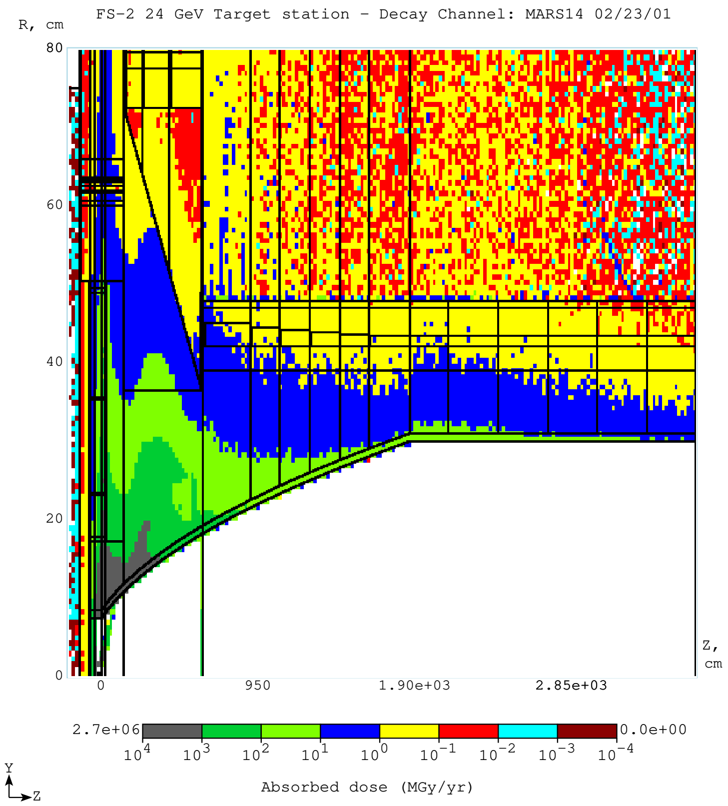

Figure 3.21: Absorbed radiation dose in the target system and decay channel for $-2 < z < 36$ m and $r < 0.8$ m.

3.3.3 Radial Leakage of Radiation from the Target Module

The mercury target is positioned in such a manner that it points downward at 100 mrad, and the proton beam points down at 67 mrad. Thus, the emerging shower of particles starts off in a downward direction. The charged particles are under the influence of the surrounding magnetic field, but the neutral particles propagate straight on. Any leakage flux from the target module will exhibit this overall pattern.

The results in Table 3.11 for radial leakage at the position of the mercury pool show the expected azimuthal variation, with more leakage in the direction of the proton beam. The gamma ray leakage is approximately an order of magnitude below that of the neutron leakage. The energy spectrum of the latter was also determined, and is given in Table 3.12.

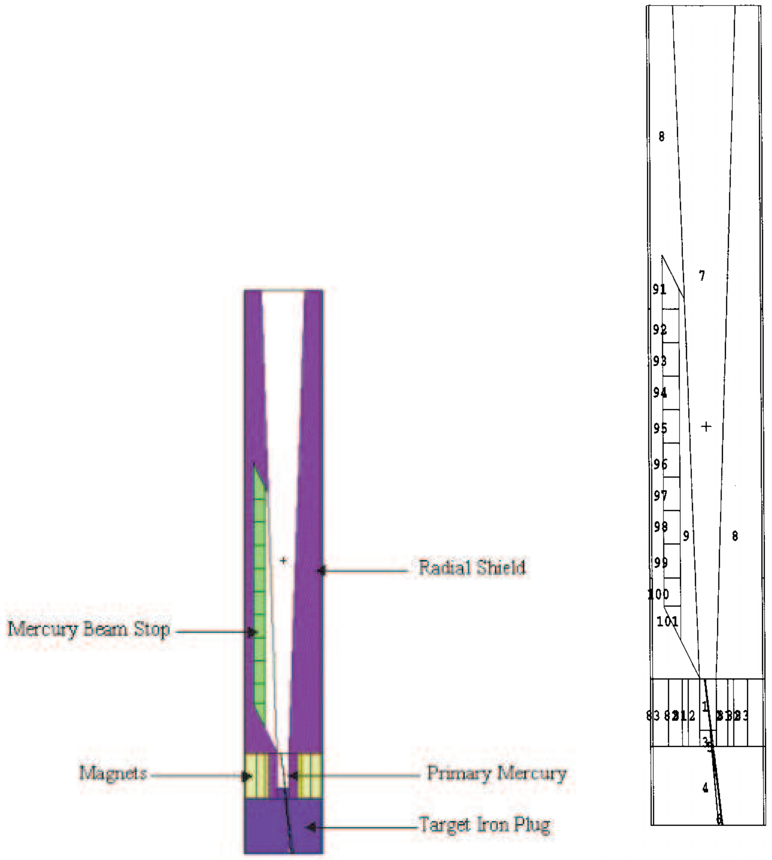

Figure 3.22: Longitudinal section through target module, with cell numbers shown on the right.

There is a significant neutron flux leakage above the MeV energy range, which will affect the operational life of components near the target magnet system.

3.4 Pion Capture Magnet

An efficient Neutrino Factory should capture nearly all the pions that the high-energy proton beam generates when it bombards the target. To do so, we employ a solenoidal magnetic field to bend the pion trajectories into helices bound to the surface of cylinders that enclose an invariant amount of flux. A solenoid captures those pions with trajec-

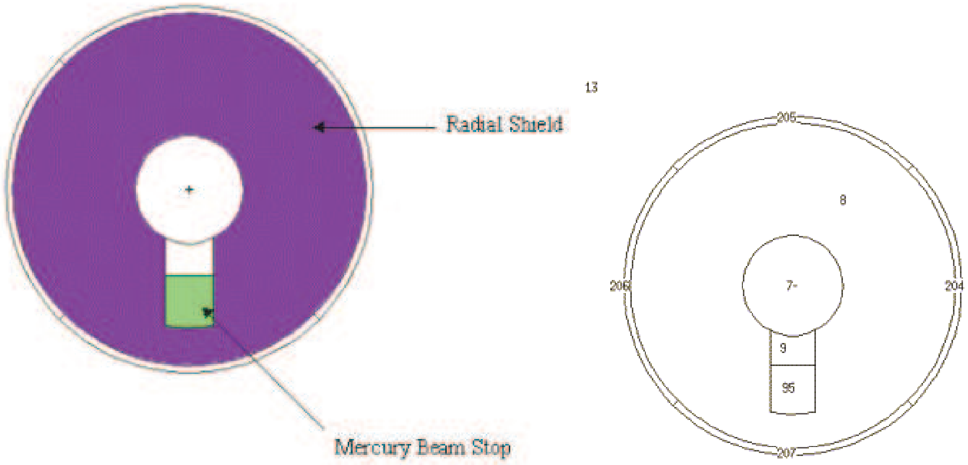

Figure 3.23: Radial section through the target module at $z = 4$ m, with cell numbers shown on the right.

tories small enough to fit inside its bore. Pions of high transverse momentum require a solenoid of large bore and intense field. For example, capture of transverse momenta up to 225 MeV/c, the baseline for Feasibility Study-II, requires a product of field and bore of 3 T·m. Study-II employs a capture field of 20 T, about the maximum that is feasible; the corresponding bore is 0.15 m.

The least costly magnet of this transverse-momentum reach has a large bore but only modest field. However, such a magnet would require that the magnets and other downstream components all be inconveniently large. Minimum overall system cost dictates a modest bore but high field.

The desired field profile of the pion capture magnet is uniform over the target, followed by a gradual transition to the much lower field of subsequent components of the Neutrino Factory, as shown in Fig. 3.8. For minimal particle loss the optimum field profile is

$$B(z) = \frac{B_0}{1 + kz/L}\,, \tag{3.2}$$

where B_0 is the field at $z = 0$, the downstream end of the target, and $(k + 1)$ is the ratio of B_0 to the field at $z = L$, the downstream end of the transition region. For Study-II, $B_0 = 19$ T, $k = 14.2$ and $L = 18$ m. Within the target region itself, $-l < z < 0$, where $l = 0.6$ m, the field need be only approximately uniform. Near the upstream end $(z = -l)$ the drop in field should be at most 5%, in order to limit shearing of the incoming jet of

Table 3.6: Neutron flux in various target system cells for 1 MW of 24-GeV protons.

Cell Number	Total neutron flux ($\mathrm{cm}^{-2}\mathrm{s}^{-1} \times 10^{12}$)
8	1.27
12	8.64
2	8.02
3	9.32
81	3.27
82	1.29
83	0.26
91	4.07
92	3.51
93	3.12
94	2.88
95	3.28
96	4.63
97	6.43
98	8.98
99	10.06
100	7.56
101	6.49

mercury by the field gradient. Near the downstream end ($z = 0$) the field drops a similar amount in order to blend smoothly, satisfying $\nabla \cdot \mathbf{B} = 0$, with the rapid decrease with z of the field at the upstream end of the transition region.

To generate this field we employ magnets of three types: superconducting (SC), resistive, and iron. SC magnets generate the entire field everywhere except in the vicinity of the target. There, the intense field and high density of energy deposition from radiation make it more economical to supplement the SC magnet with a resistive one. Contributing to the field at the very upstream end of the target region is a stepped cylinder of ferromagnetic material. A cobalt-iron alloy such as Permendur could contribute nearly 1.2 T, but cobalt may be undesirable from the standpoint of activation. Pure iron would contribute slightly more than 1 T. More valuable than the modest and highly localized field contribution is the favorable field gradient, which corrects much of the field inhomogeneity of the other coils that would otherwise cause excessive shear of the jet of mercury

Table 3.7: Activation in Curies for selected cells. (x) stands for $\times 10^x$.

Cell	Time after shutdown				
Number	0	4 hrs	1 day	7 days	30 days
8	1.59(6)	2.63(5)	2.01(5)	1.37(5)	8.92(4)
12	7.67(3)	4.12(3)	2.58(3)	1.16(3)	5.45(2)
2	1.34(5)	2.11(4)	1.62(4)	1.11(4)	7.35(3)
3	6.26(2)	4.09(2)	2.95(2)	2.51(2)	1.87(2)
81	5.08(4)	3.32(4)	1.12(4)	2.12(2)	1.67(2)
82	7.85(4)	5.15(4)	1.74(4)	2.06(2)	1.59(2)
83	2.83(4)	1.85(4)	6.25(3)	8.53(1)	6.86(1)
91	1.24(3)	7.77(2)	5.08(2)	2.03(2)	8.93(1)
92	2.36(3)	1.46(3)	9.57(2)	3.87(2)	1.61(2)
93	2.44(3)	1.52(3)	9.99(2)	3.99(2)	1.62(2)
94	1.78(3)	1.15(3)	7.49(2)	2.99(2)	1.26(2)
95	1.75(3)	1.12(3)	7.41(2)	2.99(2)	1.25(2)
96	2.39(3)	1.52(3)	1.03(3)	4.05(2)	1.66(2)
97	2.78(3)	1.83(3)	1.24(3)	4.88(2)	1.99(2)
98	3.25(3)	2.15(3)	1.44(3)	5.40(2)	2.23(2)
99	2.98(3)	1.99(3)	1.35(3)	4.94(2)	1.96(2)
100	1.82(3)	1.25(3)	8.55(2)	3.00(2)	1.17(2)
101	9.93(2)	7.18(2)	5.04(2)	1.91(2)	7.55(1)

entering the target region.

Figure 3.24 shows the on-axis field profile of the proposed pion capture magnet with parameters $B_{\rm max} = 20$ T, $B_0 = B(-l) = 19.0$ T, $k = 14.2$, and $B(L) = 1.25$ T. Figure 3.25 sketches the magnets and cryostat for the region $-l < z < 6$ m. Tables 3.13 and 3.14 list the most important parameters of the hollow-conductor and first eight superconducting coils of the pion capture magnet.

Note that, Table 3.13 incorporates minor modifications to many of the coil parameters, that have not been taken into account in Table 3.2. For example, coils downstream of 6 m are shorter and more numerous; this is a consequence, of trying to maintain the field quality, in spite of the larger intercoil gaps, introduced to facilitate cryostat construction and installation.

Table 3.8: Activation for cell 92 (mercury) 30 days after shutdown. Only elements with more than one Curie are listed.

Isotope	Activation (Ci)	Isotope	Activation (Ci)
Hg-203	41.09	Lu-173	0.35
Au-196	0.87	Lu-172	1.19
Au-195	33.09	Lu-171	0.48
Pt-188	3.49	Yb-169	6.81
Ir-190	0.51	Cs-131	1.78
Ir-189	9.89	Xe-127	1.36
Ir-188	4.20	I-125	1.38
Os-185	10.71	Te-121	1.60
Re-183	7.99	Te-118	0.13
W-181	5.74	Sr-85	1.34
Ta-179	0.54	Rb-84	0.65
Ta-178	3.09	Rb-83	0.62
Hf-175	2.64		
Total 141.6 (Table 3.7 total 161.4)			

3.4.1 Hollow-Conductor Resistive Coils

In the baseline design of this Study, the resistive insert that surrounds the target region employs hollow conductors rather than a Bitter magnet, as was used in Feasibility Study-I [4]. The penalty in performance is significant, (see Section A.2.3), but this technology should survive much better in the harsh radiation environment around the target.

The hollow-conductor magnet also presents formidable engineering challenges. Radiation doses and neutron flux densities are very high. According to calculations using the MARS code [11], each operational year (taken for radiation estimates to be 2×10^7 s) adds a dosage of $\approx 10^9$ J/kg (10^9 grays, or 10^{11} rads) and a neutron flux of $\approx 2\times10^{19}/\text{cm}^2$, despite ≈ 10 cm of shielding by water-cooled tungsten carbide that attenuates the neutron flux by more than an order of magnitude and the gamma dose by a factor of about 40. The intense ambient field, combined with the fairly large bore and fairly high current density, induces hoop stresses that are high compared with the low strength of typical hollow conductors, whose copper is in the annealed state for ease of processing. The neutron flux will strengthen the conductor to values associated with considerable cold work, but will also embrittle the conductor [15] so that the conductor must be supported

Table 3.9: Activation for cell 8 (tungsten-light water) 30 days after shutdown. Only elements with more than hundred Curies are listed.

Isotope	Activation (Ci)	Isotope	Activation (Ci)
Re-183	305.7	Gd-146	215.9
Re-184	171.6	Eu-149	276.5
W-181	40850.0	Eu-148	42.6
W-185	5779.0	Eu-147	256.9
W-178	9075.0	Eu-146	240.1
Ta-183	147.7	Eu-145	15.43
Ta-182	3122.0	Sm-145	115.2
Ta-179	3958.0	Pm-143	111.9
Ta-178	9077.0	Ce-139	174.0
Hf-175	5666.0	Cs-131	187.1
Hf-172	616.1	Xe-131	202.0
Lu-174	23.48	I-127	175.3
Lu-173	1104.0	Te-121	94.47
Lu-172	660.3	Te-118	9.849
Lu-171	576.6	Sn-113	101.3
Yb-169	2090.0	Ag-109m	47.96
Tm-170	9.611	Ag-105	190.1
Tm-168	27.28	Pd-103	105.4
Tm-167	274.0	Rh-103m	113.1
Dy-159	335.8	Rh-101	25.71
Gd-153	157.9	Rh-99	72.91
Gd-151	219.3	Be-7	1038.0
Gd-149	55.88	H-3	0.001
Total 88114.0 (Table 3.7 total 89210.0)			

as if it were glass. The alternative is to operate the conductor at 150°C or more (barely acceptable because of the penalty in conductor resistivity) or periodically to heat the conductor to that temperature, so as to anneal out much of the embrittlement before it becomes too severe.

The Study-II baseline design employs mineral insulated conductor (MIC) such as developed [16] for the Japan Hadron Facility. The insulation is a layer of MgO sandwiched between the conductor and its copper sheath. The conductor, shown in Fig. 3.26, is

Table 3.10: Gamma ray source (γ/s) in selected cells following machine shutdown. (x) stands for $\times 10^x$.

Cell	Time after shutdown			
Number	0	4 hrs.	1 day	30 days
8	1.31(17)	1.49(16)	9.76(15)	3.58(15)
12	1.01(15)	6.32(14)	2.98(14)	4.10(13)
2	1.11(16)	1.22(15)	8.13(14)	2.99(14)
3	4.35(13)	2.46(13)	1.44(13)	5.71(12)
81	1.54(15)	7.09(14)	2.43(14)	9.05(12)
82	2.26(15)	1.09(15)	3.71(14)	8.58(12)
83	8.26(14)	3.44(14)	1.34(14)	3.74(12)
91	2.05(14)	1.44(14)	6.49(13)	7.39(12)
92	2.95(14)	1.99(14)	1.07(14)	1.52(13)
93	4.29(14)	3.08(14)	1.39(14)	1.55(13)
94	3.02(14)	2.21(14)	1.03(14)	1.23(13)
95	2.45(14)	1.71(14)	8.85(13)	1.19(13)
96	3.48(14)	2.45(14)	1.23(14)	1.54(13)
97	4.36(14)	3.14(14)	1.57(14)	1.99(13)
98	5.10(14)	3.88(14)	1.89(14)	2.28(13)
99	4.86(14)	3.66(14)	1.69(14)	1.80(13)
100	2.86(14)	2.17(14)	1.02(14)	1.01(13)
101	1.47(14)	1.16(14)	5.49(13)	5.86(12)

Table 3.11: Integrated neutron and gamma ray flux per proton leaking radially outward from the target system at $z = 4$ m, the location of the mercury pool.

Cell Number	Neutron flux ($cm^{-2}s^{-1} \times 10^{-4}$)	Gamma ray flux ($cm^{-2}s^{-1} \times 10^{-5}$)
204	1.72	4.10
205	1.29	3.14
206	1.69	4.24
207	3.94	1.11

Table 3.12: Neutron energy spectrum for cell 207, the cell below the mercury pool. (x) stands for $\times 10^x$.

Energy bin (MeV)	Flux
0.0- 0.01	6.40(-5)
0.1- 0.1	6.01(-5)
0.1 - 1.0	1.31(-4)
1.0- 5.0	5.89(-5)
5.0 - 10.0	1.49(-5)
10.0 - 100.0	5.05(-5)
100.0 - 1000.0	1.37(-5)
1000.0 - 24000.0	2.237(-8)
Total	3.936(-4)

Table 3.13: Parameters of the hollow-conductor magnets.

	H-C 1	H-C 2	H-C 3
Avg. current density (A/mm^2)	244	191	149
Winding inner radius (cm)	17.8	23.2	35.3
Winding outer radius (cm)	23.2	35.3	49.0
Radial build of windings (cm)	5.4	12.2	13.7
Upstream end, z_1 (cm)	-71.2	-71.2	-71.2
Downstream end, z_2 (cm)	3.7	16.5	36.1
Coil length, $z_2 - z_1$ (cm)	74.9	87.7	107.3
Volume of windings (m^3)	0.052	0.196	0.389
Approx. peak field (T)	20.0	18.6	16.1
Avg. hoop tension (MPa)	118	124	115
Conductor fraction (%)	33.2	32.9	33.4
Copper fraction (%)	48.9	48.3	49.2
Structural fraction (%)	11.2	12.1	10.7
Copper mass (tons)	0.243	0.893	1.77
Stainless steel mass (tons)	0.048	0.194	0.334

18 mm square, with a cooling hole that is 10 mm square, surrounded by insulation 1.8 mm thick and a copper sheath 1.1 mm thick, for an overall size of 23.8 mm. As employed

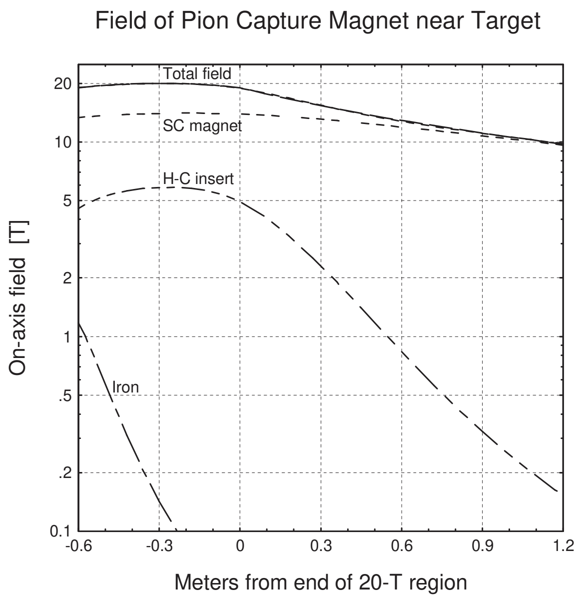

Figure 3.24: On-axis field of the pion capture magnet near the target region, $-0.6 < z < 1.2$ m. At $z = -0.3$ m, the superconducting magnet generates about 14 T and the resistive insert 6 T. The iron improves the entry of the mercury jet into the region by reducing the field inhomogeneity by a factor of two.

by the JHF, in lengths of 60 m and with only modest water pressure, the conductor can carry 3 kA. By limiting each hydraulic length to 15 m and using a high water pressure differential, 30 atm, as used at the National High Magnetic Field Laboratory (NHMFL), such a conductor will carry the required current, 15.5 kA, with a bulk temperature rise limited to 60°C. With an inlet water temperature of 10°C, as at the NHMFL, the peak conductor temperature is 80°C.

Figure 3.27 shows the cross section and a longitudinal section of the resistive insert magnet, built from three grades of such hollow conductor. The magnet consists of three nested coils, the innermost of two layers and the outer two coils of four layers each. Surrounding each coil is a reinforcing cylinder of Inconel 718, maraging steel, or other high-strength material. These cylinders hold the downstream flange against the downstream load of ≈ 0.6 MN (60 metric tons) from the other magnets in the system. Simultaneously, the cylinders contain the conductor against the high Lorentz forces. To restrict all terminations to the upstream end, the conductor spirals to the downstream

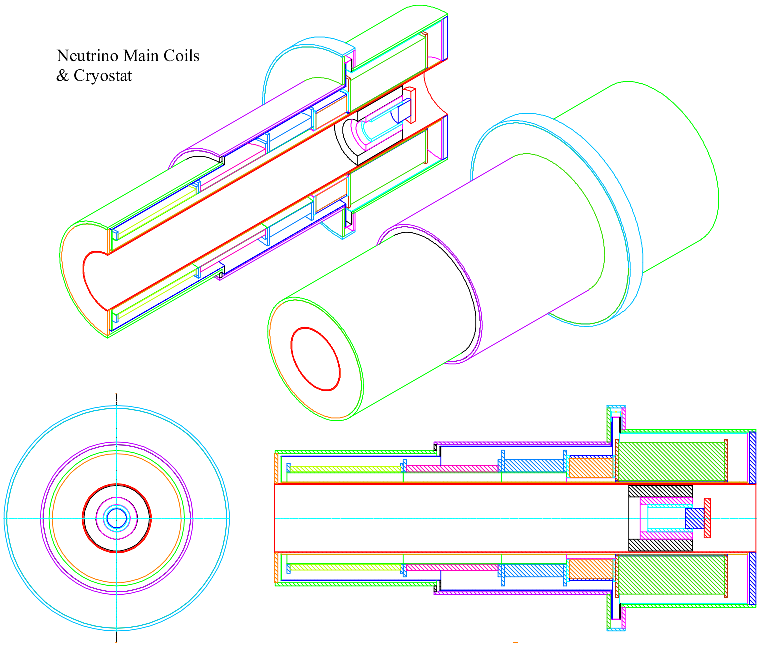

Figure 3.25: Cryostat and coils of the pion capture magnet in the region $-1 < z < 6$ m. The proton beam enters from the right of the section view in the lower right of the figure. Shown: iron plug (of stepped, T cross section), hollow-conductor (H-C) insert magnet, tungsten shielding outside H-C insert, cryostat, and first five superconducting (SC) coils. The bores of the SC coils range from 1.27 to 1.55 m. The first SC coil generates 14 T; the field at the downstream end of the fifth coil is 3.3 T. Not shown: conical beam tube and shielding between it and cryostat. Further downstream are additional SC coils to extend the field tail to 1.25 T at $z = 18$ m.

end in odd-numbered layers and back in even-numbered layers. To achieve water flow adequate to limit the bulk temperature rise to 60°C with conductors within the capacity of the JHF drawing bench, all layers have six conductors hydraulically in parallel, *i.e.*, a six-in-hand winding. That is, all conductors are electrically in series and hydraulically in parallel.

The inner coil uses conductor exactly as shown in Fig. 3.26. The other coils use conductor of the same proportions, to permit fabrication from billets of the same dimensions

Table 3.14: Parameters of the upstream eight superconducting solenoids of the pion capture system.

	SC 1	SC 2	SC 3	SC 4	SC 5	SC 6	SC 7	SC 8
Avg. current density (A/mm^2)	234	255	297	383	484	679	705	705
Winding inner radius (cm)	63.6	68.6	77.6	77.6	77.6	42.4	42.2	42.2
Winding outer radius (cm)	127.8	101.1	98.8	88.3	84.1	45.1	45.9	45.9
Radial build of windings (cm)	64.2	32.5	21.2	10.7	6.56	2.69	3.69	3.69
Upstream end, z_1 (cm)	−125.3	62.8	145.7	255.6	420.6	600.8	657.7	720.7
Downstream end, z_2 (cm)	52.8	135.7	245.6	410.6	606.5	643.7	707.3	770.3
Coil length, $z_2 - z_1$ (cm)	178.1	72.9	99.9	155.0	185.9	42.9	49.6	49.6
Volume of windings (m^3)	6.88	1.26	1.17	0.866	0.619	0.032	0.051	0.051
Approx. peak field (T)	14.0	11.8	8.74	6.21	4.33	3.33	3.03	3.03
Avg. hoop tension (MPa)	209	206	201	184	163	96	90	90
Conductor fraction (%)	7.8	6.2	5.3	5.5	6.2	8.2	8.3	8.3
Copper fraction (%)	10.4	10.9	12.1	16.4	21.8	38.5	39.9	39.9
Structural fraction (%)	31.8	32.9	32.6	28	22	3.4	1.8	1.8
Vol. of superconductor (liters)	538	79	62	48	38	3	4	4
Copper mass (tons)	6.42	1.24	1.28	1.27	1.21	0.11	0.18	0.18
Stainless steel mass (tons)	17.1	3.24	2.98	1.89	1.06	0.01	0.01	0.01

as that for the inner coil. These outer coils, being longer as well as larger in diameter, have longer passages that require bigger conductor, 26.8 mm for the coil of intermediate size and 30.6 mm for the outer coil. Each conductor in the outermost double layer is 35 m long, with a mass equivalent to 57 m of 23.8 mm square conductor. This is within 5% of the maximum so far produced on the JHF drawing bench, and thus sets the limit on conductor size throughout the magnet.

3.4.2 Superconducting Coils

One of the superconducting coils of the pion capture magnet is also a formidable engineering challenge: SC 1, with its 14-T field and 1.3-m bore. Fortunately there are two precedents for this coil. One, is a collaboration of MIT and the NHMFL for its 45-T hybrid magnet [17]. It can generate 15 T when operated alone, and therefore not restricted to 14 T by the need for current margin to survive the current surge from a tripout or burnout of the insert coil of the hybrid system. However, the bore of this magnet is only half that of pion capture magnet SC 1. More relevant is the central solenoid model coil

Figure 3.26: Mineral-insulated hollow conductor developed for Japan Hadron Facility. The end-on view shows the white layer of powdered MgO insulation sandwiched between the copper hollow conductor and its sheath, also of copper. Of the cross section, 17% is cooling passage, 37% conductor, 28% insulation and 18% sheath. The side view shows a conductor termination, brazed of several parts that confine the MgO and hold the glossy white ceramic ring that keeps the sheath isolated from the current-carrying conductor.

(CSMC), shown in Fig. 3.28, for ITER, the International Thermonuclear Experimental Reactor [18]. The coil has generated 13 T in a bore 26% bigger than necessary for SC 1. The CSMC weighs 140 tons and stores 600 MJ, the same as the entire pion capture magnet, including the coils in its 18-m-long transition region.

The pion capture magnet has the additional complexity of energy deposition from radiation, up to 1 kW/m^3, despite shielding about 30 cm thick. However, it does not have to cope with energy deposition from the high sweep rate that the CSMC must survive. It also does not have to cope with so high a discharge voltage, 15 kV for the CSMC. Therefore, its insulation need not be so thick, nor its current density quite so low.

Cable-in-conduit conductor (CICC) will be used in the highest field superconducting coils of the pion capture magnet, coils SC 1–5. Figures 3.29 and 3.30 show the CSMC conductor, which is about 50 mm square and can carry 46 kA in a field of over 13 T. Liquid helium in the central tube flows through the spiral gap in its wall to cool the strands

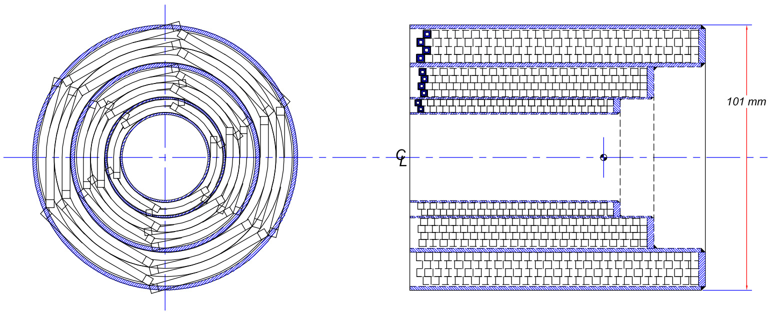

Figure 3.27: End view (left) and vertical section (right) of the resistive insert of the hollow-conductor magnet. Every layer employs six hydraulic paths in parallel to achieve the short hydraulic path length necessary for adequate water flow. The conductor is mineral-insulated conductor (MIC) of the sort developed for the Japan Hadron Facility, shown in Fig. 3.26. The thick-walled cylinders reinforce the conductor against the radial Lorentz hoop stresses engendered by the combination of high field (20 T) and large bore (0.36 m).

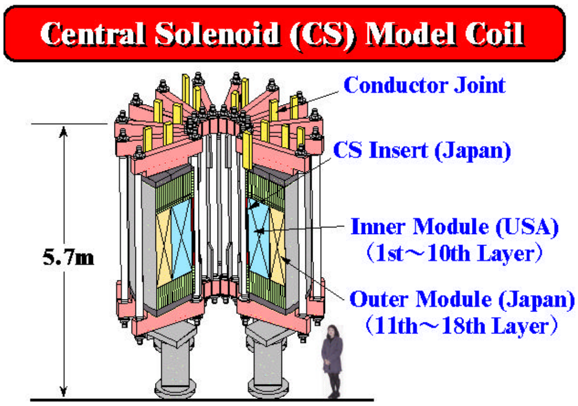

Figure 3.28: Superconducting magnet of the same scale as the pion capture magnet. The CSMC for ITER weighs 100 tons, generates 13 T in a 1.6 m bore, and stores 600 MJ.

of superconducting cable that parallel the tube. The fine strands have a high ratio of surface to volume, to keep each strand at nearly the same temperature as the helium.

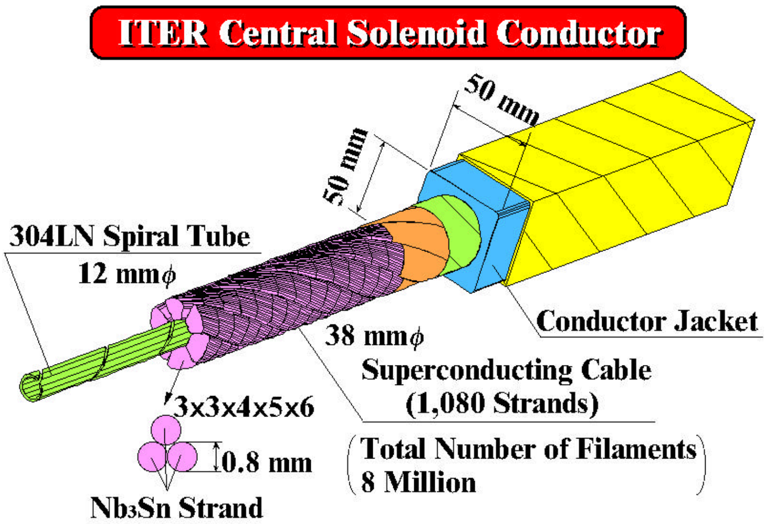

Figure 3.29: Concept of high-current cable-in-conduit conductor needed by the intense-field coils of the pion capture magnet. Liquid helium in the central tube flows through the spiral gap in its wall to cool the strands of superconducting cable that parallel the central tube. The outer jacket, typically of stainless steel or Inconel, provides most of the mechanical strength.

The outer jacket, typically of stainless steel or Inconel 908, protects the delicate strands within and provides almost all of the mechanical strength to resist huge Lorentz forces in large magnets that generate intense fields. Cable-in-conduit conductor is appropriate for large magnets operating at 10 kA or more. For the downstream coils of the pion capture magnet, which experience lower hoop and much lower axial loads, solid conductors or Rutherford cables are simpler and more economical.

3.4.3 Magnetic Forces

The axial loads on the upstream, high-field coils of the pion capture magnet are immense. Figure 3.31 shows that the peak cumulative axial load (which is at the downstream end of SC 1) to be over 100 MN, or 10,000 metric tons. All of the biggest loads involve only the first five SC coils. To manage this load, we support the coils with a structure that is cold at both ends to minimize heat leaks into the cryostat. The obvious way to do this is to house them all in the same cryostat. This is the only feasible way given that the

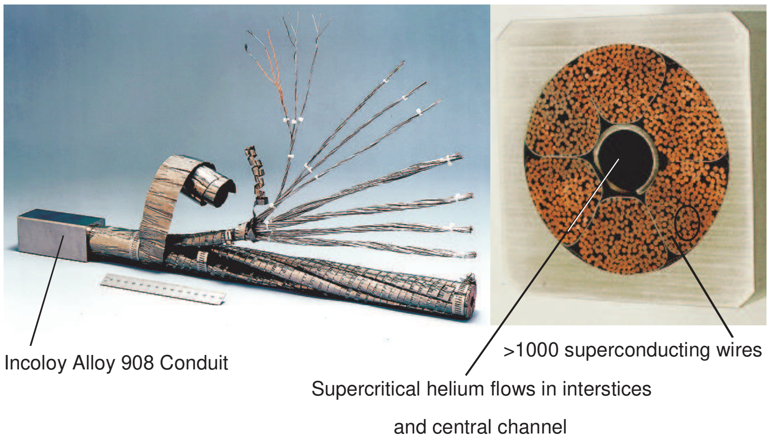

Figure 3.30: The cable-in-conduit conductor for the ITER central solenoid.

separation between consecutive coils is 10 cm, which is not enough for two sets of coil flanges and cryostat walls. The loads on all the low-field coils (beyond $z = 6$ m) sum to only 2.5 MN. We group these coils in sets, as in the case of phase rotation coils, with each cryostat of convenient length.

3.4.4 Field Quality

The gaps between consecutive coils can introduce considerable field ripple, especially beyond $z = 6$ m, the downstream end of the proton beam absorber, where the coils are of smaller bore. Fig. 3.32 shows the field ripple for coils with 14 cm gaps as indicated in Table 3.14. Whereas Table 3.2 had only 7 coils downstream of $z = 6$ m, Table 3.14 has 19 coils, each of only ≈ 50 cm in length. This geometric distribution maintains the field ripple within 5.3% peak-to-peak and 10% rms. An on-axis field ripple of this size does not affect the transmission of pions to the phase rotation region.

3.5 Beam Windows

3.5.1 Upstream Proton Beam Window

The upstream and downstream beam windows isolate the incoming proton beam transport and pion decay channel from the mercury vapor atmosphere near the target.

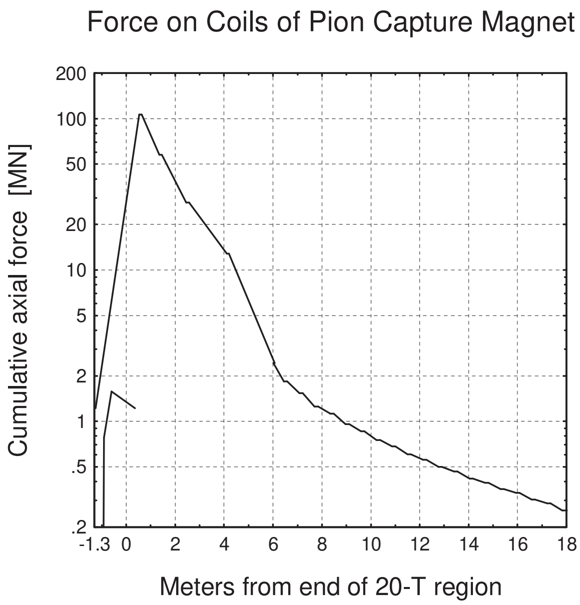

Figure 3.31: Cumulative axial force on components of the pion capture magnet. Upper curve: the peak force is over 100 MN, or about 10,000 metric tons. The forces between the first five superconducting coils, with their high field and large size, dictate that they share a common cryostat. The forces on coils beyond $z = 6$ m are much less, and allow individual cryostats for each coil or convenient group of coils. Lower curve: the force on the resistive insert magnet and iron is only 1.2 MN (note the semi-logarithmic scale).

The upstream proton beam window will see the full beam before it hits the target. The resulting pulsed energy deposition excites pressure waves that must be sustained by the window for over 10^8 cycles per year. Since the lifetime of the window is expected to be limited, provisions for its periodic replacement are part of its design.

The proton beam window is a double wall structure with a gap between the two walls that allows for active cooling. The interior face of the window will be exposed to mercury vapor, so the window material must be mercury compatible. Candidate window materials include beryllium and Ti90-Al6-V4 alloy (whose short-term compatibility with mercury has recently been verified).

To assess the viability of candidate window materials, an ANSYS finite-element analysis was performed, including both the thermal aspect of the beam/window interaction

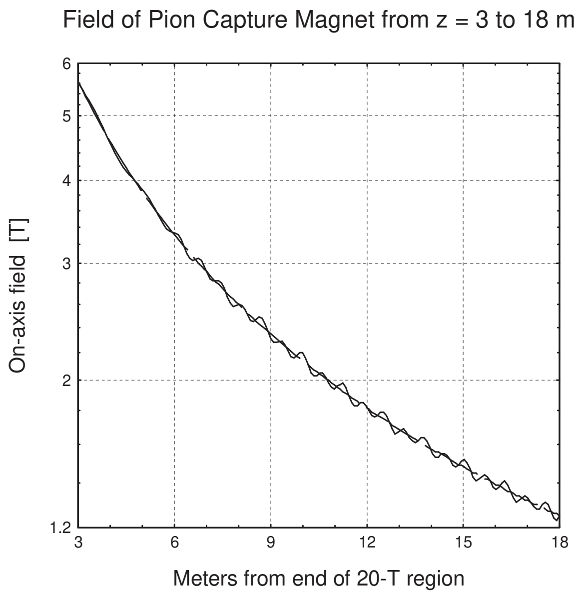

Figure 3.32: On-axis field of the pion capture magnet from 3 to 18 m downstream of the target region, where the solenoids have 0.42 m inner radius and 0.50 m length separated by axial gaps 0.14 m. The desired field (dashed line), to maximize the adiabatic retention of captured pions, declines from 19 T at $z = 0$ to 1.25 T at 18 m according to Eq. 3.2. The actual field (solid line) differs from the desired value by 5.3% peak-to-peak (from −2.5% to +2.8%), with an rms deviation of 1.0% (Note the semi-logarithmic scale).

and the resulting thermal shock. The energy deposition in the window material was computed using the MARS code [10]–[11]. Figure 3.33 shows results for a 1-mm-thick beryllium window intercepting six pulses of 1.7×10^{13} 24-GeV protons with $\sigma_r = 1$ mm. Figure 3.33 (left) shows the temperature rise of one of the walls of the beryllium window during a train of six micro-pulses that arrive 20 ms apart. Bunches of these six micropulses arrive at a frequency of 2.5 Hz. The temperature rise per micro-pulse, at the center of the beam, is approximately 10°C. In steady-state conditions, coolant flowing between the walls, would limit the temperature in the window to ≈ 116°C above ambient, assuming a heat removal coefficient of 100 W/m^2 · °C.

Figure 3.33 (right) shows the von Mises stress induced in the Be window by a single micropulse. The peak stress is about 90 MPa while the yield strength of beryllium is

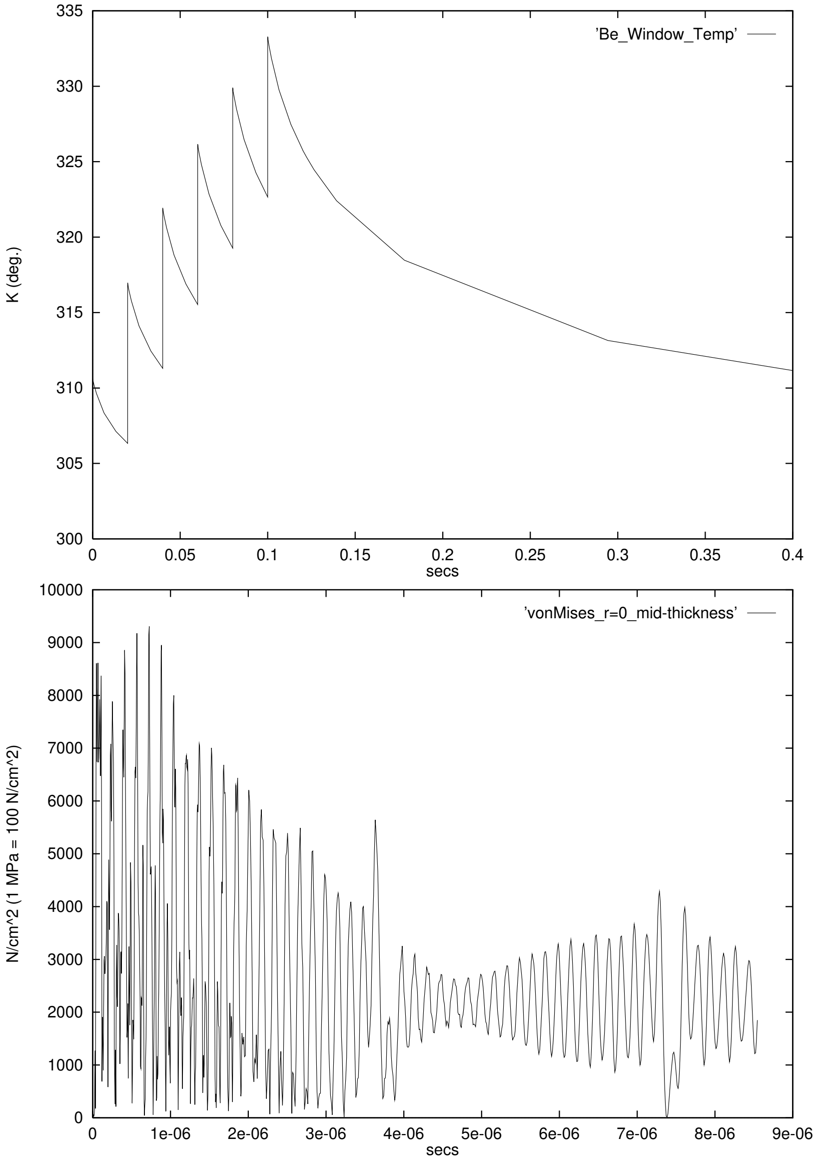

Figure 3.33: ANSYS model of a 1-mm-thick beryllium window subject to a train of six micro-pulses of 1.7×10^{13} 24-GeV protons per pulse with $\sigma_r =$ 1 mm). Top: transient thermal response; bottom: von Mises stress.

between 186 and 262 MPa. We note that the beam spot on the window will certainly be larger than that assumed here. The spot size at the window is related to that at the target by

$$\sigma_{r,\mathrm{window}} = \sigma_{r,\mathrm{target}}\sqrt{1 + \frac{L^2_{\mathrm{window}}}{\beta^{\star 2}}}, \tag{3.3}$$

where, $\sigma_{\mathrm{target}} = 1.5$ mm, L_{window} is the distance from the window to the target, and $\beta^\star$ is the betatron parameter of the beam focus (not yet determined). Clearly, large L and small $\beta^\star$ provide greater safety margin for the beam. In the present design, $L_{\mathrm{window}} \approx 3.3$ m, but parameters of the proton beam focus, including $\beta^\star$, have not been set. In any case, we have taken a very conservative estimate of the spot size, so we have a significant safety margin.

3.5.2 Downstream Beam Window

The downstream beam window is located on the magnetic axis at $z = 6$ m and will be approximately 36 cm in diameter. It intercepts forward secondary particles, but not the unscattered proton beam. The baseline window design is a pair of 2-mm-thick Be plates with active cooling between them.

A MARS calculation of the power deposition and radiation dose in the Be window is shown in Fig. 3.19. The dose is high enough that the Be window is not a lifetime component. A preliminary concept for window replacement is shown in Fig. 3.39.

The mechanical design of the downstream window is governed by the following:

- Large window diameter (36 cm)
- Pressurized active coolant in the gap of the double wall
- Vacuum environment on the downstream side

The principal design challenge is to maintain mechanical integrity against the pressure differential over the large window area. Failure due to beam-induced stress is a lesser concern for this window.

Three variations of the basic design concept are being considered, as shown in Fig. 3.34. For a window with flat plates, as in Fig. 3.34 c), the stress at the edge of the plates due to a one atmosphere pressure differential is above the yield strength. To relieve the stress the windows should be curved, as in Fig. 3.34 a) and b). Option a) in which the two windows have equal but opposite curvature, appears to be more favorable, with a steady-state temperature gradient of only 30°C. If no coolant were used, the temperature gradient would be 250°C.

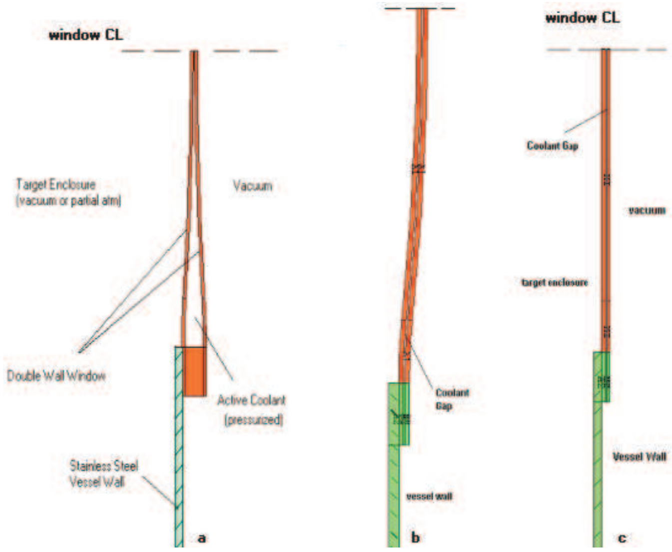

Figure 3.34: Three double layer designs for the downstream beam window.

3.6 Mercury Deflectors

Two components of the mercury handling system present unusual design challenges in view of the disruptive effect of the proton-mercury interaction: i) the mercury jet nozzle and ii) the entrance baffles to the mercury pool that serves as the proton beam absorber.

3.6.1 Mercury Jet Nozzle

Pressure waves generated in the mercury jet during its interaction with the proton beam will travel back to the nozzle, which must withstand the pressure wave. An ANSYS model of the effect of a pulse of 1.7×10^{13} 24-GeV protons on a 5-mm-radius mercury jet indicates a peak stress of 3800 MPa. The resulting pressure wave propagates to the nozzle in about 100 μs where the pressure pulse will be about 100 MPa, as shown in Fig. 3.35.

The nozzle must be constructed of a material with yield strength well above 100 MPa to have the desired lifetime of $> 10^8$ cycles.

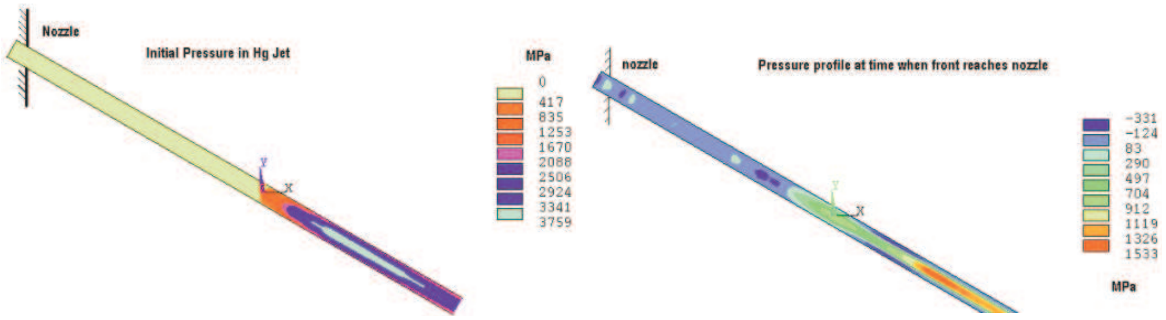

Figure 3.35: ANSYS model of the pressure wave in the mercury jet induced by a pulse of 1.7×10^{13} 24-GeV protons. Left: the pressure profile just after the proton pulse; right: the pressure profile when the wave reaches the nozzle after 100 μs.

3.6.2 Entrance Baffles to the Mercury Pool

Both the unscattered proton beam and the undisrupted mercury jet enter a pool of mercury at $2.25 < z < 5$ that serves as the proton beam absorber. Details of this concept are shown in Fig. 3.36.

The undisrupted mercury jet has mechanical power $\pi\rho r^2 v^3/2 \approx 10$ kW for $r = 5$ mm and $v = 30$ m/s. This power will agitate the mercury pool unless the impact of the jet is mitigated by a set of diffusers submerged in the pool. The diffusers will consist of stainless steel mesh and a bed of tungsten balls.

The unscattered part of the proton beam retains about 10% of the initial beam power, which is sufficient to disperse a significant volume of mercury as it enters the pool. A set of stainless-steel-mesh baffles will direct the ejected mercury droplets back into the pool. The design must be robust enough to survive at least one pulse in which the mercury jet was not present and the full proton beam entered the pool.

3.7 Mercury Flow Loop

The mercury-jet target system consists of the process flow loop, a replaceable nozzle assembly mounted in the bore of the iron plug magnet, a mercury containment vessel that is part of the decay channel downstream to $z = 6.1$ m, and the beam absorber, which is located at $2.5 < z < 5.5$ m. A dedicated hot cell that contains the flow loop components is located at the tunnel level. Figure 3.37 is a schematic diagram of the

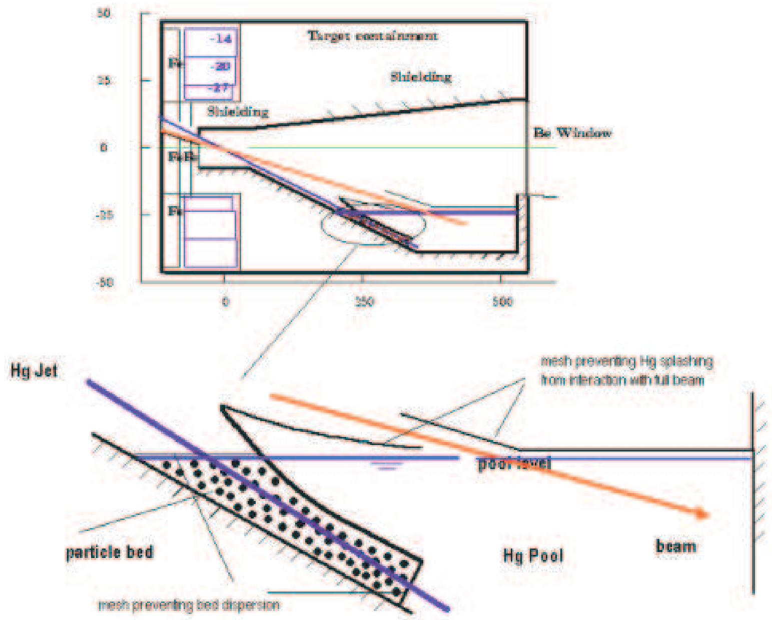

Figure 3.36: Schematic of the mercury pool that serves as the proton beam absorber.

overall system.

3.7.1 Process Flow Loop and Absorber

The process flow loop contains 110 liters of mercury distributed as follows: 30 liters in the beam absorber pool, 7 liters in the heat exchanger, 35 liters in the sump tank, and 38 liters in miscellaneous piping and valves. A 200 liters tank provides storage for the mercury when the system is shut down or undergoing maintenance. The piping is sloped towards the storage tank, and the elevation of the main (jet) pump, the heat exchanger, the beam absorber pool, and the storage tank are arranged so that the mercury level can be easily controlled among the components. Various valves are used to isolate portions of the system for storage, flow, or drainage into the storage tank, and drainage is by means of gravity. The system components are located in the target hot cell and are arranged to be accessible by the wall-mounted manipulators. The various valves are pneumatically actuated, but they can be manually operated using through-the-wall manipulators, if necessary.

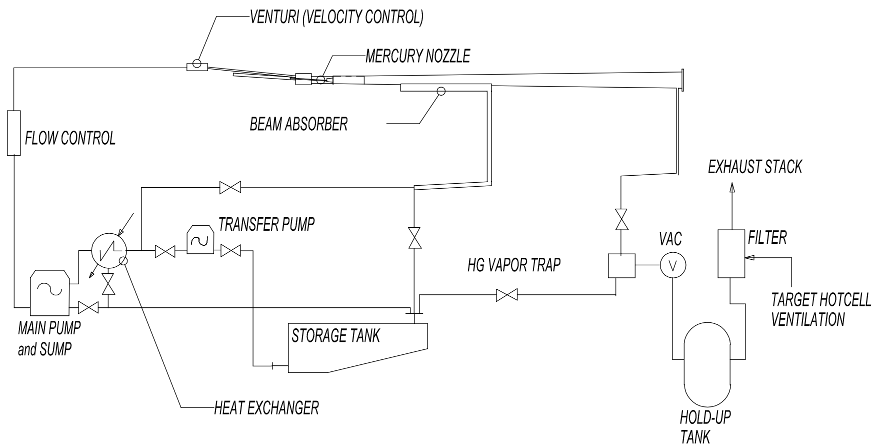

Figure 3.37: Mercury flow loop schematic layout.

The pumps for the flow loop have centrifugal magnetic drives. The low-capacity transfer pump is self-priming and can pump at a rate of 3-6 gpm. This pump is used to transfer mercury from the storage tank into the flow loop by first filling the heat exchanger and the sump tank of the main pump. The volume of the sump tank includes Hg for the absorber pool as well as the main pump volume, *i.e.*, 65 liters. The high-capacity main pump initially transfers 30 liters of mercury into the pool before the high-field magnets are energized. During system operation, it pumps at a rate of 35–50 gpm to circulate mercury at 30 m/s through the nozzle assembly.

The heat exchanger is a welded-tube and shell construction with a closed-loop water system. The inlet temperature of the mercury is 122°C; the outlet temperature is 20°C. The water inlet temperature is 20°C; the outlet temperature is 47°C. These values are based on water flowing through the shell of the exchanger at 4 liters/s. Figure 3.38 is a view of the flow loop components located in the target hot cell.

The mercury storage tank is located under the shield floor in the target hot cell. The full inventory of mercury is stored there when the system is shut down. This is accomplished by closing and opening the appropriate valves in the flow loop for gravity flow into the tank. There are drain lines from the sump pump, the heat exchanger, and the beam absorber pool. In addition, there is a secondary drain/vent located at $z = 6.0$ m. Its purpose is to extract and condense mercury vapors prior to maintenance operations that require opening the mercury containment vessel in the capture/decay region. The vent line is connected in series to a mercury trap (condenser) and a vacuum scroll pump. The condensate is returned to the storage tank by means of a bypass line and the vacuum exhaust passes into the first hold-up tank. Gases and mercury vapors are passed through a filter system containing sulfur-treated charcoal filter modules before passing into the facility ventilation exhaust.

Mercury, mercury vapor, and rare gas reaction products are contained in the target/capture region by means of windows. The upstream Be window is mounted on the target nozzle insert at the proton beam line axis; the downstream beryllium window is mounted to the vacuum vessel at SC 6. Figure 3.39 shows the location of the beryllium window.

The average beam power deposited in the jet is 400 W/g (100 kW) and the remainder of the 1-MW proton beam power is deposited in the shielding that lines the target magnet system, including the mercury pool that serves as the proton beam absorber. Even if 900 kW were deposited in the beam absorber, the bulk temperature rise of mercury in the absorber pool would be only 102°C, well below the boiling point. However, this assumes homogeneous mixing occurs in the pool due to the mercury jet that enters the pool at a rate of 2.4 liters/s.

3.7.2 Target System Maintenance

The various components that make up the target system fall into three categories. Class 1 are limited-lifetime components that require frequently scheduled remote replacements during the life of the facility. They are designed for remote handling and minimal impact

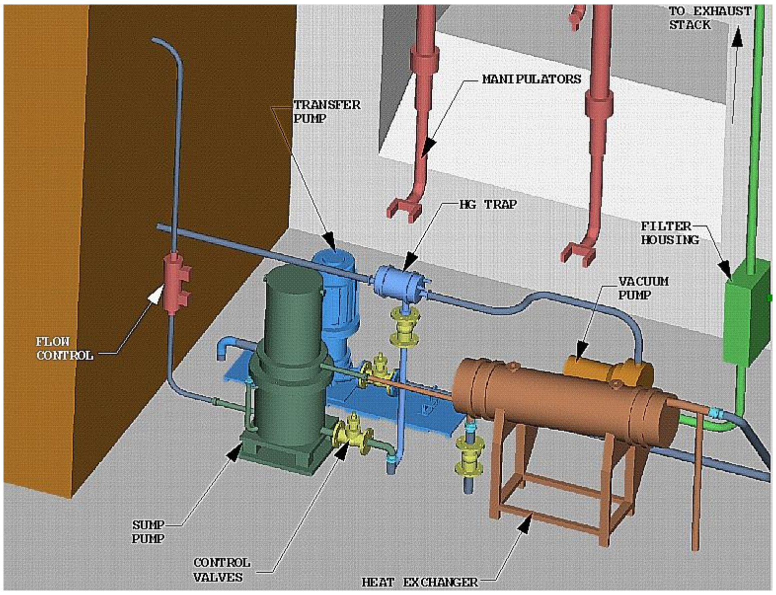

Figure 3.38: Arrangement of the mercury flow loop components in the target hot cell.

on operating availability, and remote handling tools and equipment are included in the design. Class 2 are lifetime components having activation levels that preclude hands-on replacement, and whose failure shuts down the facility. They have a finite probability of at least one failure. These components are designed for remote handling, but remote handling tools and equipment are not included in the design (unless they are used for initial installation). Their replacement would impact operating availability since spare components are not assumed to be on hand. Class 3 components are expected not to fail during the facility lifetime.

Replacement of target system components must be done using remote-handling equipment because of high levels of activation, and the presence of (radioactive) mercury contamination. The target system contains many components that are considered to be life-of-the-facility (Class 3), numerous components that could require infrequent replacement (Class 2), and several that are life limited (Class 1). The maintenance requirements for this system are summarized in Table 3.15. The table is based on an operating year of 2×10^7 seconds, which is the equivalent of 8 months of continuous full-intensity beamline operation.

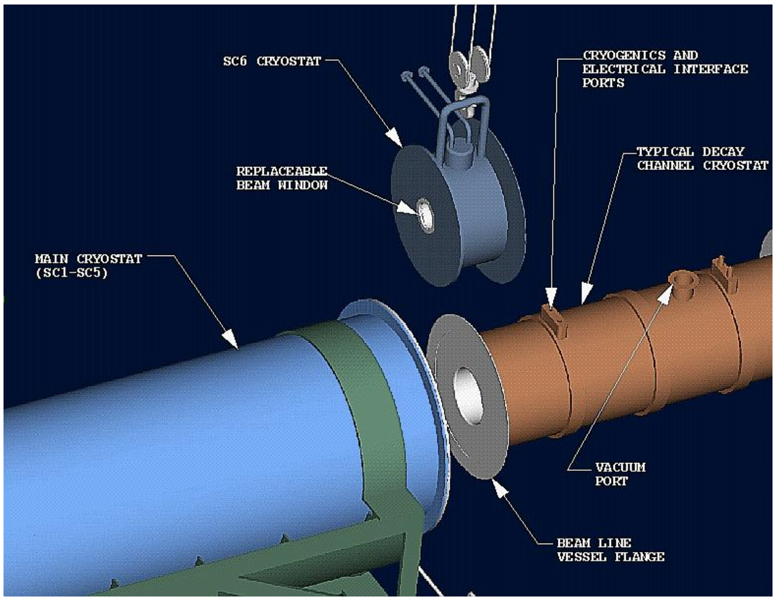

Figure 3.39: The beryllium window is mounted to a readily replaceable solenoid.

Table 3.15: Maintenance requirements for the target system components, based on 8-hour maintenance shifts.

Component	Class	Failure Mode	Dose Rate (rad/h)	Expected Life (yrs)	Replacement Time (days)
Nozzle insert	1	erosion, embrittlement	$> 10^6$	2–3	11–16
Be window	1	embrittlement	10^4–10^5	2	7–11
Isolation valve	1	mechanical	10^4–10^5	5–7	1–2
Filters	1	saturated	Contam.	2	2–3
Pumps, valves	2	mechanical	Contam.	7.5	2–3
Heat exchanger, Piping, tanks	3	mechanical	Contam.	> 40	5–8

3.8 Target Support Facility

The geometry for the target support facility (see Fig. 3.12) is defined around the intersection of the mercury jet, the proton beam, and the magnetic axis of the solenoid magnets. The proton beam interacts with the jet over a region whose downstream end is at $z = 0$ cm. The three axes intersect at $z = -15$ cm. The locations of the coils and other components are measured from $z = 0$. The decay channel extends to $z = 35.6$ m, which is the facility interface with the first induction linac. Figures 3.40 and 3.41 show the basic geometry of the facility.

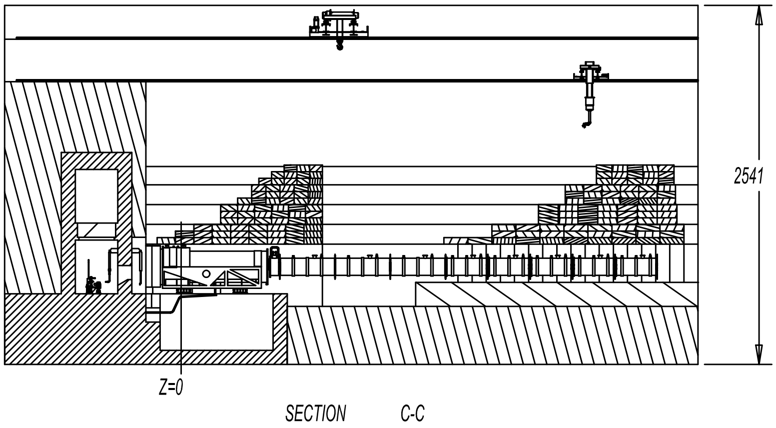

Figure 3.40: Side view of the target facility. Dimensions are in cm.

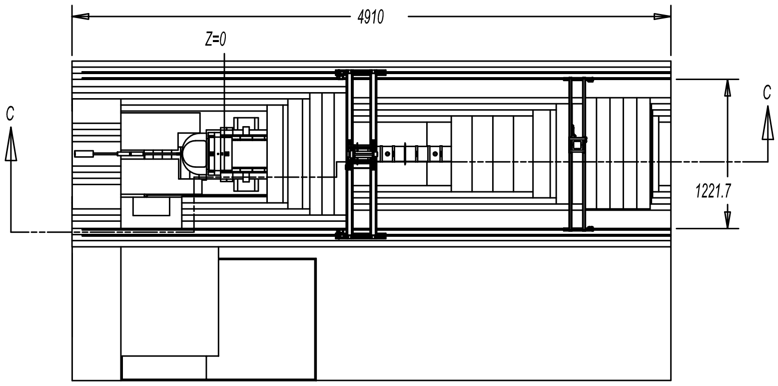

Figure 3.41: Plan view of the target facility. Dimensions are in cm.

The incoming proton beam window is located at $z = -330$ cm and is connected to the core vacuum vessel with a removable section of beam pipe, as shown in Fig. 3.42. This design permits the window assembly to be close to the target region, yet readily removable to replace the window or the mercury jet nozzle, or provide clearance for the replacement of the inner solenoid module should that ever become necessary.

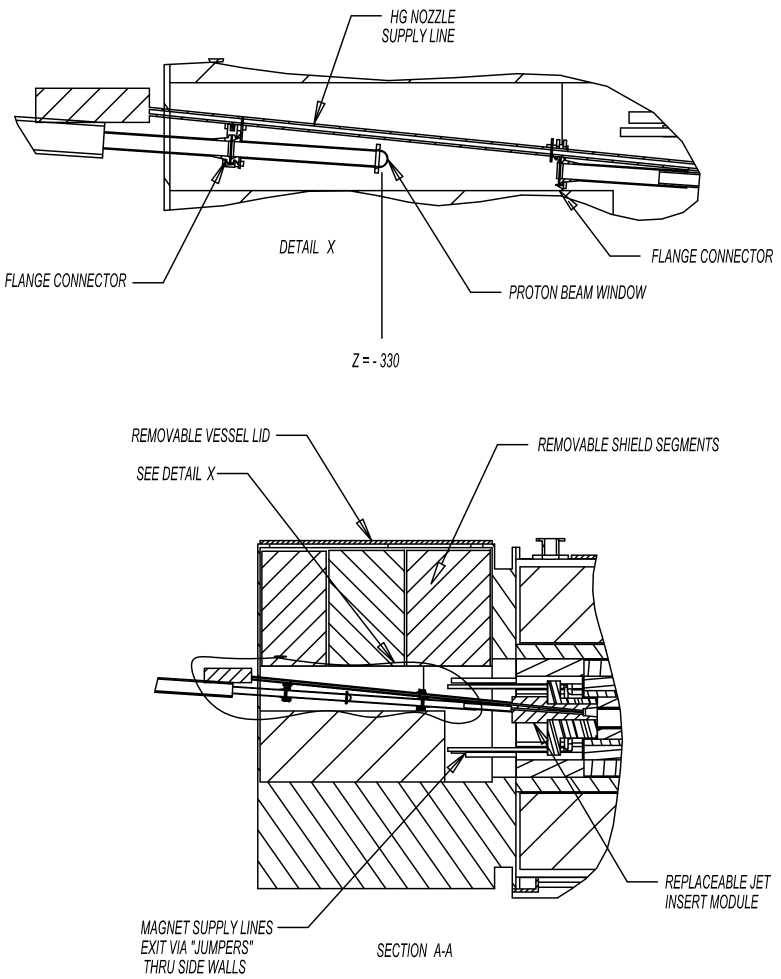

Figure 3.42: Vacuum vessel upstream of the target region.

It is important to keep in mind that virtually all of the components that make up the target and capture facility will be highly radioactive. Replacing components after start-up operations must be done using remote handling equipment and tools. The development of the facility arrangement was based on considering the initial assembly and installation of the various subsystems, and also on modularization of components to simplify remote handling and have minimal impact on the operating availability.

3.8.1 Solenoid Magnets

The solenoid magnets are located in the capture and decay tunnel of the support facility, and although they are considered to be lifetime components, the facility design is based on their remote replacement. The tunnel begins in the target region upstream of the proton beam window and extends to $z = 35.6$ m. The first five solenoids (SC 1–5) are contained in a common cryostat that extends to $z = 6.1$ m. The cryostat is designed so that its inner shell is the outer shell of part of the tungsten-carbide shield. Therefore, there is a shield cylinder attached to the cryostat that is 16-20 cm thick and contains inner rib supports to stiffen this cylindrical beam. The ribs are also partitions for the cooling flow channels of the shield. Figure 3.43 is a section through the main cryostat that shows the magnet arrangement and the shield-beam. Figure 3.44 shows the rib structure of a typical shield module and the coolant line connections.

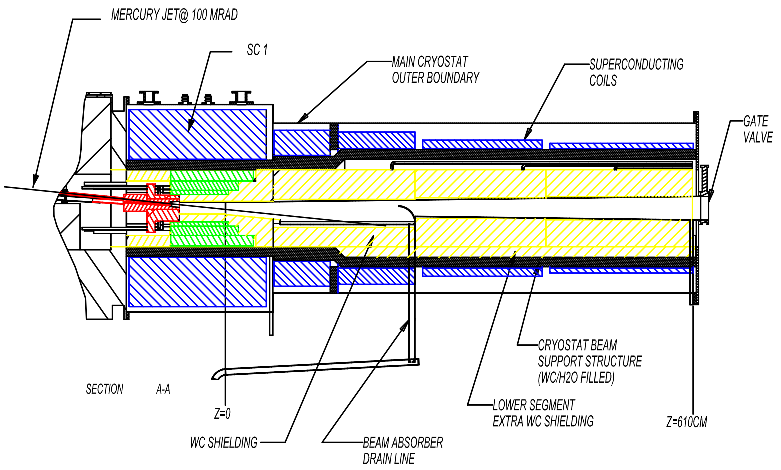

Figure 3.43: Main cryostat containment for SC 1–5.

There is a separate module for the resistive magnets and shielding contained within the bore of SC 1. It consists of an iron plug, three resistive, water-cooled magnets (H-C 1–3), and tungsten-carbide shielding. The combination of these coils and SC 1 provides the 20 T field in the target region. Figure 3.45 shows the resistive coil module along with the nozzle insert for the mercury jet. Figure 3.46 shows a section cut and end view of the resistive module. The target nozzle insert is mounted in the off-center cut-out in the iron plug.

The magnets downstream of the main cryostat are two-coil solenoids contained in 4-m-long cryostats, except for SC 6, which has a 0.5-m cryostat. These magnets extend

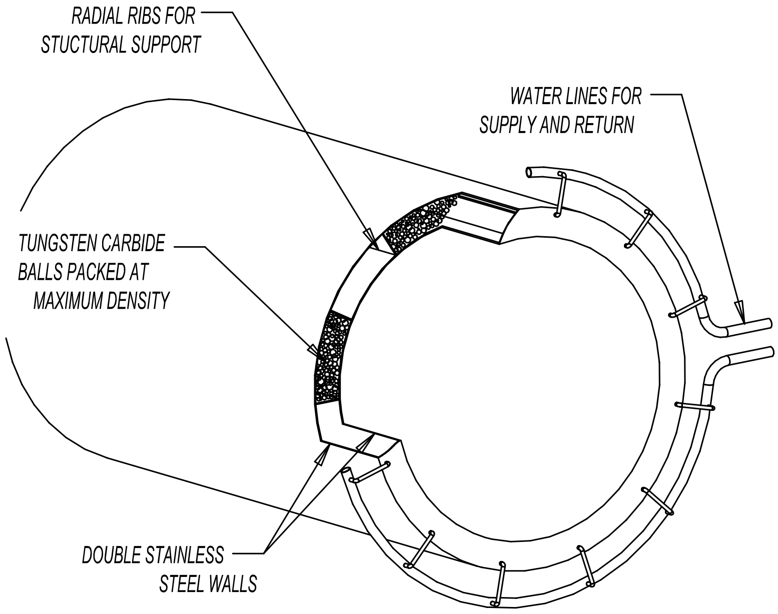

Figure 3.44: Typical construction of the shield modules.

from $z = 6.1$ to 17.6 m and make up the remainder of the transition coils (SC 6–25). Figures 3.12 and 3.39 show the transition coils. In this region, the axial field decreases until it is 1.25 T at $z = 17.6$ m.

Coil SC 6 is smaller and is designed to be the mounting support for the beryllium window located at $z = 6.1$ m. The window is the downstream containment boundary for the mercury target vessel. The window is replaced every two years by removing SC 6 and installing a spare SC 6 module with the replacement window already mounted. Figure 3.39 shows SC 6 in the process of being removed.

The magnets from the end of the transition region to the end of the decay channel are contained in 3-m-long cryostats, each containing three coil pairs. Figure 3.47 is a section- and end-view of a typical cryostat module. The nuclear shielding for these magnets is similar to the upstream coils except that a homogeneous mix of stainless steel balls is used instead of the tungsten carbide balls.

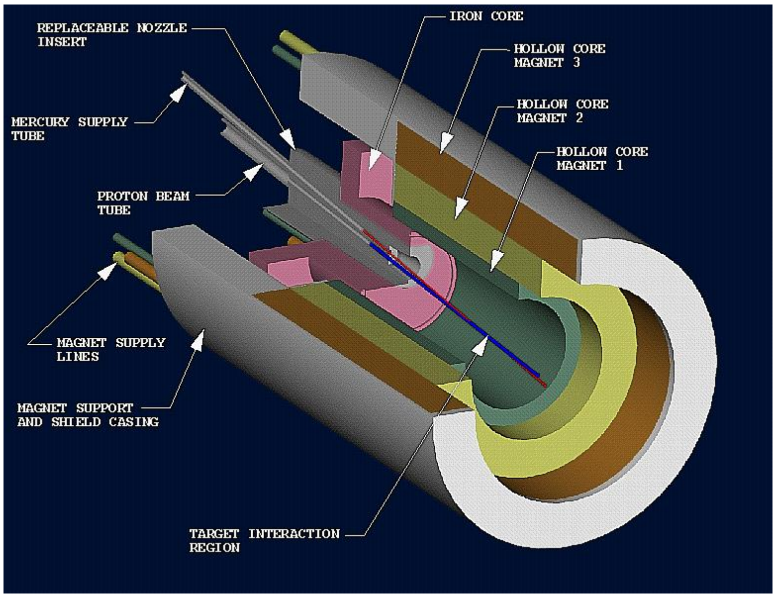

Figure 3.45: Cutaway view of the resistive insert magnets that surround the proton beam and mercury jet.

3.8.2 Assembly and Installation

The assembly and installation of the magnet system was the major consideration for determining the facility arrangement. The coil/shield modules are the heaviest and largest components and were the basis for establishing the building height and width, and determining the crane capacity needed for installation operations and subsequent maintenance.

The overall dimensions of the coil modules and their respective component weights are given in Table 3.16. The largest module weight was used to determine the lifting requirement in the crane hall. Installing the tungsten-carbide shield for SC 4–5 is the heaviest lift at approximately 43 tons. A 50-ton bridge crane with a 46-ft span was chosen.

3.8.3 High-Field Region

The high-field coils providing a 20-T field in the target region comprise three resistive coils (H-C 1–3), an iron plug surrounded by a water-cooled tungsten-carbide shield (Figs. 3.45-3.46), and an outer superconducting coil (SC 1, Figure 3.43). The H-C coils and part of the shield constitute a single module that is installed into the cryostat of the high-field

Table 3.16: Solenoid coil sizes and weights, and shield module weights.

Component	Outer Diam. (cm)	Length (cm)	Module Wt. (lb)
Resistive Module	110	180	47,500
Iron Plug	-	-	-
H-C 1	-	-	-
H-C 2	-	-	-
H-C 3	-	-	-
W-C Shield	-	-	-
Main Cryostat + Shield Beam	270	740	73,600
SC 1	256	178	61,000
SC 2–3	202	183	21,700
Shield 2–3	128	183	59,600
SC 4–5	176	351	17,900
Shield 4–5	148	351	86,400
SC 6 + Shield	104	50	$< 4,000$
SC 7 + Shield	104	185	11,800
SC 8 + Shield	104	185	10,800
SC 9 + Shield	104	185	9,600
SC 10 + Shield	104	185	8,400
SC 11 + Shield	104	185	7,700
SC 12 + Shield	104	185	6,600
Decay Coils + Shield (6)	87	296	12,600

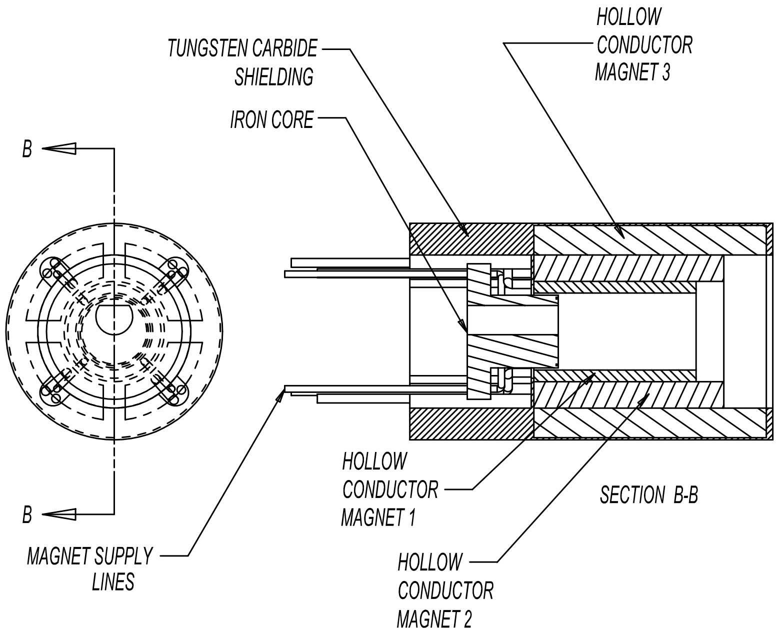

Figure 3.46: Section cut and end view of the resistive coil module.

superconducting coil.

3.8.4 Coil-to-Coil Forces, Method of Support and of Assembly

The net force on coils SC 1–25 is nearly zero, meaning it is a balanced system. SC 1 reacts to the forces of SC 2–25 with an equal and opposite force. However, the coil-to-coil forces between individual magnets are large. SC 1 reacts to the accumulated forces of the downstream coils with 23 million pounds (102.5 kN). The forces from SC 2–5 are, respectively, 1.0×10^6 lb, 6.6×10^6 lb, 3.4×10^6 lb, and 2.3×10^6 lb. (The force contributions from the remaining SC coils are ignored here since they are small by comparison.)

To minimize heat leaks into the SC 1–5 cryostat caused by large-area cold-to-warm-to-cold supports, use of a common cryostat was chosen by the solenoid coil designers. Therefore, the coil-to-coil supports are cold, but the cryostat structure must support the total gravity load of coils SC 1–5. This is accomplished by making a cylindrical portion of the radiation shield part of the cryostat (Fig. 3.43). The cryostat is assembled from two sections onto a continuous cylindrical beam that is part of the radiation shield. The cryostat/beam assembly is lowered into the target region of the tunnel, onto a pair of

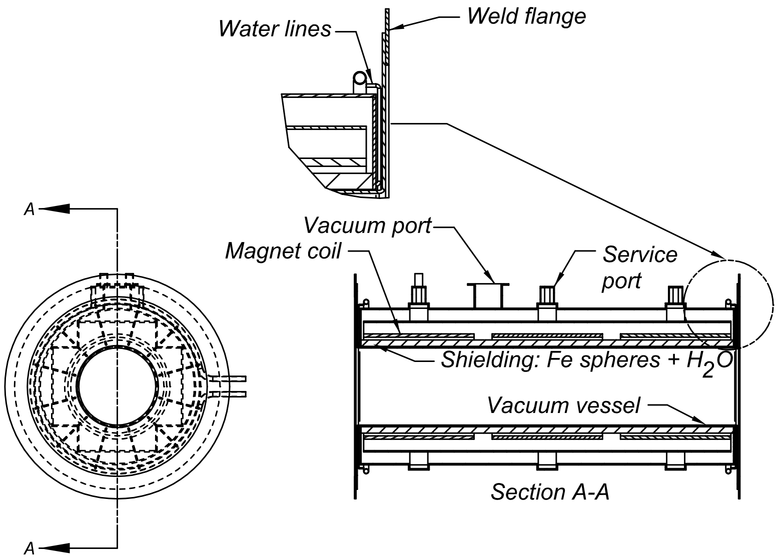

Figure 3.47: Decay channel cryostat module.

trunnion supports (see Fig. 3.48). The trunnion is located midway along the cryostat to minimize the depth of pit area under SC 1–5, and to minimize the elevation of the crane for installing SC 4–5. The cryostat is rotated so that the upstream end points up for the installation of SC 1. The weight of the SC 1 is 61,000 lb. The bridge crane is used to assist lowering the main cryostat so that the downstream end points up and the coil module consisting of SC 2–3 is installed followed by its inner shield. The cryostat is then rotated again, with assistance from the crane, so that the upstream end points up. The resistive coil module (iron plug, H-C 1–3, and shielding) is then installed into the inner bore of the shield-beam. The cryostat position is reversed again and module SC 4–5 is installed, followed by its inner shield. This sequence avoids exceding the 50-ton load limit of the crane. Figure 3.48 shows the installation sequence of the coils in the main cryostat.

3.8.5 Decay Channel Coils

Each of the remaining cryostat modules contains a radiation shield 5-cm-thick, beam mounted to the inner diameter of the cryostat shell. For the coils downstream of $z = 6.1$ m, the shield material is water-cooled copper or stainless steel. A homogeneous mix of stainless steel balls ($2 < d < 6$ mm) is judged to be the most cost-effective approach, and was used for the design.

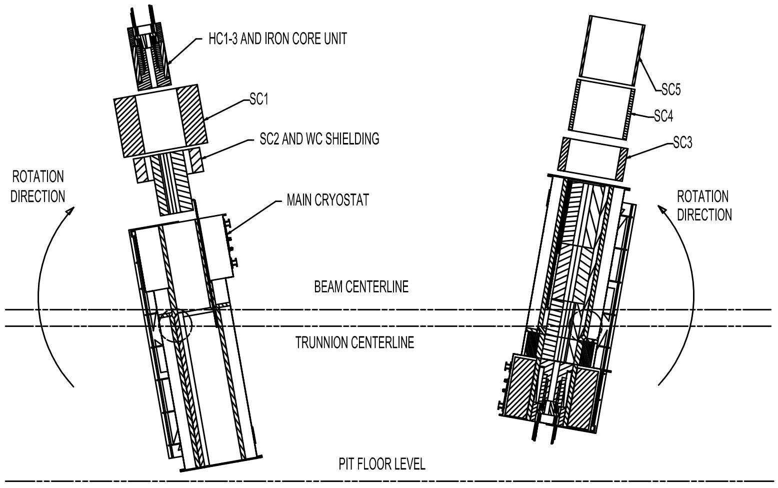

Figure 3.48: Installation sequence for the high field coils SC 1 and H-C 1–3, and transition coils SC 4–5.

A separate vacuum boundary for the muon decay channel is pre-installed to the inner shell of each shield/cryostat assembly. These are assembled so that the outer flange of the vacuum boundary shell can be seal-welded to the flange of adjacent modules, and subsequently cut for disassembly. Figure 3.47 shows typical side and end views of the decay channel magnets, the vacuum flange attachments, and clearance for coolant lines.

3.8.6 Coil Replacement and Remote Handling

The solenoid magnets are designed to be lifetime components. However, they are configured for remote replacement in the event of failure, since they will become highly activated, and since the ability to replace any of them is critical to the operation of the facility. The reverse of the assembly procedure described above is the disassembly method to replace any of the coils. Removal of any solenoid cryostat requires removing at least 24 shield slabs covering the tunnel. Each shield piece weighs 45 tons; ample space has been provided on the crane hall floor to stack the shielding. Once the process of removing shielding is started, personnel access to the crane hall is not permitted and removal operations must be done remotely using the bridge-mounted manipulator system. The maintenance cell located above the target hot cell is configured to accommodate the cryostat modules for subsequent dismantling and waste disposal. The maintenance cell is located adjacent to the staging area where new components are delivered and where waste disposal casks are shipped out of the facility. Figure 3.49 shows the maintenance cell and its relation to the target region and the staging area.

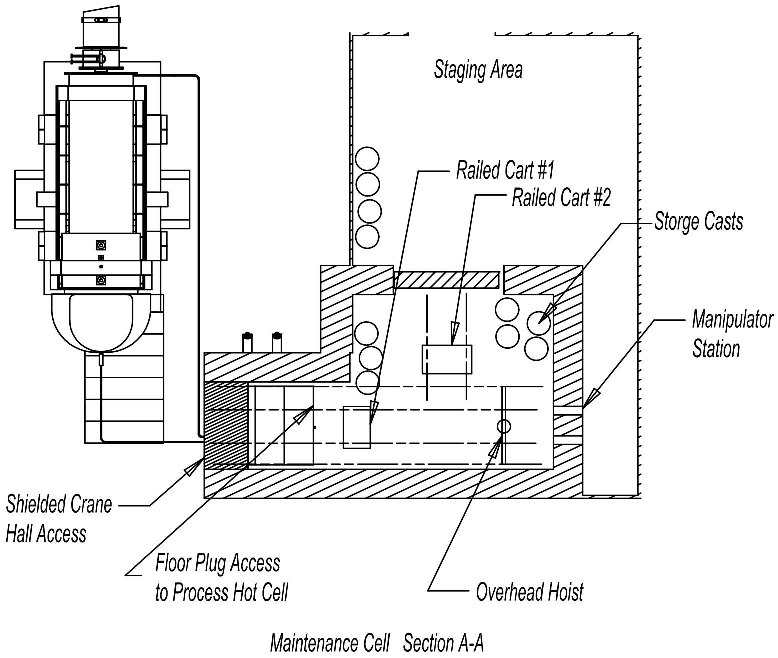

Figure 3.49: The target facility maintenance cell.

3.8.7 Facility Shielding

The facility shielding is designed to permit unlimited access to radiation workers in the crane hall. The shield material and thickness limit the dose rate at the crane hall floor to 0.25 mrem/h (0.0025 mSv). A Monte Carlo neutron, photon, charged particle transport code (MCNPX) using cylindrical geometry was prepared for neutronic calculations. The results show that the shield over the target region should be 5.8 m thick and the shield over the decay channel should be 5.2 m thick. For the purpose of this design, an average thickness was used throughout, consisting of 5.2 m of steel to attenuate fast neutrons and 0.3 m of concrete to attenuate slow neutrons. The model analyzed the shielding requirement downstream to $z = 36$ m, but it is clear that beyond the decay channel, into the first induction linac and beyond, similar facility shielding is needed, and the solenoid components will have dose rates too high to permit hands-on maintenance. Therefore, the crane hall and the remote handling access that it provides to the target/capture magnets should extend well beyond the end of the decay channel. It may be assumed that the same crane hall configuration could be used to service the linear accelerator regions downstream.

Figure 3.50 is a typical cross section in the decay channel showing the arrangement of removable shield slabs. The dimensions for each shield piece are determined by limiting their weight to 45 tons. The amount of shielding needed to limit the dose rate in the crane hall to 0.25 mrem/h is 5.2 m of steel, covered with a 30-cm concrete layer. Each slab layer is 46-cm thick, but the length and width varies, so each layer has offset joints that avoid a streaming path to the crane hall. It should be noted that the width of the tunnel decreases from 7 m in the target region to 5.2 m at approximately $z = 7$ m because of the smaller diameter of the magnets downstream from SC 7.

The shielding requirement upstream of the target region to attenuate backscattering is 2.6 m of steel. This thickness was chosen to limit dose rate to 1 rem/h. A stacked assembly of steel blocks is located in the 3-m-diameter vacuum vessel that encloses the proton beam window and the mercury-jet nozzle. The beam window is located at $z = -3.3$ m and is attached to the beam pipe feedthrough with a Grayloc© or Reflange© remote connector. (The beam pipe diameter is assumed to be 25 cm, although that is not a limiting factor for the remote connector.) This type of connector is well suited for reliable, robust operations that are done frequently. Figure 3.42 is a section view of the vessel showing the arrangement of the components it contains and the relation with the target system. Removal of the nozzle insert and resistive coil module is through the vacuum vessel after removing shield segments.

3.8.8 Maintenance Operations

The components in the target/capture facility fall into three maintenance categories, as discussed for the target system. The basic maintenance requirements for the facility are summarized in Table 3.17.

3.9 Target System Summary

This chapter has presented conceptual designs of components to generate pions by bombarding a jet of mercury with high-energy protons, and then to capture the pions with a solenoidal field that bends the pion trajectories into helices that fit within the 0.15-m-diameter solenoid bore.

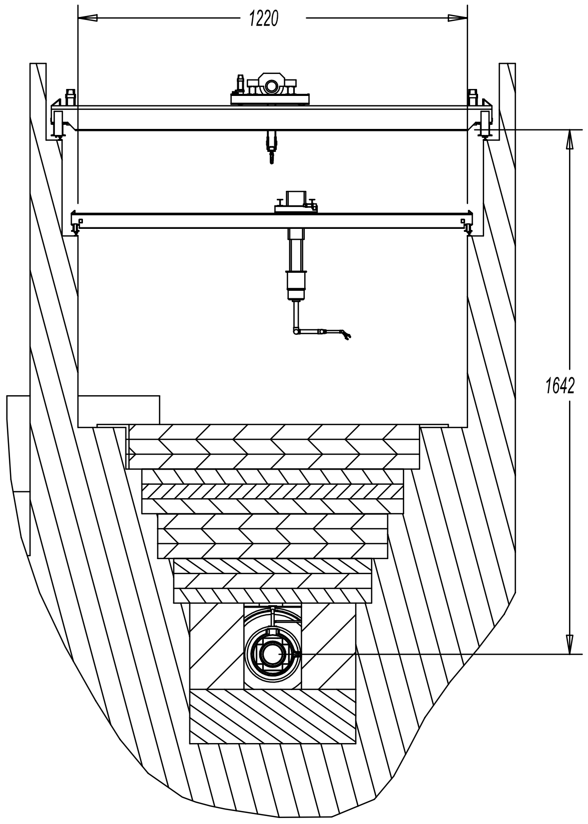

Figure 3.50: Facility shield over the decay channel.

The high-field region is 0.6 m long, with a peak field of 20 T. Downstream the field drops adiabatically by a factor of sixteen to 1.25 T over a distance of 18 m, while the bore increases by a factor of four. The mercury jet is 1 cm in diameter, with a speed of 30 m/s and a tilt angle of 100 mrad relative to the axis of the magnetic field. An analytical estimate predicts that the jet should enter the target region with little deceleration and deflection. However, these calculations suggest that the jet must not encounter any strong field gradient, if it is to avoid excessive shear and distortions in shape. We allow the field to droop only $\approx 5\%$ over the 0.6-m-long target region. Confirmation of the need for field uniformity comes from preliminary results from FronTier, a sophisticated hydrodynamic code that can track the free interface of the jet as it deforms in a magnetic field or breaks

Table 3.17: Maintenance requirements for the target/capture components. The replacement times for the solenoid include the time for fabricate a replacement.

Component	Class	Expected Life (yrs.)	Replacement Time wks.)
Proton beam window	1	2	1
Vacuum pumps, valves, ...	1	7	1-2
Resistive solenoid module	2	> 40	30-40
High-field solenoids	2	> 40	50-60
		30-40 (includes time to	
Transition solenoids	2	> 40	30-40
		20-30 (includes time to	
Low-field solenoids	2	> 40	20-30

up from shock waves.

Finite element analysis predicts that pressure waves from the instantaneous heating of the mercury to several hundred degrees by the proton beam will splatter the jet completely. To replenish the 0.6-m-long jet in only 20 ms, the desired time interval between proton bunches, dictates the 30 m/s jet velocity.

Radiation emanating from the target is intense. The computer code MARS predicts that the neutral flux rate through the beam pipe is up to 3×10^{20} per cm^2 per year for neutrons, and an order of magnitude higher for gamma rays. Charged particle flux rates are 10^{20} per cm^2 per year for hadrons and for electrons. The power dissipation is up to 2 W/g and the total radiation dose up to 4×10^{10} Gy/yr. These levels require shielding of many components, such as the pion capture magnet.

The pion capture magnet system is a hybrid, with many coaxial superconducting coils and a resistive insert. The system stores 600 MJ, with a superconducting coil that generates 14 T in a bore of 1.3 m. The resistive insert receives radiation so intense that only ceramic insulation will survive. The baseline design for the insert uses water-cooled hollow conductor insulated with a layer of magnesium oxide between its copper conductor and sheath. To generate 6 T in a large volume, the coil consumes 12 MW and requires many conductors in parallel in each layer to limit the hydraulic path length. For a design lifetime of many years rather than a few months, the bore accommodates a layer of water-cooled tungsten carbide ≈ 10 cm thick to attenuate the radiation by a factor of 30. The pion capture magnet employs superconducting coils of two types. High-field, large-bore coils employ cable-in-conduit conductor. The lower-field, smaller-core coils that ramp the field down to 1.25 T employ Rutherford cable (as do the phase-rotation coils farther downstream). All coils require shielding to limit the power deposition to < 1 W/m^3, to avoid quenching, and to limit the radiation dose to < 10 MGy/yr to enable organic insulation to survive.

Additional engineering challenges are mercury containment, mercury jet capture and diffusion, beryllium-window integrity and remote handling. The computer code MCNPX predicts nearly 2 MCi of activation after only a hundred days of operation, with 105 Ci remaining after 30 days of cool-down. The remote handling for maintenance and repair must deal with masses up to 45 tons and with components with limited accessibility. All of these components will benefit from additional research and development. Nevertheless, all aspects of the technology appear feasible.

Bibliography

[1] H.G. Kirk, *Pion Producion Cross Sections from E910 and MARS*, 2nd Intl. Workshop on Neutrino Beams and Inst. (Fermilab, Sept. 6-9, 2000), http://pubweb.bnl.gov/users/kirk/www/e910/fnal00/hkirk.pdf

[2] C.M. Ankenbrandt *et al.*, *Status of Muon Collider Research and Development and Future Plans*, Phys. Rev. ST Accel. Beams 2 081001 (1999)

[3] N.V. Mokhov, *Particle Production for a Muon Storage Ring: I. Targetry and π/μ Yield*, MUC0169 (Sep. 2000), http://www-mucool.fnal.gov/mcnotes/muc0169.pdf

[4] N. Holtkamp and D. Finley, eds., *A Feasibility Study of a Neutrino Source Based on a Muon Storage Ring*, Fermilab-Pub-00/108-E (2000), http://www.fnal.gov/projects/muon_collider/nu-factory/nu-factory.html

[5] B.J. King, N.V. Mokhov, N. Simos and R.V. Weggel, *A Rotating Inconel Band Target for Pion Production at a Neutrino Factory, using Study II Parameters*, MUC0199 (Apr. 9, 2001), http://www-mucool.fnal.gov/mcnotes/muc0199.pdf

[6] R. Samulyak, W. Oh and K.T. McDonald, *Numerical simulation of liquid jets in magnetic fields and applications* (Apr. 3, 2001), http://pubweb.bnl.gov/users/rosamu/www/MHD/Papers/mhd_jets.ps

[7] J. Gallardo et al., *First order perturbative calculations for a conducting liquid jet in a solenoid* (Feb. 21 2001), http://pubweb.bnl.gov/people/palmer/

[8] P. Thieberger, *Estimated perturbations of the axial motion of a liquid-metal jet entering a strong magnetic field*, MUC0182 (Nov. 8, 2000), http://www-mucool.fnal.gov/mcnotes/muc0182.pdf

[9] N.V. Mokhov, *MARS Code System User's Guide*, Fermilab-FN-628 (1995); http://www-ap.fnal.gov/MARS/

[10] N.V. Mokhov, *MARS Code Developments, Benchmarking and Applications*, in *Proc. ICRS-9 Int. Conf. on Rad. Shielding* (Tsukuba, Ibaraki, Japan, 1999), J. Nucl. Sci. Tech. **1**, 167 (2000).

[11] N. Mokhov, *Particle Yield and Radiation Fields in Feasibility Study-2 Target Capture System*, MUC0194 (Mar. 21, 2001), http://www-mucool.fnal.gov/mcnotes/muc0194.txt

[12] MCNPX Users Manual - Version 2.15, L.S. Waters, ed. Los Alamos National Laboratory, TPO-E83-G-UG-X-00001 (1999).

[13] MCNP-A General Monte Carlo N-Particle Transport Code, version 4A, J.F. Breismeister, ed. Los Alamos National Laboratory, LA-12625-M (1993).

[14] R.E. Prael and H. Lichtenstein, *User Guide to LCS: The LAHET Code System*, Los Alamos National Laboratory, LA-UR-89-3014 (1989).

[15] S.A. Fabritsiev et al., *Low-temperature radiation embrittlement of alloys*, J. Nucl. Mat. 233 (1996).

[16] K.H. Tanaka et al., *Development of Radiation-Resistant Magnet Coils for High-Intensity Beam Lines*, IEEE Trans. Magn. **30** (1994).

[17] J. Brooks et al., *World's Most Powerful Magnet Tested*, NHMFL Reports **7:2**, 1 (Spring 2000), http://www.magnet.fsu.edu/publications/reports/spring00screen.pdf

[18] R.J. Jayakumar et al., *The USHT-ITER CS Model Coil Program Achievements*, IEEE Trans. Appl. Supercon. **10:1** (2000).

[19] M.A. Green et al., *Superconducting Solenoids for the Muon Collider*, MUC0162 (Sep. 27, 1998), http://www-mucool.fnal.gov/mcnotes/muc0162.pdf

Chapter 4

Decay and Phase Rotation Channel

4.1 Concept

The function of the phase rotation section of the Neutrino Factory is to reduce the energy spread of the collected muon beam to a manageable level that will allow reasonable throughput to subsequent system components. We see in Fig. 4.1 the consequences of allowing the beam to drift without the application of properly phased acceleration. In Fig. 4.2 we see the longitudinal structure of the beam after the application of our proposed three-stage phase rotation system.

For a Neutrino Factory the requirements on the longitudinal phase space are quite different than those for a muon collider. Unlike the muon beam for a muon collider we can permit the captured muon beam to grow in its longitudinal dimensions and then put it through a buncher system that will permit the cooling section downstream to be operated with rf cavities having relatively high frequency.

If the process is done with a single drift and single induction linac, relativistic effects cause a distortion of the rotated bunch such that the initially high energy particles end up with a larger energy spread than the initially low energy ones. The use of at least two induction linacs, with a drift between them, allows this distortion to be greatly reduced.

It is natural for both these induction linacs to be bipolar, with initial deceleration and later acceleration. For technical reasons, such bipolar voltage pulses have been avoided in the baseline design. In the case of the first linac, a hydrogen absorber is placed immediately after it to reduce the beam energy, allowing the first linac to be unipolar. This absorber also reduces the emittance, and is thus referred to as a “minicooler.” The absorber is in two parts, with a field reversal between them to avoid the generation of angular momentum.

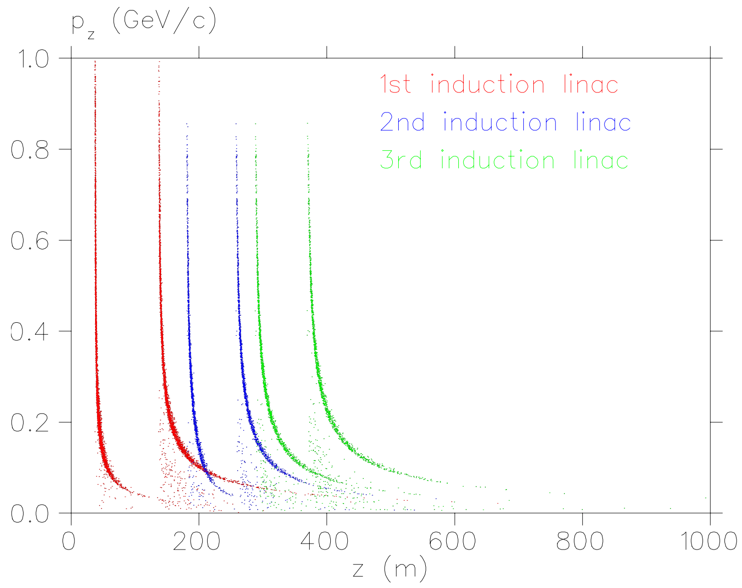

Figure 4.1: Beam longitudinal profile without phase rotation.

To avoid a bipolar second linac, it has been replaced with two linacs: the first unipolar decelerating, the second unipolar acceleration (A slightly less conventional bipolar second linac solution is discussed in Section A.2.4).

4.2 Drift Sections

A principal strategy for the drift sections of the capture/decay channel is to avoid the π-resonances that will be present due to the necessary periodic structure of the solenoidal magnetic field (resulting from gaps between the superconducting coils). Examples of these resonances are located at the minimum (odd-π) and maximum (even-π) points shown in Fig. 4.3. For drift sections, these nπ-resonance points are approximated by

$$p = \lambda \frac{Bc}{2\pi n} \tag{4.1}$$

where p is in units of eV/c, B is the average solenoidal field in Tesla, c is m/s and the period, λ, is in meters.

Particle losses in a 3 T periodic solenoidal system are confirmed in Fig. 4.4 where the spectrum of surviving particles after a 50 m drift is compared with the spectrum of the

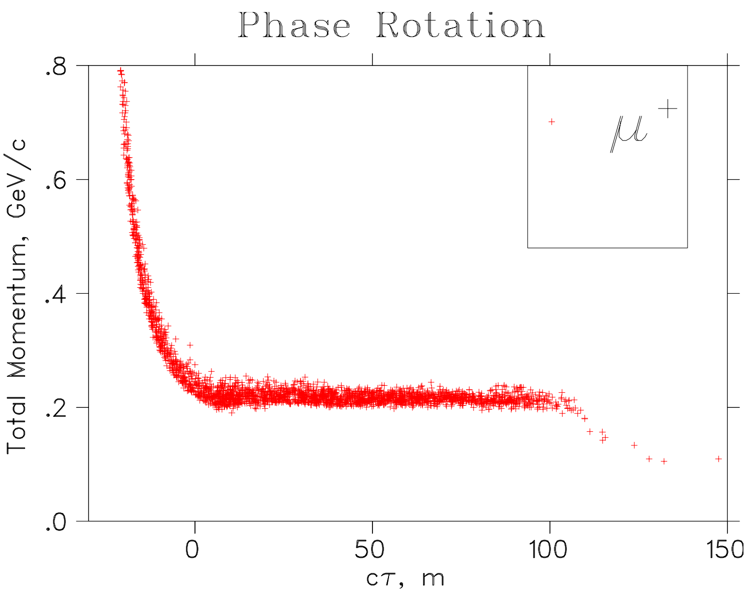

Figure 4.2: Beam longitudinal profile with non-distorting phase rotation.

source particles. The particle tracking for this example is done with ICOOL. Note the appearance of particle losses in the momentum band of 150–200 MeV/c which agrees well with the predictions seen in Fig. 4.3. Hence, if we wish to avoid particle losses in the momentum region of 100 to 300 MeV/c then a channel based on a 1.5 T solenoidal field and a 1 m period should be suitable.

We choose as the baseline for our decay channel the parameters $B = 1.25$ T and a period of 0.5 m. We extend this periodicity throughout the capture channel to include also the induction linac section, so that only the minicool section, with its single-flip solenoidal field does not exhibit this 0.5 m periodicity. Using ICOOL, we have compared the results of transporting the MARS-generated particles at the target through the exit of the third induction linac for both the case of 0.5 m periodicity and an artificial constant 1.25 T solenoidal field throughout the channel (excluding the minicool segment). We find that the total throughput of muons at the exit of the third induction linac is the same for both cases.

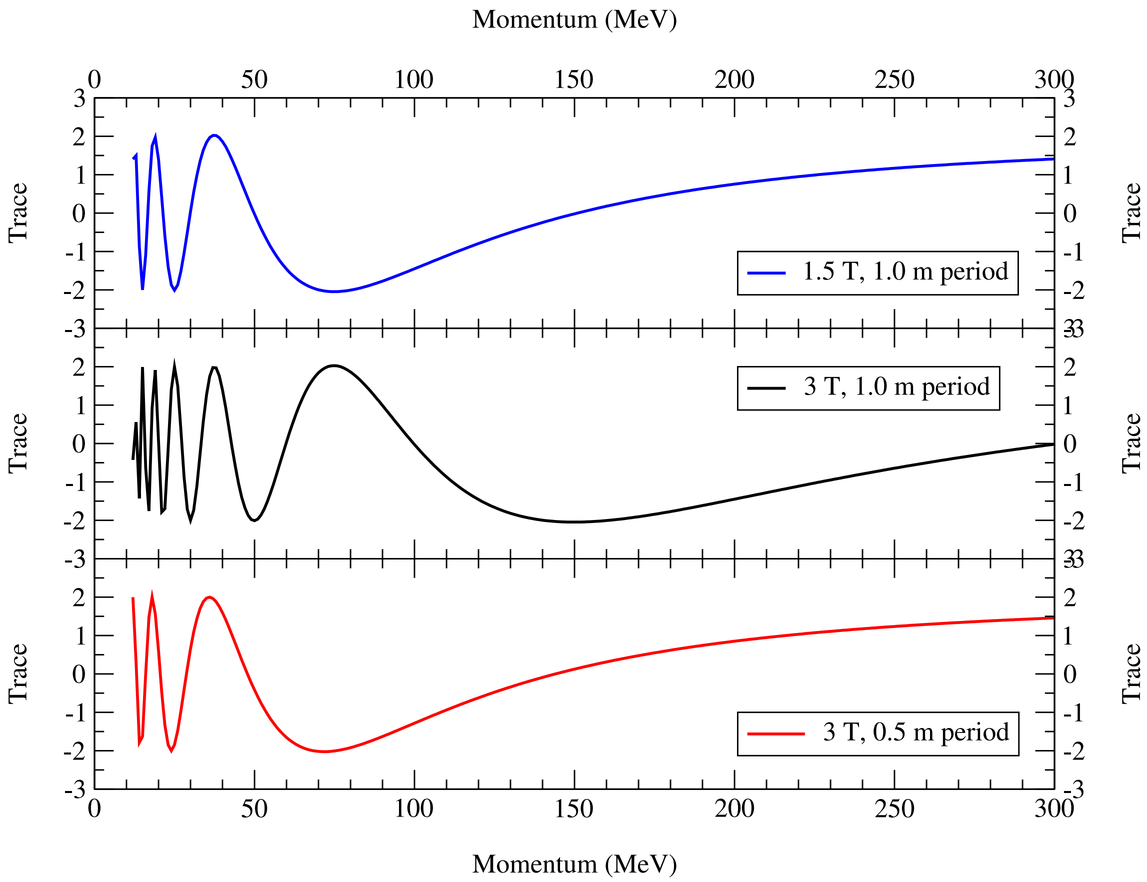

Figure 4.3: Location of nπ-resonances in a periodic solenoidal field.

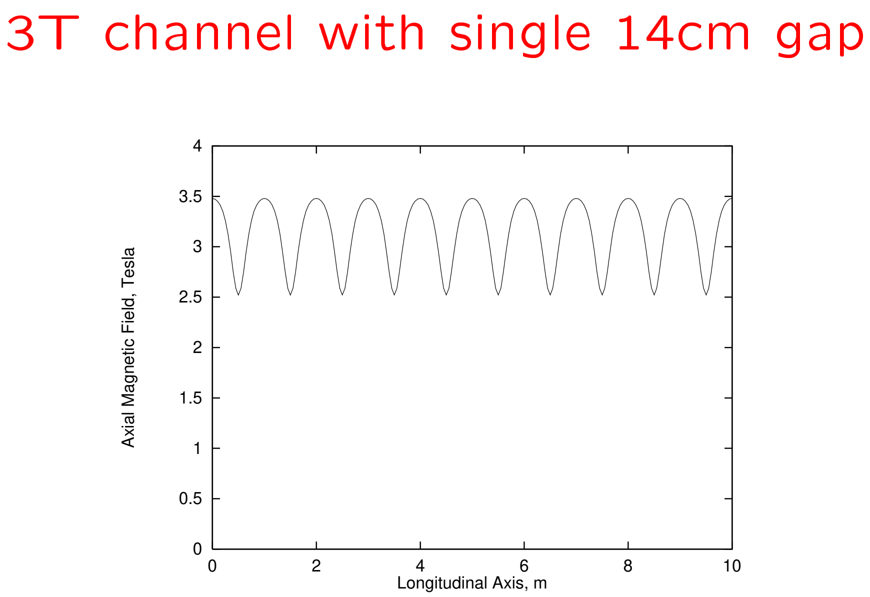

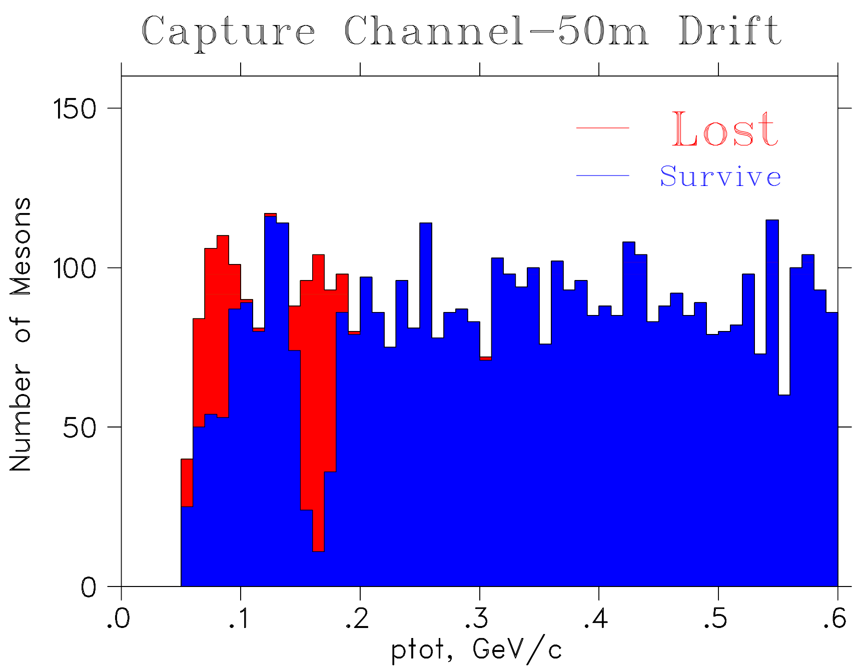

Figure 4.4: Particle losses after a 50 m drift in a 3 T, 1 m periodic solenoidal field

4.3 Induction Linacs

The muons drift first to spread out in time. The induction linacs then decelerate the early particles and accelerate the later ones. Three induction linacs are used with lengths of 100, 80 and 80 m, in a system that reduces distortion in the phase space of the rotated muon bunch and allows the induction linacs to operate with unipolar pulses. One additional feature of this design is that the 1.25 T transport solenoids are placed inside of the induction cores to avoid saturation of the ferrites. The induction linac units are similar to those being built for the DARHT project [1]; technical details are discussed in Chapter 9.

Figure 4.5 shows the pulse shapes of three induction linacs and Fig. 4.6 depicts a cross section of two units of the induction linac. The gaps in the solenoidal focusing, which lead to the periodicity described in Section 4.2, are apparent.

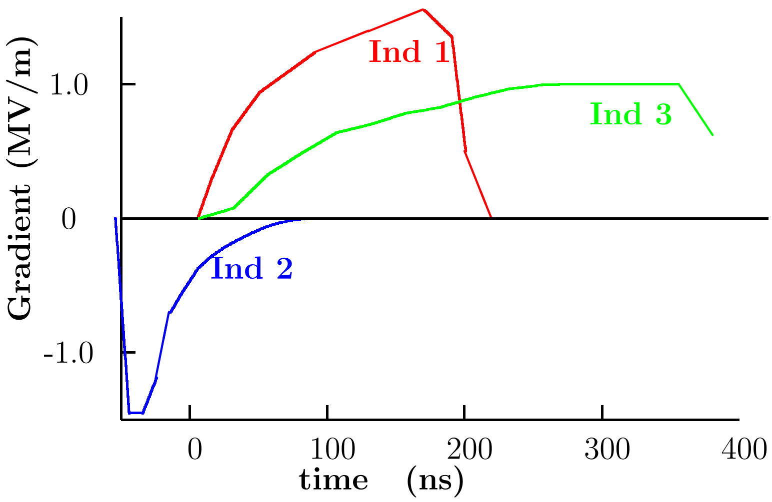

Figure 4.5: Pulse shapes of the three induction linacs.

4.4 The Solenoids

The decay and phase rotation region includes the IL1, the mini-cooler, IL2 and IL3, and extends from $z = 18$ m (from the target) to $z = 356$ m. Within this region, there are four types of solenoids.

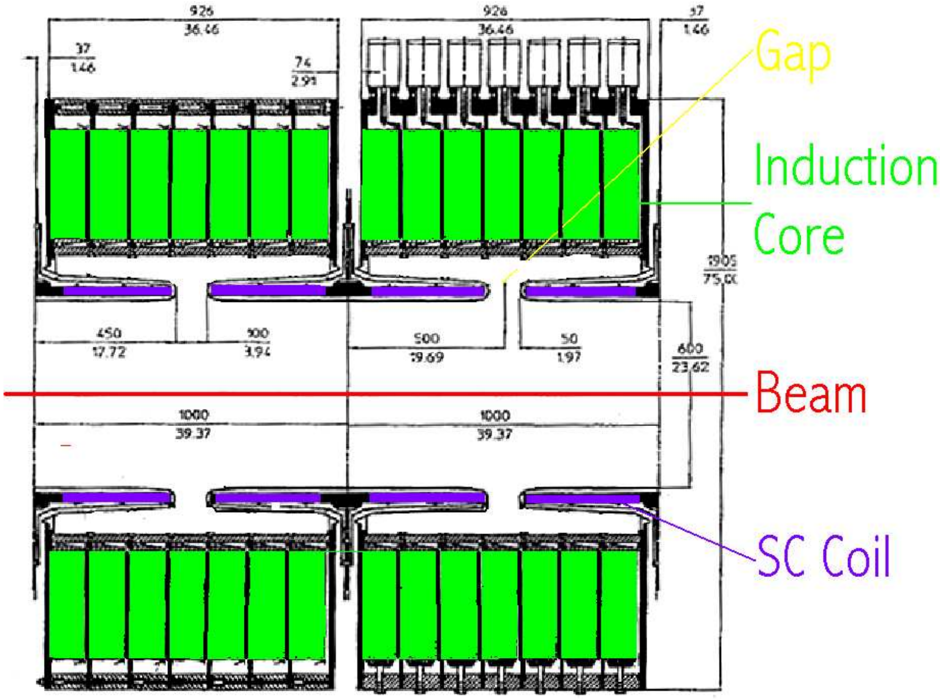

Figure 4.6: Cross section of two induction units.

1. From $z = 18$ m to $z = 36$ m, there is a decay section that has a warm bore diameter of 600 mm. Around this warm bore is a water-cooled copper shield that is 100 mm thick. The solenoid cryostat warm bore is thus 800 mm. The 18 m of decay solenoid is divided into six cryostats each 2.9 m long. This same type of magnet is used for the 9 m long mini-cooling sections on either side of the field-flip solenoid. As a result, there are twelve magnets of this type.

2. The IL1 solenoids, which extend from $z = 36$ m to $z = 146$ m, have a beam aperture of 600 mm diameter. Around the bore is a 10 mm thick water-cooled copper radiation shield. The warm bore of this magnet cryostat is thus 620 mm in diameter. There are 110 magnets of this type.

3. IL2 and IL3 and the drift between them extend, from $z = 166$ m to $z = 356$ m. These solenoids do not require a radiation shield and have a cryostat warm bore diameter of 600 mm. There are 190 magnets of this type.

4. The field-flip solenoid between the two mini-cooling sections is 2 m long with a warm bore diameter of 400 mm. There is only one such magnet.

Table 4.1 shows the design parameters for the induction linac solenoids and the solenoids in the decay channel and mini-cooling channel. The 2-meter long field flip solenoid is not included in this table. Technical details of the magnets are discussed in Chapter 10.

4.5 Minicooling Absorbers

The baseline design includes two "minicooling" liquid-hydrogen absorbers, each 30 cm in radius and 1.75 m long, preceded by a thin beryllium sheet and separated by a field flip. ICOOL simulations have been used to propagate MARS-generated secondary particles from the primary target through the initial induction linac module to the minicool absorbers. Tables 4.2 and 4.3 give the estimated power deposition in these absorbers for each important particle species generated at the target. For each mode the total power deposited in the absorber is about 5 kW. As seen in Fig. 4.7, the power dissipation in the first absorber is peaked at the absorber's upstream end. This energy dissipation peak is due to the arrival of low-energy protons which are generated at the target and conducted down the capture/decay channel. They are not removed by the induction linac because they are out of time with the higher velocity mesons and electrons. A beryllium sheet placed immediately before the liquid hydrogen absorber is used to absorb the low-energy protons and reduce the peak energy deposition in the first several cm of liquid hydrogen. However, even without this beryllium absorber foil, we find the volume power density in the liquid hydrogen to be manageable.

4.5.1 Handling the Average Heat Load

Even without detailed refrigeration studies, we can be confident about the overall power-handling capability of these absorbers based on experience with the Fermilab 15-foot bubble chamber. The 15-foot bubble chamber was cooled by a 6.7 kW refrigerator [2]. While considerably larger than a minicooling absorber, the bubble chamber had substantially lower beam-induced power dissipation; the large refrigeration plant was required to remove the heat generated by the work done on the fluid by the rapid-cycling expansion piston.

Each minicooling absorber will have refrigeration requirements comparable to that of the 15-foot bubble chamber. On the other hand, Table 4.4 shows that the refrigeration

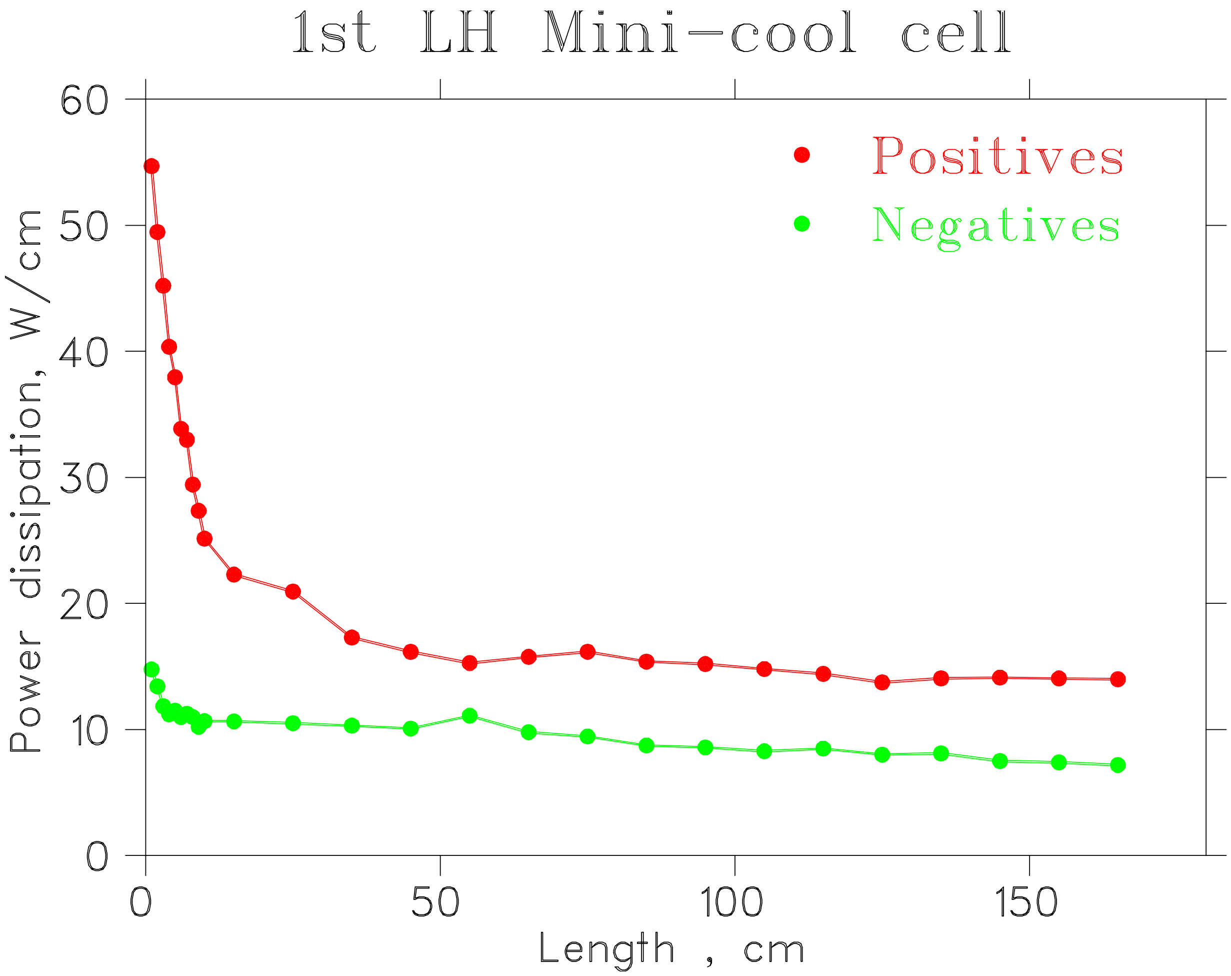

Figure 4.7: Power deposition along the length of the first minicool section.

needed for the minicooling absorbers dominates that of the cooling channel itself (see Section 5.3.6) and the extra complexity and reliability impact of operating two 15-foot-bubble-chamber equivalents is worth avoiding if a practical alternative is available; these considerations motivate the minicooling alternatives considered in Section 14.4.

4.5.2 Handling the Peak Power Density

Figure 4.7 shows the power dissipation *vs.* position along the absorber, and Fig. 4.8 shows the transverse distribution. For comparison, the liquid-hydrogen target built for SLAC Experiment 158 [3] is designed to handle 700 W, uniformly distributed over 1.5 m of length but with about 1 mm rms transverse beam size. While the power per cm at the upstream end of the first minicooling absorber is more than 10 times that in SLAC E158, the power per cm^3 is only about 10^{-3} of that in E158. We therefore conclude that the peak power density will not pose a problem and can be handled using one or the other of the approaches described elsewhere in this report (see Section 5.3.6).

4.5.3 Window Design

Unlike the case for the SFOFO absorbers, in the minicooling absorbers muon multiple scattering is dominated by the hydrogen, and muon-cooling performance hardly depends on the details of the window design. Furthermore, a hemispherical window shape, which minimizes the window thickness for a given strength, is practical for absorbers such as these, whose length far exceeds their diameter. The American Society of Mechanical Engineers (ASME) [4] specifies the minimum acceptable thickness for a hemispherical window as

$$t = \frac{0.5PR}{SE - 0.1P}, \tag{4.2}$$

where P is the differential pressure across the window, R the vessel radius, S the maximum allowable stress, and E the weld efficiency. For S, we follow ASME recommendations and use the smaller of 1/4 of the ultimate strength, S_u, or 2/3 of the yield strength, S_y; in practice, for aluminum alloys, it is the ultimate strength that matters. If we machine the window with an integral flange out of a single disk of material, as for the cooling channel absorbers, there are no welds and we can take $E = 1$. For 1.2 atm operation, and given the ASME specification for 6061-T6 aluminum alloy, $S_u = 289\,\text{MPa}$ and we obtain $t = 250\,\mu\text{m}$. While a detailed finite-element analysis (taking into account the stresses imposed on the spherical shell by the stiff flange) may result in a somewhat thicker window, even windows as thick as 1 mm have been shown by simulation to have negligible effect on muon-cooling performance.

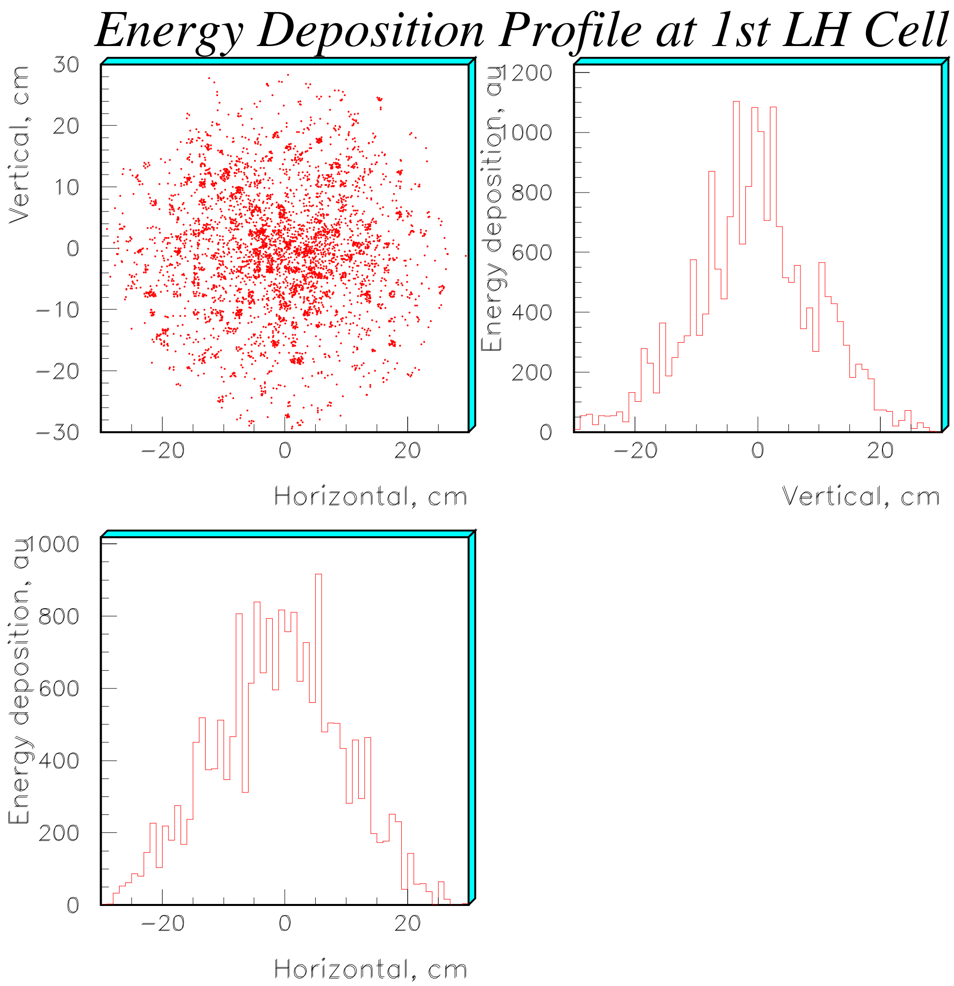

Figure 4.8: Transverse power deposition in the first minicool section.

4.6 Summary

The guiding principle of the design for the Capture/phase rotation section of the front end for the neutrino factory has been to achieve good performance while utilizing components based on at-hand technology. Key components include large aperture superconducting solenoids, 260 m of induction linac, and 3.5 m of liquid hydrogen absorbers. The gradients required for the induction linacs are between 1.55 and 1.0 MV/m. The muon beam delivered to the buncher has an rms energy spread, $\frac{\delta E}{E}$ of 4.4% and contains 0.49 μ/p within the $\pm 3.5\sigma$ boundaries of this energy spread.

Table 4.1: Decay, phase rotation, and minicool solenoid parameters.

	IL1 Magnets	IL2,IL3 Magnets	Decay Channel Magnets
Magnet Mechanical Parameters			
No. of cells of this Type	110	190	12
Cell length (mm)	1000.0	1000.0	3000.0
Magnet cryostat length (mm)	900.0	900.0	2900.0
Magnet coil package length (mm)	860.0	860.0	860.0
Number of coil packages per cell	1	1	3
Number of coils in the coil package	2	2	2
Length of each SC coil (mm)	360.0	360.0	360.0
Inner cryostat radius (mm)	310.0	300.0	400.0
SC coil inner radius (mm)	334.0	324.0	429.0
SC coil thickness (mm)	9.6	9.6	9.6
Support structure thickness (mm)	6.4	6.4	6.4
Magnet cryostat thickness at ends (mm)	55.0	55.0	80.0
Magnet cryostat thickness at center (mm)	80.0	80.0	80.0
Cold mass per magnet cell (kg)	207.6	201.1	911.1
Overall mass per magnet cell (kg)	277.3	268.0	1151.1
Magnet Electrical Parameters			
Average central induction (T)	1.25	1.25	1.25
On axis induction variation (%)	± 2.5	± 2.5	± 2.2
Peak induction in the windings (T)	~ 1.6	~ 1.6	~ 1.6
Number of turns per cell	2532	2532	7596
Magnet design current (A)	392.8	392.8	392.8
Magnet design operating temperature (K)	4.4	4.4	4.4
Conductor critical current at operating T (A)	~ 1600	~ 1600	~ 1600
Magnet stored energy per cell E (kJ)	224	211	1103
Magnet self inductance per cell (H)	2.90	2.74	14.3
Superconductor matrix J (A mm^{-2})	249	249	249
EJ^2 limit per magnet cell (J A^2 m^{-4})	1.39×10^{22}	1.31×10^{22}	6.86×10^{22}
Quench protection method	quench-back	quench-back	quench-back

Table 4.2: Power dissipation in the μ^+ collection mode.

	Power (kW)				
	e	μ	π	K	p
positives	0.42	2.02	0.14	0	0.86
negatives	0.43	1.29	0.24	0	-

Table 4.3: Power dissipation in the μ^- collection mode.

	Power (kW)				
	e	μ	π	K	p
positives	0.42	1.45	0.19	0	0.94
negatives	0.45	1.90	0.14	0	-

Table 4.4: Absorber parameters.

Absorber	Length (cm)	Radius (cm)	Number	P (kW)	P_{tot} (kW)
Minicool	175	30	2	$\approx$5	$\approx$10
SFOFO lattice 1	35	18	16	$\approx$0.3	$\approx$4
SFOFO lattice 2	21	11	36	$\approx$0.1	$\approx$3

Bibliography

[1] M.J. Burns, et al., *DARHT Accelerators Update and Plans for Initial Operation*, Proc. 1999 Acc. Conf., p.617.

[2] P.C. VanderArend, et al., *15-Foot Bubble Chamber Safety Report*, National Accelerator Laboratory Report NAL-48-A-2624, July 1972, Vol. 3.

[3] R. W. Carr *et al.*, *E158 Liquid Hydrogen Target Milestone Report*, April 21, 1999, http://www.slac.stanford.edu/exp/e158/documents/target.ps.gz.

[4] *ASME Boiler and Pressure Vessel Code*, ANSI/ASME BPV-VIII-1 (American Society of Mechanical Engineers, New York, 1980), part UG-32.

Chapter 5

Buncher and Ionization Cooling

In this Chapter, the Buncher and SFOFO cooling channel are introduced and described. Performance, systematic errors and tolerances are discussed. Design of the LH_2 absorbers is included here, in Section 5.3.6. Design of the rf components and superconducting solenoid magnets are discussed in Chapters 8 and 10, respectively.

The designs presented here for the bunching and cooling channels employ a variety of magnetic-focusing lattices. In these lattices, the solenoidal magnetic field is periodically reversed in order to modulate the beta function, producing periodic minima and maxima of beta, typically with local secondary minima and maxima located in between (see Fig. 5.6). To be specific in our descriptions, we here define a "cell" to be that portion of apparatus extending from one beta minimum to the next (for example, from one liquid-hydrogen absorber to the next in the SFOFO cooling lattice described below). Note that one cell of such a lattice thus corresponds to a half-period of the magnetic field.

5.1 Matching Section from the Induction Linac to the Buncher.

After the energy spread of the beam has been reduced in the induction linacs, the muons are distributed continuously over a distance of about 100 m. It is then necessary to form the muons into a train of bunches prior to cooling and subsequent acceleration. First, an 11-m-long magnetic lattice section (four 2.75 m cells) is used to gently transform the beam from the approximately uniform solenoidal field used in the induction linacs to the so-called "super-FOFO," or SFOFO, lattice used in the remainder of the front end. This is followed by the 55-m-long rf buncher itself, which consists of rf cavity sections interspersed with drift regions. These two functions are performed sequentially for design simplicity.

There is a significant advantage in using the same lattice in the buncher section as in the cooling region to follow, since it avoids adding another complicated 6-dimensional matching section.

Two distinct computer codes were used to simulate this buncher and the cooling channel: ICOOL [1] and Geant4 [2]. There is no shared code between the two programming environments: Fortran for ICOOL and C++ for Geant4. The Geant4 and ICOOL implementations were based solely on the parameters listed below. After optimization, good agreement between these two codes was obtained, as shown in the performance section. Thus, we have high confidence that the simulated cooling performance is realistic.

5.1.1 The Transverse Matching Section

The purpose of the transverse matching section is to transform the muon beam smoothly from the approximately uniform 1.25 T focusing field in the induction linac to the 2 T alternating polarity SFOFO lattice. The 4% rms momentum spread entering the matching section is relatively small, so chromatic corrections are less critical than in the minicooling field reversal. Table 5.1 gives coil dimensions and current densities for the solenoid magnets used in the matching simulations.

Table 5.1: Matching section magnets.

z (m)	dz (m)	r (m)	dr (m)	j (A/mm^2)
0.358	1.375	0.300	0.100	-9.99
1.733	0.330	0.300	0.110	-15.57
2.446	0.187	0.330	0.330	-33.40
2.963	0.187	0.330	0.330	35.19
4.008	0.330	0.770	0.110	67.41
5.146	0.187	0.330	0.330	43.75
5.663	0.187	0.330	0.330	-43.75
6.708	0.330	0.770	0.110	-66.12
7.896	0.187	0.330	0.330	-43.75
8.413	0.187	0.330	0.330	43.75
9.458	0.330	0.770	0.110	66.12
10.646	0.187	0.330	0.330	43.75

The magnet configuration at the beginning of the section, the axial magnetic field on-axis, and the beta functions for three momenta are shown in Fig. 5.1. The magnetic lattice

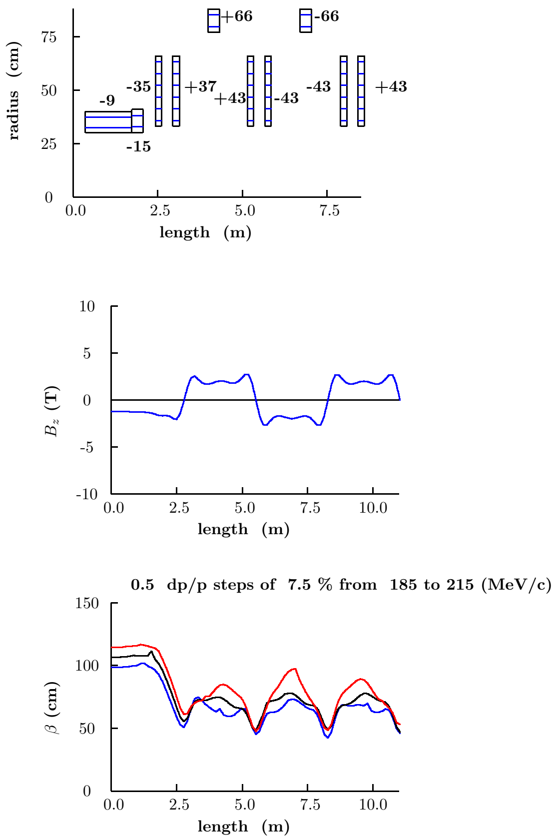

Figure 5.1: Magnet configuration, axial magnetic field and beta function of the matching section to the SFOFO lattice.

goes from a series of constant radius solenoids to an SFOFO cell structure consisting of small radius coils at each end of a cell and a large radius coil in the middle. The axial magnetic field in a cell peaks symmetrically near the two ends and has a smaller secondary peak in the middle. The beta functions across the match are similar for the three momenta shown, which vary in momentum steps of 7.5% from 185 to 215 MeV/c.

5.2 Buncher Section

The design principles for the lattice and details concerning the rf and other technical components for the buncher section will be described later. Only the beam dynamics and performance will be described here.

The buncher magnetic lattice is identical to that used in the first cooling section. It contains rf cavities in selected lattice cells and no absorbers. The main rf frequency was chosen to be 201.25 MHz in the front end, so that the beam would fit radially inside the cavity aperture. Power sources and other technical components are available at this frequency. The 201.25 MHz cavities are placed at the high-beta locations in the lattice, just as in the cooling section. Harmonic cavities running at 402.5 MHz are placed at minimum-beta locations, corresponding to where hydrogen absorbers are placed in the cooling section.

The buncher comprises 20 lattice cells, each 2.75 m long. Maximum bunching efficiency is obtained by breaking the region into three rf stages, separated by drift regions. The locations and lengths of the buncher components are given in Table 5.2.

Second harmonic (402.5 MHz) cavities are used at the entrance and exit of the first and second stages to linearize the shape of the rf pulse. All cavities are assumed to have thin Be windows at each end. They are modeled in the simulation codes as perfect TM_{010} pillboxes. The window radii and thicknesses are given in Table 8.5. The electric field gradient in the buncher ranges from 6 to 8 MV/m. A long drift is provided after the first stage to allow the particles to begin overlapping in space.

Figs. 5.2 and 5.3 show the momentum-time distributions at the start, and after each of the three buncher stages. Distributions are also shown at the ends of the first and second cooling stages. In the last three distributions, ellipses are drawn indicating the approximate acceptance of the cooling channel.

It can be seen that, at the end of the buncher, most, but not all, particles are within the approximately elliptical bucket. About 25% are outside the bucket and are lost relatively rapidly, and another 25% are lost in the cooling channel as the longitudinal emittance rises due to straggling and the negative slope of the dE/dx curve with energy.

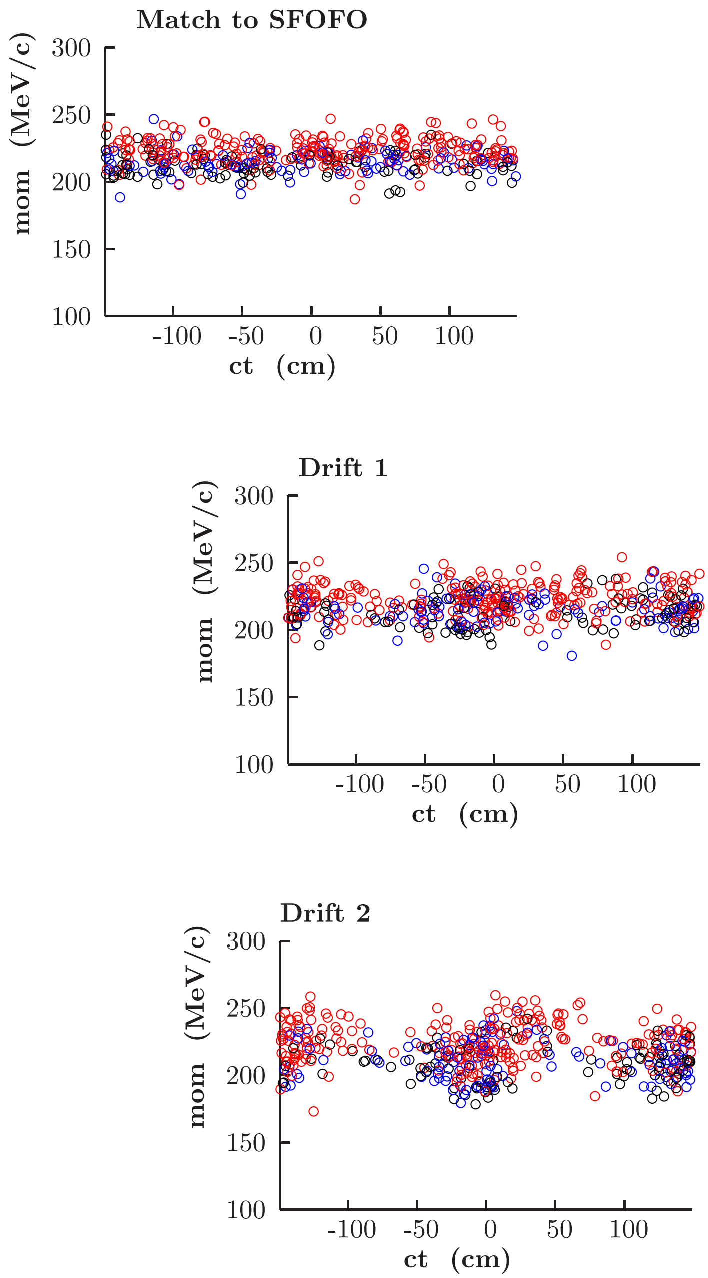

Figure 5.2: Momentum-time distributions through the buncher.

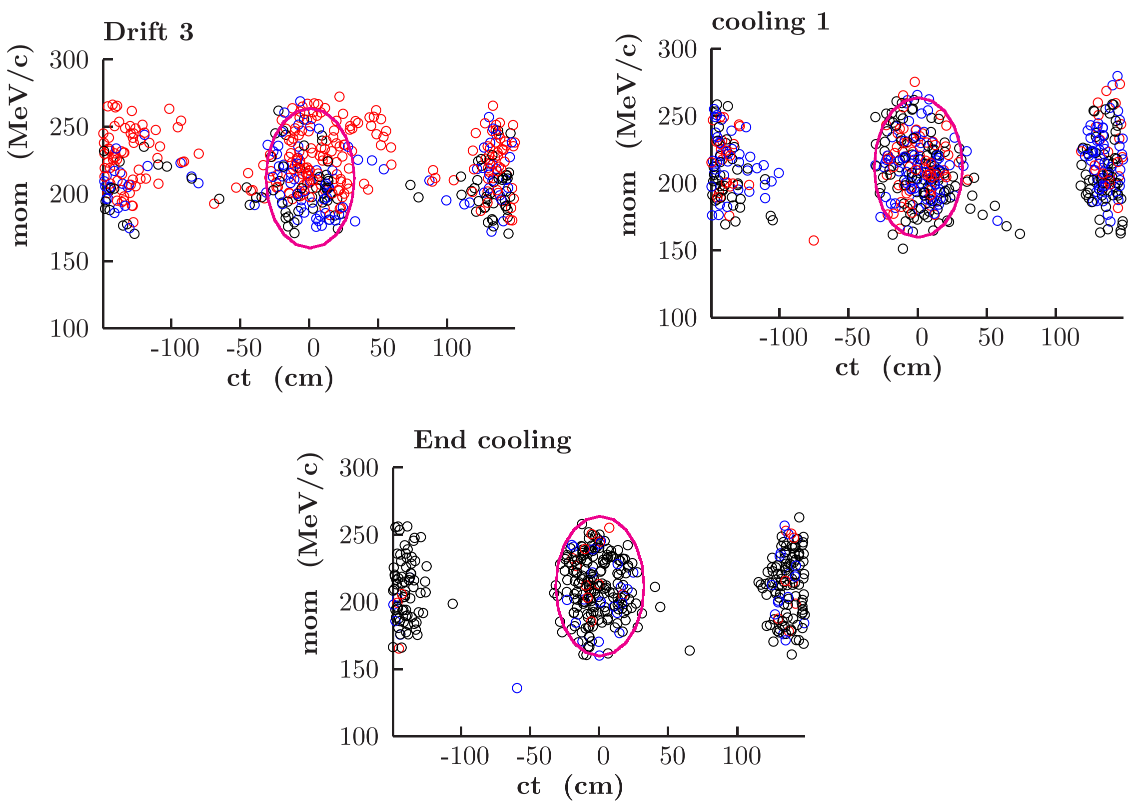

Figure 5.3: Momentum-time distributions through the buncher (continued).

5.2.1 Longitudinal-Transverse Correlation

A significant coupling develops in these pre-cooling stages of the Neutrino Factory (including the induction linac) between a particle's longitudinal and transverse motions. This occurs because particles with different transverse displacements, or angular divergences, take different amounts of time to move axially down the solenoidal lattice. They thus arrive at the cavities at different points in the rf cycle, or at a different time with respect to the induction linac pulse, thereby obtaining different accelerations and velocities. The resulting correlation, shown in Fig. 5.4, can be expressed as

$$p = p_o + CA^2, \tag{5.1}$$

where C is the correlation coefficient and the transverse amplitude is defined as

$$A^2 = \frac{r^2}{\beta_\perp^2} + \theta^2. \tag{5.2}$$

This quantity is evaluated at a waist in the transverse plane.

The magnitude of the momentum-amplitude correlation coefficient is seen from Fig. 5.4 to be 0.7 GeV/c. This is a higher value than the 0.45 GeV/c that would be obtained without the minicooling. Ideally, the correlation should be such that forward velocity in the following lattice is independent of transverse amplitude. A value of approximately 1.1 GeV/c would be required for this.

Figure 5.4 shows also that there is little correlation between momentum and angular momentum after the induction linacs, indicating that the field reversal in the minicooling is correctly located with respect to the induction linacs.

5.3 Ionization Cooling Channel

The rms transverse emittance of the muon beam emerging from the induction linac must be reduced to ≈ 2 mm·rad (normalized) in order to fit into the downstream accelerators and be contained in the storage ring. Ionization cooling is currently our only feasible option [3]. The cooling channel described below, as well as the one described in the appendix, are based on extensive theoretical studies and computer simulations performed in the same context as our previous studies [4, 3, 5, 6].

5.3.1 Principle of Ionization Cooling

In ionization cooling, the beam loses both transverse and longitudinal momentum by ionization energy loss while passing through an absorber. The longitudinal momentum

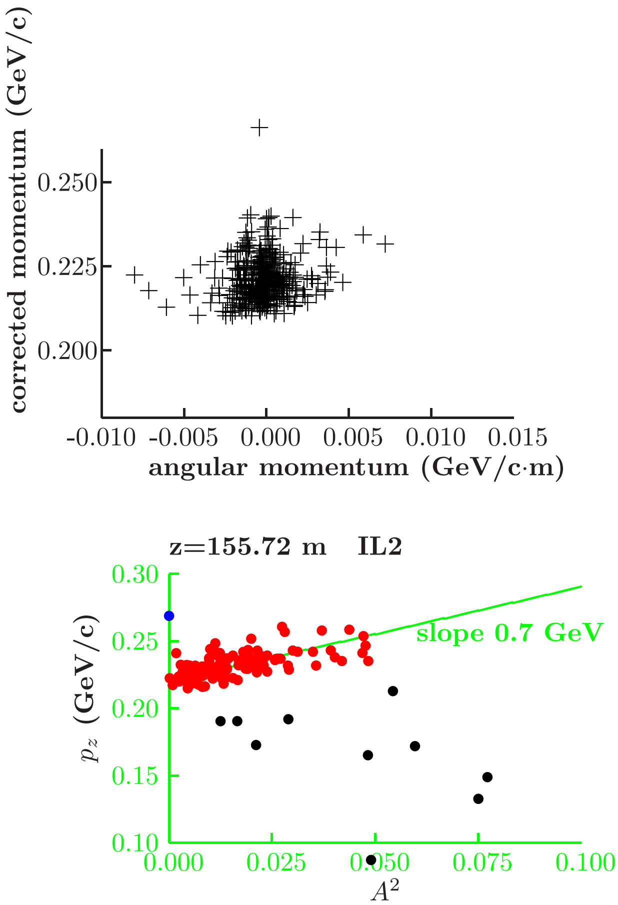

Figure 5.4: (top) Correlation between momentum and angular momentum; (bottom) correlation between longitudinal momentum and transverse amplitude (see Eq. 5.2), after the induction linac (IL2).

is then restored to the beam in rf accelerating cavities. This sequence, repeated many times, results in a reduction of the angular spread and thereby reduces the transverse emittance.

Ionization cooling is limited by multiple Coulomb scattering (MCS) in the absorbers. To minimize the MCS effect on cooling channel performance, we must have rather strong focusing at the absorber, with $\beta_{\perp,min} \approx 0.4$ to 0.2 m at a momentum of 200 MeV/c. Strong solenoidal fields are used for this purpose. Weak focusing, *i.e.*, too large $\beta_\perp$ at the absorbers, leads to excessive emittance growth due to MCS. Too strong focusing is hard to achieve for such large aperture beam transport, but can also be detrimental to the 6D beam dynamics. As the angles, or beam divergence, get too large, the longitudinal velocity decreases too much, leading to the wrong longitudinal-transverse correlation factor and thereby resulting in unacceptable growth of the longitudinal emittance. Choosing the right range of $\beta_{\perp,min}$ with respect to the operating momentum is a key to a successful design [3, 6].

The approximate equation for transverse cooling in a step ds along the particle's orbit is [4]

$$\frac{d\epsilon_N}{ds} = -\frac{1}{\beta^2}\frac{dE_\mu}{ds}\,\frac{\epsilon_N}{E_\mu} + \frac{\beta_\perp(0.014\mathrm{GeV})^2}{2\beta^3 E_\mu m_\mu\, L_R}, \tag{5.3}$$

where β is the normalized velocity, E_μ is the total energy, m_μ is the muon mass, ϵ_N is the normalized transverse emittance, $\beta_\perp$ is the betatron function at the absorber, dE_μ/ds is the energy loss per unit length, and L_R is the radiation length of the absorber material. The betatron function is determined by the strengths of the elements in the focusing lattice. Together with the beam emittance, the beta function determines the local size and divergence of the beam. (Note that the energy loss dE_μ/ds is defined here as a positive quantity, unlike the convention often used in particle physics.) The first term in this equation is the cooling term, and the second describes the heating due to multiple scattering. The heating term is minimized if $\beta_\perp$ is small (strong focusing) and L_R is large (a low-Z absorber).

The minimum normalized transverse emittance that can be achieved for a given absorber in a given focusing field is reached when the cooling rate equals the heating rate in Eq. 5.3,

$$\epsilon_{N,min} = \frac{\beta_\perp(14\mathrm{MeV})^2}{2\beta m_\mu \frac{dE_\mu}{ds} L_R}. \tag{5.4}$$

For a relativistic ($\beta \approx 0.87$) muon in liquid hydrogen with a beta function $\beta_\perp = 8$ cm, which corresponds roughly to confinement in a 15 T solenoidal field, the minimum achievable emittance is about 340 mm·mrad.

The equation for energy spread is

$$\frac{d(\Delta E_\mu)^2}{ds} = -2\, \frac{d\left(\frac{dE_\mu}{ds}\right)}{dE_\mu} \langle (\Delta E_\mu)^2 \rangle + \frac{d(\Delta E_\mu)^2_{\mathrm{stragg}}}{ds} \tag{5.5}$$

where the first term describes the cooling or heating due to energy loss, and the second term describes the heating due to straggling. ΔE_μ is the rms spread in the energy of the beam.

Ionization cooling of muons seems relatively straightforward in theory, but requires simulation studies and hardware development for its optimization and application. There are practical problems in designing lattices that can transport and focus the large emittance beam. There will also be effects from space charge and wake fields, if the beam intensity is sufficiently high.

We have developed a number of tools for studying the ionization cooling process. First, the basic theory was used to identify the most promising beam properties, material type and focusing arrangements for cooling. Given practical limits on magnetic field strengths, this gives an estimate of the minimum achievable emittance for a given configuration. Next several tracking codes were written, or modified, to study the cooling process in detail. These codes use Monte Carlo techniques to track particles one at a time through the cooling system. The codes attempt to include all relevant physical processes (*e.g.*, energy loss, straggling, multiple scattering), and use physically correct electromagnetic fields.

5.3.2 Concept of the Tapered SFOFO Cooling Channel

For optimal performance, the solenoidal field should not be kept constant during the entire cooling process. In a cooling channel with a constant solenoidal field, the transverse momentum of each particle will decrease, while the position of the Larmor center will not, causing the net angular momentum of the beam to grow. To avoid this, we flip the field while maintaining good focusing throughout the beam transport and low $\beta_\perp$ at the absorbers. One of the simplest solutions (the FOFO lattice), is to vary the field sinusoidally. The transverse motion in such a lattice can be characterized by its betatron resonances, near which the motion is unstable. The stable operating region is between the low momentum (2π) and high momentum (π) phase advance per half-period of the lattice. (Note that a half-period of the lattice is one "cell" in our notation.) The SFOFO lattice [7] is based on the use of alternating solenoids, but is a bit more complicated. We add a second harmonic to the simple sinusoidal field, producing the axial field shown in Fig. 5.5. As in the FOFO case, the axial field vanishes at the $\beta_{\perp,min}$ position, located at

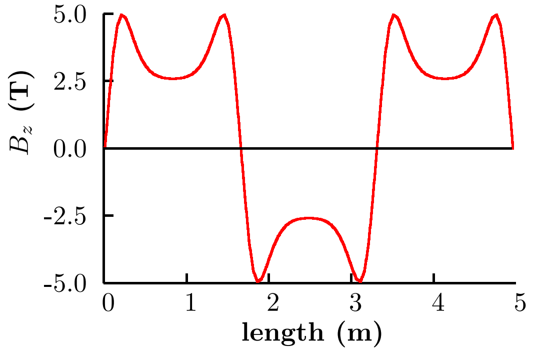

Figure 5.5: The longitudinal component of the on axis magnetic field, B_z, for a typical SFOFO lattice.

the center of the absorber. This is accomplished by using two short *focusing* coils running in opposite polarity. However, unlike the FOFO case, the field decreases and flattens at $\beta_{\perp,max}$, due to a *coupling* coil located midway between the focusing coils, around the rf cavity. The transverse beam dynamics is strongly influenced by the solenoidal field profile on-axis and by the desired range of momentum acceptance.

This SFOFO lattice has several advantages over the FOFO:

- The betatron resonances are usually a nuisance, since they inevitably restrict the region of stable motion. However, in this case they give us a strong, approximately constant, focusing result (*i.e.*, flat $\beta_\perp$) across the relevant momentum range, as we operate between the 2π and π resonances. This is illustrated in Figs. 5.6 and 5.7. Within this (albeit limited) momentum range the transverse motion is stable.

- For a given $\beta_{\perp,min}$, the SFOFO period is longer than the corresponding FOFO period, allowing longer absorbers per lattice cell, thereby reducing the relative amount of multiple scattering in the absorber windows. The longer period also allows more room for all other components.

- The focusing coils can be located just around the absorbers, adjacent to the rf cavity. Since the absorber has a much smaller outer diameter than does the rf cavity, this arrangement allows the diameter of these high-field magnets to be reduced considerably, with concomitant cost savings.

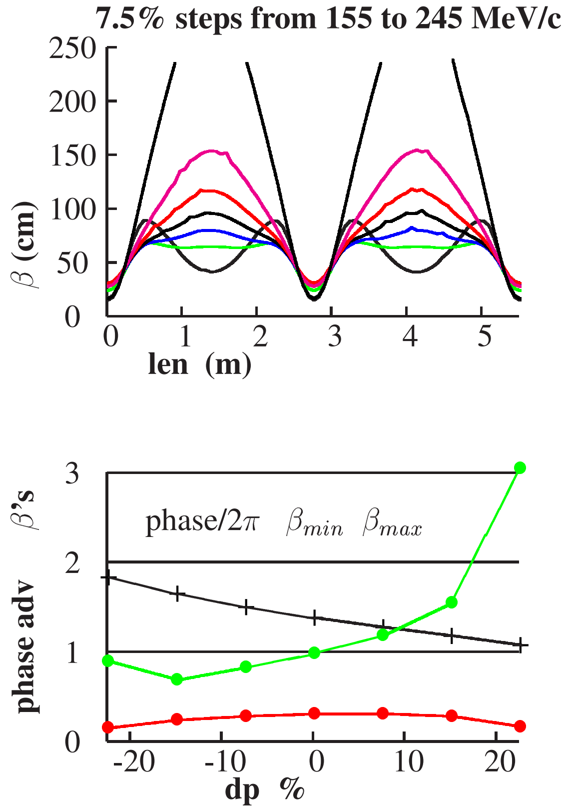

Figure 5.6: (top) Beta functions in the (1,3) cooling lattice section, at small transverse amplitude, for 7 different momenta, spanning the entire operating range from 155 to 245 MeV/c above the 2π and below the π resonance. (bottom) $\beta_{\rm min}, \beta_{\rm max}$ and phase advance as a function of relative momentum. The lower curve corresponds to $\beta_{\rm min}$ and the second curve from the bottom to the phase advance. The black crosses show the $\beta_{\rm max}$ function.

Table 5.2: RF buncher component locations used in the simulations.

	Length (m)	Frequency (MHz)	Phase (deg.)	Gradient (MV/m)
Harmonic rf	0.186	402.5	180	6.4
Space	0.443			
rf	4 × 0.373	201.25	0	6.4
Space	0.443			
Harmonic rf	0.186	402.5	180	6.4
Drift 1	10 × 2.75			
Harmonic rf	0.186	402.5	180	6
Space	0.443			
rf	4 × 0.373	201.25	0	6
Space	0.443			
Harmonic rf	2 × 0.186	402.5	180	6
Space	0.443			
rf	4 × 0.373	201.25	0	6
Space	0.443			
Harmonic rf	0.186	402.5	180	6
Drift 2	3 × 2.75			
Space	0.629			
rf	4 × 0.373	201.25	12	8
Space	0.629			
Space	0.629			
rf	4 × 0.373	201.25	12	8
Space	0.629			
Drift 3	2 × 2.75			

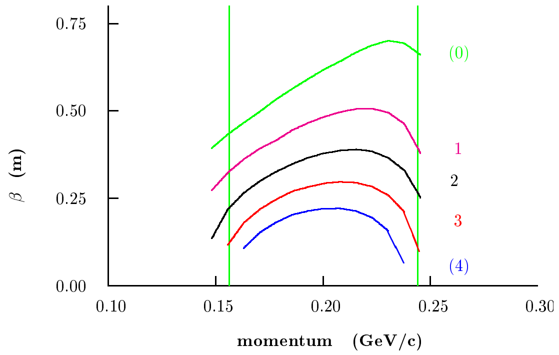

Figure 5.7: The $\beta_\perp$ function versus momentum for the five SFOFO lattices described below.

For a given lattice period, one can adjust independently the location of the two betatron resonances, or, equivalently, the nominal operating momentum and the $\beta_{\perp,min}$ at that momentum. By adjusting these two parameters, we can keep the $\beta_\perp$ symmetric about the required nominal momentum, and independently reduce the central $\beta_\perp$ value. However, this is true over only a limited momentum range. As we decrease the coupling field and increase the focusing field, the momentum acceptance will shrink as the π and 2π resonances move closer to the nominal momentum. At this point, we are forced to change the lattice period.

This brings us to the second improvement over the FOFO channel used in the previous feasibility study: $\beta_{\perp,min}$ can be "tapered" along the cooling channel. One can slowly increase the focusing strength at a fixed operating momentum, while keeping a reasonable momentum acceptance. Were we to use a fixed $\beta_{\perp,min}$, as the cooling progresses, the rms angle would decrease. The cooling rate would then also decrease as the heating term due to multiple scattering becomes relatively more important. By slowly increasing the focusing strength (decreasing $\beta_{\perp,min}$), we can maintain large rms angles at the absorbers ($\sigma_{x'} = \sigma_{y'} \approx 0.1$ rad), thereby keeping the relative effect of multiple scattering to a minimum.

5.3.3 Description of the SFOFO Cooling Channel

In this subsection, we describe the cooling channel from the viewpoint of the simulation effort. Engineering details will be given later.

5.3.3.1 Lattices

The channel operates at a nominal momentum of 200 MeV/c. There are six sections with steadily decreasing $\beta_{\perp,min}$. In the first three lattices, labeled (1,i), i=1,3, the lattice cell length is 2.75 m, and in the other three lattices, (2,i), i=1,3, it is 1.65 m. A cell of the cooling lattice comprises one absorber, one linac and three coils. The matching sections between these sections also consist of cooling cells, which differ from the regular cooling cells only by the current circulating in the coils, with one exception: A different coil length must be used in the matching section between the (1,3) and (2,1) lattices, where the cell length decreases from 2.75 m to 1.65 m. The lengths of these lattice sections are specified in Table 5.3. Coil dimensions and current densities are specified in Table 5.4. In the simulations, it is assumed that the current density is uniform across the thickness of the coil.

Table 5.3: Lengths of the sections and integrated length from the start of the cooling channel.

Section	Length (m)	Total length (m)
Cool (1,1)	$4 \times 2.75 = 11$	11
Match (1,1-2)	$2 \times 2.75 = 5.5$	16.5
Cool (1,2)	$4 \times 2.75 = 11$	27.5
Match (1,2-3)	$2 \times 2.75 = 5.5$	33
Cool (1,3)	$4 \times 2.75 = 11$	44
Match (1,3) - (2,1)	4.4	48.4
Cool (2,1)	$12 \times 1.65 = 19.8$	68.2
Match (2,1-2)	$2 \times 1.65 = 3.3$	71.5
Cool (2,2)	$8 \times 1.65 = 13.2$	84.7
Match (2,2-3)	$2 \times 1.65 = 3.3$	88
Cool (2,3)	$12 \times 1.65 = 19.8$	107.8

The design of the matching sections between regular sections of the same cell length goes as follows. In all cases, a matching section is inserted that consists of two lattice

Table 5.4: Geometry and current densities for the solenoids used in the simulations. The j(1,n) coil types refer to the 2.75-m-long cell, and the j(2,n) coils to the 1.65-m-long cell. The position refers to the upstream edge of the coil and starts from the beginning of a cell. The radius refers to the inner radius of the coil. The current indices refer to the nomenclature used in the previous table.

Type	Position (m)	Length (m)	Radius (m)	Thickness (m)	j(1,1) (A/mm^2)	j(1,2) (A/mm^2)	j(1,3) (A/mm^2)
Focusing	0.175	0.167	0.330	0.175	75.20	84.17	91.46
Coupling	1.210	0.330	0.770	0.080	98.25	92.42	84.75
Focusing	2.408	0.167	0.330	0.175	75.20	84.17	91.46
					j(2,1)	j(2,2)	j(2,3)
Focusing	0.066	0.145	0.198	0.330	68.87	75.13	83.48
Coupling	0.627	0.396	0.792	0.099	95.65	88.00	76.52
Focusing	1.439	0.145	0.198	0.330	68.87	75.13	83.48

cells, the first as in the previous cells, the second as in the following cells, except that the currents in the central pair of focus coils are set to an average of the currents in the previous and following focusing coils. For instance, Table 5.5 describes the match between the (1,1) and (1,2) lattices.

The match where the cell length changes from 2.75 m down to 1.65 m requires further attention. Although the proposed solution is not a perfect match, its mechanical simplicity and relatively short length may actually outweigh the benefit we might get with a slow, adiabatic match from one cell length to the other. Note that the absorber in the matching cell is removed, allowing us to run the upstream and downstream rf cavity phases closer to the bunching condition and giving us a slight local increase of the rf bucket size, as well as ease of mechanical assembly. Coils and currents are listed in Table 5.6. The magnetic field on axis for the entire cooling channel is shown in Fig. 5.8.

5.3.3.2 Cooling rf

The lengths of the rf cavities are constrained by the lattice design, as the focusing coils have a bore smaller than the rf cavities, and by the rf cell length, which must be optimized to give the high R_S required to reach high gradient (see Chapter 8). In the simulations, cavities are always placed in the middle of the lattice cell. Each rf cell can be phased individually. In order to improve the shunt impedance of the cavity, the iris of the cell

Table 5.5: Geometry and current densities for the solenoids in the first matching section. Coil locations are given with respect to the start of the channel. The coil dimensions are specified in Table 5.4.

Type	Location (m)	j(1,i) (A/mm^2)
	last (1,1)	
Focusing	11.175	75.20
Coupling	12.210	98.25
Focusing	13.408	75.20
	match	
Focusing	13.925	-75.20
Coupling	14.960	-98.25
Focusing	16.158	-80.07
Focusing	16.675	80.07
Coupling	17.710	92.42
Focusing	18.908	84.17
	first (1,2)	
Focusing	19.425	-84.17
Coupling	20.460	-92.42
Focusing	21.658	-84.17

Table 5.6: Geometry and current densities for the solenoids in the matching section between the (1,3) and (2,1) lattices. Coil locations are given with respect to the start of the channel.

Type	Location (m)	Length (m)	Radius (m)	Thickness (m)	j (A/mm^2)
			last (1,3)		
Focusing	41.425	0.167	0.330	0.175	91.46
Coupling	42.460	0.330	0.770	0.080	84.75
Focusing	43.658	0.167	0.330	0.175	91.46
			match		
Focusing	44.175	0.167	0.330	0.175	-91.46
Coupling	45.210	0.330	0.770	0.080	-84.75
Focusing	46.393	0.198	0.330	0.175	-95.24
Focusing	46.816	0.145	0.198	0.330	56.39
Coupling	47.377	0.396	0.792	0.099	95.65
Focusing	48.189	0.145	0.198	0.330	68.87
			first (2,1)		
Focusing	48.466	0.145	0.198	0.330	-68.87
Coupling	49.027	0.396	0.792	0.099	-95.65
Focusing	49.839	0.145	0.198	0.330	-68.87

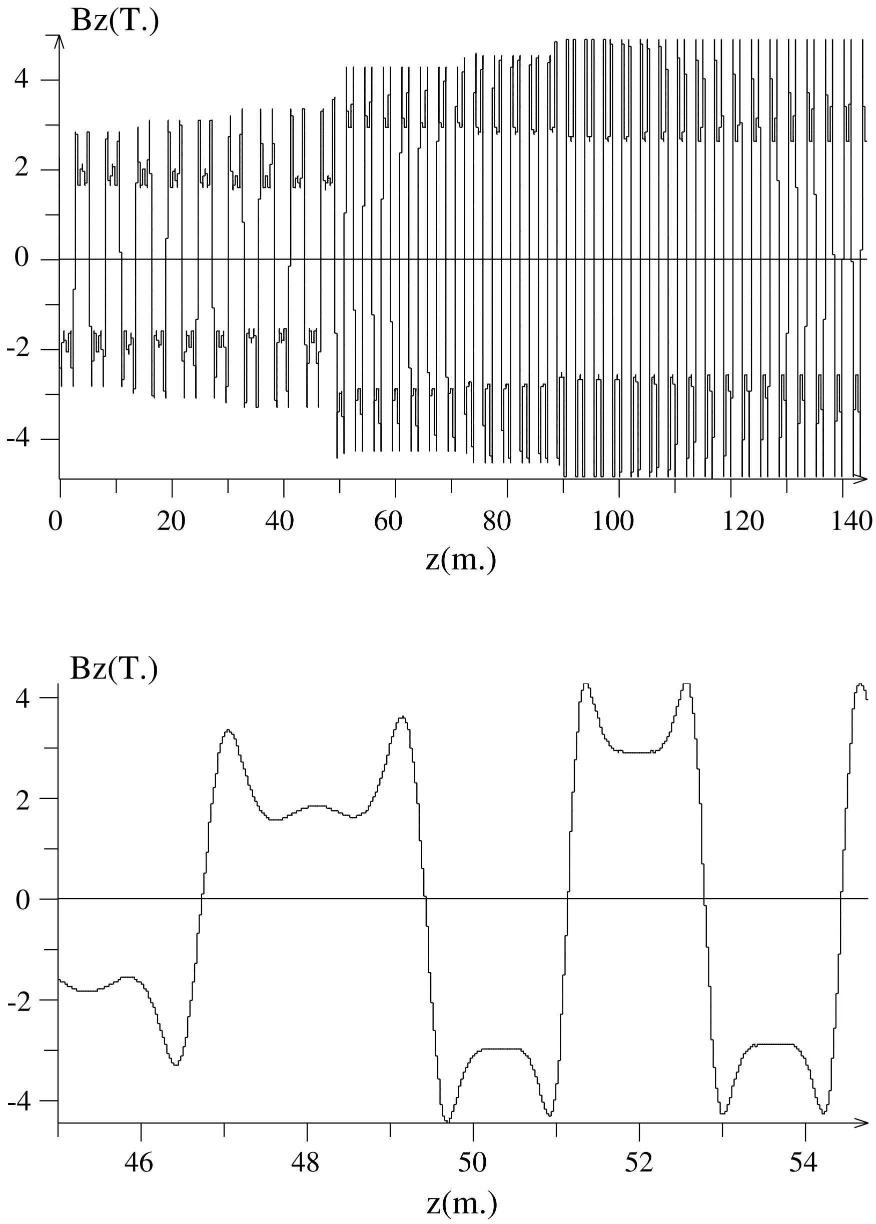

Figure 5.8: B_z on axis for the entire SFOFO cooling channel (top) and for the matching section between the (1,3) and (2,1) lattices (bottom).

is closed with a foil. Our baseline design calls for a thin, pre-stressed beryllium window with thickness that increases with radius. This arrangement is described in Chapter 8. Radius-dependent foil thickness is used because power dissipated in the foil goes like the fourth power of the radius (for small radius). Therefore, we benefit from more thickness at higher radius to remove the heat. In addition, particles at large radius tend to have large transverse amplitude and are "warmer" than the central core. Thus, a bit more multiple scattering can be tolerated at large radius. Windows at the end of a cavity dissipate half as much power as windows at the boundary between two adjacent rf cells. These end windows can be made thinner than those in the center of the cavity. The cavity parameters used in the simulations are listed in Table 5.7. The rf window parameters are in Table 8.5.

Closing the cavity iris with thin aluminum tubes arranged in a Cartesian grid can also be considered, as briefly discussed in Chapter 14.5.

Table 5.7: Geometry and rf parameters for the cavities in the cooling channel used in the simulation study.

Lattice type	No. of rf cells	Cell length (m)	Peak field (MV/m)	Phase (deg.)
(1,i), i=1,3	4	0.466	15.48	40
match	4	0.466	15.48	18.8
(1,3)-(2,1)	2	0.559	16.72	18.8
(2,i), i=1,3	2	0.559	16.72	40

5.3.3.3 Absorbers

The absorber material is liquid hydrogen (LH_2). The LH_2 vessels are equipped with thin aluminum windows; their thicknesses are 360 (220) μm , with radii of 18 (11) cm, for the (1,i) and (2,i) lattices, respectively.

The density of LH_2 is approximately 0.071 g/cm^3. The energy loss, as given by the Bethe-Bloch formula [8] with a mean excitation energy of 21.9 eV, is 4.6 MeV·cm^2/g. The absorber length is 35 cm for the (1,i), i=1,3 lattices and 21 cm for the (2,i) lattices, respectively. The muons lose $\approx$ 12 MeV per lattice cell for the (1,i) lattices and $\approx$ 7 MeV for the (2,i) lattices, including the energy loss in the absorber windows.

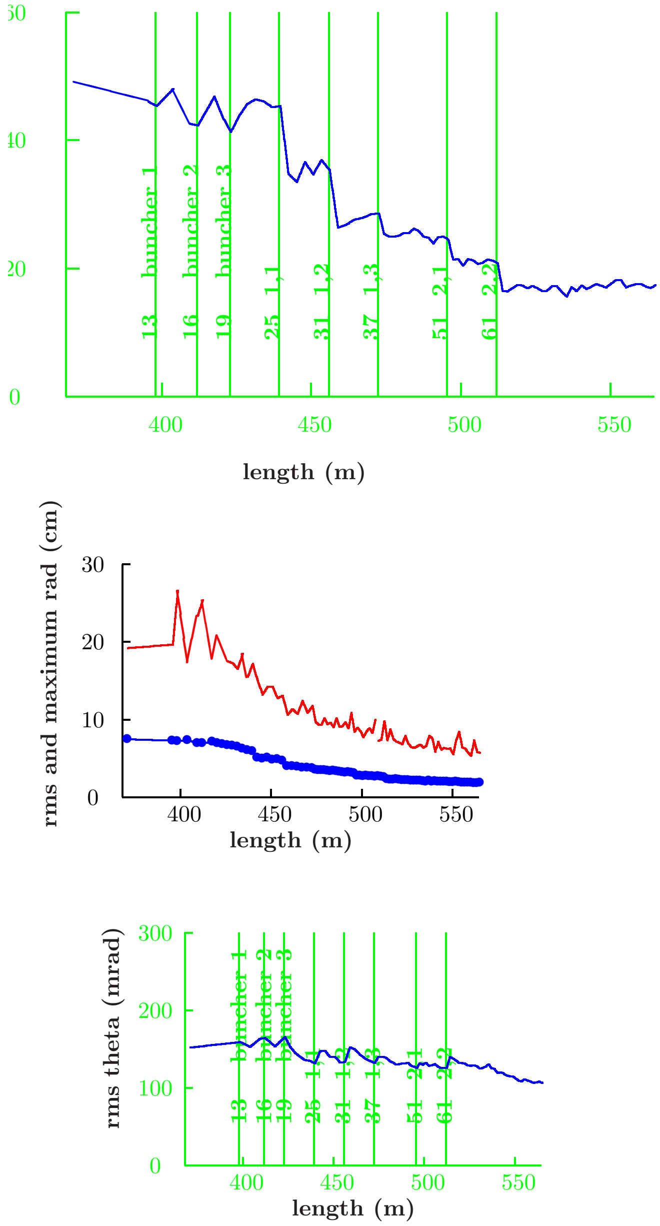

Figure 5.9: Beta function in the buncher and cooling section; rms and maximum beam radius; rms divergence. These results were obtained with ICOOL.

5.3.4 Performance

Fig. 5.9 shows the beta functions, which step down with each new section of the cooling lattice; also shown are the beam radius and beam divergence. The beam divergence at the absorbers is kept approximately constant in order to minimize the effects of multiple scattering. The $\beta_{\perp,min}$ function, derived from the beam second-order moments at the absorber centers, is shown in Fig. 5.10.

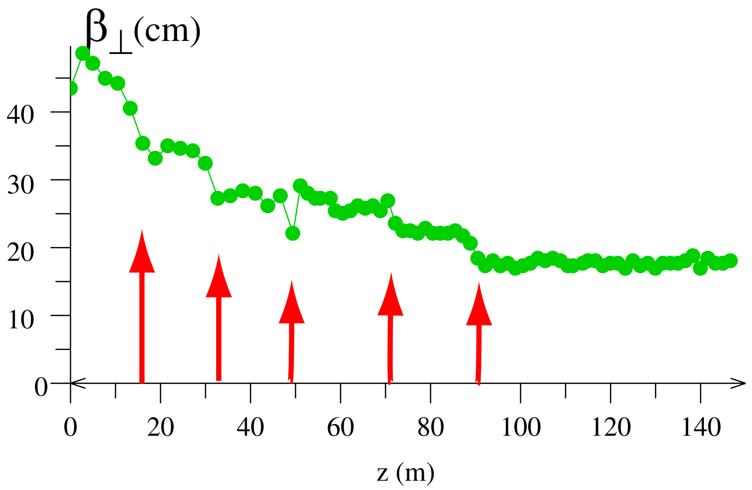

Figure 5.10: The $\beta_{\perp}$ function for the entire SFOFO cooling channel, averaged over the relevant momentum bite and measured from the second-order moments of the beam itself, as the cooling progresses. The five arrows indicate the beginning of the (1,2), (1,3), and (2,i), i=1,3 lattice sections. (Geant4 result.)

The transverse and longitudinal emittances through the cooling system are shown in Fig. 5.11 and Fig. 5.12. They were obtained using the ICOOL simulation code and the code ECALC9 [9], respectively. Emittances are computed in ECALC9 using diagonalized covariance matrices. These normalized emittance values are corrected for correlations among the variables, including the strong momentum-transverse-amplitude correlation.

The transverse emittance cools from 12 to $\approx$ 2 mm·rad. The longitudinal emittance shows an initial rise, and then, as particles outside the rf bucket are lost, an approach to an asymptotic value set by the bucket size. This longitudinal emittance should naturally rise

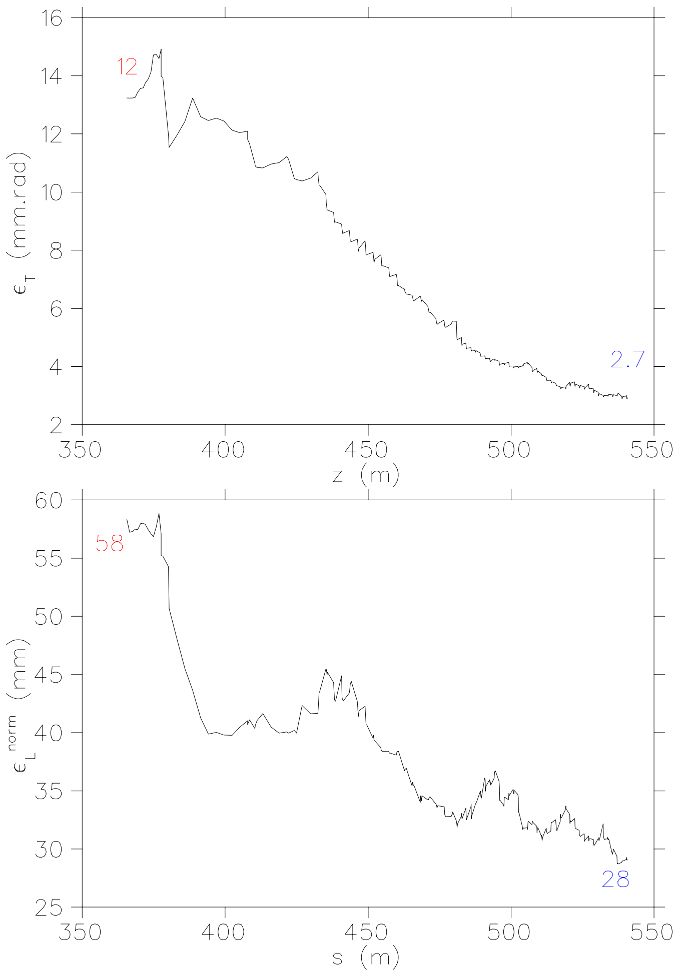

Figure 5.11: Transverse (top) and longitudinal (bottom) emittances in the cooling section, obtained with the ICOOL code. The initial and final values are indicated.

due to straggling and the negative slope of the energy loss curve with energy. However, since the rf bucket is already full, instead of an emittance growth we have a steady loss of particles (*i.e*, "longitudinal scraping"), as seen in the top curve of Fig. 5.13.

Despite this overall loss, the number of particles within the accelerator acceptance increases. The lower two curves in Fig. 5.13 give the number of particles within the baseline longitudinal and transverse acceptance cuts. The middle curve gives the values

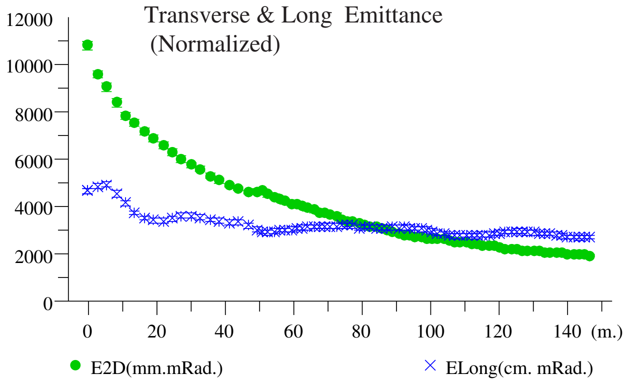

Figure 5.12: The longitudinal and transverse emittances, obtained with the Geant4 simulation code. Notice that the length of the last lattice (2,3), has been extended by ≈ 20 m to investigate the ultimate performance of the cooling channel.

used in this Study (FS2). The lowest curve, shown for comparison, gives the values for the acceptances used in Feasibility Study-I (FS1) [3]. These acceptance cuts are based on the 6D normalized beam emittances derived from the moments of the simulated beam distribution and the estimated transverse and longitudinal beta functions:

- Longitudinal (FS1 & FS2): $(dz^2)/\beta_s \; + \; (dp/p)^2 \; \beta_s \; (\beta\gamma) \; < \; 150$ mm
- Transverse (FS2): $(x^2+y^2)/\beta_\perp \; + \; (x'^2+y'^2)\beta_\perp \; (\beta\gamma) \; < \; 15$ mm·rad
- Transverse (FS1): $(x^2+y^2)/\beta_\perp \; + \; (x'^2+y'^2)\beta_\perp \; (\beta\gamma) \; < \; 9.35$ mm·rad

where β_s is the synchrotron beta function ($\beta_s = \sigma_z/\sigma_{dp/p}$), and $\beta_\perp$ is the transverse β function. Transverse and longitudinal emittances obtained with Geant4 are shown in Fig. 5.12. At equilibrium, a transverse emittance of 2.2 mm·rad is reached, consistent with the ICOOL result.

It is seen that the gain in muons due to cooling within the accelerator acceptance is a factor of ≈ 3 (or ≈ 4 if the Study-I acceptances were used). Similar performance is obtained with the Geant4 code, as shown in Fig. 5.14. If the particle loss from longitudinal emittance growth could be eliminated, as might be the case if emittance exchange were used, then these gains might double.

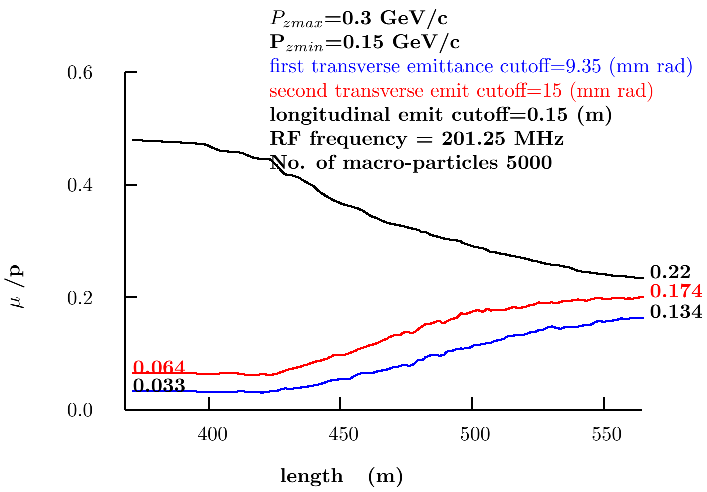

Figure 5.13: Particle transmission: number of muons per incident proton on target in the buncher and cooling sections. Top curve is overall transmission; lower two curves are for 150 mm longitudinal acceptance with two different transverse acceptance cuts: (middle) 15 mm·rad transverse acceptance; (bottom) 9.35 mm·rad transverse acceptance. This result was obtained with ICOOL.

The beam characteristics in the buncher and cooling sections are summarized in Table 5.8. This table lists the properties of all the muons in the beam that survive to a given location. The beam is cylindrically symmetric in this lattice, so the x and y properties are similar. We see that the beam size steadily decreases as we proceed down the channel. The angular divergence is kept approximately constant, maximizing cooling efficiency. The momentum spread of the entire beam is still large after the induction linac, but this includes very low and very high energy muons that do not get transmitted through the subsequent SFOFO lattice. For example, the range of momenta accepted in the acceleration linac is 150–300 MeV/c. The rms momentum spread for muons that lie inside this momentum range varies from 16 MeV/c after the third induction linac to 21 MeV/c after the 1.65 m cooling lattice.

The decrease in energy spread shown in Table 5.8 is due to particle losses, since there is no longitudinal cooling or emittance exchange. Likewise, the average momentum of the

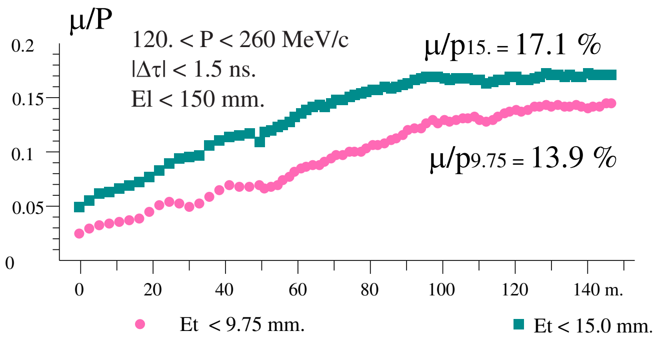

Figure 5.14: The muon-to-proton yield ratio for the two transverse emittance cuts, clearly showing that the channel cools, *i.e.*, the density in the center of the phase space region increases. Since the relevant yield μ/p_{15} no longer increases for $z \leq 110$ m, the channel length was set to 108 m. This is a Geant4 result.

Table 5.8: Beam characteristics summary.

Location (end of)	σ_x (cm)	$\sigma_{x'}$ (mrad)	σ_p (MeV/c)	σ_t (ns)	$\langle p \rangle$ (MeV/c)
Induction linac	8.6	95	118		237
Matching section	5.8	114	115		247
Buncher	5.1	104	101	0.84	238
2.75 m cooler	3.0	89	64	0.55	219
1.65 m cooler	1.6	94	28	0.51	207

beam decreases until it matches the acceptance of the SFOFO lattice. The time spread refers to a single bunch in the bunch train.

The longitudinal emittance remains more or less stable, at around 30 mm. This is somewhat deceptive. The anti-damping slope of the energy loss curve, straggling, and imperfections in the longitudinal-to-transverse correlation[1] cause particles to fall out of the rf bucket and be scraped away due to the strong betatron resonances. In fact, the buncher delivers a full rf bucket to the cooling section and the longitudinal emittance cannot grow any larger. This scraping occurs on the combined time scales of the synchrotron period, about 20 m, and the growth time of the betatron resonance instability.

The performance of the cooling channel is influenced by both multiple scattering and the limited momentum acceptance. Without multiple scattering, the μ/p_{15} and $\mu/p_{9.35}$ yields would increase by approximately 20% and 40%, respectively.

5.3.5 Tolerances & Systematics

The performance of the cooling channel has been evaluated based on computer simulations using two distinct codes. However, some parameters or assumptions in the calculations are common in the two simulations. Since no such channel has been built yet, it is fair to question whether the estimation of the cooling performance is robust against small changes in these parameter values. In addition, we need to consider the tolerances on the mechanical alignment in such a long beam transport system.

5.3.5.1 Sensitivity to multiple scattering model

ICOOL treats multiple scattering by using a straightforward Moliere model, imported from the Geant3 package. Geant4 uses an improved version of the Moliere model, but has a tunable parameter. We have studied the sensitivity of the rms value of the scattering angle to this parameter, in relation to the known uncertainties in the measured values for these rms scattering angles for low-Z materials. The sensitivity of the μ/P_{15} yield in the relevant range of this tunable parameter has been measured. The systematic error due to this uncertainty is approximately 10%.

5.3.5.2 Control of the energy loss in LH_2 and energy gain in the linac

Because of the relatively narrow momentum acceptance of the channel compared with the beam momentum spread, the energy loss and the energy gain must be known in the

[1]See Fig. 5.4 in the previous section.

channel to better than $\approx 0.25\%$. This tolerance can be achieved in the rf cavities, where the peak voltage and accelerating voltage can be controlled to better than a few tenths of a percent.

Nonuniform heat deposition within the absorbers may cause density variations in the vicinity of the core of the beam. These could result in reduced beam cooling as well as a net acceleration of the beam through the cooling channel, since the reduced energy loss would then be overcompensated by the rf accelerating gradient. While the absorber R&D program has not yet reached the point where such variations may be predicted in detail, we believe that they will be small in view of the success of the SAMPLE collaboration at Bates Laboratory in maintaining constant target density within tenths of a percent with 500 W of beam heating [20].

We have also explored, by simulation, the effects on muon cooling performance of reduced absorber density. As a first approximation the absorber density has been reduced uniformly throughout all absorbers by 1, 3, 5, 10, and 20%. For density decreases up to 5%, the cooling performance is unaffected within the few-percent level of simulation statistics.

The cooling channel will require about 72 12-MW klystrons. It is likely that one will fail occasionally. If so, emptying an LH_2 vessel and rephasing the downstream rf cavities will keep the beam on the nominal momentum. As an example, we have simulated the loss of rf power in a (1,1) or a (1,3) cooling cell. We find that emptying the absorber vessel and rephasing the remaining rf cavities results in a performance degradation of about 5% (relative), allowing us to keep the cooling channel running productively.

5.3.5.3 Magnet alignment

The design of the cooling channel was optimized using ideal magnetic fields from cylindrical current sheets. In an actual magnetic channel, imperfections that occur in the fabrication and assembly of the solenoids result in magnetic fields that deviate from the ideal used in the simulations by some small error field $\delta\vec{B}(x, y, z)$. A state-of-the-art magnet construction results in field errors $\frac{\delta B}{B} \leq 0.1\%$. These field errors produce effects, in general detrimental, that tend to increase with the length of the channel. If left uncorrected, these errors lead to mismatching and betatron oscillations, which in turn result in degradation of the cooling performance of the channel and to a decrease of the channel transmission.

We have considered the following analytical treatment of the detrimental effects of magnet alignment errors. As the muon beam propagates along the periodic channel with a prescribed beta function, it encounters a series of errors of various origins, which are assumed to be described by a stochastic function $\delta B(\vec{s})$ (we neglect the transverse coordinate dependence). The muons experience a series of random forces or "kicks," which result in a random walk of the centroid of the beam. Statistically, the rms magnitude of the transverse deviation $\sqrt{< (\delta x(s))^2 >}$ is a function of the length of the channel, s. In principle, it should be possible to develop a correction algorithm such that strategically located correction coils bring the centroid back to the ideal trajectory, thereby minimizing the deterioration of the cooling process.

A first look at the effects of errors and the sensitivity of the present design of the cooling channel to them has been carried out in references [10] and [11]. Studies of the error fields due to misalignment of individual coils and current sheets are found in references [12],[13].

There are several sources of magnet imperfections that may contribute to the overall deviation from the ideal fields of the channel:

1. Geometric (*macroscopic*) survey errors:

   a) transverse misalignment of solenoids, characterized by a vector $\vec{d} = \vec{d}(\cos\theta, \sin\theta, 0)$ of magnitude d and direction θ. In the simulations the values of d are chosen from a Gaussian stochastic function.

   b) transverse tilt of the solenoid, characterized by two angles: θ direction with respect to the x-axis, and the tilt, by the magnitude ψ, with respect to the z-axis.

   The Cartesian coordinates $\vec{r} = (x, y, s)$ transform as

$$\vec{r'} = \vec{r} - \vec{d} \tag{5.6}$$

   for a translation in the transverse plane and

$$x'_i = \mathcal{M}_{ij} x_j \tag{5.7}$$

   for a tilted magnet. The magnetic fields are calculated as

$$\vec{B}(x, y, s) = \vec{B}'(x', y, s') \qquad B_i(\vec{r}) = \mathcal{M}^{-1}_{ij} B'_j(\mathcal{M}\vec{r}) \tag{5.8}$$

   for a translation and tilt respectively. The transformation matrix is

$$\mathcal{M} = \begin{bmatrix} \cos\psi + \cos^2\theta(1-\cos\psi) & \sin\theta\cos\theta(1-\cos\psi) & \sin\theta\sin\psi \\ \sin\theta\cos\theta(1-\cos\psi) & \cos\psi + \sin^2\theta(1-\cos\psi) & \cos\theta\sin\psi \\ \sin\theta\sin\psi & -\cos\theta\sin\psi & \cos\psi \end{bmatrix} \tag{5.9}$$

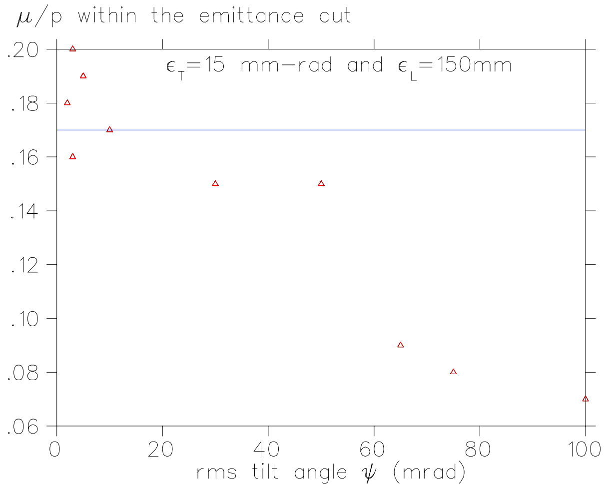

Figure 5.15: Transmission of the front end for different *rms* tilt angles.

2. Power supply fluctuations resulting in current fluctuations

3. Geometric conductor positioning, which leads to random *microscopic* field errors.

Here we only consider the first type, *i.e.*, geometric *macroscopic* field errors introduced by mispositioning of entire magnet cryostats.

We have performed two studies with ICOOL [1]. The buncher and SFOFO cooling channel have been simulated with independent Gaussian random tilt angles and translation of the coils roughly every 5 m. The results are shown in Figs. 5.15 and 5.16.

An independent analysis of alignment tolerance issues (microscopic field errors) has been done using the Geant4 package. The simulations of the buncher and cooling channels are run in the following modes:

1. Random polar tilts. A Gaussian model was used to generate the tilts, polar angles ψ, for each coil. Since large transverse displacements of coils are expected to be relatively easy to find and correct, we have truncated the distribution at $2\sigma_\psi$. The azimuthal θ angles were chosen randomly, between zero and 2π. The μ/p_{15} yield was measured for tens of such simulated channel assemblies. The histogram in Fig. 5.17 shows that a σ_ψ of 0.5 mrad gives no statistically significant degradation of the channel performance. However $\sigma_\psi \approx 2.5$ mrad would be unacceptable.

2. Random transverse displacements. Since the coils are about 15 cm long, a tilt of 0.5 mrad gives a lateral displacement at one end of about 75 μm. Evidently, the coil

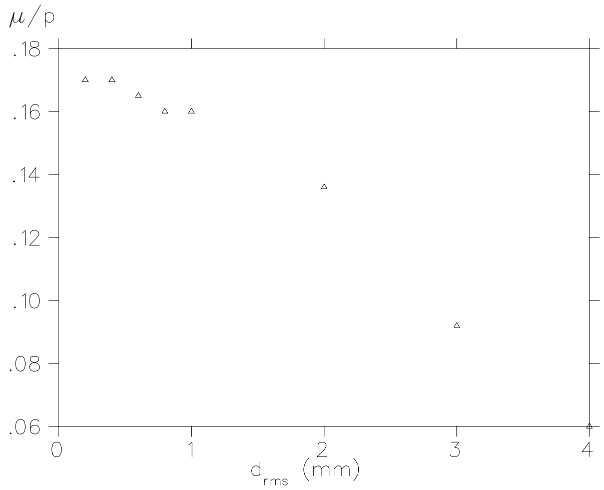

Figure 5.16: Transmission of the front end for different rms translation errors d.

could also shift laterally by about the same amount. We verified that a 2σ truncated displacement of 100 μm has no significant impact on the channel performance.

Since the typical tolerance on accelerator magnet alignment is about 100–μm, we believe that such a channel can be assembled to the required accuracy.

5.3.5.4 Space charge

The nominal number of muons per bunch is $N_\mu \approx 5\times10^{10}$, which corresponds to $Q \approx 8$ nC. An estimate of the deleterious effect of space charge on the beam dynamics can be found by calculating the self-electric field of a Gaussian distribution of charge represented by the Basetti-Erskine-Kheifets formula [14]

$$\Phi(r,z,s) = \frac{2Q}{\epsilon_o\sqrt{\pi}} \int_0^\infty dt \frac{e^{-\frac{r^2}{2\sigma_\perp{}^2+t}}}{(2\sigma_\perp{}^2+t)} \frac{e^{-\frac{z^2}{2\sigma_3{}^2+t}}}{\sqrt{(2\sigma_3{}^2+t)}}. \qquad (5.10)$$

The variable z is defined as $z = s - c\beta t$, with s the longitudinal coordinate, assuming that the centroid of the bunch is at $s = 0$ at time $t = 0$. The argument s in $\Phi(r, z, s)$ is there to indicate that the rms transverse size $\sigma_\perp$ and longitudinal size σ_z of the beam are functions of s. This is important because the beta function varies from moderate to small values at the absorbers.

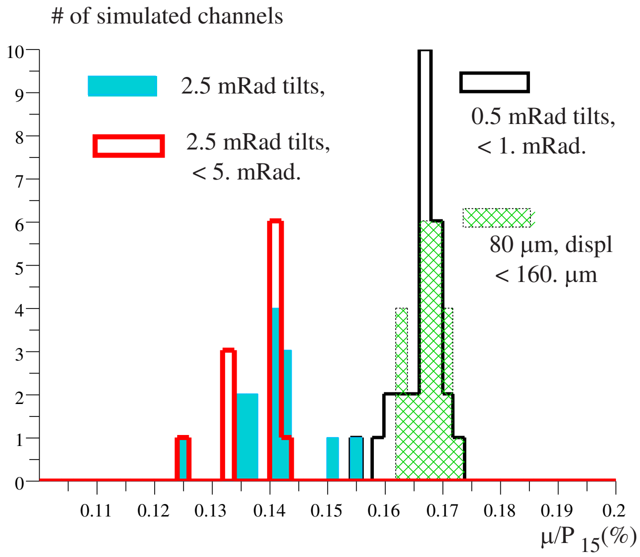

Figure 5.17: A histogram of the performance of 35 SFOFO cooling channels built with tolerances of 0.5 and 2.5 mrad tilts and small translations.

From Eq. 5.10 and the corresponding expression for the vector potential $A_s(r, z, s) = \beta\Phi(r, z, s)$ we can calculate the electric field components $E_r(r, s, t)$ and $E_s(r, s, t)$ [15]. ICOOL contains this formulation and systematic studies have been carried out. The results are shown in Fig. 5.18, where it can be seen that the number of muons per proton μ/p at the end of the cooling channel is rather insensitive to the number of muons in the bunch up to values $N_\mu^{critical} \approx 1 \times 10^{12}$, some 20 times our intensity.

This approach is approximate and leaves aside potentially important phenomena: first, the effects of induced charge in the walls of the beam pipe and in the metallic (Be) rf windows; second, the short-range wake potential created by the $\beta < 1$ muon beam inside the cavities. The effect of the walls of a cylindrical beam pipe on a bunch of charged particles was also considered and has been computed with ICOOL with no noticeable effects. We note here that the presence of Be windows should mitigate any space charge effects. However, it is rather difficult to calculate this with precision.

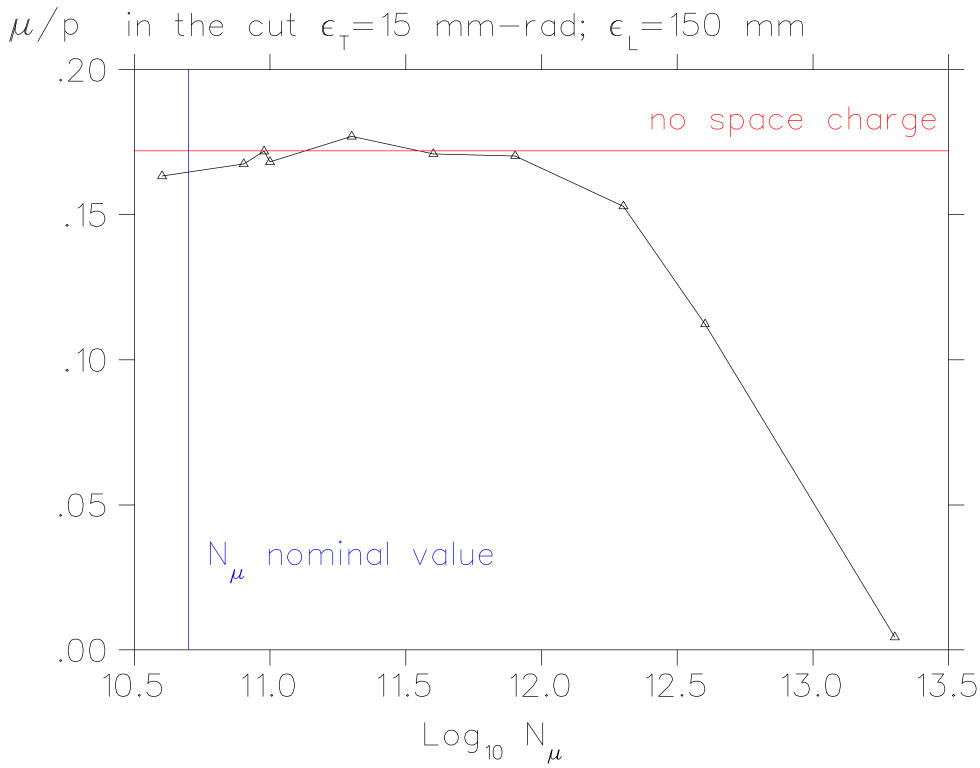

Figure 5.18: μ/p *vs.* N_μ in a bunch, assuming a Gaussian self-field.

5.3.6 Liquid Hydrogen Absorbers

5.3.6.1 Power handling

We estimate the maximum power dissipation per absorber to be about 300 W, dominated by the ionization energy loss of the muons (See Table 4.4, which shows the absorber lengths, radii and the number of absorbers of each type). The main technical challenge in the absorber design is to prevent boiling of the hydrogen near the beam axis, where the power density is greatest. This requires that the hydrogen flow have a significant component transverse to the beam. We are investigating two ways to achieve this: "flow-through", a design in which the absorber connects to an external heat-exchange and temperature-control loop, and "convection", a design in which the absorber vessel is itself the heat exchanger, and heat transfer within the absorber is accomplished dominantly by convection.

The flow-through design resembles previous high-power liquid-hydrogen targets [19, 20], which have been operated successfully at power dissipations as high as 500 W [20] and have been proposed for operation at even higher dissipations [21, 22]. In this approach the hydrogen is pumped around a loop that includes the absorber vessel, as well as a heat exchanger and a heater. In the heat exchanger, which runs at a constant power level, the hydrogen is cooled by counterflowing cold helium gas. The heater is used in feedback to regulate the hydrogen temperature and compensate for changes in beam intensity.

Given the small emittance of conventional particle beams, liquid-hydrogen targets tend to be narrow transverse to the beam, leading to designs in which the natural direction of hydrogen flow is parallel to the beam. To avoid boiling the liquid in the high-intensity beam core, various design strategies are then necessary to ensure transverse flow of the liquid [20, 23]. In contrast, in our flow-through design the hydrogen enters the absorber vessel from below and exits at the top, ensuring automatically that the flow is transverse to the beam. The flow pattern is controlled by means of nozzles, which must be configured so as to avoid dead regions or eddies and to ensure adequate flushing of the windows.

In the convection design (Fig. 5.19), the interior wall of the vessel is equipped with cooling tubes through which cold helium gas circulates. A heater located at the bottom of the vessel is used to compensate for changes in beam intensity. The design of the convection-cooled absorber is being guided by two-dimensional fluid-flow calculations. The flow-through approach is less amenable to calculation, but will be tested on the bench to verify the efficacy of the nozzle design, first in a room-temperature model and later at cryogenic temperature. Prototype construction and testing programs for both designs are now under way and will lead to high-power beam tests.

5.3.6.2 Window design

To minimize heating of the beam due to multiple scattering, the absorbers must be equipped with thin, low-Z windows. Yet, the windows must be strong enough to withstand the pressure of the liquid hydrogen. We have devised a window design that satisfies these requirements and also allows quite thin absorbers to be built. While a hemispherical window shape minimizes the window thickness for a given strength, the desire to build absorbers that are thinner relative to their diameter than a sphere leads to the "torispherical" shape. In the version specified by the American Society of Mechanical Engineers (ASME) [24], the torispherical head for pressure vessels is composed of a central portion having a radius of curvature (the "crown radius") equal to the diameter of the cylindrical portion of the vessel, joined to the cylindrical portion by a section of a toroidal surface with a radius of curvature 6% of the crown radius (see Fig. 5.20).

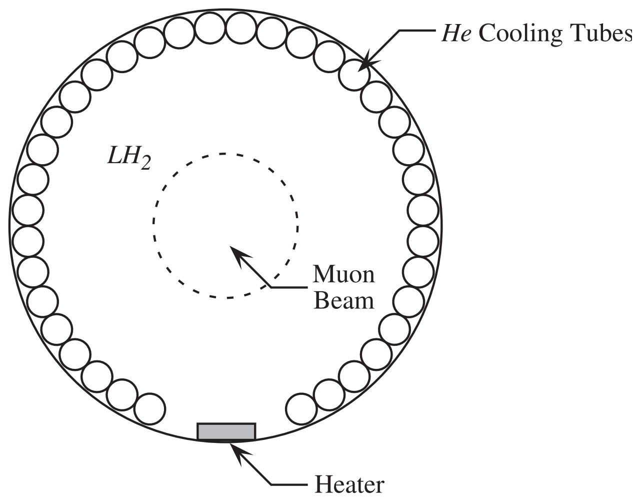

Figure 5.19: Schematic of convection design.

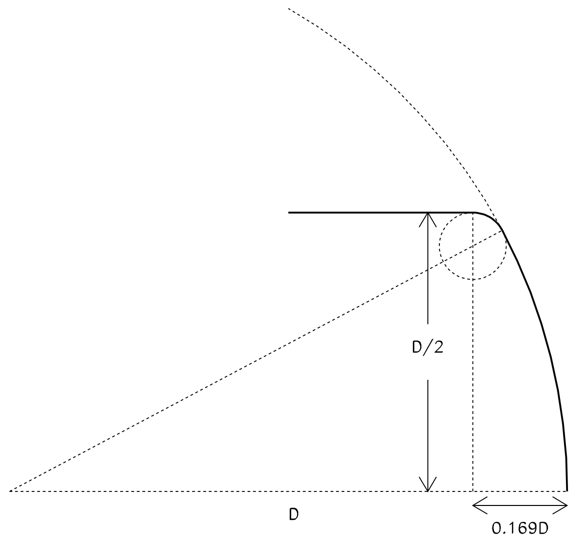

Figure 5.20: Schematic of ASME torispherical head on cylindrical vessel of diameter D: solid curve shows upper half section, with dashed lines and curves indicating the spherical and toric surfaces from which it is composed.

ASME specifies the minimum acceptable thickness of the torispherical head as

$$t = \frac{0.885PD}{SE - 0.1P}\,, \tag{5.11}$$

where P is the differential pressure across the window, D the vessel diameter, S the maximum allowable stress, and E the weld efficiency. Although previous high-power liquid-hydrogen targets have operated at 2 atm [19, 20], to keep the windows as thin as possible we have designed for 1.2 atm. For S, we follow ASME recommendations and use the smaller of 1/4 of the ultimate strength S_u or 2/3 of the yield strength S_y (in practice, for aluminum alloys it is the ultimate strength that matters). We will machine the window with an integral flange out of a single disk of material (Fig. 5.21), with the flange fastened to the assembly by bolts (Fig. 5.22). Thus, there are no welds and we take $E = 1$. For 1.2-atm operation, and given the ASME specification for 6061-T6 aluminum alloy, $S_u = 289\,\mathrm{MPa}$, we obtain $t = 530\,\mu\mathrm{m}$ for the "Lattice 1" absorbers ($D = 0.36\,\mathrm{m}$) and $t = 330\,\mu\mathrm{m}$ for the "Lattice 2" absorbers ($D = 0.22\,\mathrm{m}$). If necessary, the windows can be made thinner than this by tapering their thickness as described below. In addition, less easily machinable, but stronger, aluminum alloys (such as 2090-T81) may allow further reduction in thickness.

In addition to eliminating the weld, machining the window out of a single disk allows detailed control of the window shape and thickness profile. We have used the ANSYS finite-element-analysis program to optimize the window shape and profile so as to minimize the window's thickness in its central portion, where most of the muons traverse it. The resulting shape and thickness profile are shown in Fig. 5.21. Therefore we have used in the simulation the smaller thicknesses of 360 μm and 220 μm for the (1,i) and (2,i) cooling lattices, respectively.

5.3.7 Diagnostics and Instrumentation Issues in the Cooling Channel

There are a number of unique instrumentation problems involved in optimizing and monitoring the performance of the cooling line [25]. The beams will be large and intense, and a variety of precise measurements will be required that are both novel and difficult.

There will be significant backgrounds in all detectors, due either to other particles from the target coming down the line with the muons, or to x-rays and dark currents generated by the rf cavities. We must consider the angular momentum of the beam, perhaps for the first time with any high energy physics beam. The beams will be intense enough so that thermal heating of the detectors is significant. The environment will have high magnetic fields, a large range of temperatures, and high-power rf cavities. In addition, under normal circumstances the access will be very limited, since the rf cavities and liquid hydrogen absorbers will occupy most of the available space. Standard loss monitors will not be useful for the low energy muons because the range of such particles

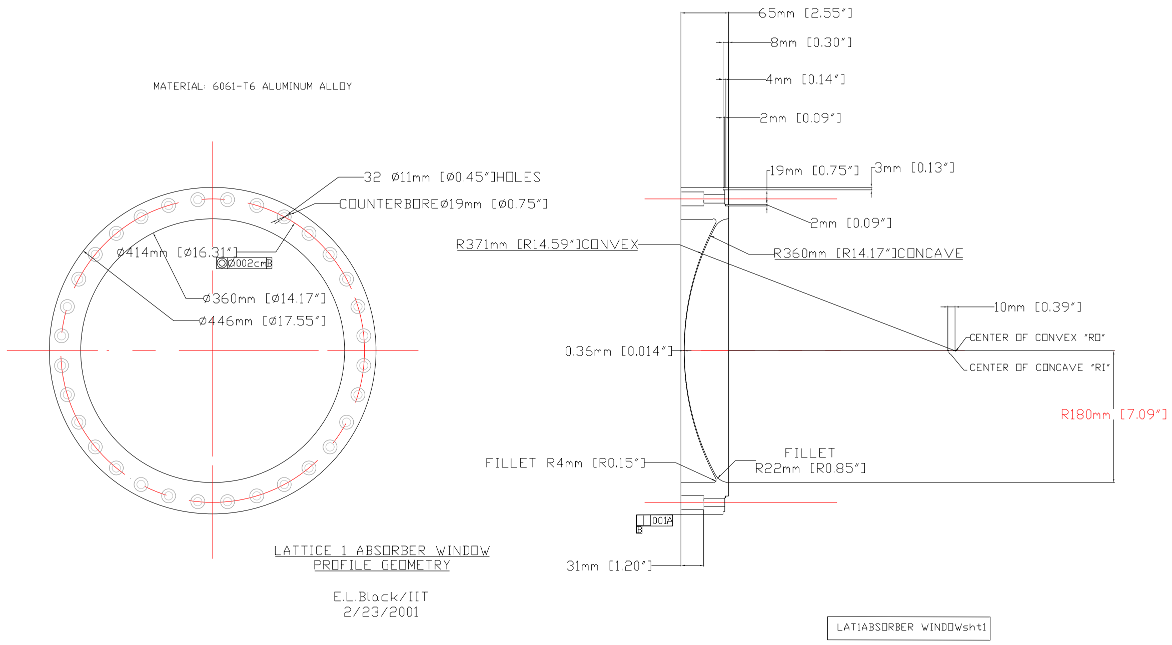

Figure 5.21: Window design for the SFOFO Lattice 1 absorbers.

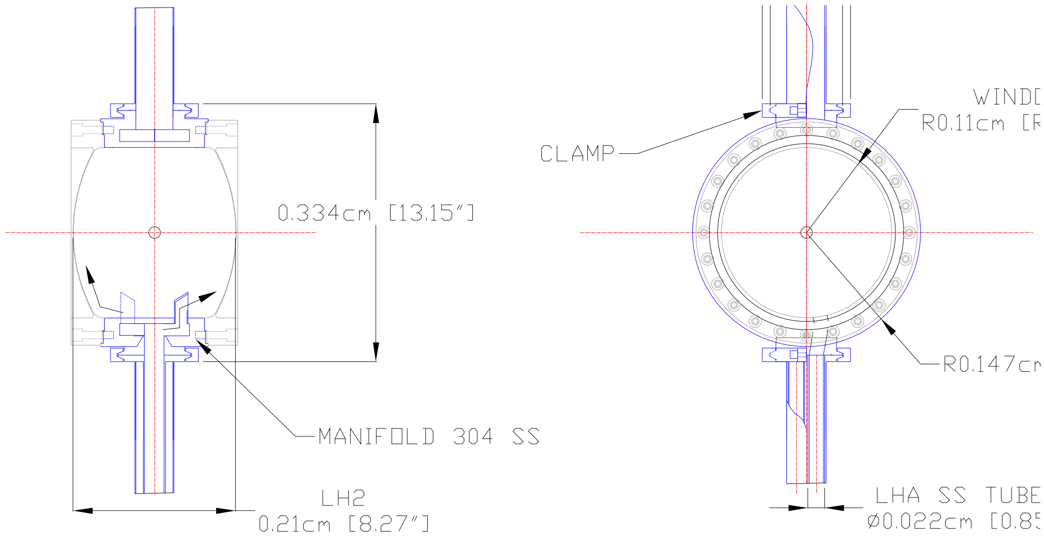

Figure 5.22: Absorber assembly for SFOFO lattice 2 (flow-through design shown).

is so short (6 cm in Cu) and they produce no secondaries. An R&D program is under way to look at the sensitivity and usefulness of different diagnostic techniques and evaluate them in the environment of rf backgrounds and high magnetic fields.

On the other hand, there are a number of reasons why the tune-up and operation of the cooling channel could be fairly straightforward. The cooling channel will have been very thoroughly simulated by the time of initial construction. In addition, there are a relatively small number of variables that control the behavior of the beam, such as currents in solenoids, rf parameters and liquid-hydrogen-absorber parameters, and these can be measured with high precision. While the change in transverse beam emittance, $\epsilon_\perp$, between individual cells may be difficult to measure, $\Delta\epsilon_\perp/\epsilon_\perp < 0.01$, the overall size and profile of a beam with $\sim 10^{12}$ particles per macro-bunch is a comparatively straightforward measurement.

5.3.7.1 Measurement precision

The sensitivity of the system to alignment errors was described in Section 5.3.5. Related issues involve sensitivity to various other effects: transverse and longitudinal mismatches between the cooling line and the bunching section, arc-down and temporary loss of an rf cavity, boiling or loss of hydrogen in the absorber section, inadvertent introduction of a collimator or thick diagnostic, and mismatches at the ends of the cooling line. These mismatches can be either first-order (beam centroid position, energy, or angle errors), or second-order (discontinuities in Twiss parameters). Mismatches will slow down the cooling process and could significantly affect beam losses.

A mismatch due to problems with the rf or absorbers would change both the mean beam momentum and the measured β function downstream. An example is shown in Fig. 5.23, where the beta functions are plotted through regions where the momentum has changed, corresponding to an empty hydrogen cell or a single rf cavity that is turned off, giving the scale of the effects that might be produced. The changes in β functions are a few percent at some positions, while at other points the β functions are essentially unchanged. Thus, it is necessary to have beam profile measurements done at a number of positions. Mismatches in the beam optics would persist until chromatic effects caused decoherence of

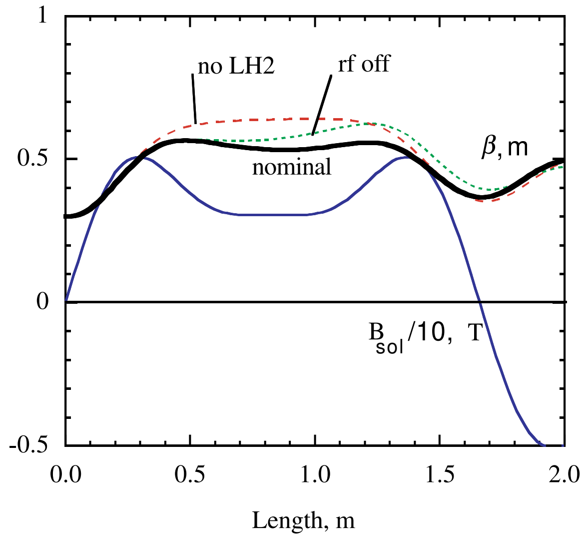

Figure 5.23: The scale of discontinuities in β function when rf or absorbers are perturbed, corresponding to empty liquid-hydrogen absorber (dashed line) or shorted rf cavity (dotted line).

the betatron motion (and perhaps subsequent recoherence due to synchrotron motion). The ultimate emittance growth, due to filamentation, would be of the same order of magnitude as the change in β functions. If a change in momentum persisted through the end of the cooling line, it could be detected in dispersive areas of the beam transfer lines, but the synchrotron motion could cancel the energy fluctuation. Thus, it is desirable to diagnose the beam using the transverse optics.

An R&D program is under way to look at the sensitivity and usefulness of different diagnostic techniques and evaluate them in the environment of rf backgrounds and high magnetic fields. Modeling is also required to understand mismatches and realistic errors better.

5.3.7.2 Angular momentum

Angular momentum plays an important role in solenoidal ionization cooling channels, unlike the quadrupole channels commonly used elsewhere in high energy physics. Due to the rotational symmetry of the solenoid focusing field, the canonical angular momentum is a conserved quantity when the cooling material is absent. When absorbers are present, however, the beam angular momentum can change, thereby yielding a residual angular momentum at the end of a cooling channel. Non-zero beam angular momentum creates coupling between the two transverse degrees of freedom and causes problems for matching the beam into a downstream quadrupole channel. Furthermore, the angular momentum intrinsically couples with the beam emittance in the cooling dynamics. For optimum cooling in a periodic channel, the change in the net angular momentum should be zero. This requirement becomes the following condition [26]

$$\int_0^{\lambda} \eta(s)\beta_{\perp}(s)B(s)ds \sim 0 \tag{5.12}$$

where λ is one period, $B(s)$ is the on-axis magnetic field, $\beta_{\perp}(s)$ is the envelope function, and $\eta(s)$ is the ionization energy loss rate.

Measurement of beam angular momentum is a new subject. Beam profile monitors, which measure beam distributions in x and y, can measure the beam emittance, but do not provide sufficient information to directly determine the angular momentum in a solenoid cooling channel. We are investigating whether it is possible to indirectly measure the angular momentum by comparing the measured emittance-damping rates. Clearly, such measurements will be difficult. Novel ideas are being explored to directly measure the correlation terms $\langle xp_y \rangle$ [27].

Since the energy loss rate, absorber thickness, and magnetic field are known, or can be measured with an accuracy much better than one percent, and an envelope function measurement is likely to be accurate to a few percent, it should be possible to determine whether Eq. 5.12 is approximately satisfied. For machine operation purposes, beam angular momentum measurements are helpful, but not absolutely necessary.

5.3.7.3 Backgrounds

There are a number of backgrounds that will impact beam diagnostics. These backgrounds come primarily from three sources: 1) backgrounds produced by the incident protons at the target; 2) backgrounds produced in the cooling line, primarily from rf cavities; and 3) backgrounds from decay electrons. We assume that the decay electrons can be simulated and subtracted from all measurements.

5.3.7.3.1 Beam backgrounds The solenoidal beam transport channel for muons will also transport all other particles whose transverse momentum is less than ∼100 MeV/c. Thus, hadronic showers from 3 GeV protons, for example, can be expected in the liquid hydrogen absorbers well down the cooling line. A large number of species are produced: K, n, γ, $e^{\pm}$, D, He^3, He^4, and other nuclear fragments should be seen in detectable quantities. Most low-energy backgrounds from the target will be stopped in the first minicooling absorber, but the high energy particles that are left will be comparatively unaffected by the rf in the line. Timing should be very effective in identifying and discriminating against these particles.

5.3.7.3.2 RF backgrounds X-ray production from rf cavities results from dark-current electrons hitting the body of the cavity and nearby solid components. The bremsstrahlung x-ray flux produced is then scattered and attenuated by both the production material and by transmission through any external structure. While the dark-current electron orbits will be influenced by magnetic fields along the beam axis, the x-rays, particularly those around 1-2 MeV, will scatter and diffuse freely up and down the cooling line. The dark-current electrons from single-cell cavities, and the x-rays they produce, are expected to be in the 1–10 MeV range. The electron and x-ray fluxes produced in this environment have recently been measured using a 1.3 GHz high-gradient cavity [28]. Other experiments are planned using an 805 MHz cavity. Data taken from a variety of pulsed cavities suggest that rf breakdown limits the total dark current, and thus the x-ray flux that can be produced, somewhat independent of frequency.

Fluxes of dark-current electrons and x-rays measured in the 1.3-GHz cavity were on the order of 10^{10}–10^{11} electrons per rf pulse, or $10^7 - 10^8$ electrons per bucket, a more relevant parameter. The number of bremsstrahlung photons is of the order of $n_e r/L_R$ where n_e is the number of dark-current electrons, r is their range, usually a few mm, and L_R is the radiation length for the material, *e.g.*, 1.44 cm for Cu. Because the energies are low, complex showers do not develop. The photons, however, do diffuse through the system.

There are several ways of altering the flux of dark-current electrons and the x-ray flux seen by the beam diagnostics:

- the geometry of the system can be changed so that dark-current electrons do not appear near the beam axis (the double-flip cooling channel option described in Section B does this, because the rf cavities are inside of a uniform solenoidal field and, consequently, it is less likely that dark-current electrons will be guided into the diagnostic device)
- rf electric field, E_{rf}, can be reduced since $I_{dark} \propto E_{rf}^{10}$
- cavity can be coated with a material having low secondary electron yield.

All of these methods are to some extent applicable to the cooling line.

5.3.7.4 Access in the cooling line

It is desirable to be able to insert, park, and possibly remove any instrumentation in the line without disrupting the beam vacuum. There are a number of options for insertion of diagnostics into the cooling line.

Analogous to FODO accelerator structures, it is desirable to insert diagnostics at every major focusing element. While there is limited space in the cooling line, instrumentation modules compatible with the 3.7 cm expansion section that is a part of every cell can be used. Figure 5.24 shows a possible location for inserting diagnostics in the cooling cell.

Special SFOFO sections, without hydrogen absorbers and with only enough rf voltage to contain the bunch, could also be used for specific Cherenkov counters or other devices that require more access than would be available in a standard cell. We have not made use of this concept as part of this Study, but it is compatible with the cooling channel.

5.3.7.5 Making and using pencil beams

We anticipate that pencil beams will be very useful in assessing the alignment of all cooling, accelerator, and storage ring components. Since the range of the roughly 200 MeV/c muons in the cooling line is only about 6 cm in Cu, and scattering angles are large, collimation works very well. Thus a variety of collimators could be used at locations in the bunching and cooling lines to produce low transverse emittance beams, on or off axis.

Producing a 6D "pencil" may be even more useful, since this could be used to track the longitudinal evolution of the bunch through all of the acceleration and storage ring optics. In principle, the 6D bunch can be produced from a 4D bunch by reducing the rf voltage in the cooling line, so that only the center of the longitudinal phase space is

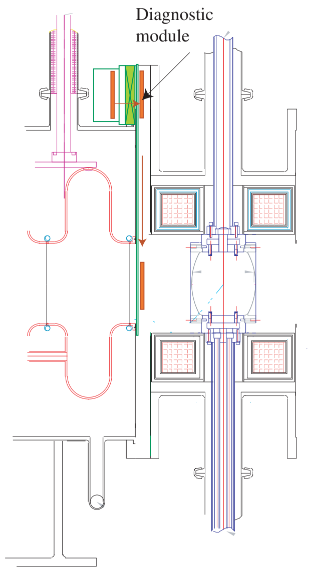

Figure 5.24: Possible location for diagnostic instrumentation in a standard cooling lattice cell. The arrows show how a diagnostic module could be removed from its parked position and inserted into the beam temporarily for measurements.

transmitted. While the intensities will be reduced, muon beams in the range of 10^{10} to 10^{11} particles should be useful and quite easily measured.

5.3.7.6 Instrumentation options

Although high-energy particles, dark-current electrons and x-rays will be present, the signal from the primary muon beam should dominate these backgrounds. Nonetheless, we will look first at instrumentation options that offer very fast time response; these will be relatively less sensitive to backgrounds. From this perspective, segmented secondary emission monitors (SSEMs) and Faraday cups offer a significant advantage. These devices have been shown to have a useful resolution time of the order of 150 – 200 ps. Since this time response is significantly less than the bucket length, these devices would be able to provide some information on the bunch shape and thus on the longitudinal emittance of the beam. Faraday cups could be used essentially interchangeably with the SSEMs. However, they would provide about two orders of magnitude more dynamic range, and the possibility of some particle discrimination using range.

These devices can be used both to measure the beam parameters, and to provide consistency checks for evaluating measurements by other methods. One possibility being considered is a curtain of scintillating fibers, with an actuator to slide the fibers into place when beam diagnostics are needed and a safe parked area out of the way during normal operating conditions. Likewise, a telescoping 2D pixel-array SEM is envisioned that can be inserted to diagnose the center or edge of the beam region.

It is possible that detectable scintillation may occur when the muon beam passes through the liquid-hydrogen absorbers. If this is verified in cosmic-ray tests, it would provide a diagnostic that is always present and does not add any additional material in the beam. The scintillation should provide a signal with good time resolution and 2D position information.

Semiconductor arrays of polycrystalline CdTe would be able to provide high-precision x and y beam profiles in a single measurement [29]. The detector consists of an array of charge-sensitive elements, each providing a signal with amplitude proportional to the intercepted muon beam density. Finally, bolometers are being developed that can measure xy profiles from the heating in the metallic windows of the liquid-hydrogen absorbers. We are also looking at high-rate ion chambers, which would be generally useful for a wide range of measurements. Tests of how these various devices perform in the high x-ray-flux environment of a cooling channel will be done as part of the R&D program.

5.3.8 Engineering Considerations

The fully-integrated layout of the cooling cells for the (1,i) lattices and the (2,i) lattices are shown in Figs. 5.26 and 5.25.

This design takes into account the constraints from the solenoid magnet subsystem (see Figs. 5.27, 5.28 and 10.6) described in Chapter 10, the rf cavities discussed in Chapter 8, and the absorber detailed in Section 5.3.6. The basic dimensions of the cooling cells are taken from the conceptual design presented above. However, the exact placement of various components may depart slightly from the layout used in the simulation package. For instance, the rf cavities are slightly off-center longitudinally with respect to the coils (by 3.7 cm) to facilitate servicing; this will not affect beam-cooling performance. In addition, space for diagnostics is potentially available at that location, as detailed in Sec. 5.3.7.4. Note also that some rf feeds need to be tilted due to the space constraint imposed by the coupling coil cryostat. The piping and auxiliary hardware for the absorber shown in the figures correspond to the through-flow absorber design; they would, however, be very similar to those used in the convection absorber design.

Deviation from the simulation design driven by engineering or cost considerations will

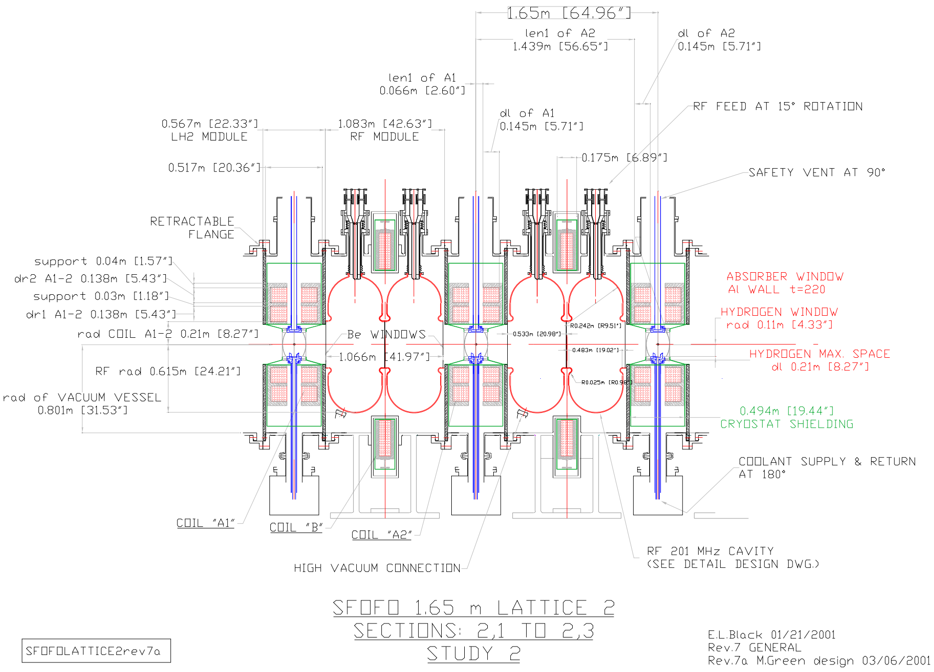

Figure 5.25: Engineering rendering of the 1.65 m cooling lattice cell.

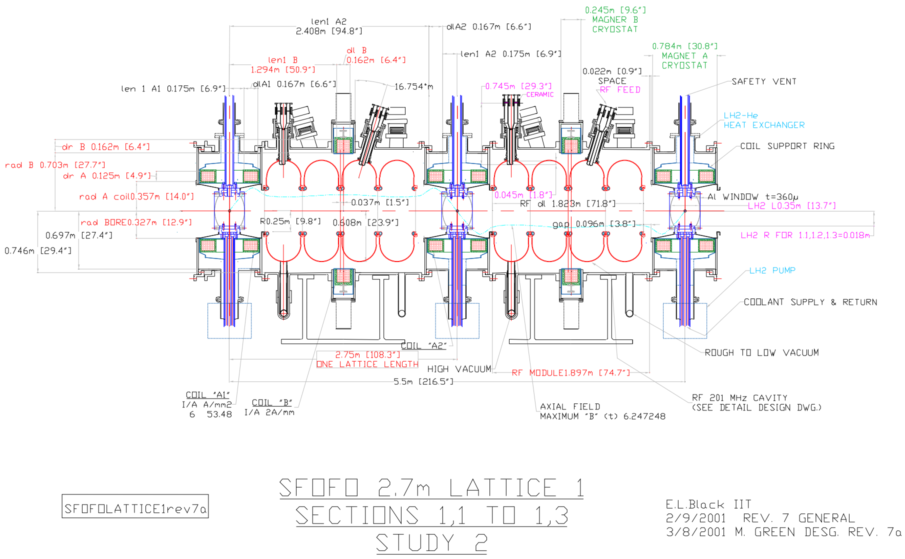

Figure 5.26: Engineering rendering of the 2.75 m cooling lattice cell.

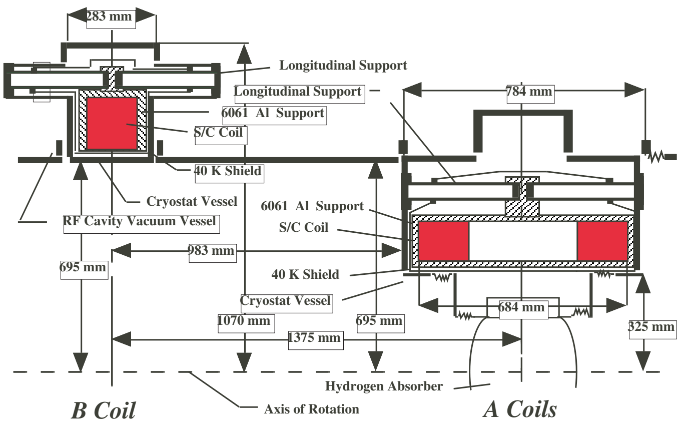

Figure 5.27: Magnet cross section for the 2.75 m long cooling cell. The coils labeled "A" is the focusing coil and "B" is the coupling coil.

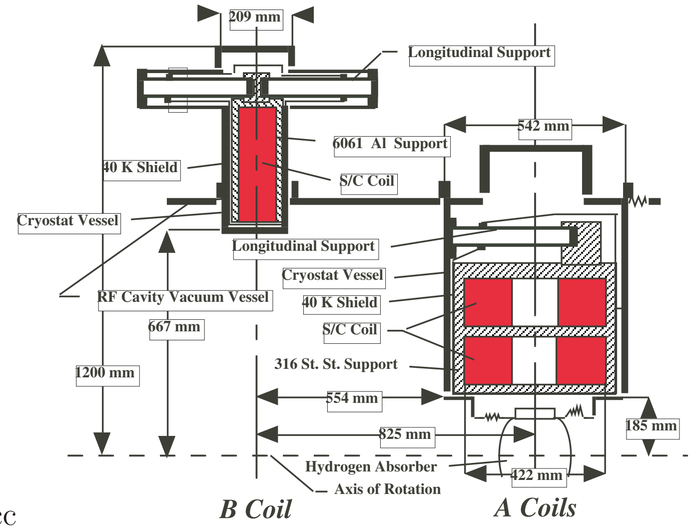

cc

Figure 5.28: Magnet cross section for the 1.65-m-long cooling cell. The coils labeled "A" is the focusing coil and "B" is the coupling coil.

most likely occur. Indeed, some items have been discovered in the course of this study and are listed below:

- Coil configuration: The coil positions, sizes, and current densities used in the simulations (see Tables 5.4–5.6) differ somewhat from those listed in Chapter 10, which have been engineered to reduce cost and to allow more room, both for the absorbers and for insertion of the rf feeds. We have verified that the revised fields on-axis are the same as for the original configuration, and that the slight discrepancies in the off-axis fields do not affect the cooling performance.

- Winding structural support: To handle the large forces exerted on the windings, the focusing coil ("A coil") in the (2,i) cooling lattices has been split into two windings with a structural stainless steel plate inserted in between (see Fig 5.28.) However, the simulations have been made assuming a current density uniformly distributed over the entire radius of the coil. We can easily readjust the current densities of these two windings to obtain the required magnetic field profile.

- Absorber details: Our simulation studies have assumed cylindrically-shaped liquid-hydrogen absorbers with flat windows of constant thickness. However, in practice the shape will be as indicated in Fig.5.22, with approximately spherical ends, and with tapered windows as shown in Fig. 5.21. A closer approximation has recently been implemented in Geant4, with the absorber ends represented as spherical caps and the correct window thickness profile, with no adverse effects on cooling performance.

- rf-window design: In the rf cavities used in the simulation, the beryllium windows are stepped in thickness, with their thickness suddenly increasing at the radius r_1 (see Chapter 8). In practice, the mass distribution near r_1 may well be smoother (for instance, if the change in thickness is brought about by means of chemical etching). We have verified that, as expected, a smooth transition does not affect the cooling performance.

5.4 Conclusion: Performance of the Entire Front End

The transverse emittance along the entire front end is plotted in Fig. 5.29. The emittance is seen to be reduced in the minicooling at 150 m (from 17 to 13 mm·rad), remains approximately constant through the induction linacs, althought large-amplitude particles are lost, and falls quickly in the final cooling section (from 12 to 2.8 mm·rad).

The muon-to-proton ratio along the full system is given in Fig. 5.30. Particle losses prior to the buncher come primarily from the loss of very high and very low momenta (30%), plus losses from muon decay ($\approx$ 20%). The losses in the cooling section come

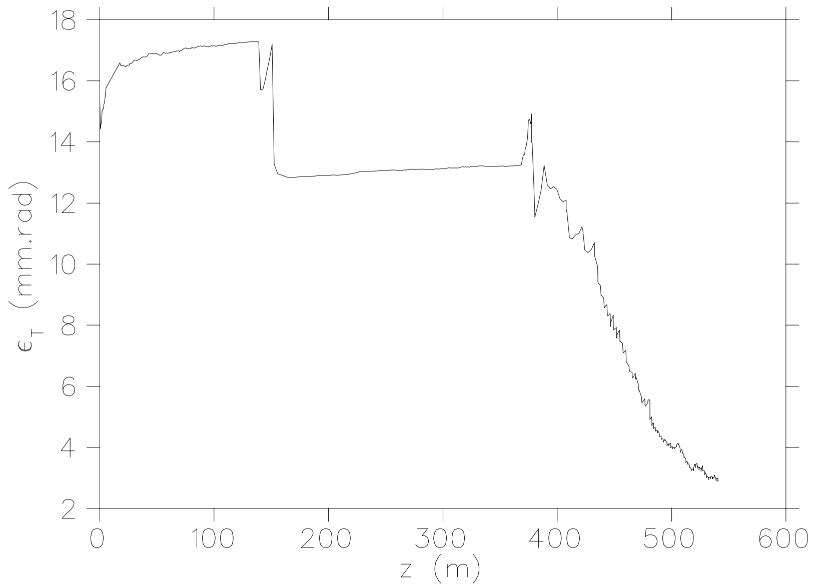

Figure 5.29: Transverse emittance as a function of distance along the front end.

from bunching inefficiency ($\approx$ 25%) and from loss of particles from the rf bucket as the longitudinal emittance grows in this section ($\approx$ 25%).

As shown in the left panel of Fig. 5.31, we are able to collect the muon phase space over a substancial kinetic energy range, *i.e.*, approximately 50–250 MeV. The peak collection efficiency occurs for kinetic energy around 100 MeV, where about 35% of the pions yield accepted muons. Note the falling efficiency for pions with kinetic energy above 300 MeV.

The SFOFO cooling channel increases the number of muons per proton in the 15 mm·rad transverse acceptance cut by a factor of 3.5, or a factor of 5.75 in the 9.35 mm·rad acceptance. This is the Geant4 estimate; ICOOL numbers, listed above, are slightly lower, consistent with systematic errors in the calculations. The factor of 5.75 should be compared with the corresponding enhancement achieved in Feasibility Study I, which was approximately 2 to 2.5 [3]. The better performance of the front-end is due primarily to our progress in understanding phase rotation and to the advantages of the SFOFO cooling lattice compared with the FOFO lattice used in Study-I.

Engineering and mechanical tolerances have been studied. We now know that such a channel can be assembled and aligned with known techniques.

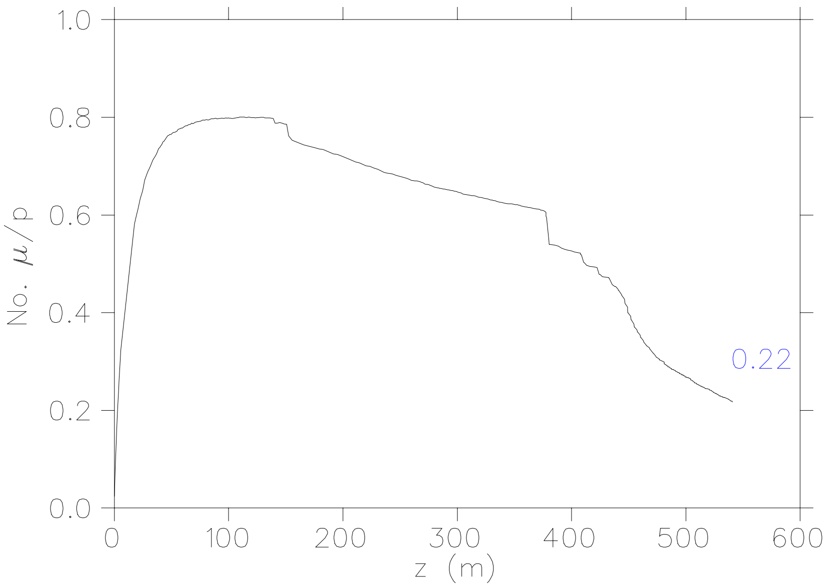

Figure 5.30: Muons per incident proton as a function of distance along the front end.

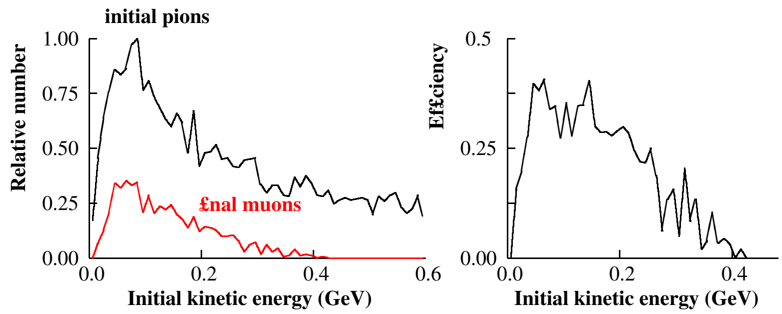

Figure 5.31: Left plot: Kinetic energy distribution of initial pions (upper curve) and of pions that decay into muons that exit the cooling channel (lower curve). Right plot: efficiency distribution for an initial pion to produce an accepted muon by the channel.

5.5 Matching Cooling to Acceleration

5.5.1 Method

The matching from the end of the cooling section to the start of the acceleration is achieved by adiabatically changing the lattice parameters from the short (1.65 m) low beta (0.18 m) SFOFO lattice (2,3) at the end of the cooling section to a longer (2.75 m) and higher beta (0.6 m) FOFO lattice. The transition is made in 10 cells.

Initially there are seven 1.65-m cells, all identical in dimensions, but with currents modified to gradually raise the central value of the beta function, and change the form of the beta function *vs.* momentum from the SFOFO shape (Fig. 5.5) to a monotonic slope. This is followed by 3 cells with all longitudinal dimensions scaled up to further increase the beta function. The beta functions at the ends of the various matching cells are shown as a function of momentum in Fig. 5.32.

Finally, after a lone coupling coil, followed by a reversed-direction coil to bring the axial field down to zero, the beta function is allowed to rise toward the value needed for the optics of the superconducting linac. Coil dimensions and axial fields are shown in Fig. 5.33.

5.5.2 RF Cavities

We introduce rf to keep the bunch together and to raise the average momentum. All currents are scaled with increasing momentum. The rf fields (on-crest) average 8 MV/m over 19 m. Average energy gain is 3 MV/m. Each cavity consists of two rf cells, except that there are three cells in cavity 10 and a single-cell cavity beyond the final focus coils, for a total of 22 cells. Each rf cell is identical to those in the 1.65-m cooling lattice. The total acceleration required (on crest) is 152 MeV, corresponding to 6.9 MeV per cell. The cavity phase is set to give an actual mean acceleration of 2.6 MeV per cavity.

5.5.3 Superconducting Coils

The coils have the same radial dimensions as those in the final cooling lattices, but different currents and, in the final cells, different lengths. Parameters of the matching coils are summarized in Table 5.9. The current densities in some coils are very low and the dimensions of the coils could be reduced, provided the total currents and current centers are maintained.

Table 5.9: Coil parameters for the cooling channel to acceleration section match.

Start (m)	dl (m)	r (m)	dr (m)	J (A/mm^2)
0.066	0.145	0.198	0.330	83.76
0.627	0.396	0.792	0.099	80.10
1.439	0.145	0.198	0.330	81.31
1.716	0.145	0.198	0.330	-81.66
2.277	0.396	0.792	0.099	-88.55
3.089	0.145	0.198	0.330	-78.99
3.366	0.145	0.198	0.330	79.32
3.927	0.396	0.792	0.099	95.67
4.739	0.145	0.198	0.330	77.58
5.016	0.145	0.198	0.330	-77.89
5.577	0.396	0.792	0.099	-103.02
6.389	0.145	0.198	0.330	-75.99
6.666	0.145	0.198	0.330	76.29
7.227	0.396	0.792	0.099	111.46
8.039	0.145	0.198	0.330	74.23
8.316	0.145	0.198	0.330	-74.52
8.877	0.396	0.792	0.099	-122.79
9.689	0.145	0.198	0.330	-72.31
9.966	0.145	0.198	0.330	72.58
10.527	0.396	0.792	0.099	130.03
11.339	0.145	0.198	0.330	73.92
11.616	0.145	0.198	0.330	-74.18
12.246	0.462	0.792	0.099	-106.28
13.193	0.169	0.198	0.330	-54.23
13.517	0.169	0.198	0.330	54.42
14.240	0.528	0.792	0.099	89.45
15.322	0.194	0.198	0.330	41.57
15.692	0.194	0.198	0.330	-41.71
16.509	0.594	0.792	0.099	-76.98
17.726	0.218	0.198	0.330	-32.94
18.142	0.218	0.198	0.330	29.74
19.052	0.660	0.792	0.099	47.20
21.378	0.660	0.792	0.099	-1.42

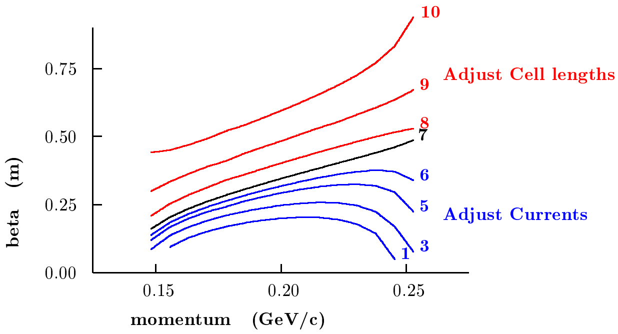

Figure 5.32: Beta functions at the end of various cells of the matching section.

5.5.4 ICOOL Simulation

Simulation of this matching section uses a file of tracks from the end of the baseline cooling simulation. It is important to point out that: i) No rf windows have yet been included in the simulations; ii) the window apertures have been set to 21 cm; and, iii) no optimization of the design has been attempted. We also note that the acceleration section was designed and without the present matching. Thus, the small amount of energy gain in the matching line will lead to the elimination of a portion ($\approx$ 39 m) of the initial preacceleration linac, described in Chapter 6. (This change was accounted for properly in the cost estimate)

Figures 5.34–5.37 show the behavior of a number of important quantities as a function of distance along the cooling-channel-to-acceleration-section matching line. The minimum of the β function shown in Fig. 5.34, varies from 18 cm at the beginning to $\approx$ 1 m at the end of the section. Figure 5.36 shows there is a net acceleration from 210 to 270 MeV/c, and also that the total muon loss due to the matching is only 1.25%. The loss inside the accelerator acceptance, shown in Fig. 5.37, is 2.4%. The selected μ/p ratios fluctuate because ECALC9 does not correct for angular momentum when it applies the transverse acceptance cuts. The values are correct only at locations where B_z is zero; these correspond to the maxima of μ/p in Fig. 5.37 (bottom). There is negligible growth in the normalized transverse and longitudinal emittances.

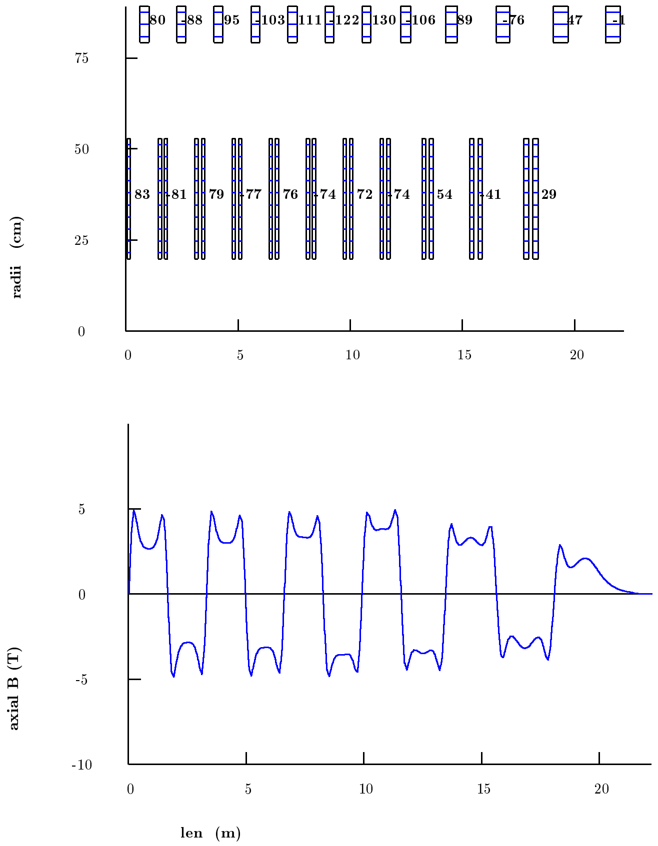

Figure 5.33: Coil dimensions and axial fields for the cooling-channel to acceleration-section matching section.

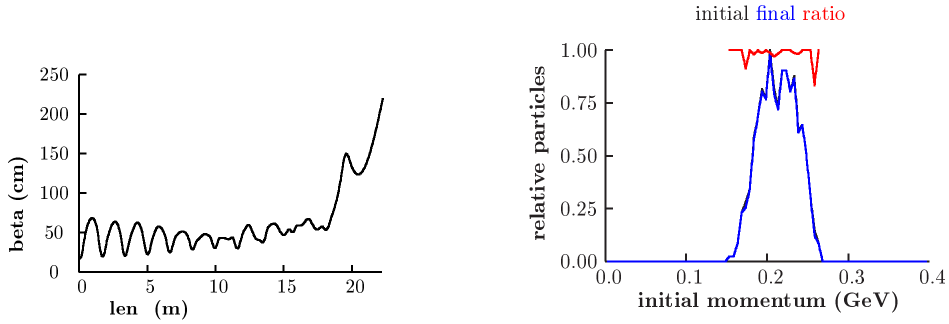

Figure 5.34: $\beta_\perp$ function *vs.* distance along the cooling-channel-to-acceleration-section matching (left); muon momentum distribution (right).

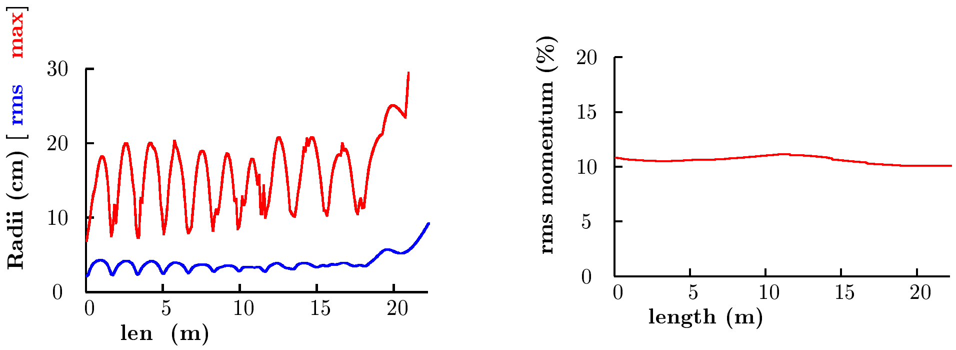

Figure 5.35: Rms and maximum radius *vs.* z (left); rms fractional momentum spread *vs.* z (right).

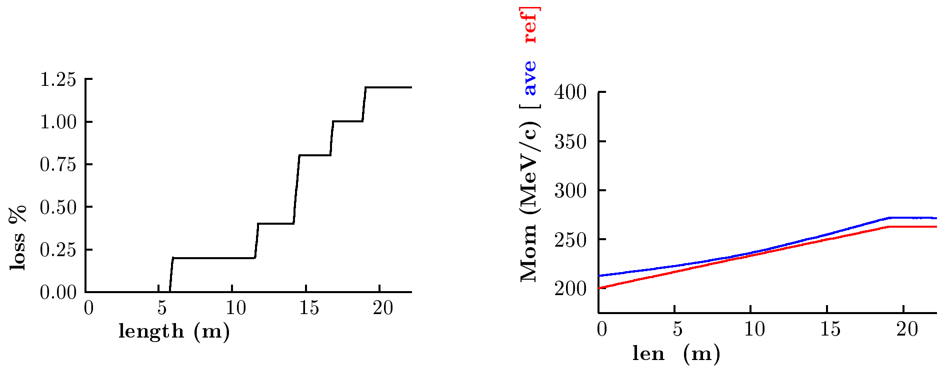

Figure 5.36: Loss in % (left); momentum *vs.* z (right), along the cooling-channel-to-acceleration-section matching line.

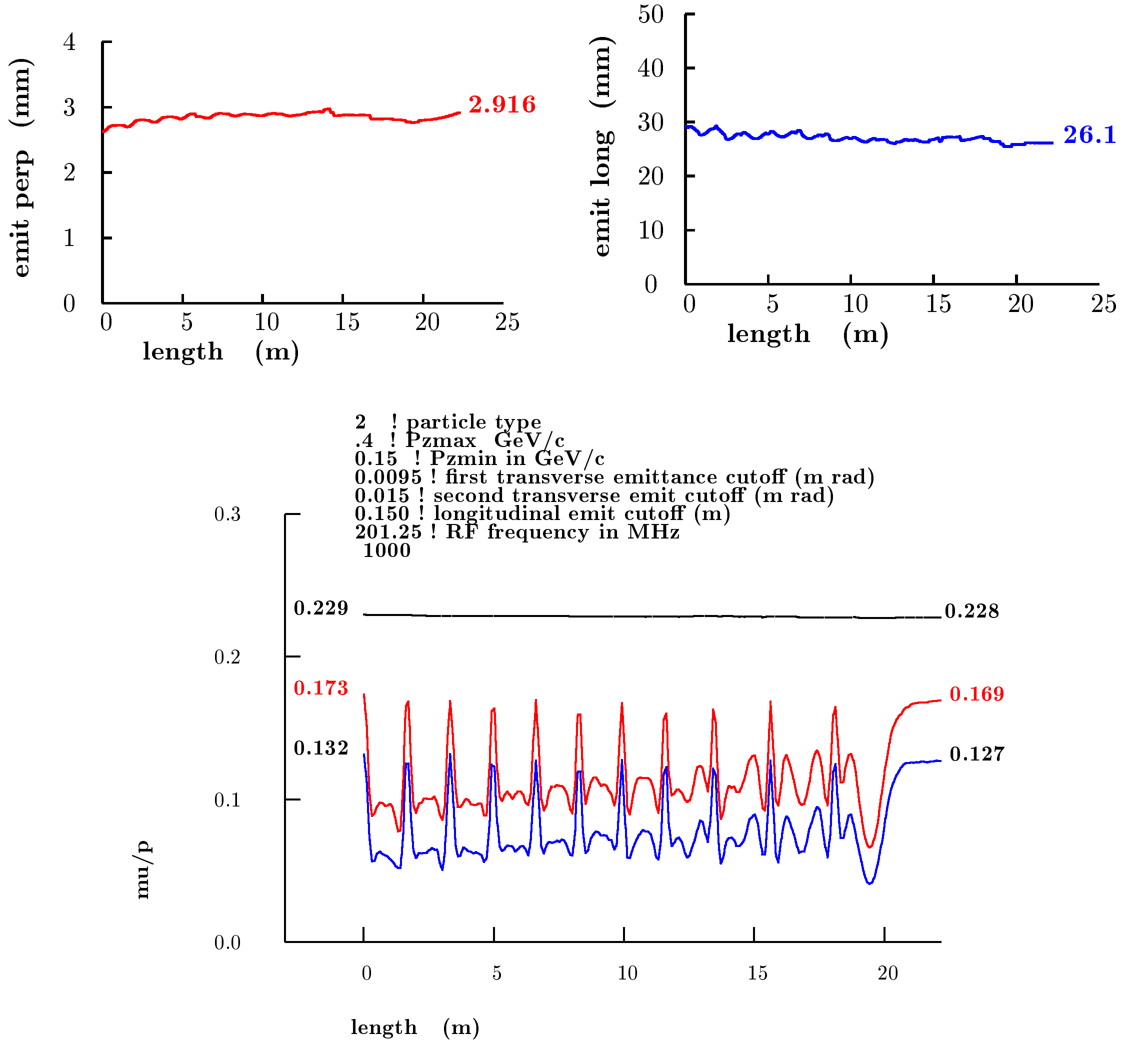

Figure 5.37: ϵ_T (top-left), ϵ_L (top-right), and μ/p (bottom) *vs.* z. The three curves in the bottom figure are: (top) total number of μ/p; (middle) within the ϵ_T=0.015 m·rad and ϵ_L=0.15 m cuts; (lower) within ϵ_T=0.0095 mm·rad and ϵ_L=0.15 m cuts.

Bibliography

[1] R. Fernow, *ICOOL, A Simulation Code for Ionization Cooling of Muons Beams*, Proceedings of the 1999 Particle Accelerator Conference, A. Lucio and W. MacKay, eds. (IEEE, Piscataway, NJ, 1999) p. 3020.

[2] The Geant4 Tool Kit is available at *http://wwwinfo.cern.ch/asd/geant4/geant4.html*

[3] *A Neutrino Source Based on an Intense Muon Storage Ring*, ed. N. Holtkamp and D. Finley, available at http://www.fnal.gov/projects/muon_collider/nu-factory/nu-factory.html

[4] C.M. Ankenbrandt *et al.* Phys. Rev. ST Accel. Beams 2, 081001 (1999)

[5] G. Penn *et al.*, Phys. Rev. Lett. 85 (4) pp. 764-767. July, (2000).

[6] J. Monroe *et al.*, *Design and Simulation of Muon Ionization Cooling Channels for the Fermilab Neutrino Factory Feasibility Study*, Phys. Rev. ST Accel. Beams 4, 041301 (2001).

[7] First suggested by A. Sessler, LBNL.

[8] The Particle Data Group, *Review of Particle Physics*, Eur. Phys. J. C **15** (2000) 163.

[9] This code was written by G. Penn, LBNL.

[10] R. Fernow, *Effect of a dipole error on the performance of the alternating solenoid lattice*, http://www-mucool.fnal.gov/mcnotes/muc0035.pdf

[11] P. Lebrun, *Sensitivity of the 15 T. Alternate Solenoid Cooling Channel to Dipole Errors caused by misalignment of the Solenoids* http://www-mucool.fnal.gov/mcnotes/muc0073.ps

[12] J. Gallardo, *Errors in a continuous solenoid* , http://www-mucool.fnal.gov/mcnotes/muc0041.ps; *Errors in a discrete solenoid* http://www-mucool.fnal.gov/mcnotes/muc0037.ps

[13] J. Gallardo, *Note on Vector potential for a Solenoid and Errors*, unpublished (1999).

[14] M. Bassetti and G.A. Erskine, *Closed Expression for the Electric Field of a Two-Dimensional Gaussian Charge*, CERN Report **CERN-ISR-TH/80-06**, 1980; S. Kheifets, *Potential of a Three-Dimensional Gaussian Bunch*, DESY Report **PETRA** Note 119 (1976).

[15] F. Zimmermann and T. Raubenheimer, *Longitudinal space charge in final-focus systems*, Nucl. Instrum. Meth., 1997; J. Gallardo, *Space Charge in Gaussian Beams: A Collection of formulas*, http://www-mucool.fnal.gov/mcnotes/muc0038.ps

[16] H. Wang, *Analytical approach to the short-range wakefields*, http://www-mucool.fnal.gov/mcnotes/muc0117.pdf

[17] MAFIA is available from CST GmbH, Buedinger Strasse 2a, 64289 Darmstadt, Germany (www.cst.de).

[18] J. Gallardo, *Implementing space-charge effects in cooling simulations*, BNL Report: Muon Tech. Notes Mu-019, 1998.

[19] J.W. Mark, SLAC-PUB-3169 (1984) and references therein.

[20] E.J. Beise *et al.*, Nucl. Instrum. Meth. **A378** (1996) 383.

[21] R.W. Carr *et al.*, SLAC-Proposal-E-158, July 1997.

[22] D.J. Margaziotis, in *Proc. CEBAF Summer 1992 Workshop*, F. Gross and R. Holt, eds., AIP Conf. Proc. **269**, American Institute of Physics, New York (1993), p. 531.

[23] R.W. Carr *et al.*, "E158 Liquid Hydrogen Target Milestone Report," April 21, 1999, http://www.slac.stanford.edu/exp/e158/documents/target.ps.gz.

[24] *ASME Boiler and Pressure Vessel Code*, ANSI/ASME BPV-VIII-1 (American Society of Mechanical Engineers, New York, 1980), part UG-32.

[25] J. Norem, *Instrumentation issues for the Neutrino Source* http://www-mucool.fnal.gov/mcnotes/muc0085.ps

[26] Kwang-Je Kim and Chun-xi Wang, Phys. Rev. Lett. **85** (760) 2000

[27] A. Blondel is working to develop a system based on a ring imaging Cerenkov technique.

[28] J. Norem, A. Moretti and M. Popovic, *The Radiation Environment in and near High Gradient RF Cavities*, http://www-mucool.fnal.gov/mcnotes/muc0178.pdf

[29] M. Placidi *et al.*, *A CdTe Detector for Muon Transverse Profile Measurements*, CERN-NUFACT-Note 068, contributed to the MuCool Instrumentation Workshop, IIT, Chicago, Nov. 10-11 (2000).

Chapter 6

Acceleration: Recirculating Linear Accelerator

Acceleration of a muon beam is a challenging task because of its large phase space and short lifetime. In the design concept presented here, acceleration starts after ionization cooling at 210 MeV/c and proceeds to 20 GeV, where the beam is injected into a Neutrino Factory storage ring. The key technical issues, beyond the basic physics parameters of Table 6.1, are:

- choice of acceleration technology (superconducting versus normal conducting cavities) and, related to it, rf frequency choice
- choice of acceleration scheme
- capture, acceleration, transport and preservation of a large-phase-space muon beam
- accelerator performance issues, such as potential collective effects (*e.g.*, cumulative beam breakup) resulting from the high peak current.

To minimize muon decay, the highest possible accelerating gradient is required; that is the main driver for the proposed scheme. The muon accelerator driver consists of a 2.87 GeV linac and a four-pass recirculating linear accelerator, as shown in Fig. 6.1.

Very large transverse and longitudinal accelerator acceptances drive the design to low rf frequency. If we were to use normal-conducting rf (NCRF) cavities, the required gradients would be of the order of 15 MV/m, which, in turn, demands extremely high peak power rf sources. Superconducting rf (SCRF) cavities are a much more attractive solution. RF power can then be delivered to the cavities over an extended time, and thus

Table 6.1: Main parameters of the muon accelerator driver.

Injection momentum (MeV/c)/Kinetic energy (MeV)	210/129.4
Final energy (GeV)	20
Initial normalized acceptance (mm-rad)	15
rms normalized emittance (mm-rad)	2.4
Initial longitudinal acceptance, $\Delta p L_b/m_\mu$ (mm)	170
momentum spread, $\Delta p/p$	± 0.21
bunch length, L_b (mm)	± 407
rms energy spread	0.084
rms bunch length (mm)	163
Number of bunches per pulse	67
Number of particles per bunch/per pulse	$4.4 \times 10^{10}/3 \times 10^{12}$
Bunch frequency/accelerating frequency (MHz)	201.25/201.25
Time structure of muon beam	6 pulses at 50 Hz; 2.5 Hz repetition rate
Average beam power (kW)	150

the rf source peak power can be reduced. Another important advantage of SCRF cavities is that their design is not limited by a requirement of low shunt impedance, and therefore their aperture can be significantly larger then would be practical for NCRF cavities. Taking into account the required longitudinal and transverse acceptances, and that the beam is already bunched at 201.25 MHz at the source (ionization cooling), a 201.25 MHz rf frequency has been chosen for both the linear accelerator and the recirculator. This choice provides adequate stored energy to accelerate multiple passes of a single-pulse bunch train without the need to refill the extracted energy between turns.

The short muon lifetime essentially excludes use of a conventional circular accelerator, and demands either a high-gradient conventional or recirculating linac (FFAG rings could be also considered). While recirculation provides significant cost savings over a single linac, it cannot be utilized at low energy for two reasons. First, at low energy the beam is not sufficiently relativistic and will therefore slip in phase on subsequent passes, thus significantly reducing acceleration efficiency. Second, there are major difficulties associated with injection of a beam with the large emittance and energy spread characteristic of a muon source. Beam pre-acceleration in a linear accelerator to about 2.5 GeV makes the beam sufficiently relativistic, and adiabatically decreases the phase-space volume, so that further acceleration in recirculating linacs is possible.

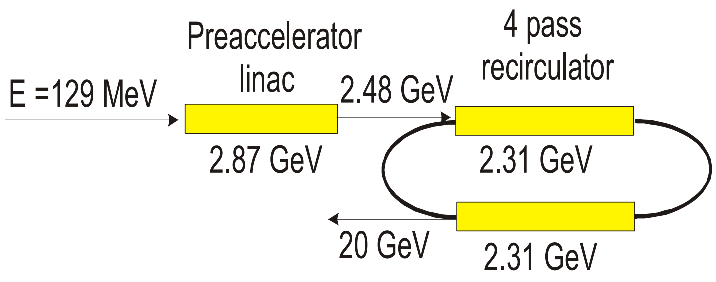

Figure 6.1: Layout of the muon accelerator driver.

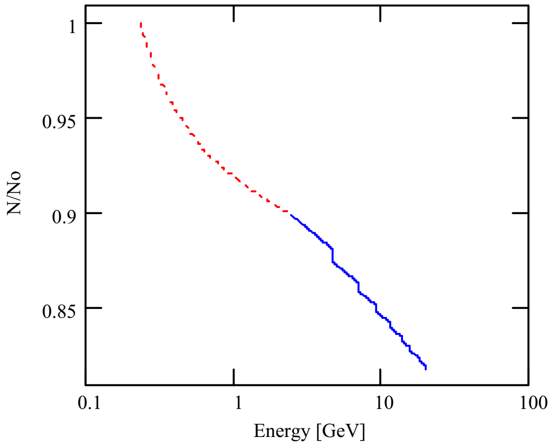

Figure 6.2: Decay of muons in the course of acceleration. The dotted line is the decay in the linac, and the solid line is the decay in the recirculator. Vertical drops correspond to the beam transport in arcs.

Cost considerations favor multiple passes per stage, but practical experience commissioning and operating recirculating linacs dictates prudence. Experience at Jefferson Lab suggests that for a given large initial emittance and energy spread, a ratio of final-to-injected energy below 10-to-1 is prudent, and the number of passes should be limited to about five. We therefore propose a machine architecture (see Fig. 6.1) featuring a 0.13-to-2.48 GeV straight "preaccelerator" linac, followed by a 2.48-to-20 GeV four-pass recirculating linac (RLA). Figure 6.2 shows the loss of muons during the course of acceleration. While the RLA gives a significant contribution, the major loss fraction comes from the linac. Note that the arcs (vertical drops in Fig. 6.2) do not contribute much to the decay, which justifies the choice of normal conducting bends, and triplet focusing discussed below.

Table 6.2: Main parameters of linear accelerator.

Injection momentum (MeV/c)/Kinetic energy (MeV)	210/129.4
Final momentum (MeV/c)/Kinetic energy (MeV)	2583/2480
Total linac length (m)	433
Acceptance: initial/final (no emittance dilution) (mm-rad)	7.5/0.62
Momentum spread: initial/final	$\pm$0.21/$\pm$0.075
Total bunch length: initial/final (mm)	814/190
(deg.)	197/46
Total installed accelerating voltage (GeV)	2.87

6.1 Linear Accelerator

6.1.1 Matching

It is important to provide a section that matches the beam ellipse from what it is in the cooling section to what it is in this linac. That matching section is described in Section 5.5. The lattice not only matches the beam ellipses, it accelerates by a small amount, approximately 59 MeV. Using the phase graph in Fig. 6.11, we compute that approximately the first 38 m of the linac described in this Chapter is no longer required, that is, only the last 4 short cryomodules are needed. In this Chapter, however, we ignore the acceleration in the matching section, and assume that we start accelerating at a momentum of 210 MeV/c.

6.1.2 Linac General Parameters and Lattice Period Layout

The requirement for a large acceptance of the accelerator necessitates a large aperture and tight focusing at its upstream end. Considering the large aperture, the tight space, the moderate beam energy and the need for strong focusing in both planes, solenoidal focusing is superior to triplet focusing, and has been chosen for the entire linac. To achieve a manageable beam size in the initial portion of the linac, short focusing cells are used for the first 11 cryomodules. As the beam size adiabatically damps during acceleration, intermediate-length cryomodules can be used and finally, when the energy reaches 0.75 GeV long (standard) cryomodules are utilized for the remainder of the linac. In comparison with the standard 13 m cryomodules, the short and intermediate-length cryomodules have increased aperture and, consequently, reduced accelerating gradient. The main parameters of the linac and its three cryomodule types are presented in Tables 6.2 and

Table 6.3: Parameters for the linear accelerator cryomodules.

	Short	Intermediate	Long
Number of periods	11	16	19
Total length of one period (m)	5	8	13
Number of cavities per period	1	2	4
Number of cells per cavity	2	2	2
Number of couplers per cavity	2	2	2
Cavity accelerating gradients (MV/m)	15	15	17
Real-estate gradient (MV/m)	4.47	5.59	7.79
Aperture in cavities ($2a$) (mm)	460	460	300
Aperture in solenoids ($2a$) (mm)	460	460	360
Solenoid length (m)	1	1	1.5
Solenoid maximum field (T)	2.1	2.1	4.2

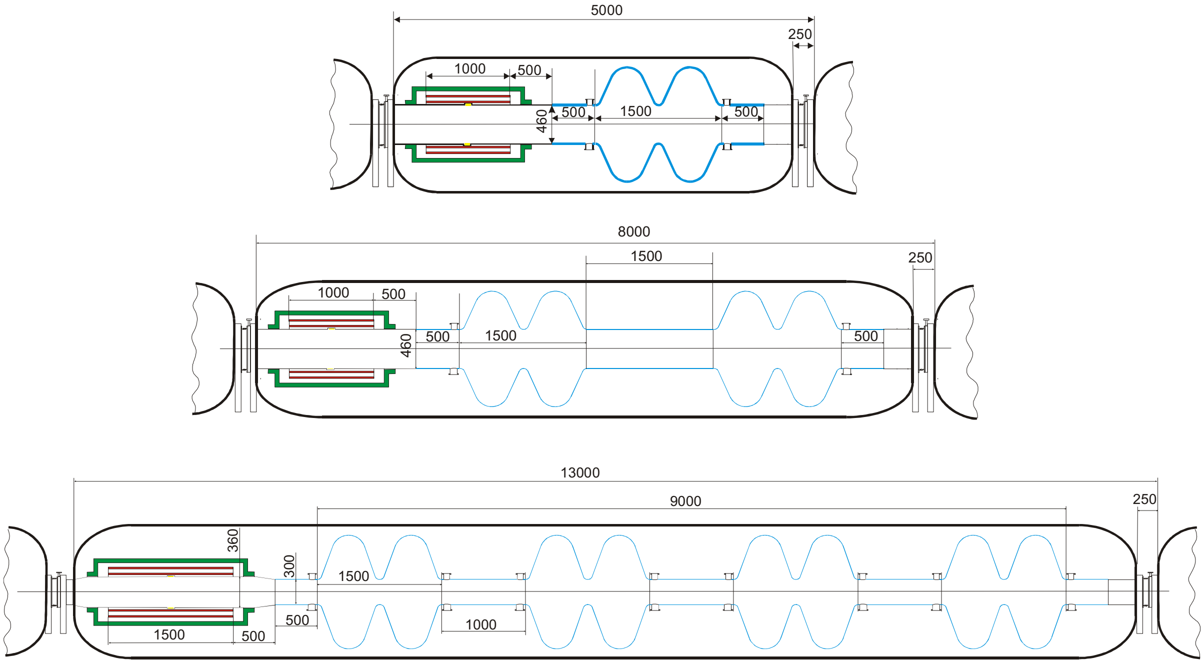

Figure 6.3: Layouts of short (top), intermediate (middle) and long (bottom) cryomodules. Blue lines are the SC walls of the cavities. Solenoid coils are indicated in red, and BPMs in yellow.

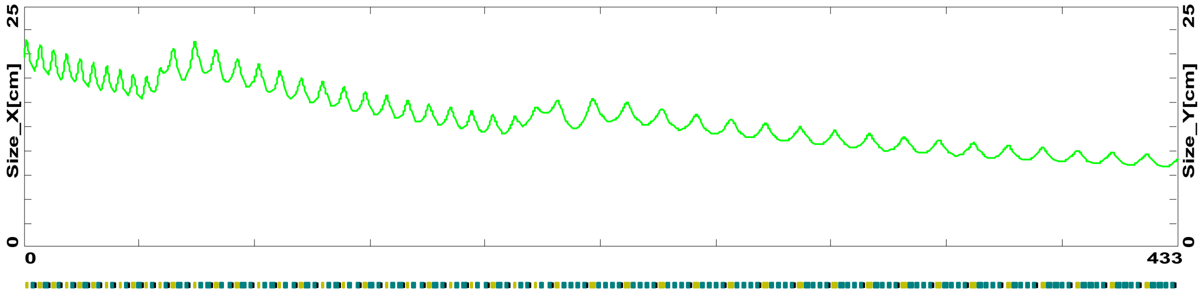

Figure 6.4: Beam envelopes of the entire beam (2.5σ) along the linear accelerator.

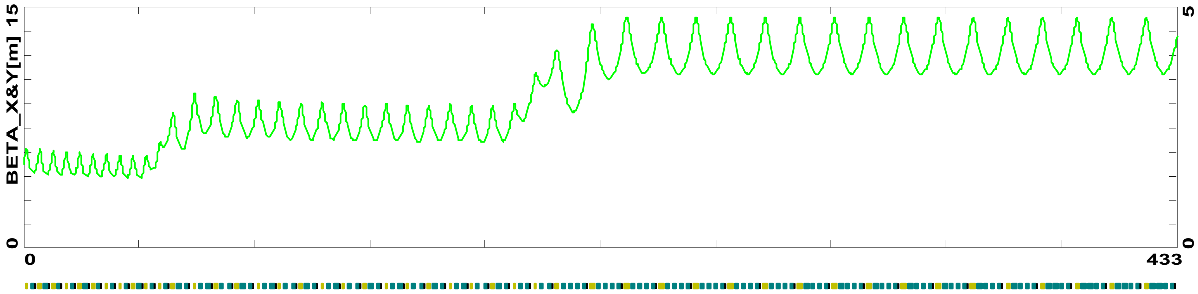

Figure 6.5: Beta functions along the linear accelerator. The beta functions are computed in the frame that rotates with angular frequency $\omega = eB_s/2pc$, so that the beam motion is decoupled.

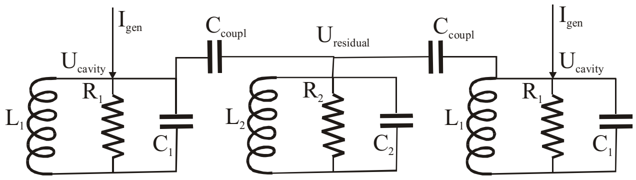

Figure 6.6: Electrical circuit model for calculation of cavity coupling.

6.3. Figure 6.3 depicts the layouts of short, intermediate-length and long cryomodules. Figures 6.4 and 6.5 present the beam envelope and beta-function along the linac.

The layout of cryomodules and the arrangement of SC cavities are determined by the requirement to keep power through the fundamental coupler at an acceptable level and to have cavities sufficiently decoupled. The coupler power limitation (below 0.5 MW) requires 1 coupler per cell, so there is a coupler at each end of the two-cell cavity.

The coupling coefficient determined as $\delta = C_3/C_1$ (see Fig. 6.6), should be sufficiently

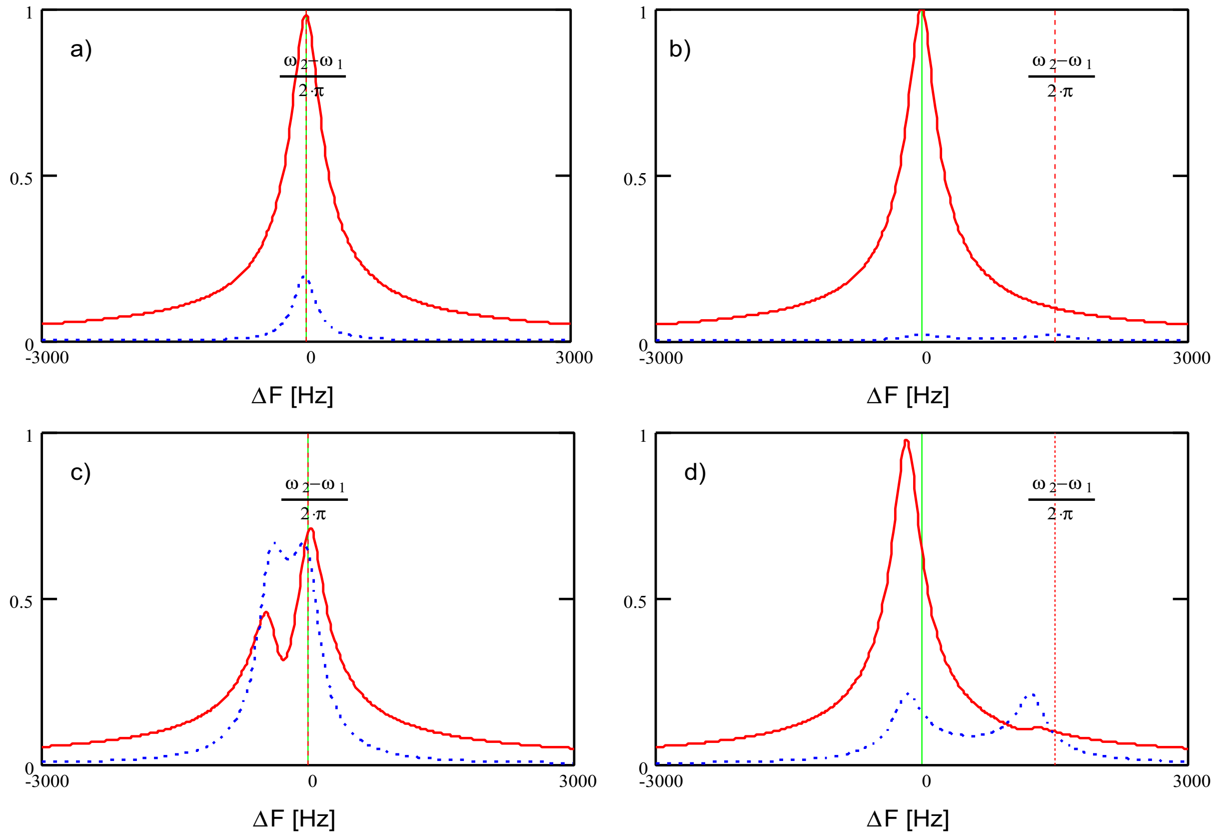

Figure 6.7: Dependence of cavity voltage on frequency. Solid lines: voltage for normally powered cavity; dashed line: voltage for improperly functioning cavity with corresponding power generator off. Left figures, cavity is not detuned; right figures, cavity is detuned by 5 bandwidths. Top figures, $\delta = 0.1/Q$; bottom figures, $\delta = 1/Q$.

small,

$$\delta \leq \frac{1}{10Q}, \tag{6.1}$$

to have a possibility to bypass cavities not functioning properly. Figure 6.7 demonstrates the effects of cavity coupling and detuning on the cavity voltage. For a loaded Q of 5×10^5, the required cavity decoupling should be below 2×10^{-6}.

Such decoupling requires significant distances between nearby cavities. For an estimate, we take the coupling between cavity cells to be 5%, and then, using results presented

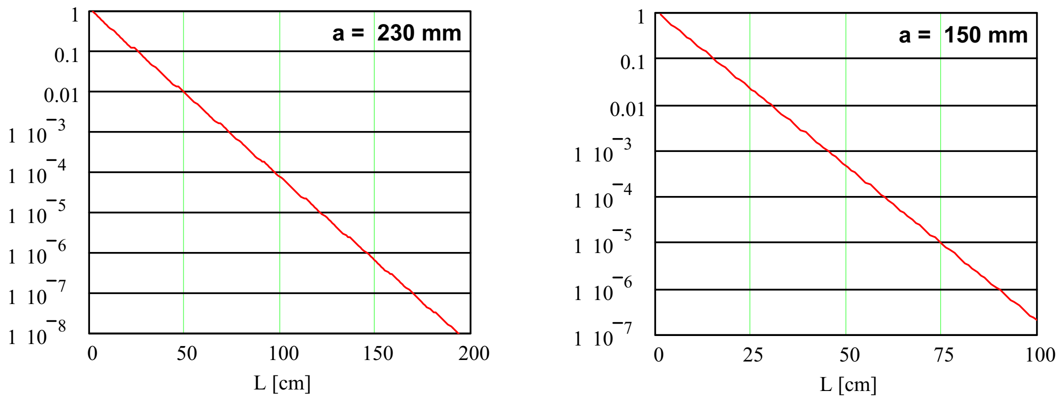

Figure 6.8: Attenuation of electromagnetic waves between two cavities for short (left) and long (right) cryomodules. The attenuation is approximated by $\delta = \exp(-L\sqrt{(\mu_0/a)^2 - (2\pi/\lambda)^2})$.

in Figure 6.8, find that the distance between cavities has to be more than 110 cm for short cryomodules and 70 cm for long cryomodules. Taking into account that the fundamental and HOM couplers are located in the same space, these distances were increased to 150 and 100 cm, respectively. BPMs are located inside the solenoids to reduce effects of EMI coming from the rf cavities.

There is an additional limitation on the layout of the linac determined by a requirement that all cavities be treated and placed under vacuum in a clean room and then kept under vacuum thereafter. To accomplish this, each cryomodule must have vacuum valves at both ends, with corresponding transition modules from liquid-helium temperature to room temperature. To achieve the maximum real-estate accelerating gradient, the focusing solenoids are also located inside the rf cryomodules.

Considering the large aperture required by the beam size, the question of focusing linearity of the solenoids must be addressed. The dependence of focusing strength on radius can be approximated by the following expression:

$$\Phi \equiv \frac{1}{F} \approx \left(\frac{e}{2pc}\right)^2 \left(\int B^2 ds + \frac{r^2}{2}\int B'^2 ds\right) \approx L\left(\frac{eB_0}{2pc}\right)^2 \left(1 + \frac{r^2}{3aL}\right), \tag{6.2}$$

where L and a are the solenoid length and radius. As can seen from Eq. 6.2, to reduce the nonlinearity one needs to increase the solenoid length and aperture. Increasing length directly decreases the real-estate gradient; increasing the aperture requires a larger distance between the solenoid and cavity to shield the magnetic field and, in the final analysis, also decreases real-estate gradient. An aperture increase also makes solenoids

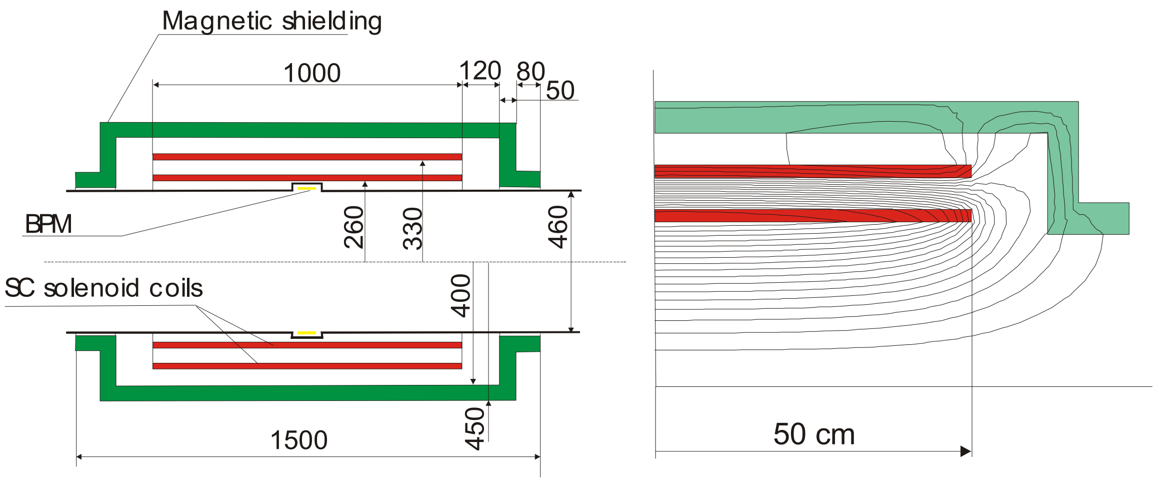

Figure 6.9: Layout of short solenoid and plot of its magnetic field lines.

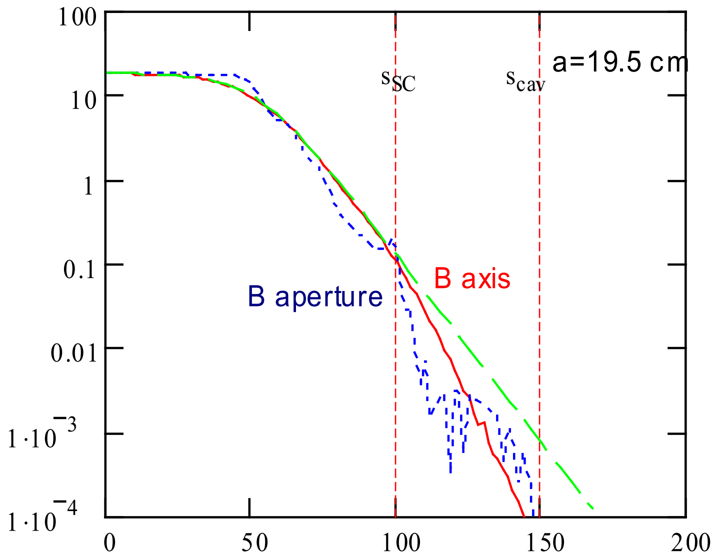

Figure 6.10: Dependence of magnetic field on longitudinal coordinate. The solid line is the field on axis; the dotted line is the field at the cavity radius (23 cm); the dashed line is a fit to $B(s) = (B_0/2)\{1 - \tanh[(s - L/2)/a]\}$, where $a = 19.5$ cm. Vertical lines show positions where the SC screen and cavity start.

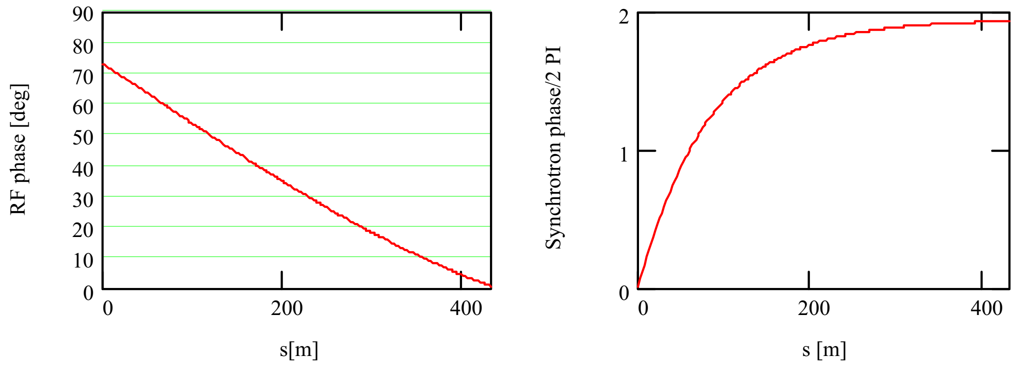

Figure 6.11: RF (left) and synchrotron (right) phases along the linac.

more expensive and less reliable. The length of the short solenoid has been chosen to be 1 m, as a compromise between these conflicting requirements. The length of the long solenoids is determined by the magnetic field limitation and is chosen to be 1.5 m. The concept of the short solenoid and plots of magnetic lines are shown in Fig. 6.9. Design details are given in Chapter 10. To achieve fast field drop between the solenoid and the cavity, the solenoid has an outer bucking coil that cancels its magnetic flux. It also has a SC shield at its outer surface. Together, these give a magnetic field less than 0.1 G inside the cavity, as depicted in Fig. 6.10.

6.1.3 Longitudinal Beam Dynamics

Because the initial bunch length and energy spread are very large, the bunch length is more than a half rf wavelength ($\Delta\phi = \pm 89°$), and the momentum spread is about $\pm 21\%$. Decreasing these values (via adiabatic damping) to a manageable level is the most important assignment of the beam acceleration in the linac. The final linac energy is determined by demanding a velocity sufficiently close to the velocity of light that there is no significant rf phase slip for higher passes in the subsequent recirculator.

To perform adiabatic bunching, the rf phase of the cavities is shifted by 73° at the beginning of the linac and is gradually changed to zero at the end of the linac, as shown in Figure 6.11. In the first half of the linac, when the beam is still not sufficiently relativistic, the offset results in synchrotron motion, which prevents a sag in acceleration for the bunch head and tail, and allows bunch compression in both length and momentum spread to $\Delta p/p = \pm 7.5\%$ and $\Delta\phi = \pm 23°$. However, the rf phase offset also reduces the effective accelerating gradient, so that a total voltage of 2.87 GV is required to provide a beam acceleration of 2.35 GeV. To maximize longitudinal acceptance, the initial position of the

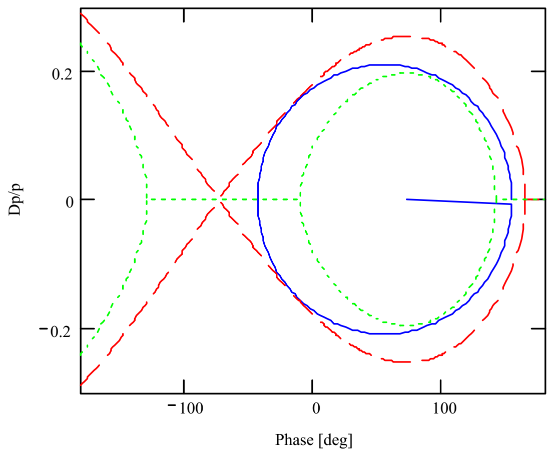

Figure 6.12: Beam boundary (solid line) inside separatrix (dashed line) shown at the beginning of the linac.

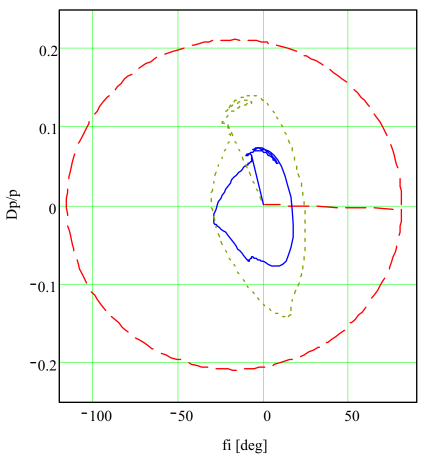

Figure 6.13: Beam boundary at the beginning (dashed line), in the middle (dotted line), and at the end of the linac.

beam is shifted relative to the center of the bucket. Figure 6.12 depicts the position of the beam boundary inside the separatrix; Figure 6.13 shows how the initially elliptical boundary of the bunch longitudinal phase space is transformed to the end of the linac.

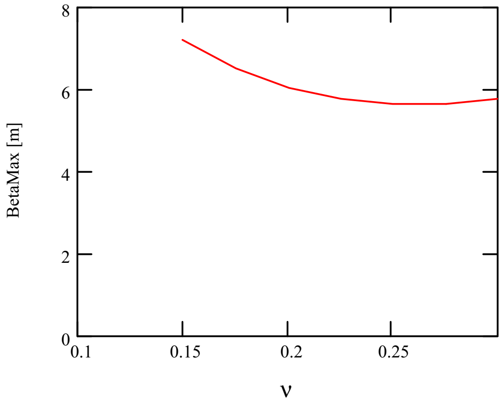

Figure 6.14: Dependence of maximum beta function on phase advance per cell for a beam line with solenoidal focusing and period length 6 m.

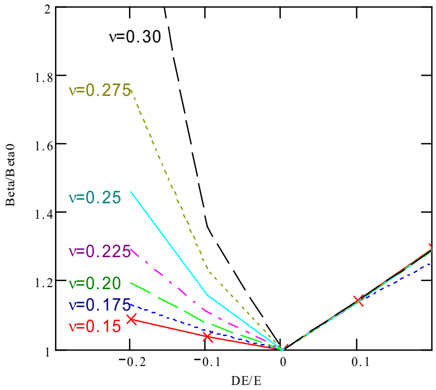

Figure 6.15: Dependence of relative change of the maximum beta function on the relative momentum change for different values of the phase advance per cell.

6.1.4 Transverse Beam Dynamics and Tracking

Betatron phase advance per cell, ν, is an important parameter to determine the properties of the beam transport in the linac. There are a few considerations that must be taken into account. First, large beam emittance and limited aperture in the cavities require minimization of the beam size for a given period length. As seen from Fig. 6.14, this requires ν close to 0.25. Second, we must minimize the dependence of the beta function

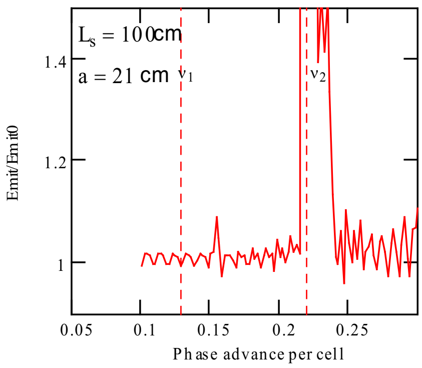

Figure 6.16: Relative emittance change after passing 50 solenoidal lenses of 1 m length. $\varepsilon_n = 15$ mm-rad; vertical lines show betatron tune spread in the beam: $\Delta\nu/\nu \approx \Delta p/p = \pm 26\%$.

on momentum. For the same initial conditions, the beta function oscillates relative to its nominal value if the momentum is changed. Figure 6.15 shows the ratio of maximum beta function achieved in the course of oscillations to the maximum beta function at equilibrium energy. For a momentum spread of $\pm 20\%$ a phase advance below 0.25 is clearly preferred. Third, the solenoids are short compared with their aperture, and therefore they have significant non-linearity in their focusing. From Eq. (6.2), for $a = 19$ cm, $r = 23$ cm and $L = 1$ m, there is a change of focusing strength of 9% at the beam boundary. Such nonlinear fields can cause strong nonlinear resonances, even for a small number of lattice periods. Figure 6.16 shows how the beam emittance changes for different values of the phase advance per cell after traversing a channel with 50 solenoidal lenses. One can see the very strong effect of the 1/4-resonance, which spreads over the 0.21–0.24 tune range. The 1/6-resonance is also visible, but does not produce so large an effect. In reality, this effect would be much smaller, because of adiabatic damping of the beam size with acceleration. Taking everything into account, we choose a phase advance of 0.175.

The particle distribution for tracking has been chosen to be Gaussian in 6D phase space, but the tails of the distribution are truncated at 2.5 σ, corresponding to the beam acceptance presented in Table 6.1. Despite the large initial energy spread, particle tracking through the linac does not exhibit any significant emittance growth, with 0.2% beam loss coming mainly from particles at the longitudinal phase space boundary. Figure 6.17 presents longitudinal phase space at the beginning and the end of the accelerator. Figure 6.18 shows the beam emittance, beam envelope, and beam intensity along the linac. The sudden increases and then decreases of the envelopes correspond to a particle motion instability, with subsequent particle scraping. The decay of muons is not taken into

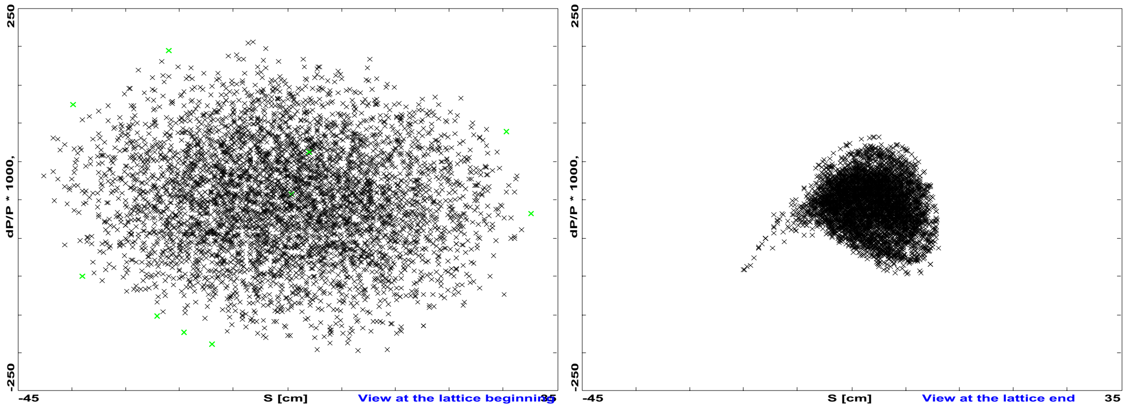

Figure 6.17: Longitudinal phase space at the beginning (left) and the end (right) of the linac.

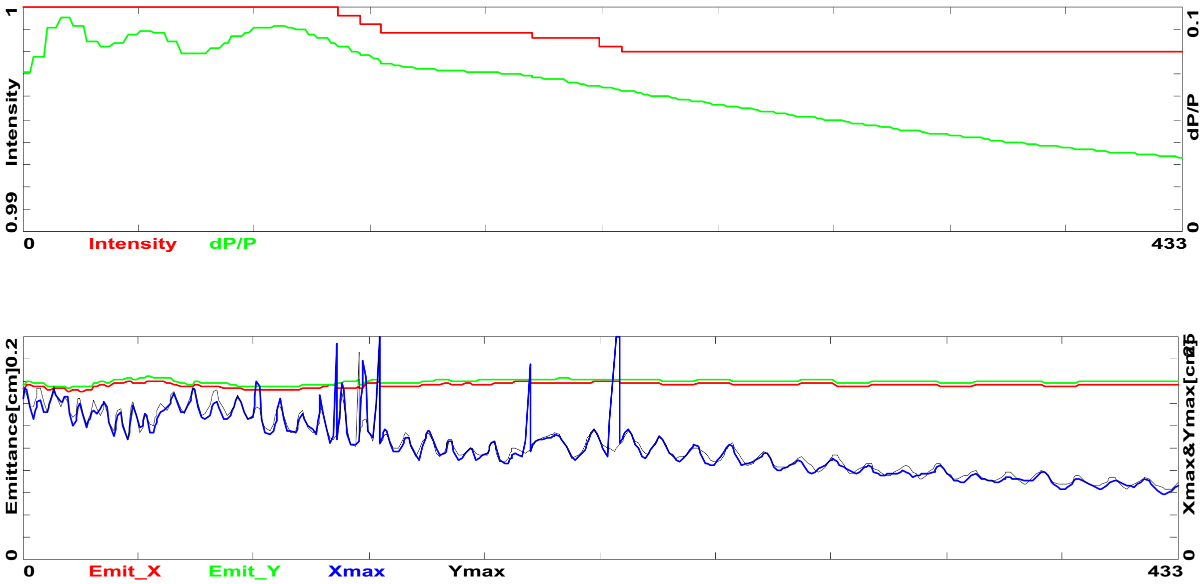

Figure 6.18: Beam intensity, rms momentum spread (top), beam emittances (normalized to the initial linac energy) and beam envelopes (bottom) along the linac.

account in this beam intensity plot.

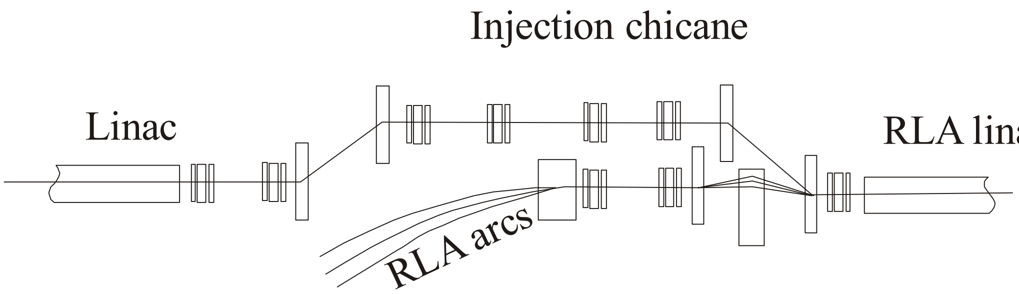

Figure 6.19: Diagram of the injection chicane.

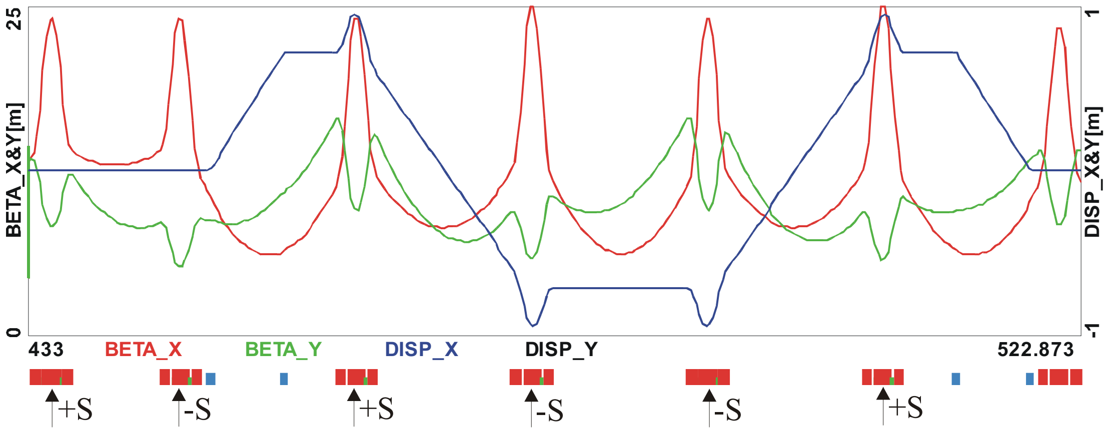

Figure 6.20: Beta functions and dispersion in the injection chicane.

6.1.5 Injection Chicane

An injection chicane is used to inject the beam into the RLA. A simplified scheme is presented in Figure 6.19. The chicane is built from four dipoles with four quadrupole triplets between them to form an achromat. A standard three-dipole chicane cannot be used because the chicane has to be sufficiently long to bypass the incoming higher energy arcs. In addition, two quadrupole triplets are used immediately before the chicane in place of the solenoidal focusing in the linac. An advantage of triplet focusing is that it easily provides the long straight sections necessary for beam separation at injection. Triplet focusing also naturally matches the solenoidal focusing. The period length is 15 m to coincide with the period length of the downstream RLA linac. The betatron phase advance per cell is chosen to be 90°, as this is preferable from the viewpoint of compensating chromatic effects. Figures 6.20 and 6.21 depict beta functions, dispersion,

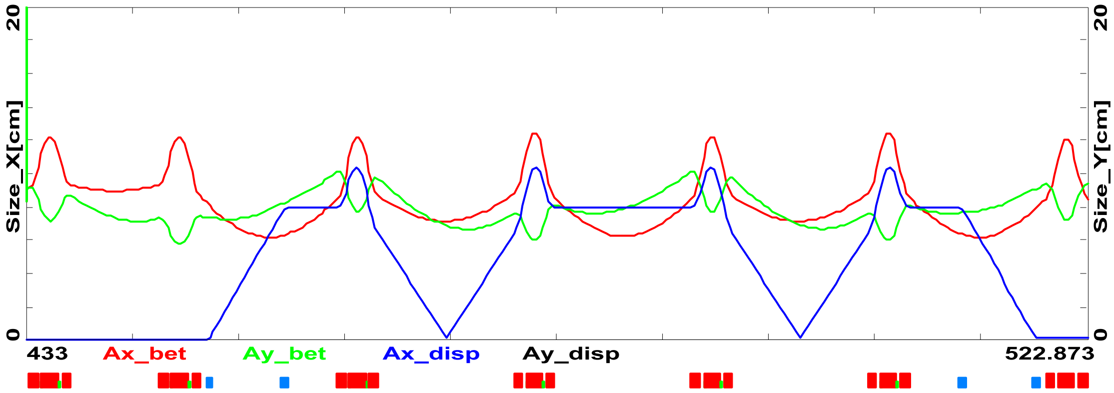

Figure 6.21: Beam envelopes in the injection chicane.

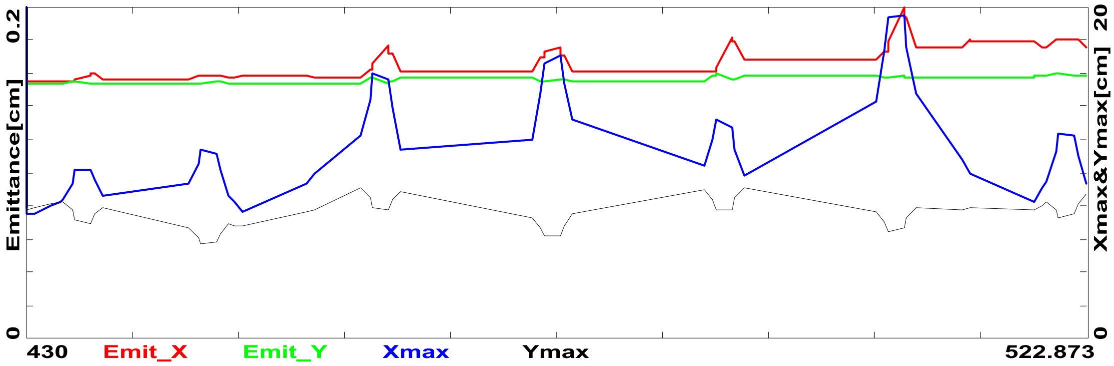

Figure 6.22: Variation of beam emittance (normalized to the initial linac energy) and beam envelopes along the linac.

and beam envelopes in the chicane.

In the linac, chromatic effects are suppressed by the periodicity of the focusing and do not require special correction. Unfortunately, it does not quite work the same way when we introduce bends; a sextupole chromatic corrector is required for the horizontal plane. This is achieved by introducing sextupole components into the field of the focusing quadrupoles of the six triplets. Four of these quadrupoles are located at the maximum of the dispersion function for chromaticity compensation and the other two are located in front of the chicane for compensation of the nonlinearity introduced by the strong chromaticity-correction quadrupoles, as shown in Fig. 6.20. Tracking studies showed that the nonlinearity of the sextupole fields can be cancelled for a small beam momentum spread, but only partial cancellation can be achieved for a momentum spread

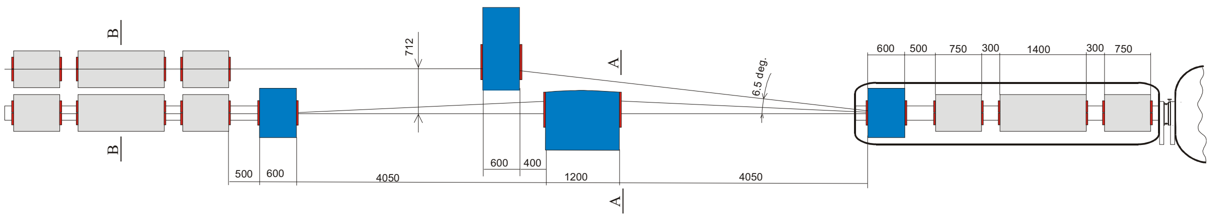

Figure 6.23: Layout of the injection chicane at the separation point.

Table 6.4: Parameters of the injection chicane quadrupoles.

	Number of magnets	Maximum gradient (T/m)	Length (m)	Aperture (m)	Built-in sextupole, S/G (m^{-1})
Focusing quad	3	4	1.40	0.15	0
Defocusing quad	14	4	0.75	0.15	0
Large aperture quad	4	4	1.40	0.181	0.355

as large as $\pm 10\%$, the value at the end of the linac (see Fig. 6.17). Strong sextupole components, required for good correction of second-order dispersion, cause emittance growth that is too large, due to inadequate cancellation of nonlinearities, and therefore a partial compensation of second-order dispersion is preferable. In tracking studies, values of all six sextupole components were varied independently to minimize the overall emittance growth through the chicane. It was found that if all sextupole components are proportional to the corresponding quadrupole components (the preferable technical choice), the emittance growth is close to its minimum value. Such a choice required only one additional type of quadrupole, and therefore it was adopted. The optimal ratio of sextupole to quadrupole components is $S/G = 0.355\ \mathrm{m}^{-1}$, which corresponds to a 7% correction of quadrupole gradient at a radius of 20 cm. Figure 6.22 depicts the beam envelopes and the beam emittances normalized to the initial linac energy, $\varepsilon\gamma\beta/\gamma_0\beta_0$. The horizontal emittance grows by 13% and the vertical by 3%, with no losses. Maximum horizontal beam size occurs at the last chicane triplet and is equal to ± 19 cm.

Figure 6.23 shows the injection chicane in the vicinity of the separation point. To minimize emittance growth, the bend angles of the chicane dipoles are chosen to be as small as possible. The separation is determined by the beam sizes and the space required for the septum magnet coil. Figures 6.24 and 6.25 show cross sections of the injector chicane at the separation point and in the center of the focusing quad. Taking into account the large apertures of the magnets (about 30 cm) and their comparatively

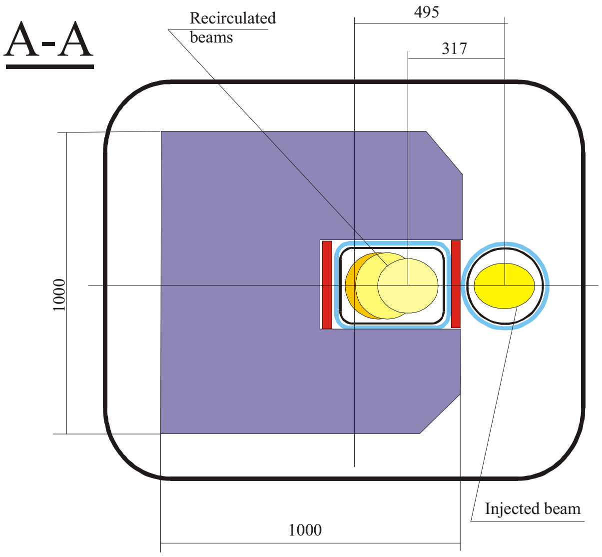

Figure 6.24: Cross section of the injection chicane at the separation point.

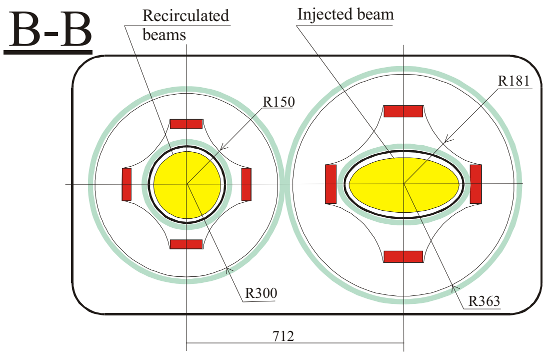

Figure 6.25: Cross section of the injection chicane at a focusing quadrupole.

modest magnetic fields (< 2 T), it looks preferable to use magnets with SC coils but with the field formed by the cold-iron core. Such a choice allows compact magnets and a significant reduction in required power. Tables 6.4 and 6.5 present parameters of dipoles and quadrupoles used for the injection chicane.

6.1.6 Solenoid Magnets

The linac contains several different solenoid magnets to provide focusing. The end of the matching section consists of a pair of low-stray-field solenoids with adjustable currents

Table 6.5: Parameters of injection dipoles.

	Number of magnets	Maximum field (T)	Length (m)	Gap (m)	Width (m)
Short dipole	4	1.7	0.6	0.30	0.30
Long septum	1	1.7	1.2	0.30	0.38
Short septum	1	1.7	0.6	0.30	0.38

for tuning. The short and intermediate modules have a 1-m focusing solenoid with a 1.25-m straight section at each end. Likewise, the long modules have a 1.5 m solenoid with a 1.25-m separation to the first rf cavity cell.

Unlike focusing quadrupoles, focusing solenoids produce a stray field that reaches far from the magnet. Superconducting rf cavities are sensitive to magnetic fields even at the gauss (10^{-4} T) level, so as noted in Section 6.1.2}, a key parameter in the superconducting focusing solenoid design is getting rid of the solenoid stray field in the rf cavities. The approaches one can use to eliminate the stray field in the rf cavities are described in Chapter 10.

6.2 Recirculating Linac (RLA)

6.2.1 Arc Optics, Spreaders, and Recombiners: Design Choices

For multiple practical reasons, horizontal rather than vertical beam separation was chosen. If vertical separation were chosen, one of the drawbacks would be an enormous vertical aperture of the vertical spreader/recombiner dipole. Furthermore, instead of having to suppress vertical dispersion created by the spreaders and recombiners we can use horizontal separation with no dispersion suppression; it is matched to the horizontal dispersion of the arc. Finally, to ensure a compact arc architecture, very short matching sections (three triplets) were implemented in the spreaders and recombiners.

The 4-pass RLA beam transport system uses a single dipole separation of beams at the end of each linac to allow independent recirculation of each pass. Individual recirculation arcs are based on a periodic triplet-focusing structure, which is a smooth continuation of the linac focusing. Betatron phase advance per cell is chosen to be 90°, which is preferable from the point of view of compensating chromatic effects. The period length (about 11 m) is slightly shorter than for the linacs, to achieve the desired small value of

M_{56} (about 1.4 m).

Triplet focusing has a few advantages over the FODO focusing structure. First of all, it has larger distance between quadrupoles, which significantly simplifies spreader/recombiner design. Spreading and recombining the beams with a FODO lattice would be much more complicated. Furthermore, triplet focusing allows simple and smooth beam envelope matching from linac to recirculating arc, which is very important for beams with such a large energy spread. Finally, triplet focusing has only half the chromaticity of the vertical beam envelope compared with FODO focusing, so it requires chromatic corrections in only one plane.

Another crucial beam transport issue is to maintain manageable beam sizes in the arcs. This calls for short cells and for putting stringent limits on dispersion and beta functions (beam envelope). Since spreaders and recombiners were chosen in the horizontal plane, the uniform focusing and lattice regularity is broken in that plane, and the horizontal beam envelope requires special attention. On the other hand, the vertical beam size remains small due to maintaining uniform focusing (unbroken periodic symmetry) and small beta functions in that plane.

Furthermore, there is a need for high periodicity and a smooth transition between different types of optics, *e.g.*, linac-arc-linac, to alleviate emittance dilution due to chromatic aberrations (second-order-dispersion).

Finally, the required large momentum acceptance necessitates introduction of a chromatic correction scheme using three sextupole families for the off-momentum orbit and path length. As in other recirculating linacs, and unlike storage rings and synchrotrons, correction of betatron "tunes" is unnecessary. Figure 6.26 shows a geometric layout of arcs 1, 3, 5 and 7.

6.2.2 Longitudinal Dynamics in Recirculating Linac

The beam bunch length and energy spread are still too large at the RLA input, and further compression is required in the course of the acceleration. To achieve this, the beam is accelerated off-crest with non-zero M_{56} (momentum compaction). This causes synchrotron motion, which suppresses the longitudinal emittance growth related to nonlinearity of the accelerating voltage. Without synchrotron motion, the minimum beam energy spread would be set by the nonlinearity of the rf voltage at a value of $(1 - \cos\phi) \approx 6\%$ for a bunch length of $\phi = 20°$.

Synchrotron motion causes particle motion within the bunch and equalizes the total average energy gain of particles in the tail and particles in the core. The parameters of acceleration are presented in Table 6.6, and corresponding boundaries of longitudinal

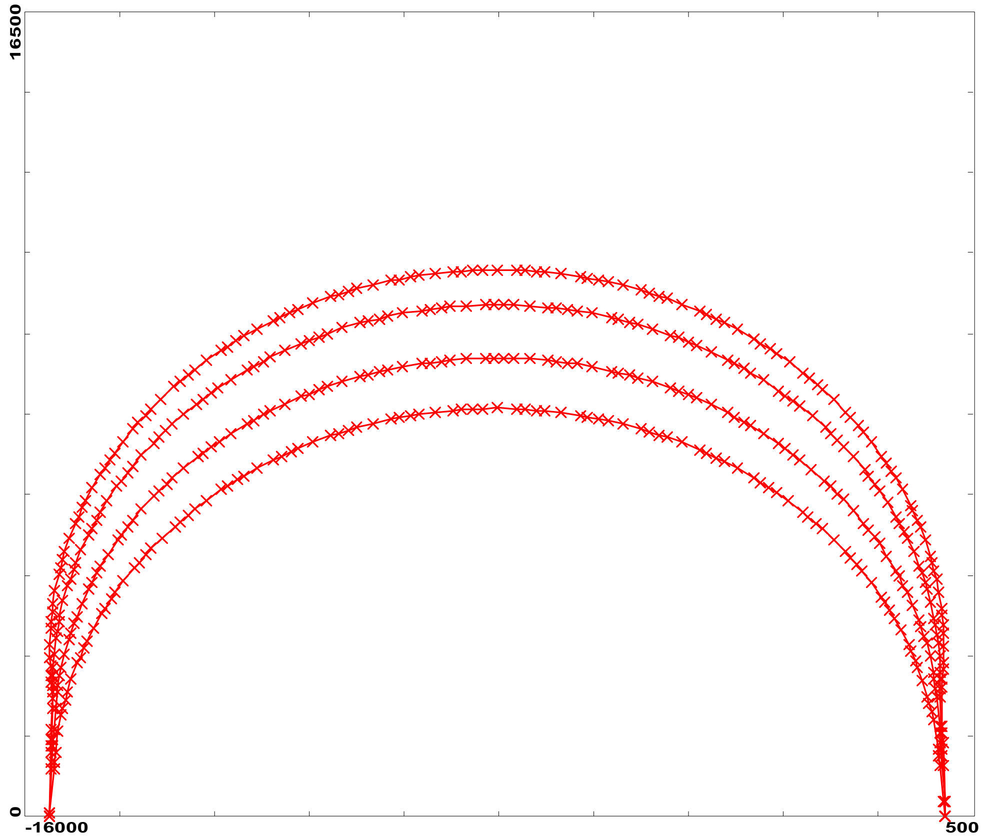

Figure 6.26: Geometric layout (bird's eye view) of odd numbered arcs, including spreader/recombiner configuration. Crosses mark locations of magnets (dipoles and quadrupoles). All distances are in cm.

phase space are presented in Figure 6.27. We chose to have approximately the same M_{56} for all the arcs; the optimum value is about 1.4 m. Optimal detuning of the rf phase from the on-crest position is different for different arcs. Although longitudinal motion is still quite nonlinear, it is possible to reduce the energy spread by a factor of 4.7, to $\pm 1.6\%$, with emittance dilution of about 75%. In these calculations for arc optics we assume that the longitudinal displacement is a function of momentum only, given by the linear function, $\Delta L/L = M_{56}\Delta p/p$. The horizontal and vertical acceptances of the arcs listed in Table 6.6 are presented with emittance dilutions of 9% to 4% per arc. This is supported by preliminary tracking results. Final details of the beam dynamics depend on the beam transport optics and can be determined only by tracking (discussed below).

Table 6.6: Parameters for acceleration in the recirculator.

	Kinetic energy (GeV)	Gang phase (deg)	Total energy spread, $2\Delta p/p$ (%)	Horizontal acceptance (mm-mrad)	Vertical acceptance (mm-mrad)
Entrance	2.480	0	15.0	669	638
Arc 1	4.756	-23	11.3	384	350
Arc 2	6.884	-23	8.9	292	253
Arc 3	9.017	-23	6.7	244	202
Arc 4	11.140	-23	5.8	216	171
Arc 5	13.284	-20	5.0	198	150
Arc 6	15.462	-16	4.4	187	134
Arc 7	17.690	-5	3.4	178	122
Exit	20.000		3.2	157	108

Since the beam intensity is high, beam loading has to be taken into account. It causes the rf voltage to droop by about 0.6% per pass, yielding about 2.4% loss in acceleration for the tail bunch of the last pass. This is comparable with the energy aperture of the later arcs and their optics tuning must be done with energy droop taken into account. In this scenario, the first and the last bunches see different accelerating voltage and experience different longitudinal dynamics. Fortunately, accelerating off-crest resolves this issue as well. In this case, after acceleration in the first linac, the last bunch experiences less acceleration; but then, because of smaller energy, the bunch comes faster through the first arc and is accelerated with smaller rf phase, causing higher acceleration, in the next linac. In other words, the bunch center of the last bunch experiences synchrotron motion relative to the center of the first bunch. This suppresses the effect of accelerating voltage droop. Figure 6.28 shows the longitudinal phase space for the first and the last bunches at the end of the accelerator. The acceleration has been optimized so that the energy spread of both bunches is the same. Although the beam loading significantly changes the bunch shape, the energy droop cannot be seen.

6.2.3 General Parameters and Period Layout of RLA Linac

Both RLA linacs have the same period. One period comprises a cryomodule with four SC cavities and a cryomodule with a quadrupole triplet; the layout is presented in Figure 6.29. The design and parameters of the cavities are the same as for the cavities of the long cryomodule of the preaccelerator linac (see Table 6.3). However, in contrast to

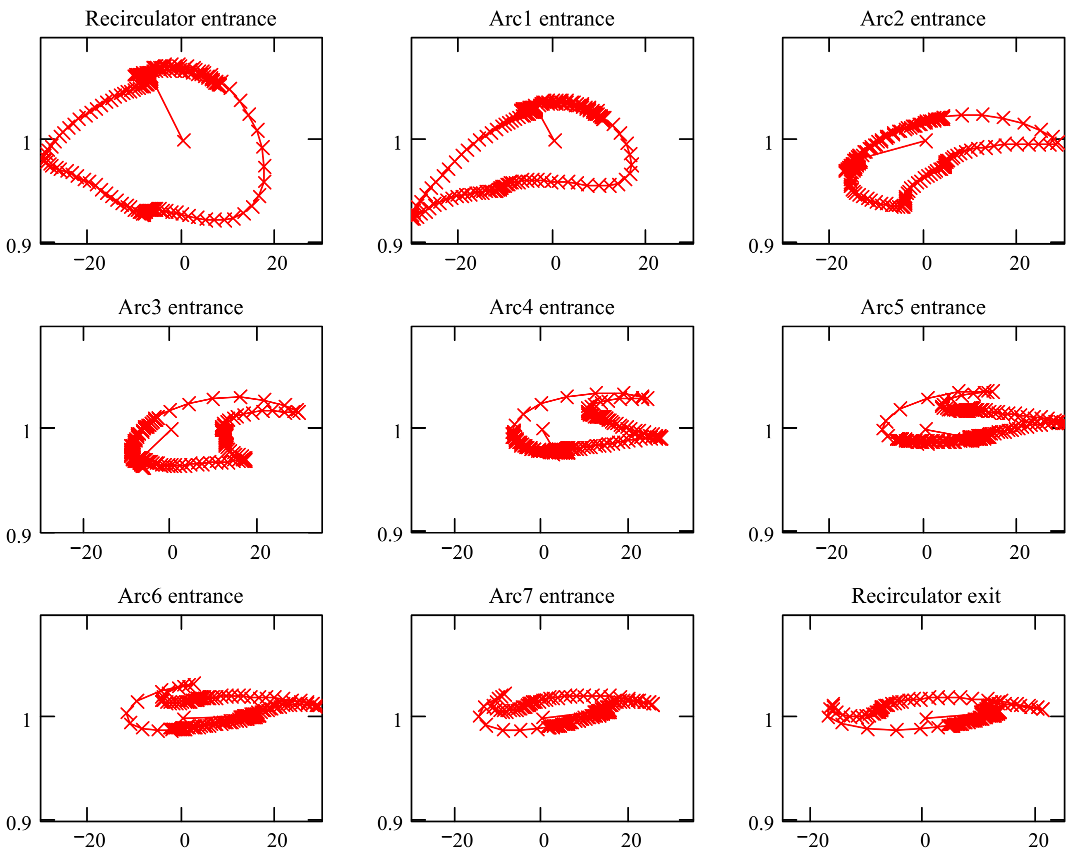

Figure 6.27: Boundaries of the beam longitudinal phase space at different locations in the recirculator; $M_{56} = 1.4$ m.

the preaccelerator linac, which has just one cryomodule per period, the RLA period has separate cryomodules for cavities and for magnets. This solution is preferred due to the increased length of the RLA period. The design and parameters of the triplets of the first RLA linac are similar to those of the small triplets of the injection chicane, but with higher focusing gradients ranging from 3.2 – 6.7 T/m. Quadrupoles of the second RLA linac have a similar design but with 1.5 times smaller aperture (100 mm). Their focusing gradient ranges from 6.2 – 9.7 T/m.

Figures 6.30–6.33 show the beta-functions and beam envelopes for the first and the last passes in the first RLA linac. Beta functions of the first pass in the second RLA linac are the same as for the first RLA linac. The last pass beta functions of the second RLA linac are smaller than the corresponding beta functions of the first RLA linac because

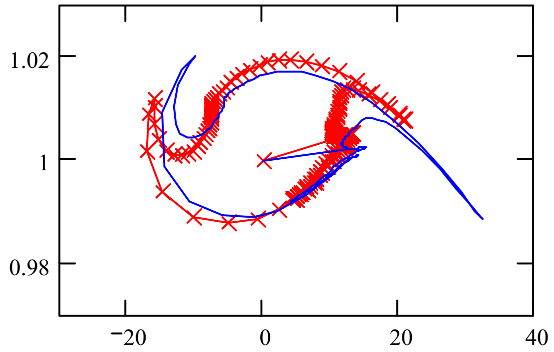

Figure 6.28: Boundaries of the beam longitudinal phase space at the end of the recirculator for the first bunch (line with crosses) and the last bunch (solid line). $M_{56} = 1.4$ m; the energy droop of 0.5% per pass corresponds to 3×10^{12} muons in the bunch train.

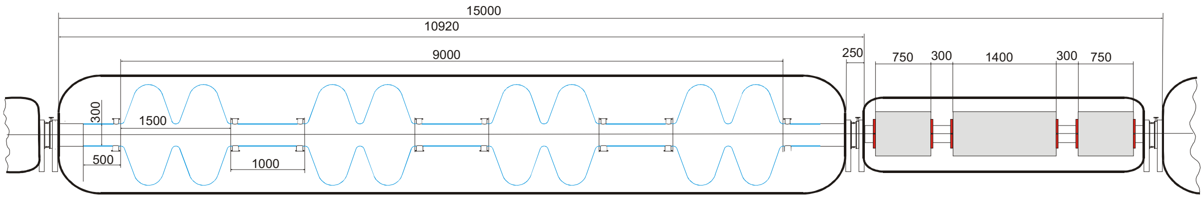

Figure 6.29: Layout of an RLA linac period.

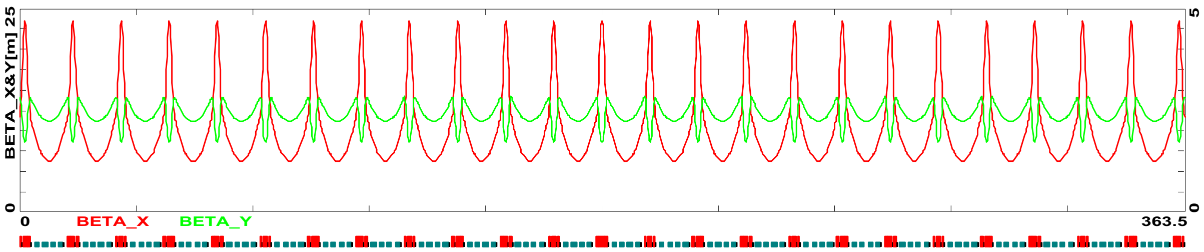

Figure 6.30: Beta functions for the first pass of the first RLA linac.

of a smaller energy difference between the last and the first passes. Figures 6.34 and 6.35 show the beam envelopes for the first and the last passes in the second RLA linac. The difference between the vertical and horizontal beam sizes for the last pass is related to a larger horizontal emittance resulting from higher horizontal emittance growth. The focusing structure for both linacs is chosen to give the same betatron phase advance per cell for the first-pass beam. The requirement to have similar horizontal and vertical beta

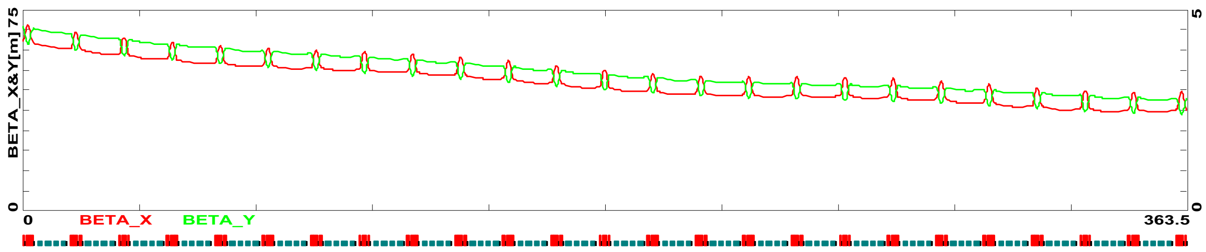

Figure 6.31: Beta functions for the last pass of the first RLA linac.

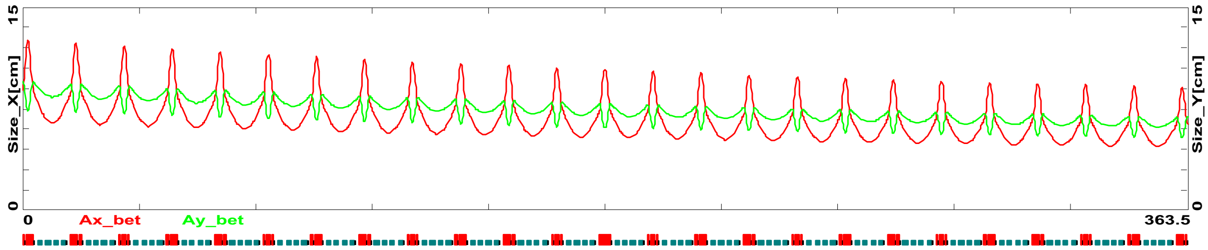

Figure 6.32: Beam envelopes for the first pass of the first RLA linac.

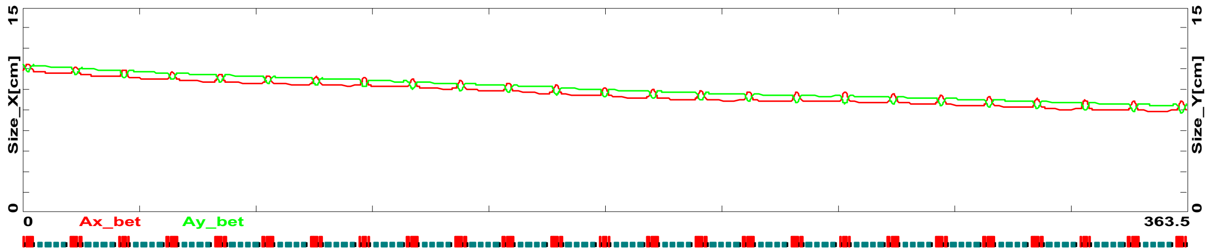

Figure 6.33: Beam envelopes for the last pass of the first RLA linac.

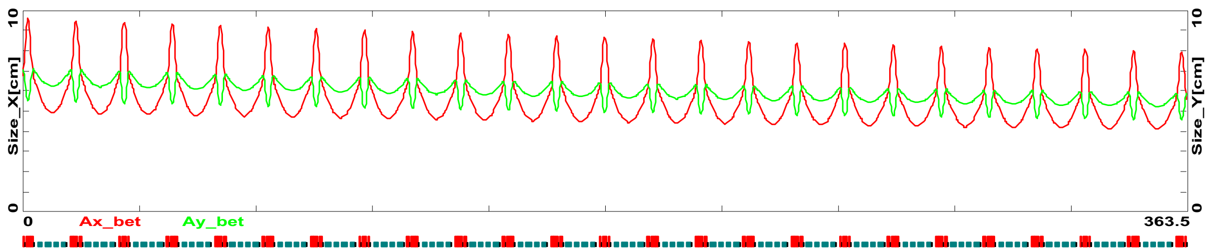

Figure 6.34: Beam envelopes for the first pass of the second RLA linac.

functions for the higher passes determines that the horizontal and vertical phase advances are not equal. Figure 6.36 shows the line on the tune diagram where the horizontal and

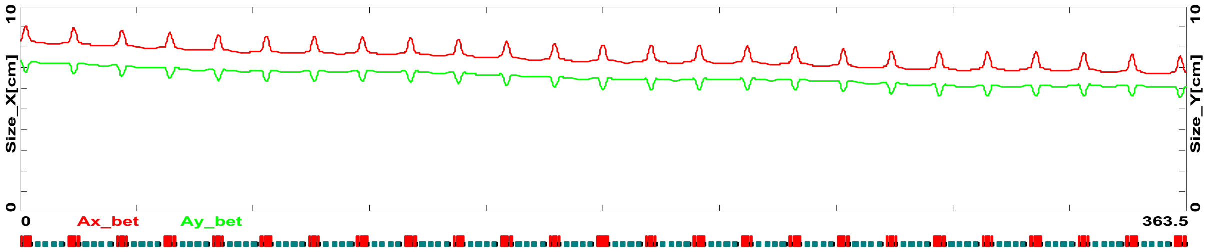

Figure 6.35: Beam envelopes for the last pass of the second RLA linac.

Table 6.7: Parameters of the RLA linac periods.

	Linac 1	Linac 2
No. of periods	24	24
Total length of one period (m)	15	15
No. of cavities per period	4	4
No. of cells per cavity	2	2
No. of couplers per cavity	2	2
Cavity accelerating gradient (MV/m)	17	17
Aperture in cavities, $2a$ (mm)	300	300
Aperture of quadrupole, $2a$ (mm)	300	200
Focusing quad length (m)	1.4	1.4
Defocusing quad length (m)	0.75	0.75
Quadrupole gradient (T/m)	3.2–6.7	6.2–9.7

vertical beta functions are approximately equal for the last pass of the first RLA linac. Parameters of linac periods are presented in Table 6.7.

Each cavity cryomodule has vacuum valves at both ends and is delivered to the tunnel under vacuum. These valves are slow; it is not feasible to build a sufficiently fast valve to prevent a major vacuum failure in a chamber of so large an aperture. Therefore each linac is separated from the arcs with 0.5-mm beryllium windows. This approach also resolves the question of differential pumping between the high vacuum in the RLA linacs and the low vacuum in the arcs, which otherwise would be a major issue with a vacuum chamber of such large aperture. The design and size of the windows are similar to the beryllium windows used for the ionization cooling. Altogether there are 5 windows: one in the injection chicane, and one at each end of both RLA linacs. Multiple scattering causes the total emittance growth of about 5% for windows of 0.5-mm thickness. The contribution to emittance growth from different passages through the windows is almost even: the

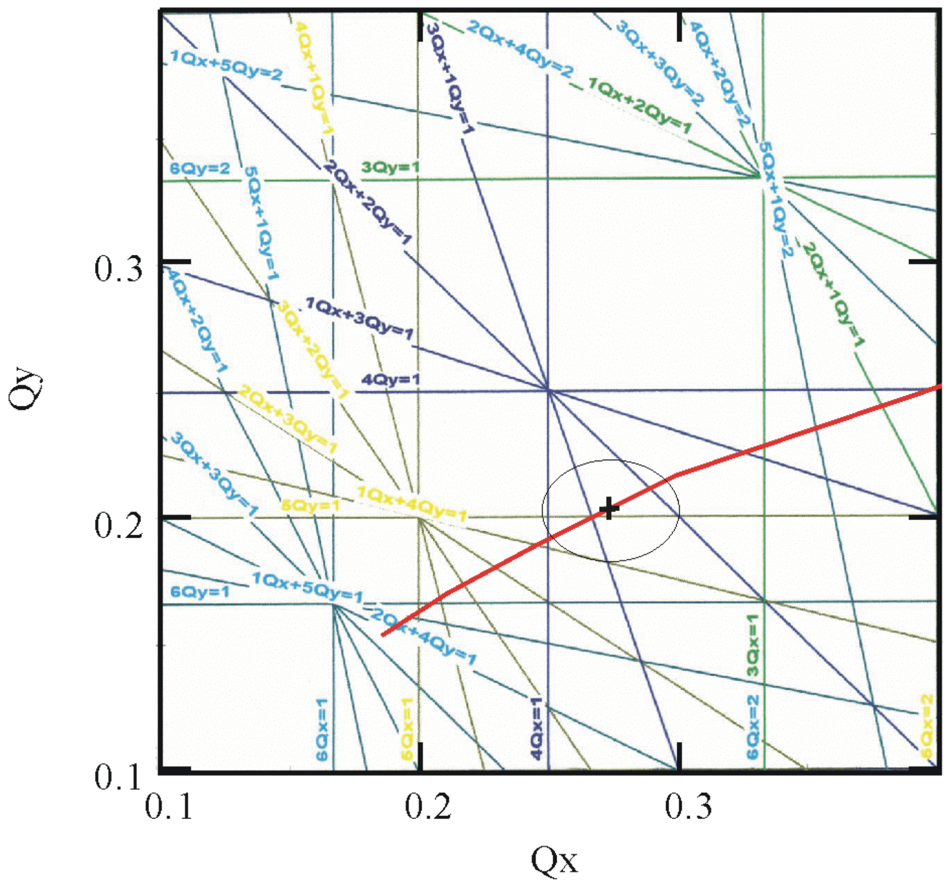

Figure 6.36: Tune diagram for one period of the first pass in the RLA linac. Solid line shows tunes where $\beta_x = \beta_y$ for the highest energy pass. The cross shows the chosen tune, $Q_x = 0.273$, $Q_y = 0.204$, and the circle around it corresponds to the tune changes corresponding to 10% energy spread.

beam of higher energy experiences smaller scattering, but it has a proportionately larger beta function in the RLA.

6.2.4 Beam Dynamics in the RLA Linacs

To choose a working point we took into account the following considerations. First, due to the symmetry of the quadrupole field, the lowest nonlinearity of its field has sixth-order

Table 6.8: Acceptable nonlinear fields of quadrupoles.

	4th order (octupole)	6th order	8th order
$\lvert F_n \rvert$	< 0.015	< 0.02	< 0.02

symmetry, so we would like to avoid sixth-order resonances. Second, the beam size should be close to its minimum for a given period length. Third, the chromaticity of the beam envelopes should be minimized. The chosen tunes of $Q_x = 0.273$, $Q_y = 0.204$ satisfy the above requirements. For higher passes, the phase advance per cell is not constant and grows from the beginning to the end of the linac, causing the tune to cross a few resonances. The most sensitive is the second pass, during which tunes cross the sixth-order resonances. Nevertheless, the tracking showed that all higher passes are less sensitive to quadrupole nonlinearity than the first pass. The first RLA linac is more sensitive to quadrupole nonlinearity because it has larger beam size for all passes. Therefore, it sets the limit for acceptable quadrupole nonlinearity. For simulations we assumed that nonlinear terms are proportional to the quadrupole gradients. The nonlinearity is described by the parameter

$$F_n = \frac{1}{Ga}\frac{a^{n-1}B_n}{n!}, \tag{6.3}$$

which determines a relative correction of the gradient at the reference radius a. Table 6.8 summarizes results of simulations performed for the first RLA linac. The values correspond to a reference radius of 10 cm, which is close to the beam envelope in the focusing quadrupoles. We find that the requirements for quadrupole nonlinearity are very modest and should be easily met. Summarizing, we can conclude that an accuracy of the quadrupole field integral better than 1% at the reference aperture of 100 mm is sufficient. With this assumption, tracking in the linacs did not exhibit any significant emittance growth, demonstrating that the periodicity of motion is not badly broken in the arcs.

As was already mentioned, there is a significant rf phase slip for the beam during different passes because of different particle velocities at different energies. Figure 6.37 presents rf phases for the beam at different passes, assuming that the cavity phases are set so that the second-pass beam is on crest. We see that the first-pass beam in the first RLA linac has phase variations in the range of about -19 to $12°$. This reduces the effective accelerating gradient by 1.2%, but it does not otherwise produce any significant effect for higher passes.

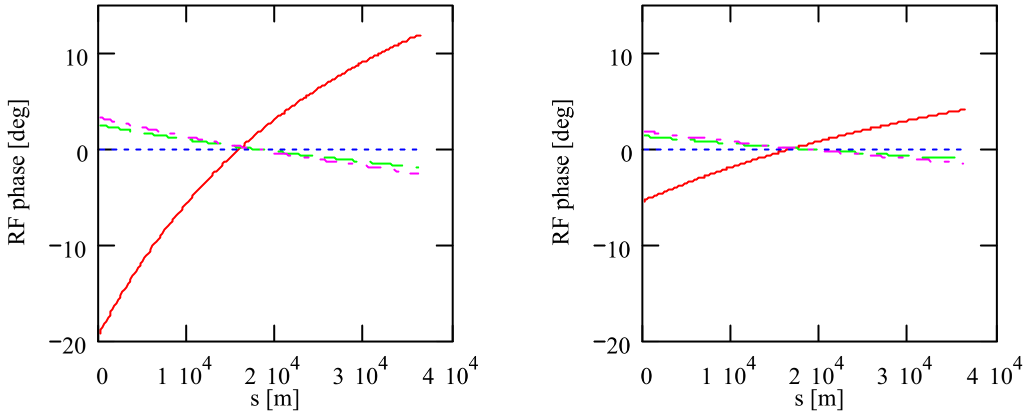

Figure 6.37: RF phase for different passes through the first (left) and second (right) RLA linacs. The solid line is pass 1, the dotted line is pass 2, the dashed line is pass 3, and the dot-dashed line is pass 4.

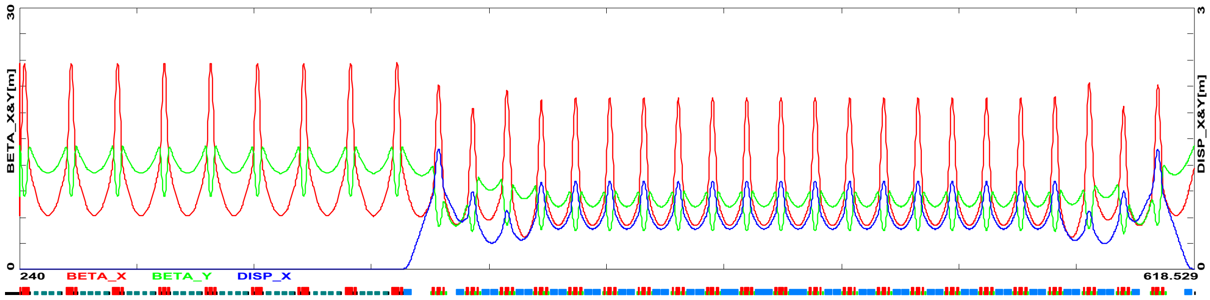

Figure 6.38: Arc 1 optics. Beta functions and the horizontal dispersion for the end of linac 1 and arc 1 (matched to both adjacent linacs).

6.2.5 Odd Arcs: Proof-of-principle Lattice Design

Lattices for four odd arcs and one even arc of the RLA are illustrated in terms of the beta functions and dispersion in Figs. 6.38–6.42. Short matching sections in spreaders and recombiners (consisting of six quadrupoles) allow us to match all Twiss functions and to smoothly join regions of different optics of the adjacent linacs.

The number of periodic cells in the arc was chosen and tuned so that the desired value of momentum compaction factor required for optimum longitudinal phase space compression ($M_{56} = 1.4$ m) is built into the arc optics.

Similar optics for one full turn in the RLA (linac1-Arc1-linac2-Arc2), as illustrated in Figures 6.38 and 6.39, was put to the test for beam transport properties in Study I. A

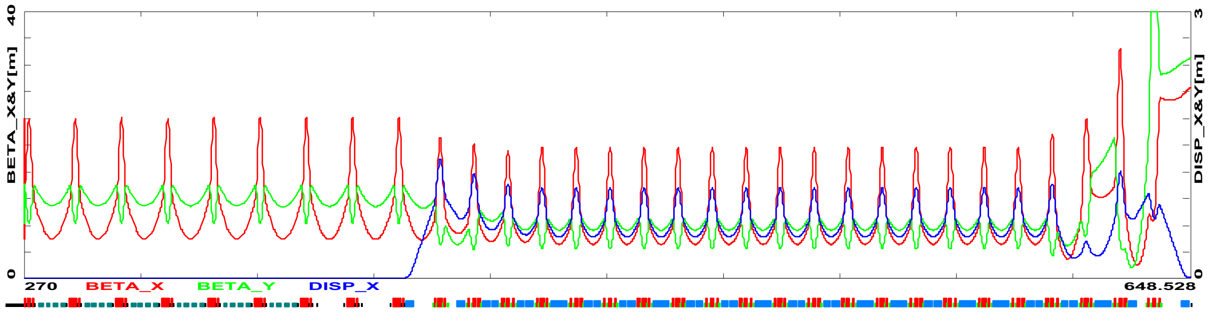

Figure 6.39: Arc 2 optics. Beta functions and the horizontal dispersion for the end of linac 2 and arc 2 (matched to both adjacent linacs).

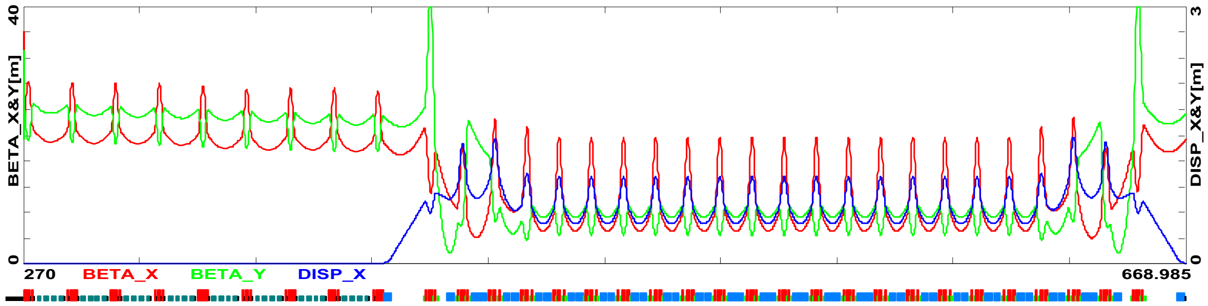

Figure 6.40: Arc 3 optics. Beta functions and the horizontal dispersion for the end of linac 3 and arc 3 (matched to both adjacent linacs).

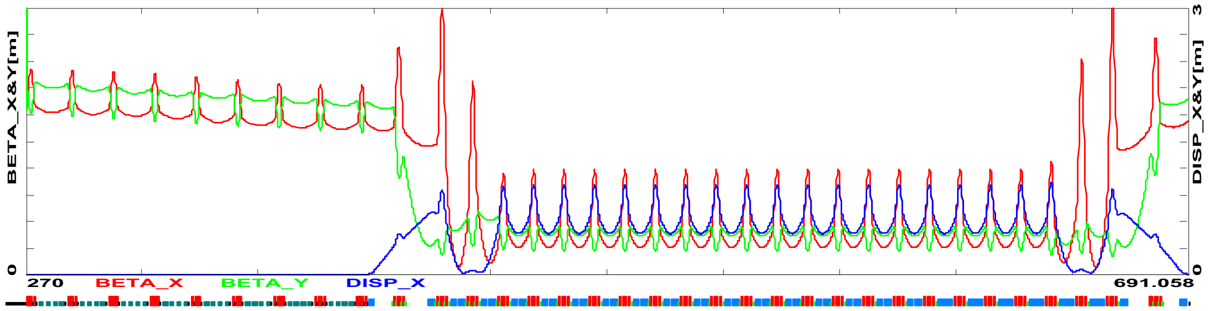

Figure 6.41: Arc 5 optics. Beta functions and the horizontal dispersion for the end of linac 5 and arc 5 (matched to both adjacent linacs).

multi-particle simulation was carried out for a particle distribution having a realistic large momentum spread (10%). The particle distribution used for tracking was Gaussian in 6D phase space with the tails of the distribution truncated at 2.5σ, corresponding to the

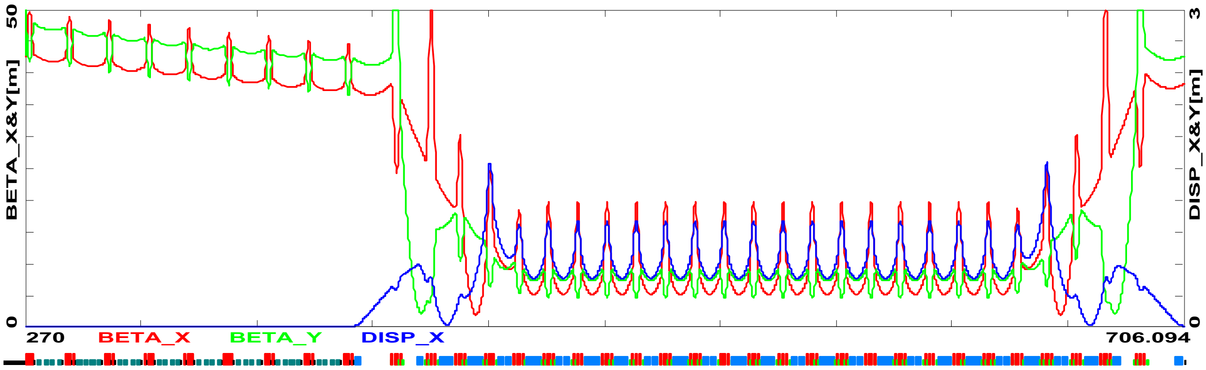

Figure 6.42: Arc 7 optics. Beta functions and the horizontal dispersion for the end of linac 7 and arc 7 (matched to both adjacent linacs).

beam acceptance presented in Table 6.6. Despite the large initial energy spread, particle tracking through the linac does not exhibit any significant emittance growth. There was less than 0.5% beam loss, coming mainly from particles at the longitudinal phase space boundary. The simulation also showed that the chromatic corrections via three families of sextupoles in the spreaders/recombiners are a very effective means of emittance dilution control.

Chapter 7

Muon Storage Ring

7.1 Overall Design Motivation

The storage ring is the part of the Neutrino Factory that delivers the neutrino beam to the detector. As such, its effectiveness can be defined by the ratio of the number of neutrinos aimed in the direction of the detector to the total number of muons injected into the storage ring. Since we consider here sending neutrinos to a single detector, we use the storage ring geometry shown in Fig. 7.1. The straight sections are aligned parallel to a line from the storage ring to the detector. Thus, the muons decaying in one of the two straight sections (the "production" straight) contribute to the neutrinos headed toward the detector, while muons decaying in the rest of the ring do not. The effectiveness f_S of the storage ring is the ratio of the length of the production straight section to the circumference of the storage ring:

$$f_S = \frac{L_S}{C} = \frac{L_S}{2(L_S + L_A)}, \tag{7.1}$$

where L_S is the length of one straight section, and L_A is the length of 180° of arc.

In the case of a detector at the WIPP facility, the storage ring must be tilted 13.1° from horizontal to have a straight section pointing toward the detector. It follows that there must be a substantial elevation change from the top of the ring to the bottom. For this study, we have constrained ourselves to keep the bottom of the storage ring tunnel at least 10 feet above the water table. At the Brookhaven site, the water table averages 48 feet above sea level, with a seasonal variation of ±5 feet. Thus, the bottom of the storage ring tunnel will be at 63 feet above sea level. The highest ground elevation on the Brookhaven site where the storage ring could be realistically placed is about 90 feet above

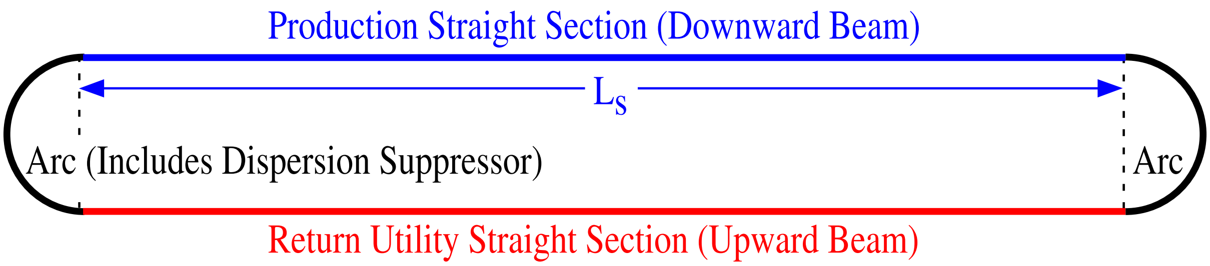

Figure 7.1: Storage ring diagram.

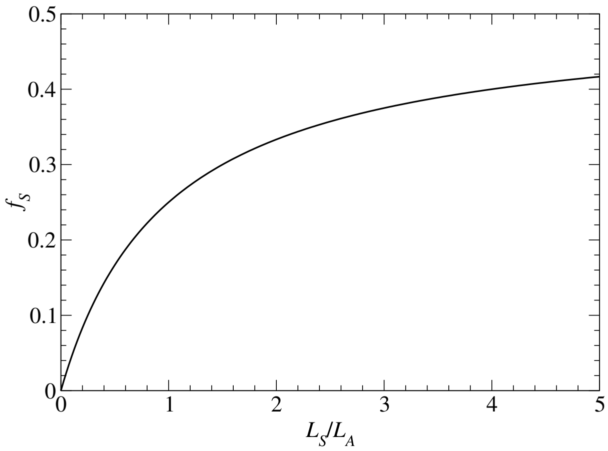

Figure 7.2: Fraction of decays in a straight (f_S) as a function of the ratio of the length of a straight to the length of an arc.

sea level. Thus, there is not enough room to keep the entire storage ring underground, and a hill is needed. For large L_S, the height of the hill increases linearly with L_S, and the volume of fill required for that hill increases as L_S^3. Thus, there is an economic incentive to keep the ring circumference small.

One can see from Eq. (7.1) that f_S depends only on the ratio L_S/L_A. That dependence is plotted in Fig. 7.2. One can conclude two things from Fig. 7.2. First, for a given f_S, the shorter the arc is, the shorter the straight section can be. Second, beyond $L_S/L_A \approx 2$, it takes a very large change in L_S/L_A to increase f_S by even a small amount.

We summarize in Table 7.1 the values of some parameters of the storage ring.

Table 7.1: Muon storage ring parameters.

Energy (GeV)	20
Circumference (m)	358.18
Normalized transverse acceptance (mm-rad)	30
Energy acceptance (%)	2.2
Arc	
Length (m)	53.09
No. cells per arc	10
Cell length (m)	5.3
Phase advance (deg)	60
Dipole length (m)	1.89
Dipole field (T)	6.93
Skew quadrupole length (m)	0.76
Skew quadrupole gradient (T/m)	35
$\beta_{\max}$ (m)	8.6
Production Straight	
Length (m)	126
$\beta_{\max}$ (m)	200

7.1.1 Design Choices for Optimizing Arcs

It is clear from Fig. 7.2 that it is beneficial to minimize the arc length. Whereas Study-I focused on a storage ring with an energy of 50 GeV, here we consider a 20 GeV storage ring, at least partly for this reason. (there are several other reasons, related to machine cost and the insensitivity of CP violation physics to the beam energy, that contributed to this decision as well.)

One way to decrease the arc length of the storage ring is to use high-field bending magnets. Nb_3Sn superconductor can achieve very high fields, but due to its brittle nature, it is difficult to wind a $\cos\theta$ magnet using it. However, winding a pancake-type coil (Fig. 7.3) is not a problem with Nb_3Sn. For this reason, we have chosen to use Nb_3Sn pancake coil magnets in the arcs.

Another consideration for the arc magnet design is the decay of the muons. The superconducting magnet coils must be shielded from the decay electrons, which remain primarily in the horizontal plane of the beam. For a $\cos\theta$ magnet, this would be accomplished by putting a tungsten shield inside the magnet, increasing the required magnet aperture. The pancake coil configuration has the advantage that it can be designed with

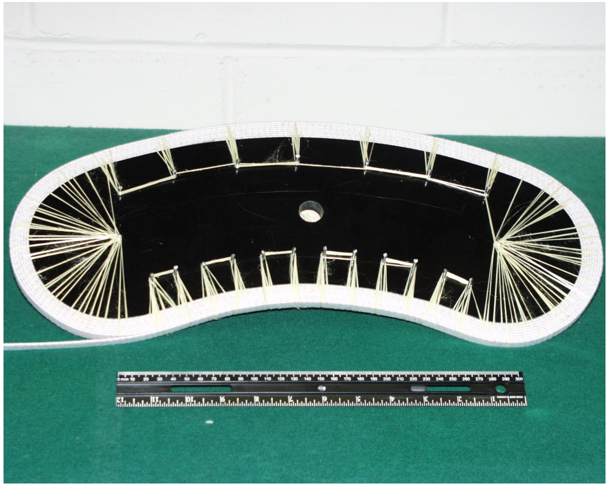

Figure 7.3: Photograph of a pancake coil. This also illustrates a method to provide sagitta and reverse bend using Kevlar strings.

no coil in the midplane, eliminating the necessity for coil shielding.

One of the primary obstacles to reducing the arc length is the required spacing between magnets. As demonstrated in Fig. 7.4, if one simply scales the magnets from the 50 GeV storage ring in Study-I by 40%, the arc is in fact longer than 40% of the 50 GeV arc length, since the inter-magnet spacing must remain roughly the same. Indeed, it might be necessary to increase the inter-magnet spacing due to larger beam sizes, and thus larger magnet aperture, at the lower energy. Some gain can be achieved by eliminating some of the gaps by using combined-function magnets. Ideally, it would be best to eliminate the inter-magnet gaps altogether. The pancake coil design achieves this by using coil configurations where one coil (of two) continues through each transition between magnets.

7.1.2 Choice of Straight Length

Once the length of the arc is minimized, the length of the straight determines the number of neutrinos decaying in the direction of the detector. For this study, there is an added consideration: a hill must be built to accommodate the storage ring. Thus, we chose a goal of $f_S = 0.35$. In the design a straight length of $L_S = 126$ m was chosen along with an arc length of $L_A = 53.09$ m. This requires a hill with a height of 43 m and having 6.4×10^5 m^3 of fill.

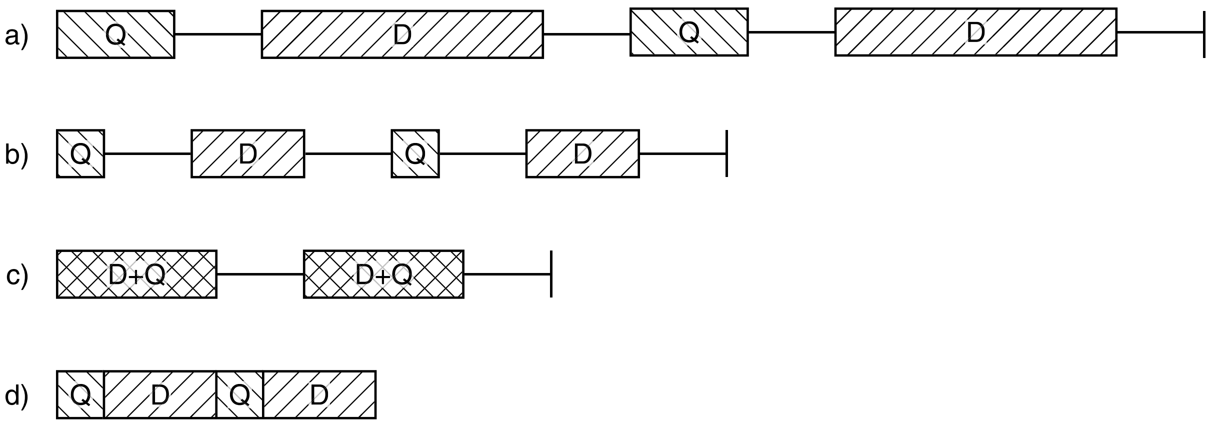

Figure 7.4: Demonstration of the effect of inter-magnet spacing on arc length. The top drawing (a) is the arc cell for a 50 GeV lattice from the Fermilab design study. Scaling that lattice to 20 GeV, but leaving the inter-magnet spacing fixed, does not reduce the cell length to 40% of the original length (b). In (c), we see that using combined-function instead of separated-function magnets can reduce the cell length substantially. In (d), we show what happens if the inter-magnet spacing is completely eliminated.

Table 7.2: Input beam parameters.

Energy (GeV)	20
Normalized transverse acceptance (mm-rad)	30
Ratio of full width to rms width	2.4
Relative momentum spread (full) (%)	$\pm$1.9

7.1.3 Lattice Parameters

The input beam parameters are given in Table 7.2. There two primary issues related to these parameters that need to be dealt with. First, since the magnets operate at very high field, their aperture should be kept small to minimize peak fields and maintain field uniformity. Second, to give a reasonable uncertainty at the detector, the angular spread in the beam must be kept well below the angular spread in the neutrinos due to decays. Specifically, we require that $\sigma_\theta < 0.1/\gamma = 0.53$ mrad.

The first constraint requires that, in the arcs, the beta functions must be kept small. The second constraint requires that, in the production straight, the Twiss parameter gamma ($\gamma = (1 + \alpha^2)/\beta$) be small. Note that, in the production straight, not only does

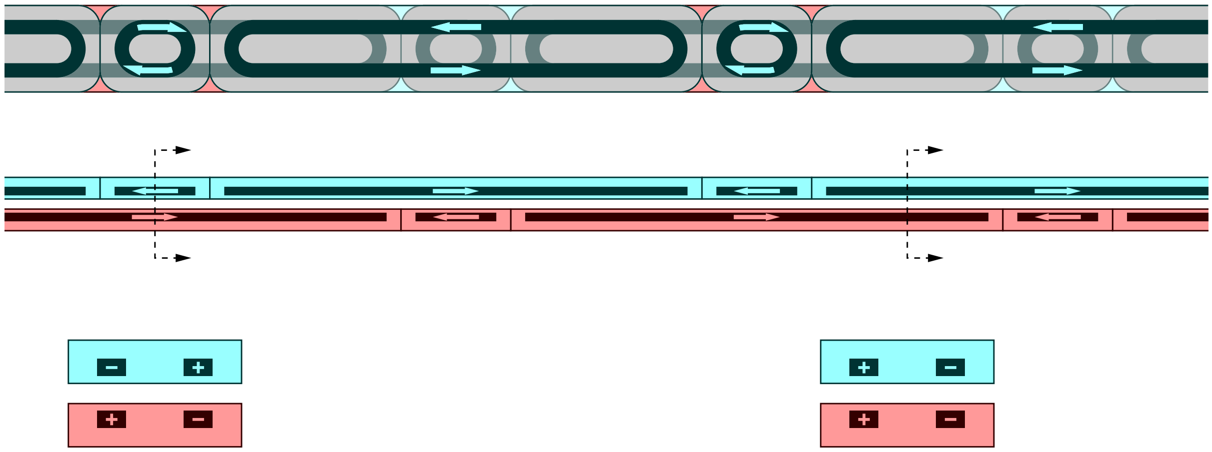

Figure 7.5: Arc magnet layout. Above is a top view of the arc (straightened out); in the middle is a side view. At the bottom are two cross sections of the magnet lattice, at the points indicated in the side view. Coil current directions are indicated, with + being out of the page.

β need to be large, but α must be small. The above requirement on σ_θ means that $\gamma < 0.011\ \mathrm{m}^{-1}$ in the production straight. It will turn out that this constraint is not met for that lattice as is; later in this chapter we describe changes that must be made to achieve this. The reason for the difficulty is that, since β goes from being very small in the arcs to being very large in the production straight, there is necessarily an intermediate region which has moderate β and large α.

7.2 The Lattice

7.2.1 Effect of Magnet Choice on Lattice Design

Figure 7.5 shows a diagram of the arc cell layout. The arcs will consist of two sequences of racetrack coils, one placed above the other, but with the magnets overlapping. The direction of the current alternates from one magnet in the sequence to the next. There are two types of magnetic fields in this lattice, illustrated in the two cross sections in Fig. 7.5: dipole fields (the right cross section), and *skew* quadrupole fields (the left cross section).

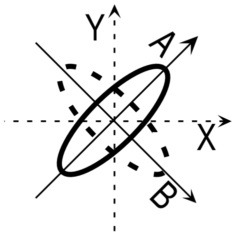

Figure 7.6: Eigenplanes for the pure skew decoupled lattice used for this storage ring. The eigenplanes are rotated 45° with respect to the horizontal.

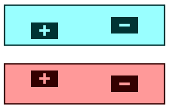

Figure 7.7: Raising part of each coil to generate an upright quadrupole component in the bend.

Note that this lattice gives rise to skew quadrupole fields rather than upright quadrupole fields. A single coil on top covers one quadrupole and both bends in any given cell. That coil has no ends (and therefore no wasted space) at the ends of the skew quadrupole field in the section that it overlaps. The lower coils at that same skew-quadrupole region do in fact have ends. But, from an efficiency standpoint, those ends are not "wasted": they merely create a transition from a bending region to a skew quadrupole region. In essence, the transition is really a combined-function section, rather than an empty section.

Thus, the lattice is completely skew, with the eigenplanes shown in Fig. 7.6. However, since the dipoles are focusing in the horizontal plane, which is not one of the eigenplanes, they introduce coupling between the two skew planes. To avoid this we create an upright quadrupole with

$$\frac{dB_y}{dx} = -\frac{eB_y^2}{2p}, \tag{7.2}$$

where p is the reference momentum. Then, the focusing is the same in the horizontal and vertical planes, and therefore cylindrically symmetric. Cylindrically symmetric focusing does not produce coupling between the skew planes. This upright quadrupole is created by raising or lowering one side of each coil pack within the bending region, as shown in Fig. 7.7. The amount that the coils need to be raised or lowered is actually very small, about 1 mm. Generating this amount of vertical shift in the coils will be straightforward.

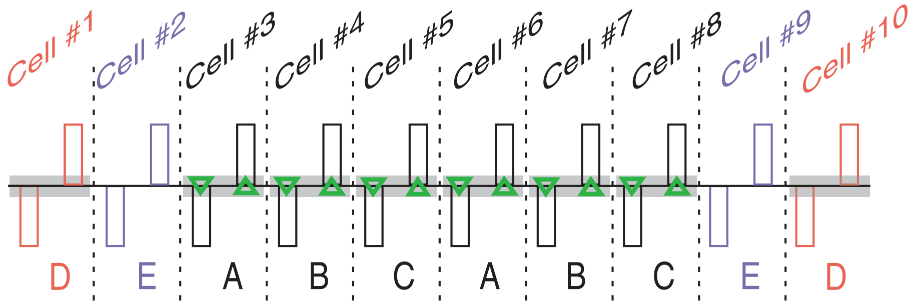

Figure 7.8: Layout of the arc. The "E" cells have no dipoles. The linear magnets in the central six cells are identical, and are the same as those in the "D" cells. The triangles indicate the placement of sextupoles.

7.2.2 Lattice Design

Figure 7.8 shows the layout of an arc. The phase advance per cell is chosen to be 60°. This gives reasonable values for the cell length, the beta functions, and the dispersion. It also gives a reduced swing in the dispersion functions, leading to a lower vertical dispersion.

To accomplish dispersion suppression, we employ the pattern of cells shown in Fig. 7.8. There are six central cells, surrounded by two cells having no bend, and on the ends there are two cells that are identical to the central cells. For a 60° phase advance per cell, this gives dispersion suppression and matches the dispersion in the central cells automatically. Arc cells with no dipoles will contain warm quadrupoles. This permits the use of collimation in those cells, and confines the decay shower to a region with warm magnets.

As discussed above, the production straight has large beta functions, so as to minimize the angular spread of the neutrinos decaying toward the detector. The other straight, where we inject, has beta functions roughly twice those in the arcs. That section will also be used to adjust the overall ring tunes.

Table 7.3 gives the parameters for the magnets used in the storage ring.

Lattice functions for the 20 GeV muon storage ring using compact skew combined function arc cells are shown in Figs. 7.9 and 7.10. Here the beta functions, (β_A, β_B), are given for the 45°-rotated betatron eigenplanes (A,B) shown in Fig. 7.6, but the eigenplane dispersion functions (η_A, η_B) are projected to dispersion in the normal horizontal-vertical coordinate system according to the relationships, $\eta_x = \dfrac{\eta_A + \eta_B}{\sqrt{2}}$ and $\eta_y = \dfrac{\eta_A - \eta_B}{\sqrt{2}}$.

By design, the dispersions in the A and B eigenplanes are nearly equal, so the effective vertical dispersion is much smaller than the horizontal dispersion. With this skew lattice,

Table 7.3: Magnet parameters. Only four of the utility straight quadrupoles require the strength shown; others are as low as 6.7 T/m. The arc dipole and SC quadrupole parameters are really idealized parameters for a lattice made from standard magnets; the actual fields are provided by overlapping coils as described in the text.

	Number	Length (m)	Field (T)/ Gradient (T/m)	R_{pole} (mm)	B_{pole} (T)
Arc dipole	32	1.89	6.93		
Arc SC quadrupole	32	0.76	35		
Arc NC quadrupole	16	0.65	27.2	47	1.28
Production straight quadrupole	2	1.85	5.0	175	0.87
	2	5	3.6	200	0.72
	2	2.25	6.4	125	0.8
	2	0.76	23.2	50	1.16
Utility straight quadrupole	28	1.9	11.6	70	0.81

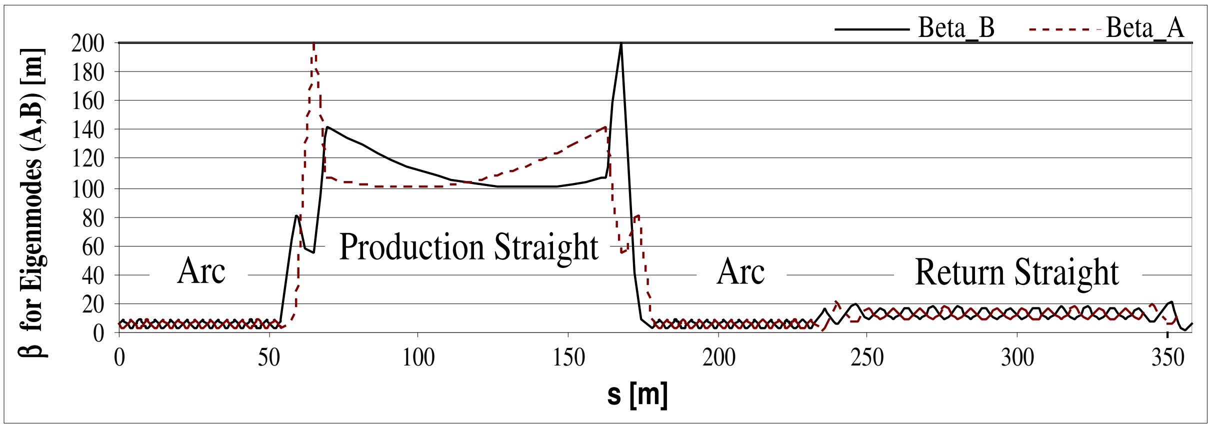

Figure 7.9: Beta functions for the storage ring, in the 45°-rotated eigenplanes.

the horizontal dispersion is nearly constant across the arc, whereas the vertical dispersion oscillates with small amplitude about zero. The arc cells without bending match the dispersion to zero for both eigenplanes in the straight sections.

The lattice shown in Fig. 7.9 has a ratio between the lengths of arcs and straight sections such that the geometric decay ratio, f_s, is just over 35%. The central 93 m of the production straight has a Twiss gamma function of 0.01 m^{-1}, which meets the requirements for the angular divergence described in Sec. 7.1.3. Within that central

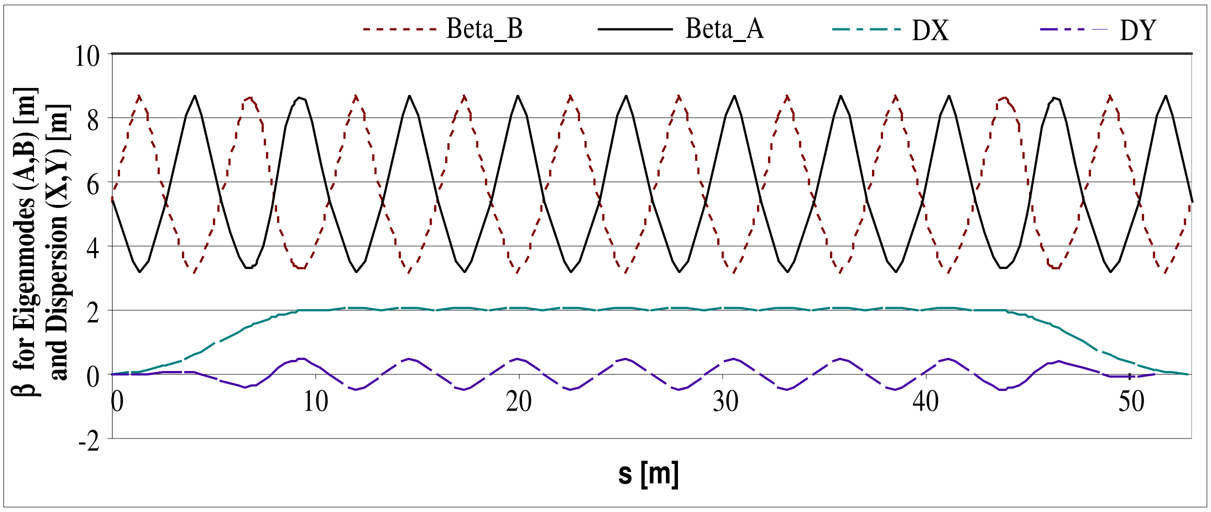

Figure 7.10: Beta functions and the dispersion function for an arc of the storage ring. The beta functions are in the 45°-rotated eigenplanes, while the dispersion functions are projected into the standard horizontal and vertical planes.

section, there are no quadrupoles; this appears to be the most straightforward way to minimize α, and therefore γ, in that section. Beta functions in the return straight are intermediate in magnitude between the values in the arcs and the production straight in order to facilitate injection.

7.2.3 Chromatic Correction Sextupoles

For chromatic correction, a skew sextupole has been placed at each skew quadrupole in the central section of the arcs (see Fig. 7.8). A skew sextupole, like the dipole and skew quadrupole magnets, requires no coil in the midplane of the magnet. These sextupoles must be very strong, since they correct not only the chromaticity generated in the arcs, but also the chromaticity generated in the straights. Since the straights are significantly longer than the arcs, the sextupoles require high strengths.

The sextupoles are divided into A, B, and C families, as indicated in Fig. 7.8. All sextupoles in a given family have identical strengths (this is true separately for the sextupoles at focusing and defocusing quadrupoles). Due to the 60° phase advance per cell, there is an automatic first-order cancellation between the nonlinear terms from these sextupoles, as shown in Fig. 7.11. The families can be chosen to give a second-order cancellation of

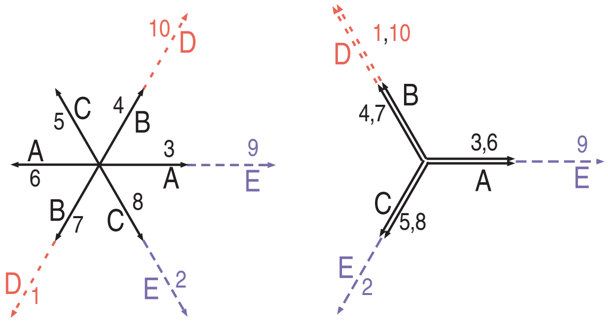

Figure 7.11: Diagram showing cancellation of the sextupole nonlinearities due to the choice of families and the 60° phase advance per cell. The left diagram shows the first-order cancellation, the right diagram shows that, given the right relationship between the A, B, and C family strengths, there will be a second-order cancellation as well. Note that putting sextupoles in the D or E regions would not give a similar cancellation.

the nonlinearities as well, as illustrated in the second part of Fig. 7.11.

The required sextupole strength to achieve zero chromaticity is $S = B'' = 78$ T/m^2. This sextupole strength could be reduced by putting sextupoles in the remaining arc cells, but there is no simple cancellation scheme for the nonlinearities in that case, as illustrated in Fig. 7.11.

With one degree of freedom in our three families needed to correct the chromaticity, and another needed to correct the second-order nonlinearities, there is still one remaining degree of freedom in each plane. We use this to minimize the nonlinear momentum dispersion in the production straight. Writing the transverse momentum of the closed orbit in the center of the production straight as a function of $\delta = \delta p/p$) as $p_{x0}(\delta) = D_{p1}\delta + D_{p2}\delta^2 + \cdots$, the sextupoles could be used to eliminate D_{p2} (note that D_{p1} is already eliminated in our dispersion suppression scheme).

7.2.4 Coil End Effects

There are two end effects with which we will be primarily concerned. The first is a solenoid generated by the ends of the coils. The reason for the solenoid field is seen in Fig. 7.12. Where one coil ends, there is a transverse current, which leads to a longitudinal field. (In standard magnet designs, the symmetry of the return coils eliminates this solenoid field. Since our design lacks this symmetry, there is a net solenoid field.)

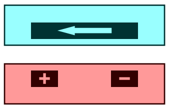

Figure 7.12: Arc magnet cross section at the skew quadrupole end of the upper coil pack.

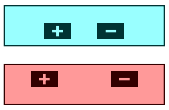

Figure 7.13: Cross-section as one approaches the end of the top coil, showing the coils on top moving closer to each other. This has a nonzero sextupole field.

It is important to note that this solenoidal field will affect the linear lattice; it is not just a nonlinear effect. There are two effects: the first is a rotation, the other is a focusing effect. The focusing can just be taken into account in the linear lattice, but the rotation is more difficult since it can couple the eigenplanes together. The coupling can be removed from the lattice, if necessary, by rotating the skew quadrupoles by the amount that each end rotates. One quadrupole sign is rotated in one direction; the other is rotated in the opposite direction. The amount of rotation can be calculated precisely knowing only the current in the coil and the height of the coil above the axis. The coils need to be displaced by only about 1 mm to put this rotation in, which is comparable to the coil displacement we already must achieve to put the upright quadrupole field into the bending sections.

The second end effect we consider is a sextupole contribution. This is not the sextupole-order contribution caused by the longitudinal derivative of the dipole field. Rather, it comes from the fact that the coil symmetry changes when the coil starts to cross at the end. Consider the dipole cross section in Fig. 7.5. That cross section will have a nonzero sextupole field unless the coils are placed in precisely the correct places. (For a single wire coil, that would be along a line through the center, 30° from horizontal.) The main body of the magnet is designed with the coils placed to eliminate that sextupole contribution. However, when the coils are moved out of the position that zeros the sextupole contribution so that they can cross over, as depicted in Fig. 7.13, there will be a net sextupole field at that point. This sextupole field can be hundreds of times as large as the sextupole component in the body of a realistic magnet.

Uncorrected, this sextupole field would decrease the dynamic aperture of the ring.

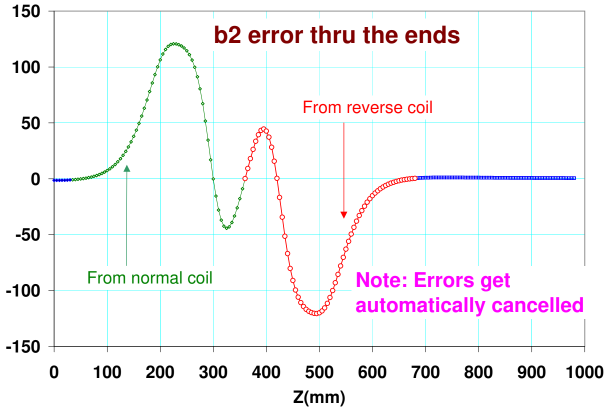

Figure 7.14: Longitudinal variation in the sextupole field at the transition from the dipole to the skew quadrupole region.

However, immediately adjacent to the end that generates this sextupole is another coil end that generates an opposite sextupole. As shown in Fig 7.14, the integrated sextupole is zero over a very short distance (a few tens of cm), and should not be a problem for beam dynamics.

7.2.5 Correction and Tuning

In principle, since the short coils in the skew quadrupole regions can be powered separately from the longer coils, it is possible to perform both dipole and quadrupole corrections by varying their current. To create a "pure" correction requires more than one magnet working in concert, since one coil does not produce a pure dipole or a pure skew quadrupole at a given point.

Alternatively, an additional coil could be added opposite the short coil to allow pure dipole or pure skew quadrupole corrections at a given point. The coil could be either superconducting or normal conducting, since it need not generate large fields.

To adjust the overall tune of the ring, the quadrupoles in the utility straight will be used.

7.2.6 Tracking

Tracking studies were performed on a single arc cell using COSY INFINITY [1]. A more detailed analysis is given in [2]. The arc cell used is slightly different from the one described earlier in this chapter. A diagram of the cell used in the tracking is shown in

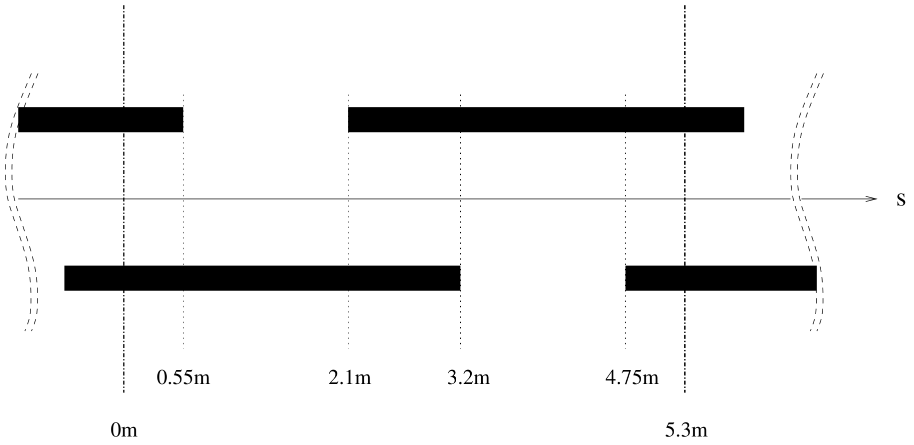

Figure 7.15: Arc coil configuration used for tracking.

Fig. 7.15. Note that the short coils with a reversed current direction are missing. Instead of having a pure skew quadrupole section, there is a combined-function section which is part dipole and part skew sextupole. The phase advance in this cell is 60°, just as in the actual lattice. We expect the results from tracking this cell to be similar to what we find from tracking the actual lattice, since the only real difference between the two is a slight redistribution of the linear components. Table 7.4 lists the magnet parameters used in the COSY-INFINITY tracking. In the combined-function areas, there are regions of overlapping bend, upright quadrupole, skew quadrupole, and skew sextupole (these are the regions with only a single coil, labeled as (b)/(b') and (e)/(e') in Table 7.4). To model this properly in COSY INFINITY, these sections are divided into 10 subsections of length $\Delta L = 0.155$ m, each of which consists of a bend/upright-quadrupole section of length ΔL, a negative drift of length $-\Delta L$, and a skew-quadrupole/skew-sextupole section of length ΔL. The skew sextupole strength is chosen to be sufficient to precisely cancel the chromaticity. COSY INFINITY also uses the full kinematic Hamiltonian (the full square root, as opposed to simply $p_x^2/2 + p_y^2/2$) in its tracking.

Figure 7.16 shows tracking results for the arc cell as described above. The dynamic aperture for this idealized lattice is much larger than needed. Figure 7.17 demonstrates, that for amplitudes within the magnet aperture, the lattice is extremely linear and well decoupled.

The next step is to add end fields to these magnets. An Enge-function falloff model [3] was used to model these end fields. Fig. 7.18 shows the results. Note that there is now significant coupling between the planes. Linear coupling is, in principle, correctable as described earlier, but there is a nonlinear coupling that will inevitably be there, as is

Table 7.4: Optical description and parameters for the arc cell. $k_1 = (\partial B_y/\partial x)/(B\rho)$, $k_2 = (\partial^2 B_y/\partial x^2)/(B\rho)$, $(B\rho)$ for a 20 GeV muon is 67.064332 Tm, B_D is the dipole field strength, and B_Q and B_S are the quadrupole and sextupole field strength at the aperture, r = 6.5 cm, divided by 7.02296 T.

Section	Starting position (m)	Length (m)	Tilt angle (°)	Deflection (B_D)	k_1 (m^{-2}) (B_Q)	k_2 (m^{-3}) (B_S)
(a)	0.00	0.55	45	57.6 mrad (7.02296 T)	-0.00548 (-0.02389 T)	0
(b)	0.55	1.55	45	81.8 mrad (3.51148 T)	-0.00137 (-0.00597 T)	0
(b')			0	0 mrad	-0.30269 (-1.31950 T)	-0.01932 (-0.002737 T)
(c)	2.10	0.55	45	57.6 mrad (7.02296 T)	-0.00548 (-0.02389 T)	0
(d)	2.65	0.55	45	57.6 mrad (7.02296 T)	-0.00548 (-0.02389 T)	0
(e)	3.20	1.55	45	81.8 mrad (3.51148 T)	-0.00137 (-0.00597 T)	0
(e')			0	0 mrad	0.30269 (1.31950 T)	0.01317 (0.001866 T)
(f)	4.75	0.55	45	57.6 mrad (7.02296 T)	-0.00548 (-0.02389 T)	0

the case in an upright lattice. The beam still is well within the dynamic aperture.

Next, multipole components in the body of the magnets are added. We started with multipole components from a 2D model of the region with both coils, which was computed using Poisson [4, 5] and Opera 2D. Independently, we performed a 3D field simulation using a bar magnet model, where the field can be expressed analytically [6, 7]. Two models were used: one where the bar magnets were infinite in extent, and a second where there were four magnets laid out as in Fig. 7.15. The bar magnet models were constructed to match as closely as possible the 2D model described above. The multipole fields in the real system were computed by starting with the values from the original 2D model, and scaling them by the ratio of the values in the second bar magnet model to those in the

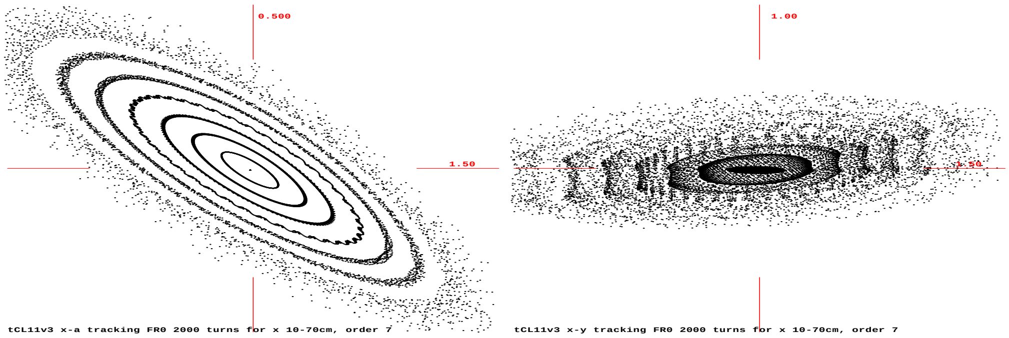

Figure 7.16: Tracking particles in the arc cell starting at $A = 10, ..., 70$ cm, showing A-p_A motion (left) and A-B motion (right). The scales of the pictures cover ±150 cm in the A plane, ±100 cm in the B plane, and ±0.5 in the p_A plane. Recall that A and B are the diagonal eigenplanes.

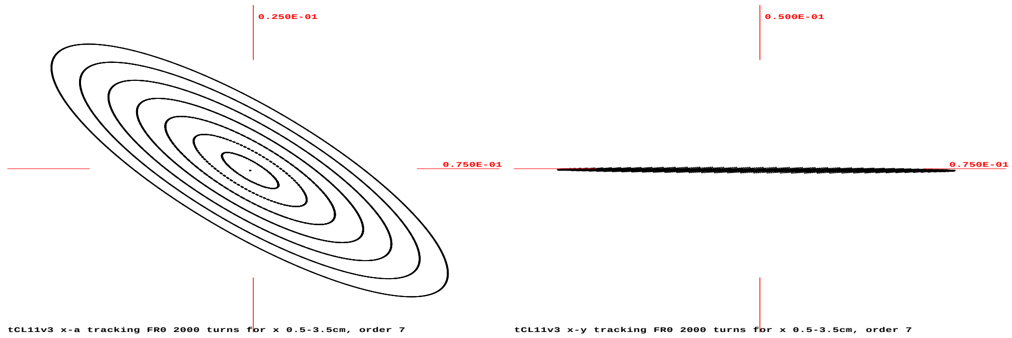

Figure 7.17: Tracking particles in the arc cell, starting at $x = 0.5, ..., 3.5$ cm, showing A-p_A motion (left) and A-B motion (right). The scales of the pictures cover ±7.5 cm in the A plane, ±5 cm in the B plane, and ±0.025 in the p_A plane.

first bar magnet model. The values of these computed multipole components are given in Table 7.5.

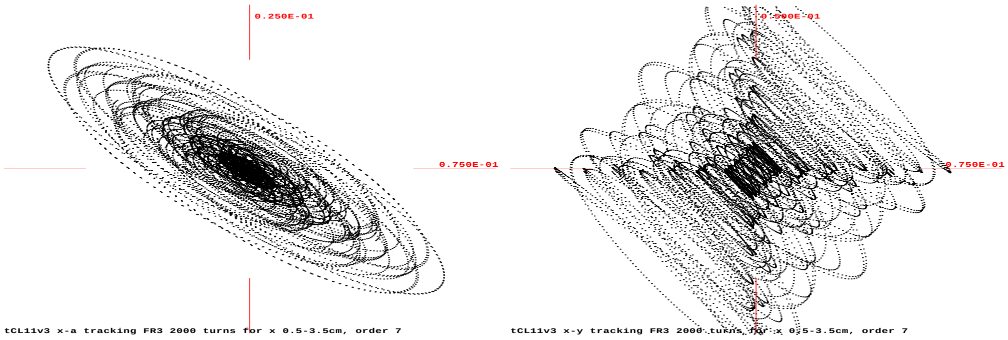

Figure 7.18: Tracking with end fields. Initial conditions and scales as in Fig. 7.17.

Table 7.5: Multipole components in the arc cell. The value given in the table is the maximum of the magnetic field in Tesla for that multipole component at a radius of 6.5 cm.

		Double Coil Region	Single Coil Region (b)	
		Normal	Normal	Skew
2	Sextupole	−0.721874127471	−0.360937063736	0
3	Octupole	0	0	0.100208577080
4	Decapole	−0.325677875510	−0.162838937755	0
5	Dodecapole	0	0	0.105845309541
6	14-pole	−0.048154527567	−0.024077263783	0
7	16-pole	0	0	−0.111799108203

Results of tracking with these multipole components are shown in Fig. 7.19. The dynamic aperture is unacceptably small. However, the multipole components shown in Table 7.5 are extremely large. As described later in Sec. 7.3.1, we believe we can make those multipole components much smaller. It was found that if the sextupole, skew octupole, and decapole components were reduced to 10% of the values in Table 7.5, the dynamic aperture was acceptable, even with fringe fields (see, Fig. 7.19).

The bar magnet model gives a solenoidal field as shown in Fig. 7.21. In that model, the solenoidal field doesn't become small anywhere. The solenoidal field was modeled using several short solenoids with a Gaussian-shaped profile. There are three effects of this

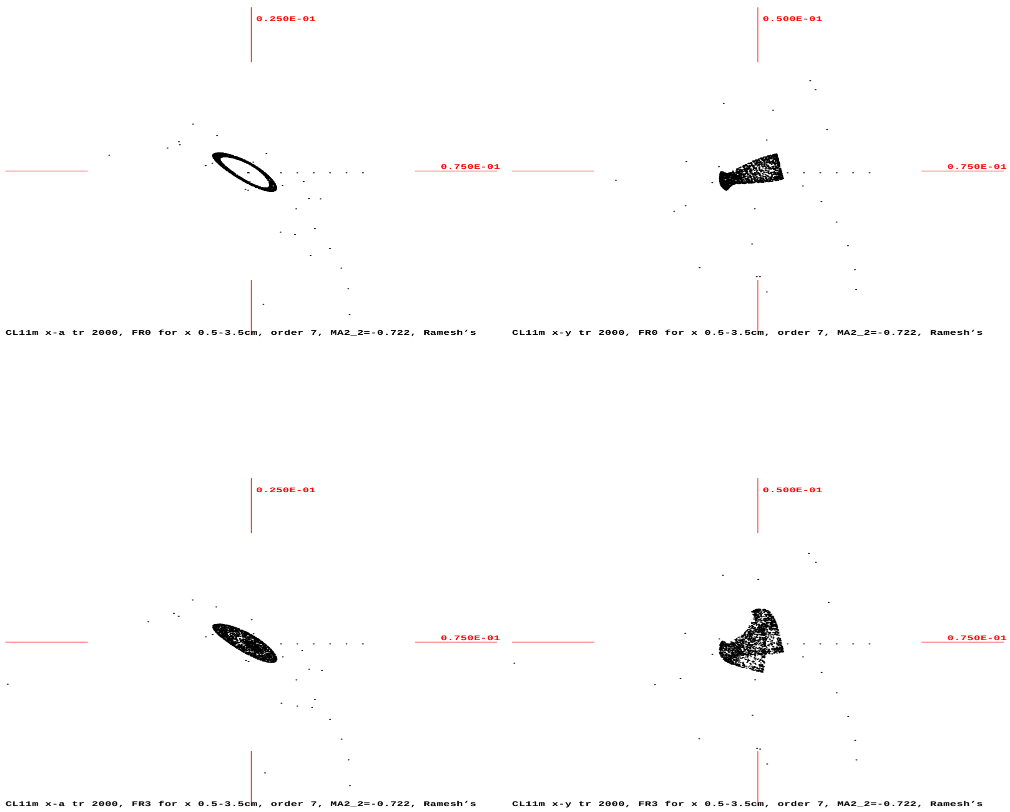

Figure 7.19: Tracking the arc cell with the additional multipole components in Table 7.5. Without (top two) and with (bottom two) fringe fields.

solenoidal field: linear coupling, linear focusing, and additional nonlinearities (from the longitudinal derivative of the field). Figure 7.22 shows the results of tracking with these solenoidal fields added. The solenoidal fields have a significant impact on the dynamic aperture of the machine. Further study is needed to examine to what extent this effect can be mitigated.

Table 7.6 indicates the strong effect of the solenoidal fields on the tune. In particular, the correction scheme described in Sec. 7.2.3 for canceling geometric nonlinearities will not work as well when the phase advance is not exactly 60°. The tune split comes from coupling from the solenoids, which can be corrected as described in Sec. 7.2.4. Thus, this

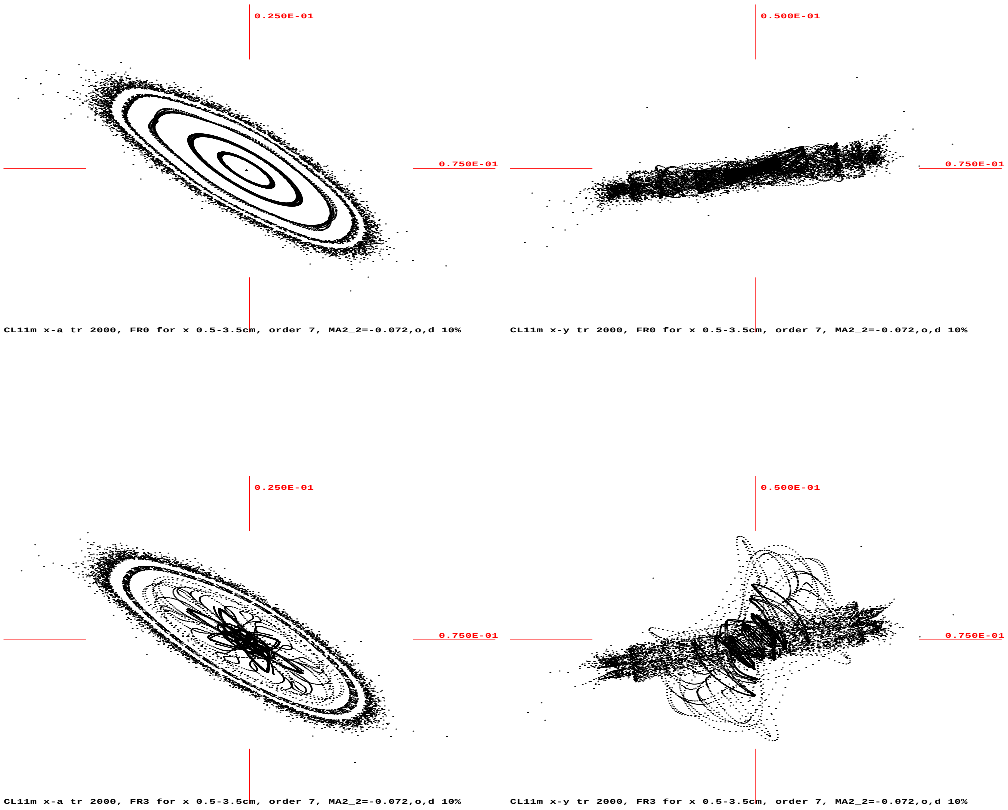

Figure 7.20: Tracking with the additional multipole components, with the normal sextupole, skew octupole and normal decapole strengths reduced to 10% of their initial values. Without/with (top/bottom) fringe fields.

decoupling, along with an adjustment of magnet strengths to compensate for the focusing effect from the solenoids, may restore the dynamic aperture.

7.3 Magnets

Figures 7.23 and 7.24 show diagrams of the arc magnets to be used in the storage ring. Each coil pack with its associated hardware will be built in the lab, and the individual cryostats will then be connected together appropriately in the tunnel.

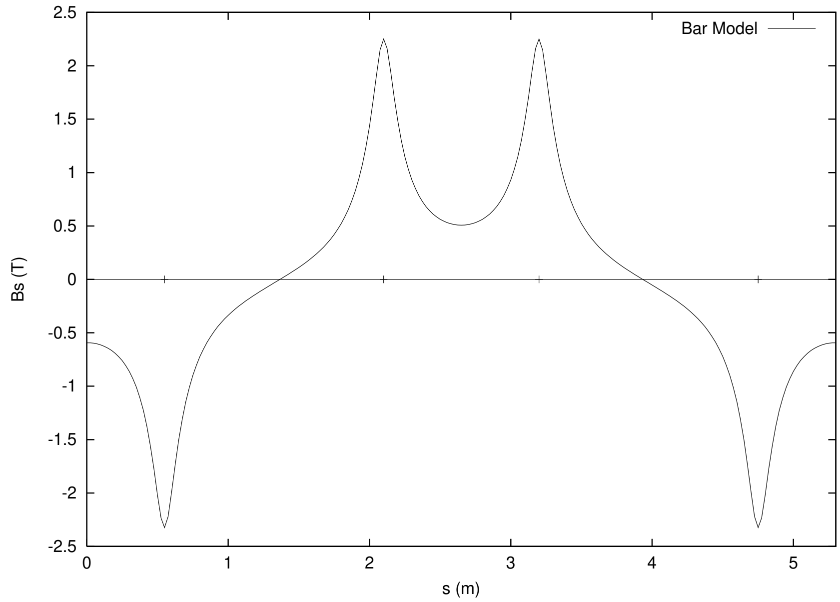

Figure 7.21: Field profile of solenoidal field component from the bar magnet model.

Table 7.6: Linear tunes in each study case for the two orthogonal planes.

	No fringe field effects	With fringe field effects
Initial approximation	0.166667 0.166667	N/A
Thick lens model	0.168422 0.168422	0.168040 0.166919
With solenoids	0.162584 0.174157	0.162190 0.172703

The vertical aperture of the dipole is 80 mm. The actual vertical separation between the upper and lower coils is 130 mm, to accommodate space taken by the support structure, heat shield, and cryostat. The aperture in the horizontal plane is much larger than in the vertical plane, since the space under the coils is also available due to the open-midplane design (see Figs. 7.23 and 7.24). The actual horizontal coil aperture, 240 mm, is dictated by the minimum bend radius at the end of 120 mm. Of course the beam cannot take advantage of the region under the coil, since the field quality is poor there. It is important to know the field in this region, however, since it is needed for tracking of

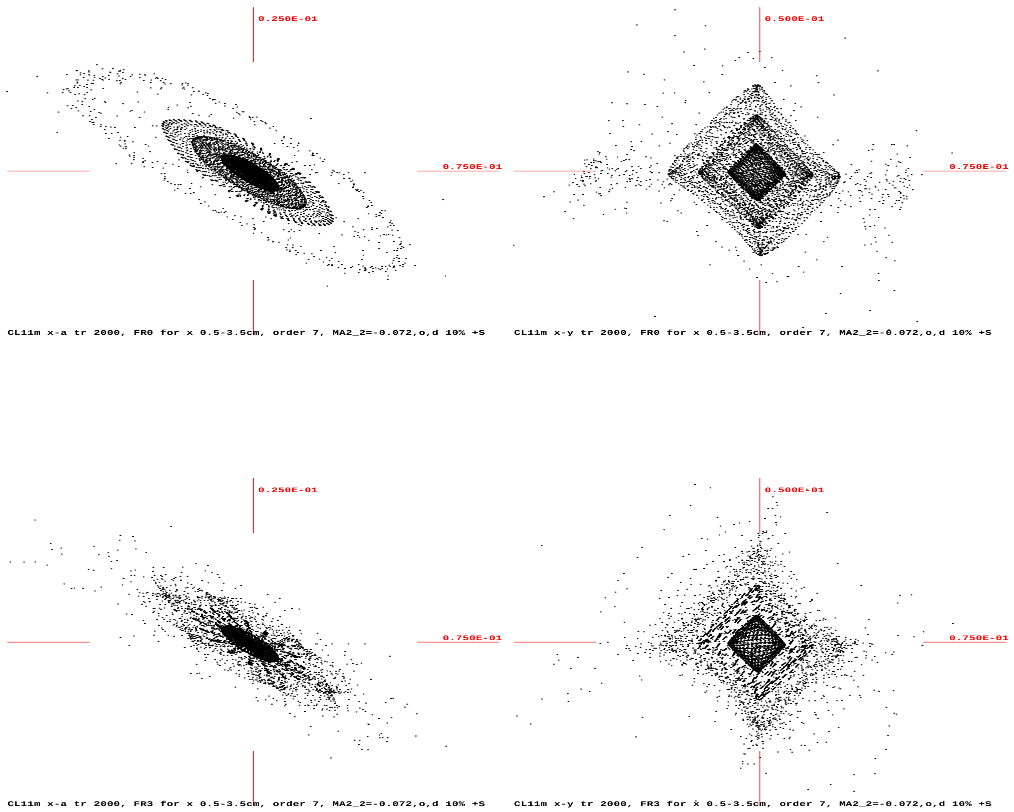

Figure 7.22: Adding the solenoid components to tracking with the additional multipole components, with the sextupole, octupole and decapole strengths 10% of the initial. Without/with (top/bottom) fringe fields.

decay electrons. The region of good field quality can be determined from the harmonics given in Section 7.3.1, or by a field profile within the beam tube.

The operating field of the dipole is 6.93 T, and the quench field is over 8 T. This gives an operating field margin of over 15%. As mentioned earlier, the maximum field on the conductor at quench excludes the possibility of using NbTi at 4.2 K operating temperature. The coils, therefore, are made of Nb_3Sn superconductor. Large bend radius in the ends allows the use of the "react and wind" technique in a pancake (racetrack) coil geometry. These pancake coils must have a large sagitta, due to the small size of the

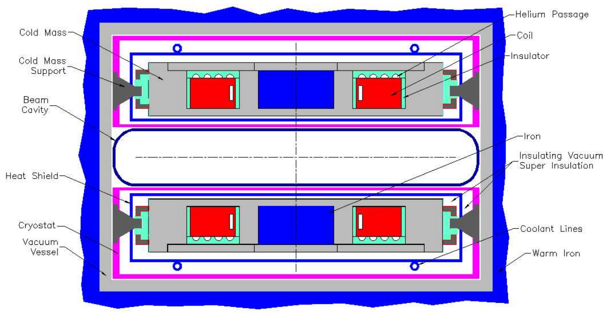

Figure 7.23: An engineering design of the magnet cross section.

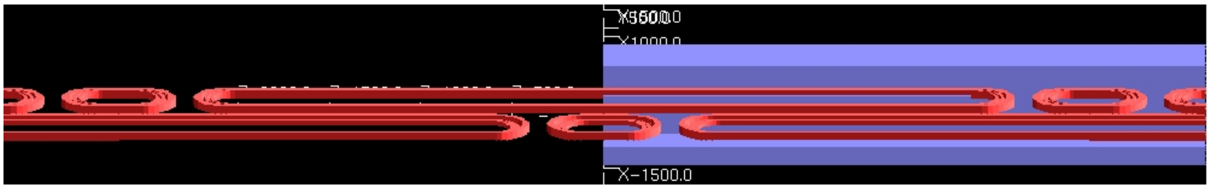

Figure 7.24: Three-dimensional view of the storage ring magnets. Iron (blue) is shown for only half the length.

ring. The reverse curvature in the coil is provided by Kevlar strings as shown in Fig. 7.3.

In this design, most of the energy from the decay particles is deposited in the warm-iron yoke. A warm-iron design allows the heat generated by decay particles to be removed efficiently. This means that a tungsten inner liner to protect the superconducting coils is not needed.

An engineering design of the magnet is shown in Fig. 7.23. The coils are located in a cryostat that is placed inside the warm iron yoke. Upper and lower coils will have separate cryostats that are placed in a common vacuum vessel. A major design consideration is to minimize the cryostat volume, in particular the vertical separation between the upper and lower coils.

The Lorentz forces are large, due to the high field and large aperture of this magnet. Horizontal forces are contained in a self-supporting collar structure. The vertical forces are transmitted to the cryostat with a coldmass support post, which in turn is connected to the iron and contains the force. The posts are designed to minimize the heat leak, which in the present design is comparable to the heat load from the decay products.

Table 7.7: Estimated field errors in the pure dipole magnet section at a 20 mm reference radius. $\langle b_n \rangle$ and $\langle a_n \rangle$ are the expected means of the normal and skew terms. $d(b_n)$ and $d(a_n)$ are systematic uncertainties arising from design and manufacturing errors, and $\sigma(b_n)$ and $\sigma(a_n)$ are the random uncertainties in those values. Note that $n = 2$ corresponds to the sextupole term.

n	$\langle b_n \rangle$	$d(b_n)$	$\sigma(b_n)$	$\langle a_n \rangle$	$d(a_n)$	$\sigma(a_n)$
1	0	0.2	0.2	0	1	2
2	−1	1	2	0	0.1	0.5
3	0	0.1	0.1	0	0.3	1
4	−1	1	1	0	0.05	0.2
5	0	0.03	0.03	0	0.1	0.5
6	−0.3	0.2	0.1	0	0.03	0.1
7	0	0.03	0.01	0	0.03	0.1
8	−0.1	0.1	0.02	0	0.03	0.1
9	0	0.03	0.01	0	0.03	0.1
10	−0.03	0.02	0.02	0	0.03	0.1

7.3.1 Magnetic Design

The magnet cross section is based on two double-layers of pancake coils (total four layers) with a curvature that approximately follows the beam trajectory. The total height of the coil pack is 40 mm (made with four stacks of 10-mm-wide cable), and the width is 60 mm. The cross section has spacers (equivalent to the wedges in a cosine theta design) to optimize the field quality and to reduce the peak field in the conductor. The peak field in the conductor is higher when the coil and magnet are made compact, in particular, when there is a large gap between the upper and lower coils at the midplane of the magnet. In the present design, the peak field is about 50% of the central field.

The expected skew and normal harmonics are given in Tables 7.7 and 7.8. These are not final values, as the magnetic design is not yet optimized. Table 7.7 gives the field errors in the dipole section, where the upper and lower coils have the same polarity, and Table 7.8 gives the field errors in the skew quadrupole section, where the upper and lower coils have opposite polarity. Field harmonics are expressed in terms of the normal and

Table 7.8: Field errors in the skew quadrupole magnet section at a 20 mm reference radius. See Table 7.7 for definitions.

n	$\langle b_n \rangle$	$d(b_n)$	$\sigma(b_n)$	$\langle a_n \rangle$	$d(a_n)$	$\sigma(a_n)$
1	0	0.2	0.2	0	1	2
2	-0.5	0.5	1	0	1	0.5
3	0	0.1	0.1	2	2	1
4	-0.5	0.5	0.5	0	0.05	0.2
5	0	0.03	0.03	1	1	2
6	0	0.2	0.1	0	0.03	0.1
7	0	0.03	0.01	0.5	0.5	0.3
8	0	0.1	0.05	0	0.03	0.1
9	0	0.03	0.01	0.1	0.03	0.1
10	0	0.02	0.01	0	0.03	0.1

skew harmonic coefficients, b_n and a_n, defined by

$$B_y + iB_x = 10^{-4} B_0 \sum_{n=0}^{\infty} (b_n + ia_n) \left(\frac{x + iy}{R} \right)^n , \tag{7.3}$$

where x and y are the horizontal and vertical coordinates, R is the reference radius, and B_0 is the field strength at $x = R$ and $y = 0$ in the dipole straight section. Field harmonics are normalized to this same B_0 in both sections. The reference radius R is 20 mm.

7.4 Beam Flux to Detector

There are really two quantities that we must deliver to the detector: a sufficient flux of neutrinos, and a sufficiently small uncertainty in that flux. It turns out that the latter may be the more difficult challenge. To understand this, consider Fig. 7.25. In that figure, we show event rate as a function of beam divergence (for a round beam), and fit a curve to that. This is based on the fact that, for an elliptical Gaussian beam divergence, with angular divergences of σ_p and σ_q in the two directions, and a Gaussian divergence of the neutrino decays with RMS divergence σ, the central flux is expected to be proportional to

$$\frac{1}{\sqrt{(1 + \sigma_p^2/\sigma^2)(1 + \sigma_q^2/\sigma^2)}} . \tag{7.4}$$

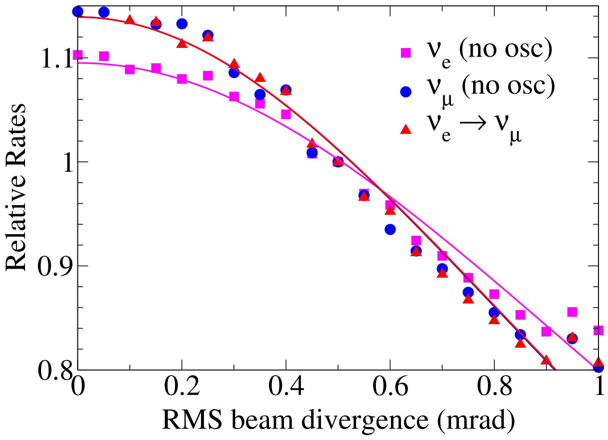

Figure 7.25: Relative event rate at the detector for a 30 GeV muon beam as a function of the rms beam angular divergence, with data taken from [8]. Curves are fit to this data with the functional form $A/(1+\sigma_\theta^2/\sigma^2)$, where σ_θ is the beam divergence, and σ and A are fit parameters. This form is the central flux of two overlapping Gaussians, one with divergence σ_0 (the beam) and the other with divergence σ (the decay divergence). The fit σ_0 values are 1.64 mrad (ν_e) and 1.41 mrad (ν_μ and $\nu_e \to \nu_\mu$).

While the basis for this model is not particularly accurate, it nonetheless gives a reasonably accurate representation of the simulated data when you fit to σ. Based on the fit to the data in Fig. 7.25, we take $\sigma = 0.42/\gamma$.

From this curve, one can understand why a larger divergence beam contributes more to the uncertainty: the uncertainty comes from the uncertainty in the angular spread times the slope of that curve. When one has a larger divergence, the curve has a larger slope. Another way to view this is that if the angular spread in the beam is much smaller than the angular divergence from the decays, the uncertainty in that angular spread has little effect on the total angular spread in the beam. Using this model, we can plot the flux and the uncertainty in that flux relative to a beam with zero angular spread. This is shown in Fig. 7.26. The resulting relative flux is 0.759 ± 0.014. Thus, despite the fact that the flux uncertainty from the middle of the straight section is almost exactly 1% (add the two planes in quadrature), the ends of the production straight contribute disproportionately to the uncertainty, despite their relatively small contributions to the total flux. Also, note the reduced flux: instead of having 35% of the muons decaying in a very low divergence beam toward the detector, we have only 27% of the muons decaying

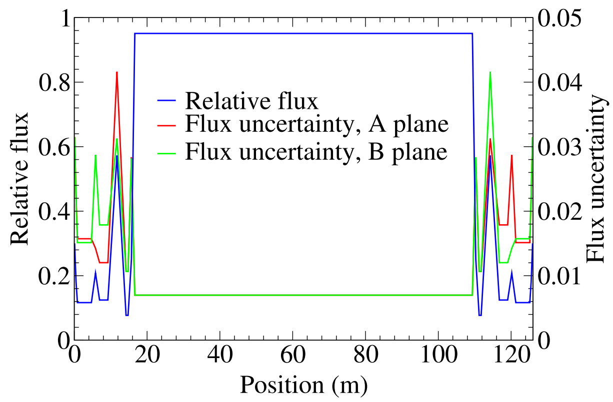

Figure 7.26: Flux at the detector, and the uncertainty in that flux, as a function of position in the production straight. A relative uncertainty in the angular divergence of 15% in each plane is assumed and, within a given plane, those uncertainties are assumed to be completely correlated. The correlation assumption is correct for the contribution to the uncertainty from the emittance uncertainty, but only partially correct for the contribution from the uncertainty in the lattice functions (the uncertainties must be propagated properly).

from the low divergence portion of the straight section.

It is clearly important to eliminate this uncertainty from the ends of the production straight. These ends are a matching section from the relatively low beta functions in the arcs to the high beta function in the straight. Thus, they will necessarily have a large angular divergence. One workaround is to point the matching sections in a different direction from that of the detector by bending slightly less than 180° in the arcs, and inserting a bend just before the "good" section of the production straight. One drawback to this is that the production straight becomes shortened. However, since the ends contribute relatively little to the total flux, not much is lost: whereas originally the relative flux was 0.759 ± 0.014, the relative flux would become 0.700 ± 0.007 after the workaround.

The required bending angle has been estimated to be 29 mrad. This calculation assumed that the ends produced a flat beam with an angular spread in the wide dimension equal to the largest angular spread anywhere in the end, and required that this beam contribute less than 0.1% to the total flux.

Table 7.9: Required precision for muon beam measurements [8].

momentum	δp_μ	$\leq$	0.3%
momentum spread	$\Delta\sigma_p/\sigma_p$	$<$	0.17
divergence	σ_θ	$\leq$	$0.1/\gamma$
	$\delta\sigma_\theta/\sigma_\theta$	$\leq$	0.2
polarization	δP_μ	$<$	0.01
direction	$\delta\theta_\mu$	$<$	$0.6\ \sigma_\theta$

7.5 Instrumentation

The storage ring presents some new beam instrumentation problems. There are of course the usual measurements of emittance, divergence, closed orbit, injection, extraction, beam loss and beam energy. However, since we are interested in the properties of the neutrino beam produced by the muon beam, it is helpful to have additional information. The precision with which the parameters of the muon beam must be known to achieve sufficient precision in the neutrino beam flux have been determined by Geer [8], and these are listed in Table 7.9. As indicated in this table, for instance, the polarization of the muon beam should be measured, and precision measurements of the beam direction in the straight section would be useful. The majority of instrumentation for the muon beam in the storage ring should utilize proven technology. The primary difficulty is that precision measurements are complicated by the presence of decay electrons in the beam, since electrons can cause showers.

The fraction of primary decay electrons in the beam is $L/\gamma\tau c$, where L is a path length in the storage ring, and $\gamma\tau c \sim 125$ km is the decay length at 20 GeV. In bending magnets, these electrons would be swept out within a few meters of their creation, so the electron contribution would be negligible. Quadrupoles produce less efficient sweeping. The fraction of muons that will decay in the 126 m straight sections, however, is ~ 0.001, and the electron/muon ratio at the downstream end of the straight will be $\sim 0.001F_s$, where F_s is a factor that depends on the probability of electrons showering and being swept from the vacuum pipe. These backgrounds are relatively low, but they may not be insignificant. Since estimates of the electron background are difficult, it may be desirable to have precision measurements external to the ring for determining the neutrino beam direction, profile and divergence.

We anticipate that the 6D "pencil" beams used to tune up the accelerator will also be useful in tuning up and operating the storage ring.

Semertzidis and Morse [9] have looked at using the $g-2$ frequency of the muons to determine the muon beam energy. They consider measurement using the very substantial signal from synchrotron radiation from decay electrons. Synchrotron radiation is non-linear in energy, which amplifies the oscillations. The beam momentum spread is also measurable using $g-2$, since the beam will be dephased by the spread in γ.

The beam size and divergence in the quadrupole-free decay straight section of length, $2L$, can be measured by comparing beam profile measurements at the ends, σ_e, and middle, σ_m, of the straight section. We assume that $\alpha = 0$ in the center of the straight section. The beam divergence is $\sigma_\theta = \sqrt{\sigma_e^2 - \sigma_m^2}/L$, and the beam emittance is $\epsilon_\perp = \sigma_m \sigma_\theta$. Since there will be no focusing in this part of the straight section, it should be possible to perform a Monte Carlo calculation and subtract the contributions from any decay electrons. The beam size can be measured using visible transition radiation from foils inserted in the beam, or a variety of other fast detectors.

In order to separate the contributions to the neutrino flux from decays in the upstream and downstream matching sections, bending magnets have been introduced. Using a near detector located a few hundred meters from the straight section, the precise profile of the contributions from the three sections to the downstream detectors can be evaluated with statistics 10^5 times larger than will be available in the far detector. We assume a dense, fine-grained detector consisting of tungsten or other heavy plates interspersed with hodoscopes or liquid-argon calorimeters. This could be located in a 52 m deep shaft, 200 m downstream of the decay straight, where the three "beams" would have a Gaussian radius of about 1 m. Rates could be high, on the order of 25 events/fill for a 1-m-thick detector ($\sim$0.5 kHz). With this rate, it may be possible to measure and subtract the background contribution of neutrinos produced in the upstream and downstream matching sections. Such a system needs further analysis, and is not considered part of the baseline design.

The polarization of the muons in the storage ring can be measured by looking at the momentum distribution of the decay electrons moving in the beam direction. Roughly 8×10^4 decays/m per turn will generate about 100 W/m of signal. These electrons are produced close to the beam as part of the fan of electrons that is swept inward by the bending magnets. The muon beam polarization is measured from the electron decay spectrum. A shower calorimeter, which can absorb the shower from forward-going electrons close to the beam, can be instrumented to look at the power deposition rate at the μs time scale. Detection with a calorimeter should be relatively linear with electron energy. The precision with which the Monte Carlo calculations could be done would be crucial, and this work is under way.

Bibliography

[1] M. Berz. COSY INFINITY Version 8 reference manual. Technical Report MSUCL-1088, National Superconducting Cyclotron Laboratory, Michigan State University, East Lansing, MI 48824, 1997. see also http://cosy.nscl.msu.edu.

[2] K. Makino, C.J. Johnstone, M. Berz and B. Erdelyi. Nonlinear effects in the 20-GeV Feasibility II muon storage ring. Technical Report MSUCL-1197, National Superconducting Cyclotron Laboratory, Michigan State University, East Lansing, MI 48824, 2001.

[3] M. Berz, B. Erdelyi, and K. Makino. Fringe field effects in small rings of large acceptance. *Physical Review ST-AB*, 3:124001, 2000.

[4] K. Halbach, "A Program for Inversion of System Analysis and Its Application to the Design of Magnets," Lawrence Livermore National Laboratory report UCRL-17436 (1967); CONF-670705-14

[5] J. H. Billen and L. M. Young, "POISSON/SUPERFISH on PC Compatibles," Proceedings of the 1993 Particle Accelerator Conference, Vol. 2 of 5, 790-792 (1993).

[6] M. Berz. *Modern Map Methods in Particle Beam Physics.* Academic Press, San Diego, 1999.

[7] M. M. Gordon and T. Taivassalo. The z^4 orbit code and the focusing bar fields used in beam extraction calculations for superconducting cyclotrons. *Nuclear Instruments and Methods*, 247:423, 1986.

[8] C. Crisan and S. Geer, *How well do we need to know the beam properties at a neutrino factory?* MUC Note 87 and FERMILAB-TM-2101, February 13, 2000.

[9] Y. Semertzdis and W. Morse, Unpublished Note, BNL (2000).

Chapter 8

High-Power RF systems: 201.25 and 402.5 MHz

8.1 Introduction to rf Systems

The rf systems for the buncher and the cooler are required to match the muon beam into the longitudinal acceptance of the cooling channel and to replenish the beam energy lost during ionization cooling. Since they must operate inside the strong solenoid fields they must be normal conducting. These systems require a large number of rf cavities operating at high gradient, and a large amount of pulsed rf power. They are technically challenging and expensive, and have therefore been the focus of continued development during Study-II. The cooling channel layout has continued to evolve since Study-I, with emphasis on integration of realistic components into the available space along with optimization of the channel performance. The buncher and cooling channel systems must accommodate liquid-hydrogen absorbers, high-gradient rf cavities, windows, tuners, superconducting solenoids, diagnostics, pumping, harmonic cavities and other equipment. The system must be designed in such a way as to allow assembly and access for maintenance. The buncher and cooling channel comprises a large number of modules (cells). The cell layouts are described in Section 8.4. Each module contains two or four 201.25 MHz closed-cell cavities and is powered by one or two high-power multibeam klystrons. The density of equipment in the building is therefore high and the systems must be carefully laid out to allow access for installation and maintenance. Following the cooling channel is a matching section containing rf and solenoids, but no absorbers.

The proposed buncher, cooling channel, and matching section is approximately 183 m long and requires 184 cavities and 84 klystrons at 201.25 MHz and an additional 6 cavities and 3 klystrons at 402.5 MHz. The total installed power is approximately 780 MW ($\approx$ 1.56 MW average), and the installed voltage is 1080 MV.

The cooling channel is followed by an acceleration section employing 299 two-cell superconducting rf cavities operating at 201.25 MHz. These structures are also challenging because of the high gradient and large physical size. Peak power requirements for the acceleration section are not as high as for the normal conducting rf sections, but the pulse length is much longer. Many superconducting cavities can be powered from a single klystron station. Several multi-cell rf cavities may share a common cryostat. The final energy at the end of the accelerating section is 20 GeV, compared with the 50 GeV of Study-I. This reduces the size and cost of the acceleration section significantly.

8.2 NCRF Specifications for Buncher and Cooling Channels

Table 8.1 summarizes the inventory of normal conducting rf cavities (NCRF). The cooling channel simulations were based upon ideal pillbox cavities with lengths determined by the space available in the chosen lattices (and zero space between cavities). The gradients and phases of these cavities were adjusted to optimize the cooling channel performance while keeping the gradients and rf power requirements within feasible limits. Table 8.2 shows the peak cavity power and klystron output power to meet these requirements, and the total power for each cavity type. Both tables also show how the required voltages are obtained using realistic re-entrant or "omega" shaped cavities with closed-off irises of finite thickness. The loss of active length in the realistic case is compensated by the greater efficiency of the rounded design. To be conservative, the iris diameter used for the omega cell was sufficient to accommodate any reasonable beryllium foil. In practice, the foils may be smaller and in any case will decrease in size towards the end of the cooling channel. Ideally, the cavity shape would be optimized for each foil size. This would maximize the efficiency and minimize the power cost. Note that the rf power requirements are dominated by the cooling sections (1,1)-(1,3) and (2,1)-(2,3), which have the largest number of cavities and the highest gradients.

8.3 RF Station Description

Each rf station consists of a modulator for two klystrons, a distribution system, and low-level rf and controls driving two or more cavities. The modulator must provide a flat top DC pulse of up to 125 μs with a recharge time of less than 20 ms. (This is equivalent to

Table 8.1: Parameters for the ideal (pillbox) and practical (omega) NCRF cavities. *Note: Kilpatrick number is about 15 MV/m at 201.25 MHz.

Ideal pillbox dimensions used in the simulations (see Chapter 5)						
Section	Radius (m)	Length (m)	Freq. (MHz)	No. of cavities	E^*_{pk} (MV/m)	V_{eff} (MV)
b1	0.570	0.373	201.25	4	6.40	2.07
b2	0.570	0.373	201.25	8	6.00	1.94
b3	0.570	0.373	201.25	8	8.00	2.59
(1,1)-(1,3)	0.570	0.466	201.25	68	15.48	5.76
(2,1)-(2,3)	0.570	0.559	201.25	74	16.72	6.71
match	0.570	0.559	201.25	22	16.72	6.71
b1 402.5 MHz	0.285	0.186	402.5	2	6.40	1.03
b2 402.5 MHz	0.285	0.186	402.5	4	8.00	1.29
Omega cavities						
Section	Radius (m)	Length (m)	Freq. (MHz)	No. of cavities	E^*_{pk} (MV/m)	V_{eff} (MV)
b1	0.607	0.405	201.25	4	7.41	2.07
b2	0.607	0.405	201.25	8	6.95	1.94
b3	0.607	0.405	201.25	8	9.27	2.59
(1,1)-(1,3)	0.607	0.405	201.25	68	20.62	5.76
(2,1)-(2,3)	0.615	0.483	201.25	74	23.06	6.71
match	0.615	0.483	201.25	22	23.06	6.71
b1 402.5 MHz	0.308	0.288	402.5	2	6.57	1.03
b2 402.5 MHz	0.308	0.288	402.5	4	8.21	1.29

a repetition rate of 50 Hz, but not every 50 Hz pulse is required. The output from the AGS appears as 6 pulses spaced at 20 ms followed by a 300 ms gap, with a repetition rate of 2.5 Hz.) The *average* duty factor is $\approx 1.9 \times 10^{-3}$.

Each rf station must provide approximately 10 MW of peak power to drive two cavities. The power source is a multi-beam klystron, which should give good reliability and a long operational lifetime.

Power distribution will be via high-power coaxial lines, with the power split between two or more cavities using appropriate delays to maintain the proper phase . The cavities will use coaxial feedthroughs and loop-type couplers. The high peak power requirements require careful design of the components, although the average power, of about 10 kW

Table 8.2: Voltage and power requirements for the NCRF cavities.
† Rs, calculated, $= V^2/P$, * Real cavity, Q_0 assumed 85% of theoretical;
** Klystron forward power for 3τ filling.

Section	$Veff$ (MV)	$Rs^{\dagger}$ ($M\Omega$)	$P_c{}^*$ (MW)	$P_{kly}{}^{**}$ (MW)	No. of cavities	P_{tot} (MW)	Sum (MW)
Ideal pillbox							
b1	2.07	8.899	0.567	0.628	4	2.51	
b2	1.94	8.899	0.499	0.552	8	4.42	
b3	2.59	8.899	0.886	0.982	8	7.85	
(1,1)-(1,3)	5.76	10.701	3.646	4.038	68	274.60	
(2,1)-(2,3)	6.71	11.428	4.635	5.134	74	379.91	
match	6.71	11.428	4.635	5.134	22	112.95	782.0
b1 402.5 MHz	1.03	6.275	0.200	0.222	2	0.444	
b2 402.5 MHz	1.29	6.275	0.313	0.347	4	1.387	1.8
Omega cavities							
b1	2.07	10.220	0.494	0.547	4	2.19	
b2	1.94	10.220	0.434	0.481	8	3.85	
b3	2.59	10.220	0.77	0.855	8	6.84	
(1,1)-(1,3)	5.76	10.220	3.818	4.228	68	287.54	
(2,1)-(2,3)	6.71	11.794	4.491	4.974	74	368.09	
match	6.71	11.794	4.491	4.974	22	109.43	778.0
b1 402.5 MHz	1.03	8.368	0.150	0.166	2	0.333	
b2 402.5 MHz	1.29	8.368	0.235	0.260	4	1.040	1.4

per coupler, is quite modest. Provision is made for adjusting the phase of individual cavities and for handling the reflected power during the initial part of the cavity fill time.

Each station includes a water distribution system and a rack of low-level rf hardware and controls.

8.3.1 Power Source and Equipment

The bunching, ionization cooling channel, and the match to the acceleration system requires high peak rf power sources at 201.25 MHz and 402.5 MHz to efficiently bunch, cool the muon beam and prepare it for acceleration. Table 8.2 lists the peak rf power requirements for each section. There are 184 201.25-MHz cavities in the channel that require 782 MW of rf power for a pulse length of 125 μs at 15 Hz (average) and six

402.5 MHz cavities that require 1.8 MW at 15 Hz.

An examination of the requirements shows that an rf source of about 6 or 12 MW would be ideal for the 201.25 MHz cavities and a source of 500 to 750 kW for the 402.5 MHz cavities. The rf power for the 201.25 MHz cavities could be supplied by existing gridded tubes at about the 5 MW level. However, the low gain and lifetime of gridded tubes make the R&D effort to develop an alternative most attractive. Preliminary calculations at SLAC [1] have shown that a 201.25 MHz klystron could be built with a reasonable amount of R&D. The gain, efficiency, and lifetime are all higher than a gridded tube at 50 dB, 50-70% and 50,000 hours, respectively. SLAC has examined two designs, a single-gun diode design, and a multibeam klystron (MBK). The multibeam klystron is the more attractive in that it reduces the overall length of the tube from 7.5 m to about 3.5–4.0 m. The length reduction factor of the multibeam klystron, and its potential for higher efficiency, make it the optimum candidate for the Neutrino Factory. Moreover, the length of the multibeam klystron is consistent with the manufacturing capabilities of current tube manufacturers, whereas the manufacture of a 7.5 m diode tube would be a big step and would require new and costly facility upgrades. Figure 8.1 shows a 7 beam MBK developed by Thompson for TESLA. Two such tubes have been built and tested, and have demonstrated efficiencies of $63-66\%$ [2]. To provide rf power overhead for dynamic regulation of the rf phase and amplitude, a 12 MW multibeam klystron has been selected as the high-power rf source for the Neutrino Factory. This provides an rf power overhead margin of about 20% for regulation. The design will be a fully integrated horizontal package incorporating the tube, solenoid, and high-voltage terminal, as pioneered at CERN for LEP. This facilitates the replacement and installation of tubes in the facility. Another advantage of the horizontal design, besides the ease of handling, is the reduced cost of the rf building because of the lower building height requirement. With a mean-time-between-failures (MTBF) of 50,000 hours and 84 tubes, one tube will need to be replaced about every 30 days (after the initial break-in period). Since there is a comparable number of klystrons for the acceleration system, the rate of klystron failures for the facility as whole will be about two per month, on average. Many of these failures towards the end of life are gradual, and replacement can be scheduled for routine maintenance periods. Because of the large size and high cost of waveguide, the transmission lines from the tubes to the cavities will be large coaxial lines of 0.31 to 0.36 m diameter, pressurized to 1.75 atmospheres of dry air. Power splitters divide the rf power from each tube to supply the cavities. Sections b1 and b2 of the buncher (see Chap. 5.1 and, in particular, Table 5.2) will require a 12-way splitting of the power; section b3 an 8-way split, and sections (1,1) to (2,3) of the cooling a 2-way split. Splitters with proper built-in phase delays further divide the power to each cell or cavity section of the cooling channel.

Figure 8.1: Thomson TH 1801 multi-beam klystron.

The 402.5 MHz system can use currently existing 900 kW diode rf klystron amplifiers. Because of their long length, it would be advisable to fund a small R&D effort aimed to development of an integrated horizontal package for the tube. As for the multibeam klystron, this would improve the efficiency of tube handling and provide cost savings because of reduced building height requirement. Coaxial transmission lines with splitters would be used to provide the rf power to the cavities. Only 3 klystron tube amplifiers are required to supply the requirements of the 402.5 MHz buncher rf.

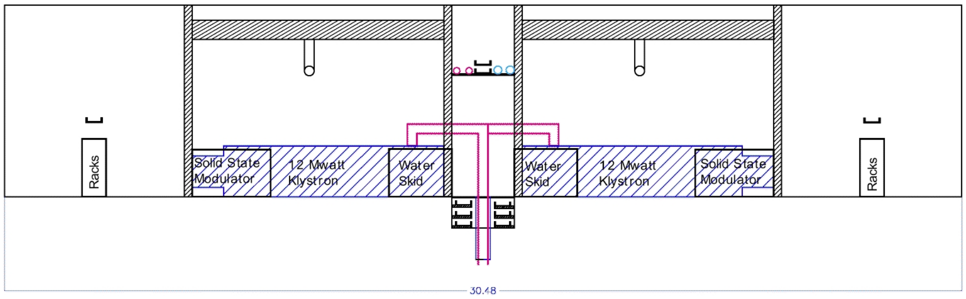

Figure 8.2: Cross section of cooling channel equipment gallery.

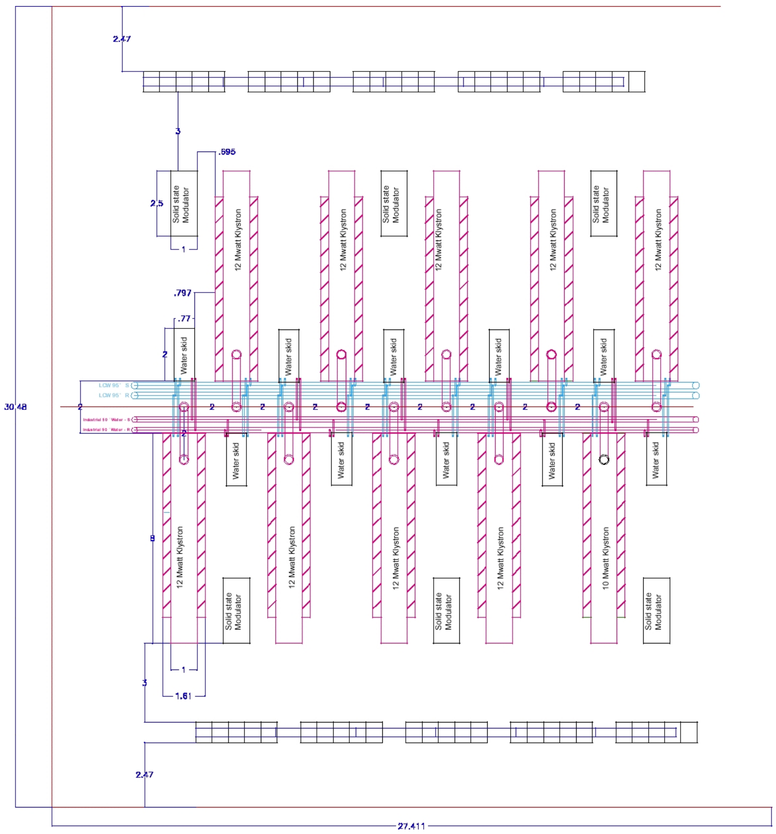

Figure 8.3: Cooling channel equipment gallery, plan view.

Figures 8.2 and 8.3 show a cross section and plan view of a portion of the rf building gallery along a 201.25 MHz section. The rf building is approximately 190 m long and 30 m wide. With horizontal packaging of the 201.25 and 402.5 MHz klystrons, the height of the building roof line need only be 5.5 m. Because of the large footprint of the equipment, the klystrons are arranged side by side and on both sides of the gallery. Not shown in the figures are the transmission line splitters, required to supply the rf power to the cavities, and the utilities. The 402.5 MHz klystron system footprint will be much the same, but about half the size, and these klystrons will be located in sections b1 and b2 interspersed between the 201.25 MHz equipment.

8.3.2 Station Controls and Low-Level rf

The low-level rf (LLRF) and control system provides the drive power for the final klystron amplifier, contains feedback loops for phase, amplitude and cavity frequency control, and circuitry for personnel safety and equipment protection. A frequency reference line running the length of the complex provides an rf phasing reference to which each cavity is locked. A microprocessor in each rf station processes error information to control the amplitude and phase and thus keep the cavity tuned to the reference frequency. The microprocessor communicates with, and accepts directions from, the central control room. The system is similar to systems currently in use at Fermilab or planned for the SNS project. The LLRF system will include fast circuits to detect sparks and malfunctions and immediately inhibit the rf to protect the equipment and cavities. Other, hard-wired, fast circuits will monitor for high rf leakage from equipment or contact with high-voltage and current, and then activate interlocks for personnel protection. The equipment would be housed in five standard racks next to the klystron and associated equipment, Fig. 8.3.

8.3.3 High-Voltage Modulator and Power Supply

The high-voltage modulator and power supply for the 201.25 MHz rf system will use the latest solid-state design. Currently available Insulated Gate Bipolar Transistor (IGBT) modulator technology will be built by industry to provide the pulsed power requirements of the klystron, see Fig. 8.4. The Neutrino Factory will use IGBT modulators similar to designs currently being built for the SNS project. They are very reliable, efficient, and cost effective. A 19-beam klystron, the basis of this design, has a calculated efficiency of 70% and a klystron tube perveance of 0.5×10^{-6}. The specifications for the modulator and power supply are given in Table 8.3. The overall efficiency of the modulator and power supply from the AC mains is about 95%.

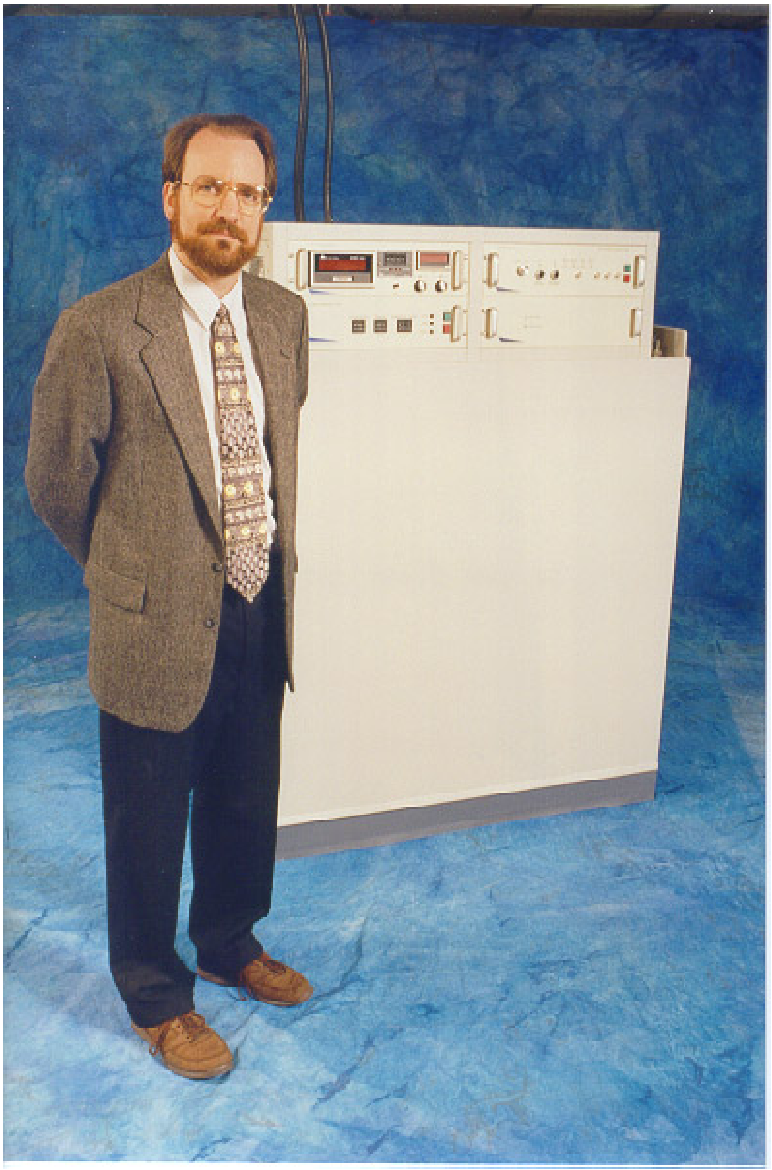

Figure 8.4: Compact modulator from Diversified Technologies, Inc., Medford, MA (Capacitor bank and regulator not shown in this picture).

Table 8.3: High-voltage modulator parameters.

Klystron frequency (MHz)	201.25	402.5
High-voltage (kV)	80	60
Current (A)	215	31
Duty factor (%)	0.19	0.0525
Average power (kW)	33	1.0
Voltage droop (%)	0.1	0.1

8.3.4 NCRF AC Electrical Power and Water System

The AC power for the normal conducting rf must support 84 tubes with 33 kW average power and three tubes with 1.0 kW average power, solid-state amplifiers and solenoid power supplies, cooling water systems and miscellaneous other loads. These all require a 480-V three-phase supply. In addition to this, AC power is required at 120 V and 208 V for racks and other miscellaneous equipment. This gives a total AC power requirement of 6.8 MW. Table 8.4 shows a summary of the AC power requirements.

Table 8.4: NCRF systems AC power requirements.

Item	Power (MW)
Klystron modulators (95% efficiency)	2.9
Amplifiers & supplies	1.0
Cooling + miscellaneous loads	2.3
Racks etc.	0.6
Total	6.8

The cooling water system will be sized to accommodate the average power of 6.8 MW with a proper temperature rise for safe and efficient operation of the equipment. Each klystron station requires 75 gpm of low-conductivity water (LCW) for cooling the klystron and associated equipment, and 20 gpm LCW to cool and provide temperature control of the cavity. This gives a total water requirement of 7,980 gpm. This could be divided up between room-temperature (and above) water and chilled-water systems for cavity control at 20 gpm per station. For all these systems, we assume a supply header pressure of 100 psi and return pressure of 40 psi.

8.4 Specification of NCRF Cavities for Cooling

The 201.25 MHz normal-conducting cavities in the cooling sections must operate at very high accelerating gradients. This would be impractical with conventional open-iris structures, given the large size of the beam iris required. A great improvement can be made in the shunt impedance of the cavity by closing the iris with a thin conducting barrier. This barrier must use the smallest amount of material to minimize scattering of the muon beam. In the design we close the irises with thin beryllium foils. Alternative methods of closure, such as grids of thin-walled tubes will be evaluated in the future. The foils must be thick enough to conduct away the heat from the rf currents and keep the temperature below a predetermined level. The foils are pre-stressed in tension during manufacture in order to keep them flat. This method ha2 been tested experimentally and works well up to the point where the thermal expansion exceeds the pre-stress and the foils begin to move. Foil thicknesses have been chosen for Study-II that will keep the temperatures below this critical level. The use of tapered foils, or foils with stepped thickness, can reduce the amount of material intercepted by the core of the beam, reducing the amount of scattering significantly. Table 8.5 shows the thickness of the foils used in the simulations of the various types of cavities in the buncher and cooling channel.

The normal-conducting cavities in the buncher are the same design as those in the first cooling section, though they are operated at lower gradient, allowing the use of thinner foils. The buncher section also contains harmonic cavities operating at 402.5 MHz. These fit into the spaces that are occupied by the liquid-hydrogen absorbers in the cooling cells farther downstream. For these cavities, the foils occupy most of the diameter of the end walls, but the gradients are sufficiently low that the losses in the foils are manageable.

The normal-conducting cells must have some cooling to remove the average power losses in the walls and to stabilize the frequency. The Study-II design is based upon room temperature operation, although the option of operating at reduced temperature (*e.g.*, liquid-nitrogen temperature) has been kept open. This option would lower the wall resistance and reduce the peak power requirements, at the expense of adding an additional refrigeration system.

8.4.1 201.25 MHz Closed-Cell Description

The cooling channel simulations were based upon simple pillbox cavities that have continuous, flat, conducting end walls from the center all the way to the outer radius. The cavity lengths assumed for the simulations are just the available space divided by the appropriate number of cells. In practice the cavities must be closed by assemblies of foils or grids that are demountable to permit assembly or repair. This requires a non-

Table 8.5: Beryllium foil thicknesses for various cells in the buncher and cooling channel. * dual values imply a stepped-thickness foil.

Type	Section	Frequency (MHz)	Length (m)	Gradient (MV/m)	Thickness* (μm)	Radius* (cm)
end	b1	402.5	0.186	6.4	75	18
end	b2	402.5	0.186	6	75	18
end	b1	201.25	0.3728	6.4	10	21
middle	b1	201.25	0.3728	6.4	120/240	14/21
end	b2	201.25	0.3748	6	100	21
middle	b2	201.25	0.3748	6	105/210	14/21
end	b3	201.25	0.3748	8	180	21
middle	b3	201.25	0.3748	8	187/374	14/21
end	(1.1)	201.25	0.466	15.48	200/400	12/18
middle	(1,1)	201.25	0.466	15.48	700/1400	14/21
end	(1,3)-(2,1)	201.25	0.5592	16.72	248/495	12/18
middle	(1,3)-(2,1)	201.25	0.5592	16.72	917/1834	14/21
end	(2,1)	201.25	0.5592	16.72	128/256	10/15
middle	(2,1)	201.25	0.5592	16.72	495/990	12/18

zero thickness for each iris, reducing the length available for rf and lowering the effective shunt impedance. We have mitigated the losses by rounding the outer walls of the cavity to improve the quality factor and restore the shunt impedance. Any practicable assembly of foils (or grids), requires some space for flanges and access. We used a minimum spacing of 50 mm between cavities, as shown in Fig. 8.5. The dimensions of the cavities were adjusted to fit the remaining available space. Note that the resulting cavity lengths are significantly shorter than the optimum for a particle of this velocity ($\beta = 0.87$). A cavity length that is more optimal could be achieved by adjusting the total cell length appropriately and this will be done as part of the overall optimization process later. The cavity shape is slightly reentrant in order to maximize the inductance, minimize the capacitance, and, hence, get the highest shunt impedance [3]. Figures 8.5 and 8.6 show the cavities separated by a pair of foils. This allows variable thickness foils to be used where the stepped side is not exposed to rf. Figure 8.7 shows a MAFIA simulation of the electric field in two half-cells separated by a pair of foils. Some field enhancement can be seen on the noses. Alternatively, a single foil of twice the thickness could be used in the center of the iris, heated from both sides (except for the end cells). Another advantage of the closed-cells is that there is no rf coupling through the iris, so the cavities can be individually phased for optimum performance of the cooling channel. One penalty of the omega shape is some field enhancement on the nose, see Figs. 8.8 and 8.9. Although the nose is made with as large a radius as practical, it still has an enhancement factor of about 1.7 over the field on axis. However, the highest surface field in Table 8.2 is only about 1.5 times the Kilpatrick number for this frequency. Furthermore, a positive aspect of this field concentration is that it is not on the foil but on the solid copper. A breakdown to this point may be less of an issue. Figure 8.9 shows the azimuthal magnetic field. The distribution on the foil, and therefore the rf heating, is similar to the pillbox model, although there is some shielding due to the noses. Figure 8.10 shows the profile of the cavity from the downstream part of the cooling channel where only two cavities are used per cooling cell (Lattice 2). The cavities are longer and closer to the optimum for this particle velocity (though there is still room for some improvement). Figures 8.11 and 8.12 show the 2D electric and magnetic field profiles for this case.

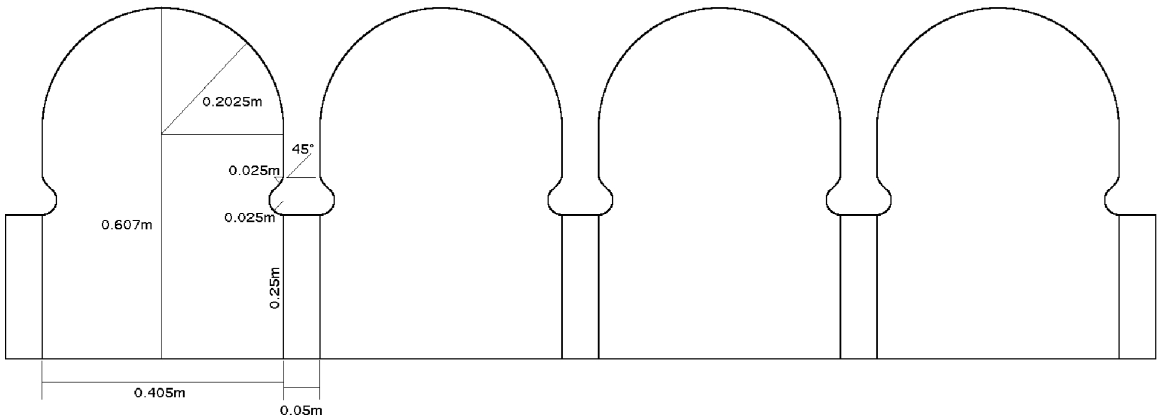

Figure 8.5: Profile of cavities for buncher and Lattice 1 cooling section.

8.4.2 Foil Requirements

The closed-cell cavity design described above assumes that beryllium foils will be used to seal off the beam irises. Other methods, including grids of thin-walled tubes, have been discussed, and show promise, but are not as far advanced in understanding or testing as the foils. Hence pre-stressed foils have been chosen as the baseline design for Study-II. The foils are made of thin high-purity beryllium sheet bonded to a thicker ring of slightly

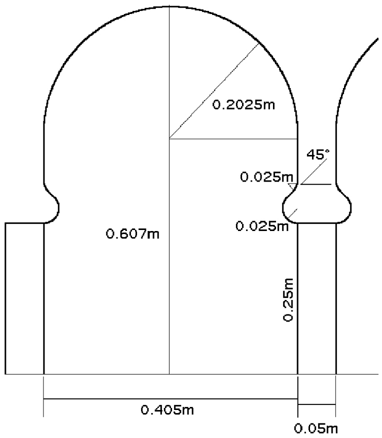

Figure 8.6: Section of one cavity.

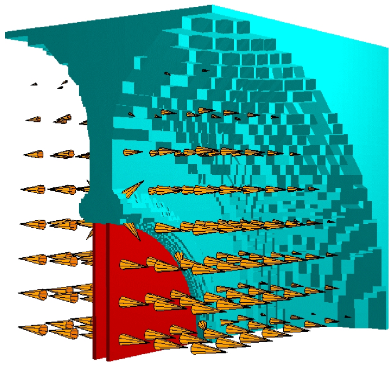

Figure 8.7: MAFIA model with two foils.

lower grade material, see Fig. 8.13. The exact details of this process are proprietary but the combination of materials used results in a small but significant difference in the thermal expansion of the foil relative to the ring assembly. This produces a tensile pre-stress on cool down from the joining operation, which helps to keep the foil flat.

When the foils are heated by rf, and only cooled by conduction to the edges, they assume an approximately parabolic temperature profile, see Fig. 8.14. The calculated rf-induced profile is slightly flatter than parabolic and can be used in ANSYS as a load set for the stress calculations. Figure 8.15 shows an example of the temperature distribution in a thin foil from such an analysis.

The foils remain flat until the thermal expansion exceeds the tensile pre-stress. At this point compressive stress is generated in the foil, and it starts to deflect by buckling into a gently bowed shape, see Fig. 8.16. The maximum allowed temperature difference is about 35 $^\circ C$ and is approximately independent of the radius and thickness. Of course a thicker foil can take more power before reaching the buckling temperature, as shown in Fig. 8.17. A set of foils (Table 8.5), has been specified for the set of cavities used in Table 8.1, that keeps the temperatures below the critical point. For the larger irises, the foils become quite thick and the scattering of the muon beam becomes significant. One way to reduce this is to make the windows thinner in the middle, where the core of the beam passes, and thicker towards the outside, where there are fewer particles, see Fig. 8.18. It is thus possible to reduce the scattering while maintaining the same temperature rise in the foil. Figure 8.19 shows the temperature profile for a thin window of uniform thickness and for windows with thicker profiles starting at different radii. As can be seen from the

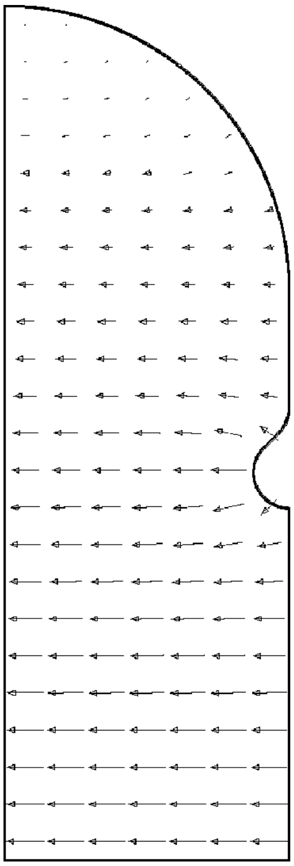

Figure 8.8: URMEL 2D E-field.

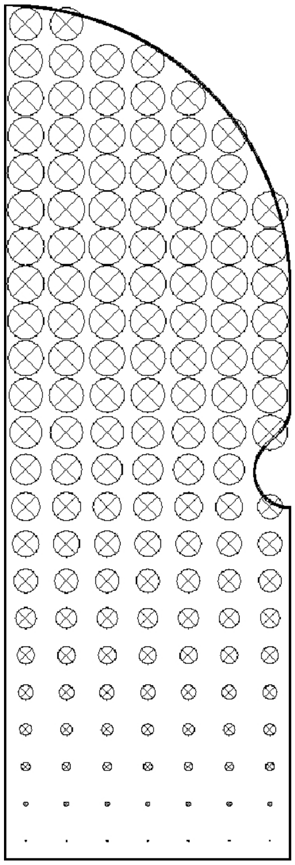

Figure 8.9: URMEL 2D azimuthal H-field.

figure, adding material at large radius has a significant effect on the temperature profile up to about one third of the way in. Beyond this point, there is diminishing return and much past halfway there is little to be gained by adding more material. Simulations have shown that such a stepped window reduces the multiple scattering significantly compared with a uniform foil for the same temperature. Going to multiple steps in thickness, or to a continuous taper, should yield further small improvements in scattering but the simulations do not show a significant improvement in transmission through the cooling channel.

The pre-stressed foil properties have been investigated experimentally in a low-power test cavity at 805 MHz using a halogen lamp as a heat source [4]. These experiments used small (160 mm diameter) foils and the results have been extrapolated to larger foils. We

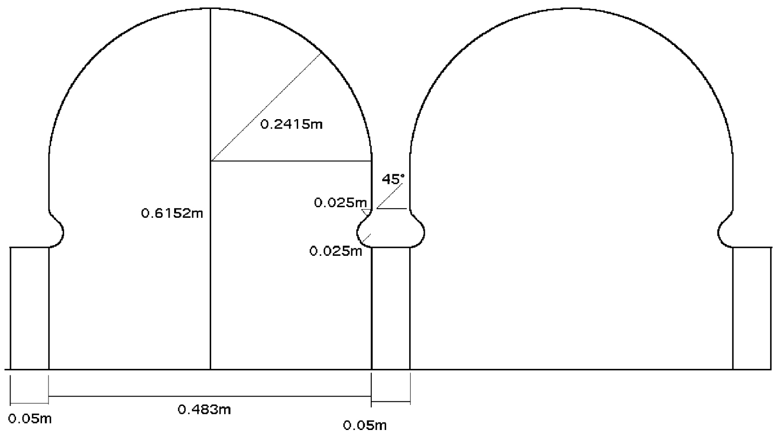

Figure 8.10: Profile of cavities for Lattice 2 cooling section.

have assumed that the same pre-stress can be achieved in the larger foils, but this must be validated experimentally as part of the future R&D program. It should be straightforward to obtain the desired pre-stress by adjusting the combination of materials in the outer ring but some experimentation may be required to find the optimum combination.

One issue with the closed-iris structures is the possibility of multipactoring due to the high secondary yield of beryllium or aluminum (foils or tubes). This could cause outgassing and possibly breakdown in the cavity, which might damage the delicate structures. Persistent multipactor discharge may also heat the surfaces involved. Unlike copper, the secondary yield of aluminum does not reduce with rf conditioning because of a stable surface oxide layer. It is expected that beryllium may behave similarly, although the handbook values for beryllium oxide are lower than those for aluminum oxide. It is proposed to suppress this problem by the application of low secondary emission coatings, such as titanium nitride (TiN). This issue will be investigated experimentally in a high-power cavity as part of the ongoing Muon Collaboration 805 MHz R&D program. The cavity is designed to use demountable foils or copper blank-off plates and can be conditioned to very high-gradient using the high-power klystron test stand in the Lab G facility at FNAL. The foils will be coated on one side with TiN and conditioning tests can thus be run with all-copper surfaces, uncoated beryllium windows, coated beryllium windows or combinations of these. Windows of various thickness and with stepped profiles will be tested and the conditioning can be attempted with a wide range of magnetic fields in an available 5 T superconducting solenoid.

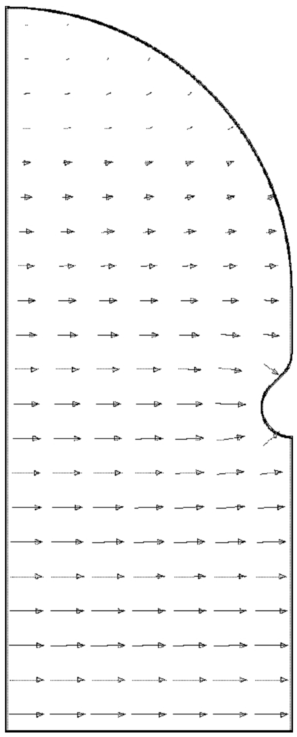

Figure 8.11: Lattice 2 cooling cavity. URMEL 2D E-field.

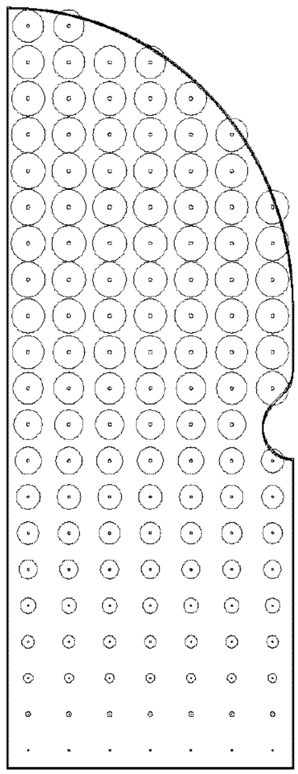

Figure 8.12: Latice 2 cooling cavity. URMEL 2D azimuthal H-field.

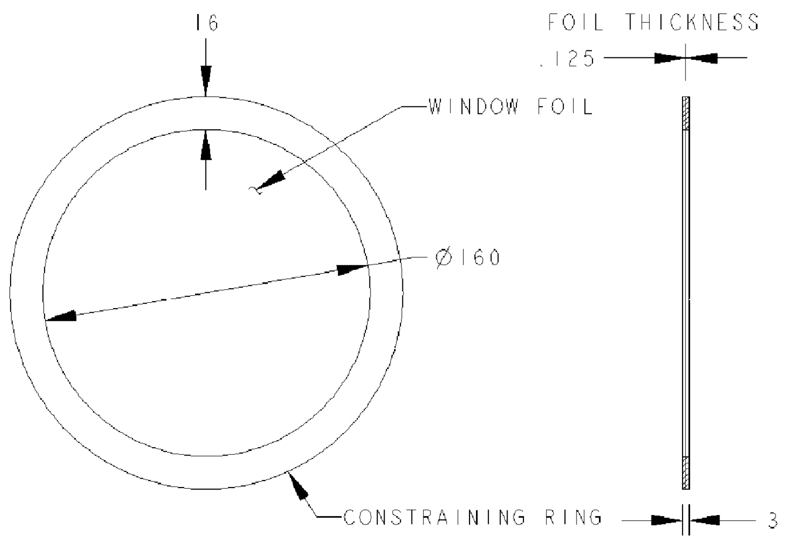

Figure 8.13: Layout of beryllium test window (all dimensions in mm).

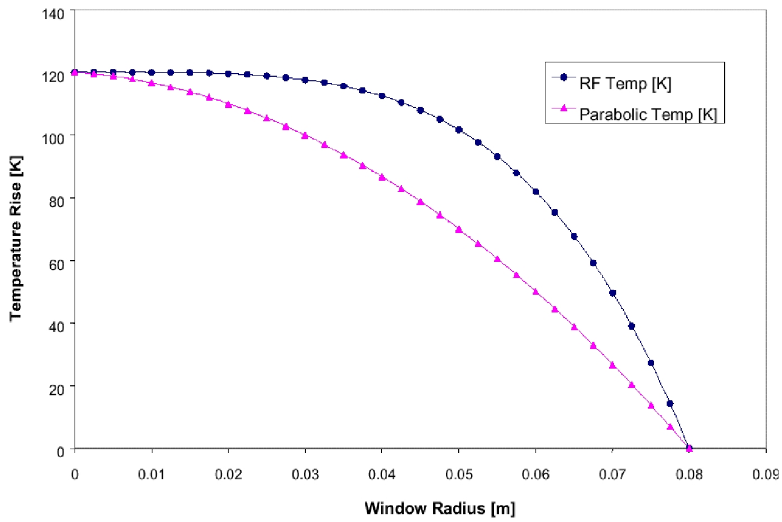

Figure 8.14: Actual temperature profile for rf heating and parabolic approximation from halogen lamp tests.

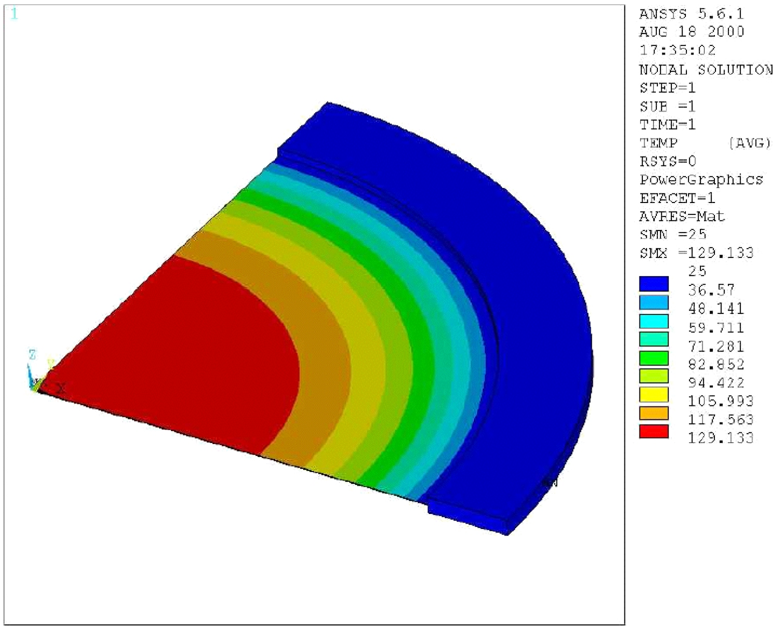

Figure 8.15: ANSYS calculated temperature profile for thin window with 60 W loading.

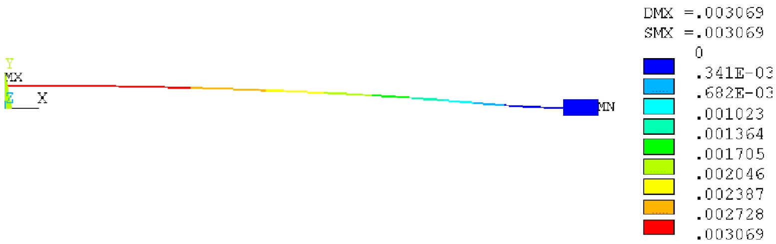

Figure 8.16: ANSYS model showing example of buckling displacement (dimensions in m).

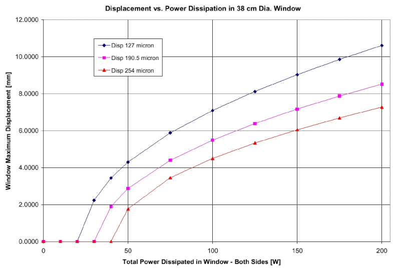

Figure 8.17: ANSYS calculated displacement *vs.* power for larger windows. The three curves represent three window thicknesses, 127μm, 190.5μm, and 254μm.

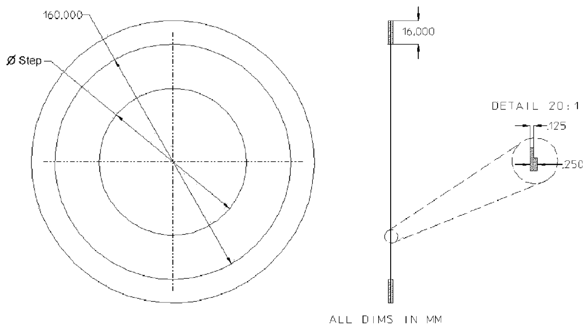

Figure 8.18: Stepped window concept.

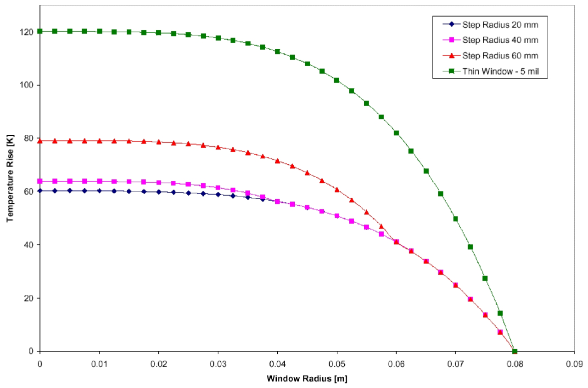

Figure 8.19: Temperature profile of uniform thin window and windows with steps to thicker outer region starting at various radii.

8.4.3 2.75 m Lattice Implementation (Lattice 1)

The cooling channel lattice is a tightly packed assembly of equipment including liquid-hydrogen absorbers, superconducting solenoids, high-gradient rf cavities, instrumentation, vacuum equipment, etc. Our studies show that it is possible to integrate all these components into the available cell length. Several iterations have been performed on this layout to try to make the most efficient use of the space. Constraints include the size of the rf cavities, which is dictated by the frequency, the size of the absorbers, which is determined by the beam size, and the cell length, which has been fixed for this Study at 2.75 m for the buncher and Lattice 1 cooling section and 1.65 m for the Lattice 2 cooling section. The two lattice cell dimensions will be re-evaluated as part of the overall system optimization.

The sizes of the coil packs and cryostats have been chosen to allow practical current densities and the coil diameters have been kept small to minimize the amount, and therefore the cost, of superconductor required. The largest coil is the central one ("coupling coil") that surrounds the rf cavities. The inner diameter of this coil is left large enough to allow the cavity structures to pass through during assembly. The rf feeds must come out through the wall of the cryostat, and may be angled to give clearance to other hardware. Pumping ports will be short and wide to give good conductance and may also penetrate the cryostat. Clearance is required at the end of each cooling cell for installation or removal of one absorber/rf module from the channel. This is achieved by using a collapsible flange in the outer cryostat wall, which is reinforced after it is made up in order to handle the possible magnetic forces. RF shields will be used to keep beam-induced signals from escaping into the outer cryostat and vacuum system.

Figure 8.20 shows the proposed cooling channel layout for the first cooling section lattice, including all major components except the beam instrumentation package, which will occupy the clearance opening at the end of each cell or, possibly, the space between the rf cavities and the hydrogen absorber. The space in the cryostat outside of the cavities will be evacuated to minimize the load on the rf structures. This approach would provide insulation for the cavities if they were operated below room temperature. It also obviates the need for UHV connections between each cavity and between the cavities and the hydrogen absorbers. The flanges are required only to provide rf continuity (for screening) and to separate the UHV of the rf system from the guard vacuum of the cryostat.

8.4.4 1.65 m Lattice Implementation (Lattice 2)

The 1.65 m lattice for the downstream part of the cooling channel will use a layout similar to the upstream part, but with smaller hydrogen absorbers and only two rf cavities per

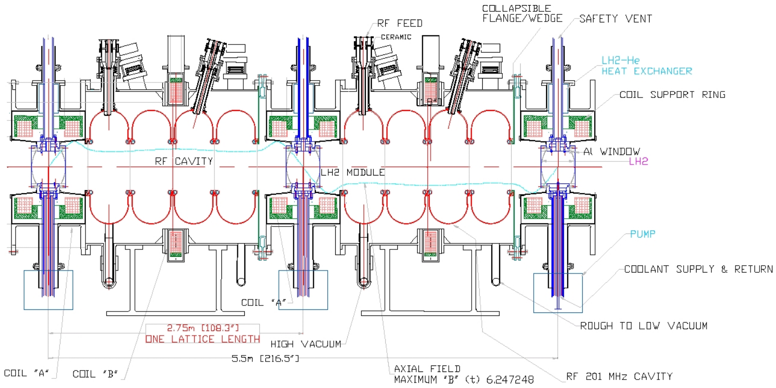

Figure 8.20: Cooling channel Lattice 1, four cavities per cell.

cell. The density of equipment is similarly high. In this case the cavity lengths are closer to the optimum for this particle velocity, but could still be improved if the cell length were increased slightly. Figure 8.21 shows the proposed cooling channel layout for lattice 2, including all major components except the instrumentation package.

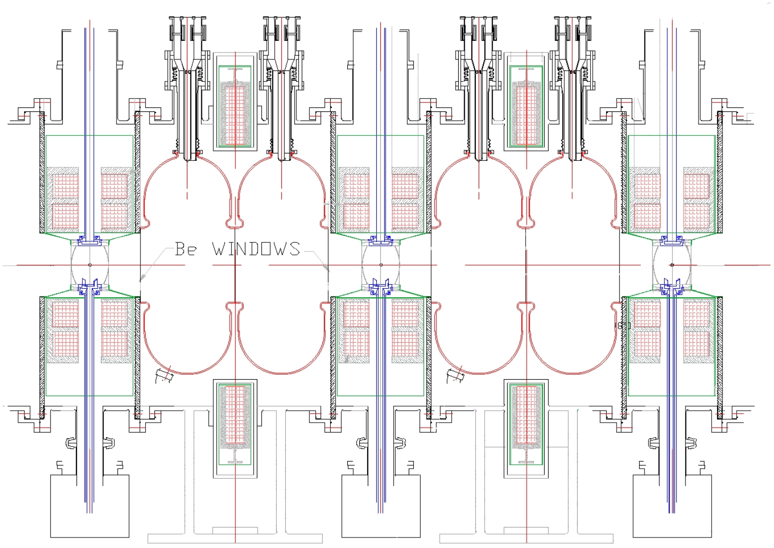

Figure 8.21: Cooling channel Lattice 2, two cavities per cell.

8.4.5 402.5 MHz Buncher Cavity

The buncher harmonic cavities, Fig. 8.22, are smaller, simpler versions of the 201.25 MHz cavities. They are rounded pillboxes and are closed by similar foils that are smaller and thinner than those used for the large cavities. There is adequate space for the cavities to be the optimal length for this particle velocity. Though the power requirements are modest, cooling water is used to stabilize the frequency and remove the small amount of average power dissipated in the walls. Harmonic cavities are installed in some of the buncher cells in the location corresponding to that where the hydrogen absorbers are placed in the normal cooling sections, *i.e.*, inside the bore of the focusing solenoid coils.

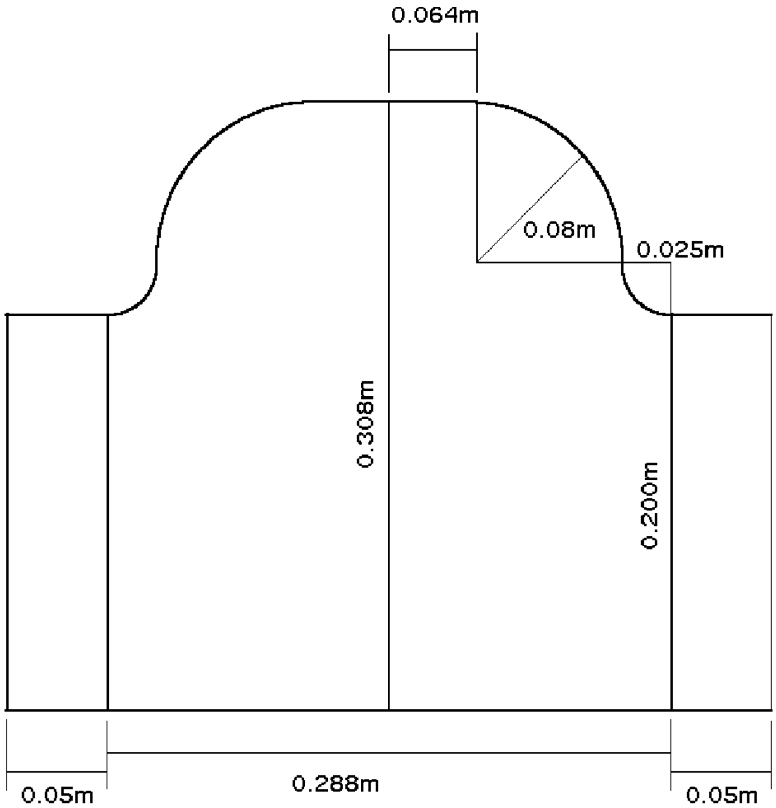

Figure 8.22: 402.5 MHz buncher harmonic cavity.

8.4.6 Tuning Requirements

Since there is negligible beam loading, the tuning requirement for the cavities is simply to compensate for temperature variations due to water supply changes and rf heating. If we assume bulk water temperature fluctuations are of the order of 1°C or less, and a thermal expansion coefficient of copper of approximately 17 ppm/°C, then the frequency variation would be about 3.4 kHz. Since the average power is modest, it should be easy to limit the temperature rise due to rf heating to 10°C or less. A worst-case cold start with the cavities around 0°C and a normal operating temperature of 40°C would produce a frequency detuning of about 136 kHz. Simple 2D calculations show that if the length of the cavity is varied from the nominal value, the frequency sensitivity is about 236 kHz/mm, so a small range of motion would be adequate to achieve the required tuning range. A tuning scheme similar to that used for superconducting cavities, where the cavity is mechanically stretched or compressed within elastic limits, will easily achieve this range of motion. Alternatively, a moving plunger tuner can be used to tune the cavity inductively but this would require an additional aperture in the cavity and would be harder to package within the confines of the cryostat.

It would also be possible to tune the cavities over a limited range by controlling the water temperature, but the water stability would have to be a fraction of a degree to keep the frequency stable to within the bandwidth of the cavity (3.3 kHz unloaded, 6.6 kHz critically coupled). Moreover, each cavity would then require an independent water circuit and controller, which would be inconvenient.

Depending on the elastic range of motion of the cavities, it may be desirable to have some kind of *fixed* tuning after assembly to account for manufacturing tolerances (analogous to the “dimpling” of linac cavities). This could be a specific part of the cavity which is designated to be deformed or the cavity as a whole could be designed such that it can be stretched or compressed beyond the elastic limit to achieve a permanent tuning. If detailed analysis shows that the cavity has a sufficiently large elastic tuning range, it may even be possible to relax the requirement of keeping the foils flat and allow some movement to take place. (Pre-bowing of the foils would ensure that this happens in a predictable manner.) This would allow thinner foils to be used with a concomitant reduction in scattering.

In the event that vibrations of the foils or other parts of the system should produce troublesome fluctuations in the rf fields, the deforming type tuner could be augmented with a fast piezo-electric actuator allowing feedback at audio frequencies. This has been demonstrated to reduce the effect of microphonics in superconducting cavities.

8.4.7 Vacuum Requirements

The operating vacuum in the high-gradient cavities should be in the 10 nTorr range or better. Operating much above this range is likely to produce more frequent arcing and would require significantly longer time to condition the cavities initially and after any vent. The reliability of the rf window is also strongly influenced by the vacuum level. The frequency of window arcs and the lifetime of anti-multipactor coatings on the ceramic are both degraded by operating at pressures above about 100 nTorr. These conditions will require strong pumping and good conductance to the rf cavities. Because of the presence of strong solenoid magnetic fields, ion pumps may not be used in close proximity to the cavity during operation, though they may be useful during initial conditioning with solenoids off. Cryopumps or titanium sublimation pumps may be useful close to the cavities with magnetic fields on. It would be advantageous to pump the cavities through the rf coupler if there proves to be sufficient conductance, since this will ensure the best possible vacuum at the rf input window. A large diameter coaxial feed with a short distance to the pump may have sufficient conductance by itself. If not, it can be supplemented by an additional pumping port on the cavity body. A thorough bakeout to above 150°C after assembly would be advantageous but may be incompatible with the superconducting components. In that case, the individual components will be baked separately before final assembly into the cryostat.

8.5 SCRF Cavities for Acceleration

Based on the high-real estate gradient desired to minimize muon loss, superconducting cavities are selected for the acceleration section of the Neutrino Factory to provide an active gradient of 15-17 MV/m, and a real-estate gradient of 7.4 MV/m. At such high-gradients, the peak rf power demand for copper cavities that provide 7.5 GV would become prohibitively expensive. By virtue of low losses, SC cavities can be filled slowly, reducing the peak power demand to roughly 0.5 MW per cell for a 3 ms rise time.

As a result of experience at LEP, CEBAF, TTF, Cornell, KEK and CEA-Saclay, the science and technology of superconducting cavities and associated components are highly developed [6]. In all, SCRF systems totaling 1 km in active length have been installed in a variety of accelerators and routinely operated to provide a total of 5 GV. The largest installation was at LEP-II, where 500 m of niobium-coated copper cavities provided more than 3 GV of acceleration [7]. The Neutrino Factory calls for nearly 500 m to provide 7.4 GV.

Although the sheet-metal Nb cavites used for TESLA are capable of providing gradients of the order of 20 MV/m and higher [8], we have chosen Nb/Cu technology, developed at CERN [9] for LEP-II, for several reasons:

- Because of the low rf frequency (201.25 MHz), and the accompanying thicker wall (*e.g.*, 6 mm), the cost of raw sheet niobium would be prohibitive for the roughly 600 cells needed.

- High thermal conductivity copper provides better stability against quenching of superconducting cavities than does sheet Nb. This is especially beneficial at 201.25 MHz because of the high stored energy per cell (roughly 1 kJ per cell at design gradient).

- The wall thickness of 201.25 MHz cavities may need to be even greater than 6 mm for mechanical stability against atmospheric load, for reducing Lorentz force detuning, and for avoiding microphonics from external vibrations.

- A coated copper cavity allows the use of pipe cooling instead of the more usual bath cooling. Pipe cooling saves liquid-helium inventory (estimated at 100,000 L for standard bath cooling of 600 cells). It also opens additional avenues for improving the mechanical stability for large scale cavities.

Recent results from CERN [10] on 400 MHz Nb/Cu cavities (Fig. 8.23) demostrate accelerating gradients of 15 MV/m at 2.5 K at a Q of 2×10^9. Because of the lower frequency used here, we can expect the Q to be four times higher. We have chosen an operating temperature of 2.5 K and a Q value of 6×10^9. Extrapolating LEP results at 4.5 K would imply a much lower $Q < 2 \times 10^9$ at the design gradient for the Neutrino Factory, even when scaled for the lower frequency. Moreover, LEP cavities never reached the Neutrino Factory design gradients at 4.5 K.

Modeling the Q *vs.* E (Fig. 8.24) obtained for LHC 400 MHz cavities and incorporating the Q increase for 201.25 MHz, ANSYS studies conclude that it will not be possible to reach E_{acc} =15–17 MV/m at a Q of 6×10^9, unless the operating temperature is reduced to 2.5 K. Figure 8.24 shows the peak magnetic field expected for 17 MV/m in a 2-cell cavity with 300 mm beam aperture. It corresponds to E_{acc} = 13 MV/m for the LHC cavity geometry because of the relatively smaller beam pipe and optimized cavity. (The Neutrino Factory cavity geometry is discussed below.)

Accelerator physics studies show that an aperture of 300 mm (diameter) is acceptable for the Neutrino Factory, except for the first 1000 MeV of the pre-accelerator linac, where an aperture of 460 mm has been chosen. Because of the higher peak fields arising from the larger aperture, the gradient for the first section of the pre-accelerator has been reduced

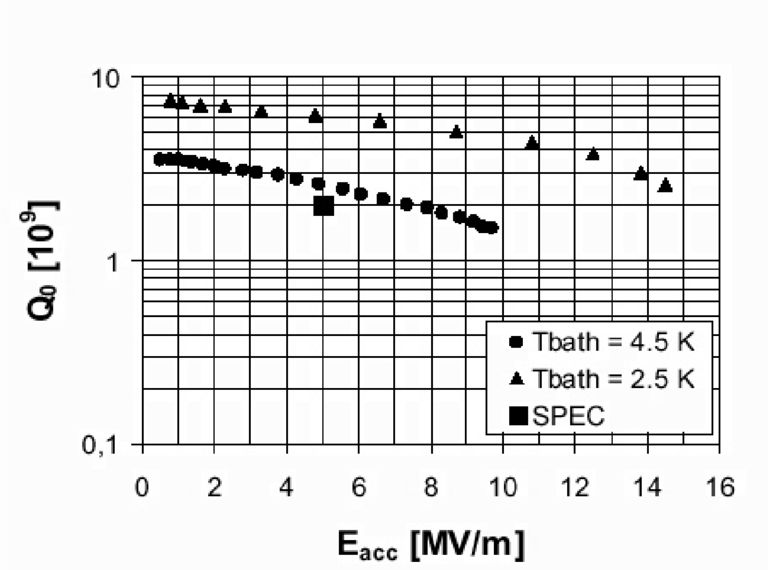

Figure 8.23: Q_0 *vs.* gradient for Nb/Cu CERN 400 MHz, LHC cavity.

to 15 MV/m. The corresponding surface magnetic field is still 12% less than the peak magnetic field for the LHC cavity at 15 MV/m.

In selecting the rf pulse length (T_{rf}), a trade-off must be made between peak rf power on the one hand, and refrigerator load, tolerance to microphonics and Lorentz force (LF) detuning on the other hand. Increasing T_{rf} will lower the peak power, but increase the average rf power and the refrigeration load. Increasing T_{rf} will also drive Q_L toward higher values, decreasing the cavity bandwidth and thereby increasing its sensitivity to LF detuning and microphonics. The peak rf power (P_{pk}) needed to establish the fields depends on the stored energy (U), the cavity time constant ($\tau = \frac{Q_L}{\omega}$) and the amount of detuning $\delta\omega$ expected from Lorentz force and microphonics, as follows [6]

$$P_{pk} = \frac{U(\frac{\omega}{Q_L})\left\{(Q_L\frac{\delta\omega}{\omega})^2 + \frac{1}{4}\right\}}{\left\{(1 - \exp -\frac{T_{rf}}{2\tau})\right\}^2} \tag{8.1}$$

Once the fill time and detuning tolerance are selected, the loaded Q of the cavity can be found to minimize the peak power required. A conservative estimate for detuning tolerance in these large 201.25 MHz structures is 40 Hz. Cavities at TTF and CEBAF show microphonic excitation of < 10 Hz [11]. For a fill time of 3 ms, the optimum Q_L

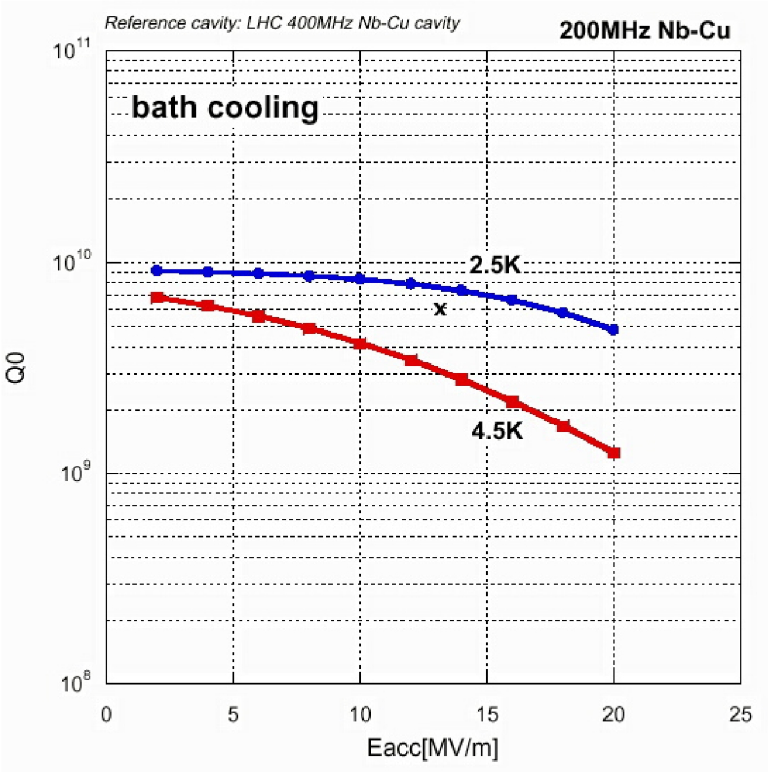

Figure 8.24: Qo *vs.* gradient expected for 201.25 MHz cavity. Although the Neutrino Factory design is $Q_0 = 6 \times 10^9$ at $E_{acc} = 17$ MV/m, for a 2-cell, 300 mm aperture cavity, it corresponds to only 13 MV/m (marked X) for the LHC cavity geometry due to the smaller aperture of this cavity and the optimized geometry.

is 1×10^6 (bandwidth = 200 Hz) and the required peak power is about 500 kW per cell. Coaxial couplers developed for KEKB [12] have delivered 380 kW CW to a 1 A beam. In pulsed mode, higher power performance is expected. For a wall thickness of 8 mm, the calculated Lorentz force detuning at 17 MV/m is 128 Hz. Most of this can be handled with feed-forward techniques developed at TTF for TESLA [13].

8.5.1 SCRF Structures at 201.25 MHz

To improve the real-estate gradient, it is important to have a large filling factor of cavities in the cryomodule. This pushes structures towards multi-cell cavities. On the other hand, because of the low frequency and high-gradient, the coupler power and stored energy per structure increase with the number of cells. Also, the mechanical resonance frequency of multi-cell cavities drops, demanding stiffening schemes. Compromising between these factors, 2-cell units are chosen. In the first 1000 MeV of the preaccelerator linac, where apertures of 460 mm are needed, gradients are lowered to 15 MV/m to keep the peak surface fields comparable to those of the 300-mm bore cavity at 17 MV/m; input coupler power is kept at the 500 kW level by providing one coupler at each end. The performance

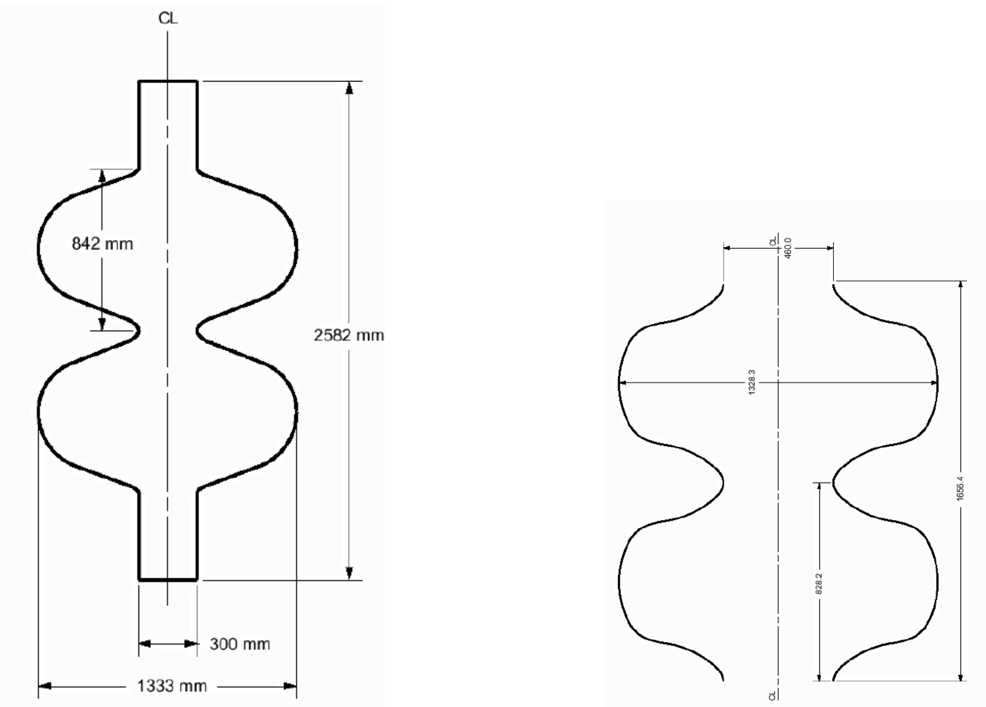

Figure 8.25: Two-cell geometry: (left) small aperture; (right) large aperture.

of a superconducting cavity depends on the peak surface fields. Minimizing E_{pk} is important to avoid field emission that lowers the cavity Q and increases heat load. Minimizing H_{pk} is also important, since the Q of these cavities falls with surface magnetic field, one of the characteristic features of Nb/Cu cavities (Fig. 8.23). In the 400 MHz LHC cavity, which reached E_{acc} = 15 MV/m, the corresponding peak surface fields were E_{pk} = 33

MV/m and H_{pk} = 750 Oersted. The LHC cavity has a beam pipe diameter of 300 mm. Keeping the same beam pipe diameter for 201.25 MHz, 2-cell cavities, it is possible to improve the Neutrino Factory cavity geometry (see Fig.8.25) to reduce the peak fields to 14% below LHC-cavity values. Relative to CERN cavity performance, there is adequate safety margin for both improved structure choices. Tables 8.6 and 8.7 list the properties of the 2-cell 300 mm aperture unit and the 2-cell large aperture unit, respectively. Figure 8.25 (left panel) shows the 2-cell geometry with 300 mm aperture and (right panel) shows the 2-cell geometry with 460 mm aperture. Figure 8.26 shows the deformation (exaggerated) due to Lorentz force detuning for the 2-cell, 300 mm diameter cavity.

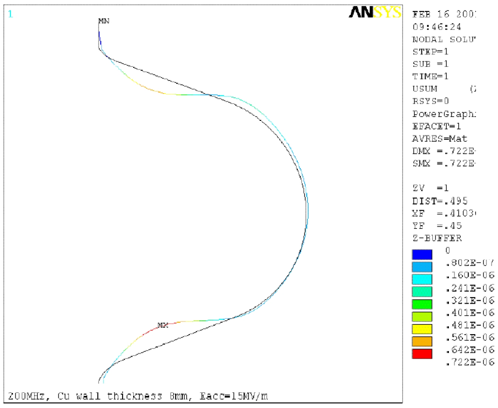

Figure 8.26: Lorentz force detuning for 8 mm wall thickness cavity.

8.5.2 Input Power Coupler

The antenna type coaxial design was chosen based on the successful experiences of CERN (LEP-II), DESY (HERA and TTF) and especially the success of the input coupler for KEKB [12]. Figure 8.27 shows the dimensions of the KEK, 508 MHz coupler, which will be scaled proportionately to 201.25 MHz. The lengths of the various sections will be adjusted to fit the final cavity and cryostat designs adopted. The waveguide-to-coaxial transition is of the door-knob variety. As in all high-power applications, the main window will be at room temperature and remote from the cavity. At KEKB, it is a disk shaped, water cooled, 95% pure alumina ceramic with a central hole for the inner conductor. A teflon coaxial centering disk between the window and doorknob serves to limit the flow of air to the cavity in the unlikely event of a ceramic window break. The inner conductor is

Table 8.6: 2-cell, 300 mm-diameter cavity parameters.

RF freq (MHz)	201.25
No. of cells per cavity	2
Active cavity length (m)	1.5
No. of cavities	268
Linac	76
RLA	192
Aperture diameter (mm)	300
E_{acc} (MV/m)	17
Energy gain per cavity (MV)	25.5
Stored energy per cavity (J)	2008
R/Q (Ω/cavity)	258
E_p/E_{acc}	1.43
H_p/E_{acc} (Oe/MV/m)	38
E_{pk} at 17 MV/m (MV/m)	24.3
H_{pk} at 17 MV/m (Oe)	646
Q_0	6×10^9
Bandwidth (Hz)	200
Input power per cavity (kW)	1016
RF on-time (ms)	3
RF duty factor (%)	4.5
Dynamic heat load per cavity (W)	18.9
Operating temperature (K)	2.5
Q_L	10^6
Microphonics detuning tolerable (Hz)	40
Wall thickness (mm)	8
Lorentz force detuning at 15 MV/m (Hz)	128

made of OFHC copper pipe and is water cooled. The outer conductor is made of copper plated (30 mm) stainless steel and has fins cooled by a 4.5 K stream from the refrigerator. This reduces both the dynamic and static heat leaks associated with the coupler.

Benefiting from simulation codes recently available for calculating and avoiding multipacting [14], dimensions of the inner and outer conductors are chosen so that multipacting will not be a serious problem. The coaxial design also permits application of a DC bias voltage between the two conductors to curtail any possible multipacting that may develop near the window or other sensitive regions.

Table 8.7: 2-cell, 460 mm-aperture cavity parameters.

RF freq (MHz)	201.25
No. of cells per cavity	2
Active cavity length (m)	1.5
No. of cavities	43
Aperture diameter (mm)	460
E_{acc} (MV/m)	15
Energy gain per cavity (MV)	22.5
Stored energy per cavity (J)	1932
R/Q (Ω/cavity)	208
E_p/E_{acc}	1.54
H_p/E_{acc} (Oe/MV/m)	44
E_{pk} at 15 MV/m (MV/m)	23.1
H_{pk} at 15 MV/m (Oe)	660
Q_0	6×10^9
Bandwidth (Hz)	200
Input power per cavity (kW)	980
RF on-time (ms)	3
RF duty factor (%)	4.5
Dynamic heat load per cavity (W)	18.3
Operating temperature (K)	2.5
Q_L	10^6
Microphonics detuning tolerable (Hz)	40

The coupler will be equipped with standard diagnostics for vacuum, gas species, temperature and light monitoring. Vacuum and light levels can be used to trip the rf power source in case of arcs.

The Q_{ext} value of the input coupler is fixed after initial adjustment of the position of the inner conductor by the use of appropriate spacing washers during final assembly. From experience at KEK, we expect that the Q_{ext} for the non-accelerating modes of the fundamental pass band will be of the same order as the Q_{ext} for the accelerating mode, *i.e.*, a few $\times 10^5$.

8.5.3 Higher-Order Mode (HOM) Couplers

The function of the HOM couplers is to damp the higher-order modes to Q_{ext} values of $10^4 - 10^5$ to prevent resonant build up of beam-induced fields that may make the beam unstable or increase the HOM power. The HOM couplers extract beam-induced HOM power from the cavity and deposit it in room-temperature loads. In view of the large muon bunch length, we do not expect HOMs to be a serious issue.

Two couplers are needed, with a relative azimuthal angle of about 90° to ensure damping of both polarizations of dipole modes. One coupler is attached to each end of the cavity. The HOM couplers must reject the accelerating mode by means of a narrow-band filter built into the coupler.

Detailed calculations will be carried out during the prototyping stage for the HOM spectra, possible trapped modes, and expected HOM power. Codes exist and procedures have been well established for electron applications. Our baseline device is a loop type coupler (Fig. 8.28) because it is demountable, compact, has relaxed mechanical tolerances, and provides demonstrated performance in mode damping [15]. The plane of the loop is orthogonal to the beam axis. The loop couples mainly to the magnetic field of dipole modes and mainly to the electric field of longitudinal modes. The rejection filter is formed by the inductance of the loop and the capacitance between the loop end and the outer conductor. The loop is capacitively coupled to the external load via a type-N connector, and is cooled by conduction through an upper stub. Final tuning of the filter can be carried out outside the clean room once the coupler is attached and the cavity sealed. Q_{ext} values are typically 10^3 to 10^5 for high impedance modes in a 9-cell TESLA cavity. These Q value will be even lower for the 2-cell cavities.

Power tests carried out for TESLA cavities under CW operating conditions showed good thermal behavior up to an accelerating field of 21 MV/m.

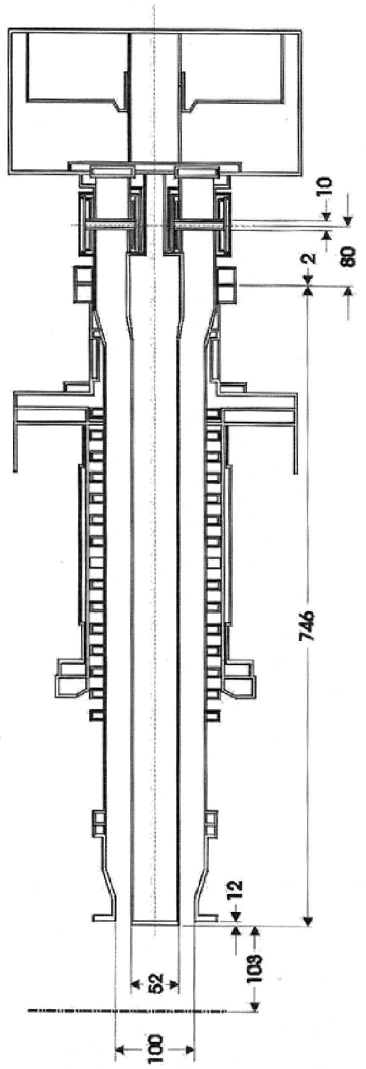

Figure 8.27: KEKB 508-MHz coupler.

8.5.4 Tuner

The function of the tuner is to match the cavity resonance frequency to the desired accelerator operating frequency. If the cavity is not being used for acceleration, the tuner must detune the cavity frequency a few bandwidths away from resonance, so that the beam will not excite the fundamental mode. During accelerator operation, the tuner

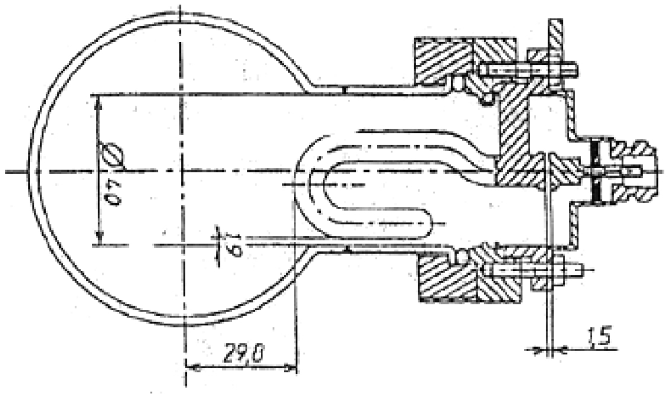

Figure 8.28: TESLA-type HOM coupler.

must correct for slow changes in the cavity frequency due to changes in the liquid-helium bath-pressure, or in the lengths of the cavity and He vessel support system. Tuning is achieved by varying the total length of the cavity within its elastic limit, so that the field flatness is preserved. The tuning coefficient of a 2-cell cavity is of the order of 50 Hz/mm. (Plunger tuners are not advisable in superconducting cavities because of moving parts and the danger of dust.)

With a mechanical tuner, the length of the cavity is controlled by an electromechanical system acting differentially with respect to the cavity body. If each cavity is enclosed in its own helium vessel, the latter must have some flexibility built in.

A mechanical tuning system is generally composed of a stepping motor, a gear box, a screw and nut assembly, and a lever arm with a flex mechanism attached. A fast piezoelectric element can be added for fine tuning, compensating Lorentz force detuning, Fig. 8.26, as well as microphonics. Figure 8.29 shows the lowest frequency vibrational mode of the two-cell cavity that could be excited by vibrations. The stiffness will be increased to raise the frequencies of this and other mechanical modes.

Alternatively a thermal tuner could be considered, modeled after the LEP system [16]. This uses three Ni tubes as tuner bars located in the cryomodule insulation vacuum. The tuner rib cage can also help increase the mechanical resonant frequency of cavity longitudinal modes. For slow tuning in one direction (constriction) the temperature of the tubes is lowered by flowing cold helium gas. For tuning in the opposite direction the temperature is raised by centrally located electric heaters. The typical tuning speed is 10 Hz/sec. Heat losses are minimized by counter-flowing cold He gas through the tuner

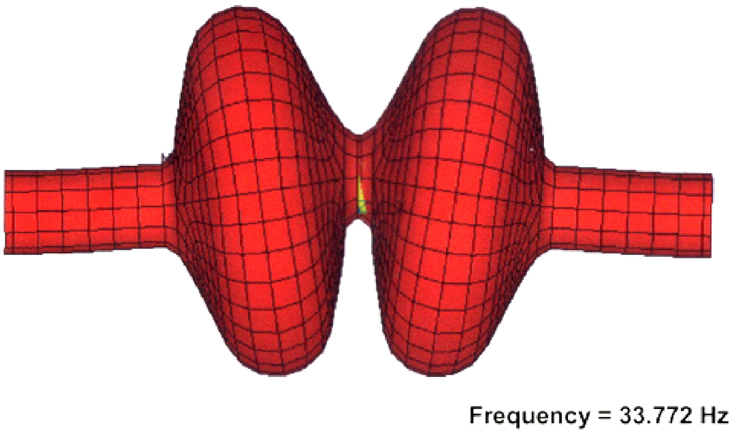

Figure 8.29: Lowest vibrational mode of 2-cell cavity.

tubes. For fast tuning, coils can be wound around the Ni tubes to produce a magnetic field that changes the length of the tubes by the magnetostrictive effect. Rapid (ms) tuning ranges of kHz are possible.

Tuners are an active part of the complete rf low-level control system, which stabilizes the frequency, amplitude and phase variations induced by sources such as the rf drive, beam current variations, Lorentz force detuning, and microphonics.

8.5.5 Cryogenics for SCRF

Figure 8.30 shows a 3D CAD model of the long cryomodule with four 2-cell units and a focusing magnet. Each cavity has two input couplers, one on each end, and two HOM couplers, also one on each end. Mature cryomodule designs (see Fig. 8.31), available at CERN for LEP-II and LHC will be adapted to the Neutrino Factory needs. Based on scaling from LEP 12.5-m long cryomodules, 4.5 K static heat leaks of 100 W per cryomodule are expected. Thin beryllium windows will be placed on the beam line at each end of the cryomodule to protect the cavity vacuum and to keep the cavity surfaces clean during installation into the beam line. Tables 8.8, 8.9 and 8.10 give cryomodule parameters. Table 8.11 gives a summary for the total SCRF requirements. The hardware implementation of the refrigerator is described in Chapter 11.

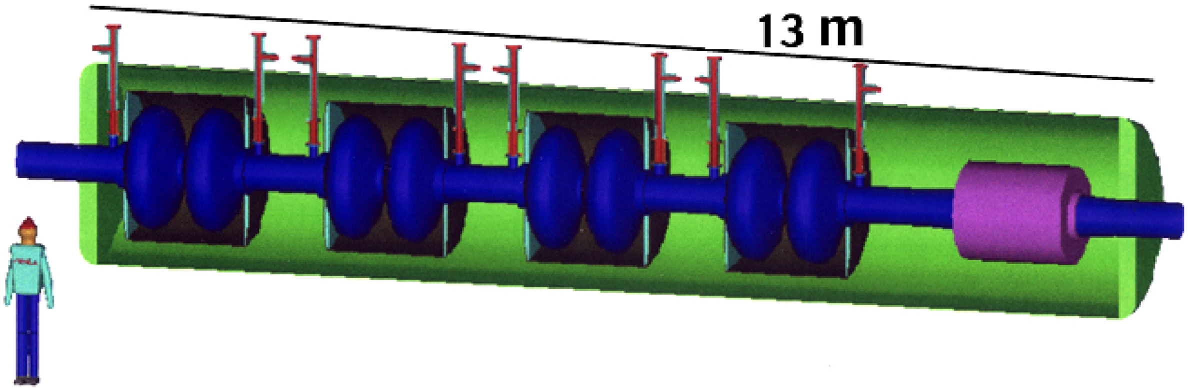

Figure 8.30: Long cryomodule.

Figure 8.31: LEP cryomodule.

Table 8.8: Short cryomodule parameters.

No. of cryomodules (in linac)	11
No. of 2-cell cavities in one cryomodule	1
No. of input couplers	2
Overall length (m)	5
Active length (m)	1.5
Cavity dynamic heat load at 2.5 K (W)	18
Couper dynamic heat load at 2.5 K (W)	1
Coupler static heat load at 2.5 K, 5–8 K, 40–80 K (W)	2, 4, 40
Cryomodule static heat load at 2.5 K, 5–8 K, 40–80 K (W)	6, 60,600
Total 11 cryomodule heat load @ 2.5 K, 5–8 K, 40–80 K (W)	300, 700, 7000

Table 8.9: Intermediate cryomodule parameters.

No. of cryomodules (in linac)	16
No. of 2-cell cavities in one cryomodule	2
No. of input couplers	4
Overall length	8 m
Active length	3 m
Cavity dynamic heat load at 2.5 K (W)	36
Couper dynamic heat load at 2.5 K (W)	2
Coupler static heat load at 2.5 K, 5–8 K, 40–80 K (W)	4, 8, 80
Cryomodule static heat load at 2.5 K, 5–8 K, 40–80 K (W)	7, 70, 700
Total 16 cryomodule heat load at 2.5, 5–8 K, 40–80 K	790, 1250, 12,500

8.5.6 Power Source for SCRF

The superconducting linac and recirculating linear accelerator (RLA) designs employ a total of 311 cavities. The linac contains 119 cavities running at a gradient of up to 17 MV/m. (The early part of the linac operates at a gradient of 15 MV/m). The rf pulse length is 3 ms and the average repetition rate is 15 Hz, although the recovery time between pulses is only 20 ms. Each cavity is driven by two 500 kW couplers. With a 20% rf power overhead, this works out to 1.2 MW per cavity and a total rf requirement of 375 MW.

Examination of the average power requirement demonstrates that a very high efficiency source is required. The best candidate for the required source is again a multi-

Table 8.10: Long cryomodule parameters.

No. of cryomodules (19 linac + 48 RLA)	67
No. of 2-cell cavities in one cryomodule	4
No. of input couplers	8
Overall length (m)	13
Active length (m)	6
Cavity dynamic heat load at 2.5 K (W)	$4 \times 19 = 76$
Couper dynamic heat load at 2.5 K (W)	$8 \times 0.5 = 4$
Coupler static heat load at 2.5 K, 5–8 K, 40–80 K (W)	8, 16, 160
Cryomodule static heat load at 2.5 K, 5–8 K, 40–80 K (W)	10, 100, 1000
Total 67–cryomodule heat load at 2.5 K, 5–8 K, 40–80 K (kW)	6.6, 7.8, 78

Table 8.11: SCRF overall parameters for a Neutrino Factory.

No. of cryomodules	94
No. of 2-cell cavities	311
No. of input couplers	622
Overall length (m)	1054
Active length (m)	467
Filling factor	0.44
Total voltage (GV)	7.5
Average real estate gradient (MV/m)	7.8
Total heat load at 2.5 K, 5–8 K, 40–80 K (kW)	7.7, 9.7, 94
Cryo load (with ×1.5 safety factor) 2.5 K, 5–8 K, 40–80 K (kW)	11.6, 14.6, 141
Assuming efficiency multipliers of 600, 225 , 20	
AC power for refrigeration (MW)	13
Total peak rf power (with 20% margin for control/losses)(MW)	362
Average rf power (MW)	16.3
AC power for rf (efficiency multiplier = 2) (MW)	35.6
Total AC power (MW)	49

beam klystron (MBK). This could be the same basic design as that used for the NCRF system but with increased thermal capacity to handle the increased duty factor. Thompson has developed a 7-beam MBK with an efficiency near 70%, see Section 8.3.1 and reference [2]. Scaling this design to 201.25 MHz would produce a 5 MW, 19 beam MBK with each beam having a perveance of 5×10^{-5}. The tube, with gun and collector, would be about 5.7 m in length and could be manufactured by industry after some initial R&D. A 37-beam MBK has also been developed by other groups [5].

Each tube will drive four cavities through 8-way power splitters. The specifications for the modulator, an IGBT-type like that described in Section 8.3.3 for the NCRF, are 50 kV at 142 A, with an average power of 320 kW. To save costs, the modulator will be designed to operate two 5 MW tubes, requiring twice the current and average power rating. A total 0f 78 tubes and 39 modulators are required to supply the rf power requirements. The multi-beam klystron may be designed with a vapor-cooled collector to save on the cooling water requirement. Such a system is at least ten times more efficient than conventional water cooling. With vapor cooling, each tube will require 120 gpm of near-room-temperature cooling water with a total installed capacity of 9,360 gpm. Assuming an efficiency of 95%, each modulator station will require 694 kW of installed AC power for a total of 27 MW.

8.6 Conclusions

The normal conducting and superconducting systems have continued to evolve since Study-I. Both cavity designs have been studied in some detail and feasible solutions have been developed for the required cooling channel and acceleration parameters. Ongoing R&D programs are addressing the practical aspects of cavity fabrication and conditioning. The cooling channel layout, though densely packed, has shown the feasibility of assembling all of the vital components. There is room for further optimization of the cooling channel, notably by adjusting the total cell length, to reduce the rf power requirements and reduce the superconducting magnet costs. The superconducting rf accelerating section has been developed using design choices that are consistent with the state of the art at various laboratories around the world.

Bibliography

[1] Daryl W. Sprehn, *MBK Calculations*, Feb 26, 2001; N. Holtkamp and D. Finley, eds., *A Feasibility Study of a Neutrino Source Based on a Muon Storage Ring*, Fermilab-Pub-00/108-E (2000), Chapter 10, p. 10-17, and 19.
http://www.fnal.gov/projects/muon_collider/nu-factory/nu-factory.html

[2] A. Beunas, G. Faillon, THOMSON TTE, France, S. Choroba, A. Gamp, DESY, Germany *A High Efficiency Long Pulse Multi Beam Klystron For The Tesla Linear Collider*, Submitted to PAC 2001.

[3] R.A. Rimmer, N. Hartman, D. Li, Al. Moretti, T. Jurgens *Closed-Cell 201.25 MHz rf Structures for a Muon Cooling Channel*, submitted to PAC 2001.

[4] N. Hartman, D. Li, J. Corlett, *Thin Beryllium Windows - Analysis and Design Status*, http://www-mucool.fnal.gov/mcnotes/muc0180.pdf.

[5] A. Larionov, International Workshop on Pulsed RF Sources For Linear Colliders (RF93), July 5-9, 1993, Dubna-Protvino, Russia.

[6] H. Padamsee, J. Knobloch and T. Hays, *RF Superconductivity for Accelerators*, John Wiley and Sons, 1998.

[7] P. Brown et al., *Proceedings of the 9th Workshop on rf Superconductivity* (1999) ed. by B. Rusnak, p. 1.

[8] D. Proch, *Proceedings of the 9th Workshop on rf Superconductivity* (1999) ed. by B. Rusnak, p. 19 and D. Trines.,*ibid.*, p. 605.

[9] E. Chiaveri, *Proceedings of the 1996 European Particle Accelerator Conference*, ed., S.Myers et al., Barcelona, Spain, IOPP Publishing, Bristol, p. 200 (1996).

[10] E. Chiaveri, *Proceedings of the 9th Workshop on rf Superconductivity* (1999) ed. by B. Rusnak, p. 352. and S. Bauer et al., *ibid.* p. 437.

[11] C. Reece, *Proceedings of the 8th Workshop on rf Superconductivity*, ed. by V. Palmieri and A. Lombardi (1998) p. 138.

[12] T. Furuya et al., *Proceedings of the 9th Workshop on rf Superconductivity* (1999) ed. by B. Rusnak, p. 31.T; and S. Mitsunobu, *ibid.* p. 505.

[13] S. Simrock et al., *Proceedings of the 9th Workshop on rf Superconductivity* (1999) ed. by B. Rusnak, p. 92.

[14] E. Somersalo et al., *Proceedings of the 1995 Particle Accelerator Conference*(1996), Dallas Texas, p. 1623.

[15] J. Sekutowicz, TESLA Note, 94-07 (1994).

[16] G. Cavallari et al., *Proceedings of the 3rd Workshop on rf Superconductivity* (1988) ed. by K. Shepard, p. 625.

Chapter 9

Induction Linac

9.1 Induction Accelerators for the Phase Rotator System

The principle of magnetic induction has often been applied to the acceleration of high-current beams in betatrons and in a variety of induction accelerators [1]. The induction linac (IL) consists of a simple nonresonant structure where the drive voltage is applied to an axially symmetric gap that encloses a toroidal ferromagnetic material. The change in flux in the magnetic core induces an axial electric field that provides particle acceleration. This simple nonresonant (low-Q) structure acts as a single-turn transformer that can accelerate beams of hundreds of amperes to tens of kiloamperes, limited only by the drive impedance. The IL is typically a low-gradient structure that can provide acceleration fields of varying shapes and time durations from tens of nanoseconds to several microseconds. The efficiency of the IL depends on the beam current, and can exceed 50% if the beam current exceeds the magnetization current required by the ferromagnetic material. The acceleration voltage available is simply given by the expression $V = AdB/dt$. Hence, for a given cross sectional area A of material, the beam pulse duration influences the energy gain. Furthermore, there is a premium put on minimizing the core diameter, as this impacts the total weight, or cost, of the magnetic material. Indeed, the diameter doubly impacts the cost of the IL, since the power to drive the cores is proportional to the volume as well.

To meet the waveform requirements during the beam pulse, we make provisions in the pulsing system to maintain the desired $\frac{dB}{dt}$ during the useful part of the acceleration cycle. This can be done in either of two ways: by using the final stage of the pulse forming network (PFN) or by using the pulse-compensation network in close proximity

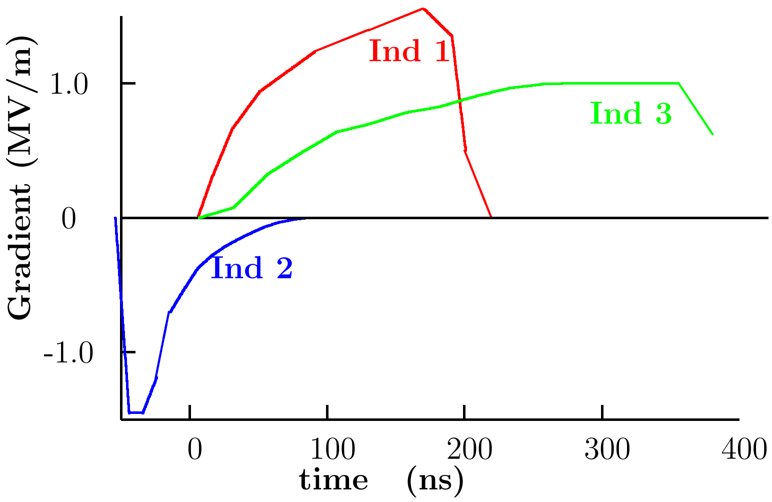

Figure 9.1: Acceleration waveforms for induction 1, 2 and 3.

to the acceleration cell.

The choice of magnetic materials is made by testing various materials, both ferromagnetic and ferrimagnetic; not only to determine the properties that are essential in this application, possible materials will include the nickel-iron, silicon steel, amorphous, and various types of ferrites, but on the energy losses in the magnetization process, which directly impact the cost.

9.1.1 Accelerator Waveforms

Parameters and pulse shapes from this study, compared with Study-I [2] have evolved toward considerably improved physics performance and less demanding accelerator waveforms, avoiding the need for multipulsing.

The present baseline design results in the acceleration waveforms shown in Fig. 9.1. The waveforms for IL1, IL2, and IL3 are all unipolar.

Although IL1 and IL3 could possibly be combined, it became preferable for technical reasons, and to reduce the risk factors, to separate the two functions (with a small penalty in economics). (A combined IL2 and IL3 would require the application of *branched magnetics* to achieve two waveforms that are independently controllable in shape and timing. The branched magnetics approach could lead to a 5-10% cost savings, but at more risk, since this approach has only been applied to small benchtop prototypes but not to presently operating induction accelerators. This approach will be examined in Appendix B.)

9.1.2 Magnetic Material

A number of induction linac have been constructed in the past that cover the pulse duration of the three units required by the Neutrino Factory. None of these accelerators, however, has gradients and energy gains that are as high. To satisfy the requirements in an economically reasonable design, it is imperative to choose a magnetic material, and a pulsing system, that minimize the cost but still achieve the reliability and performance required.

In the past two decades, great strides have been made in the development of a magnetic material that is replacing all previous ones in the 60-Hz power industry because of its low loss, ease of manufacturing, and low cost. Several alloys are made in ribbon form by rapidly quenching a stream of molten material on a cold rotating drum. The ribbon thickness is typically 25 μm and can be of any width from 5 to 20 cm. Because the ribbon is so thin, and has higher resistivity than other ferromagnetic materials, it is directly applicable to short pulse applications. In short pulse applications where the rate of magnetization (dB/dt) is very high, tens of volts are generated between the layers of ribbon when it is wound into a toroid. Thin insulation such as 2-4 μm Mylar must be used between layers to insure that the ribbon layers are sufficiently insulated to hold off the voltage generated.

The soft magnetic properties can be improved by annealing. Unfortunately, this procedure, although well below the crystallization temperature, embrittles the material, making it nearly impossible to wind into a toroid. Annealing can be done after winding if the insulating material between layers has a sufficiently high melting point. Annealing is not an option when Mylar is used. Coatings have been developed that allow annealing after winding, but at the present time they are not fully developed and do not hold off sufficient voltage per turn. Because the losses at high magnetization rates are almost entirely due to the eddy current losses, very little is lost in our application using the material "as cast" or unannealed.

To choose the appropriate alloy of this amorphous material it is important to measure the properties such as flux swing (ΔB) and magnetization (ΔH) at the appropriate pulse duration or magnetization rate (dB/dt). Figure 9.2 shows the losses in J/m^3, at different rates of magnetization. It can be seen that above T/μs the losses increase linearly with magnetization rate. From Fig. 9.2 it appears that the lowest loss material is the alloy 2705M with the lowest ΔB of about 1.4 T while the highest loss material is 2605CO

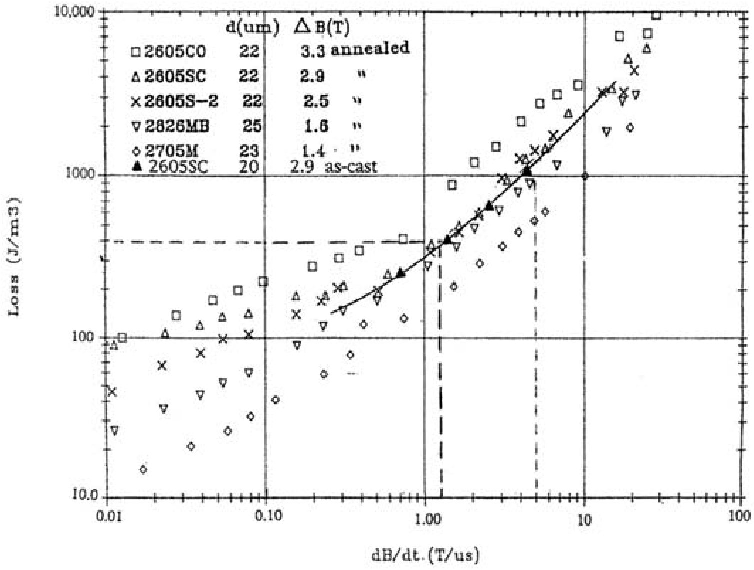

Figure 9.2: Losses (J/m^3) of several amorphous alloys as a function of magnetization rate (dB/dt).

with a ΔB of about 3.3 T. The optimum material is selected by considering the ΔB, the losses (J/m^3) and the cost per kilogram. Two alloys which are not plotted on this chart (Fig. 9.2) are the 2605SA1, used exclusively in the 60-Hz power industry, and the 2605S3A, which is used in pulse transformer applications. The SA1 material offers the potential for greatest savings since it is mass produced for the power industry, but it has not been investigated as thoroughly as the SC or S3A materials at the very short pulse regime of interest here. For this reason the SC alloy is chosen here since it has been used recently in an induction accelerator for radiography at the Los Alamos National Laboratory and extensive technical and cost data exist. The S3A also offers a good choice since it has been used extensively in the AVLIS program at the Lawrence Livermore National Laboratory. The SA1 alloy will be investigated in the near future as part of our R & D program since, as mentioned previously, it offers the greatest possibility for cost savings.

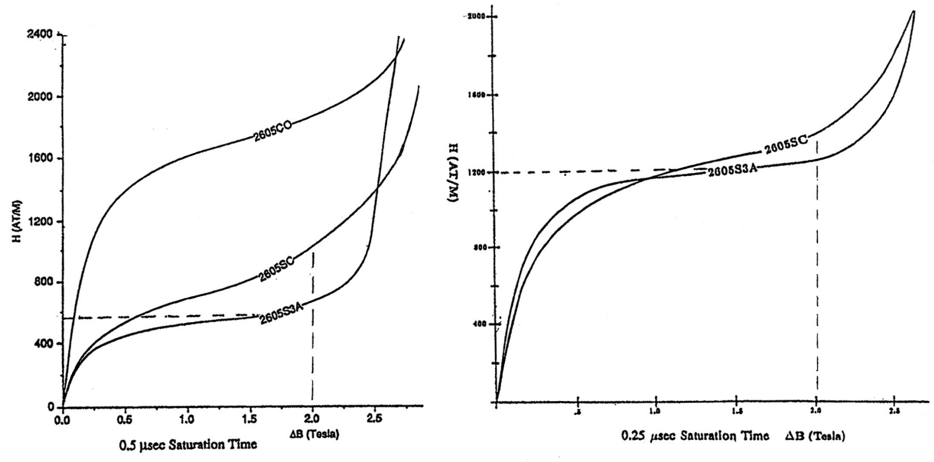

Figure 9.3: Hysteresis for 2605SC and 2605S3A at two different magnetization rates.

9.1.3 Induction Linac 1 Cell

From the specifications 1 in this Study, IL1 is 100 m in length and has the acceleration waveform shown in Fig. 9.1. The waveform has a full-width-half-maximum (FWHM) of about 180 ns, with an approximately exponential rise time of 100 ns and a fast fall time. The significant portion of the acceleration cycle is during the rise time; the fall time is unimportant. In fact, the fall time will be longer than indicated by the waveform since the energy stored in the cell inductance will decay with a time constant $t = L/R$ of the drive circuit. The L/R of the fall time will be similar to the rise time, hence, the actual FWHM will be about 250 ns. Since a 1-m section must allow axial space for the cryogenic feed lines and for vacuum pumping, the maximum allowable space for the core is 712 mm. To obtain the lowest cost for the amorphous material, the alloy should be cast in widths of 101.6 mm (4") or greater. Manufacturing limits, therefore, dictate a maximum number of cells that is a multiple of 101.6 mm. For our case, we select 7 cells.

From the required gradient we now have a basis for calculating the cross-sectional area of the magnetic material for IL1. From $V = A(dB/dt)(\mathrm{PF})$ we can calculate the ΔR knowing the ΔZ and the packing factor (PF=0.75). The hysteresis loop for the two alloys, 2605SC and 2605S3A, are shown in Fig. 9.3.

Although the total flux swing to saturation is over 2.5 T, the actual working flux swing (ΔB) is chosen as 2.0 T so that the pulse generator drives into a more linear load.

The required voltage for each of the seven cells that constitute one meter of acceleration is 214.3 kV. The actual cross-section is

$$A = (r_2 - r_1) * w = \frac{V\Delta t}{\Delta B(PF)} \tag{9.1}$$

so

$$(r_2 - r_1) = frac(214.3 \times 10^3)(250 \times 10^{-9})(2.0)(0.75)(r_2 - r_1) = 0.325 \text{ m}. \tag{9.2}$$

The inside radius of the core is set by the outside radius of the superconducting solenoid at a minimum of 0.4 m. Preliminary calculations of the leakage flux at the solenoid gaps indicate that this flux, which is orthogonal to the magnetization flux, can be of the order of a few thousand gauss at the 0.4 m radius. From previous tests for the Advanced Test Accelerator (ATA) and the Dual-Axis Radiographic Hydro Test (DARHT) [3] accelerator, this is acceptable. Nonetheless, this issue should be investigated further with laboratory tests to insure that the flux swing of the induction cell is not reduced by this stray flux. To be conservative, we set the inside radius of the actual amorphous material at 500 mm. The magnetizing current and the losses can now be calculated. The magnetizing force $\Delta H = \Delta I/\pi d$ where d is the average diameter or $d = r_2 + r_1 = 1.35$ m. From Fig. 9.3 for a 0.25 μs saturation time we find that the magnetizing force is $\Delta H = 1200$ A/m or $\Delta I = 5{,}087$ A, and the loss is $U = V\ \Delta I\ \Delta t$ or $U = (214.3 \times 10^3)(5.087 \times 10^3)(250 \times 10^{-9}) = 272.5$ J/cell. The magnetic material volume, including the mylar insulation is $V = \pi(r_2^2 - r_1^2)(\Delta z)$, or V=0.151 m^3. With a packing factor of 0.75, the actual volume of amorphous material is 0.113 m^3, and at a density of 7290 kg/m^3 it weighs 825 kg. The core losses could also have been calculated from Fig. 9.2, which shows that the losses per cubic meter at a magnetization rate $dB/dt = 2.0$ T/0.25 μs, are 2 kJ/m^3 for a total of 262 J, slightly lower than the estimate above. The loss calculations above determine the drive power required by the pulse generator for one cell. For seven cells $P = 7VI$, and with $V = 214.3$ kV, $I = 5.09$ kA, $P = 7.63$ GW and the impedance $Z = V/7I = 6.0\Omega$.

9.1.3.1 High Voltage Design of Cell

Figure 5.8 shows a cross section of the induction cell. The cell is driven by two high voltage cables at 180°. The high voltage cables plug into two connections, of the type used on the DARHT accelerator, that are part of the compensation network box. The acceleration gap is 1 cm and is oil filled. From Fig. 9.5, which shows the voltage breakdown in oil for different pulse durations and surface areas, it appears that the safety factors are more than adequate, that is, the actual breakdown is about twice the operating voltage. The highest voltage stress occurs at the outside radius of the core where one half of the driving

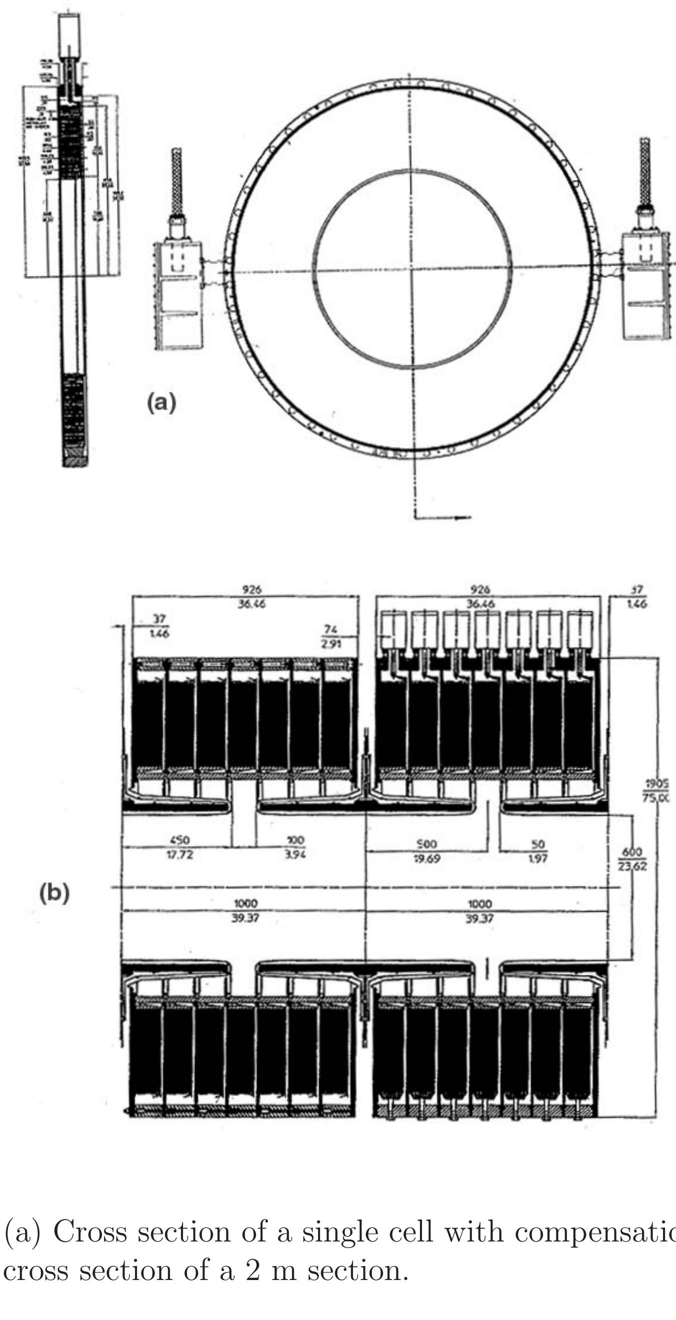

Figure 9.4: (a) Cross section of a single cell with compensation network boxes; (b) cross section of a 2 m section.

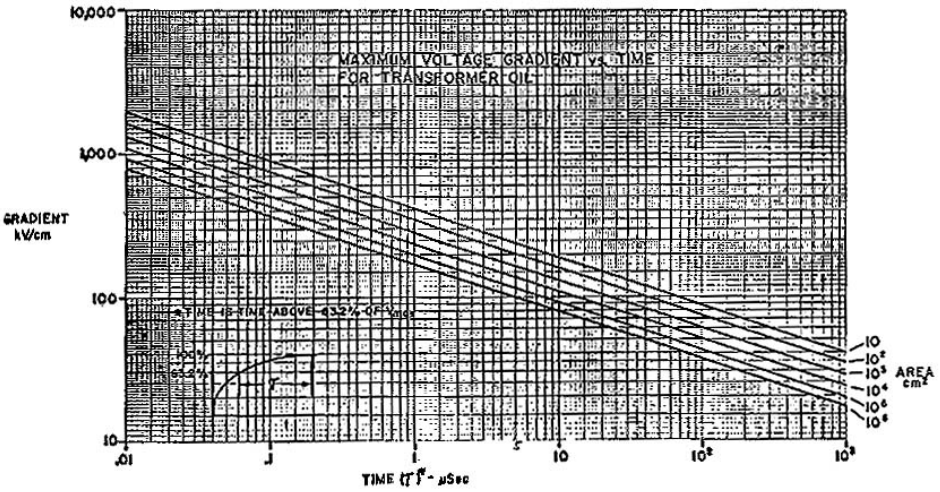

Figure 9.5: Short-pulse voltage breakdown in oil.

voltage appears from each side of the core to ground. Insulation is done with ten layers of 50 μm mylar with oil impregnation.

The oil-to-vacuum interface insulator is designed so that on the vacuum side the field lines form a 30° or greater angle with the insulator to achieve the highest possible voltage holding. The empirical curve in Fig. 9.6 shows the voltage flashover for different angles. For our design, the maximum surface gradient on the insulator is nearly one order of magnitude lower.

The highest voltage gradient occurs between the solenoid housings. Here the spacing is 100 mm and the radius is 30 mm. Using a cylindrical geometry, the maximum gradient is about 150–200 kV/cm. Figure 9.7 shows field emission after 200 ns for different types of surfaces. A standard electropolished stainless steel surface is marginally acceptable for our purposes. To be prudent, the surfaces should be greened. In a subsequent optimization, the gradient will be reduced somewhat by redesigning the nose pieces.

9.1.4 Induction Linac 2 Cell

From the specifications shown in Fig. 9.1 for IL2, the deceleration pulse has an unspecified rise time (from zero to a negative value) and a fall time of about 50 ns (from a negative

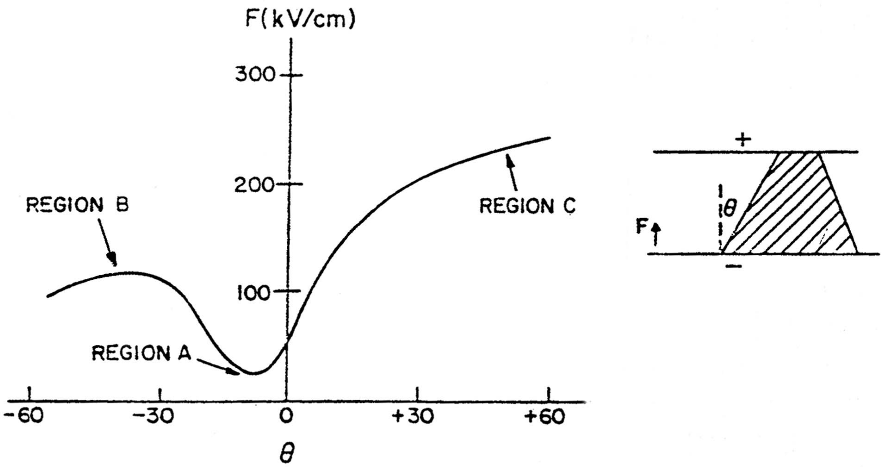

Figure 9.6: Flashover voltage with a 30-ns pulse for different cone angles.

value back to zero) that is a significant portion of the waveform.

Induction accelerators with pulse durations of less than 100 ns have traditionally used nickel-zinc ferrites as the magnetic material of choice. This choice was the appropriate one a decade or two ago when the last short-pulse induction accelerator was built, since the amorphous materials at that time were not of a very high quality and were more expensive than they are today. The choice of ferrites also was logical if one compares their losses to those of amorphous materials at saturation times of 50 ns. We can see from Fig. 9.8 that, if full saturation is achieved in 50 ns, the losses for ferrites (CMD 5005) are about 800 J/m^3 while the losses for amorphous materials (2605SC) are about one order of magnitude higher. That is, even though the flux swing for amorphous materials is five times greater than those of the ferrites, the losses are more than ten times greater (at full saturation). On the other hand, the cost of ferrites has quadrupled in the past two decades while the cost of amorphous materials has decreased considerably. This makes it imperative to take another look at using amorphous materials of the same cross section (volume) as the ferrites. Then the flux swing would be much lower than that at full saturation, as would be the magnetization rates, and hence, the losses. To make the best comparison, designs were made using both the ferrites and the amorphous materials. Using the standard 101.6 mm width (w) and a ΔB (from Fig. 9.9) for the ferrite CMD-5005 the area $A = w(r_2 - r_1) = V\Delta t/\Delta B$. From Fig. 9.1 the significant part of the

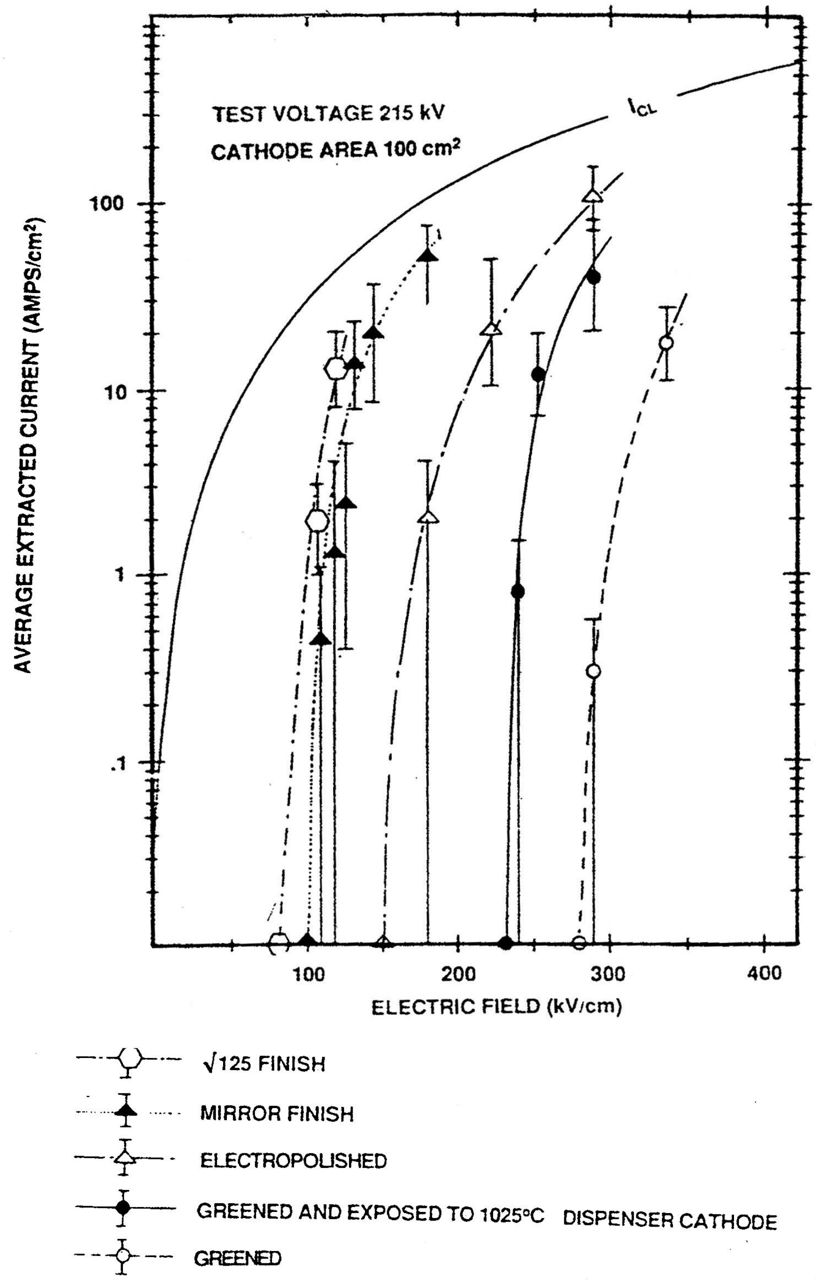

Figure 9.7: Current density after 200 ns for different surface preparations.

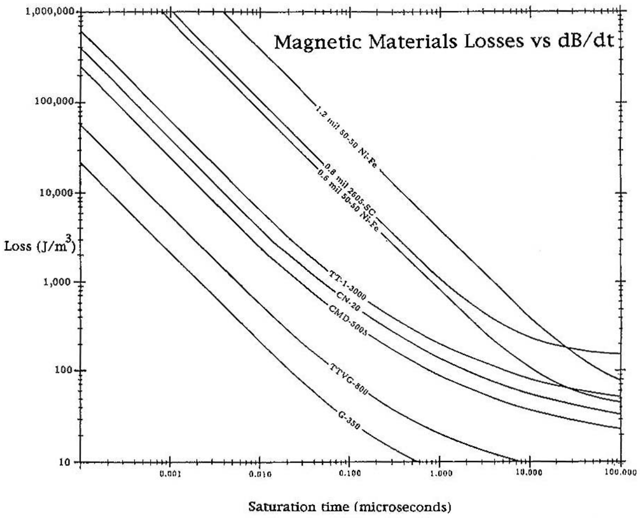

Figure 9.8: Magnetic material losses for different saturation times.

acceleration waveform is the fall time while the rise time is unspecified and is determined by the pulse generators. Because of the large gap capacitance and the impedance of the pulse generator, the rise time will be nearly the same as the fall time so that the FWHM will be about 100 ns.

Using 100 ns as Δt and the voltage per cell V = 188 kV, the outside radius r_2 = 870 mm. From Fig. 9.9, the hysteresis curve for CMD-5005 indicates that ΔH = 1000 A/m and the losses will be 500 J/m^3. The ferrite volume, $V = \pi(r_2^2 - r_1^2) =$ 0.162 m^3 will result in 81 J of losses per cell requiring a drive current $I = 4.3$ kA. Taking the same cross-sectional area, but using the proporties of amorphous materials, we can compare the losses. Because the packing factor of the amorphous material will be 0.75 instead of 1, the flux swing will be 0.667 T and the magnetization rate $dB/dt = 6.67$ T/μs (for, 100 ns saturation). From Fig. 9.2, the losses for 2605SC are about 1400 J/m^3. The total losses, U, for the amorphous material will be U = (1400 J/m^3)(0.162 m^3)(0.75) or U = 170 J/cell. We conclude that losses using the amorphous material are about twice as high as those of the ferrites and, therefore, the cost of the pulse generator will be that much greater. Surprisingly, the economics still favor the amorphous material because its cost is about one-fourth of that of the ferrites. Even though the pulse generator doubles in cost, the net result is a saving of about 10%.

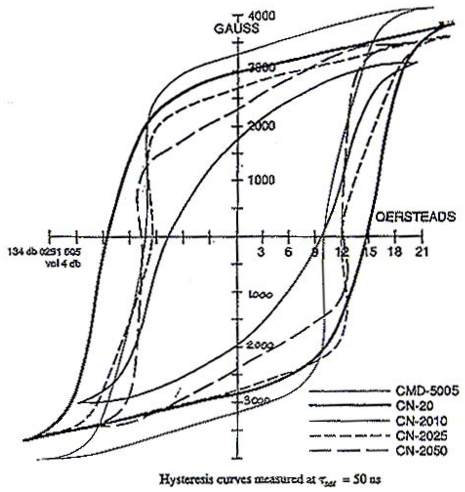

Figure 9.9: Hysteresis curves for various ferrites.

It is interesting to note that the design for IL2 is nearly identical to IL1, that is, $r_2 = 0.85$ m for IL1 and $r_2 = 0.87$ m for IL2, so in actuality, for manufacturing and design cost saving, the two cells can be identical. Since IL2 is a decelerating gradient, the induction cells for this accelerator are simply installed rotated 180° from those of Induction 1.

9.1.5 Induction Linac 3 Cell

Applying the same arguments used in the design of IL1, the FWHM for IL3 is 380 ns and the acceleration voltage $V = 143$ kV. The outside radius of this cell can now be calculated from $V\ \Delta t = A\Delta B(\mathrm{PF})$. The magnetization rate for this cell is lower since the saturation time is longer. For the same ΔB as in IL1, or $\Delta B = 2.0$ T, $dB/dt = 5.26$ T/μs, and the magnetization will be the average between the two cases shown in Fig. 9.3 or $\Delta H = 900$ A/m. Applying these parameters to the design of IL3, from $w(r_2 - r_1) = \frac{V\Delta t}{\Delta B(PF)}$ we get $r_2 = 857$ mm. The magnetizing current is $I = \pi H(r_2 + r_1) = 3.84$ kA and the cell losses $U = VI\Delta t = (143 \times 10^3)(3.84 \times 10^3)(380 \times 10^{-9}) = 209$ J. The volume of material is $V = \pi(r_2^2 - r_1^2)w = 0.155$ m^3, and the weight with a PF = 0.75, is 846 kg. Table 9.1 summarizes important parameters for the three induction accelerators.

It is evident from Table 9.1 that the three induction accelerators can be mechanically identical as far as induction cells are concerned. Each pulsing system will, of course, be

Table 9.1: Induction accelerator parameters.

Unit	MV/m	Length (m)	Δt (ns)	IR (m)	OR (m)	V_{cell} (m^3)	W_{cell} (kg)	ΔB (T)	ΔH (A/m)	Voltage (kV)	Current (kA)	Energy (J)	Weight (tons)
IL1	1.5	100	250	0.5	0.85	0.151	826	2.0	1200	214	5.09	273	578
IL2	1.5	80	100	0.5	0.87	0.162	886	0.67	2100	188	9.05	170	496
IL3	1.0	80	380	0.5	0.86	0.155	846	2.0	900	143	3.84	209	474

different.

The amorphous alloy taken for this Study was not optimized but was chosen because the most reliable information exists for it in the short-pulse applications and the most accurate cost data was available from a recent induction linac constructed at LANL for radiography. It is very likely that the alloy being mass produced for the power industry, 2605SA1, can be substituted for the 2605SC. The SA1 material has great potential for cost reduction, since it is mass produced in very large quantities. We will pursue testing samples of SA1 in the near future as part of the R&D program, and will begin negotiations with the scientific staff at Honeywell (Allied Signal) to explore making the material in thinner ribbon and less expensive than the SC material.

9.1.6 Pulsing System

IL1, IL2, and IL3 are driven by pulse generators with output voltages from 100–200 kV and currents in the tens of kiloamperes at pulse durations from 50 ns to 300 ns. The peak power levels exceed 1 GW and, except for spark gaps, no switches exist that are capable of operating reliably at the required repetition rates and power levels. The prefered option, then, is the nonlinear magnetic pulse compression modulator.

The use of saturable reactors for generating very high peak power levels was described by Melville [4] in 1951. The basic principle behind magnetic pulse switching [5] is to use the large changes in permeability exhibited by saturating ferri-(ferro) magnetic materials to produce large changes in impedance. The standard technique for capitalizing on this behavior is shown on Fig. 9.10. By using multiple stages, as shown, it is possible to compress a pulse of relatively low power and long duration into a pulse of very high peak power and very short duration, maintaining the same energy (except for a small core loss) per pulse. This is exactly the technique that allows us to use available thyratrons or solid-state devices to initiate the pulse and then pulse compress it to the desired peak power levels.

The principle of operation of the magnetic pulse compressor has been covered extensively in the literature but is briefly described here for completeness. Referring to Figure

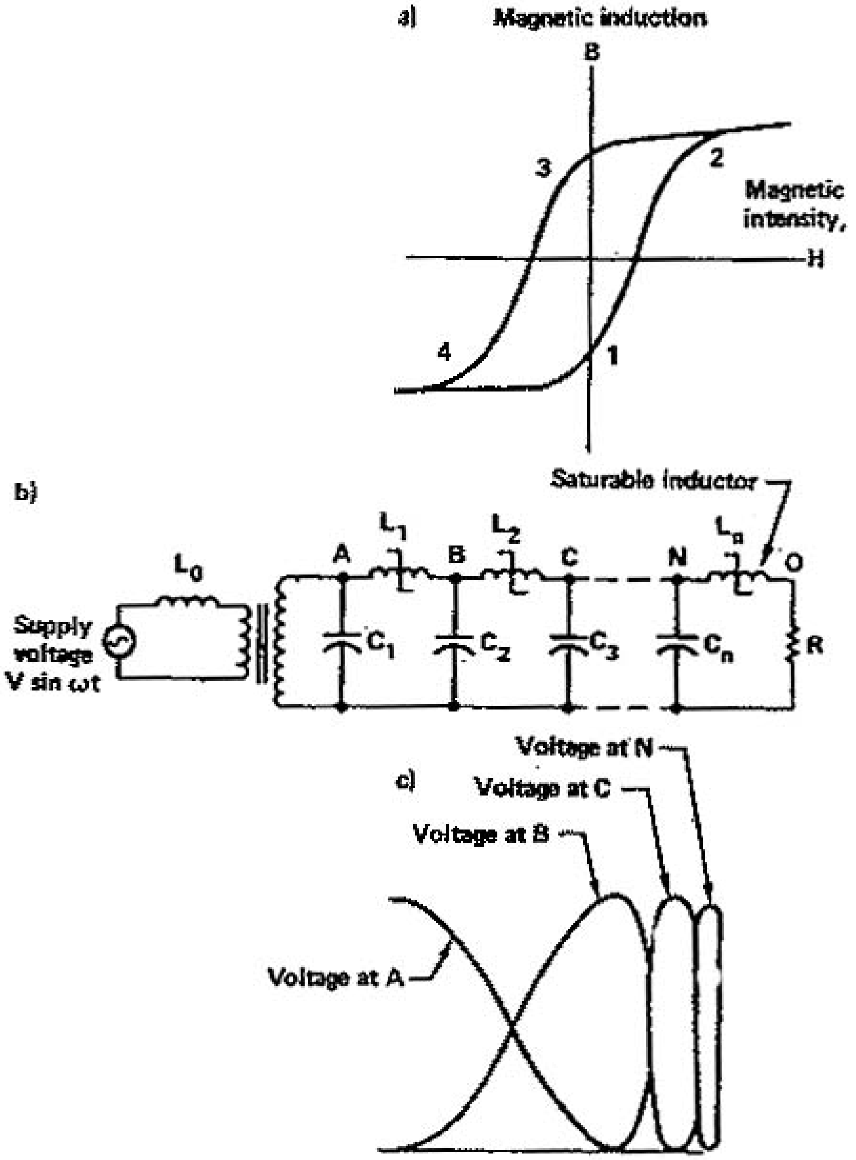

Figure 9.10: Principle of magnetic pulse compression.

5.14, capacitor C_1 charges through inductance L_0 until inductance L_1 saturates, becoming much less than L_0. Once this happens, C_2 will begin to charge from C_1 through L_{1sat} but since L_{1sat} is much less than L_0, C_2 charges more rapidly than C_1 did. This process continues through the successive stages until C_n discharges into the load through L_{nsat}.

To make this process efficient, we design each of these successive stages so that saturation occurs at the peak of the voltage waveform. Segment 1 to 2 in the hysteresis loop of Fig. 9.10 is the active, or high-permeability, region during which the inductor impedes current flow; the leveling off of the curve at point 2, reached at the peak of the voltage waveform, indicates core saturation when the inductor achieves a low impedance. During segment 2 to 4, the core is reset to its original state, ready for the next cycle.

9.1.6.1 IL1 pulse compressor

The requirement for IL1 is to generate an acceleration pulse shape and gradient shown in Fig. 4.5. Each accelerator cell previously described produces a voltage of 214 kV; after the beam traverses 700 of these cells it has gained 150 MV of energy. From Table 9.1, the necessary drive current for one cell is 5.09 kA for a duration (FWHM) of 250 ns. As previously mentioned, no switches exist that can produce this type of pulse directly. By investigating the optimum operating voltage and current of the switches, the required stages of compression are decided. Since thyristors have limits in dI/dt of several kA/μs and voltage limits of a few kV it can be seen that a large number of them in series and parallel combination will be required. Thyratrons also have limits on dI/dt and voltage but these limits are at least one order of magnitude greater than thyristors. Thyristors have practically unlimited life while thyratrons have an operating life of the order of 20,000 hours. Even taking into consideration replacement costs, the thyratrons offer a simpler and more economical pulse compression system (fewer stages).

For technical and economic reasons, the pulse compression system is designed to drive one meter or seven induction cells. The total energy required is $U = 273 \times 7 = 1.9$ kJ plus that needed to make up the additional losses incurred in the pulse compression scheme. The 500 J pulse compression system (Fig. 9.12), designed to replace the Advanced Test Accelerator spark gaps, achieved efficiencies greater than 90%. Allowing for 5% losses in the thyratron switches, 5% losses in the resonant charging and 5% in the power supply, the total input energy per pulse needed is 2.5 kJ and, at 15 Hz average repetition rate, the power for seven cells $P = 38.2$ kW; the total power for IL1 is $P_t = 3.82$ MW.

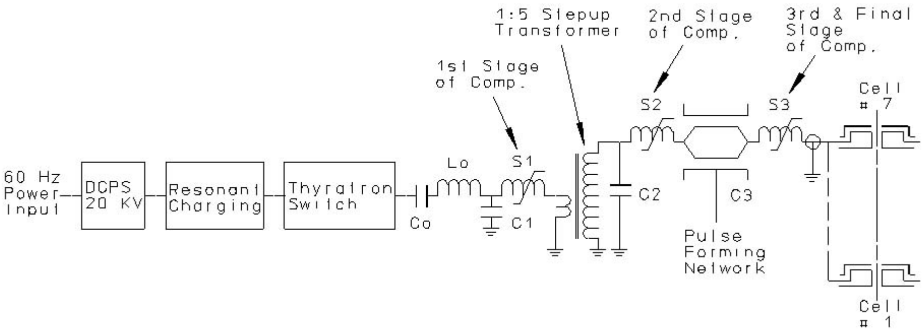

Figure 9.11: Simplified diagram of IL1 7-cell pulse generator.

9.1.6.2 IL1 7-Cell pulse generator

Figure 9.11 shows a simplified diagram of the pulse generator that will drive 7 cells of IL1 with a voltage pulse of 214 kV, 35.6 kA and a pulse duration FWHM = 250 ns. The resonant charger initiates the sequence by charging capacitor C_0 to $2 \times V_{DCPS}$ or 30–40 kV. The charging current through C_0 will have the effect of partially resetting the first stage compression and the step-up transformer. The reset of the other stages and the induction cells will be done by a separate pulse generator just prior to initiating the pulse sequence. The optimum saturable reactor is obtained by designing a time compression of about 3:1 and with three stages the total compression will be about 27:1. The thyratron switch will discharge C_0 in about 6.8 μs. As the magnetic switch, $S1$, saturates, it will discharge C_1 into the transformer primary with a time period of 2.25 μs. This primary voltage of 30 kV will be stepped up to 428 kV and charge C_2 with a $l - \cos(\omega t)$ waveform. The magnetic switch S_2 is designed to saturate at the peak of this waveform, which will charge the pulse forming network in 750 ns. Finally, the saturable reactor S_3 switch the PFN energy at the peak of that waveform, delivering the energy to the seven cells. The desired waveform will be achieved by tailoring the temporal impedance of the PFN to that of the nonlinear load of the cells. Further waveform tailoring is done with series inductors and an RC compensation network in the boxes on each side of the cells.

The total energy that must be switched by the thyratrons includes the system losses, and amounts to 2.5 kJ. This energy is stored in capacitor $C_0 = 5.66$ μF and is switched into C_1 through inductor $L_1 = 0.828$ μH with a series impedance $Z_0 = 0.382$ Ω, resulting

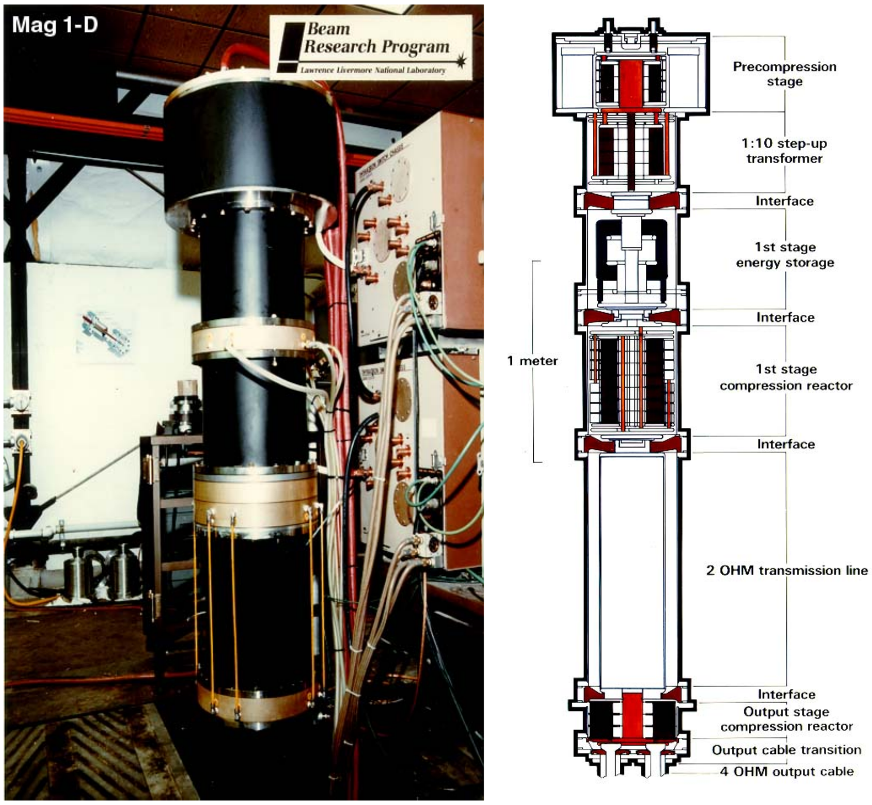

Figure 9.12: 500 J Mag 1-D magnetic pulse compression modulator driving the ETA II accelerator.

in a peak half-sine-wave current of 28 kA, for a peak power of 2.3 GW. Several thyratron options are available. The highest continuous-power thyratrons are the ceramic-envelope units, while the glass-envelope units are capable of nearly as high a peak power with low average power capability. Since the average power is moderate (38 kW) the appropriate choice for technical and economic reasons is the glass- envelope unit. To carry the 78 kA peak current, twelve parallel devices are used. To insure current sharing, each thyratron will switch its own capacitor which is $C_0/12 = 0.47$ μF. Except for thyratron replacement every 20,000 hours or more of operation, the pulse compression systems should be maintenance free since all components are passive devices.

9.1.6.3 IL2 pulse compressor

The pulse for the IL2 accelerator has a duration (FWHM) of 100 ns. Assuming an additional 5% loss (since the pulse compression system has to go one step further), the total input energy for seven cells would be $U = 1.6$ kJ and, at 15 Hz, would result in a power requirement of 24 kW. The total power requirement for IL1 is 1.9 MW, and its pulse duration is 100 ns FWHM. The shorter pulse duration would dictate an additional stage of pulse compression on the system described for IL1. However, since the energy for IL2 is 68% of IL1, it is possible to achieve the shorter pulse duration with the same number of stages simply by initiating the compression process with a shorter pulse. The design of each stage, of course, will be different and the transformer will have a step-up of 12:1. For IL2, $C_0 = 3.78$ μF and the compression for three stages is 36 for an initial discharge time of 3.6 μs with $L_0 = 0.347$ μH and $Z_0 = 0.303\Omega$. The peak current required of the twelve thyratrons is 99 kA, or 8.25 kA each.

9.1.6.4 IL3 pulse compressor

The pulse duration for IL3 is 380 ns FWHM. A pulse compression similar to IL1 with three stages is used. The transformer will have a step-up of about 10:1, and the three saturable reactors will be similar to those in IL1. The energy at the input is $U = 2$ kJ and, at 15 Hz average repetition rate, the input power per seven cells is 29.3 kW and the total imput power is $P_t = 2.34$ MW. With the input energy of 2 kJ, the capacitor C_0 $= 4.34$ μF and with an initial discharge time $t_0 = 10.3\mu$s, the inductor $L_0 = 2.46$ μH, and the series impedance $Z_0 = 0.753\Omega$, which results in a peak current of 40 kA. The total power required for IL1, IL2 and IL3 at 15 Hz average repetition rate is 8.2 MW. Including the efficiency of 90% for the DC charging power supplies, the total 60-Hz power requirement (see Table. 9.2) will be very nearly 9 MW.

Table 9.2: Energy and power requirements. * Assuming 90% efficiency.

Unit	Length (m)	Pulser energy (J/m)	Total energy (kJ)	P_{total} (15 Hz)* (kW)
IL1	100	2548	254.8	4247
IL2	80	1590	126.9	2115
IL3	80	1951	156.1	2602
Total power required from grid				8964

9.1.7 Mechanical Systems

In order to achieve the desired gradient for the three induction linacs, the induction cells are driven by the pulsing system in units of seven. Hence, these cells are mechanically assembled into one module by bolting together seven cells.

The individual cores would be assembled at the plant. The mandrel on which the amorphous material is wound supports the complete core. An additional support cradle is included on the OD of the core to insure that there is no sagging (Fig. 9.13). As specified under electrical requirements, the cores are wound with 101.6 mm wide ribbon with 3 μm mylar between layers and protruding 3 mm beyond the ribbon. As assumed earlier in this section, the complete core has a packing factor (PF) of about 75%.

The high-voltage insulator, which is the oil-to-vacuum interface, is assembled in seven sections for each module and voltage grading of each section is provided by making contact with the appropriate cell. Each section has a gradient ring, which insures that the field lines enter the insulator at an angle of about 30° to provide maximum voltage holding (Fig. 9.6). The seven section insulator is made of "Mykroy/Mycalex" and will be glued together as in the DARHT accelerator (Fig. 9.14). The induction module housing is fabricated and assembled using seven large rings fastened together by outside fixtures similar to those used in the Relativistic Two-beam Accelerator (RTA) at LBNL. The whole module is supported on the OD from these rings by a six-strut support system (Fig. 9.15). The support system allows for excellent alignment of each module with respect adjacent modules and the absolute beam line.

The vacuum system will consist of turbo pumps and cryopumps located every 5-10 modules. These pumps will be connected to a roughing line alongside the accelerator. Beam position and total current diagnostics will also be located at the pump-out station. Each module with its downstream SC solenoid magnet is assembled and aligned prior to installation in the beamline. After installation in the beamline, the module is aligned and the vacuum seal is fastened.

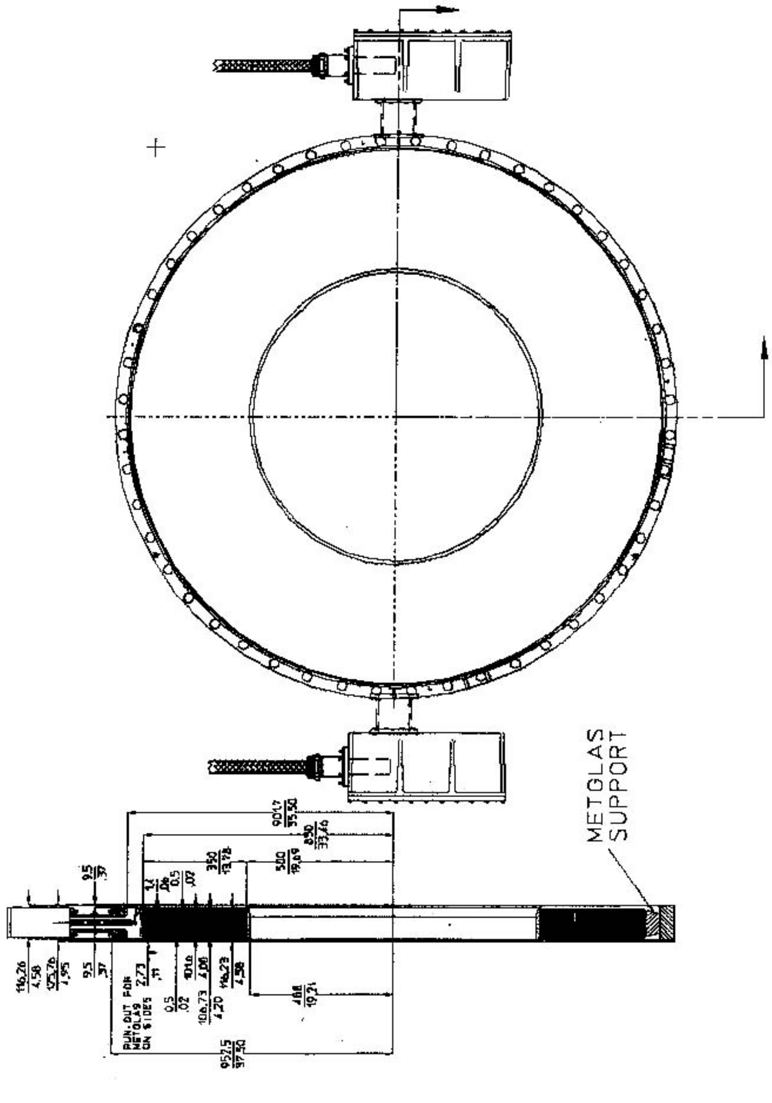

Figure 9.13: Metglas single-cell assembly.

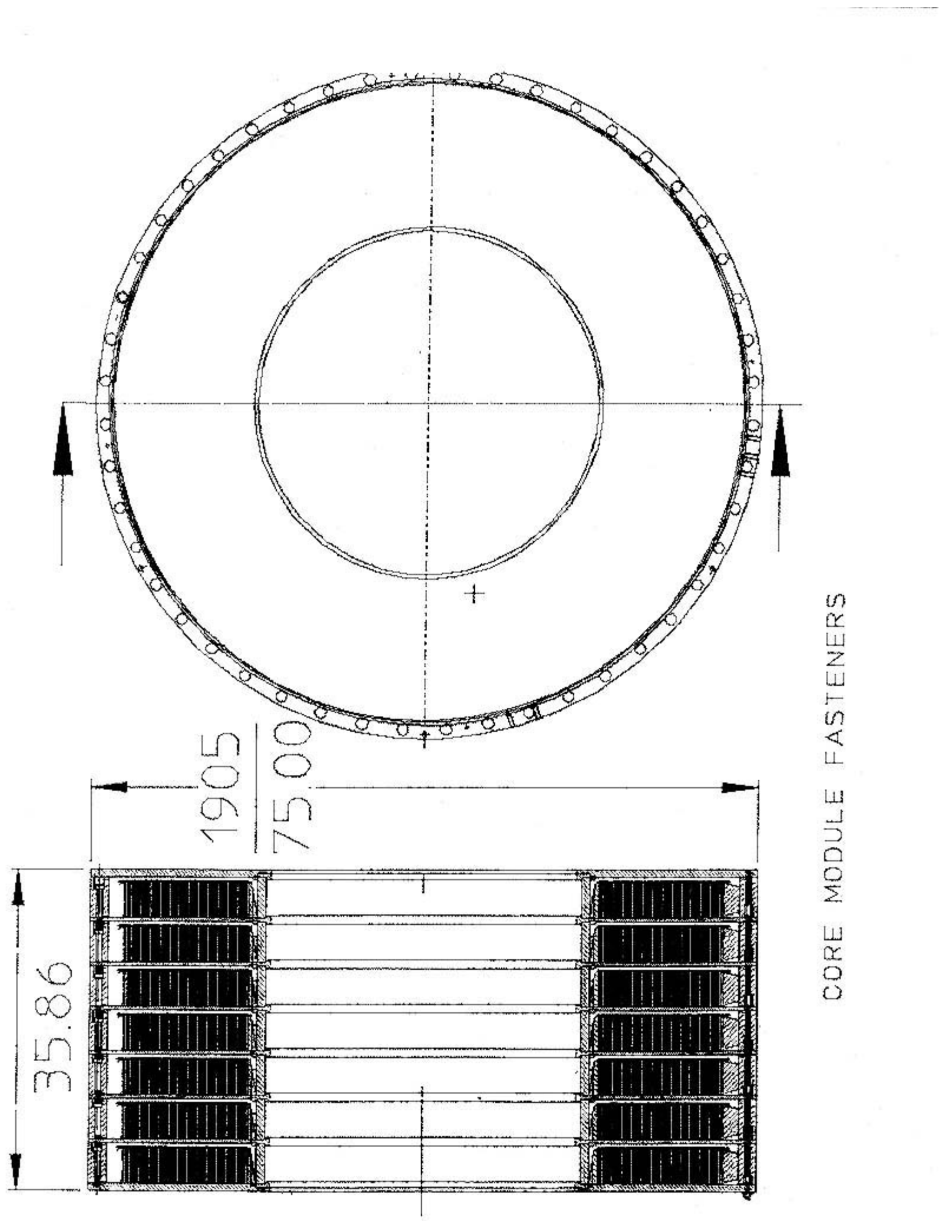

Figure 9.14: Seven-cell housing that forms one accelerator module.

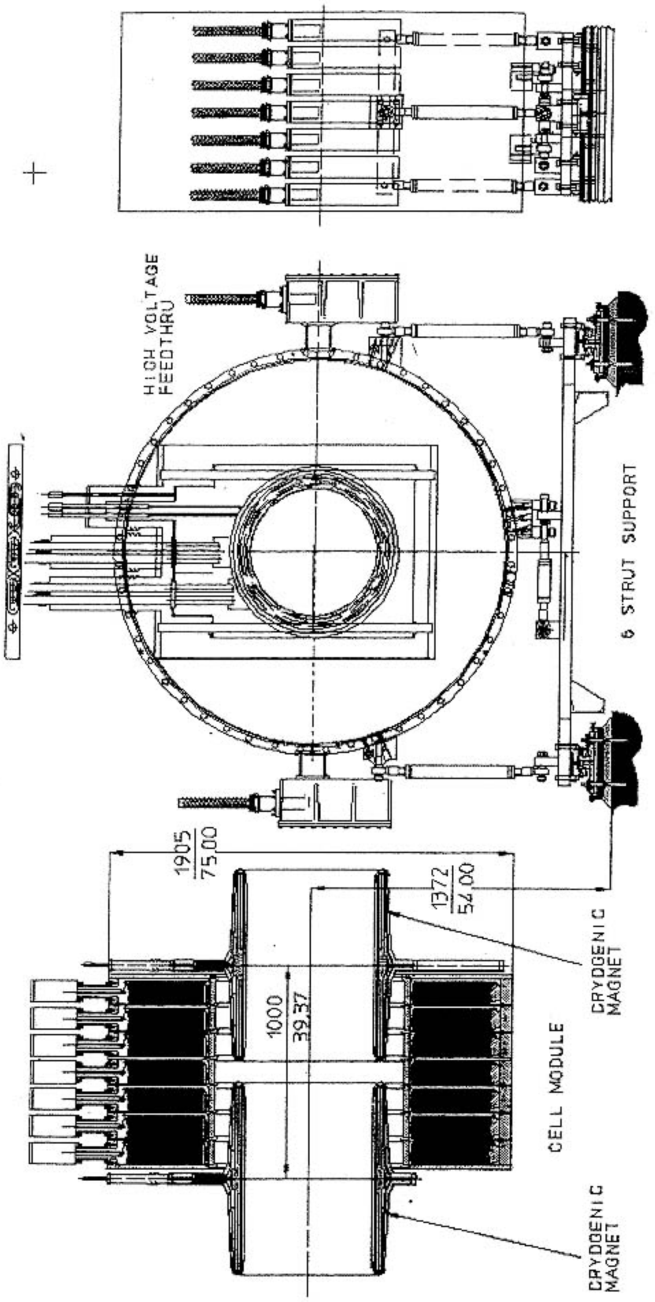

Figure 9.15: Six-strut module support system.

Bibliography

[1] N.C. Christofilos, *High-Current Linear Induction Accelerator for Electrons*, Rev. Sci. Instrum., **35**, July (1964).

[2] N. Holtkamp and D. Finley, eds., *A Feasibility Study of a Neutrino Source Based on a Muon Storage Ring*, Fermilab-Pub-00/108-E (2000), Chapter 5, p. 5-4. http://www.fnal.gov/projects/muon_collider/nu-factory/nu-factory.html

[3] M.J. Burns, et al., *DARHT Accelerators Update and Plans for Initial Operation*, Proc. 1999 Acc. Conf., p.617.

[4] W.S. Melville, *The Use of Saturable Reactors as Discharge Devices for Pulse Generators*, Institute of Electrical Engineers, **98**-Part III, May (1951).

[5] D.L Birx, *An Investigation into the Repetition Rate Limitations of Magnetic Switches*, UCRL-87278, (1982), Lawrence Livermore National Laboratory.

Chapter 10

Superconducting Solenoid Magnets

10.1 Introduction

The Neutrino Factory [1], [2], [3], beyond approximately 18 m from the target, requires three solenoid-based magnetic channels. In total, more than 530 m of solenoids with different magnetic strengths and bore sizes are used in order to prepare the muon beam for injection into the muon acceleration system. This is followed by the pre-acceleration linac with several different low-stray-field solenoids.

10.2 Decay and Phase Rotation Channel Solenoids

The decay and phase rotation region includes the muon decay channel, an induction linac (IL1), the mini-cooler and two additional induction linacs (IL2, IL3). This region extends from $z = 18$ m (from the target) to $z = 356$ m; within it, there are four types of solenoids.

- From $z = 18$ m to $z = 36$ m, the decay section has a warm bore diameter of 600 mm. Around this warm bore is a water-cooled copper shield that is 100 mm thick. The solenoid cryostat warm bore is 800 mm. The 18 m of decay solenoid is divided into six cryostats, each 2.9-m long. This same type of magnet is used for the 9-m long mini-cooling sections on either side of the field-flip solenoid. As a result, there are twelve magnets of this type.

- The IL1 solenoids, which extend from $z = 36$ m to $z = 146$ m, have a beam aperture of 600 mm diameter. Around the bore is a 10-mm-thick water-cooled copper radiation shield. The warm bore of this magnet cryostat is 620 mm in diameter. There are 110 magnets of this type.

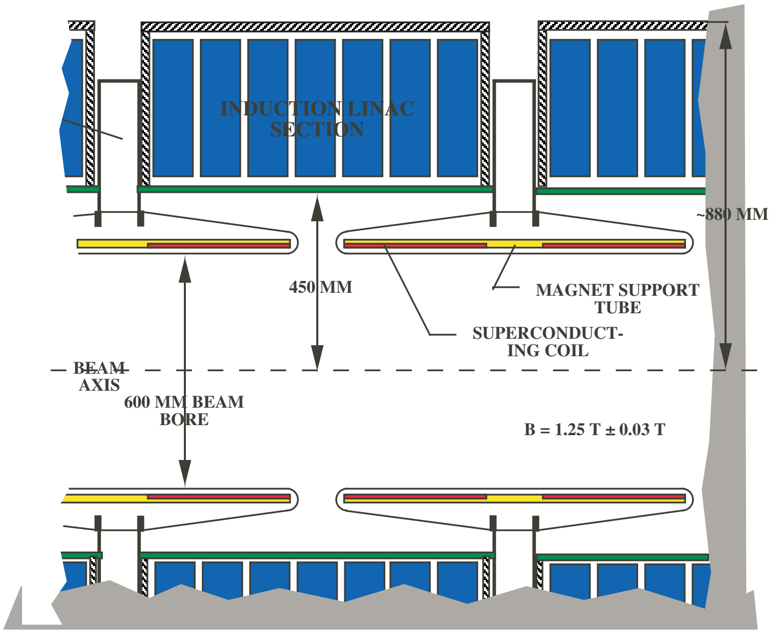

Figure 10.1: Cross section of the induction cell and mini-cooling solenoids.

- The IL2 and IL3 solenoids, and the drift between them, extends from $z = 166$ m to $z = 356$ m. These solenoids do not require a radiation shield and have a cryostat warm bore diameter of 600 mm. There are 190 magnets of this type.

- The field-flip solenoid between the two mini-cooling sections is 2.0-m long with a warm bore diameter of 400 mm. There is only one such magnet.

Table 4.1 shows the design parameters for all of these magnets; the last magnet, the 2-m long field-flip solenoid is not included. Figure 10.1 shows a cross section of the induction cell and mini-cooling solenoids.

The basic requirements for the phase rotation solenoids, from $z = 36$ m through $z = 146$ m and from $z = 166$ m through $z = 356$ m, are as follows: The magnetic induction in the phase-rotation and mini-cooling channel has been set to 1.25 T and the beam pipe diameter is 600 mm. The periodicity of the varying magnetic field on axis of the phase rotation channel has been set to 0.5 m, to avoid potential particle losses due to resonances in the channel. This constraint requires the coils in the cell to be of equal length with equal length gaps between them. A 1.0 m cell has two equal length coils and two equal length spaces between coils, yielding a period length for the magnetic field of 0.5 m. The radial thickness of the solenoid cryostat is minimized to permit the induction linac structure to be brought as close as possible to the axis of the machine. The distance of the induction cell from the magnetic field axis is also influenced by the magnetic flux leakage through the gaps between the superconducting coils. Therefore, the space between the induction linac cells must be minimized; this means that the space used for the cold mass support system, the electrical leads, and the cryogenic feed system must be kept to a minimum. In addition, steering dipoles are mounted on the inside of the solenoid coils. The pair of dipoles is 1.0 mm thick and they can correct alignment errors up to 5 mrad.

Figure 10.2 shows a cross section of a typical superconducting solenoid designed to generate an average induction of 1.25 T on the axis of the phase rotation induction linac. The inner bore radius of the solenoid cryostat is 300 mm. This allows a 200 MeV/c muon beam with a nominal diameter of 600 mm to pass through the solenoid without loss (except from muon decay). The distance from the end of the superconducting coil to the outside end of the cryostat is reduced to 20 mm. (If an additional support clip were needed at the end of the coil, the coils can shortened to accommodate the clip in the space shown.) The coils in the solenoid shown in Fig. 10.2 have a length of 360 mm. The gap between the coils is 140 mm and the space between a coil in one magnet and the coil in the next magnet is also 140 mm.

The conductor for the coils shown in Fig. 10.2 is a standard MRI magnet conductor that is 1 part Nb-Ti and 4 parts RRR = 70 Cu. This conductor has fifty-five 85μm filaments with a twist pitch of 12.7 mm. The bare matrix dimensions of the conductor are 0.955 mm by 1.65 mm. The conductor insulation is 0.025-mm thick. The coils are designed to be 6 layer, each one 9.6-mm thick, including 2 mm of ground-plane insulation. At an average design induction of 1.25 T on axis, the coil design current is 393 A. The peak induction in the coil winding is 1.6 T, which gives a coil operating temperature margin of over 2.5 K.

The coils can be wound and cast on a form that is removed after the coil is cured. After curing, the coils are removed from the mold and machined at the ends and on the outer radial surface. After the coil is machined, it can be shrunk fit into a 6061 Al support structure that has been machined so that the coils closely fit within it. The 6061 Al support structure on the outside of the coils serves the following functions: 1) it limits the coil strain by carrying some of the magnet hoop forces; and 2) it serves as a shorted secondary to protect the magnet during a quench. A single magnet is entirely self-protecting through quench-back from the support structure.

The longitudinal space at the center of the magnet, 85 mm, is available for leads, cryogenic services and cold mass supports. The cold mass of the phase-rotation solenoids

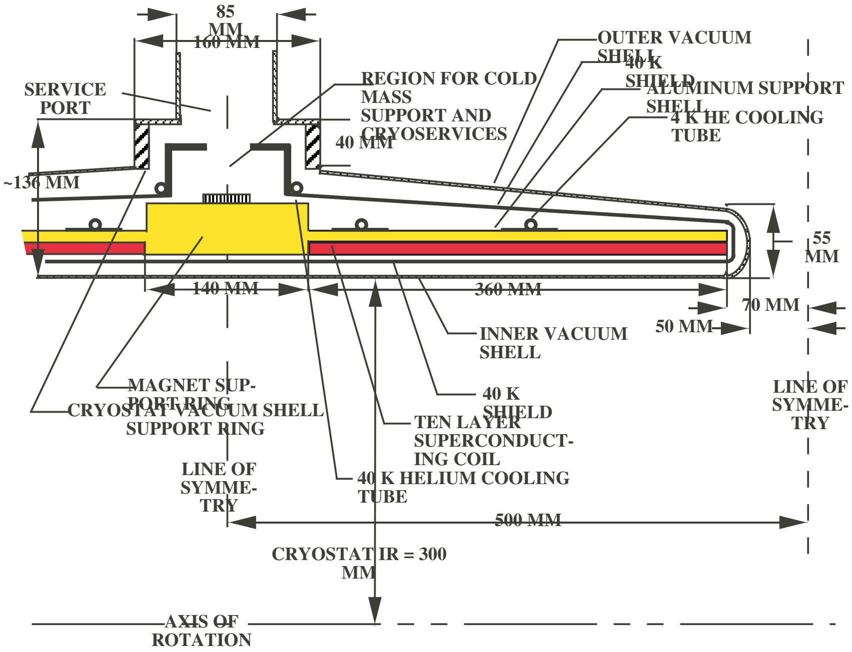

Figure 10.2: A cross section of the induction linac superconducting coil and cryostat.

(including the 40 K shield and lower lead assembly) is about 210 kg. The largest forces that will be seen between the cold mass and room temperature will be forces due to shipping and forces introduced due to unbalanced magnetic fields. The magnet cold-mass supports are designed for a force of 20,000 N in any direction. A pair of 60 mm diameter oriented carbon fiber tubes (with a wall thickness of 3 mm) will be used to carry forces from the cold mass to room temperature.

Since there is a solenoid magnet every meter down the phase rotation channel and the drift spaces between the phase rotation linac sections, leads must be brought out for each of these magnets. All of the magnets in 25-m long sections are hooked in series and powered from a common power supply. Interconnects between the solenoids use conventional copper cable. A long string of magnets can be run from a single power supply in this case because the magnet coils are closely coupled inductively to each other and to the support structure.

Quench-back is the primary mode of quench protection for the string of magnets. We use quench-back to protect a string of these magnets as well. When a quench is detected in one magnet, the current in the string is discharged through a varistor resistor, causing all coils to go normal through quench-back from the support structure. Quench-back eliminates the forces between solenoids that would result when only one goes normal. Each 1 m magnet section has its own set of leads to room temperature. The leads between 4 K and 50 K are made from high-temperature superconductor (HTS). The leads from room temperature to the top of the HTS leads at 50 K are gas cooled. Gas from the refrigerator that is used to cool the magnet shields and cold mass support intercepts can also be used to cool the gas-cooled leads. This gas must be returned to the refrigerator compressor intake at room temperature. See Fig. 10.3 for a schematic representation of the cold mass support system, the helium supply system, and the current leads. The cross section shown in Fig. 10.3 is taken at the center of the magnet along the magnet axis.

The solenoids for the decay channel and the mini-cooler section use basically the same magnet design as those in the induction linac cells. The primary difference is the inside diameter of the superconducting coil (858 mm bore versus 648 mm for the induction cell coils). Another difference is that three coil modules share a single cryostat vacuum vessel. Each module has its own cold-mass support system, but the three modules are hooked together using superconducting bus bars cooled with two-phase helium. There is a single set of external leads powering the modules in the magnet cryostat. In the magnets that are next to the flip region, individual power supplies are used to power the coils to shape the magnetic field within the flip region.

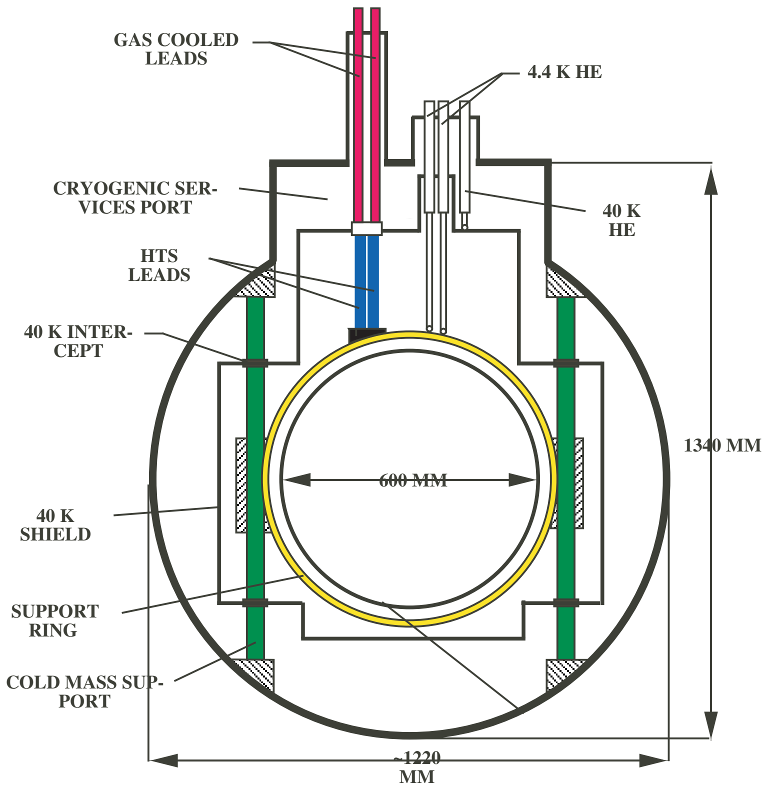

Figure 10.3: Induction cell solenoid cold mass support system and leads.

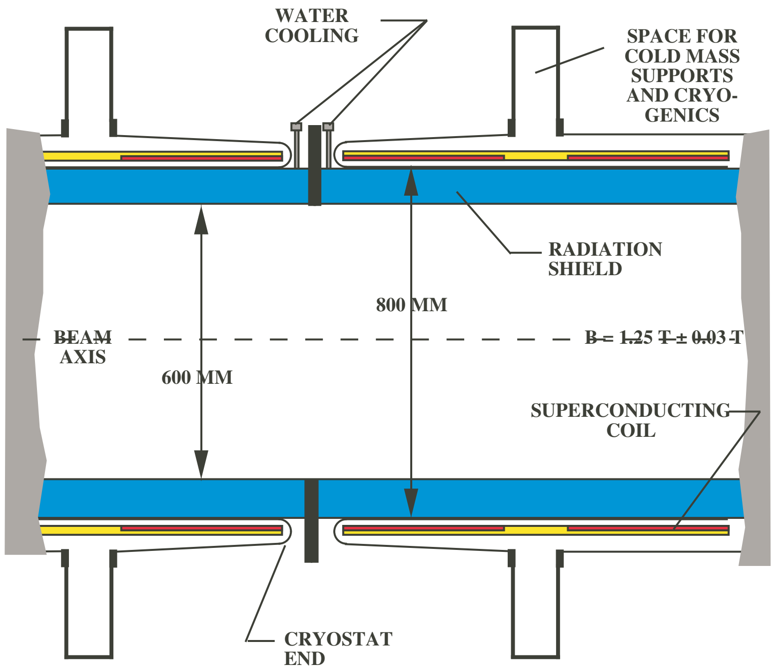

Figure 10.4: A cross section of the solenoids in the pion decay channel.

The solenoids for the flip region of the channel are the same as those used for the decay channel, except that the warm bore diameter of the magnet sections is set at 800 mm. This diameter should provide enough space for the 1.75 m hydrogen absorbers that have window diameters of 600 mm. It allows for a 50 to 70 mm space on the outside of the absorber for cooling of the hydrogen within the absorber. The hydrogen absorbers will use helium coming from the refrigerator at 16 K. About 5,500 W of refrigeration at 16 K is needed to cool the absorbers. This is equivalent to 1,600 W of cooling at 4.4 K. The cryogenic services to the hydrogen absorber go through the 100 mm space between the magnet cryostats. Additional room for services for the hydrogen absorber could be made available by going through the magnet cryostat between magnet coil modules.

Figure 10.4 shows a schematic representation of the solenoids in the decay region. All the solenoids in the decay channel will be powered from the same power supply. Field correction dipoles are mounted on the inside of the solenoid coil. These coils are 1 mm thick and can correct magnet alignment errors up to 5 mrad.

As noted earlier (see Section 4.5), the decay region and the first induction cell solenoids are subject to additional heat loads caused by radiation emanating from the target.

Depending on the location, the radiation heat loading is estimated to vary between 2 and 20μ W/g of cold mass. For the well-shielded decay solenoids, the maximum heat leak per module is about 2.4 W. However, the first magnet modules of IL1 may have heating rates as high as 4.5 W per magnet module. The additional heat load goes down over an order of magnitude farther down the channel. Spent particles from the target that remain beyond IL1 will be absorbed by the first hydrogen absorber of the minicooling. Half of the radiation heat from the target is deposited in the magnet coils. The number of coil layers was increased to six in order to maximize the magnet temperature margin where the magnet is subjected to radiation heating. The induction cell solenoids and the decay channel solenoids are cooled by conduction from the 6061 Al support structure. The Al support structure itself will be cooled by two-phase helium flowing in attached tubes. Two-phase helium cooling is commonly used to cool large detector magnets; its advantages are:

- there is very little helium inventory within the magnet
- the two-phase helium tubes have a high pressure rating; this means that the magnet cryostat itself need not be a pressure vessel
- two-phase helium cooling does not require a cold compressor or a helium pump to circulate the helium through the magnet cooling system
- the temperature of the helium in a two-phase helium cooling circuit decreases as it moves along the flow circuit
- the pressure drop along a two-phase helium flow circuit is lower than for a supercritical helium forced-flow circuit

About twenty to twenty-five magnets are cooled in series from the two-phase helium refrigerator and control cryostat, requiring a mass-flow rate through the flow circuit of about 2.5 g/s. The two-phase helium tube is attached to the superconducting coil support structure, the base of the HTS leads and the attachment points of the cold mass supports. The static heat load into a typical 1 m magnet cryostat at 4.4 K and 40 K is summarized in Table 10.1.

The heat that is added to the two-phase helium flow stream at 4.4 K in each meter of solenoid varies from 0.45 W to 5.0 W, depending on the heat input due to ionizing radiation from the target. The peak temperature at the inside of the superconducting coil when the ionizing radiation heat load is highest (a maximum value of 4.5 W in the first solenoid of IL1) will be less than 5.5 K. Except for heat from ionizing radiation from the target, the heat load at 4.4 K is dominated by the heat leak down the HTS

Table 10.1: Sources of heat at 4.4 K and 40 K in a 1-m induction cell magnet.

Source of Heat	4.4 K load (W)	40 K load (W)
Heat flow down the cold mass supports	0.12	1.9
Thermal radiation through the multi-layer insulation	0.05	2.0
Heat flow down the helium bayonet joints	0.03	1.3
Heat flow down the cold mass supports	0.12	1.9
Heat flow down instrumentation wires	0.02	0.1
Heat flow down the 400 A magnet current leads	0.25	—
Heating due to ionizing radiation from the target	0.0–4.5	0–0.5
Total heat load per meter	0.47–5.0	5.3–5.8

current leads. The heat load into the shield circuit stream is expected to vary from 5.3 W to 5.8 W, again depending on the heat input due to the ionizing radiation from the target. The shield gas comes from the refrigerator at a temperature between 30 and 35 K. (In the region of the mini-cooler, the shield cooling gas comes from the refrigerator and will enter at a temperature of 16 K.) This gas enters the magnet cryostat through a single vacuum-insulated tube. The helium flow in this tube is dictated by the needs of the gas-cooled leads between 50 K and room temperature. The 400 A gas-cooled leads require need 0.05 g/s. The shield gas stream picks up heat from the cold mass supports and from thermal radiation on the shield, helium bayonet joints, and the instrumentation wires. In most of the induction cells, the expected heat load into this stream is about 5.3 W/m. In the first cells of IL1, the shield circuit may pick up as much as 5.8 W. (The extra 0.5 W is due to ionizing radiation from the target heating the 40 K shields.) The helium stream temperature entering the shield circuit from the refrigerator increases from 22 to 24 K as it flows to the base of the gas-cooled leads. The gas used to cool the shields and the cold mass support intercepts is also used to cool the gas-cooled leads between about 60 K and room temperature. The HTS leads are designed to operate with their top end temperature below 70 K. The gas exiting the room temperature end of the gas-cooled leads returns warm to the refrigerator compressor suction. Fig. 10.5 shows the proposed two-phase helium cooling system for a typical 1-m long phase-rotation solenoid. The refrigerator and cryogenic distribution system for the decay solenoids, induction cell solenoids, and the mini-cooling section solenoids are described in Chapter 11.

A string of twenty-five induction cell solenoids has a self-inductance of 68.5 to 72.5 H, depending on which induction linac they are in. A string of six 3-m solenoids for the decay channel and the minicooler will have a self-inductance of 85.8 H. The magnets in

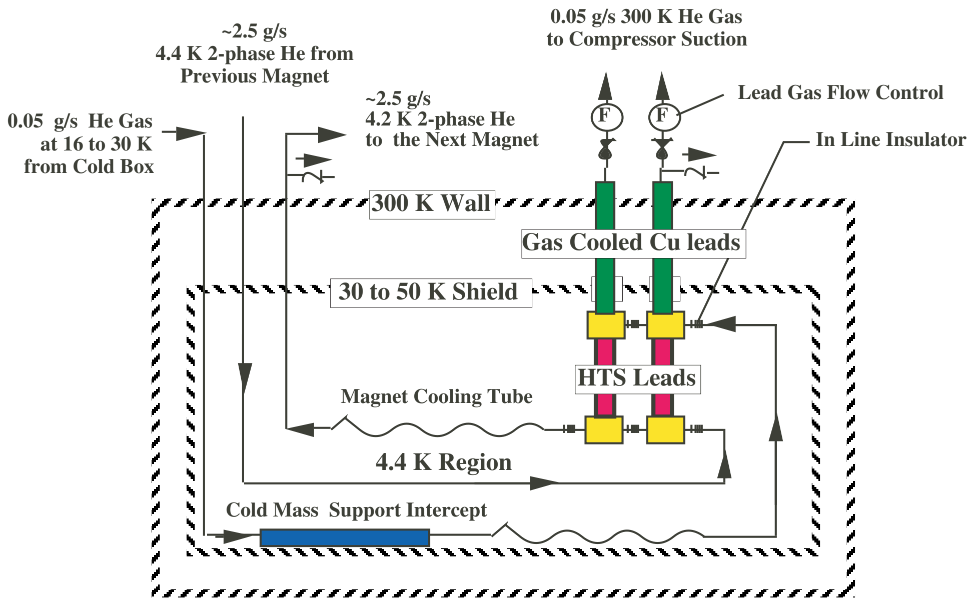

Figure 10.5: Cryogenic cooling system for a typical induction cell.

any of the strings can be charged to full field in less than 1,800 s, by a power supply that delivers 500 A at voltages up to 50 V. The power supply controllers regulate on the voltage across the magnet during magnet charging. When the magnets are charged, the current must be kept constant. Because the magnets are closely coupled, a quench in one magnet of the string will trigger quenches in all of the magnets in that string. A simple resistor across the magnet string leads can protect the entire string during a magnet quench. A typical magnet quench will raise the temperature of the magnet cold mass to about 45 K. The helium refrigerator is sized to allow the magnet to be cooled back down to 4.4 K in less than two hours. To meet this requirement, the helium refrigeration system must deliver helium at 10 to 15 K to the magnets at rate of 4.5 g/s.

10.2.1 Stray Fields

The ferrite cores will carry much of the return flux; what they do not, will be carried in the air between the ferrite cores and the superconducting coils. The induction field at $R = 1.5$ m is below ≈ 0.05 T and at $R = 2$ m it will be ≈ 0.025 T.

10.3 Buncher and Cooling Channel Solenoids

10.3.1 Solenoid Layout and Parameters

We proceed downstream starting at the end of the induction linacs [4]. The matching section between the last induction linac and the beginning of the bunching section consists of four 2.75 m long cells. The focusing solenoids in this matching section must be designed to withstand longitudinal forces of up to 60 metric tons that are imparted on them by the matching solenoids located upstream, at the end of the last induction linac. The bore aperture of the focusing coils for a 2.75-m-ong cooling cell must be about 650 mm in order to accommodate a liquid-ydrogen absorber (se Fig. 5.27). The warm bore aperture for the focusing coils in the bunching section must also be ≈ 650 mm, in order to accommodate the 402.5 MHz rf cavitiies.

Room temperature service ports to the 402.5 MHz rf cavity can go out between two focusing coils running in opposite polarity (*i.e.*, in the flux-reversal region), through the magnet cryostat servicing these two coils. Table 10.2 shows the number of cells of each type, the minimum aperture requirements for the magnets and the maximum coil current densities for the coils in each cell type. Included in Table 10.2 is the magnetic field 9.9 m from the beam axis. Because the bunching and cooling cell solenoids are constantly changing polarity, there is almost no stray field from these solenoids at a radius $R = 10$ m.

Magnet parameters and a magnet cross section for the 2.75-m-long bunching and cooling cell magnets are shown in Table 10.3 and Fig. 5.27. Magnet parameters and a magnet cross section for the 1.65-m-long cooling cell magnets are shown in Table 10.4 and Fig. 5.28.

Figures 5.27 and 5.28 show a cross section of the bunching and cooling cell solenoids. The plane for the cross sections is taken through the warm to cold supports that carry axial forces. These cross sections also show the magnet cryostats, the coils, the coil support structure, the 30 K shields, and the vacuum vessel around the rf cavities. The cryostat vacuum systems are separated from the vacuum around the rf cavities and the beam vacuum. The penetration of the hydrogen absorber plumbing through the space between the focusing coils is not shown in Figs. 5.27 and 5.28.

Figure 10.6 shows a cross section through the center of the 1.65-m-long cell focusing coil pair ("A"). Note the location of the longitudinal cold mass supports and the cold mass supports that carry forces in both directions perpendicular to the solenoid axis. This figure illustrates how magnet electrical leads, and helium refrigeration can be brought into the cryostat. Figure 10.6 is a typical cross section that can be applied to all of the bunching and cooling cell solenoids.

Figures 5.27 and 5.28 show the location of the hydrogen absorbers within the bore of

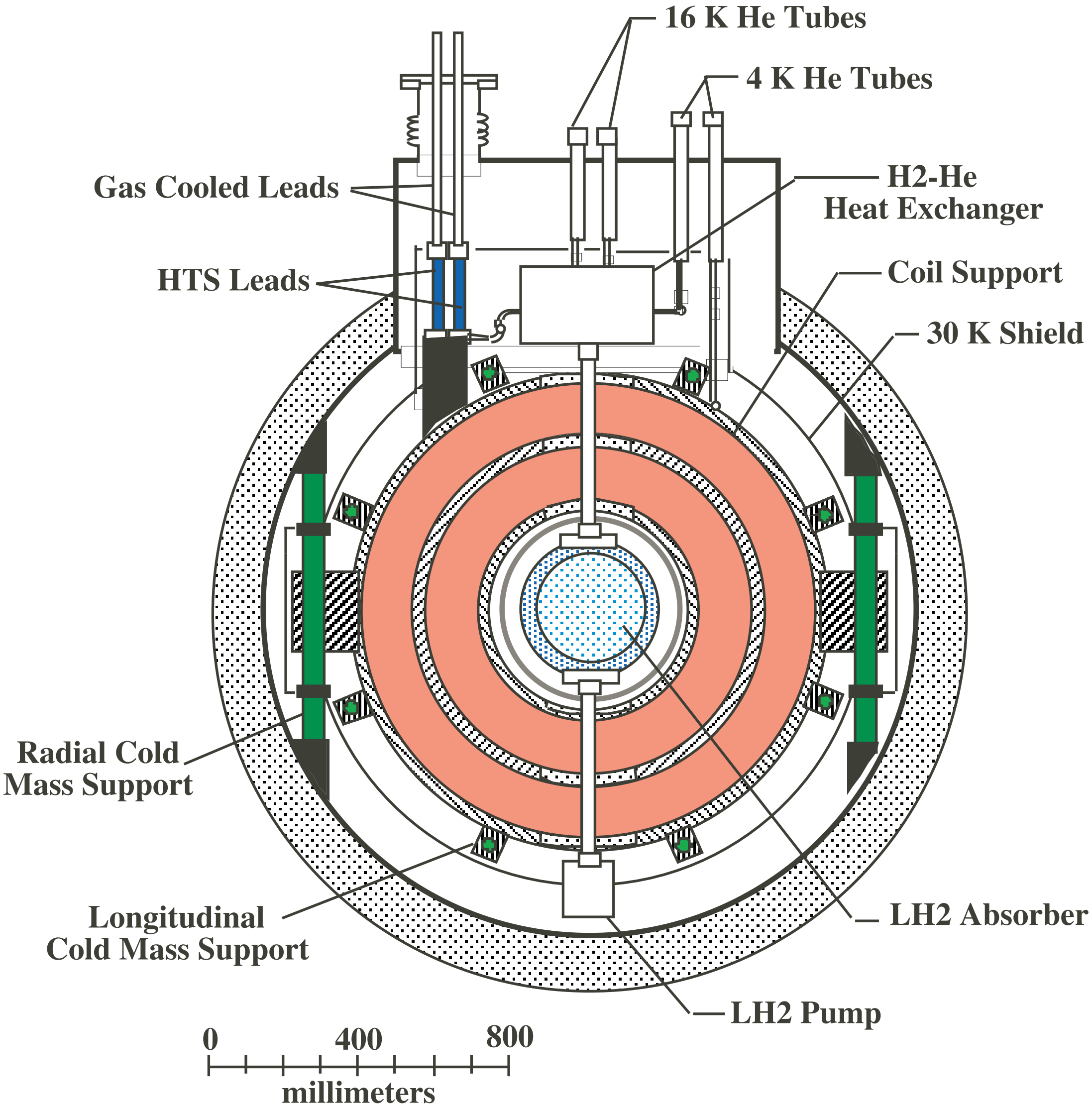

Figure 10.6: Cross section of the 1.65 m cell focusing magnets, perpendicular to the beam.

Table 10.2: Basic parameters for the bunching and cooling cells.

Parameter	2.75 m cell	1.65 m cell
Number of cells of this type	37	37
Cell length (mm)	2750	1650
Maximum space for the rf cavity	1966	1108
Number of 201.25 MHz rf cavities per cell	4	2
Number of 402.5 MHz rf cavities per bunching cell	1	NA
Focusing magnet cryostat length (mm)	784	542
Focusing magnet cryostat length (mm)	283	209
Aperture for the focusing magnet (mm)	650	370
Aperture for the coupling magnet (mm)	1390	1334
Maximum focusing coil current density (A mm^{-2})	128.04	99.65
Maximum coupling coil current density (A mm^{-2})	99.24	109.45
Maximum cell stored energy (MJ)	13.2	17.6
Maximum longitudinal warm to cold force (MN)	0.74	1.20
Number of longitudinal supports per coil	4	6 to 8
Peak induction 9.9 m from the cell axis (T)	1.18×10^{-5}	2.62×10^{-5}

the focusing coil pair. The hydrogen absorber will share the same cryostat with the focusing coils. The hydrogen absorber and these magnets will have a common vacuum. The hydrogen absorber will be supported from the coil package by a low thermal conductivity support system made from a titanium tube. Figure 10.6 illustrates schematically that connections to the hydrogen absorber can be made between the focusing coils through the support structure that carries the large magnetic forces generated by these coils.

10.3.2 Forces

Forces in the longitudinal direction are a serious issue for the bunching and cooling solenoids. The focusing coils, running in opposite polarity, generate large forces (up to 1950 metric tons) pushing them apart. These forces must be carried by a 4.4 K metallic structure between the two coils. The magnitude of the forces pushing these coils apart depends on the spacing between the coils, the average coil diameter and the current carried in each coil. The inter-coil forces are carried by either aluminum or stainless steel shells on the inside and the outside of the coils. The forces are transmitted to the coil end plates, which are put in bending. Large stresses are developed at the point where the end plates meet the shells inside and outside the coils. Since the force between the focusing coils in the 1.65-m-long cooling cells is so large, these coils must be divided in

Table 10.3: Solenoid parameters for the 2.75-m-long bunching and cooling cell.

	Focusing	Coupling
Mechanical Parameters		
Magnet cryostat length (mm)	784	283
Magnet cryostat bore diameter (mm)	650	1390
SC coil length (mm)	167	162
Inner radius of the coil (mm)	355	729
SC coil thickness (mm)	125	162
Distance between coils in z direction (mm)	350	NA
Inner support structure thickness (mm)	15	0
Outer support structure thickness (mm)	20	25
Number of turns per magnet	2304	1472
Magnet cold mass (kg)	1430	1245
Magnet overall mass (kg)	1870	1570
Electrical Parameters and Magnetic Forces		
Maximum magnet design current (A)	2320.2	1779.9
Peak induction in the windings (T)	7.5	6.5
Magnet stored energy at design current (MJ)	≈7.9	≈7.7
Magnet self inductance per cell (H)	≈2.9	≈4.9
Superconductor matrix $J(A\mathrm{mm}^{-2})$	155	119
E J^2 limit per magnet cell (JA^2 m^{-4})	1.89×10^{23}	1.09×10^{23}
Force pushing the focusing coils apart (metric tons)	329	NA
Peak fault force on a coil (metric tons)	75.3	75.3

the radial direction in order to reduce the bending stress in the end plates. The large stress in the end plates of these focusing coils in the 1.65-m-long cooling cell dictate that the end plates and shells must be made from 316 stainless steel.

If the currents in all of the focusing coils and all of the coupling coils were the same from cooling cell to cooling cell, there would be no net longitudinal force on any of the coils. However, the currents in the cooling cell coils vary as one goes down the channel. This generates a longitudinal force in various magnet coils. The largest longitudinal forces will be generated at the ends of the string or when one coil quenches and adjacent coils do not quench. One can attach all of the coils together with cold members, but further examination suggests that this approach would make it difficult to assemble and disassemble the muon cooling system. As a result, every magnet is assumed to have cold to warm longitudinal supports. The cold-to-warm supports in the magnets in the 2.75-

Table 10.4: Solenoid parameters for the 1.65-m-long cooling cell.

	Focusing	Coupling
Mechanical Parameters		
Magnet cryostat length (mm)	542	209
Magnet cryostat warm bore diameter (mm)	380	1334
SC coil length (mm)	145	109
Inner radius of inner coil	210	687
SC coil thickness (mm)	138	326
Distance between coils in z direction (mm)	132	NA
Inner support structure thickness (mm)	20	0
Center support structure thickness (mm)	30	NA
Outer support structure thickness (mm)	40	25
Number of turns per magnet	4480	1974
Magnet cold mass (kg)	1995	1750
Magnet overall mass (kg)	2430	2290
Electrical Parameters and Magnetic Forces		
Maximum magnet design current (A)	1780.5	1896.7
Peak induction in the windings (T)	8.4	6.5
Magnet stored energy at design current (MJ)	≈10.7	≈11.0
Magnet self-inductance per cell (H)	≈6.8	≈6.1
Superconductor matrix J (A mm^{-2})	119	126
E J^2 limit per magnet cell (J A^2 m^{-4})	1.51×10^{23}	1.74×10^{23}
Force pushing the focusing coils apart (metric tons)	1950	NA
Peak fault force on a coil (metric tons)	122	122

m-long cells are designed to carry 80 metric tons (the maximum force during a magnet fault). These forces can be carried by four oriented fiverglass epoxy cylindrical supports that are 50 mm in diameter with a 4-mm-thick wall. Oriented fiberglass rods can carry stresses up to 600 MPa in either tension or compression.

The 1.65-m-long cell magnets have longitudinal cold-to-warm supports that are designed to carry 120 metric tons. Figure 10.6 shows the location of eight of these supports on the 1.65-m-long cell focusin magnet. A six-support longitudinal support system would also be practical. The support shown for the focusing coil in Fig. 5.28 is designed to operate in both tension and compression. Further engineering can define an optimum cold mass support system for these magnets. Compared with other heat loads into the magnets, the longitudinal cold mass supports represent about one quarter of the total heat leak into the magnet cryostat.

10.3.3 Conductor

The magnet conductor that is assumed for all of the coupling solenoids is a conductor that is 7 parts copper and 1 part niobium-titanium. This conductor consists of strands with a copper-to-superconductor ratio of 1:1.3. The twist pitch in the superconductor is about 10 mm. The strands of this conductor are attached to a pure copper matrix.

The overall dimensions for the finished conductor for all of the bunching and cooling solenoids are 3 mm by 5 mm. This conductor will carry 5100 A at 5 T and 4.2 K. At 7.5 T, the proposed conductor will carry about 2500 A at 4.4 K. The same conductor could be used in the 2.75-m cell focusing coils but the margin is rather tight. However, it could not be used in the 1.65-m long cell focusing magnet, where the peak magnetic field reaches is 8.4 T within the coil. Therefore, this coil must be operated at reduced temperature (say 2.5 K). To allow for greater temperature margin, all the focusing coils in both lattices will use a conductor with a 4:1 copper-to-superconductor ratio. The focusing coils in the 1.65-m long cell will be cooled to 2.5 K.

The conductor will have a varnish insulation that is 0.05 mm thick. The layer-to-layer fiberglass epoxy insulation is 0.4 mm thick. The ground plane insulation around the coils is 1.6 mm thick. This permits the superconducting coils to be discharged with a voltage across the leads of up to 1200 V. Each focusing coil set and each coupling coil is powered separately. A quench-protection voltage of 1200 V is adequate to protect any of the coils in the cooling cells. Because the conductor current density is high, the focusing coils in the 2.75-m-long cells have the smallest safety margin when it comes to quench protection. Re-optimization of these coils can improve their quench protection.

The conductor currents and current densities are given for the focusing and coupling coils in Tables. 10.3 and 10.4. Listed also are the peak values that would occur in the cells operating at the highest current. The estimated stored energy occurs at the peak design current in the coils. In general, when the current density is high in the focusing coil, the current density in the coupling coil is low. The stored energy for the cooling cells changes very little along the cooling channel. The cell stored energy shown in Table 10.2 is the average stored energy for that type of cell. Table 10.5 shows the average coil current density and coil current for the focusing and coupling coils in the various regions of the bunching and cooling channel.

There are 41 pairs of focusing coils and coupling coils that make up the 2.75-m-long matching, bunching and cooling cells. Likewise, there are 37 sets of coils that make up the 1.65-m-long cooling cells.

Table 10.5: Coil average j and I for various sections of the bunching and cooling channel. The matching sections between lattices have been taken into account.

Section	focusing j (A mm^{-2})	focusing I (A)	coupling j (A mm^{-2})	coupling I (A)
Bunching cells	105.28	1907.7	98.83	1762.0
Cooling (1,1)	105.28	1907.7	98.83	1762.0
Cooling (1,2)	117.84	2135.3	92.42	1657.5
Cooling (1,3)	128.04	2320.2	85.25	1519.9
Cooling (2,1)	82.34	1471.1	105.53	1899.7
Cooling (2,2)	89.83	1604.9	95.99	1727.9
Cooling (2,3)	99.81	1783.2	84.42	1519.7

The last three meters of the induction linac channel must have thicker coils with a separate power supply on each coil. The 1.25 T solenoids at the end of the induction cells must have separate longitudinal warm-to-cold supports to carry forces (up to 60 metric tons) generated by the magnets in the first cells of the bunching section.

The end of the short cell cooling section must be matched to the accelerator section downstream (see Sec. 5.5). This matching section consists of seven standard short cooling cells with varying currents in the coil and no hydrogen absorbers. The last three cells in this section are longer than the standard 1.65-m cooling cell, but the coupling coils can be made identical to the standard coupling coils. The three focusing coils in the last three cells are special coils with larger spacing between the flux reversal coils. The final two coils have the same diameter as the short-cell coupling coils, but they are longer and powered differently. The last two coils are considered to be part of the solenoids in the superconductiong linac section.

10.3.4 Refrigeration

Refrigeration to the muon cooling magnets and hydrogen absorbers is supplied at 16 K and 4.4 K. The 4.4 K refrigeration is used to cool the superconducting coils except for the focusing coils in the 1.65-m-long cell, which are cooled to 2.5 K. The 2.5 K cooling requires an additional heat exchanger and a vacuum pump to produce nearly 0.3 W of cooling at 2.5 K. Most of the heat into the 1.65 m cell focusing coil package is intercepted at 4.4 K. The hydrogen absorbers are cooled from the same refrigerator as the solenoid magnets. Refrigeration for the hydrogen absorbers is drawn off at 16 K. The 16 K helium used to cool the liquid hydrogen returns to the helium cold box at 19 K. The absorbers in the 2.75-m-long cell contain 35.6 liters of liquid hydrogen. The 1.65-m-long cell absorbers contain about 8 liters of liquid hydrogen. The estimated heat load to the absorbers is between 120 and 130 W. Table 10.6 shows the refrigeration requirements for the 2.75-m-long cells and the 1.65 m long cells with hydrogen absorbers. The equivalent 4.4 K refrigeration reflects the Carnot ratios from 4.4 K to 16 K and the refrigeration lost when helium returns to the compressor by bypassing the refrigerator heat exchangers. The equivalent 4.4 K refrigeration for the bunching cells is 13.3 W per cell. About 10.5 W of equivalent 4.4 K refrigeration are used to cool two pairs of 2000-A gas-cooled leads from 300 K to 40 K.

Figure 10.7 shows a schematic representation of the refrigeration for a pair of focusing coils with a hydrogen absorber. Two-phase helium at 4.4 K is used to cool the superconducting coils. If nineteen magnets are cooled from a single flow circuit, the mass flow of two-phase helium should be 8 to 10 g/s. The flow circuit can have up to 20 magnet coils in series before the helium is returned to the control cryostat. The shields, intercepts, current leads, and hydrogen absorbers are cooled by helium that comes from the refrigerator at 16 K. The helium used to cool the shields and the leads is returned to the refrigerator compressor warm. The rest of the 16 K helium returns to the refrigerator at 19 K.

The helium used to cool the magnet shield intercepts heat from the cold-mass support, the bayonet tubes, the instrumentation wires, and radiation heating through the multilayer insulation before it is used to cool the gas-cooled current leads for the magnets. For the flow circuit shown in Fig. 10.7, the flow of helium gas in the shield cooling circuit is dictated by the needs of the gas-cooled current leads. For the current leads in the cooling and bunching magnets, this flow varies from 0.15 to 0.23 g/s. Depending on the needs of the current leads, the temperature rise in the shield-gas flow circuit will vary from 14 K to 23 K. If we optimize the magnets, the lead current might be as low as 1200 A. With 1200 A current leads, the temperature at the top of the high T_c superconducting leads would be about 50 K.

oth the focusing and the coupling magnet shields will be cooled using the same 16 K source of gas from the helium refrigerator, but this is not optimum from the standpoint of overall refrigeration system efficiency. When the helium refrigerator cools both the hydrogen absorber and the magnets, there will be enough excess refrigeration capacity available to cool down the magnet coils in a reasonable time.

The flow in the 16 K circuit to the hydrogen absorber is dictated by the heat load in the absorber. Without a muon beam, the heat load could be as low as 22 W. With beam heating and the circulation heater operating, the heat load into the absorbers can approach 320 W. The temperature rise in the absorber cooling circuit should be limited to

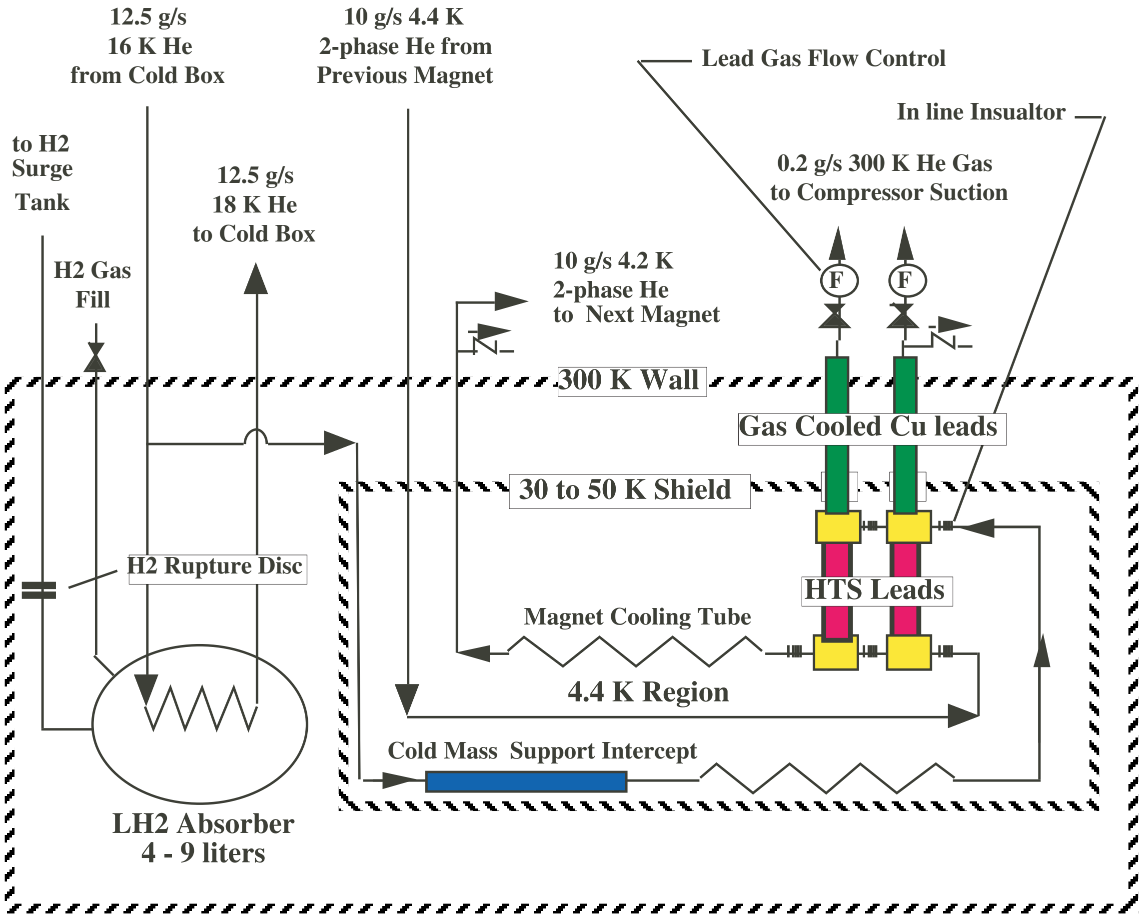

Figure 10.7: Cryogenic cooling system within a typical cooling focusing coil cryostat.

about 2 K. As a result, the helium flow circuit used to cool the hydrogen absorbers should be designed to provide 31 g/s of 16 K helium. The heat load in the hydrogen decreases along the cooling channel. At the end of the channel, the heat is load is expected to be as low as 130W[1]. Thus, the 16k helium flow rate for the 1.65-m-long cells should be set to about 15 g/s. In all cases the helium will be returned to the refrigerator cold box at around 19 K (including heating in the return transfer line).

10.3.5 Quench Protection

The bunching section has twenty focusing magnets and twenty-one coupling magnets that have the same current in the coils. The number of cooling section cells where magnets carry the same current is up to thirteen. Each magnet in the bunching and cooling sections has its own leads. The magnets can be powered individually or in strings of magnets that carry the same current. Powering magnets as a string of magnets requires a more complicated quench-protection system that uses diodes and resistors to cause the string current to bypass the quenching magnet. For sake of simplicity, each magnet has its own power supply and quench protection system. A 2500 A power supply for charging and discharging a single magnet coil (either a focusing coil or a coupling coil) should be capable of developing ±7 V. The magnet quench protection consists of a dump resistor across the magnet leads. When a quench is detected, a fast switch disconnects the power supply from the magnet. In all cases, the power supply control system should permit control of the current and the voltage across the coils as the magnet is charged and discharged. The power supply is not required to operate at both positive and negative currents. A controller is used to control the charging and discharging voltages across each coil and regulate the current once the coil has reached its set current.

10.3.6 Alignment

The coupling coils can be aligned so that the solenoid axis is correct to 0.3 mrad. The magnetic center of the coupling coil can be maintained to about 0.3 mm. The alignment of the focusing coils can probably be maintained to about 0.5 or 0.6 mrad. Correction dipoles could be installed if necessary, correcting the apparent solenoid axis of the coils by ± 1.5 mrad.

[1] This is due to beam losses

10.3.7 Magnetic Field Outside the Solenoids

The net magnetic moment of the cooling channel is essentially zero; consequently the field falls off quite rapidly away from the magnetic axis. Considering the long cell in isolation, the induction field at different distances from the solenoidal channel is given in Table 10.7

10.4 Linear Accelerator Solenoids

The requirement of a large acceptance for the pre-accelerator linac requires large apertures and strong focusing in both planes. Clearly, solenoids are superior to quadrupole triplets (see Chapter 6).

The present design contains several different solenoid magnets. The matching section has a pair of low-stray-field solenoids with adjustable currents. The short and intermediate cryomodules have a 1 m solenoid and the long one has a 1.5 m solenoid.

Solenoids produce stray fields that have adverse effects on the superconducting rf cavities; therefore, a very important design feature of the solenoids is the need to eliminate the stray fields. The solenoids satisfy the following conditions:

1. are designed to produce zero net magnetic moment. This means that the coil that produces the solenoidal field is bucked by a coil or coils that are larger in diameter.

2. The field from the bucking coils is be distributed in the same way as the solenoid field. This suggests that the bucking solenoid be around the focusing solenoid so that the return flux from the focusing solenoid is returned between the focusing solenoid and the bucking solenoid.

3. The solenoid pair is surrounded by iron, except where the muon beam passes through it.

4. An iron flux shield is installed between the solenoid magnet package and the rf cavity cells.

5. The superconducting rf cells nearest the focusing solenoid are covered with a type 2 superconducting shield. This will not shield the earth's magnetic field, but it will shield the remaining stray flux from a nearby solenoid. A superconducting shield was used to shield the stray field from a superconducting inflector magnet that is located within the good field region (good to better than 1 part in a million) of the $g-2$ experiment at BNL.

It is unlikely that all five steps will be needed to sufficiently reduce the stray field in the rf cavities arising from the adjacent solenoid. The linac solenoids are designed to have bucking solenoid coils on the outside of the main solenoid. The bucking coil is the same length as the main solenoid, and its radius and current are set so that the solenoid pair produces zero net magnetic moment. In order for a solenoid of average radius R_1 with a total current I_1 to have zero net magnetic moment, a bucking coil of radius R_2 larger than R_1, must be around it. The total current of the bucking solenoid I_2 can be calculated using the expression

$$I_2 = -I_1 \frac{R_1^2}{R_2^2}. \tag{10.1}$$

If the coils in both the outer and the inner solenoids in a system of solenoids with zero net magnetic moment are evenly distributed, the induction generated at the center of the nested solenoid pair will be given by

$$B_0 = \frac{\mu_0 I}{L}(n_1 \cos\beta_1 - n_2 \cos\beta_2), \tag{10.2}$$

where

$$\beta_1 = \tan^{-1}\left(\frac{2R_1}{L}\right) \qquad \beta_2 = \tan^{-1}\left(\frac{2R_2}{L}\right), \tag{10.3}$$

I is the current in the solenoid pair, L is the length of the nested solenoid pair, n_1 is the number of turns in the inner focusing solenoid, and n_2 is the number of turns in the outer bucking solenoid. Because of the zero net magnetic moment condition, $R_2 = (n_1/n_2)^{1/2} R_1$ with $I_1 = n_1 I$ and $I_2 = n_2 I$.

Table 10.8 presents the mechanical and electrical parameters for the short and long module focusing solenoids. The matching solenoids at the start of the channel are similar to the first focusing solenoids. All of these solenoids are designed to have zero net magnetic moment. The solenoids in Table 10.8 are assumed to have a warm bore and a warm iron shell around the solenoid pair. It should be noted that the magnet bore does not have to be warm. A cold bore solenoid will be somewhat smaller and the bore can be a cryopump for the beam vacuum. The iron shield around the magnet pair does not have to be warm either, as long as it does not carry large forces. The inner coils and the outer coils of the solenoid in Table 10.8 have an even number of layers. This allows the solenoid leads to be brought out together at one end. The outer solenoid is split with a 50 mm gap between the two coils. This allows the leads and helium cooling tube for the inner solenoid to be brought out through the outer solenoid. Electrical connections and helium into the magnet can be brought in at the center of the solenoid, thus minimizing the stray field that might be produced at or near the connection point. The solenoid pair is assumed to be supplied with current through a single set of high temperature superconductor (HTS) and gas-cooled electrical leads. Since the nested magnets are hooked in series, the focusing solenoids have zero net magnetic moment at all magnet currents.

Figure 10.8 shows a cross section of the short solenoid (1.0 m long with 2.1 T in the inner bore) in a plane that contains the magnetic axis; it also shows the separation of the inner coil and the bucking coil, as well as the magnet cryostat, an electrical lead, and the iron shield around the actively shielded solenoid. The center of the cryostat has no iron shield around it because there is very little magnetic flux leaking outside the bucking solenoid. Not shown in Figure 10.8 is iron flux shield that is about 300 mm from the end of the magnet cryostat. This shield further reduces the field in the rf cavity.

Figure 10.9 shows a cross section of the long focusing solenoid (1.5 m long with 4.2 T in the inner bore) in a plane perpendicular to the solenoid axis. Figure 10.9 shows the 24 layer inner coil and a 4 layer bucking coil; it also shows a cold mass support system that can be used for both types of focusing solenoids. The cold mass support system carries predominantly gravitational loading during magnet operation. The support system is designed to carry shipping loads due to acceleration generated by the truck. Because the focusing solenoids are decoupled magnetically from each other, there are no loads imposed on the solenoid by nearby magnets. Also shown in Fig. 10.9 are the magnet current leads and some of the 4.4 K and 40 K helium plumbing for the magnet. Figures 10.8 and 10.9 represent typical cross sections that can be applied to both types of focusing solenoids.

The focusing solenoids are cooled by conduction from the 6061-aluminum support structure. The aluminum support structure will be cooled by two-phase helium flowing in tubes attached to it. Two-phase helium cooling is commonly used to cool large detector magnets. The advantages of two-phase tubular cooling are as follows:

1. there is very little helium inventory within the magnet

2. the tubes carrying the two-phase helium have a high-pressure rating. This means that the magnet cryostat is not a pressure vessel

3. two-phase helium cooling does not require a cold compressor or a helium pump to circulate the helium through the magnet cooling system

4. the temperature of the helium in a two-phase cooling circuit decreases as it moves along the flow circuit

5. the pressure drop along a two-phase helium flow circuit is lower than for a supercritical helium forced flow circuit

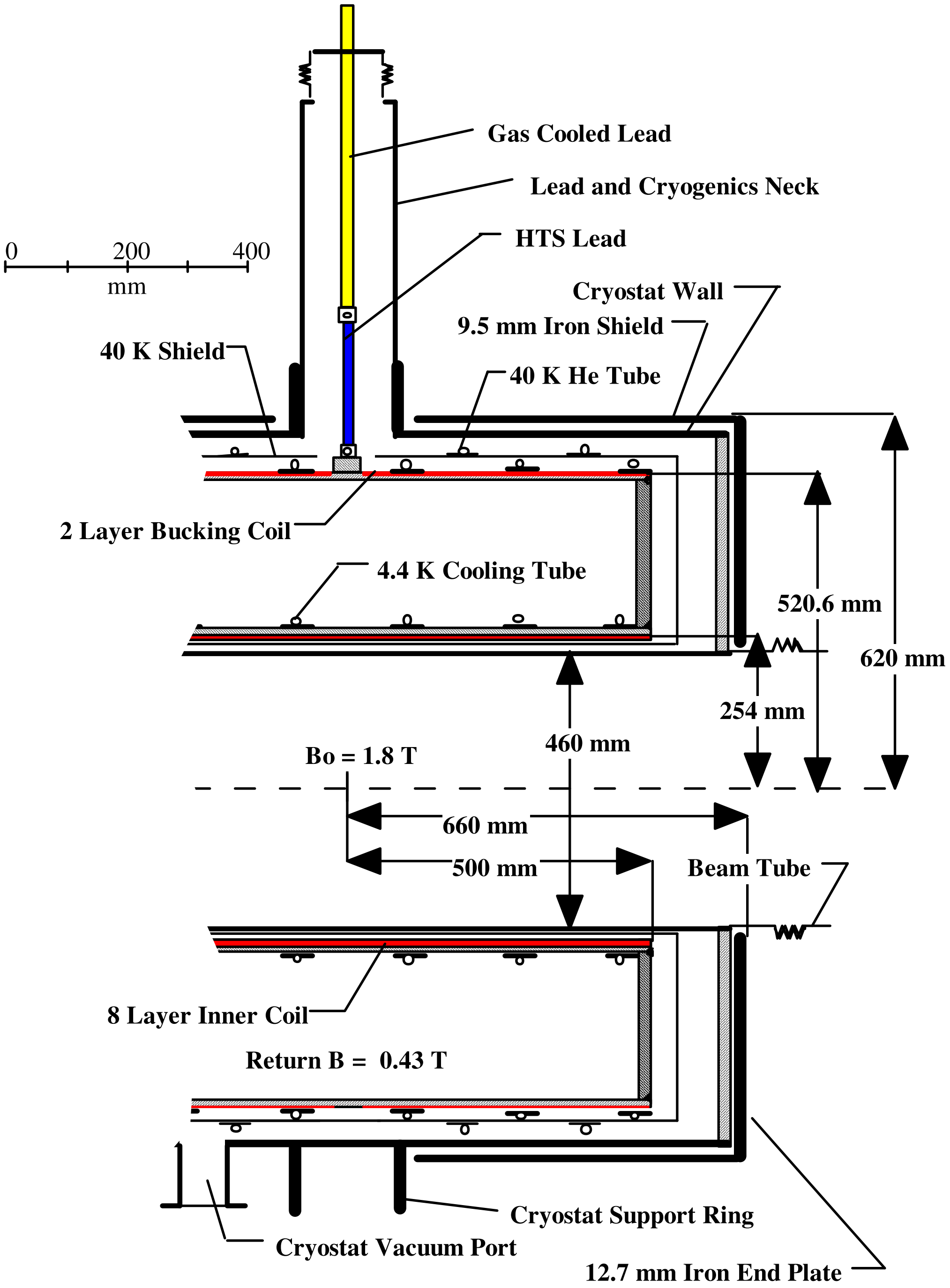

Figure 10.8: A cross section, parallel to the magnetic axis, of a short 1-m solenoid.

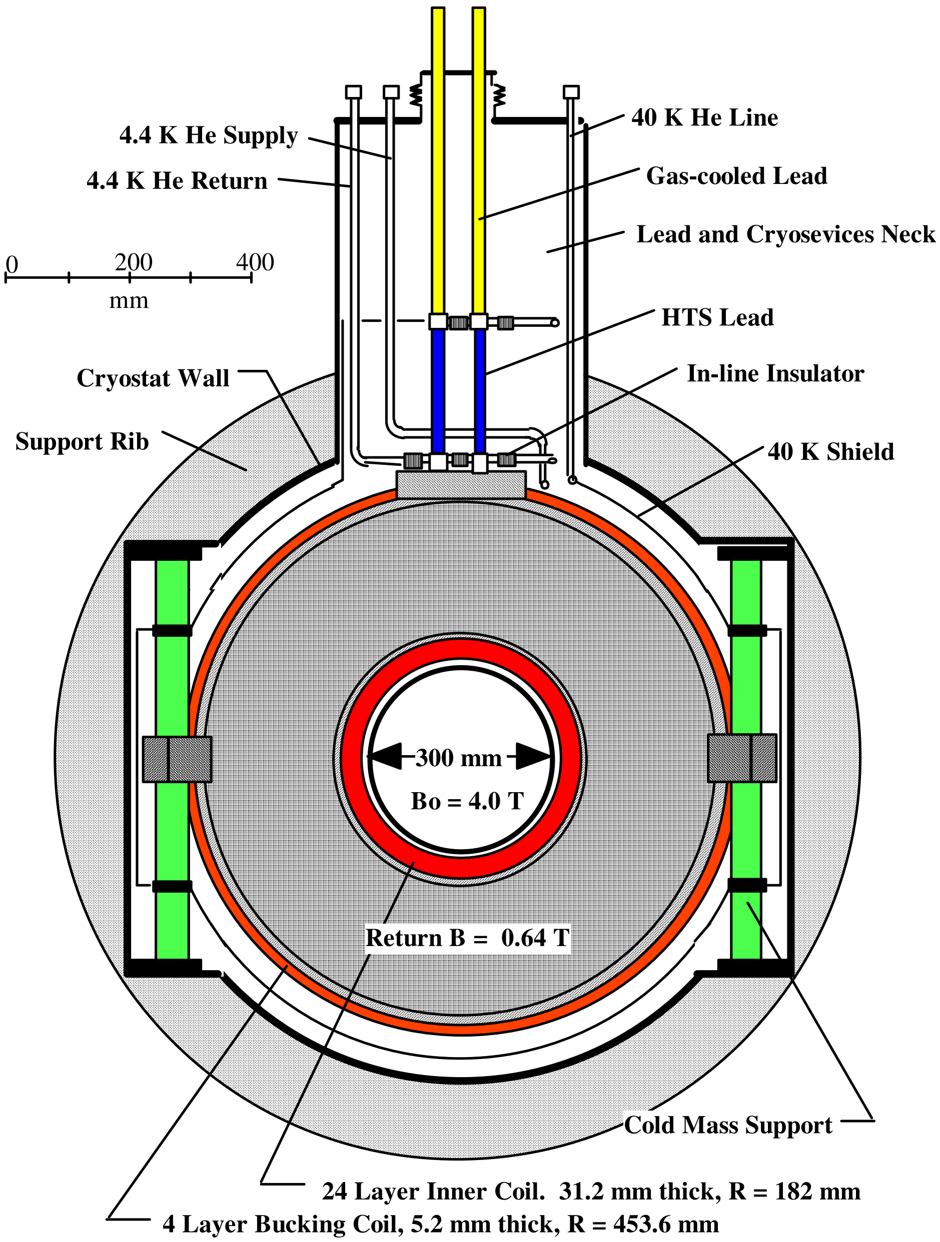

Figure 10.9: A cross section, perpendicular to the magnetic axis, of the long 1.5-m solenoid.

The static heat load into the magnet cryostat at 4.4 K and 40 K for the 1.5-m-long focusing solenoid is shown in Table 10.9. The 4.4 K heat load into a short solenoid is estimated to be about 0.50 W. Most of the difference is heat flow down the HTS leads.

All of the magnets in an acceleration section are cooled in series from the two-phase helium refrigerator and control cryostat. Whether this refrigerator is the same one that cools the superconducting RF cavities depends on the operating temperature of the rf cavities. Cooling for 23 or 24 magnets requires a mass flow rate through the two-phase 4.4 K flow circuit of about 2.5 g/s. The two-phase helium tubes would be attached to the inner coil support structure, the outer coil, the attachment points of the cold-mass supports, and the base of the HTS leads.

The heat load into the shield circuit helium stream is expected to vary from 6.1 to 7.3 W, depending on the length of the magnet. The shield gas comes from the refrigerator at a temperature of 30 K. This gas enters the magnet cryostat through a single vacuum insulated tube. The helium flow in this tube is dictated by the needs of the gas-cooled leads between 50 K and room temperature. The mass flow through the shield circuit is governed by the needs of the gas-cooled leads. The short solenoid leads will need 0.05 g/s; the long solenoid leads will need 0.035 g/s. Gas exits from the gas-cooled electrical leads at room temperature. It returns warm to the refrigerator compressor suction. In the short solenoid, the shield gas enters the gas-cooled leads at about 55 K. In the long solenoid, the top of the HTS leads will be about 70 K. The same HTS leads can be used for both magnets.

For sake of simplicity, each magnet has its own power supply and quench protection system. A 500-A power supply can be used for charging and discharging a single magnet at ± 5 V. The charge time with 3 V across the short magnet is about 600 s. The long focusing solenoid will take about 3200 s to charge with 3 V across the magnet. In all cases, the power supply control system should permit control of the current and the voltage across the coils as the magnet is charged and discharged. The power supply is not required to operate at both positive and negative currents. A controller is used to control the charging and discharging voltages across each coil and regulate the current once the coil has reached its set current. The magnet quench protection consists of a dump resistor across the magnet leads. When a quench is detected, a fast switch disconnects the power supply from the magnet. Both coils in the magnet go normal through quench-back.

The focusing solenoids can be aligned so that the solenoid axis is correctly placed to about 0.5 mrad. The magnetic center of the B coil can also be maintained to about 0.3 mm.

Table 10.6: Sources of heat at 2.5 K, 4.4 K, abd 16–40 K in the bunching and cooling cell magnets. [a] "A" denotes the focusing coil; [b] "B" denotes the coupling coil

Source of heat	2.75 m Cell(W)		1.65 m Cell(W)	
	Coil A[a]	Coil B[b]	Coil A	Coil B
Magnet heat loads at 4.4 K				
Vertical cold mass supports	0.24	0.24	0.40	0.24
Longitudinal cold mass supports	0.36	0.36	0.74	0.54
Thermal radiation through MLI	0.16	0.14	0.01	0.19
Bayonet joints and piping	0.03	0.03	0.03	0.03
Instrumentation wires	0.02	0.02	0.02	0.02
HTS current leads	0.60	0.60	0.60	0.60
Total 4.4 K heat load per coil	1.41	1.39	1.80	1.62
Magnet Heat Loads at 2.5 K				
Vertical cold mass supports	—	—	0.05	—
Longitudinal cold mass supports	—	—	0.10	—
Thermal radiation through MLI	—	—	0.11	—
Bayonet joints and piping	—	—	0.01	—
Instrumentation wires	—	—	0.00	—
HTS current leads	—	—	0.02	—
Total 2.5 K heat load per coil	0.0	0.0	0.29	0.0
Magnet shield and intercept heat loads at 16 to 40 K				
Vertical cold mass supports	3.8	3.8	3.8	3.8
Longitudinal cold mass supports	7.2	7.2	10.8	10.8
Thermal radiation through MLI	2.7	2.9	1.9	3.2
Bayonet joints and piping	1.3	1.3	1.3	1.3
Instrumentation wires	0.1	0.1	0.1	0.1
Gas cooled current leads	—	—	—	—
Total 16 to 40 K heat load per coil	15.1	15.3	17.9	19.2
Hydrogen Absorber (16 K Cooling)				
Cold mass supports	1.5	—	1.0	—
Thermal radiation through MLI	0.3	—	0.2	—
Bayonet joints and piping	1.3	—	1.3	—
Instrumentation wires	0.1	—	0.1	—
Thermal radiation to windows ($\epsilon = 0.2$)	18.4	—	6.9	—
Beam absorption heating	275	—	110.0	—
Circulation heater	≈30	—	≈30	—
Total 16 K heat load per coil	326.6	0.0	149.5	0.0
Equivalent 4.4 K refrigeration per cell	100.7		54.1	

Table 10.7: Stray field at various distances from the axis of a long cooling cell.

R (m)	B (T)
23×10^{-2}	1.5
11×10^{-2}	2.0
18×10^{-3}	4.0
56×10^{-5}	6.0
18×10^{-6}	10.0

Table 10.8: Superconducting solenoid parameters for the linear accelerator.

	Short	Intermediate	Long
Mechanical Parameters			
Beam bore diameter (mm)	460	460	300
Solenoid cryostat length (mm)	1260	1260	1710
Solenoid cryostat outer diameter (mm)	1180	1180	1060
Iron shell length (mm)	1300	1300	1750
Iron shell outer diameter (mm)	1240	1240	1120
Iron shell thickness (mm)	9.5	9.5	9.5
Coil length for both coils (mm)	1000	1000	1500
Inner coil average radius (mm)	254	254	182
Inner coil thickness (mm)	10.4	10.4	31.2
Number of inner coil layers	8	8	24
Number of inner coil turns	4840	4840	21816
Outer coil average radius (mm)	520.6	520.6	453.6
Outer coil thickness (mm)	2.6	2.6	5.2
Outer coil center gap (mm)	50	50	50
Number of outer coil layers	2	2	4
Number of outer coil turns	576	576	3512
Solenoid cold mass (kg)	376	376	746
Solenoid cryostat mass (kg)	166	166	238
Iron shell mass (kg)	485	485	581
Magnetic and Electrical Parameters			
Solenoid average magnetic induction (T)	2.1	2.1	4.2
Solenoid magnetic length (m)	≈ 1.0	≈ 1.0	≈ 1.5
Magnet design current (A)	469.6	469.6	274.0
Peak induction in the inner coil B_p (T)	≈ 2.9	≈ 2.9	≈ 5.8
Magnet conductor I_c at 4.4 K and B_p (A)	≈ 1100	≈ 1100	≈ 590
SC current density (A mm^{-2})	307	307	180
Solenoid stored energy (MJ)	0.421	0.421	1.306
Solenoid self inductance (H)	3.82	3.82	34.8
EJ^2 limit (A^{2}m^{-4}J)	3.97×10^{22}	3.97×10^{22}	4.23×10^{22}

Table 10.9: The sources of heat at 4.4 K and 40 K in a 1.5 m long focusing solenoid.

Source of heat	4.4 K load (W)	40 K load (W)
Heat flow down the cold mass supports	0.12	1.9
Thermal radiation through the multi-layer insulation	0.10	4.0
Heat flow down the helium bayonet joints	0.03	1.3
Heat flow down instrumentation wires	0.02	0.1
Heat flow down the 280 A magnet current leads	0.45	—
Total heat load per magnet	0.72	7.3

Bibliography

[1] M. A. Green, *Design Issues for the Solenoid Magnets for the Neutrino Factory Muon Cooling System,* LBNL-46357, July 2000, http://www-mucool.fnal.gov/mcnotes/muc0165.pdf.

[2] M. A. Green, Y Eyssa, S. Kenny, et al, *Superconducting Solenoids for the Muon Collider.* IEEE Transactions on Applied Superconductivity 10, No.1, p. 196, (2000), http://www-mucool.fnal.gov/mcnotes/muc0162.pdf.

[3] S. Prestemon, J. Miller, Y Eyssa, and M. A. Green *Magnet System Design with Cost Optimization,* IEEE Transactions on Applied Superconductivity 10, No.1, p. 1356, (2000).

[4] A. Green, Y. Eyssa, S. Kenny, J. R. Miller and S. Prestemon, *High Field Superconducting Solenoids for Muon Cooling,* Institute of Physics Conference Series 167, p. 1165, (2000).

Chapter 11

Cryogenic Systems

11.1 Introduction

In order to apply bulk refrigeration to accelerator components, the cooling requirements for each device need careful consideration. The specification and application of bulk refrigeration will naturally follow a thorough investigation and careful engineering of cooled components. It is this study that sets the stage for making the connection between the cooling requirements and the refrigeration system cooling arrangement and hardware. For our case, the cooled devices are rf cavities, superconducting magnets, and hydrogen absorbers, all of which are well characterized in terms of heat loads.

11.2 Cooled Components

The Neutrino Factory uses cryogenic cooling in all of its major sections. A general listing of the cryogenic cooling needs are:

- The proton driver, which has a superconducting linac (SCL) made of three sections, each with its own energy range and cavity cryostat arrangement, and all operating at 2 K.
- The target station and pion capture system, which utilize 1.9 K and 4.4 K refrigeration for the superconducting capture solenoids.
- The decay channel, which has superconducting magnets operating at 4.4 K.
- The phase rotation section, which uses superconducting solenoids that operate at 4.4 K.

- The mini-cooling section, which has solenoids operating at 4.4 K and two-phase hydrogen absorbers operating at 16-19 K.
- The bunching and cooling channel, which has superconducting solenoids operating at 4.4 K and 2.5 K, as well as liquid-hydrogen absorbers operating at 16-19 K.
- The linear accelerator section, which has superconducting rf cavities operating at 2.5 K and solenoids operating at 4.4 K.
- The recirculating linear accelerator, which again has rf cavities operating at 2.5 K and superconducting magnets operating at 4.4 K.
- The storage ring, which has superconducting dipoles and quadrupoles operating at 4.4 K.

All the superconducting magnets and superconducting rf cavities also require cooling in the 5-8 K and 50-80 K range for shields and current leads. Cryogenic cooling, regardless of temperature, is accomplished via helium refrigeration.

Large helium refrigerators are envisioned here, because they naturally provide all temperature ranges required, and typically provide a higher Carnot efficiency than do smaller units. Larger refrigerators, typically with turbine expanders, also offer enhanced cooling capacity at higher temperatures, as well as options to improve the cool-down and liquefaction processes with the addition of liquid nitrogen. The requirements of superconducting magnets, absorbers, and rf cavities will define the interface between refrigeration and cooled devices.

In the muon cooling channel and the phase rotation channel, a 16 K stream cools the magnet shields and leads as well as the liquid-hydrogen absorbers. Figure 11.1 shows the cooling circuit to a typical coupling ("B") coil in the muon cooling channel. The same type of flow circuit can be applied to the solenoids in the phase rotation section. The focusing ("A") coils in the cooling channel have liquid-hydrogen absorbers within them. The cryostat for the liquid-hydrogen absorber is a part of the magnet cryostat. The 2.75-m-long cell focusing magnets operate at 4.4 K, whereas helium delivered to the hydrogen absorber enters at about 16 K and leaves at about 18 K. Helium entering the absorber heat exchanger must remove about 330 W of heat from the liquid-hydrogen absorber when the full intensity muon beam is present. When there is no beam, the heat into the 16 K helium flow circuit is reduced to about 55 W. Figure 11.2 shows a helium flow circuit for the focusing coil and liquid-hydrogen absorber in a 2.75 m cooling cell. As seen in both Figs. 11.1 and 11.2, the shields and leads are cooled from the 16 K helium circuit. Shield and lead gas exits the cryostat at 300 K. The corresponding 16 K cooling

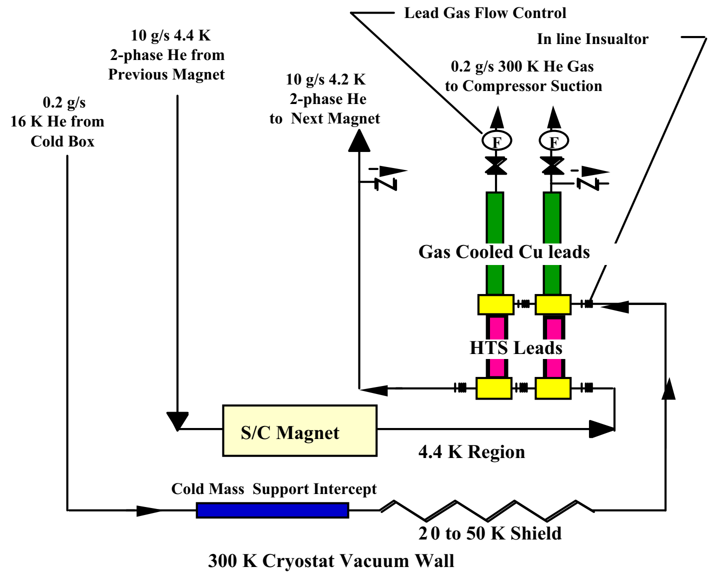

Figure 11.1: The magnet helium cooling circuit for a typical coupling ("B") coil in the cooling section.

requirement for the 1.65 m cell hydrogen-absorbers are 150 W with the muon beam on, and 40 W with the beam off.

The focusing coils in the 1.65-m cooling cell have a peak induction in the winding of 8.5 T. In order for these coils to be made from Nb-Ti, they must operate at a reduced temperature (between 2.5 and 3.0 K). The heat load into the ("A") coils comes from the cold-mass supports and from thermal radiation from the shield; there is almost no heating due to muon decay or AC losses in the superconductor. By using the 4.4 K stream to intercept heat from the cold-mass supports, shield, and leads, the heat leak into the focusing coil can be reduced from 1.8 W to about 0.3 W.

A low heat load at 2.5 K can be removed by using a small 2 K cooling circuit that operates off of the 4.4 K refrigeration circuit. The cooling circuit consists of a heat exchanger that takes liquid helium from the two-phase flow circuit. After passing through the high-pressure side of the heat exchanger, the liquid helium is throttled through an expansion valve down to a pressure of about 40 ton. The helium is now two-phase helium at 2.2 K, with evaporation cooling of the load. The low-pressure gas phase passes through the low-pressure side of the heat exchanger and is finally returned to the refrigerator compressor at 300 K. To generate 0.3 W of cooling at 2.2 to 2.5 K, a helium flow rate of

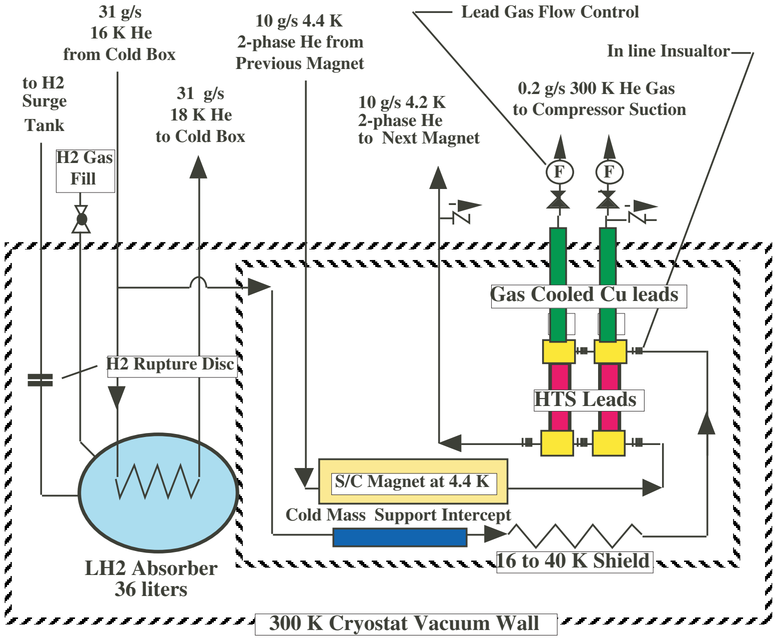

Figure 11.2: The magnet helium cooling circuit for a typical focusing ("A") coil and the liquid-hydrogen absorber in the 2.75-m cooling cell.

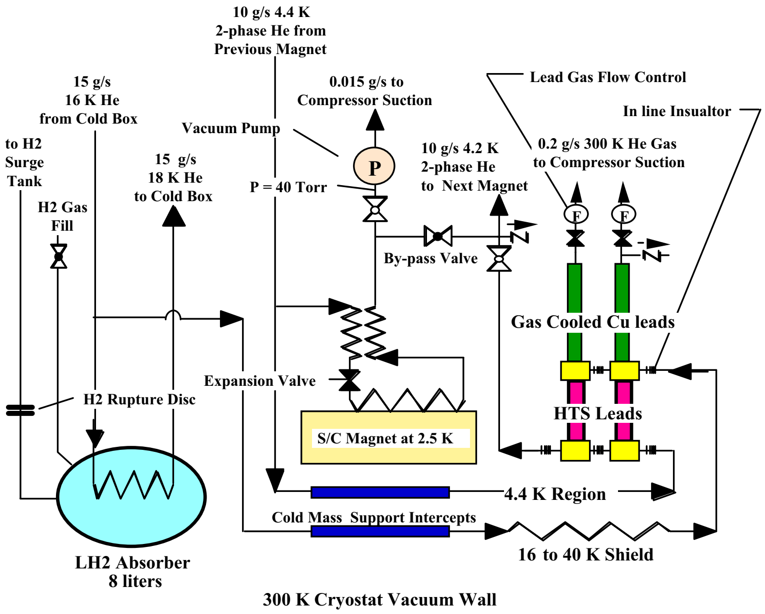

Figure 11.3: A helium cooling circuit for the focusing coils and the liquid-hydrogen absorber in the 1.65-m cooling cell.

0.015 g/s is needed. Since this helium is returned to the refrigerator warm, it is equivalent to helium liquefaction. The liquefaction of 0.015 g/s of helium corresponds to about 1.5 W of refrigeration at 4.4 K. Figure 11.3 shows the helium cooling circuit for a 1.65-m cooling cell ("A") coil and its hydrogen absorber.

11.3 Component Loads

The estimated refrigeration requirements for each cooled device, including the primary static (ambient) and dynamic (beam heating) higher temperature secondary or shield loads, and anticipated cooling arrangement (thermodynamic state) have been considered for the entire accelerator. To ease the evaluation of refrigeration component requirements, the given loads at various state points are all expressed as an equivalent load at 4.5 K. This approach gives a better feel for the refrigeration equipment, and hence a means of comparison with other installations in terms of size, capital cost, and operational demands. Considerations for reliability, helium plant economics (including standard refrigeration availability), installation costs, operation costs and difficulty, are all folded into specifying refrigerators, and in the end will define their sizes and number.

For each group of accelerator components, (see Fig. 11.4 for the approximate location of each group), Table 11.1 shows the integrated primary heat load and thermodynamic state, the secondary heat load and state, and the equivalent loads normalized to 4.5 K. The table follows the accelerator layout, starting at the source and working toward the muon storage ring. The equivalent load at 4.5 K is estimated by multiplying the primary load by the ratio of ideal work at the primary load condition to the equivalent ideal work at 4.5 K. The ideal work is found from Carnot's formula, $\frac{(T_a-2.5)}{2.5}/\frac{(T_a-4.5)}{4.5} \approx 1.8$. for the 2.5 K condition. The temperature T_a is taken as 300 K. The loads summarized in Table 11.2, are in terms of base-load at 4.5 K equivalent, and base-load-equivalent with 30% contingency added. The percentage of total equivalent load at 4.5 K for the primary and/or the secondary load is also shown to give an understanding of the areas of refrigeration concentration, and give a feeling for the relative size requirements.

The last two columns, equivalent primary and equivalent secondary loads, from Table 11.2, are combined to give a summary of the total 4.5 K equivalent loads and equivalent 4.5 K loads with 30% contingency. These values are shown in Table 11.3. It is from this table that a preliminary refrigerator sizing has been made.

11.4 Refrigeration Selection

From Table 11.3 and the accelerator layout an assessment of the number and size of refrigerators, and possible locations is possible. This is reflected in Fig. 11.4. Based upon our understanding of large refrigeration systems applied to accelerators, the choice for this application is to use a few large 4.5 K refrigerators. The low temperature (< 4.5 K) areas are covered using low temperature cold boxes, with cold pumps, tied into the local 4.5 K refrigerator. This design approach minimizes the distance between the load and the cooling system that requires sub-cooling and sub-atmospheric cold pumps. The benefit is a linear reduction of large diameter pumping lines required for this application. Large diameter vacuum insulated transfer lines are very expensive, so minimizing here is prudent. Table 11.3 gives a feeling for the location of these sub-cooling cold boxes, and also suggests ways to isolate and/or group component loads with proximity and capacity considered. A way of coalescing loads by location is shown in Table 11.4.

With reference to Table 11.4, inclusive of contingency, area specific loads at locations ("A"), ("B"), and ("C") could be divided into two 4.5 K refrigerators, for each location, of the approximate capacity of the machines in operation at the Relativistic Heavy Ion Collider at BNL [1], [2], those previously used for the LEP Electron–Positron Collider at CERN [3], ot the new refrigerators under construction for LHC project [4], [5], [6]. For

Figure 11.4: Site layout.

purposes of system design here, the 18 kW machines under construction for the LHC are used. Systems of similar size are encountered also in operation at CEBAF (Jefferson Laboratory) [7]. The feasibility of installing refrigerators of the sizes indicated above has certainly been demonstrated at many places.

Integrating local accelerator heat loads into one or more large refrigerators is cost effective in terms of initial capital investment, because it eliminates much of the duplication associated with building many smaller capacity refrigerators. Installation and operation follow the same philosophy. To support the accelerator loads other than 4.5 K, the refrigerators will incorporate process supply and return passes to meet the higher temperature requirements of items such as the shields and absorbers. These secondary loads, shown in Table 11.1, are typical and would be specified as part of a refrigerator procurement. In essence, each refrigerator will supply the 4.5 K for direct application and all higher temperature needs. Also, each refrigerator will provide the necessary refrigeration for the lower temperature cold boxes. Table 11.2 summarizes the actual loads at operating temperatures below 4.5 K.

To produce temperatures below the temperature range of the 4.5 K refrigerators, stand-alone cold boxes, containing at least one heat exchanger and a series of cold compressors are used. The production of 1.9 and 2.5 K cooling, requires pumping on saturated liquid helium to a pressure of 16 or 100 mbar, respectively. The pumping scheme is usually optimized when located as close as possible to the cooled device, so that transfer line hydraulic losses are minimized. This approach also minimizes cost, because low-pressure process pipes, connecting the pumps to accelerator components, are typically much larger diameter (possibly a factor of 4) and therefore more expensive to build than the transfer lines that connect the refrigerator to the low-temperature cold boxes. The actual cold pumps, located within the local cold box, can achieve the desired pressure with a series arrangement, usually 4 or 5 stages being required, or some pumping can be accomplished at room temperature with warm compressors, which reduces the number of cold stages to 3.

11.5 Capital Cost, Installation, and Operation

11.5.1 Capital Cost

The components that drive the capital cost of large cryogenic refrigeration systems, in descending order of relative cost, are:

- the 4.5 K refrigeration and associated warm compressor system, reduced temperature cold boxes and cold compressors

- transfer piping
- process distribution control or valve boxes
- cold and warm helium recovery
- storage volumes and controls.

Building and utility requirements are considered elsewhere (see Chapter 12); here we consider the components associated with refrigeration to the ends of each interface to each cooled device. The component installation and interface costs are specific to each cooled item. From experience with the construction of RHIC, the cost for installation materials and labor, in terms of percentage of capital cost, in descending order, comes from: transfer piping, refrigeration, valve boxes, reduced temperature cold boxes, controls, and helium recovery/storage.

Estimates for cryogenic transfer piping length are based upon the length of the particular device, which were considered as a unit (see Table 11.4) and integrated into one 4.5 K refrigeration plant. In the case of the recirculating linac the perimeter is used, and for the storage ring, with its simpler cooling requirement, the end-to-end length is chosen. A small contingency length is added to these values to allow for connection to the refrigerator (and cold boxes if they are needed).

11.6 Operational Issues

11.6.1 Power, Operations Labor, Maintenance

The operating cost, mainly electrical power, is tied directly to the cycle efficiency. This subject has been addressed in detail for the 18 kW machines at CERN [5], [6] with the present efficiency at about 30% Carnot, yielding a figure of merit (W_{in}/ W_{ref}, 4.5 K) of 250. For our case, the refrigeration with full contingency, 105 kW, corresponds to $\approx$ 26 MW of electrical power. Under normal operating conditions, estimated at 81 kW, the electrical power required is 20 MW.

The labor required to operate a facility of this nature could be derived from the models developed and used at RHIC (BNL), CEBAF (Jefferson Laboratory), or LEP (CERN). For this part of the study, the RHIC facility is used as the model and the operation of LEP is referenced. Information gathered from these operating facilities is used to project the needs for the present study. The same approach is used for maintenance of refrigeration systems. The operation of the four 18 kW plants at LEP involves a group of 37 people, the direct operation and maintenance of the refrigerators is accomplished by

15 persons. Operation of cryogenic systems at BNL includes, RHIC, with its refrigerator and warm compressors, instrumentation and controls, and ring process equipment, g–2, and experimental programs that require cryogenics. The manpower dedicated to the operation of the RHIC refrigerator directly, is on the average higher than at LEP.

11.6.2 Cryogenic Safety

It is of prime importance to consider safety as a criterion when providing refrigeration of this magnitude within the confinement of building structures. Careful attention must be paid to providing an effective means of access and egress for this facility, with its long linear dimensions, because of the possibility of an inadvertent release of cryogen at a high volumetric flow rate under certain fault scenarios. The installation and testing experience gained at RHIC, with reference to work accomplished at the SSC, FNAL, and CEBAF, has shown the prudent approach revolves around good cryogenic component design, governed by conformance to ASME pressure vessel code requirements and strict attention to the minimization of "ODH" (Oxygen Deficiency Hazard) risks. This would be accomplished by designing building ventilation systems to ensure the safest ODH class. These ODH classes range from 0 to 4, and in our case class A0 is selected.

Table 11.1: Devices and heat loads.

Primary Temperature/ State/ Primary Load at State	Cryogenic Secondary (Shield) Load/ State	Approximate Equivalent Primary Load at 4.5 K/ % Total Primary Load Equivalent	Approximate Equivalent Secondary Load at 4.5 K/ % Total Secondary Load Equivalent	
SC Linac rf Cavities / 100 m				
2.5 K/ 2 Phase/ 7.1 kW	8.3 kW/ (5–8 K) 87 kW/ (40–60 K)	12.8 kW/ 21%	8 kW (5–8 K) 8.7 kW (40–60K)/49.7%	
Matching Solenoids (Capture) / 10 m				
1.9 K/ 2 Phase/6.3 kW	0.82 kW/ (30–300)	14.8 kW/ 24%	0.3 kW/0.9%	beam loading
IL1 / 110 m				
4.4 K/ 2 Phase/ 0.55 kW	0.59 kW/ (40–60 K)	0.55 kW/ 0.9%	0.06 kW/ 0 .18%	4.5 K load = 5 W/m
Minicooling / 5 m				
16 K/ 2 Phase/ 5.5 kW		1.5 kW/ 2.4%		
IL2 and IL3 / 190 m				
4.4 K/ 2 Phase/ 0.09 kW	1.0 kW/ (40–60 K)	0.09 kW/ 0.15%	0.1 kW/ 0.3%	4.5 K load = 0.47 W/m
Matching and Bunching Solenoids / 50 m				
4.4 K/ 2 Phase/ 0.27 kW	3.0 kW (16–40 K)	0.27 kW/ 0.44%	0.8 kW/ 2.4%	
Cooling/ 100 m				
16 K/ 2 Phase/ 10.6 kW		2.9 kW/ 4.7%		
Acceleration Linac (11 short, 16 intermediate, 19 long cells) / 250 m				
2.5 K/ 2 Phase/ 1.86 kW	2.2 kW (5–8 K) 22 kW (40–60 K)	3.37 kW/ 5.5%	2.0 kW (5–8 K) 2.2 kW (40–60 K)/ 12.5 %	
continued on next page				

continued from previous page				
Primary Temperature/ State/ Primary Load at State	Cryogenic Secondary (Shield) Load/ State	Approximate Equivalent Primary Load at 4.5 K/ % Total Primary Load Equivalent	Approximate Equivalent Secondary Load at 4.5 K/ % Total Secondary Load Equivalent	
Recirculating Linac (48 long cells) / 300 m				
2.5 K/ 2 Phase/ 4.7 kW	5.57 kW (5–8 K) 55.7 kW (40–60 K)	8.5 kW/ 13.8%	5 kW (5–8 K) 5.6 kW (40–60K)/ 31.5 %	
Dipole/ Quadrupole Magnets, for Recirculating Linac				
4.4 K/ 2 Phase/ 0.47 kW	6.0 kW/ (40–60 K)	0.47 kW/ 0.76%	0.6 kW/ 1.8%	
Storage ring arcs (53 m ×2 inclined)				
4.4 K/ supercritical/ 1.0 kW (static) + 1.0 kW (dynamic)	2.0 kW/ (40–60 K)	2.0 kW (static & dynamic)/ 3.2%	0.2 kW/ 0.6%	dynamic beam loading

Table 11.2: Load summary.

Total	Primary	Secondary	Primary Equivalent	Secondary Equivalent
Total (2.5 K, 4.4 K, 16 K without contingency)	13.66 kW (2.5 K) 3.38 kW (4.4 K) 16.1 kW (16 K)			
Total (5–8 K, 16–40 K, 40–60 K without contingency)		16.1 kW (5–8 K) 3.0 kW (16–40 K) 124 kW (40–60 k)		
Total equivalent (4.5 K without contingency)			47.4 kW	33.6 kW
Total equivalent (4.5 K with 30% contingency)			61.6 kW	43.7 kW

Table 11.3: Load concentrations and percentages.

Cooled Device	% Total and Equivalent 4.5 K Load in kW (Primary Load)	% Total and Equivalent 4.5 K Load in kW (Secondary Load)	Total Equivalent 4.5 K Refrigeration, Primary plus Secondary in kW/ Total with 30% Contingency in kW
SC linac rf cavities	12.8 kW/ 21%	16.7/ 49.7%	29.5/ 38.4
Matching solenoids (capture)	14.8 kW/ 24%	0.3 kW/0.9%	15.1/ 19.6
IL1 (110 m)	0.55 kW/ 0.9%	0.06 kW/ 0.18%	0.61/ 0.8
Minicooling	1.5 kW/ 2.4%		1.5/ 1.95
IL2 and IL3 (190 m)	0.09 kW/ 0.15%	0.1 kW/ 0.3%	0.2/ 0.26
Matching and bunching solenoids	0.27 kW/ 0.44%	0.8 kW/ 2.4%	1.1/ 1.4
Cooling	2.9 kW/ 4.7%		2.9/ 3.8
Acceleration linac (11 short, 16 intermediate, 19 long cells)	3.37 kW/ 5.5%	4.2 kW/ 12.5%	7.7/ 10
Recirculating linac (48 long cells)	8.5 kW/ 13.8%	10.6 kW/ 31.5%	19.1/ 24.8
Dipole/ quadrupole magnets, for recirculating linac	0.47 kW/ 0.76%	0.6 kW/ 1.8%	1.1/ 1.4
Storage ring arcs (53 m x 2 inclined)	2.0 kW/ 3.2%	0.2 kW/ 0.6%	2.2/ 2.9
Total Load	47.4	33.6	81/ 105.3

Table 11.4: Load concentrations grouped by area, with 30% contingency.

A- SC linac rf cavities (kW)	38.4
B- Items 2–7 inclusive, from Table 11.3 (kW)	27.8
C- Acceleration and recirculating linacs (kW)	34.8
D- Storage ring (kW)	3.0

Bibliography

[1] M. Iarocci, et al., *RHIC 25 kW Refrigerator and Distribution System, Construction, Testing, and Initial Operating Experience*, Advances in Cryogenic Engineering, **Vol. 43**, P. Kittle, Ed., Plenum Press, New York (1997), p 499.

[2] M. Iarocci, et al., RHIC Accelerator Commissioning, Cryogenic Tests and Initial Operating Experience of the 25 kW Refrigerator and Distribution System, Advances in Cryogenic Engineering, **Vol. 45**, Q-S Shu, Ed., Plenum Press, New York (1999), p 1323.

[3] N. Bangert, Ph. Gayet, et al., Operation of the Four 12 kW at 4.5 K Refrigerators for LEP, Advances in Cryogenic Engineering, **Vol. 45**, Q-S Shu, Ed., Plenum Press, New York (1999), p 1293.

[4] S. Claude, et al., Specification of the Four large 4.5 K Helium Refrigerators for the LHC, Advances in Cryogenic Engineering, **Vol. 45**, Q-S Shu, Ed., Plenum Press, New York (1999), p 1269.

[5] P. Gadget, et al., Two Large 18 kW (Equivalent Power at 4.5 K) Helium Refrigerators for CERN's LHC Project, Supplied by Air Liquids, Advances in Cryogenic Engineering, **Vol. 45**, Q-S Shu, Ed., Plenum Press, New York (1999), p 1277.

[6] J. Bose, et al., Two Large 18 kW (Equivalent Power at 4.5 K) Helium Refrigerators for CERN's LHC Project, Supplied by Line Kryotechnik, Advances in Cryogenic Engineering, **Vol. 45**, Q-S Shu, Ed., Plenum Press, New York (1999), p 1285.

[7] C. H. Rode, et al., 2.0 K CEBAF Cryogenics, Advances in Cryogenic Engineering, **Vol. 35**, R. W. Fast, Ed., Plenum Press, New York (1990), p 275.

Chapter 12

Conventional Facilities

12.1 Introduction

The conventional systems for the proposed Neutrino Factory include all necessary infrastructure required to support the operation of the facility. This includes, but is not limited to, the following: site improvements, below-grade enclosures, support buildings, target hall, access shafts, utilities, and conventional cooling systems.

12.2 Structures

12.2.1 Transport Tunnel and Egress Spurs

Approximately 9500 linear feet of arch-plate tunnel will be installed in order to accommodate the accelerator. This will be made of galvanized corrugated steel with a reinforced concrete floor. The tunnel will vary in diameter from 16 to 26 feet. The steel structure can not be used in those areas where, the magnetic field is not contained and/or where high radiation is anticipated, in that case, the structure will be made of reinforced concrete. The facility requires approximately 650 linear feet of concrete tunnel. Emergency egress will be placed along the tunnel according to Life Safety requirements. Access spurs for component installation and maintenance shall be provided. Emergency ventilation for the tunnel will be provided, along with humidity control and heating.

12.2.2 Support Buildings

Four pre-engineered metal frame structures shall be built to accommodate the cryogenic plants necessary for the facility. Two of these are 19,000 S.F. each, while the other two measure 10,000 S.F. Each shall have roll-up access doors for equipment installation, personnel egress doors, HVAC, and lighting.

There will be six power supply/support buildings designed and constructed, in order to house power supplies, vacuum equipment, and instrumentation/controls. Five of these building will provide a service area of approximately 20,000 square feet each. The sixth building shall be half this size. Each structure shall have roll-up access doors for equipment installation, personnel egress doors, HVAC, and lighting.

Klystron buildings running parallel to the tunnel shall be provided. The total area required is approximately 70,000 square feet. As with the other support structures, each klystron building will have roll-up access doors for equipment installation, personnel egress doors, HVAC, and lighting.

12.3 Soils, Earthwork, and Shielding

Brookhaven National Laboratory sits on an area located within the Atlantic Coastal Plan. The basic Biotite Gneiss bedrock formation underlying the area is encountered at depths on the order of 1500 feet below mean sea level. The site is located near the center of Suffolk County, on a glacial out-wash plain. The overburden soil consists of sand and gravel deposits that extend to the bedrock surface. A few clay layers may exist, the Gardiners clay layer at a depth of 200 feet being the highest elevation. Soil borings indicate a medium-compact to compact granular soil quite suitable for building in the area of the proposed Neutrino Factory. Existing cut-and-cover technology will be used to install the facility tunnel.

It is anticipated that earthen berms will be utilized over the facility for radiation protection. Approximately 20,000 cubic yards of soil will be excavated in order to install the tunnel as outlined above. An additional 1.4×10^6 cubic yards of fill will be installed to provide a minimum of 20 feet of soil cover over the tunnel area for radiation protection. A portion of this additional fill is required to elevate the muon storage ring. Shielding in the target area shall be supplemented with 15,000 tons of steel plate and 300 cubic yards of poured concrete.

12.4 Conventional Power

The estimated essential electrical load for the facility is 150 MW of conventional power. This will require a new 138 kV overhead line from the offsite commercial grid. A further study as to whether this power is available from offsite sources is presently being carried out. For this estimate it is assumed that this power will become available from outside commercial power providers. The facility will also require three substations that will transform the 138 kV power to a usable 13.8 kV. It is anticipated that major power supplies will be designed to accommodate a 13.8 kV input voltage. Various step-down transformers providing 480 kV to the site will also be necessary.

12.5 Cooling Water

Cooling water will be required primarily in support of the facility's cryogenic system. There will also be a number of conventionally powered devices used in the facility that will directly require cooling water. Conventional cooling shall be provided via a number of evaporation, recirculating type cooling towers, pumps, and distribution piping, placed in the general vicinity of the cryogenic support buildings.

12.6 Site Improvements

While most of the facility will be built in an undeveloped section of the laboratory, there are a number of locations where the facility does impact existing utilities. These utilities will need to be rerouted or removed in order to accommodate the new construction. The existing BLIP facility will also require dismantling and demolition, or relocating, in order to accommodate the proposed Neutrino Facility superconducting linac.

New parking areas will be required for the facility. Approximately 300,000 square feet of asphalt paving will be installed for service roads and parking lots. Storm water drainage, geo-membrane material, grading, clearing and grubbing will also be required. Geo-membrane material will be installed over the target area and transport system, as well as the muon storage ring/detector area.

12.6. Site Improvements

Chapter 13

Environment, Safety and Health Considerations

13.1 Introduction

The Neutrino Factory presents a number of challenges in the general area of environment, safety, and health. Here we identify these challenges and make a preliminary assessment of how they might be addressed and of their potential impact on the project. Many of these issues are very similar to those that have been encountered and solved during the construction and operation of other accelerator facilities at BNL and elsewhere, while others are novel. The novel ones will require particular attention as the project proceeds to ensure their timely resolution in a cost-effective manner that meets the approval of the Laboratory, the Department of Energy and the public. With adequate planning in the design stages, these problems can be adequately addressed in a manner that merits their support.

13.2 Procedural/Regulatory Matters

The actual design, construction, and operation of the Neutrino Factory will have to meet a number of procedural/regulatory milestones in the area of environment, safety, and health to ensure its success. Devoting early attention to these issues is likely the best way to enhance public support of the project. Design, analytical and operational requirements are currently provided in the BNL Standards Based Management System (SBMS) Accelerator Safety and Hazard Analysis Subject Areas, as well as the applicable SBMS Subject Areas on environmental protection [1].

13.2.1 Environmental Protection

All new DOE projects are subject to the National Environmental Policy Act (NEPA). In accordance with NEPA and the Cultural Resources Evaluations Subject Area [1], the project will generate an Environmental Evaluation Notification Form and request the funding agencies (DOE and/or NSF), to make a determination on the level of documentation needed to comply with NEPA. Based on the proposed design and past determinations on other accelerator projects, an Environmental Assessment (EA) should be sufficient and would be the expectation of the determination that the funding agencies will make. The decision making process and content of the EA is prescribed in NEPA, along with the requirement to seek public comment. The conclusion of the EA process is either a Finding of No Significant Impact (FONSI) or a determination of need to prepare an Environmental Impact Statement (EIS). The NEPA process is rigorous, but one that BNL has the expertise to conduct and complete. This task must be completed, customarily by using external resources, prior to expenditure of project funds. Other procedural requirements apply in the arena of environmental protection in the form of environmental permits that will be needed for construction. This was the case for the previous RHIC Project. Any permits that apply to operations will be identified if and when the EA identifies regulated effluents. Topics covered by such permits include stormwater water discharges, discharges of cooling water, wetlands mitigation, releases of air pollutants for both non-radioactive pollutants and for radionuclides, and construction permits. Historical sites have previously been identified on the BNL site that will be reviewed in the NEPA process.

13.2.2 Environment, Safety and Health Procedural and Regulatory Compliance

The Laboratory will be required to prepare an assessment of the environment, safety, and health issues associated with this project in the form of a Safety Assessment Document (SAD). Since the project will be a Major System Acquisition, the preparation of a Preliminary Safety Assessment Document (PSAD) is required as a scooping document for the hazards involved in construction and operation. The PSAR will also be the basis for the EA and must be completed and reviewed by the funding agencies before funding is approved to start construction. The main purpose of the PSAD is to identify the relevant ES&H issues at an early stage and propose how they might be mitigated. The SAD will later document their resolution in the final detailed design of the architecture and components of the machine. It is customary for the funding agencies to review these safety documents by utilizing an external independent review team throughout the preliminary and final design stages. DOE is presently "self-regulating" in the areas of industrial safety and occupational radiation protection. This situation could change at some future time if external regulation is applied to DOE facilities. Related developments are being monitored closely to identify new requirements or procedures that might apply to new projects such as the Neutrino Factory.

13.3 Occupational Safety During Construction of the Facility

The beamlines all would be located at or just below grade, but above the water table. At this level, construction is likely to proceed by the standard "cut and fill" method. The Occupational Safety and Health Administration regulations (OSHA) in 29 CFR 1926 apply to the construction activities. These rules are delegated down to BNL staff and contractors through SBMS and general conditions specified in contracts, as appropriate. There are no unconventional occupational safety issues expected to be associated with the construction work. The beamlines and target station will be heavily shielded to reduce onsite and offsite exposure from prompt radiation. The shielding will typically be constructed with a sand berm as has been employed by other accelerators at BNL. The production target will require a more dense and complex shield matrix to reduce prompt radiation and protect the groundwater in the vicinity, but the design will not present any special problems with respect to conventional construction.

13.4 Environmental Protection During the Construction of the Facility

The Laboratory as an institution is registered to the ISO 14001 Environmental Management System (EMS) [1], which will be used as the platform to identify Environmental Aspects and Impacts during construction. The EMS process will identify Operational Controls to ensure that legal and other requirements are maintained to protect the environment and provide the framework to manage the environmental aspects.

Based on past experience with the conventional construction at RHIC, environmental protection must be addressed during the conceptual design phase. With respect to the restoration of the forested area that will be disturbed to build the beamlines, only the area of the beam enclosure will be cleared to minimize this impact. If additional fill material is needed to construct sand berms for shielding, clean fill will be brought in from off-site without disturbing any existing vegetated land. A plan to restore the environment will be required to facilitate regrowth of the vegetation on the disturbed land and over the newly constructed beamlines.

13.4.1 Ordinary Operational Occupational Safety Hazards

The operational occupational safety hazards typically encountered at BNL and other large particle accelerator facilities will be found in this facility. These have been successfully addressed by well-known techniques and are simply listed below:

- High current electrical circuits will be used in the magnets on a large scale.
- High power radio-frequency (rf) generation and distribution equipment will be used extensively.
- Large numbers of cables will be installed in cable trays, with associated fire protection implications.
- Long tunnels will be present, with corresponding egress and fire protection issues to be addressed.
- Large, heavy components will have to be moved and aligned.

13.5 Novel Occupational Safety Hazards

13.5.1 Use of Nonflammable Cryogens

The extensive use of large amounts of nonflammable cryogenics in both magnets and rf structures presents special problems, but similar to those solved at RHIC and other accelerator facilities. Portions of these cryogenic systems will reside in machine enclosures and present oxygen deficiency hazards (ODH). As was done for the cryogenic components in RHIC, the ASME Boiler Code will be used in design, as previously described in the RHIC SAD. The Oxygen Deficiency Hazards Subject Area [1] will be followed to implement worker controls in operations.

13.5.2 Use of Flammable Cryogens

The use of ionization cooling in a liquid-hydrogen (LH_2) medium presents significant fire and explosion hazards. Also, the LH_2 cells will be interleaved with RF structures and magnets that handle a great deal of electrical energy. In the past, BNL has successfully used stringent review procedures involving an internal Cryogenic Safety Committee, as well as external review committees of experienced individuals, to provide advice on the design basis and management of cryogenic systems. Because of the high level of hazard nature and expected large volume of LH_2 an intensive process of safety review will begin at the earliest reasonable stage in the design process.

13.5.3 Muon Storage Ring Life Safety (Egress) Considerations

The Muon Storage Ring (MuSR), as defined for this study, constitutes a long above-grade tunnel sloped at 13.1° with respect to the horizontal. The fire protection/egress considerations of this configuration will need to be evaluated for life safety by a fire protection professional, and others, for adequacy. Plans will need to be made for the evacuation of any injured or ill personnel through the sloped arcs.

13.5.4 Muon Storage Ring Slope Hazards

The relatively steep slope of the MuSR presents unique hazards during operation as well as during construction. There will be safety engineering considerations involved with moving heavy machine components and equipment to support installation and maintenance. The surface of the finished floor should be made sufficiently rough to provide good traction to individuals wearing ordinary shoes. Gutters should be provided to direct water flowing into the tunnel toward the large sump pits at the lower end. They might also be designed to retard the unwanted downhill movement of large items, particularly that of any portable pieces of equipment on wheels. An idea that might address this, and other considerations, is to arrange the gutters in a spiral fashion, regularly crossing the tunnel to direct such items toward one of the walls. Regular tie-down points for heavy items of equipment could be provided. These problems can be solved if they are addressed early in the design process.

13.6 Prompt and Residual Radiation Safety During Operation of the Facility

13.6.1 Proton Driver

13.6.1.1 Production Target and Prompt Radiation Shielding

The conceptual target design is a 5 mm radius liquid mercury jet with a velocity of 30 m/s. The jet is tilted vertically downward at an angle of 100 mrad with respect to a 20 T solenoidal field. A 24 GeV proton beam with an rms radius of 1.5 mm, tilted vertically downward at an angle of 67 mrad with respect to that same solenoidal field, collides with the mercury jet 45 cm from the jet nozzle. That 45 cm distance is to the intersection of the jet and beam centers; due to the finite diameter of the jet and the beam, they interact over a range of 15 cm to 75 cm from the nozzle. The nozzle is embedded in an iron pole face which helps control the uniformity of the solenoidal field, and the proton beam enters through that same pole face. Every 400 ms, 6 bunches of 1.7×10^{13} protons each, separated by 20 ms, will hit the mercury jet target.

The Proton Driver and the Neutrino Factory Target Station will require massive amounts of hadron shielding, similar in scale and type to that of other proton accelerators in this energy and intensity regime. Detailed calculations made using MARS have already been performed to assess the prompt radiation inside the target hall to determine the amount of shielding required for a similar proposal made by Fermilab [2]. The transport of beam from the synchrotron to the Target Station poses no unusual problems with respect to prompt radiation shielding, although a deployment of a Design Basis Accident (DBA) and Beam Loss Scenario, as was done for the RHIC Project, is needed to complete the detailed design of shielding for the various regions of the beamline [3]. This is also needed for analysis of the existing AGS ring, to model the current infrastructure to asses the need for additional or upgraded shielding and penetrations.

The Proton Driver, under maximal operation, will handle an expected 7-14 times the beam power of the present AGS complex. Since the impacts to the AGS ring would scale roughly with the beam power, modifications to handle such a large upgrade are planned. Direct injection to AGS from a new 1200 MeV Linac instead of the existing Booster, coupled with the improved transition crossing jump, should lead to lesser beam losses during the acceleration and ejection of beams. Therefore, it is assumed that the normal beam loss per second in the AGS will remain at, or less than, the current level. The handling of this large beam power has already received, and merits, careful attention. Efforts should continue to better control such losses of beam both from the standpoint of component activation and also with respect to soil and groundwater impacts.

Because BNL resides on a Sole Source Aquifer, activation of soil and contamination of groundwater are both considerations near the target station. The amount of high density shielding, *i.e.* steel and tungsten, must be optimized to mitigate production of ^{3}H and ^{22}Na along with moisture barriers to prevent migration of these isotopes to the water table.

A study to assess shielding of prompt radiation from the storage ring was performed using MARS. [15] For a muon beam momentum of 20 GeV/c, 2×10^{20} muons per year decay in the storage ring. The straight section is 126 m long, and the arcs are each 53 m, for 180^o of rotation, (16.87 m radius). The BNL administrative design criteria for control of off-site radiation dose equivalent is 5 mrem/yr, and the drinking water standard in DOE Order 5400.5 requires less than 1 pCi/mL tritium and 0.2 pCi/mL ^{22}Na. For shielding calculations, the Fermilab wet soil properties were used with the density of 2.24 g/cm^3 and scaled to the BNL value of 1.9 g/cm^3. For neutrino-induced radiation, the soil density is negligible; therefore the results are transferable to BNL soil. Using the above assumptions the required soil thicknesses scaled to the BNL soil density of 1.9 g/cm^3 are listed below [15]:

- During normal operation, and with a design criterion of 0.25 mrem/h for occupancy in the underground facilities (electronics rooms, etc.), there must be at least 8.3 m of shielding outward from the arc tunnel enclosure, and 3 m of shielding on all other sides of the tunnel. The radiation that is being shielded from this source is due to electron showers.

- For groundwater protection from radiation due to electron showers, a geomembrane is required to prevent water flow within 1.8 m of the tunnel in all directions. In addition, there must be a geomembrane preventing water flow through a region extending 3.5 m from the end of each straight section in the downstream beam direction of those straight sections. As for neutrino-induced activation, it results in radionuclide concentrations a factor of 800 below BNL-imposed limits for tritium, and even lower for ^{22}Na.

- To meet the off-site radiation requirement of 5 mrem/yr due to neutrino-induced radiation, a plane extending 30 m from the outside of the arc tunnel enclosure, within a band ± 10 cm from the orbit plane, must be kept on-site (see Fig. 13.1). In addition, an ellipsoid of 2 m half-width, 1300 m long, the long axis extending in the direction of the production straight, must be kept within the site (see Fig. 13.2 and discussion in Section 13.6.3.1).

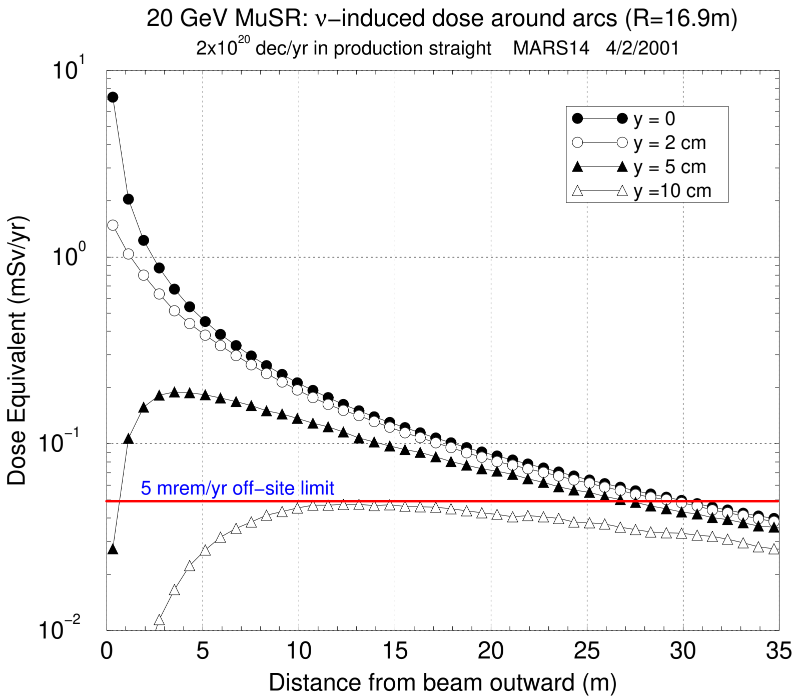

Figure 13.1: Neutrino-induced dose around the arcs as a function of the distance from the arc.

13.6.1.2 Residual Radioactivity at the Target Station

Given the high beam power, the residual activation of the Target Station merits special attention. The residual absorbed dose rates to be found in the Target Station are not presently known in detail, but will be large, of the order of krads h^{-1} (tens of Sv h^{-1}). There will also be significant activation of water used to cool the non-cryogenic components. Remote handling capabilities of the style used by other facilities, such as the Los Alamos Neutron Science Center (LANSCE) and those planned for the Spallation Neutron Source (SNS) at the Oak Ridge National Laboratory, will be needed.

Fission products will be produced from the primary interactions of protons on elemental mercury, resulting in a source term of volatile and non-volatile radionuclides. Air activation will be enhanced by the neutrons that will be produced from (p, Hg) interactions. Some of the isotopes produced in the target will exceed the thresholds for a

Non-reactor Nuclear Facility. Therefore, the target will require compliance with 10 CFR 830 Nuclear Safety Management and a funding agency approved Safety Analysis Report. Nuclear Facilities are subject to levels of safety analysis, quality assurance, and training requirements that are significantly more stringent than those normally applied to accelerator facilities. The present DOE definition of a Nonreactor Nuclear Facility excludes accelerators, such that the balance of the complex will remain regulated under the Accelerator Safety Order, DOE 420.2. Definition of the facility as a nuclear facility needs to be resolved. The target station, from a regulatory standpoint, should be segregated from the rest of the facility to the extent possible. The Laboratory continues to monitor the ongoing development of federal requirements on this topic.

13.6.1.3 Airborne Radioactivity

The production of airborne radioactivity in the vicinity of the Target Station will constitute the dominant source of airborne radioactivity emissions for the Neutrino Factory. At this early stage, a comparison with the work already done by Fermilab on the NuMI Target Station [6] may be useful, since the beam powers of the two facilities are comparable, although the source term for the Hg target is likely to exceed that from the Fermilab analysis of a carbon target and the site boundary distance may be different. The NuMI Target Station in the Fermilab proposal will operate at a beam power of 0.404 MW. It will release a total of about 15 Ci (555 GBq) annually. This is dominated by 5 Ci (185 GBq) of ^{11}C (half-life = 20.3 min.) and 9.8 Ci (363 GBq) of ^{41}Ar (half-life = 1.83 hours). Such releases will result in an annual dose equivalent of about 0.009 mrem (0.09 μSv) at the Fermilab site boundary. An evaluation of the offsite dose equivalent from airborne releases from the BNL design is required to assess whether 0.1 mrem (1 μSv) in one year may occur. If reaching that threshold is possible at the site boundary from the new beamlines at BNL, then a NESHPS Permit must be submitted. A continuous monitoring program and other requirements are specified by U. S. Environmental Protection Agency Regulations. [7] The monitoring program will have to be designed to demonstrate that the regulatory limit of 10 mrem (100 μSv) in one year is not exceeded. The design of the beam enclosure ventilation system will have to maximize the decay in transit and/or filtration from the point of production to the point(s) of release.

13.6.1.4 Radioactivity in Soil and Groundwater

The calculation of the radioactivity produced in the soil for the entire facility can be accomplished using current versions of Monte-Carlo shielding codes. As stated above, the Target Station is the most significant source. The impact of the beam loss on soil and ground water will be reassessed for new beamlines, as well as the AGS Complex, as part of the design process.

13.6.2 Cooling Stages and Muon Acceleration Stages

In the cooling stages, the collected muons from pion decays will deposit considerable energy in the LH_2 cells in the course of being "cooled." This energy will end up largely in the form of heat transferred to the hydrogen and dispersed by the refrigeration equipment. Given the low energy of the muons at this stage, only energy loss by ionization is important. It is straightforward to design shielding appropriate to ranging out "stray" muons that might miss the cooling apparatus as well as the electromagnetic cascades induced by their decay electrons. Present Monte-Carlo codes are adequate to provide accurate calculations of this effect. The forward-peaked nature of the muon decay field should minimize the lateral extent of the shielding necessary. The production of induced radioactivity in these stages is also severely limited by the energy, and the fact that leptons are the only particles present. At the higher energy stages, the scale of the muon shielding required will increase, but even the final muon energy is still relatively low since the mean range of a 50 GeV muon in soil is only about 109 m. Likewise the size and importance of the electromagnetic cascades produced by the decay electrons will grow as the energy increases. Radioactivation could be expected, but at levels much smaller than those to be experienced in the Proton Driver and Target Station.

13.6.3 Muon Storage Ring

13.6.3.1 Control of Radiation Dose Due to Neutrinos

The most unusual radiation consideration pertaining to the Muon Storage Ring is that due to the neutrinos produced by the decaying muons. Obviously, the design of the entire facility is optimized toward the production of a high fluence of neutrinos in the intended direction downward (westward). This also results, unavoidably, in a similar stream of neutrinos in the upward direction. The methods for calculating radiation dose equivalent from the neutrino fluence have been described elsewhere[9],[10]. The Department of Energy has specified annual limits on the radiation dose equivalent that can be received by occupational workers and members of the public [11]. These limits rather clearly refer to the dose equivalent that could plausibly be delivered to actual people. For individual members of the public, the limit in DOE Order 5400.5 is 100 mrem (1 mSv) in a year, not including man-made, medical, or enhanced natural radioactivity. Special reporting requirements apply when the annual dose equivalent received by an individual

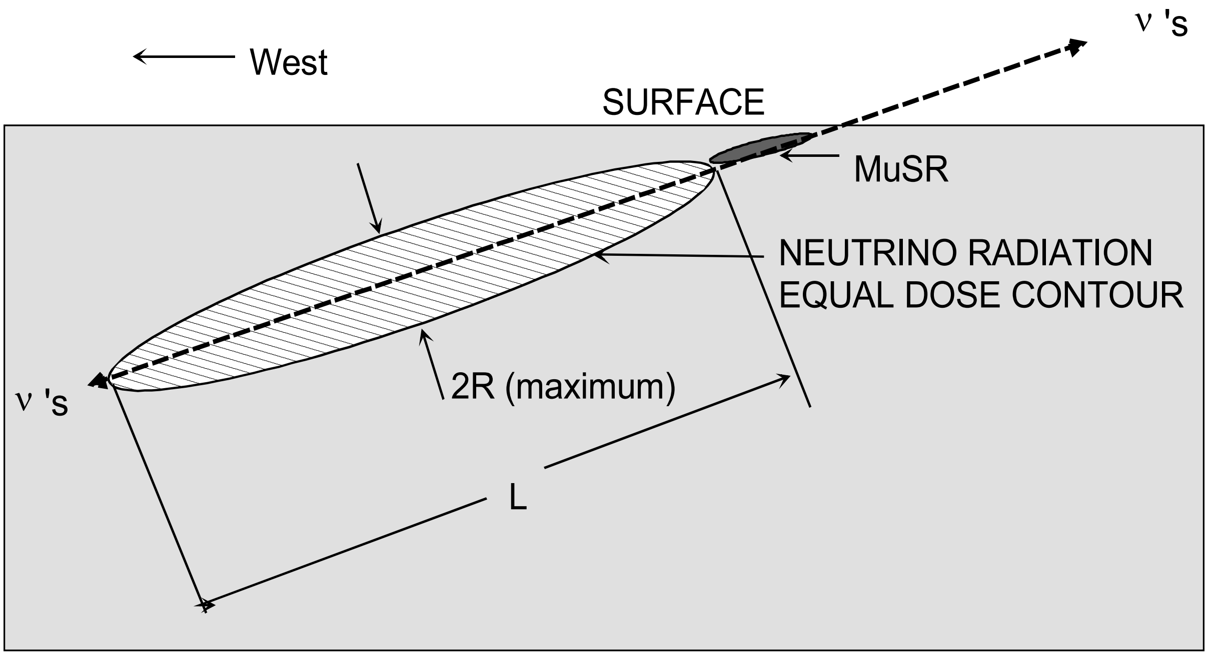

Figure 13.2: Schematic representation of the neutrino radiation fields due to muon decays in the MuSR. The gray region is the earth while the cross-hatched region is a schematic representation of the region inside of a selected contour of equal dose equivalent due to the neutrinos resulting from downward muon decays. A similar neutrino radiation lobe is to be found in the upward direction due to upward muon decays in the other straight section of the ring. The parameter L describes the intersection of this isodose contour with the centerline of the neutrino beam trajectory, while R is its maximum radial extent. The actual contours are more forward-peaked, and narrower than this symbolic ellipse. Symmetry about the centerline of the neutrino trajectories is expected.

exceeds 10 mrem (0.1 mSv) in a year. For comparison, the average annual radiation dose equivalent received by individuals living in the United States from natural sources of radiation, including exposure to radon indoors, is about 300 mrem (3000 μSv) [12]. Figure 13.2 schematically shows the "lobe" of neutrino radiation due to neutrinos produced by muon decays in the downward (westward) production straight section of the MuSR. The parameters L and R describe the length and maximum radius of a chosen contour of equal annual dose equivalent. L is measured from the end of the MuSR straight section along the centerline of the neutrino trajectory, while R is measured perpendicular to the neutrino trajectory. Cylindrical symmetry should hold about this axis for this radiation field. Due the extreme forward peaking, the dose equivalent at the surface due to these neutrinos is zero. A similar radiation field will penetrate the surface due to muon decays in the upward (eastward) return straight section of the MuSR centered about the axis of the return straight section. Mokhov has calculated these radiation fields and has plotted the results for two different contours of annual dose equivalent, 1 mSv (100 mrem) and 0.1 mSv (10 mrem) [13]. As stated in Section 13.6.1.1 and as applied to BNL, to meet the off-site radiation requirement of 5 mrem/yr due to neutrino-induced radiation, a plane extending 30 m from the outside of the arc tunnel enclosure, within a band ± 10 cm from the orbit plane, must be kept on-site (see Fig. 13.1). In addition, an ellipsoid of 2 m half-width, 1300 m long, the long axis extending in the direction of the production straight, must be kept within the site. In that regard, because the eastern site boundary is 2200 m away, the required distance of 1300 m to the east of the proposed location for the storage ring is well within the BNL site boundary. At the BNL site boundary the trajectory of the neutrino cone puts it at an elevation of 335 m. It can reasonably be assumed that a high-rise building that large will not be built, and no occupancy will occur in that aperture.

13.6.3.2 Other Radiation Sources

The bombardment of the walls of the MuSR components will involve a nearly uniform irradiation by electrons. Calculations of both the energy deposition in the superconducting magnets and the induced radioactivity due to these electromagnetic cascades were performed by Mokhov [14]. Residual dose equivalent rates due to these cascades will be small, less than about 1 mrem h^{-1} ($10\,\mu$Sv h^{-1}) after a 30 day irradiation and a 1 day cooldown. It is conceivable for the muons stored in the MuSR to be catastrophically lost in the event of a sudden power outage or some other failure of the magnets. However, given the orbit time of 6 μs, and the likely inductive time constants of the magnets, the loss of the muons during such an event would be distributed over many turns and large portions of the ring. Only a tiny fraction of them would be directed in a manner such that they penetrate the surface. Further calculations should be made to demonstrate this. It is certain that the near detector halls will be exclusion areas during operations due to neutrinos as well as the other background sources that are unavoidably present.

13.7 Non Radiological Environmental Protection Issues During Operation

13.7.1 Proton Driver, Target Station, Cooling Region, and Muon Acceleration Linacs

The issues are straightforward ones related to the control of non-radioactive wastes. Efforts should be made to prevent the creation of regulated mixed or hazardous wastes and to control environmental spills. Surface-water discharges should be managed in accordance with current Laboratory policies and any New York State SPDES permits already in place. In general, management of regulated materials will be via the ISO 14001 EMS.

13.7.2 Muon Storage Ring

The location of the MuSR over a Sole Source Aquifer demands especially stringent protection against spills. Careful attention to these problems and employment of EMS elements during the design and construction phases, should lead to their successful solution.

13.8 Summary

The Neutrino Factory provides a number of challenges in the area of environment, safety, and health. Many of these have been encountered, and effectively addressed, at BNL and other accelerator laboratories. Some of the problems are common to technological advancements in other accelerators worldwide. For these, collaborative efforts should continue to develop and improve the solutions that are needed. This project raises a few new issues that must be addressed. Continued attention to these issues is anticipated as the project proceeds.

Bibliography

[1] Brookhaven National Laboratory Standards Based Management System (SBMS), www.sbms.bnl.gov.

[2] N.V. Mokhov, *Particle Production and Radiation Fields at a Neutrino Factory Target Station*, presentation at BNL, January 29-31, 2001.

[3] A. Stevens, S. Musolino, and M. Harrison, *Design Criteria For Prompt Radiation Limits on the Relativistic Heavy Ion Collider Site*, Health Physics, 66, (1994), 300-304.

[4] M. Barbier, *Induced Radioactivity*, (North-Holland Publishing Company, Amsterdam and London, Wiley Interscience Division, John Wiley and Sons, Inc, New York, 1969).

[5] U. S. Department of Energy, *Nuclear Safety Analysis Reports*, DOE Order 5480.23, April 30, 1992. The classification criteria specified in this Order are provided in a DOE Standard, *Hazard Categorization and Accident Analysis Techniques for Compliance with DOE Order 5480.23, Nuclear Safety Analysis Reports*, DOE-STD-1027-92 Change Notice No. 1, September 1997. The criteria are augmented by additional radionuclides in LA-12981-MS, UC-940, *Table of DOE-STD-1027-92, Hazard 3 Threshold Quantities for the ICRP-30 List of 757 Radionuclides*, Los Alamos National Laboratory Report, August 1995.

[6] N.L. Grossman, D.J. Boehnlein, and J.D. Cossairt, *Production and Release of Airborne Radionuclides Due to the Operation of NuMI*, Fermilab Report TM-2089, August 1999.

[7] United States Code of Federal Regulations, Title 40, Part 61, Subpart H, *National Emissions Standard for Hazardous Air Pollutants (NESHAP) for the Emission of Radionuclides other than Radon from Department of Energy Facilities*, 1989.

[8] J.D. Cossairt, *Use of a Concentration-Based Model for Calculating the Radioactivation of Soil and Groundwater at Fermilab*, Fermilab Environmental Protection Note 8, December 1994 and J. D. Cossairt, A. J. Elwyn, P. Kesich, A. Malensek, N. Mokhov, and A. Wehmann, *The Concentration Model Revisited*, Fermilab Environmental Protection Note 17, June 1999.

[9] J.D. Cossairt, N.L. Grossman, and E.T. Marshall, *Assessment of Dose Equivalent Due to Neutrinos*, Health Physics 73 (1997) 894-898.

[10] N.V. Mokhov and A. Van Ginneken, *Neutrino Induced Radiation at Muon Colliders*, presented at the 1999 Particle Accelerator Conference, New York, New York, March 19-April 2, 1999, FERMILAB-Conf-99/067.

[11] U. S. Department of Energy, *Radiation Protection of the Public and the Environment*, DOE Order 5400.5, January 7, 1993.

[12] National Council on Radiation Protection and Measurements, Ionizing Radiation Exposure of the Population of the United State and Canada from Natural Background Radiation, NCRP Report No. 94, December 1987.

[13] N.V. Mokhov, private communication, January 2000.

[14] N.V. Mokhov, *Radiation Load on Muon Storage Ring Magnets*, presentation given at Fermilab, January 25, 2000.

[15] N.V. Mokhov, Fermilab email communication to J.S. Berg, Radiation around Storage Ring, April 2, 2001.

Chapter 14

R&D Plans

14.1 Introduction

In this section we summarize the key R&D activities required to validate the design concepts described in this Neutrino Factory Feasibility Study. Topics will be covered in the order in which they appeared in the facility descriptions given earlier in this document. Items covered here fall into two categories: i) those required to validate or improve the components that drive the fabrication costs of the facility, and ii) those required to address the performance and/or feasibility of fabrication of particular components. In the first case, R&D will mainly involve hardware fabrication and testing without beam. In the second case, performance tests with beam may be required in addition to prototyping. For each hardware area, the main R&D topics will be listed in the context of the two categories above.

The R&D items listed here fall into the broader R&D effort of the Neutrino Factory and Muon Collider Collaboration (MC). A five-year R&D plan, currently under way, has been completed by the MC and is available [1]. We will not repeat that information here. What we cover below are topics that have arisen in the context of this—and, in some cases, the previous—Feasibility Study.

It is important to note that much of the hardware development effort envisioned here requires different people at different institutions. Thus, there is no fundamental reason that the program cannot proceed in parallel on several fronts. Indeed, it *must* proceed this way if we are to complete the R&D tasks in a reasonable time frame. Clearly, however, our progress requires funding commensurate with the program needs; this is the resource over which we have the least control.

14.2 Proton Driver

The upgrade of the AGS to reach higher intensity is relatively minor, as it has already operated at 70% of the design intensity specified here. The aspect where additional work is required is related to the need for short, 3 ns, bunches. The peak current required in this case, about 400 A, is seven times higher than what the AGS has achieved to date. Efforts to reduce the ring broadband impedance below 10 Ω will be worthwhile. For example, development of bellows shields capable of operating reliably in this beam current regime should be examined. The new B Factories (PEP- II and KEKB) are operating in similar regimes of peak and average beam current without experiencing reliability problems with bellows. In parallel with this effort, it will be important to explore other means to mitigate transverse instabilities in the AGS, *e.g.*, by introducing tune spread by means of octupoles.

For the new rf cavities, the 4L2 ferrite material must be characterized in the appropriate frequency regime. (The use of 4M2 ferrite, which has been used elsewhere, is an acceptable fallback solution if the "standard" AGS cavity ferrite does not have the required properties.)

The trade-offs between using a thinner vacuum chamber wall and stronger sextupoles should be studied. In addition, it will be necessary to examine all of the power supply tracking algorithms to make sure they will work properly at a three-times-higher ramp rate. All of these kinds of issues have been solved previously in other accelerators, so there are no real unknowns here.

Experimentally, the AGS should continue with efforts to produce short bunches, to understand the present limitations and make sure that the ring impedance is well understood.

14.3 Target System

The main technical issue to deal with here concerns the survivability of a mercury jet in a 1 MW proton beam. Experiments are already under way at the AGS to study this, and an effort to predict the behavior of the mercury jet via simulations is proceeding in parallel. Ultimately, yield measurements to validate the MARS predictions should be carried out. These will include a (pulsed) 20-T solenoidal field.

Testing of a mercury jet in a high magnetic field is already in progress in Europe using a 13-T magnet at Grenoble. If necessary, tests could be repeated at the full 20-T field at the NHMFL.

The potential of failure fatigue for the jet nozzle must be studied. There is a pressure shock traveling back toward the nozzle after each proton beam pulse. A verification experiment for the shock effects, along with corresponding simulation work, should be carried out to permit a realistic means to mitigate it. Means to "pulse" the mercury jet should also be examined as a possible workaround.

Alternative designs, such as a "band" target (see Section B.2.1), should be examined. In addition to the mechanical issues of the band itself, compatibility with the solenoid configuration envisioned for the target must be assessed via a solid engineering concept.

Studies of the cost-benefit tradeoffs between capture efficiency and magnetic field should be made to optimize the target solenoid field. Present indications are that the penalty of a decrease from 20 T to 18 T is minor in terms of intensity, but the corresponding studies of magnet cost must be carried out. Studies of more optimal conductor for the hollow-conductor magnet are also needed. A conductor having wrapped ceramic insulation should have a more favorable power consumption than the MgO insulated conductor, while providing the same magnetic field. Studies of the alternative Bitter-magnet technology are also needed, focusing on issues of lifetime. The Bitter magnet is more efficient than a hollow-conductor magnet, but its resistance to corrosion in the high radiation environment must be studied.

There are a number of technical issues to consider in completing the design of the target containment area. These include:

- *Beam stop design*. A study of various materials should be undertaken to compare the advantages of low-Z and high-Z materials. Issues include secondary particle showers, residual activation, and decay heating.

- *Beam containment window design*. Adequate cooling designs must be developed, possibly including a combination of bulk coolant flow and edge cooling. If water cooling is required, adequate machine-protection interlocks must be developed. At present, beryllium looks like the most promising material. There is some commonality between the windows for the rf cavities and the beam containment that should be exploited. Since these are replaceable components, techniques for remote replacement must be developed.

- *Component cooling*. Activation of coolants, primarily light water, must be studied. In particular, ^{7}Be and tritium must be considered in the design of the cooling system.

- *Radiation damage*. The effect of radiation damage on the iron magnet "plug," the hollow-conductor copper coils, and the superconducting coil must be studied. Effects of intense radiation on mechanical properties (strength, elasticity) and buildup of corrosion products must be assessed. Materials tests in this context are already in the planning stages.

There are several R&D issues related to the facility configuration and design of the nuclear shielding for the solenoids. The first facility issue deals with the location of, and access to, the target and magnet support systems, namely, vacuum pumps, ducts, valves, cryogenic lines, electrical cables, and diagnostic equipment, to ensure that they are readily maintainable. A target hot cell is already configured with access and maintenance in mind; a more detailed iteration of the facility design would accomplish the same for the other support systems. The second facility issue is the extent to which remote handling capability and equipment are needed downstream from the target/capture region. An extrapolation of the shield analysis that was done for the floor shield over the tunnel, $-0.8 < z < 36$ m, indicates that similar requirements apply downstream. If verified, this requirement would have an impact on the overall facility design and cost.

There are several issues that deal with the nuclear shield design. These can be addressed with R&D activities that simultaneously address mechanical and thermal questions. It has been determined that the optimum shield for the high-field solenoids is 80% tungsten-carbide, 20% water, so the shield design is based on using tungsten-carbide balls. Scale model tests are needed to investigate how to distribute the balls in a homogeneous matrix, and to assess properties such as pressure drop and heat transfer coefficient. This shield is a costly component, and it is important for it to be efficiently designed.

14.4 Phase Rotation and Capture

In this Study, the induction linac (IL) design is closer to present day experience than was the case for Study-I, so the technical uncertainty is lower. Nonetheless, the gradients required are high, so a prototype induction cell, along with its magnetic pulse compression system, should be fabricated. Furthermore, there are several possibilities that might lead to a more cost-effective implementation. Development of less lossy (thinner) amorphous alloys should be undertaken, in conjunction with industry. Being able to use a mass-produced material with acceptable loss properties will result in lower capital costs initially, and lower power costs for the operating facility as well. Candidate materials need to be tested to validate the properties on which the design is based. In addition, the branched magnetics concept should be developed. If it is acceptable to drive a single core with two independent unipolar pulsers, it would eliminate one induction linac in our design. Radiation tests on the Mylar core insulation should be made, to be sure there is no degradation over the expected life of the facility.

The design of the IL core is strongly influenced by the internal superconducting solenoids, in the sense that the inner diameter of the core is set by the need to avoid the fringe field from the solenoid. Quantifying the effects on the core of the solenoid fringe field must be done. In addition, means to reduce the solenoid fringe field, thereby permitting the IL core inner diameter to be reduced, should be examined as part of a cost-benefit tradeoff study.

For the capture area, studies of the radiation heat load need to be refined, and extended through the IL region. The shielding requirements, especially for the upstream solenoids, have a strong impact on the inner diameter, and hence the cost, of these magnets, and an optimization is required. It would clearly be prudent to consider the future upgrade to 4 MW in this regard, as it would be undesirable to have to upgrade the magnets and shielding later.

The present mini-cooling absorber design is not optimized. The main requirements for mini-cooling are: *i*) energy loss equivalent to that of $2 \times 1.75\,\mathrm{m}$ of liquid hydrogen; and *ii*) low multiple scattering. Liquid-hydrogen mini-cooling, while straightforward, is technically, complicated—undesirably so. Simpler solutions involve non-cryogenic liquids or low-Z solids. It is clear that some R&D is called for to flesh out these options. Table 14.1 summarizes the lengths and corresponding radiation-length fractions for liquid hydrogen and various alternative materials.

While hydrogen minimizes scattering effects, it is likely that solid lithium or beryllium would also be acceptable. (Lithium hydride presents practical difficulties since it is neither commercially available nor readily manufactured in large, shaped pieces.) Simulations show that, compared with liquid hydrogen, solid lithium mini-cooling absorbers reduce the number of muons per proton by only about 5%, and beryllium causes only about a 10% reduction. These performance degradations are small, and they can probably be avoided by raising the solenoidal field somewhat to compensate for the increased scattering. (This would entail reoptimizing the front end.) Stronger focusing will increase the cost of the solenoids, but will reduce the size of the beam, allowing smaller absorber diameter. An overall optimization of the system, involving both simulations and engineering, should be done.

The roughly 5 kW of power dissipated in each mini-cooling absorber appears manageable. Cooling tubes affixed to the large ($\sim$1 m^2) perimeter surface can easily transfer such heat. Conductive heat transfer through the material, from the core to the periphery, requires only ~ 10°C temperature rise, small compared with the melting points of lithium and beryllium (186°C and 1350°C, respectively). Water, freon, or some other convenient refrigerant might be suitable, with a choice other than water preferred in the lithium case to reduce the risk of reaction should cracks develop in the cladding.

Table 14.1: Comparison of possible minicooling absorber materials.

Material	Length (cm)	Radiation length (%)
LH_2	175	20
LiH	38	35
Li	57	37
CH_4	49	45
Be	17	48
H_2O	25	70

On the practical side, the feasibility and cost of fabricating large cylinders of these materials must be evaluated. Preliminary contacts with manufacturers [2], [3] suggest that these are not fundamental problems. After design work, fabrication of a prototype disk, followed by bench (and perhaps beam) tests of its thermal performance, would be desirable.

14.5 Buncher and Cooling

The solenoid designs need to be cost optimized and the results put back into the simulations. In particular, the forces on the focusing coils in Lattice 2, with its 1.65-m cell length, are quite high. Lowering these forces will reduce costs. A somewhat longer cell length should help here.

Absorber development R&D is well under way. Techniques to produce very thin windows have already been developed. Pressure tests are planned to validate the safety aspects of the design. Because the power density is high, cooling of the absorber to avoid density fluctuations is challenging. A program of fluid dynamics modeling and bench tests is under way, to be followed by beam tests with 400 MeV protons at Fermilab.

Development of diagnostics is an ongoing process. Prototype devices of the types mentioned in Chapter 5 must be built and tested. Some of these tests will be carried out in conjunction with the rf cavity tests in Lab G at Fermilab. Possible backgrounds from the cavity can be assessed this way. Where possible, diagnostics devices will be tested in a beam, either the 400 MeV proton beam at Fermilab or possibly a muon beam at BNL or elsewhere.

Emittance exchange offers the potential of doubling the intensity of the facility. This is a difficult problem, presently the subject of simulation effort. This effort will be continued to see if an acceptable scheme can be developed. If a good solution is found, hardware development will follow, including new components, such as wedge absorbers, that are called for in the design concept.

In practice, the most critical technical component of the cooling channel is the rf system. The rf peak power requirement is very high for the cooling channel; means to reduce this will yield large benefits. The main issue is to optimize the cavity design for minimum power requirements at the required gradient, and then optimize the cooling lattice design with a suitable cell length. (To date, we have always done this process in inverted order, leading to a non-optimal rf cavity design.) The normal conducting rf structures for the Neutrino Factory buncher and cooling sections are challenging due to the high gradients required and the large transverse dimensions of the incoming muon beam. The solution we are pursuing is to close the beam iris with a conducting barrier of low-Z material to restore the shunt impedance. Simulations indicate that thin beryllium foils, or arrays of thin-walled aluminum tubes, restore the shunt impedance while maintaining acceptable beam scattering. For a continuous foil, the minimum thickness is determined by the power dissipation on the surface. In vacuum, at close to room temperature, the heat can only be removed by radial conduction through the foil to a water-cooled flange. This produces a temperature gradient in the foil, with the maximum temperature in the center. The result is a tendency for the center material to expand and the foil to bow, detuning the cavity. This tendency can be eliminated, up to a point, by arranging for the foil to be pre-stressed in tension. This keeps the foil flat up to that temperature at which the thermal expansion exceeds the pre-stress. Alternatively, the foils could be pre-bowed (to predetermine the direction of motion), and the movement accommodated by tuning the cavity. Such a pre-stressed foil has been simulated in ANSYS and investigated experimentally in a series of tests on small foils at 805 MHz. These will continue as part of the R&D effort, including high-power testing of a cavity with foils in the Lab G facility at Fermilab.

Other structures under consideration include grids of thin-walled tubes and other fabricated structures, see Figs. 14.1 and 14.2. An advantage of closed tubes would be the ability to flow cooling gas through the structure, potentially allowing larger apertures or less material to be used. Simulations suggest that the grids provide adequate isolation between cavities with tolerable scattering of the muon beam. The tubes themselves cause local concentrations of the electric and magnetic fields near their surfaces, but the kicks to the beam from this source are estimated to be small compared with other transverse deflections. R&D is needed to develop all of these candidate structures and test prototypes under realistic conditions. Manufacturing of pre-stressed foils large enough for the 201.25 MHz cavities needs to be investigated further. Fabrication technology for the arrays of thin-walled tubes also needs to be explored.

Cost-effective manufacturing methods must be developed for the 201.25 MHz cavities themselves. We are contemplating processes such as spinning or cold forming for the large cavity shells, and electron beam or laser welding for the joining processes. Suitable windows, tuners and ancillary equipment must be developed for the high-power and high-gradient regime we require.

Given the high rf power requirements, and the inapplicability of superconducting rf due to the high magnetic field, it is interesting to consider running the conventional copper cavities at lower temperature to improve their conductivity and thus reduce the wall losses. Anecdotal evidence suggests that wall losses may decrease by a factor of two at liquid-nitrogen temperature, although hard data for actual operating structures has not been forthcoming thus far. This would reduce the peak rf power requirements, at the expense of increased refrigeration capacity. The cost tradeoff between these two expensive systems will be evaluated. Up to this point, we have taken care to maintain the possibility of low-temperature operation in the design; none of the proposed hardware configurations preclude this option.

Large scale integration of the rf structures into the lattice will also be the subject of ongoing R&D. The close proximity of the rf cavities to superconducting solenoids, the liquid-hydrogen absorbers, and the instrumentation makes for some technical challenges and results in many tradeoffs. For example, the diameter—and therefore the cost—of the largest solenoid coil could be reduced by reshaping the center RF cavities, but at the penalty of reduced shunt impedance. The shunt impedance is also strongly dependent on the amount of longitudinal space available. Figure 14.3 shows how the shunt impedance per cavity, and per meter, varies with length. We will continue to explore the cost minima of these tradeoffs.

The cost of rf power at this high level has prompted us to adopt a multi-beam klystron (MBK), as our baseline power source for these studies. MBKs have been developed at other frequencies for applications such as the TESLA test program, and have been successful at meeting expected power outputs and efficiencies [4], Figs. 14.4, 14.5, 14.6, 14.7. Preliminary contacts with tube manufacturers suggest that development of a 201.25 MHz MBK would be technically feasible and economically viable, given the scale of the Neutrino Factory. This type of source will be investigated further as part of the ongoing R&D plans. Other potential sources might include improved tetrodes or *diacrodes* and other beam-based devices, such as inductive output tubes (IOTs) or hollow beam tubes (*hobetrons*). Figure 14.8 shows a prototype high average power IOT [5] . Table 14.2 compares this to an equivalent conventional klystron. We will continue to study these alternatives and watch developments in the field. The cost and performance of power supplies and

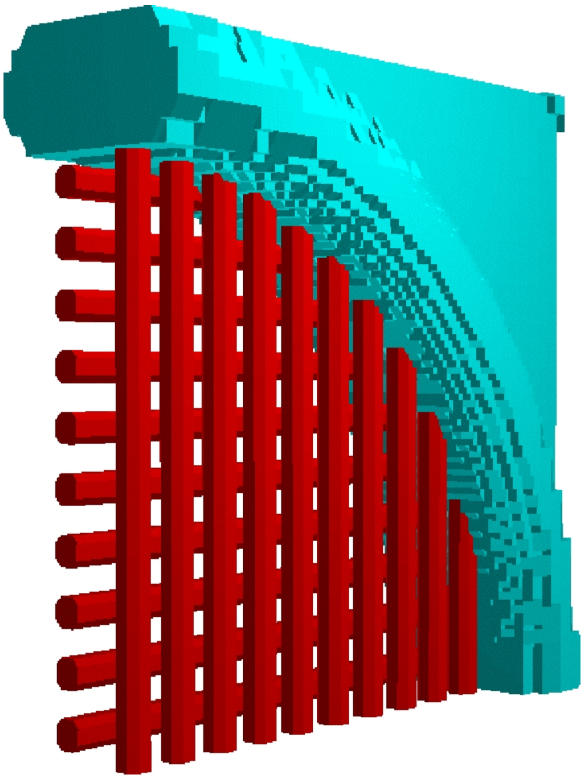

Figure 14.1: Grid of thin-walled tubes.

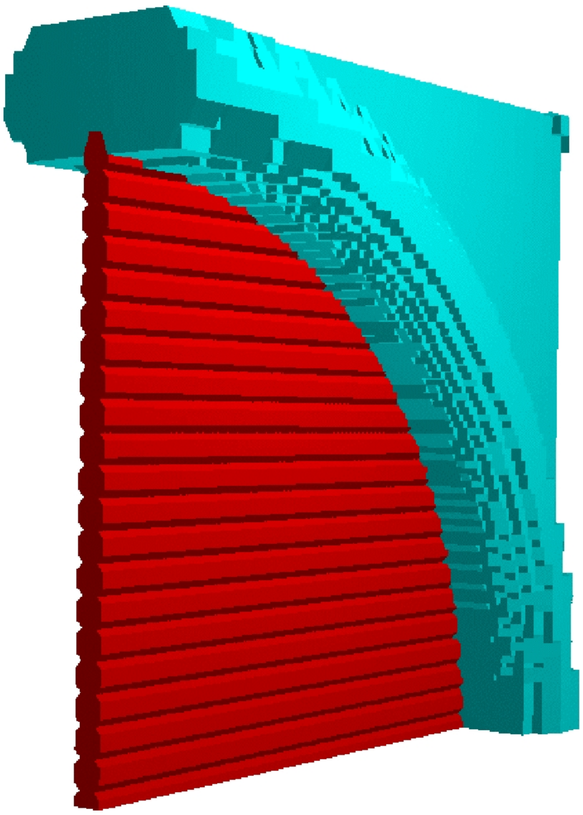

Figure 14.2: Continuous array of tubes.

modulators have improved in recent years due to developments in solid-state switching devices (such as IGBTs and SCRs), and thanks to the intensive R&D activities for linear accelerators. We will continue to refine our proposed design to take advantage of any further advances in this field.

The objectives of the R&D plan for the Buncher and Cooling Channel rf system are as follows:

- Perform high power tests of the open- and closed-cell cavities in Lab G at Fermilab
- Demonstrate that the required gradient can be achieved in the high magnetic field
- Investigate the conditioning and performance of a cavity containing beryllium foils, with varying levels of magnetic fields
- Investigate the necessity and effectiveness of anti-multipactor coatings, such as TiN
- Study the effectiveness of foils, grids, and other assemblies suitable for the 201.25 MHz cavity
- Investigate manufacturing methods for the 201.25 MHz cavity itself, and for foils or other structures suitable for the large diameter iris
- Prepare a conceptual design for a high-power 201.25 MHz test cavity, and then build and evaluate such a cavity
- Continue to work on the integration and optimization of the rf within the cooling channel layout
- Develop high-power rf windows, couplers and ancillary equipment for the cavities
- Continue to evaluate high-power rf sources and modulators, working with potential vendors to identify critical R&D items

14.6 Acceleration System

The most challenging aspect of the acceleration system is the 201-MHz superconducting rf (SCRF) cavities. The history of SCRF development for LEP, CEBAF, CESR, KEKB and TTF (TESLA) shows that it takes many years to design, prototype, and test structures in order to be ready for production. The lowest frequency at which SCRF cavities have

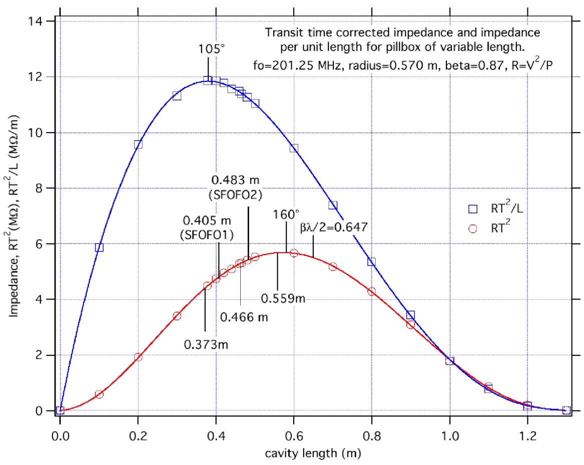

Figure 14.3: Cavity impedance versus length for an ideal pillbox, β= 0.87.

Table 14.2: Comparison between HOM-IOT (expected results) and klystron, both operated at 1 MW CW and 700 MHz.

Device	HOM-IOT	Klystron
Effective efficiency (%)	73	60
Assembly volume (ft^3)	30	200
Assembly weight (lbs)	1,000	5,000
DC beam voltage (kV)	45	90
Gain (dB)	25	46

been made for accelerating relativistic particles is 352 MHz for LEP-II. Therefore, R&D and prototyping for a Neutrino Factory at 201.25 MHz has been started now.

At present, SCRF R&D is in progress to address the following issues:

- Achieving 17 MV/m at a Q of 6×10^9 in a single-cell 201.25-MHz cavity
- Stiffening the 2-cell cavity designs to reduce Lorentz force detuning and microphonics sensitivity
- Exploring pipe cooling, both to reduce liquid-He inventory and to help stiffen multi-cell structures
- Reducing structure cost

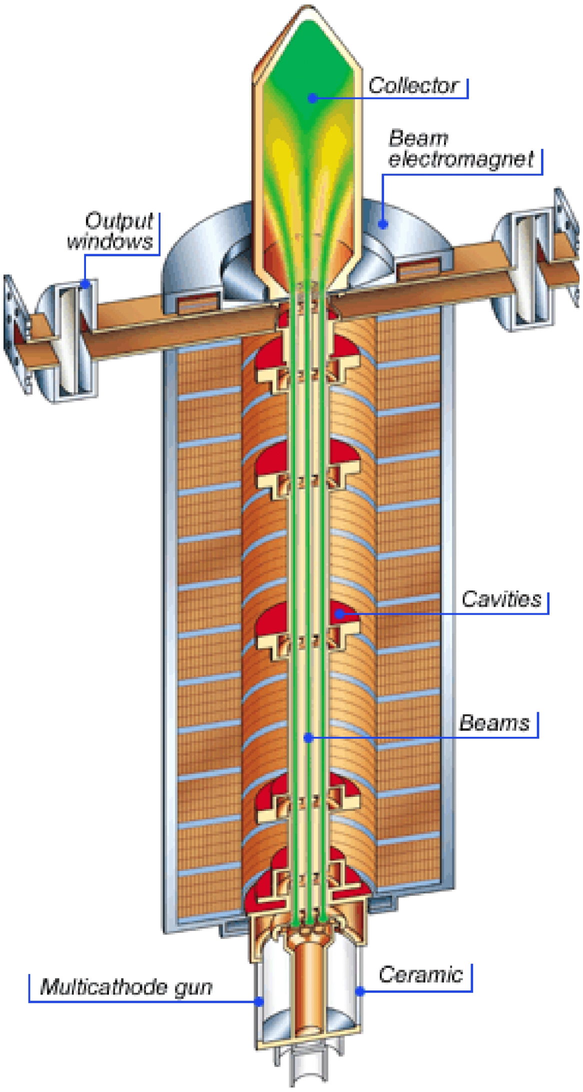

Figure 14.4: Schematic of multi-beam klystron.
http://www.tte.thomson-csf.com

Figure 14.5: Cathode of Thompson multi-beam klystron.

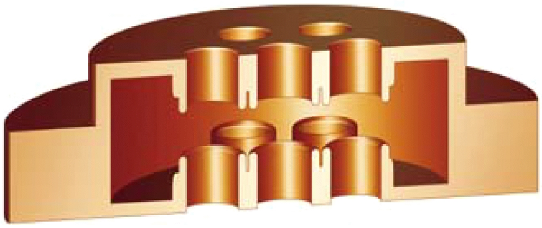

Figure 14.6: Cavity of multi-beam klystron.

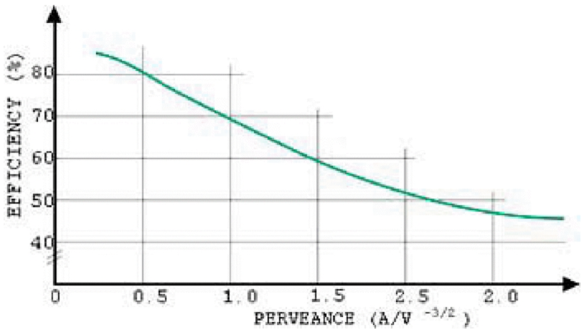

Figure 14.7: Klystron efficiency *vs.* beam perveance.

Figure 14.8: 1 MW cw HOM-IOT.

A collaboration has been set up with CERN to produce a single-cell Nb/Cu cavity at 201.25 MHz. CERN will provide the copper cavity, coat it with 1–2 μm thick niobium film using their standard DC-magnetron-sputtering technique, and send it to Cornell for testing after high-pressure rinsing and evacuation. To test the cavity, Cornell is upgrading its test facilities. Figure 14.9 shows a 3D CAD model of the CERN cavity inside the test dewar. A test pit 2.5 m diameter by 5 m deep is under excavation (Fig. 14.10) to accommodate the test dewar, which has been ordered. A 201.25-MHz, 2-kW rf test system is under construction. The clean room and high-pressure rinsing system at Cornell are being upgraded to accommodate the large cavity. ANSYS calculations have started on the 2-cell cavities to determine the mechanical resonant modes and frequencies. Not surprisingly, the resonant frequencies are low. Exploration has started on stiffening schemes, with and without pipe cooling. Figure 14.11 compares calculated Q *vs.* E curves for pipe cooling and bath cooling operations.

At 201.25 MHz, structure costs will be substantial. Multicell cavities are usually fabricated in parts that have to be machined, cleaned, and electron-beam welded. This is an expensive, labor-intensive process. We are collaborating with INFN-Legnaro in Italy to spin monolithic copper cells out of a single tube. Legnaro has experience at 1300 MHz. As a first step, they will spin a single-cell 500 MHz cavity. In a future stage, the procedure will be extended to 201.25 MHz and multi-cell cavities.

One long-term goal of the R&D is to design, construct, and high-power test a cryomodule with the first single-cell 201.25-MHz cavity, equipped with couplers and tuners. To prepare this test, continuing R&D, design, and prototyping are necessary in the following areas:

- high-power input coupler
- higher-order-mode coupler
- mechanical/thermal tuner
- piezoelectric/magnetostrictive tuner
- cryomodule
- system integration
- high-power testing

Future R&D on structure stiffening, feed-forward, and active tuning to compensate Lorentz force detuning and microphonics could lower the required peak power by reducing

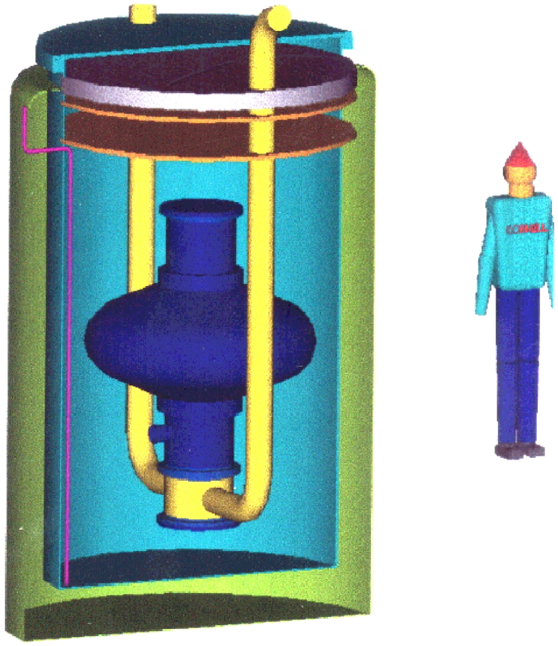

Figure 14.9: Vertical dewar test.

Figure 14.10: 200 MHz test pit (2.5 m diameter and 5 m deep) under construction at Cornell. The other pits are for testing existing cavities.

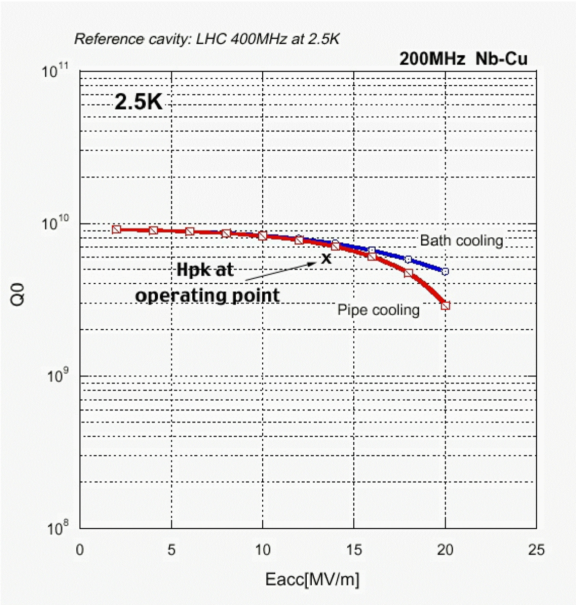

Figure 14.11: Comparison of pipe with bath-cooling at 2.5 K for a 200 MHz single-cell cavity. The He-carrying pipe diameter is 10 mm; spacing between pipes is 70 mm.

the detuning tolerance. For example, if the detuning tolerance can be lowered to 20 Hz, the input power drops to 450 kW per cell and the optimum Q_L increases to 1.5×10^6. Adopting a 4 ms fill time would then decrease the input power requirement to 350 kW per cell at the best Q_L of 1.5×10^6—a level already reached at KEKB.

The acceleration system arc design, while reasonably straightforward, requires a number of nonstandard components. Design concepts for the injection chicane and the arc magnets are needed. Depending on their complexity, prototypes might be needed for some of these.

14.7 Storage Ring

The arc magnet concept proposed here is novel, and a prototype device is certainly called for. In addition to evaluating the coil fabrication aspects, measurements of field quality suitable for the tracking studies must be performed. Thereafter, the tracking must be carried out to ensure a design with acceptable dynamic aperture for injection and storage.

Optics designs to reduce or eliminate the contributions to the detector from the ends of the straight section, where the Twiss parameters are not suitable in terms of the beam angular divergence, must be done. It should be possible to "hide" the matching regions from the detector with suitable horizontal or vertical bends, but this must be verified with an actual lattice design.

Finally, the cost-benefit tradeoffs between the present compact design and a conventional ring with a liner to protect the magnets from beam decay products must be quantified.

Bibliography

[1] http://www.cap.bnl.gov/mumu/RandD/RandD_R3.pdf

[2] D. Diesberg, Lithium Division, FMC Corp, private communication.

[3] J. Crim, Brush Wellman Corp., private communication.

[4] A. Beunas, G. Faillon, THOMSON TTE, France, S. Choroba, A. Gamp, DESY, Germany *A High Efficiency Long Pulse Multi Beam Klystron For The Tesla Linear Collider*, Submitted to PAC 2001.

[5] H.P. Bohlen *Advanced high-power microwave vacuum electron device development*, Proc. 1999 Particle Accelerator Conference, pp.445-449.

Chapter 15

Detectors

15.1 Introduction

The Neutrino Factory will open up a regime of neutrino physics that is inaccessible at existing facilities. When combined with a multi-kiloton detector located at a large distance, the proposed accelerator will allow the study of a number of unexplored neutrino oscillation parameters and a significant reduction in uncertainty of previously measured neutrino mass differences and mixing angles. The Neutrino Factory, plus its long-baseline detector, will have a physics program that is a logical continuation of current and near-future neutrino oscillation experiments in the U.S., Japan and Europe [1]. The facility will potentially enable physicists to determine values for all remaining unknown physical constants associated with current neutrino oscillation theory.

Features of the facility that allow these challenging oscillation measurements are a high neutrino intensity, a well-collimated beam, precise understanding of beam composition and spectra, and optimized energy. In addition, detector facilities located in experimental areas near the neutrino source will have access to integrated neutrino intensities 10^4–10^5 times larger than previously available (10^{20} neutrinos per year compared with 10^{15}–10^{16}). Standard neutrino physics at this facility could include physics topics such as precision $\sin^2\theta_W$, structure functions, high precision neutrino total charge current (CC) cross sections at low $\sqrt{s}$ (a few GeV), nuclear effects (shadowing at low x, anti-shadowing...), pQCD, and neutrino magnetic moments. These topics have relevance for standard model physics, nuclear physics, astrophysics and physics beyond the standard model. Finally, the Neutrino Factory will serve as a test accelerator for a high intensity muon collider and so is an R&D facility that is a significant step toward a muon collider in the future.

15.2 Beam Parameters

Neutrino beams produced at the Neutrino Factory are either (ν_μ,$\bar{\nu_e}$) or ($\bar{\nu_\mu}$,ν_e) depending on whether the machine is running μ^- or μ^+. The characteristics of the machine design guarantee that the beam is pure, with no contamination from anti-particles of the same neutrino flavor. The design intensity is 10^{20} μ decays/year, where a year is defined as 1×10^7 s. The angular dispersion of the ν-beam is $\Delta\theta/\theta = 5.3$ mrad with a momentum spread $\Delta p/p = 30\%$. The primary long-baseline target site considered in this report is the Waste Isolation Pilot Plant (WIPP) located in Carlsbad, New Mexico [2]. WIPP is located 2900 km from Brookhaven National Laboratory and requires a 13.1° dip angle in the muon storage ring. An alternative site with a smaller baseline, but with an already existing detector, Soudan, Minnesota, is discussed in the Appendix B.6. Most recently, a new alternative site has been suggested, the Homestake Mine in Lead, SD, that has been recommended as the site for the National Deep Underground Laboratory [3].

Based on design parameters in this report, the expected event rate at the WIPP site is given in Table 15.1.

Table 15.1: Event rates WIPP.

E_μ (GeV)	Baseline (km)	E_{ν_μ}	E_{ν_e}	$N(\nu_\mu$ CC) (per kt-year)	$N(\nu_e$ CC) (per kt-year)
$20_{\text{BNL-WIPP}}$	2900	15	13	740	330

15.3 Physics Signals

As discussed in detail in Section 1.3, neutrino mixing can be described by the lepton CKM matrix:

$$U = U_{23}U_{13}U_{12} = \begin{pmatrix} 1 & 0 & 0 \\ 0 & c_{23} & s_{23} \\ 0 & -s_{23} & c_{23} \end{pmatrix} \begin{pmatrix} c_{13} & 0 & s_{13}\exp^{i\delta} \\ 0 & 1 & 0 \\ -s_{13}\exp^{-i\delta} & 0 & c_{13} \end{pmatrix} \begin{pmatrix} c_{12} & s_{12} & 0 \\ -s_{12} & c_{12} & 0 \\ 0 & 0 & 1 \end{pmatrix}$$

(The possibility of light sterile neutrinos is not considered here). Three-flavor neutrino oscillations can be described by seven parameters: three $\Delta {m_{ij}}^2$ terms; three mixing angles θ_{ij}; and a CP violating term δ. The mass parameters are related by the simple identity $\Delta \mathrm{m_{12}}^2 + \Delta \mathrm{m_{23}}^2 + \Delta \mathrm{m_{31}}^2 = 0$. SuperKamiokande (SuperK) [4] has measured what appears to be non-zero values for $\Delta {m_{23}}^2$ and θ_{23} in atmospheric neutrinos. Over the next few years both K2K [5] and MINOS [6] will try to confirm the SuperK observation with accelerator-based experiments and obtain accurate values for $\Delta m_{23}{}^2$ and θ_{23}. The ν-oscillation parameters $\Delta m_{12}{}^2$ and θ_{12} are the province of solar and reactor-based experiments, either now running or planned for the next several years. The values of these parameters, hopefully, will be measured over the next 5–10 years. A long-baseline experiment at the Neutrino Factory will be able to measure θ_{13}, the sign of $\Delta m_{23}{}^2$ and possibly the CP violation term δ, providing θ_{13} is large enough. Depending on the values of the various neutrino parameters, it is conceivable that the Neutrino Factory will be in a position to measure all the remaining outstanding neutrino mixing parameters. Additionally, a long-baseline neutrino detector should be able to make the first direct measurement of the neutrino-matter oscillation effect (MSW). It would study MSW and could make a model-independent measurement of the matter parameter A, where $A = \sqrt{2}G_F n_e$. Measurements of A with 10% accuracy are possible, and may even be of interest to geophysicists.

15.4 Long Baseline Oscillation Experiment

The characteristics of a Neutrino Factory beam, $\nu_\mu, \bar{\nu_e}$ with no $\bar{\nu_\mu}, \nu_e$ contamination, naturally lend themselves to a neutrino appearance experiment. Since a μ^- beam at the Neutrino Factory will not result in any initial production of $\bar{\nu_\mu}$, a $\bar{\nu_\mu}$ signal will be due to $\bar{\nu_e} \rightarrow \bar{\nu_\mu}$ oscillations. An experiment designed to look for $\bar{\nu_\mu}$ CC events measures $P(\bar{\nu_e}\rightarrow\bar{\nu_\mu})$, where

$$P(\bar{\nu_e}\rightarrow\bar{\nu_\mu}) = \sin^2 2\theta_{13} \sin^2 \theta_{23} \sin^2(\Delta m^2{}_{13} L/4E)$$

A program to study both $P(\bar{\nu_e}\rightarrow\bar{\nu_\mu})$ and $P(\nu_e\rightarrow\nu_\mu)$ not only gives us access to θ_{13} but also tells us the sign of the $\Delta m_{23}{}^2$ and allows us to measure the matter parameter A (Fig. 15.1).

It is interesting to note that the matter parameter becomes accessible only when the beam has passed through a significant amount of material. Calculations show that the BNL-WIPP distance of 2900 km is far enough for the MSW effect to be measurable.

As stated earlier, if both the CP violating term, δ, and θ_{13} are large enough, they may be disentangled in these measurements. In addition, a spectral scan on the oscillation probabilities would potentially improve the precision of the $\Delta m_{23}{}^2$ and θ_{23} measurements by nearly an order of magnitude [7].

The experiment's concept is to start with the muon storage ring filled with μ^-, which produces a ν_μ,$\bar{\nu_e}$ beam, and look for a $\bar{\nu_\mu}$ appearance at the distant detector. The experiment would take sequential data sets with both μ^- and μ^+ storage ring fills, enabling

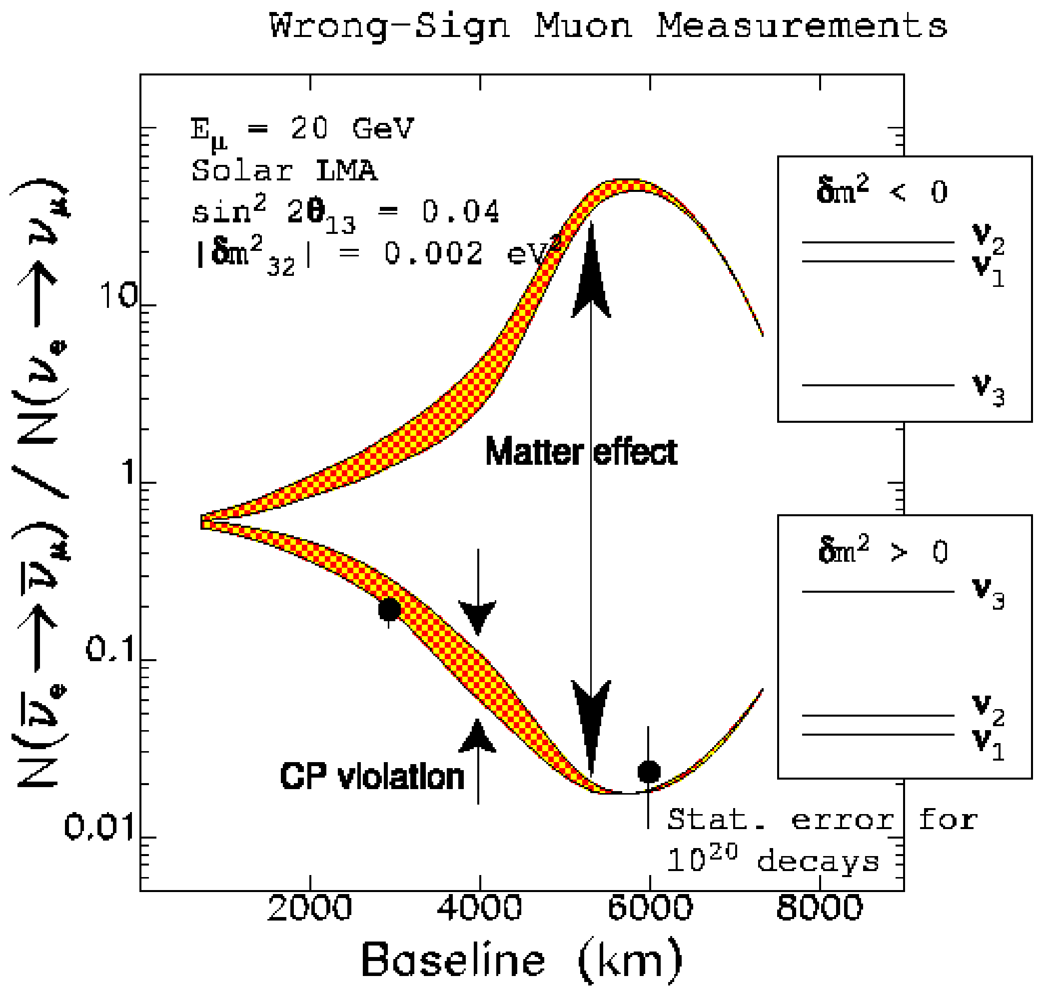

Figure 15.1: Measuring the ratio of $P(\bar{\nu_e}\to\bar{\nu_\mu})$ to $P(\nu_e\to\nu_\mu)$ enables measuring the sign of $\Delta {m_{23}}^2$ and the value of the matter parameter A.

the study of both the neutrino-matter oscillation effect and neutrino CP violations. Measuring $P(\nu_e \rightarrow \nu_\mu)$ and $P(\bar{\nu_e} \rightarrow \bar{\nu_\mu})/P(\nu_e \rightarrow \nu_\mu)$ gives access to the oscillation parameters described above.

$\bar{\nu_\mu}$ appearance experiment is typically done by looking for the leading μ^+ from the $\bar{\nu_\mu}$ CC reaction in the detector. The challenges in a search for $\bar{\nu_\mu}$ events are threefold: i) distinguishing μ^+ from the μ^- coming from the non-oscillating ν_μ's; ii) separating μ^+'s from π^+ punch-throughs; and iii) rejecting μ^+'s coming from hadronic decays. Another potential background, which depends on the detector environment, is accidentals from either cosmics or some background radiation.

There are a number of hadronic decay backgrounds for the μ^+ signal. They are:

- ν_μ CC where the primary μ^- is missed and the μ^+ from hadronic decay of the π^+, K^+, or D^+ is observed

- ν_e CC where the primary e^+ is missed and the μ^+ from hadronic decay of the π^+ or K^+ is observed (The D^+ is not a significant concern here)

- ν_μ,ν_e NC, where π^+ and K^+ again cause problems

The requirement to both measure the signal and reject the background determines a number of the detector's characteristics. Measurement of the sign of the muon is critical to the experiment, which means the detector must contain a magnetic field. Obtaining the muon spectrum is also important and can be done either through bending in the spectrometer or by range, using $\frac{dE}{dx}$. Separation of μ's from π's is accomplished through range-out in many interaction lengths of material. Rejection of hadronic backgrounds requires a combination of momentum, p_t, and isolation cuts. A detailed investigation of these backgrounds was carried out in Study-I [8]. It was determined that, to make the background manageable, a detector requires both momentum resolution and transverse segmentation (See Figs. 15.2, 15.3, 15.4). Rejection of accidental backgrounds can be handled by a detector with moderate timing resolution. Timing resolutions on the order of 100 ns would allow the experiment to only take events in phase with the machine time structure, and so reject accidentals by a factor of 200. A timing resolution of 10 ns gains an additional factor of two in background rejection by allowing a direction cut. Finally, the neutrino event rates seen in Table 15.1 indicate the need for the detector to be large, multiple ktons.

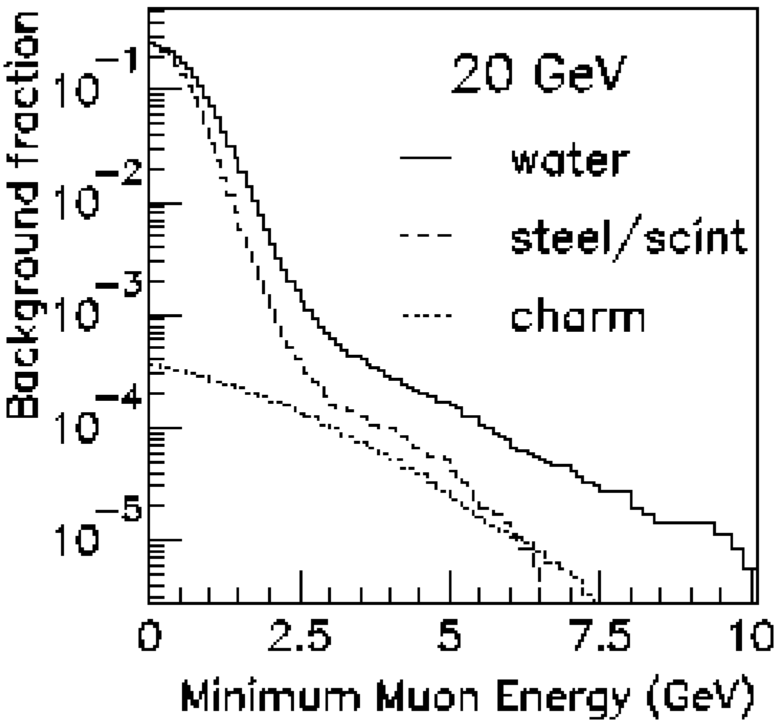

Figure 15.2: Fraction of neutrino events that produce a background signal as a function of minimum muon energy. Background sources include π and K decays, π punch-through, and charm decays.

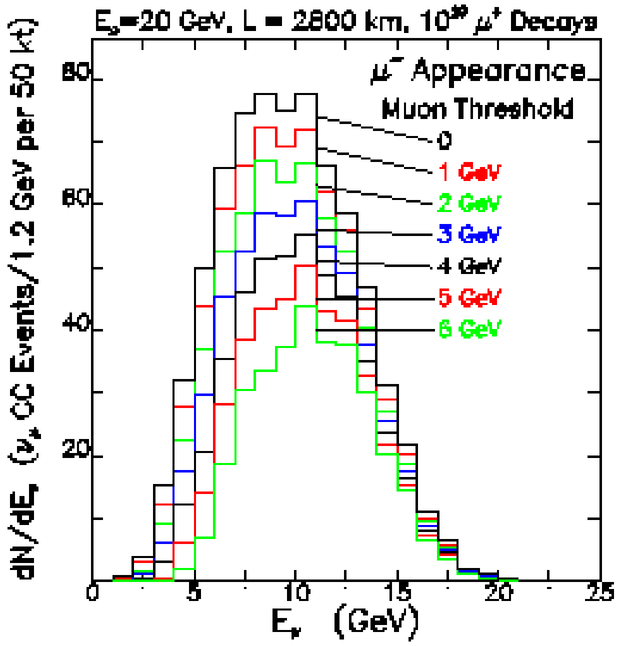

Figure 15.3: Reconstructed neutrino energy distribution for several different minimum muon energy cuts. Note that a minimum muon cut at 4 GeV reduces the signal by 30–35%.

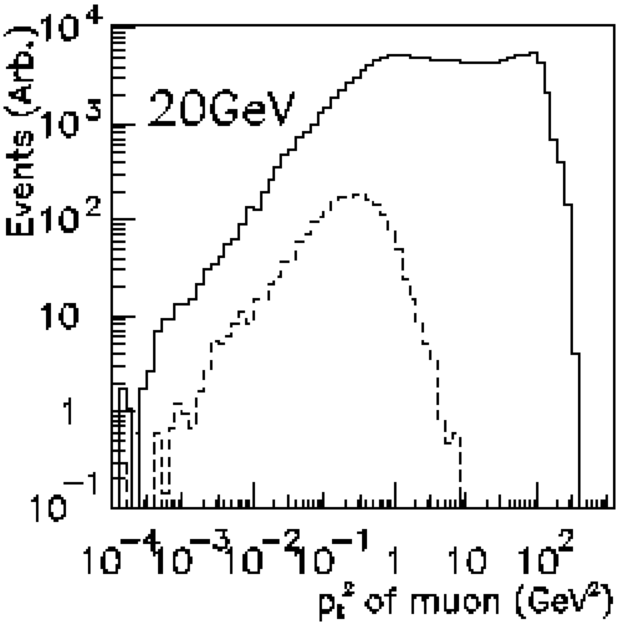

Figure 15.4: Distributions of the square of the muon momentum component transverse to the hadronic shower, p_t^2, for ν_μ CC events (solid line) and background muons (dashed line). The effectiveness of a transverse cut can be seen.

15.5 Detector Options

Specifications for the long-baseline Neutrino Factory detector are rather typical for an accelerator-based neutrino experiment. However, because of the need to maintain a reasonable neutrino rate at these long distances, the detectors considered here are between 3 and 10 times more massive than those in current neutrino experiments.

Large-mass detector designs are driven primarily by the cost of the absorbers. Limiting the detector's cost drives us to two basic options: steel-based and water-based designs. The two detector options considered for the WIPP site in this study are a 50 kton Steel/Scintillator/Proportional Drift Tube (PDT) detector and a Water Cerenkov Detector. The detector considered for the Soudan site, a 15 kton PDT detector is discussed in Section B.6.

The PDT detector would resemble MINOS, having steel absorber plates of 10–20 cm thickness, being magnetized with a toroidal field to 1–1.5 T. A combination of PDT's and scintillator slats would be interleaved with the absorber to provide longitudinal and transverse position resolution and coarse timing. In addition, the scintillator layers provide the experiment with its trigger. The thickness of the steel absorber and the ratio of PDT to scintillator slats would be optimized for momentum resolution and background rejection. The estimated electronics channel count would be of the order $1 - 5 \times 10^5$. With a neutrino event rate of a few mHz, the electronics could be highly multiplexed to reduce cost and complexity. Phototube magnetic shielding in these detector geometries has been solved by both MINOS and predecessor experiments, and so should not be an issue. Figure 15.5 shows a 50 kton detector with dimension 8 m × 8 m × 150 m. This geometry would be convenient for access and services, though designs that maximize fiducial-volume-to-edge ratios are possible. A detector of this size would record up to 4×10^4 ν_μ events/year.

A large water Cerenkov counter would be similar to SuperK but with either a magnetized water volume or toroids separating smaller water tanks. The detector could be the large water-Cerenkov UNO detector [9], currently proposed to study both proton decay and cosmic neutrinos. UNO would be a 650 kton water-Cerenkov detector segmented into a minimum of three tanks (Fig. 15.6). The gaps between the tanks may contain toroidal magnets, or perhaps large-gap dipoles to provide the B field needed to identify the charge of the leading muon (Fig. 15.7). The detector provides sufficient muon/hadron separation and muon containment up to 30 GeV/c. A water-Cerenkov detector would have background rejection of the same order as a steel/scintillator/PDT detector, though results from Study-I (Fig. 15.2) suggest muon p_t cuts would need to be 1.0–1.5 GeV/c higher in a water-Cerenkov counter to obtain the same rejection levels. UNO would be read out with 70,000 phototubes, a combination of the 20-inch SuperK tubes and 8-inch tubes.

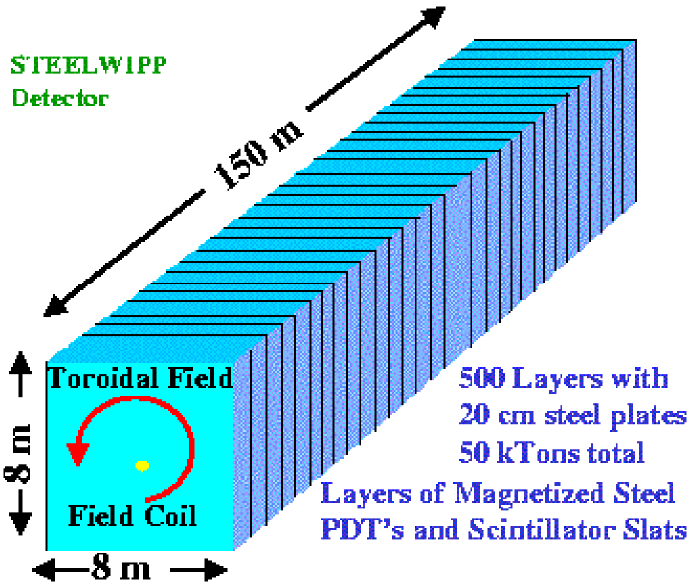

Figure 15.5: A possible 50 kton Steel/Scintillator/PDT detector at WIPP.

The timing provided by the PMT's would allow UNO to gate events in time with the Neutrino Factory beam structure. This enables UNO to work simultaneously as both a long-baseline neutrino experiment and a proton-decay experiment. The multi-faceted nature of the UNO physics program is an appealing aspect of this detector option. However, geometry of the water tanks does not provide a straightforward way to contain the spectrometer magnet fringe field, so magnetic shielding of the PMT's could be a technical challenge. UNO's active volume is large, 60 m$\times$60 m$\times$180 m (w$\times$h$\times$l), which implies an experiment hall of substantial dimensions. To provide reasonable access, the hall would need to be at least 100 m $\times$ 80 m $\times$ 300 m, and perhaps more. The detector would have an active fiducial mass of 440 ktons and would record up to 3 $\times$ 10^5 ν_μ events/year from the Neutrino Factory beam.

15.6 WIPP Site

The WIPP facility is the U.S. Department of Energy's Waste Isolation Pilot Plant located in Carlsbad, New Mexico. It is a large, underground depository for the storage of low-level radioactive waste and has been in operation since 1999 (Fig. 15.8).

The WIPP site is approximately 2900 km from Brookhaven National Laboratory. The active depository is located 650 m underground in a deep salt formation. Space is potentially available for a large underground physics facility at depths of 740–1100 m and discussions are under way between DOE and the UNO project on the possible development of such a facility. Infrastructure, such as elevator access and electricity, is currently available at the waste storage levels but new excavation and infrastructure installation would need to take place for the creation of an underground physics facility. The area should be considered a green field, albeit a very salty one.

It is worth asking here whether these experiments need to be as deep underground as proposed, or even underground at all. The effort and expense to build an experiment 700+ m underground adds significantly to the challenge of the experiment. Certainly for the UNO detector option, the experiment must be deep underground. A proton decay experiment that is searching for events with maximum rates of a few per year can tolerate little cosmic ray background. The ν interaction rate in a 50 kton steel-based detector is a few mHz at beam design intensity. At the surface, the cosmic ray interaction rate in the 50 kton detector is a few 100 kHz. These event rates would not provide significant data loading to the Data Acquisition System from either a bandwidth or archiving perspective. The main issue is the signal-to-noise (S/N) ratio of $10^{-7} - 10^{-8}$, which would be improved by gating with the Neutrino Factory beam structure, and providing a veto array around the detector. These techniques should allow the S/N to be improved to $10^{-3} - 10^{-2}$.

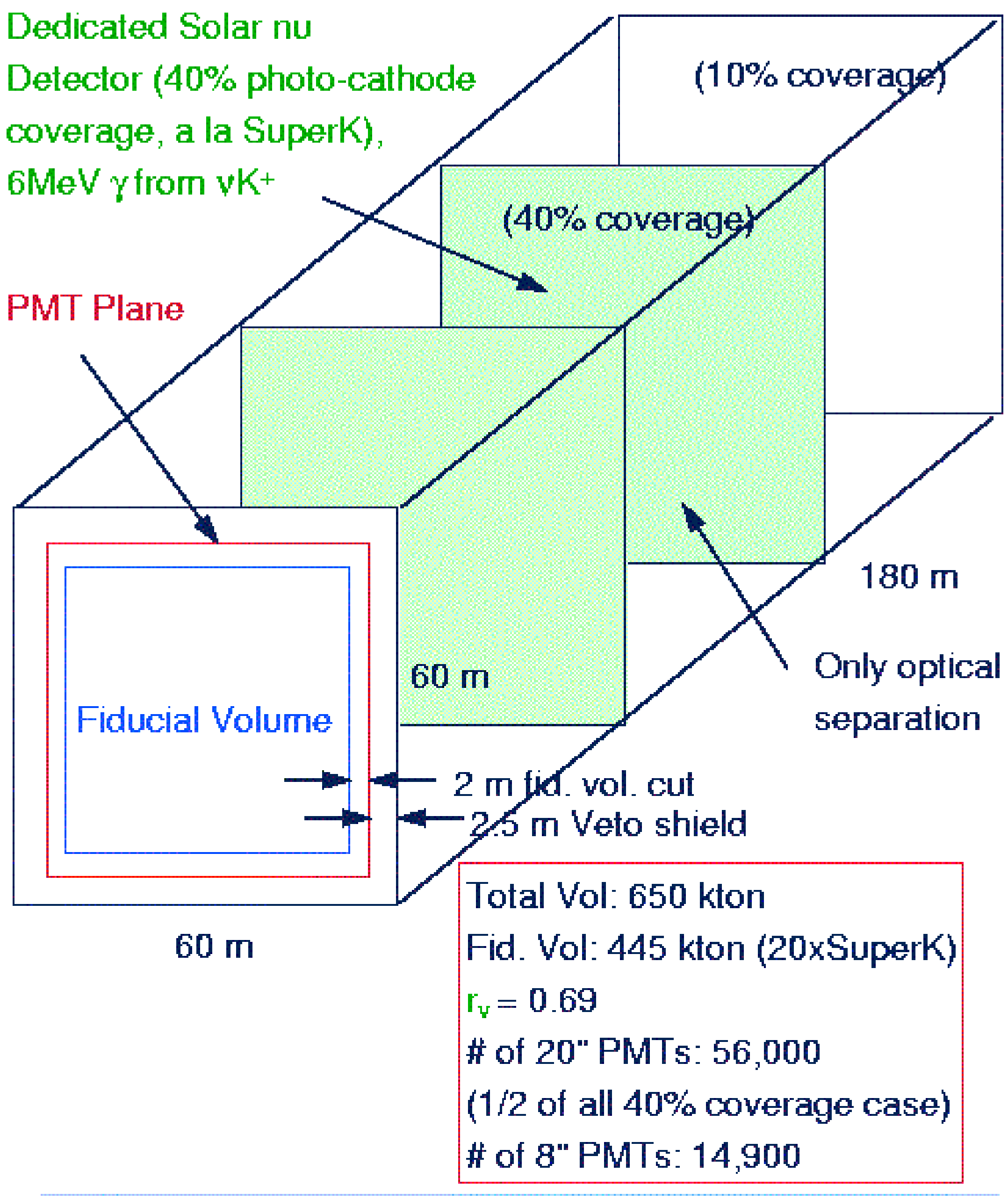

Figure 15.6: Block schematic of the UNO detector, including initial design parameters.

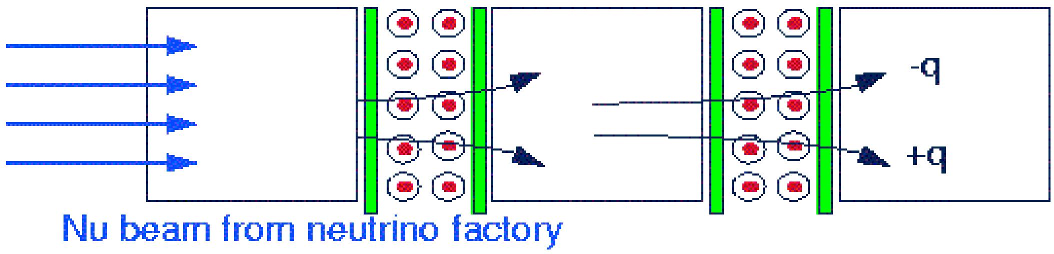

Figure 15.7: Concept of multi-water tank Cerenkov counter with magnetic field included.

Higher level software triggers could further reduce backgrounds by making cuts on event topology. A Monte Carlo study would be necessary to determine whether the remaining cosmic ray background events could be removed through data analysis.

15.7 The Near Detector

Detector facilities located on-site at the Neutrino Factory would have access to unprecedented luminosities of pure neutrino beams, well focussed with narrow energy spectra. A detector positioned 50 m from the end of the muon storage ring straight-away could expect ν-fluxes 10^4–10^5 times higher than currently available from accelerator sources. These luminosities would allow neutrino detectors to be much more compact, with higher precision in particle momentum and energy measurements. This in turn would enable standard neutrino physics studies such as $\sin^2\theta_W$, structure functions, ν cross sections, nuclear shadowing and pQCD to be performed with much higher precision than previously obtainable.

A compact Liquid Argon TPC (similar to the ICARUS detector [10]), cylindrically-shaped with a radius of 50 cm and a length of 1 m would have an active volume of 10^3 kg and a neutrino event rate O(10 Hz). The detector provides tracking, an EM energy resolution of $3\%/\sqrt{E} + 1\%$ and hadronic energy resolution of $20\%/\sqrt{E} + 5\%$. The TPC could be combined with a downstream magnetic spectrometer for muon and

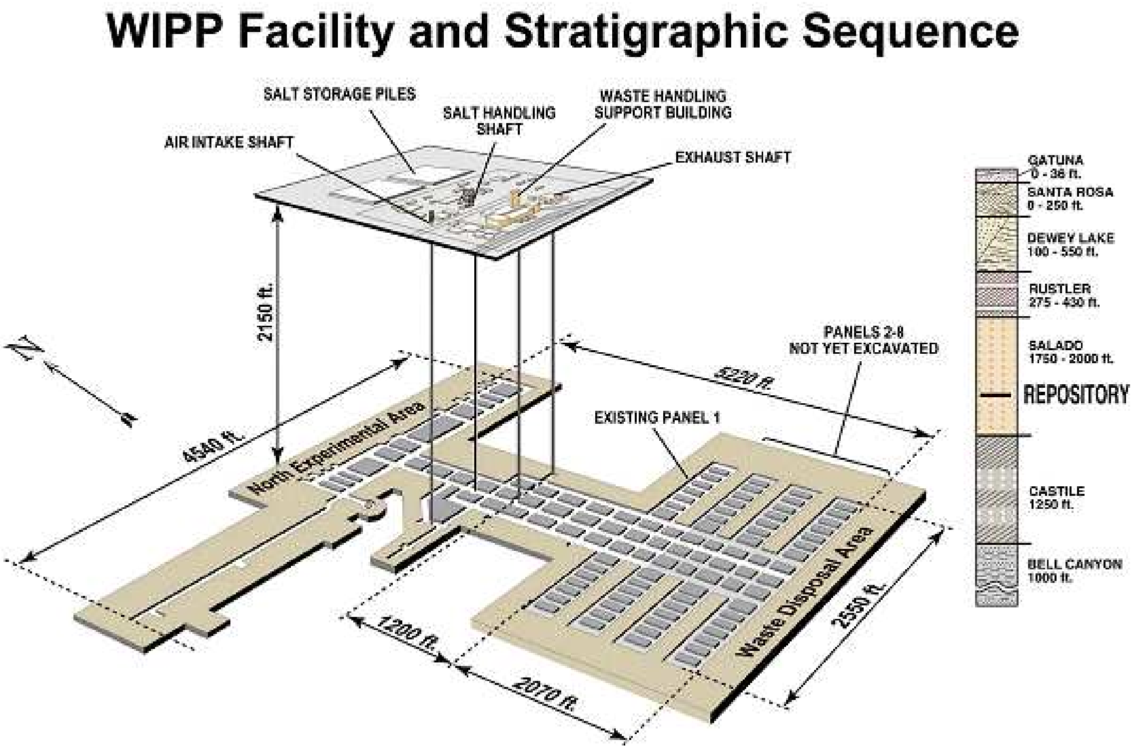

Figure 15.8: The WIPP area.

hadron momentum measurements. At these ν-luminosities it is even possible to have an experiment with a relatively thin Pb target (1 L_{rad}) followed by a standard fixed target spectrometer containing tracking chambers, time-of-flight and calorimetry with a event rate O(1 Hz). Backgrounds from neutrino interactions in the upstream shield must be considered, but should be manageable with accurate tracking to the target.

15.8 Summary

The Neutrino Factory, combined with a long-baseline detector, will allow a number of neutrino oscillation parameters to be measured (θ_{13}, sign of $\Delta {m_{23}}^2$, δ, A), some for the first time. There is the potential that by the time the factory comes online, the long-baseline experiment would be able to measure all the outstanding neutrino oscillation parameters. The experiment site considered in this study, WIPP, has space available 700+ m underground with some associated infrastructure. Detector options for the experiment include a steel/scintillator/PDT detector similar to MINOS and its progenitors, and weighing tens of ktons. The proposed 650 kton water-Cerenkov detector, UNO, is also an option. Both choices are technically feasible, though the water-Cerenkov approach has a number of outstanding technical questions. Conventional neutrino physics is also accessible at the Neutrino Factory with ν beam intensities many orders of magnitude higher than previously available at accelerator facilities.

15.8. Summary

Bibliography

[1] An index of experiments and related subjects having to do with neutrino mass and oscillations,
http://www.hep.anl.gov/ndk/hypertext/nuindustry.html

[2] The WIPP Home Web Page,
http://www.wipp.carlsbad.nm.us/wipp.htm

[3] For the recommendations by the Bahcall-Haxton committee, see http://www.sns.ias.edu/ jnb.

[4] Official Home Page,
http://www-sk.icrr.u-tokyo.ac.jp/doc/sk/index.html

[5] Long Baseline Neutrino Oscillation Experiment,
http://superk.physics.sunysb.edu/k2k/

[6] The MINOS Experiment and the NuMI beam line,
http://www-numi.fnal.gov:8875/

[7] A. Cervera et al., *Golden measurements at a Neutrino Factory*, CERN-TH/2000-40

[8] C. Albright et al., *Physics at the Neutrino Factory*, Fermilab-FN-692, 2000

[9] Official Home Page,
http://superk.physics.sunysb.edu/uno/

[10] F. Arneodo *et al.*, *Study of Solar Neutrinos with the 600-T Liquid Argon ICARUS Detector*, NIMA 455 (2000) 376-389.

Appendix A

Cost Estimates

A.1 Methodology and Facility Costs

A.1.0.1 Methodology

In this report we have described the components of a Neutrino Factory sited at BNL. The facility includes the following systems:

- Proton Driver (providing 1 MW of protons on target from an upgraded AGS)
- Target and Capture (a mercury-jet target in a 20-T superconducting solenoidal field to capture pions from the target)
- Decay and Phase Rotation (three induction linacs, with internal superconducting solenoidal focusing, to contain the muons from pion decays and provide nearly non-distorting phase rotation; a mini-cooling absorber section is included after the first induction linac)
- Bunching and Cooling (a solenoidal focusing channel with high-gradient rf cavities and liquid-hydrogen absorbers that bunches the 200 MeV/c muons into 201.25-MHz rf buckets and cools their transverse emittance from 12 mm-rad to 2 mm-rad)
- Acceleration (a superconducting linac with solenoidal focusing to raise the muon beam energy to 2.48 GeV, followed by a four-pass superconducting recirculating linear accelerator to provide a 20 GeV muon beam)
- Storage Ring (a compact racetrack-shaped superconducting storage ring in which 35% of the stored 20 GeV muons decay toward a detector located 2900 km from the ring)

As part of the Study, we have specified each system in sufficient detail to obtain a "top-down" cost estimate for it. Clearly this estimate is not the complete and detailed cost estimate that would come from preparing a full Conceptual Design Report (CDR). Neither the definition of the various systems, nor the engineering effort available for this Study would permit this. On the other hand, there is considerable experience in designing and building accelerators with similar components, so we have a substantial knowledge base from which costs can be derived. The costs obtained for this Study were obtained mainly in that way.

Where available, we have used costs from existing components—scaled as needed to reflect essential changes in the key variables—to represent the expected costs to fabricate what we need. This applies to the Proton Driver, the superconducting and normal conducting magnets and their power supplies, the rf cavities, and conventional facilities and utilities. In some cases, we were able to take advantage of the experience with designing similar components in a different context. For example, the target facility we require is closely similar to that needed for the Spallation Neutron Source (SNS) project at ORNL, for which detailed CDR-level designs already exist and construction is under way. We made use of the expertise developed at SNS to estimate the facility costs for the Neutrino Factory target area. The superconducting target solenoid is not a standard device, yet even here there is a magnet of similar size and field strength, designed for the ITER project, that serves as a convenient scaling model. Given the limited time to arrive at cost estimates, we leaned heavily on experts in the various areas who could identify the key design parameters that influence costs and then scale accordingly from known costs. In the case of rf power sources, we made use of the multi-beam klystron (MBK) example developed at DESY for TESLA, along with expertise in developing other high-power tubes at U.S. Laboratories. As was done in Study-I, for devices such as the MBK, which are a significant extrapolation from existing hardware, allowance was made for a substantial development program, whose cost was amortized over the initial complement of devices needed for the Neutrino Factory.

A.1.0.2 Facility Costs

It should be noted that the design we have described in this report has erred on the side of feasibility rather than costs. Thus, we do not claim to present a fully cost-optimized design, nor one that has been reviewed from the standpoint of "value engineering." In that sense, there is hope that a detailed design study will *reduce* the costs compared with what we estimate here. Only direct costs are included here, that is, the estimates do not contain allowances for EDIA, laboratory overhead burdens, or contingency. The breakdown by system is summarized in Table A.1; costs reported there are given in FY01 dollars. To facilitate comparison with the Feasibility Study-I estimate, we have converted the costs to FY00 dollars, shown in Table A.2, using the DOE-approved inflation factor of 2.5%. Following Study-I, we have put in Table A.2 an allowance of 10% for each of the systems to account for things we have not considered in detail at this stage.

It is interesting to compare our estimate with that of Study-I; in this study, we have **improved the performance by a factor of six** over that reached in Study-I, at a total cost (estimated in the same way for both designs) of about **3/4 of that in the original study**. This is an encouraging trend and, as noted, we have some hope that it will continue.

Table A.1: **Construction Cost Rollup per Components for Study-II Neutrino Factory.** All costs are in FY01 dollars.

System	Magnets ($M)	RF power ($M)	RF cav. ($M)	Vac. ($M)	PS ($M)	Diagn. ($M)	Cryo ($M)	Util. ($M)	Conv. Facil. ($M)	Sum ($M)
Proton Driver	5.5	7.0	66.1	9.8	26.6	2.2	28.5		21.9	167.6
Target Systems	30.3			0.8	3.5	8.0	18.8		30.2	91.6
Decay Channel	3.1			0.2	0.1	1.0	0.2			4.6
Induction Linacs	35.0		90.3	4.4	163.3	3.0	3.6		19.5	319.1
Bunching	48.8	6.5	3.2	2.7	2.1	5.0	0.3			68.6
Cooling Channel	127.6	105.6	17.7	4.3	4.8	28.0	9.5		19.5	317.0
Pre-accel. linac	46.3	68.4	44.1	7.5	3.0	6.0	13.6			188.9
RLA	129.0	89.2	63.4	16.4	5.6	4.0	28.9		19.0	355.5
Storage Ring	38.5			4.8	2.2	29.0	4.8		28.1	107.4
Site Utilities								126.9		126.9
Totals	**464.1**	**276.7**	**284.8**	**50.9**	**211.2**	**86.2**	**108.2**	**126.9**	**138.2**	**1,747.2**

Table A.2: Summary of Construction Cost Totals for Study-II Neutrino Factory. All costs are in FY01 dollars unless otherwise noted. [a]*Others* is %10 of each system to account for missing items, as was used in Study-I; [b]*Reconciliation* represents the Study-II costs given in FY00 dollars to permit direct comparison with Study-I costs. The inflation factor used is (1/1.025), per DOE official rates.

System	**Sum** ($M)	**Others**[a] ($M)	**Total** ($M)	**Reconciliation**[b] (FY00 $M)
Proton Driver	167.6	16.8	184.4	179.9
Target Systems	91.6	9.2	100.8	98.3
Decay Channel	4.6	0.5	5.1	5.0
Induction Linacs	319.1	31.9	351.0	342.4
Bunching	68.6	6.9	75.5	73.6
Cooling Channel	317.0	31.7	348.7	340.2
Pre-accel. linac	188.9	18.9	207.8	202.7
RLA	355.5	35.5	391.0	381.5
Storage Ring	107.4	10.7	118.1	115.2
Site Utilities	126.9	12.7	139.6	136.2
Totals	**1,747.2**	**174.8**	**1,922.0**	**1,875.0**

A.2 Cost Reduction Options

A.2.1 Introduction

For this study, an effort has been made to select specific and feasible technologies giving acceptable performance at reasonable cost. Nonetheless there are many alternative ideas that could be considered. In this chapter we discuss options that might lower the cost, improve performance, or be used as alternatives. In some cases, cost reductions may be possible with little sacrifice of performance; other choices would hurt performance, but by amounts that might be justifiable by the savings achieved. Some newer technologies might raise performance and lower costs simultaneously.

A.2.2 Capture Solenoid

A.2.2.1 Cost: Choice of Capture Field

Figure A.1 shows the efficiency for muon production *vs.* the axial peak field of the capture magnet. Maximum performance is achieved with the baseline value of 20 T, but the drop in efficiency is small for moderate reductions in this field. A drop from 20 T to 18 T would have an almost insignificant effect ($\approx 2\%$) and even a reduction to 15 T causes only $\approx 9\%$ reduction. The savings, even for a reduction to 18 T could be significant.

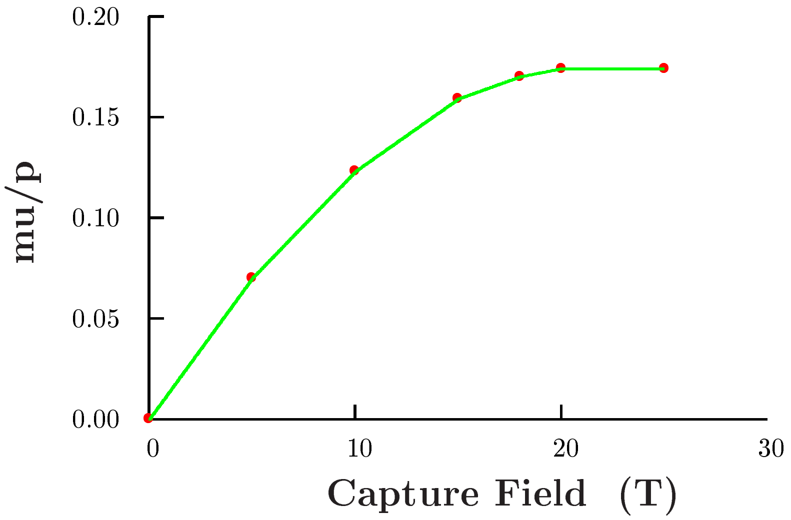

Figure A.1: Efficiency *vs.* capture field.

A.2.2.2 Cost/Performance: Use of Wrapped Insulation

Figure A.2 shows the field *vs.* power consumption for three different insert coil technologies (see Section 3.4.) The lowest curve is for the baseline design using MgO insulated hollow conductor giving 6 T with 12 MW. The dotted line above is for a wrapped ceramic insulation as being developed at CTD, Inc. [1]. With this conductor, for the same

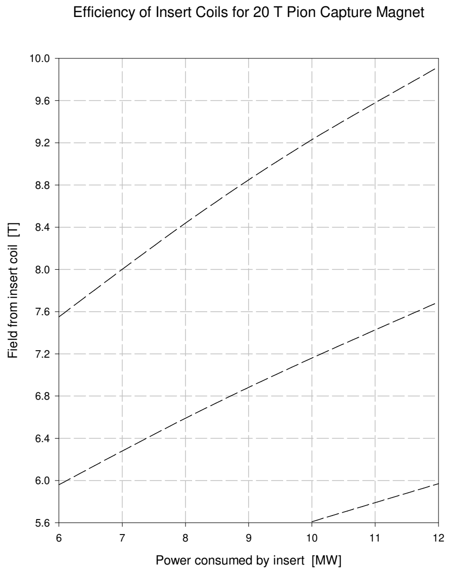

Figure A.2: Efficiency of three types of inserts in 20 T magnet; lowest curve: mineral-insulated hollow conductor as developed for the JHF; middle curve: higher-performance hollow conductor under development; top curve: Bitter coil.

power consumption, the field from the hollow conductor would rise from 6 to 7.6 T, thus lowering the field needed from the superconducting coil from 14 T to 12.4 T, and offering significant savings. Alternatively, the gain in performance could be used to reduce the power consumption, or some combination of these two options could be considered.

A.2.3 Bitter Magnet

The upper dashed line in Fig. A.2 is for a Bitter magnet.

The Bitter magnet design is the invention of Prof. Francis Bitter of MIT, who in the late 1930's first used such magnets to generate 10 T in a 5 cm bore. The design has the potential to be a very efficient insert for the pion capture magnet. The windings of a Bitter magnet are sets of thin annular plates, each like a big washer, slit along a radius, as in a lock washer. In each plate a voltage difference between the two edges of the slit forces the current to flow circumferentially, the long way around from one edge of the slit to the other, before entering the next plate. Tie rods or components of the magnet housing keep the plates in good registration and provide the axial clamping for good electrical contact over the sectors in which current transfers from one plate to the next.

The Bitter design has many virtues. It possesses great inherent strength and permits the use of a wide range of conductors, such as heavily cold-worked copper, with excellent combinations of strength and electrical conductivity. Therefore the conductor can resist the huge tensile hoop stresses that arise in generating intense fields. The fraction of conductor in a Bitter magnet typically is much higher than in a magnet built from hollow conductors. One reason is that only a thin film between adjacent plates suffices to confine the current to its desired path, because the potential difference between adjacent plates is only a few volts. Another reason is that cooling passages may be very small, because they are so short. This is true especially if one cools the magnet radially, by means of shallow grooves etched into one face of each plate (or each pair of plates; one can mate each etched plate with an unetched one). The cooling passage length in such a magnet is its “build” (outer radius minus inner radius). If, instead, one chooses to cool the magnet axially, through holes punched in each plate and insulator, the cooling passage length will be the magnet length. For the pion capture insert coil, axial passages are several times longer than radial ones—but still short, by an order of magnitude, relative to those in a magnet employing hollow conductors (See, Section 3.4). The favorable cooling geometry enables Bitter magnets to operate at very high power densities. Another virtue of the Bitter magnet design is the ease with which desired field profiles can be achieved by employing turns of the appropriate thickness in each of many axial zones. One need only change the thickness of plates comprising a turn, or change the number of plates making up each turn.

Figure A.3 plots the relative costs of various systems, each with the peak field of its associated superconducting magnet. The set labeled “unshielded” employs a Bitter magnet whose bore accommodates just the pion capture beam tube and radial clearance for an annulus to bring water to the radial cooling passages. The annulus is tapered from the upstream to the downstream end, in order to maintain a water velocity in the annulus of about 10 m/s. The annular height is at most 1.8 cm. For the set labeled “shielded” the bore accommodates 10 cm of shielding with water-cooled tungsten carbide, just as for the magnet with hollow conductors. Each magnet has an outer diameter of 80 cm if shielded, 40 cm if not—values close to the optimum.

To consider a Bitter magnet for the insert to the pion capture system will require an R&D program that validates three issues:

- verification that radiation will not immediately induce arcing so severe that a substantial fraction of current flows through the arc instead of through the copper

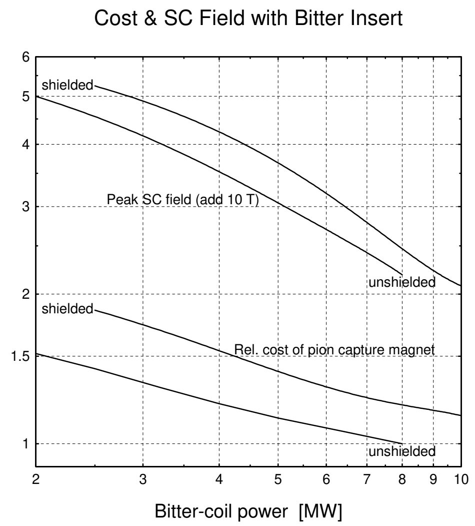

Figure A.3: Relative cost of pion capture magnet, as function of the power consumed by its Bitter magnet, with and without 10 cm of shielding with water-cooled tungsten carbide. Decreasing the power of the Bitter magnet by a factor of four from the 8-10 MW maximum plotted here entails a $\approx 50\%$ increase in system cost; the needed field contribution from the superconducting magnet rises from ≈ 12 T to ≈ 15 T.

windings

- development of an insulator—undoubtedly a ceramic—that will withstand not only the intense radiation emanating from the target but also the environment of a Bitter magnet. (Even without radiation this environment involves high clamping pressure, high temperature and high water velocities.)
- verification that conductors will not deteriorate too much in strength and ductility when irradiated for at least a few months.

If so, one can save many megawatts of power consumption and/or many millions of dollars of capital cost in superconducting magnets—a tantalizing prospect for economy for the Neutrino Factory.

A.2.4 Phase Rotation

A.2.4.1 Cost: Combining Induction Linacs 2 and 3

In the baseline design there are 3 induction linacs. The first linac must be separate from the other two in order to achieve non-distorting phase rotation, but the second and third linacs are separate only in order that they each be unipolar. A single second linac with a bipolar pulse approximately equal to the sum of the two opposite polarity pulses would perform equally well. This appears possible and would be somewhat less expensive.

A.2.4.2 Cost: Fewer Induction Linacs

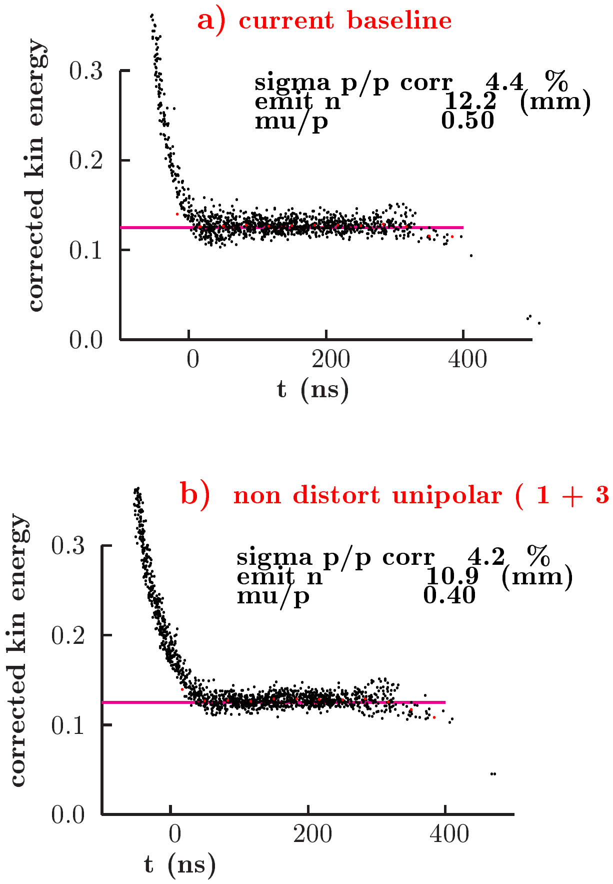

Figure A.4: Final energy *vs* time for different phase rotation systems: a) baseline; b) with IL2 removed.

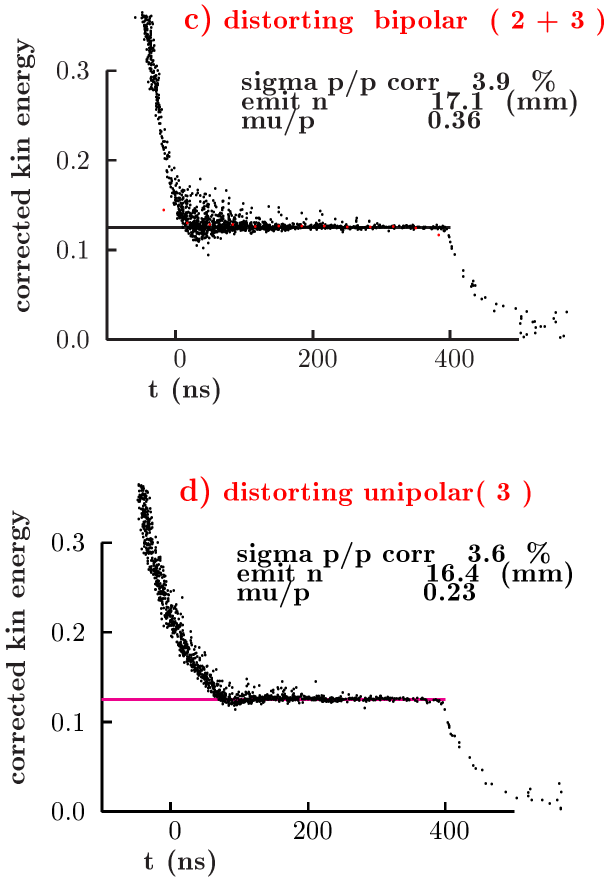

Figure A.5: Final energy *vs* time for different phase rotation systems: c) without IL1; d) without IL1 and IL2.

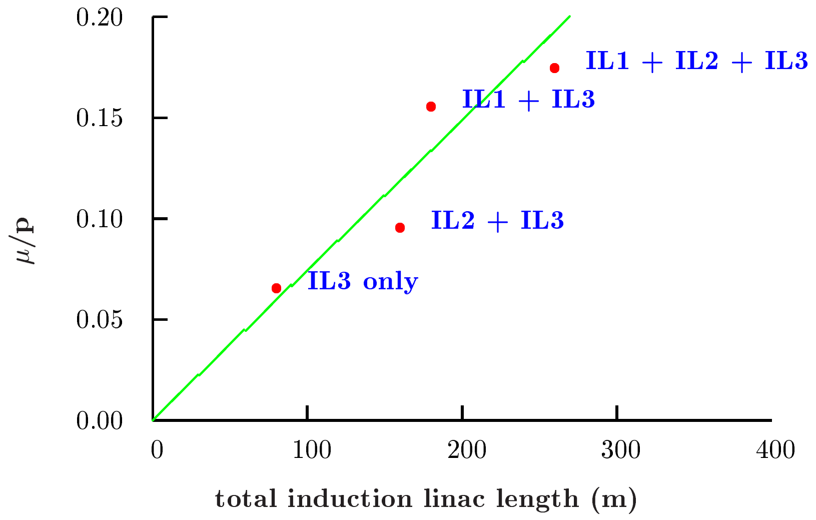

Figure A.6: Efficiency *vs.* length of induction linacs. The μ/p ratio that characterizes the performance of the front end is measured at the end of the cooling channel.

Further cost savings could be achieved if one or more of the linacs were eliminated and the remaining linacs re-optimized. This has been studied assuming a fixed geometrical layout, so that the option of upgrading to the original baseline design is retained. Figures A.4 and A.5 show 3 such cases, together with the baseline design. Figure A.6 shows the muon production efficiency (at the end of the cooling channel) for the four cases, plotted against the sum of the lengths of the remaining linacs. The losses in efficiency are large if the first linac is eliminated, but less severe (11%) if only the second linac is removed. Removing IL2 would provide a cost saving of about 4%, so its presence is favorable from a cost-benefit standpoint.

A.2.5 Cooling

A.2.5.1 Cost: Less Cooling

Figure A.7 shows the muon production into the defined accelerator acceptance as a function of length. Table A.3 shows the values for three cooling lengths. It is seen that a reduction in cooling length from 108 to 88 m, which would offer significant savings, reduces the performance by only 3.4%. Looked at in terms of marginal costs, however, we note that the baseline scenario still appears cost effective.

Table A.3: Efficiency for three cooling lengths.

Cooling length (m)	μ/p	Loss (%)	Savings (%)
108	0.174	0	0
88	0.168	3.4	2.5
68	0.150	13.8	6.7

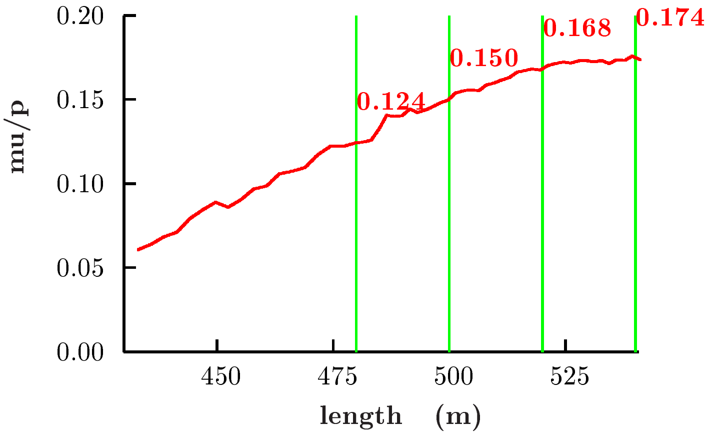

Figure A.7: Efficiency *vs.* length of cooling.

A.2.5.2 Cost: Fixed Field Alternating Gradient

Fixed Field Alternating Gradient (FFAG) acceleration offers the possibility of savings. There would be no multiple arcs, and no switchyards: the lattice would have a large enough momentum acceptance to circulate the muons from initial to final energy. The number of turns could now be raised, limited only by muon decay considerations, thus lowering the needed rf acceleration per turn.

Lattices have been designed with momentum acceptances of more than a factor of 2-3. Injection and extraction would be performed using kickers. Designs being studied at KEK [2] employ low frequency, low accelerating gradient rf and accept relatively large decay loss. Work in the US [3] has concentrated mainly on higher gradient superconducting rf with fewer turns and less loss. The main problem in this approach is assuring that the rf phase is set correctly at each pass. The ideal solution is a ring that is exactly isochronous, but the best current designs are less than ideal and require phase control of the rf corresponding to frequency variations of the order of 10^{-4}. This would be easy for conventional rf, but is difficult in a superconducting cavity. The use of ferrites weakly coupled to such cavities is being studied.

A.2.6 Summary

Although we believe that the current Study-II baseline represents a feasible and reasonably costed high performance design, there are many possibilities for cost reduction that could be considered for an initial implementation.

A.2. Cost Reduction Options

Bibliography

[1] J. Rice, DoE SBIR Phase I Final Report, *Ceramic Insulation for Heavy Ion Fusion and Other High Radiation Magnets*, DoE Grant No. DE-FG03-00ER82979 (2000).

[2] Y. Mori, *KEK FFAG Program*, presented at NUFACT01 `http:\\www-prism.kek.jp/nufact01/May25/WG3/25wg3_mori.pdf`.

[3] C. Johnstone, *US FFAG Program*, unpublished.

Appendix B

Options

B.1 Proton Driver

B.1.1 Increasing Power to 2 or 4 MW

With an increased superconducting linac energy, the proton intensity could be increased by a factor of two (from 1×10^{14} to 2×10^{14}.) A further increase of a factor of two in average proton power could be achieved by adding a 24 GeV storage ring and operating the AGS at 5 Hz. An upgrade to 4 MW beam power is possible by upgrading the AGS repetition rate to 5 Hz and increasing the linac energy to 1.5 GeV, which allows for doubling the number of protons per pulse to 2×10^{14}. To achieve the required bunch length compression a separate compressor ring would be needed. This ring will

- operate below transition
- have a small slippage factor, that is, it will be quasi-isochronous
- have low dispersion
- have an acceptance to emittance ratio > 8 (to be compatible with the tight beam loss limit)
- have a chromaticity correction system

Table B.1 summarizes the key parameters of the compressor ring. As discussed in Section B.1.2, the performance penalty of operating with longer bunches is not severe, so the cost-benefit evaluation of the compressor ring must be considered carefully.

Table B.1: Compressor ring parameters.

Circumference (m)	200
Bending field (T)	4.15
Kinetic energy (GeV)	24
Transition gamma	38.4
η	0.00074
Betatron tune, x/y	14.8/9.2
Maximum beta function, x/y (m)	12.9/19.8
Dispersion function (m)	0.12
Chamber radius (mm)	25
Maximum beam radius, x/y (mm)	7.0/8.6
Acceptance, x/y (m)	48.5/31.6
Beam emittance, x/y (m)	3.8/3.8
Accep./emit. ratio, x/y	12.8/8.3
Natural chromaticity, x/y	$-2.5/-1.7$

In operation, an unmatched bunch is injected from the AGS into the compressor ring. It is extracted immediately after a bunch rotation (bunch rotation takes a quarter of a synchrotron period, *i.e.*, 3 ms, or 4500 turns). Because of the very small slippage, a low rf voltage is required (see Table B.2.)

Table B.2: rf parameters of compressor ring.

RF frequency (MHz)	5.94
Harmonic number	4
V_{rf} (kV)	200
Bucket height, in $\delta p/p$	0.042
Bucket area (eVs)	222
Bunch area (eVs)	10
f_s, center (Hz)	91.5
f_s, edge (Hz)	82.6

The longitudinal parameters of the ring are summarized in Table B.3

Clearly, the longitudinal microwave instability threshold will be low at the injection energy, because of the small slippage factor and the low $\delta p/p$. To reduce the impedance, the vacuum chamber will have smooth tapered transitions. However, we do not plan

Table B.3: Longitudinal parameters of compressor ring.

	Injection	Extraction
No. particles per bunch (10^{14})	0.17	0.17
RMS bunch length (m/ns)	5/17	0.9/3
Peak current (A)	65	363
Momentum spread (%)	0.4	2.24
Longitudinal emittance (eVs)	10.5	10.5
Broadband impedance ($j\Omega$)	5	5
Space-charge impedance ($j\Omega$)	1.66	1.66
Keil-Schnell threshold ($j\mathrm{M}\Omega$/m)	3.75	25.5
Effective rf voltage (kV)	200	248

to shield the bellows to avoid possible problems with arcing. Despite this we expect to achieve a broad impedance of 5 Ω, which is acceptable.

We see from Table B.3 that the combination of the broadband and the space-charge impedance is 3.34 Ω, slightly lower than the Keil-Schnell (KS) threshold. Since the beam is below transition, beam instability is not expected. The overall inductive impedance below transition has a focusing effect, which increases the effective rf voltage in the bunch rotation.

Table B.4: Transverse parameters.

	Injection	Extraction
Broadband impedance ($j\mathrm{M}\Omega$/m)	0.51	0.51
BB imp. induced tune shift	0.0003	0.0017
Space-charge induced tune spread	0.003	0.016
Chromatic tune spread	0.22	1.32
Chromatic frequency (GHz)	59.4	59.4

In Table B.4 we summarize the transverse parameters of the compressor ring. We find that the transverse impedance is low, as expected for a small ring ($Z_T \propto R$). Compared with the AGS, the compressor ring is transversely more stable (this is just opposite to the situation in case of longitudinal instability). The space-charge incoherent tune spread is small and is helped by the strong focusing optics. If the chromaticity were not corrected, the chromatic tune spread would be large. This is due to the small slippage factor, the high revolution frequency, and the high tune. For these reasons, we will control the normalized chromaticity to about 1%.

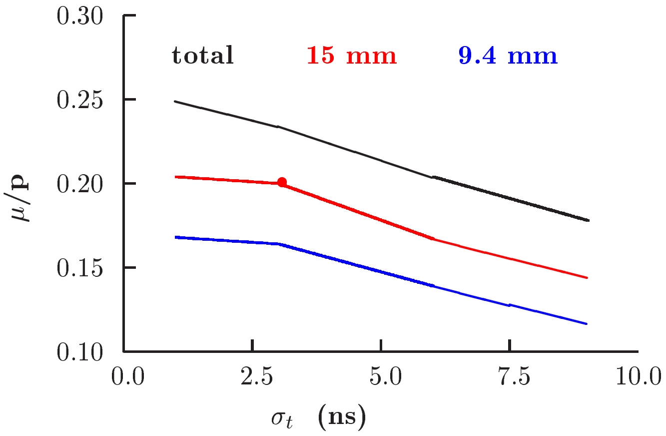

Figure B.1: Efficiency *vs.* proton bunch length.

The compressor ring design requires very low rf voltage; also, the potential-well effect facilitates the short bunch production. The required impedance is reasonable to achieve, and the acceptance/emittance ratio of 8 units is much larger than that for existing and proposed high intensity proton accelerators. In conjunction with the large momentum aperture it is reasonable to expect that beam losses can be controlled. Chromaticity control at the compressor ring is not easy, however, and needs further studies.

B.1.2 Proton Bunch Length and a Buncher Ring

The minimum proton driver bunch length achievable is set by the longitudinal emittance of the bunches and by the momentum acceptance of the AGS. For the baseline 1 MW case, we expect to achieve the specified rms bunch length of 3 ns without a bunch compressor ring.

However, if the proton bunch intensity is increased by a factor of two to reach 2 or 4 MW, as discussed in Section B.1, then the bunch length would be expected to increase,

Table B.5: Efficiency *vs.* proton bunch length.

rms bunch length (ns)	μ/p	relative
1	0.204	1.02
3	0.20	1.0
6	0.167	0.835
9	0.144	0.72

and the specified 3 ns rms bunch length could not be achieved without increasing the momentum spread above the AGS acceptance.

The consequence of such an increase in bunch length was simulated, without reoptimization. (It is not expected that any reoptimization will markedly improve the result.) The final muon per proton ratios obtained are given in Table B.5 and Fig. B.1. Note that the cooling system used in this early study had larger apertures, and thus higher performance, than the final design, but the sensitivity to bunch length is expected to be the same. It is seen that there is relatively little gain for pulse lengths less than 3 ns (the baseline value). For a 6 ns bunch the efficiency has dropped 16.5%, and for 9 ns, the efficiency has dropped by 28%.

B.2 Target

B.2.1 Rotating Inconel Band Option

If unforeseen difficulties make a liquid metal target undesirable, there are several alternatives. One of them, is a moving metal band target. The performance would be little different from the metal jet. The scheme is discussed in the next Section.

B.2.1.1 Introduction and Overview

As a backup scenario to the baseline mercury jet target design, we present here a solid-target option that is based upon an Inconel Alloy 718 target in a rotating band geometry. Similar conceptual designs for rotating band targets have been presented previously [1, 2, 3] for use at both muon colliders and neutrino factories. A more detailed report on this particular conceptual design can be found in reference [4].

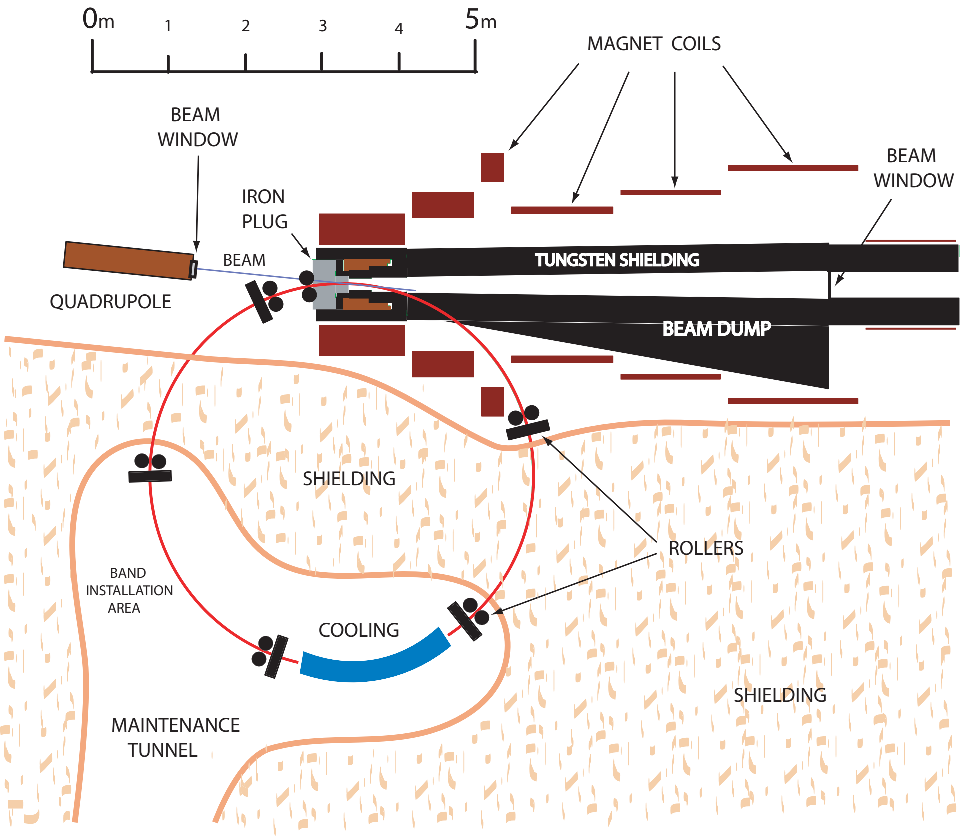

Figure B.2: A conceptual illustration of the setup for a pion production target based on a rotating inconel band.

A plan view of the targetry setup for the band target option is shown in Fig. B.2. An Inconel target band threads through the solenoidal magnetic capture channel to tangentially intercept the proton beam. The circulating band is cooled by passage through a water tank located in a radiation-shielded maintenance enclosure.

Inconel 718 is a niobium-modified nickel-chromium-iron superalloy that is widely used in nuclear reactors and particle accelerator applications because of its high strength, outstanding weldability, resistance to creep-rupture due to radiation damage and resistance to corrosion from air and water. The Inconel target band has an I-beam cross section. The band dimensions and positioning relative to the proton beam are shown in Fig. B.3. The proton pulse structure and bunch charges were assumed to be identical to the base-line target scenario. Table B.6 presents the parameter specifications that have been assumed

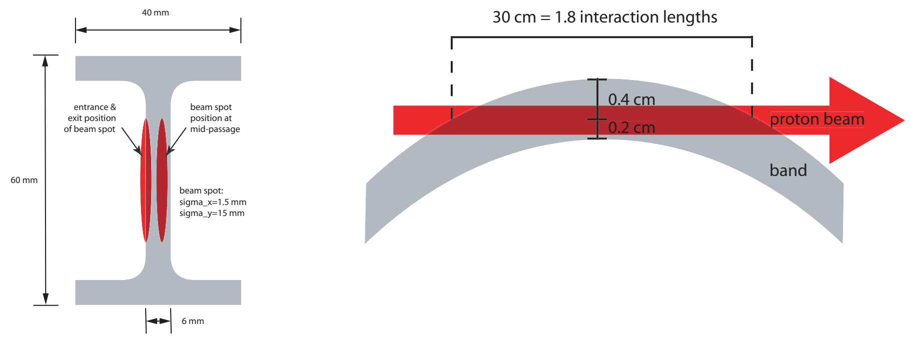

Figure B.3: Passage of the proton beam through the target band shown in cross-sectional (left) and plan (right) views. The horizontal position of the beam spot in the band webbing varies along the interaction region due to the curvature of the band. The plan view shown in the right plot is anamorphic, with a 10:1 aspect ratio.

for the Inconel target band and the incident proton beam.

B.2.1.2 Mechanical Design Considerations

As is evident from Fig. B.2, threading the target band through the pion capture channel requires only slight variations on the channel design assumed for the baseline mercury jet target option. An entry port must be incorporated into the iron plug in the upstream end of the capture solenoid and an exit port traverses the tungsten shielding and then passes between the solenoidal magnet coil blocks and out of the pion decay channel. The exit port can either be designed into the magnet cryostat or else the cryostat can be partitioned longitudinally into two cryostats so the band can exit between them. The radius of the third magnet coil block from the upstream end of the channel must be increased by approximately 10 cm relative to the baseline design in order to provide adequate space for the band to exit the channel. A modest reoptimization of the magnet coil currents in this region can restore the baseline magnetic field specifications.

No detailed consideration has yet been given to the design of the beam dump. As is clear from Fig. B.2, the target band exit port is far enough upstream from the beam dump for it to be essentially ddecopled from the beam dump design.

The band is guided and driven by several sets of rollers located around its circumference, as shown in Fig. B.2. A few hundred watts [4] of drive power will be required due to the eddy current forces from the band entering and exiting the 20 T solenoid.

Table B.6: Specifications of the Inconel target band and assumed proton beam parameters.

Target band radius, R (m)	2.5
Band thickness, t (mm)	6
Band webbing height, h (mm)	60
Full width of band flanges (mm)	40
Beam path length in band, L (cm)	30
Proton interaction lengths, λ	1.81
Density of Inconel 718, ρ (g.cm^{-3})	8.19
Mass of band (kg)	98.8
Band rotation velocity, v (m/s)	1
Proton energy (GeV)	24
Protons/bunch	1.7×10^{13}
Bunches/fill	6
Time between extracted bunches	20 ms
Repetition rate for fills	2.5 Hz
Horizontal beam-channel angle, α (mrad)	100
Beam spot size at target (horizontal), σ_x (mm)	1.5
Beam spot size at target (vertical), σ_y (mm)	15.0

Following the lead of the BNL g–2 target design [5], the roller assemblies will all incorporate self-lubricating graphalloy [6] bushings that are compatible with high radiation environments.

The pion production region of the target is in an air environment, with beam window positions shown in Fig. B.2. This simplifies target maintenance and target band replacement by avoiding any requirement to break and re-establish seals in a high radiation environment. Activated air and gases from the target and interaction region are continuously diluted and then vented from the target hall into the outside atmosphere following the procedure adopted [5] for the BNL g–2 target.

The heated portion of the band rotates through a 2-m-long cooling tank [4] whose conceptual design is shown in Fig. B.4. The band entrance and exit ports in the ends of the tank also serve as the water outlets. Both the heat transfer rates and water flow rates are found [4] to be relatively modest and the water flows due to its gravitational head alone with no need for forced flow.

The rotation of the target band has the desirable dilution effect that the rate of radiation damage on any particular section of the band material is reduced by roughly two

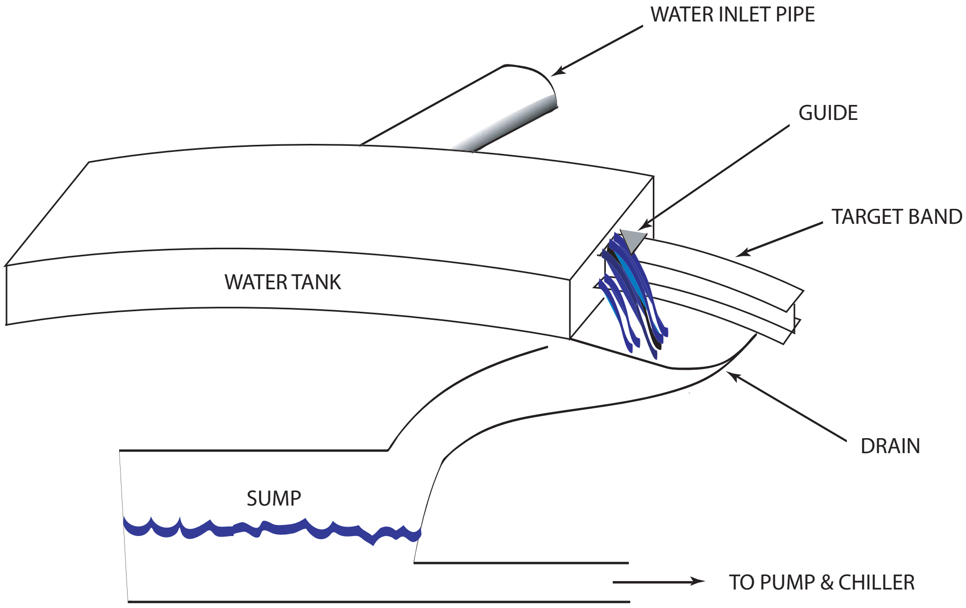

Figure B.4: A conceptual illustration of the cooling setup for the Inconel target band.

orders of magnitude relative to a fixed target geometry, since the 15.7-m-band circumference corresponds to 95 interaction lengths. Hence, each target band may last for several years [4] before requiring replacement.

The heavily irradiated used bands will be remotely extracted by progressively clamping and then shearing off 1 meter lengths and dropping them into a hot box. After the removal of the hot box, the band maintenance area can then be accessed and the new band progressively installed by welding together, in situ, eight 1.96-m-long chords of target band that have been previously cast (or otherwise prepared) into the correct I-beam cross section and circumferential curvature. Beam-induced stresses on the welds are minimized by welding on the flanges of the I-beam rather than on the central webbing; the flanges are not directly exposed to the proton beam and will also receive much smaller energy depositions from secondary particles than the central webbing.

B.2.1.3 Simulations of Pion Yields and Beam-Induced Stresses

Full MARS [7] tracking and showering Monte Carlo simulations were conducted [4] for 24 GeV protons incident on the target, giving predictions for the pion yield and energy deposition densities.

The yield per proton for pions plus kaons plus muons at 70 cm downstream from the central intersection of the beam with the target was predicted [4] to be 0.715 (positive) and 0.636 (negative) for the momentum range $0.05 < p < 0.80$ GeV/c, and 0.304 (positive) and 0.288 (negative) for the kinetic energy range $32 < E_{kin} < 232$ MeV that approximates the capture acceptance of the entire cooling channel. Note that the material in the flanges of the I-beam was not included in the calculation; their inclusion might result in a small change in the predicted yield. For comparison, the predicted yield was 18% higher for the identical geometry but with the band material artificially changed from Inconel to mercury.

Approximately 7% of the proton beam energy is deposited in the target as heat and the maximum instantaneous energy deposition from a single proton bunch is approximately 13 J/g, which corresponds to a temperature rise of approximately 29 °C. Detailed 3-dimensional maps of energy deposition densities were generated for input to dynamic target stress calculations [4] using the commercial ANSYS finite-element analysis code.

For the ANSYS simulations, the target band geometry was discretised into a 3-dimensional mesh containing approximately 30,000 elements. It was conservatively assumed that all of the deposited energy from a proton pulse is instantaneously converted into a local temperature rise.

The von Mises stress (*i.e.*, the deviation from the hydrostatic state of stress) was found to be initially zero but to develop and fluctuate over time as the directional stresses relax or are reflected from material boundaries. Figure B.5 gives a snap-shot of the predicted von Mises stress distribution at 1μs after the arrival of a proton pulse and Fig. B.6 shows the time development of the predicted stress at the position of maximum stress. For Fig. B.6, a "fixed edge" constraint has been applied to the band model with a simple rectangular cross section that is shown in the preceding figure; this is intended to better approximate the stiffening from the I-beam flanges in the actual band without the extra computing capacity required to simulate the more complicated true geometry. The predicted 190 MPa peak value, in both time and position, for the von Mises stress from a single proton bunch is much less than the the 740 MPa (or 1100 MPa) yield strength for annealed (or precipitation hardened) Inconel 718 and is also well below its fatigue strength.

The band rotation speed, 1 m/s, advances the band by 40 cm between successive beam fills. This presents a fresh 30 cm chord of target band for each beam fill, but the energy depositions from the 6 bunches within the fills are largely superimposed. However, the pile-up of stresses is not considered serious since any significant level of von Mises stress is expected to die out well within the 20 millisecond time span between successive

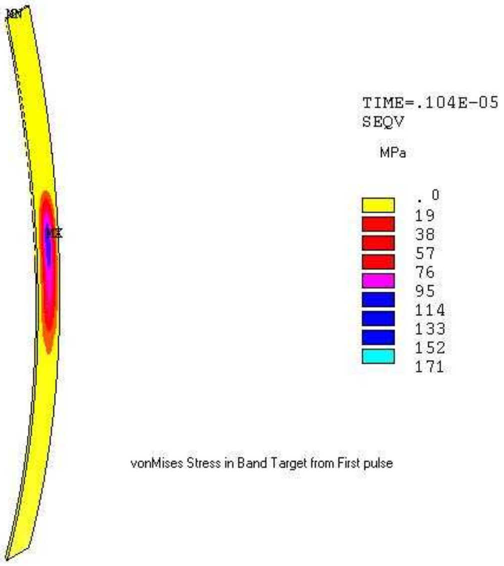

Figure B.5: Predicted von Mises stress distribution for the target band model at 1 μs after the arrival of the proton pulse. For simplicity, the flanges of the I-beam have been neglected in this particular simulation run. The maximum predicted von Mises stress at this time is 171 MPa.

bunches (*i.e.*, approximately 3000 times the time interval plotted in Fig. B.6), leaving only the relatively benign hydrostatic stresses.

B.2.1.4 Summary

In summary, the Inconel rotating band target design appears to be a promising backup option to the baseline mercury jet target. The pion yield appears slightly lower than the mercury baseline, although this has yet to be fully optimized. The engineering design looks manageable and initial simulations of target stresses are encouraging.

B.2.2 Carbon

As demonstrated in Study-I [8], a radiation cooled graphite target could be used up to 1.5 MW power level. It appears to be a relatively conservative solution (at 1 MW) but would sacrifice a factor of 2 in performance and require relatively frequent replacement. It is unclear if it could be used at 4 MW.

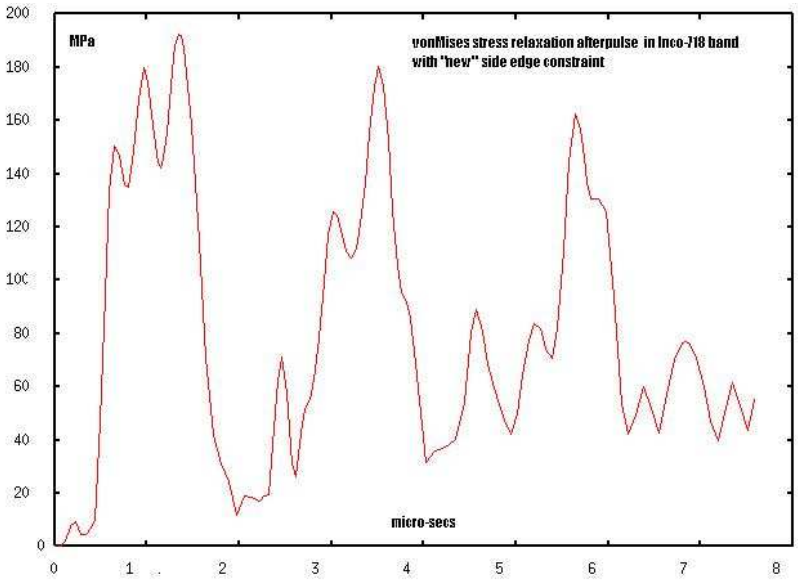

Figure B.6: Predicted time dependence of von Mises stresses on the target band. The time origin corresponds to the arrival of the proton pulse.

B.2.3 Granular

A "granular" target has also been suggested recently as an alternative approach, but this has not been examined during Study-II. [9].

B.3 Phase Rotation

B.3.1 Correlation Matching

Within the cooling lattice, particles with high transverse amplitude travel on longer orbits than those on the axis and thus, for a given momentum, move more slowly in the forward direction. In such a lattice, with active rf, the average forward velocity is controlled by the phase velocity of the rf and constrained to a fixed value. As a result, the stable momentum of a particle is dependent on its amplitude

$$\frac{dz}{dt} - \beta c \;\propto\; A^2, \tag{B.1}$$

where the approximately conserved particle amplitude is given by,

$$A \;=\; \frac{x^2+y^2}{\sqrt{\beta}} \;+\; \sqrt{\beta}\;(x'^2+y'^2). \tag{B.2}$$

Such a correlation is also generated naturally in the phase rotation process but, since the phase rotation is done in a different lattice from the cooling, the magnitude of the correlation is not the same. As a result, there is, in the present design, a mismatch in correlation at the entry to the cooling channel. Study is needed to see if performance could be improved by better matching to the optimal correlations, possibly by raising the solenoid fields used in the transport and phase rotation channels.

B.3.2 Polarization

A system of double phase rotation has been studied [10] that generated a strong correlation between the muon polarization and final time after the phase rotation. This correlation, though a little diluted, is maintained through to the storage ring and results in correlations between neutrino type and time of detection. The physics need for such correlation has not been well established, and the system requires high gradient (4 MV/m) low frequency (30 MHz) rf close (3–6 m) to the target. The viability of rf in such high-radiation environment has been questioned, but tests at CERN [11] suggest it may be feasible if it is needed.

B.3.3 Bunched Beam Phase Rotation

Cost savings may be possible by performing the phase rotation with rf after bunching of the beam [12]. As in induction linac phase rotation, the bunch is first allowed to drift to increase the bunch length and establish a correlation between time and energy, but in this case the bunching is done before the energy is corrected. The rf that performs this bunching is acting on a beam with strong time-momentum correlation; *i.e.* a beam whose time spread is still increasing with drift distance, and whose sub-bunches, as they are formed, have spacings that are also increasing. This requires that the rf wavelengths used to create and hold the bunches also rise with drift distance. After the bunches have been formed, suitable modifications to the rf frequencies and phases can be employed to accelerate the later bunches and decelerate the early ones, thus ending up with a train of bunches at a single energy, as in the conventional case.

The need to have cavities operating at many different frequencies is certainly a complication. But since the cost of conventional rf acceleration is likely to be less than that for induction acceleration, the cost of the system is expected to be less. Whether it is as efficient is less clear. For instance, non-distorting phase rotation does not seem possible with the rf-based scheme. But this scheme has the interesting feature of working on muons of both signs—the bunches of the opposite sign automatically form between the others. If both signs were subsequently accelerated through the linacs and RLA (injected in the opposite direction), and injected into the storage ring (also in the opposite direction), then a factor of two in efficiency could be achieved. This factor of two might compensate for any lower efficiency in the phase rotation of muons of one sign.

This solution is far from worked out, but seems worth evaluating. Injection into the ring must be such that timing can be used by the detector to separate the neutrinos from the two different muon trains.

B.4 Cooling

B.4.1 Limited-Flip Cooling Channels

In all solenoid focused channels used for cooling, the axial direction of the field must be reversed, at least once. If this is not done, canonical angular momentum (*i.e.*, the angular momentum of the beam once out of the axial field) rises, and it is impossible to remove it. In the SFOFO lattice, the field is reversed every cell, and significant canonical angular momentum never develops. But there are other solutions with far fewer flips: *e.g.*, single flip [13] or double flips, as in the example in Section B.4. In these cases the canonical angular momentum is allowed to build up, but is subsequently removed after a flip by cooling with the opposite field direction. The performance of such alternatives appears to be similar to that of the SFOFO, but the engineering design of the magnets is very different. The SFOFO has about five times less stored magnetic energy (often considered an indicator of cost) than the double flip design, but the forces between the coils are higher. At this time, the Super FOFO seems more cost effective, but more detailed engineering will be needed to confirm this.

There is another difference between the baseline design and the double-flip alternative (see Section B.4), that is unrelated to their differing lattices. The double-flip alternative performs its cooling at higher energy, and along the lattice. This gives a larger longitudinal acceptance, but requires more rf acceleration for a given cooling. The larger acceptance preserves more muons through the cooling channel, but does not appear to increase the muons accepted by the current acceleration scheme (see Section 6). Further optimization will be needed to assess the possible benefits of this alternative cooling channel design.

B.4.2 The Double-Flip Cooling Channel

B.4.2.1 Introduction

Unlike the baseline SFOFO channel, the Double-Flip (DF) channel [15] is based on long solenoids. Cooling is performed in a constant, or adiabatically increasing, magnetic field. This configuration provides simple transverse optics: for a matched beam there is neither modulation of the beam envelope along the channel, nor large chromatic effects.

A uniform solenoid that contains absorbers and rf cavities can only cool in two of the four transverse degrees of freedom: the Larmor radii of all the particles decrease while the positions of their Larmor centers remain unchanged. For an infinitely long channel, if we neglect scattering, the muon helices would therefore shrink to lines, and the resulting beam would be wide but without any angular spread. The magnetic field must be reversed at least once to achieve cooling in four dimensions (p_x, p_y, as well as x and y).

The field-flip section should be as short as possible (fast field flip) to avoid mismatching the beam in the region of zero field. At the flip region, the Larmor centers would move from one vertex of a parallelogram in x–y space to the opposite one, as shown in Fig. B.7 (Larmor radius $\Longleftrightarrow$ Larmor center exchange). The lengths of the channel sections with positive and negative magnetic field can be chosen to achieve a "canonical" phase ellipse on exit (an ellipse with zero angular momentum and no x–p_x correlations).

The major disadvantage of a cooling channel based on long solenoids is the perturbation of the longitudinal motion at the field flip regions. The longitudinal velocity is expressed as:

$$V_z = \frac{c}{E}\sqrt{E^2 - m^2c^4 - p_T^2c^2}\,, \tag{B.3}$$

where E and p_T are the total energy and transverse momentum of the particle. Due to the presence of an accelerating field, V_z oscillates around an equilibrium value equal to the phase velocity of the accelerating wave V_{ph}. It is possible to find the equilibrium energy that satisfies $V_z(E_{eq}) = E_{ph}$:

$$E_{eq} = E_{nominal}\sqrt{1 + p_T^2/(mc)^2}\,, \tag{B.4}$$

where $E_{nominal}$ is the usual nominal energy:

$$E_{nominal} = \frac{mc^2}{\sqrt{1 - V_{ph}^2/c^2}}\,. \tag{B.5}$$

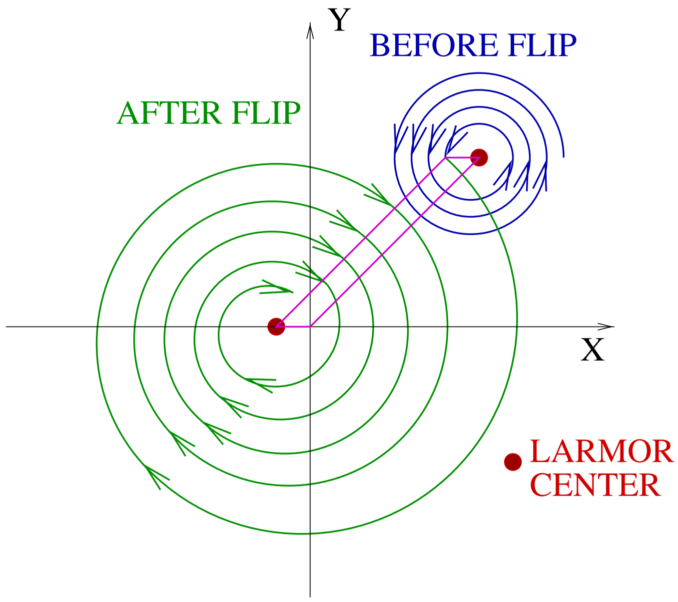

Figure B.7: Illustration of the particle motion before and after the first flip region (end view).

E_{eq}, as well as the separatrix, depends on transverse momentum and changes at the field flip. Typically, p_T is small immediately before the field reversal due to the cooling achieved in the section that precedes the flip. But after the field flip:

$$p_T \simeq \frac{eBr}{c} \tag{B.6}$$

where r is the particle radius.

The corresponding jump in the equilibrium energy leads to a strong perturbation of the synchrotron oscillations. This effect is mitigated by using a small magnetic field before and immediately after the first flip region. The field then grows adiabatically to decrease the β-function and maximize the cooling. The beam, however, would have a non-zero angular momentum its exit from such a system. A second field-flip section in the high field region, followed by a short additional cooling section, is therefore necessary to suppress the residual angular momentum. Due to the small beam radius at the end of the third section, the perturbation to the longitudinal motion at the second field flip is small. From these considerations, the DF channel is designed as follows (see Fig.B.8): the first section cools the transverse momenta of the muons using a relatively low constant solenoidal field (3 T on axis). Because the magnetic field is constant, the Larmor centers of the particle motion are unchanged and the transverse size is constant to first order. In the short region between sections 1 and 2, following the field reversal, the centers of the Larmor orbits are displaced and in section 2 the muons, to first order, execute Larmor motion about the solenoid axis. Then, the field is increased adiabatically up to -7 T in order to focus the beam more strongly, reducing the β-function for cooling of both the beam size and the transverse momentum. The second field flip is, therefore, performed at -7 T. The section lengths are chosen to obtain a canonical beam without parasitic correlations at the end of the channel. The beam is slowly accelerated to compensate for longitudinal emittance growth and avoid particle losses. The full length of the cooling channel is approximately 217 m.

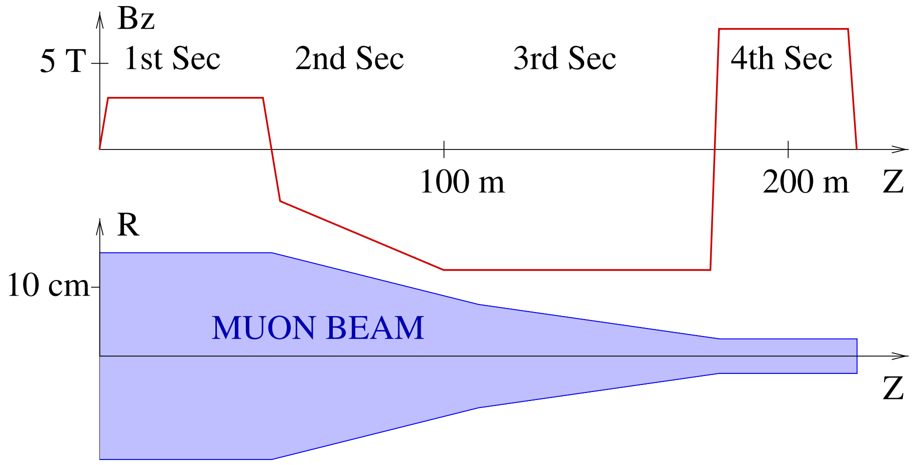

Figure B.8: Sketch of B_z on axis and the beam envelope associated with the double-flip channel.

B.4.2.2 Initial Constraints and the Input Beam

The optimization of any cooling channel is strongly coupled to the front-end design. The double-flip channel is optimized to maximize the transmission and the cooling performance for the input beam produced at the end of the pre-cooling system. The pre-cooling apparatus, and consequently the input beam for the double-flip channel, is different from the baseline system described in Chapter 5. It follows the design developed during Feasibility Study- ([16]), which is displayed in Fig. B.9. It consists of:

- **A: GeV proton beam**

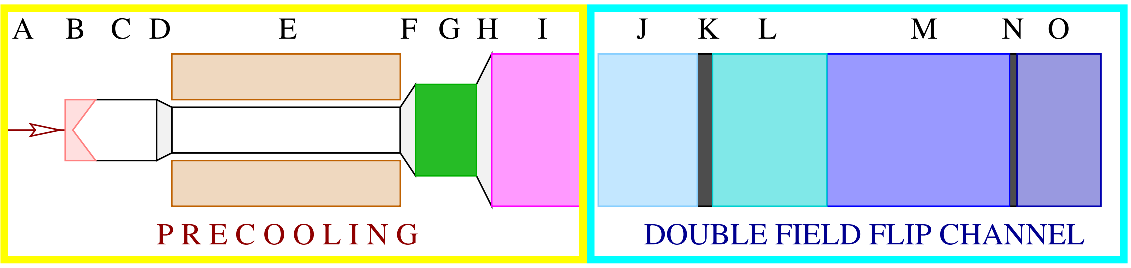

Figure B.9: Sketch of the accelerator system preceding the cooling channel (front-end).

The beam size is $\sigma_x = \sigma_y = 2.14$ mm, σ_t=3 ns.

- **B: Target station**
  A solid carbon target of 0.8-m length and 7.5-mm radius is placed in a 20-T solenoid. Then, the solenoidal field decreases adiabatically to 1.25 T in a 9 m long matching section.

- **C: Decay channel**
  A uniform solenoid, 41-m-long, with a radius of 30 cm and a field of 1.25 T on axis, is used.

- **D: 4-m-long matching section**
  The magnetic field increases from 1.25 T to 3 T, and the solenoid radius decreases from 30 cm to 20 cm, to provide a matching between the decay channel and the induction linac.

- **E: 100-m-long induction linac**
  It develops a voltage from -50 MV to 150 MV in a pulse. The accelerating voltage in the gaps is adjusted to accept muons in the energy interval 230 MeV $< E_{tot} <$ 330 MeV.

- **F: Matching section**
  A 0.6-m-long solenoid channel is used.

- **G: Minicooler**
  Minicooling is accomplished by a 2.6-m-long liquid-hydrogen (LH_2) absorber inside a 3 T solenoid with a radius of 40 cm. It produces some transverse cooling and decreases the average beam energy from 280 MeV to 200 MeV, which is optimal for bunching.

- **H: Matching section**
  A 0.3-m-long solenoid channel is used.

- **I: Buncher**
  It includes three accelerating stations and three drift spaces inside a solenoid with $r = 71$ cm, B= 3 T. Each station comprises six $f = 201$ MHz $\pi/2$ cavities, 32 cm long. The full voltages of the three stations are 15, 19.5 and 24 MV, respectively. The synchronous phase is zero at the total nominal energy of 200 MeV.

The performance of the cooling channel was tested using the beam coming from the end of the buncher (see Table B.7), as produced from a simulation of the precooling section [15]. Note that the product $\sigma_x \sigma_{p_x}/mc$ is greater than the beam transverse emittance ε_x due to the x–p_y correlations. Figure B.10 shows the distribution of particles in longitudinal phase space (energy *vs.* ct) for the "realistic" beam at the beginning of the cooling channel. Particles outside the separatrix will be lost ($\simeq$30%).

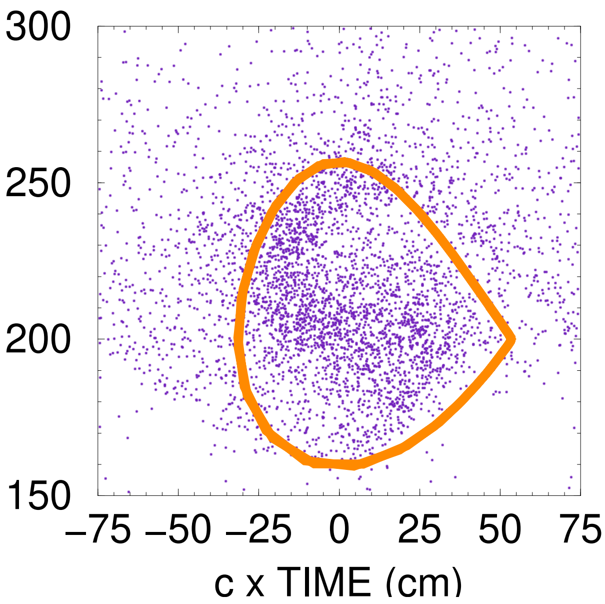

Figure B.10: Distribution of particles in longitudinal phase space for the "realistic" beam at the beginning of the cooling channel. Particles outside the rf bucket separatrix will be lost ($\simeq$30%).

The channel performance was also tested using a Gaussian beam with transverse parameters similar to those of the "realistic" beam and $\sigma_{ct} = 10$ cm, $\langle E \rangle = 200$ MeV, σ_E

= 20 MeV.

Table B.7: Parameters of the "realistic" beam (b) after bunching (input to the cooling channel), as calculated in Ref. [15]. "In bucket" means that the μ/p yield is calculated with respect to the particles inside the initial phase space bucket.

σ_x	σ_{p_x}	$\sigma_x\sigma_x/mc$	ε_x	μ/p	μ/p
(mm)	(MeV/c)	(mm)	(mm)	E < 300 MeV	(in bucket)
54.6	24.4	12.6	11.1	0.191	0.135

In the "realistic" and Gaussian beam simulations, we use μ^+ particles, which describe a clockwise helix in a field $\vec{B_z} = B_z\hat{z}$.

B.4.2.3 Description of the Channel

The cooling lattice, simulated with GEANT4 [17], comprises four sections: the first contains 20 cooling cells, 2.42-m-long, in an almost-constant magnetic field of $B_z = 3$ T on axis. Between the first and the second sections there is a 1.02 m long matching section in which the field changes polarity. The second section consists of 20 cells, 2.42-m-long, with a field on axis which adiabatically (and linearly) grows from $B_z = -3$ T to -7 T on axis. It is followed by a third section, containing 32 cells, 2.51-m-long (the first two cells are still 2.42-m-long), with a field of $B_z = -7$ T on axis. The second field flip region is 1.26-m-long and is followed by the fourth section with 15 cells, 2.51-m-long, with a field of $B_z = 7$ T on axis. A cooling cell includes 6 rf cavities that provide an effective voltage of 15 MeV/m, and a vessel containing the liquid-hydrogen absorber material (LH_2). Gaps in the long solenoids are required for flexible rf power feeds and cooling devices to reach the rf cavities and absorber. Fig B.11 shows an engineering drawing of two cooling cells of the DF channel (note that there is just one 20-cm gap every $\simeq$5 m). Correction coils could be needed to bring the magnetic field back to a uniform value in the gap regions, and avoid a degradation in the channel performance. The current simulation models neither the gaps nor the associated correction coils.

Detailed specifications of the cooling sections and the two flip regions are given in Tables B.8 and B.9. Figure B.12 shows a side view (in wire-frame mode) of a cooling cell, including the solenoid, the linac, and the absorber.

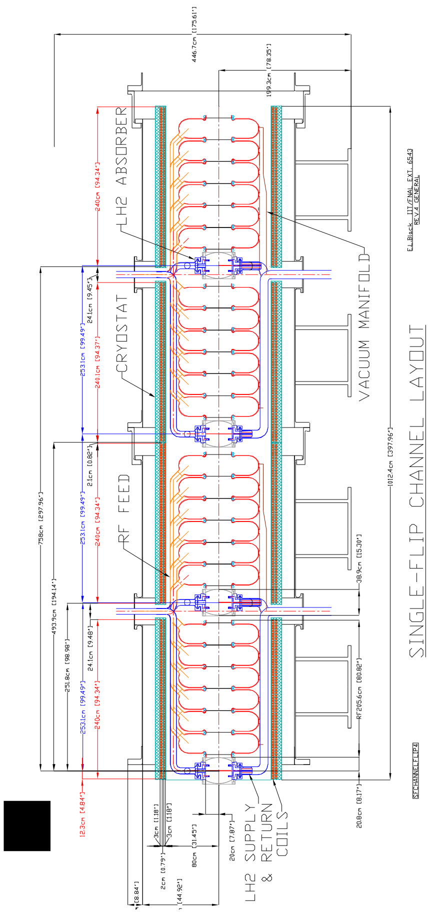

Figure B.11: Engineering drawing of a cooling channel unit cell. The gaps are not modeled in the simulation yet.

Table B.8: Lists of parameters associated with the four sections of the double flip channel.

Parameter	First	Second	Third	Fourth
Global	–	–	–	–
Length of section (m)	2.42	2.42	2.51	2.51
Magnetic field on axis (T)	3	$-3 \rightarrow -7$	-7	7
Mean current densities (A/mm^2)	68.2	$-22.7 \rightarrow -53.1$	-53.1	53.1
Coil thickness (cm)	3.5	10.5	10.5	10.5
Coil inner radius (cm)	81	81	81	81
Number of cells	20	20	32	15
Absorber	–	–	–	–
Length of hydrogen (LH_2) absorber (cm)	30	30	39	39
Density of LH_2 (g/cm^2)	0.0708	0.0708	0.0708	0.0708
Aluminum window thickness (μm)	360	360	220	220
Energy loss per cell (MeV)	10.4	11.2	$\approx$11.1	11.2
Radial aperture, in LH2 (cm)	16	16	7	7
Cavity	-	-	-	-
Length of rf cavity (m)	1.92	1.92	1.92	1.92
Number of rf cells per cavity	6	6	6	6
Frequency (MHz)	201.25	201.25	201.25	201.25
Effective voltage (MV/m)	15	15	15	15
Synchronous phase	25.5°	25.9°	24.6°	25.0°
Beryllium window thickness (μm)	300	300	25	25
Radial rf cavity aperture (cm)	16	16	7	7

B.4.2.4 Magnet

The coil blocks are modeled in the simulation as a set of infinitely thin current sheets separated 5 mm from each other in the radial direction. Each sheet shares an equal fraction of the total coil current. Figure B.13 shows the actual field, B_z on axis, as produced by the current distributions in the simulation.

The long solenoids are 81 cm in radius, and are designed so that they completely enclose the rf cavities. Coil thicknesses vary from 3.5 cm in the first section to 10.5 cm in the succeeding sections, as the magnetic field increases. The current densities of the thin and thick coils are 68.2 and 53.1 A/mm^2, respectively. The most sensitive parameter of

Table B.9: Parameters associated with the two flip regions of the double-flip channel. The main solenoid in the second flip region is made of three layers of conductor material with different current densities.

Parameter	Flip 1	Flip 2
Main Solenoid	–	(three layers)
Length (cm)	41+41	53.1+53.1
Gap length (cm)	20	20
Magnetic field at the coil (T)	3.15	6
Current density (A/mm^2)	68.2	38.6, 52.2, 68.2
Coil thickness (cm)	3.5	3.5, 3.5, 3.5
Coil inner radius (cm)	81	81, 84.5, 88
Inner solenoid	-	-
Length (cm)	10.5+10.5	24.5+24.5
Gap length (cm)	26.8	9.6
Magnetic field at the coil (T)	4.55	5.8
Current density (A/mm^2)	52.2	38.6
Coil thickness (cm)	24.42	15
Coil inner radius (cm)	21	11

the cooling channel is the gradient of the magnetic field in the field-flip regions. This gradient must be maximized in order to stabilize the longitudinal motion. Specifications for the two matching sections are displayed in Table B.9 and Figs. B.14, B.15. The 1.02-m-long first flip region consists of two outer coils, separated by 20 cm, and two 10.5-cm-long inner coils, separated by 26.8 cm from each other. The 1.26-m-long second flip region consists of the two outer coils, separated by 20 cm, and two 24.5-cm-long inner coils, separated by 9.6 cm. The magnetic fields on axis, B_z, associated with the matching sections are shown in Figs. B.16, B.17. Both sections achieve a field flip within a distance of less than 1 m.

The design of the solenoidal magnets is based on aluminum-stabilized superconductors with indirect cooling. This technique was initially developed for magnets used in particle physics detectors, which operate continuously for long periods of time in steady state conditions. Cooling of the magnets is accomplished by helium cooling tubes glued on the external face of the solenoids. In order to ensure the stability of the conductor, a minimum stability margin of 1°K is kept on the conductors. The operating point of the

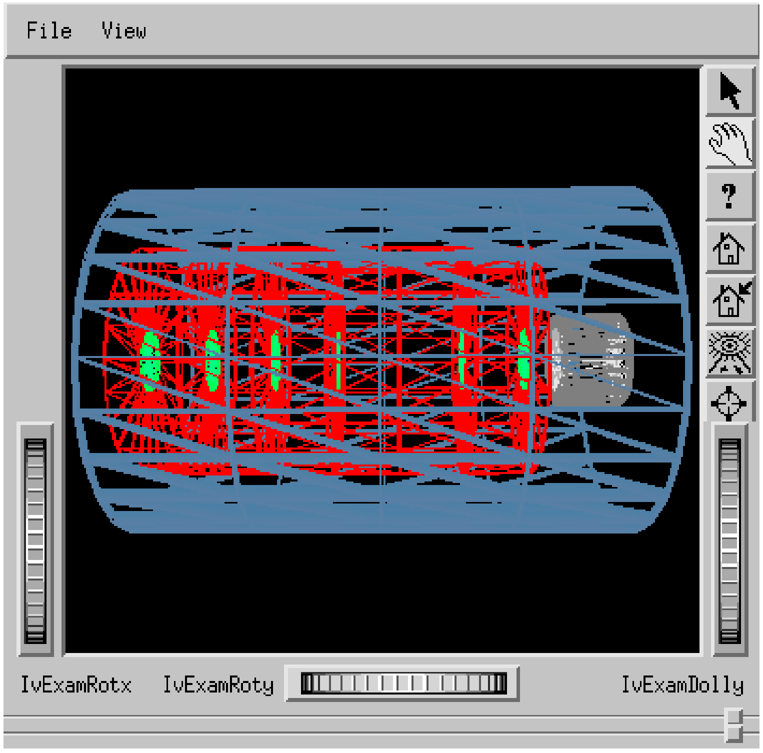

Figure B.12: Side view of a cooling cell as simulated in GEANT4 and visualized using the Open Inventor package [18].

conductor never exceeds 55% of its critical current at the operating field. The energy during a quench is dissipated inside the cold mass of the magnet. The magnets are quench protected, and the current induced in the mechanical structure during a fast discharge contributes to the propagation of the quench, thus limiting the temperature rise. The operating current is high, around 20 kA, in order to reduce the number of turns per magnet, and therefore limit their inductance. This reduces the time needed to discharge the magnets and limits the temperature rise during a quench. The aluminum stabilized conductors consist of NbTi superconducting cables around which an aluminum stabilizer is coextruded. The aluminum provides good mechanical and thermal stability, and ensures easy and safe processing during the winding (the superconducting cable is protected by the aluminum). The junction between conductors is done by TIG welding of the aluminum stabilizer. Since the critical current is strongly dependent on the magnetic field (in NbTi superconductor the critical current density decreases from 4500 A/mm^2 at 3 T to 1750 A/mm^2 at 7 T), it is advisable to use graded conductors for the cooling

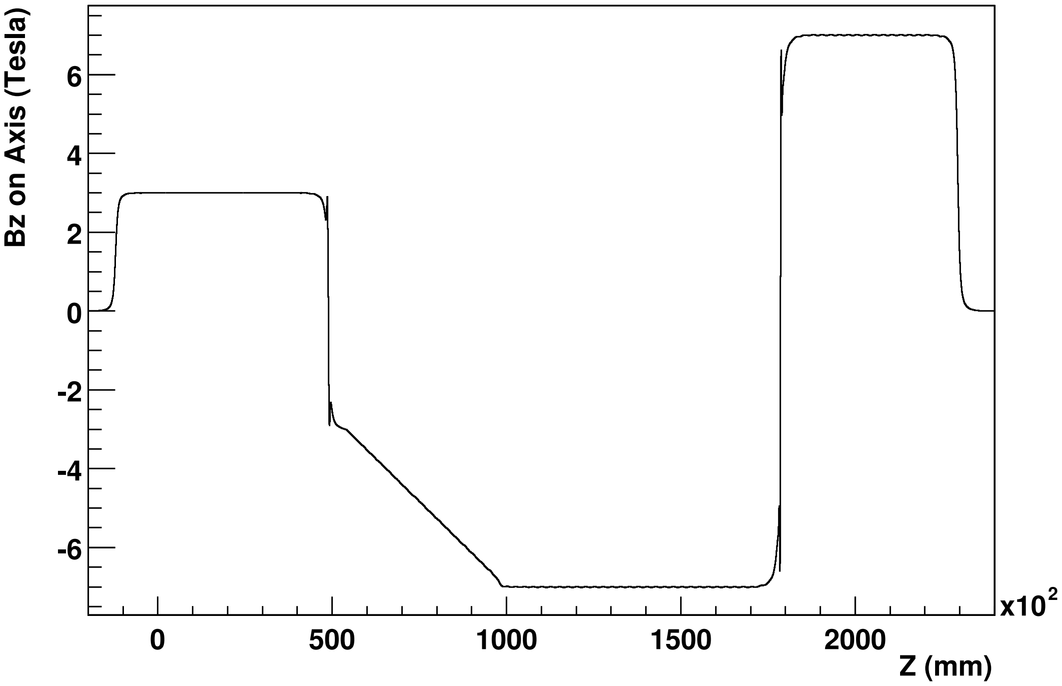

Figure B.13: B_z on axis as a function of z.

channel. In other words, the quantity of superconducting materials should be adjusted according to the location of the conductor in the magnet, leading to substantial savings in superconducting materials. As an example, a magnet operating at 20 kA, a cable having 32 strands of 1.4 mm in diameter, and a copper to superconductor ratio of 1.1 must be used in the innermost conductor layer. A cable having only 12 of the same strands is sufficient for the outermost layer. These design considerations lead to simple and safe magnets that can be easily built in industry and provide good reliability for long term operation under constant magnetic fields.

B.4.2.5 RF System

The rf system consists of one linac per cooling cell, each composed of 6 pillbox copper cavities, 32 cm long (phase advance is $\pi/2$). The radial aperture is 16 cm in the first two sections of the cooling channel and 7 cm in the third and fourth. Windows are made of Beryllium with thicknesses of 300 μm and 25 μm respectively. In the first two sections

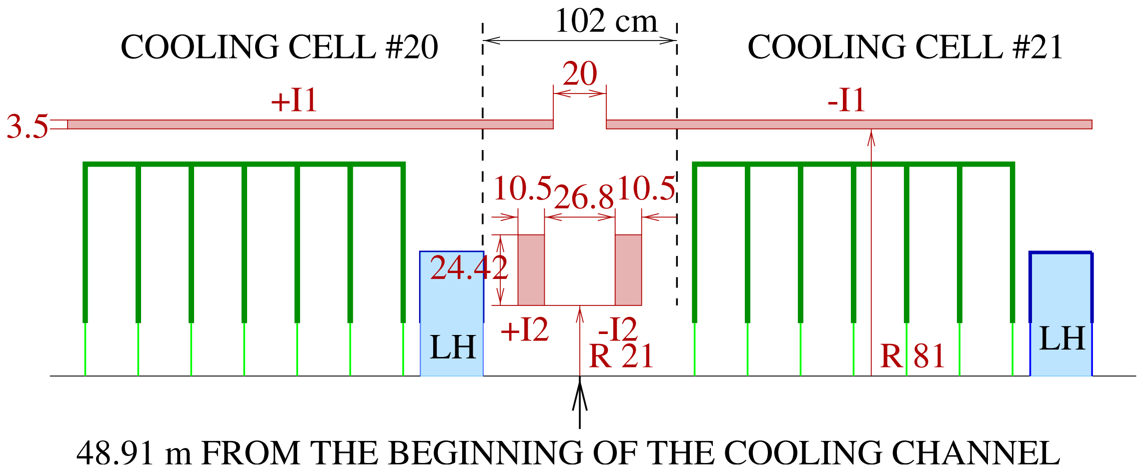

Figure B.14: The first matching section. The current densities I1 and I2 are listed in Table B.9.

the window thickness follows a step function which goes from 300μm to 600μm at 0.7 the full radius of the window. Figure B.18 shows a single r.f. cavity including the stepped window. Thin windows are preferred to reduce the transverse emittance growth due to multiple scattering. Mechanical constraints set a 25 μm lower limit to the thickness of a Beryllium window. The thickness must grow approximately as the fourth power of the radius to control the window temperature, which would rise due to the power dissipated by the high frequency electromagnetic fields. The optimal solution for the DF channel would be to adjust the window radius and thickness in each cell as the beam size decreases after the first flip. For simplicity, we changed the window size only once at the end of the second section.

A peak voltage of 16.48 MV/m, which corresponds to an effective voltage of about 15 MV/m, gives a large enough bucket to capture most of the beam from the buncher. The beam must be slowly accelerated to enlarge the bucket and compensate for the increase of the energy spread through the channel. This avoids particle losses due to longitudinal phase-space dilution. A particle with an energy of 200 MeV would lose about 10.4 MeV per cell in the first section and gain $\approx$12.9 MeV per 6-cell linac at a synchronous phase ϕ $\approx$25.5°. Fig B.19 shows the evolution of the nominal energy along the channel. It increases linearly from 200 MeV to 250 MeV in the first section. At the flip regions, the beam gains transverse momentum and its average longitudinal velocity decreases. The synchronous phases of the r.f. cavities are tuned taking into account a decrease of 15 MeV in the nominal energy of the channel at the flip regions. In the second section, the average

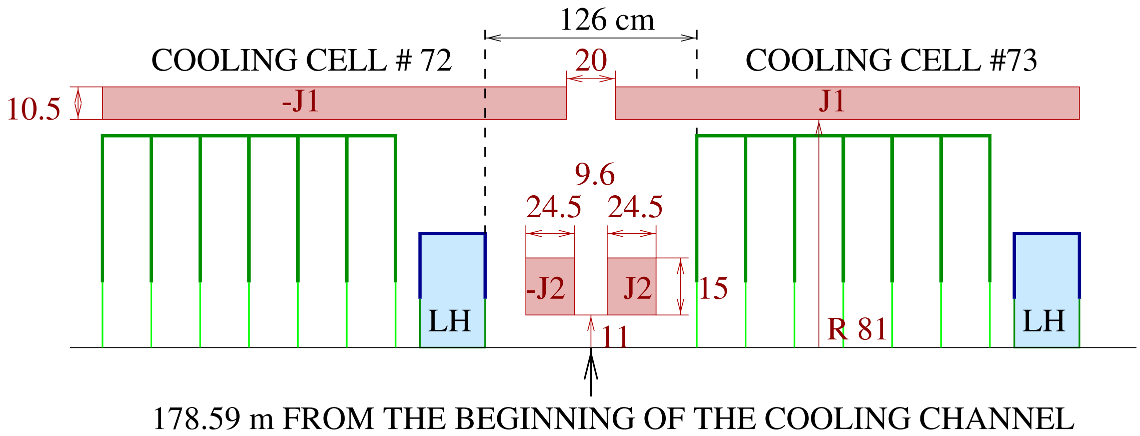

Figure B.15: The second matching section. The current densities J1 and J2 are listed in Table B.9.

net acceleration provided to the beam is the same as in the first, 2.5 MeV/cell. In the third and fourth sections, the acceleration is reduced to ≈0.85 MeV/cell. The nominal energy at the end of the fourth section is 326 MeV.

B.4.2.6 LH_2 Absorbers

The absorbers provide the energy loss necessary for the cooling mechanism. The hydrogen is contained by a cryostat vessel. The absorber length is 30 cm in the first two sections and 39 cm in the third (after the second cell) and fourth sections. This change compensates for the smaller dE/dx in the material as the energy increases, and approximately maintains the same synchronous phase throughout the channel. The aluminum windows have the same radius as the beryllium windows in the linac, but they must be thick enough to withstand the 1.2 atm pressure from the LH2. The windows are therefore 360 μm and 220 μm thick for a radius of 16 cm and 7 cm respectively. Fig. B.20 shows a downstream view of a unit cell with the absorber vessel (in grey) inside the solenoidal coils (in blue).

B.4.2.7 Performance

The performance of the channel described in the previous section, was studied using GEANT4 for both a Gaussian (a) and a “realistic” beam (b). For comparison, a third study (c) was done using a “realistic” beam through a modified version of the channel which follows more closely the design in Ref. [15]. In (c), only the windows are different: a radius and thickness of 20 cm and 125 μm for the aluminum windows in the LH2 vessels,

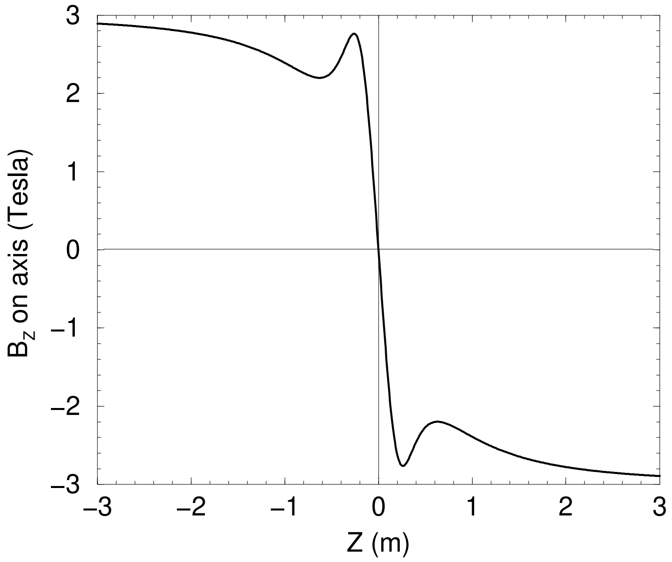

Figure B.16: The magnetic field on axis, B_z, around the first field-flip region. The z origin is placed at the center of the flip in this illustration.

and a radius and thickness of 20 cm (10 cm) and 400 μm (200 μm) for the beryllium windows in the r.f. cavities. In the three cases, muon decay is modeled and yields an $\simeq$8 % decrease in transmission. Table B.10 displays the beam parameters at the end of the cooling channel for (a), (b), (c), and Ref. [15].

Figure B.21, based on a 1000 particles simulation, illustrates the performance of the channel for the Gaussian beam (a). The transverse cooling factor is 6.5, from ε_x =12.6 cm to 1.92 cm. It is clear from Fig. B.21 that the first section of the DF channel reduces σ_{p_x} by a factor of two without changing the size of the beam envelope. The change of field polarity in the matching section causes σ_{p_x} to grow by a factor of 3. Due to the displacement of the Larmor orbits, the second section cools both σ_x and σ_{p_x}, to final values of 14 mm and 21.4 MeV/c, respectively. The second, third, and fourth sections recover from the transverse emittance growth in the field-flip regions, cool the transverse size of the beam, and restores angular momentum such that the beam is "canonical" when it exits the channel. The fractional transmission through this channel is approximately 69%.

Figure B.22, based on a 1000 particles simulation, illustrates the performance of the DF channel for the "realistic" beam (b). The final transverse and longitudinal emittances

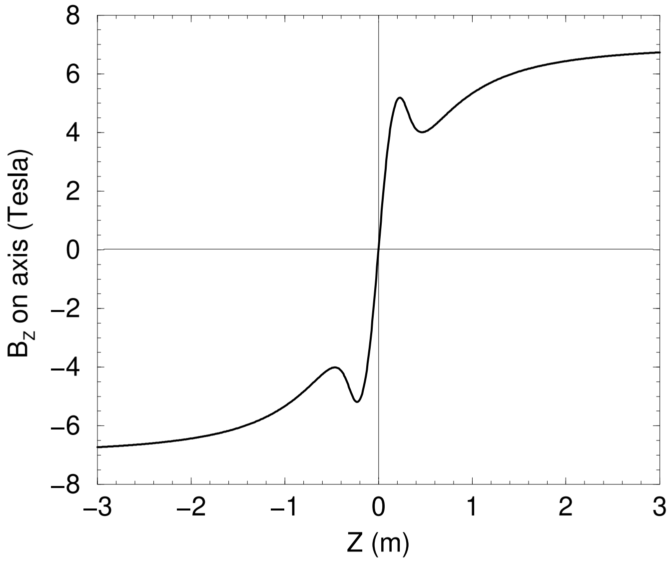

Figure B.17: The magnetic field on axis, B_z, at the second field-flip region. The z origin is placed at the center of the flip in this illustration.

(ε_x and ε_z) are 1.85 mm and 78 mm, respectively. The longitudinal emittance increases by a factor of 1.6 between the end of the first section and the end of the channel. Both σ_x and σ_{p_x} are cooled from initial values of 57 mm and 25.5 MeV/c to final values of 14.2 mm and 22 MeV/c, respectively. The transmission predicted by the GEANT4 simulation, referred to the total number of particles in the initial beam (with a E<300 MeV cut), is 40%.

Figures B.23, B.24, B.25 show the beam evolution as a function of distance from the origin. Plots number 0 and 19 correspond to the initial and cooled beam (before exiting the channel), respectively. Plots 4, 5, and 6 (13, 14, 15) show the beam immediately before, in the middle, and after the first flip (second flip) region. The rest of the plots are snapshots of the beam taken approximately every five cooling cells. The longitudinal phase space evolution in Fig. B.23 suggests that the bunch fills the 201.25 MHz r.f. bucket from the start. About half of the lost particles are muons that are not captured into the bucket; these are lost in the first few meters of the cooling channel. The remaining particle loss is due to the excitation of longitudinal motion in the first field-flip region. Low-momentum muons are lost at the maximum of the synchrotron oscillation, which is a few meters after the matching section. Thus the second section of the channel scrapes

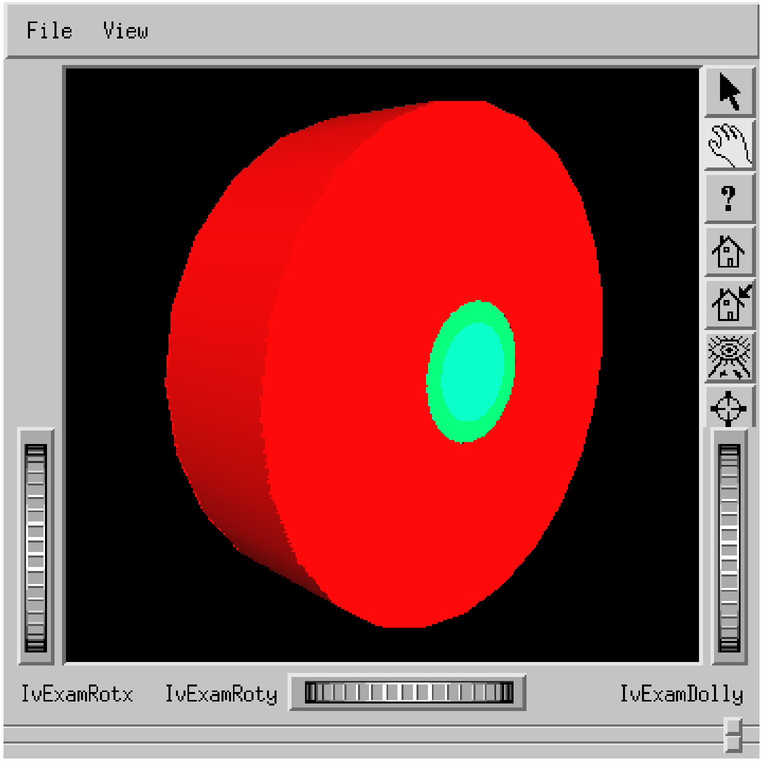

Figure B.18: Illustration of a single copper $\pi/2$ r.f. cell, 32 cm long, as simulated in GEANT4. The iris is covered by beryllium stepped windows: 300μm thick (r $< 0.7 \times$ R$_{\mathrm{window}}$), 600μm thick ($r \geq 0.7\times$ R$_{\mathrm{window}}$).

longitudinally. Figure B.24 illustrates on the transverse size of the beam, and Fig. B.25 on the angular momentum. Initially, the beam has a negative x - p_y correlation which is reversed in both field flip regions. On exit, the radial component of the fringe field would add the necessary contribution to suppress the beam angular momentum.

A "realistic" beam with non-optimized window dimensions (c) was used for comparison with results from the simpler simulation in Ref. [15]. The parameters at the end of the channel for (c) (or Ref. [15]) are in reasonable agreement: σ_x=14.4 mm (14.5 mm), σ_{p_x}=21 mm (21.1 mm), ε_x=1.74 mm (2.12 mm), ε_z=77 mm (74.6 mm). Transmission is 43% and 48% for (c) and Ref. [15], respectively.

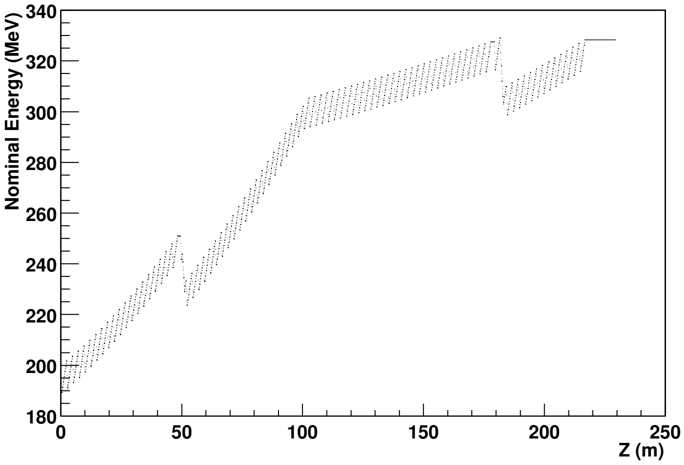

Figure B.19: Nominal energy of the channel *vs.* z. The nominal energy increases from 200 MeV to 326 MeV from the beginning to the end of the channel.

Table B.10: Parameters of the beam at the end of the cooling channel. $\star$ The longitudinal cooling factor is calculated with respect to ε_z at the end of the first section.

Case	σ_x (mm)	σ_{p_x} (MeV/c)	ε_x (mm)	Cooling factor (x)	ε_z (mm)	Cooling factor (z)	Transmission %
(a)	14.0	21.4	1.92	6.5	61.5	$0.43^\star$	69
(b)	14.2	22.0	1.85	6.8	77.6	$0.62^\star$	40
(c)	13.8	21.0	1.74	7.2	73.6	$0.69^\star$	43
Ref. [15]	14.5	21.1	2.12	6.0	74.6	$0.69^\star$	48

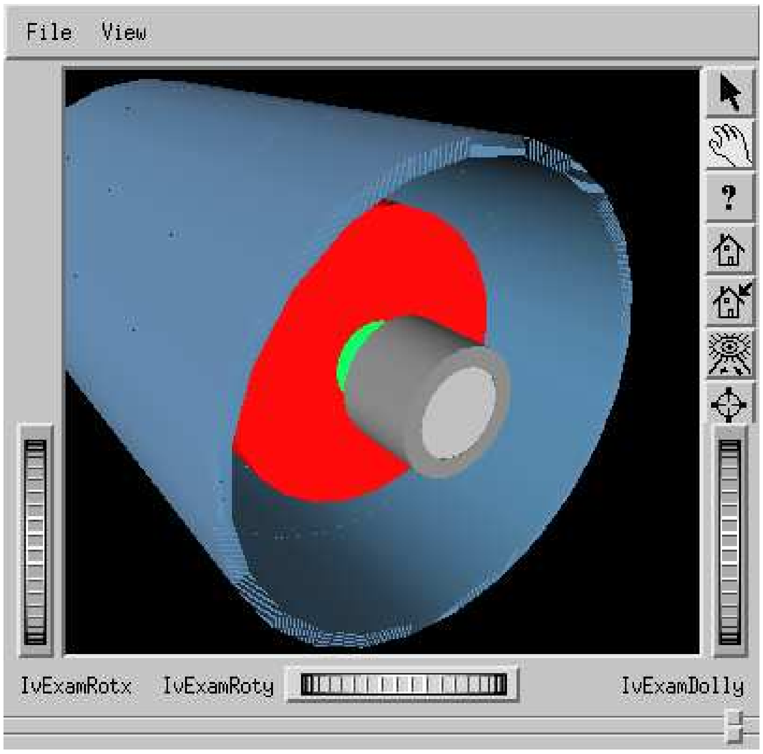

Figure B.20: The absorber vessel (in grey) is placed inside the solenoidal coils (in blue) in a unit cell. The aluminum windows are shown in light grey.

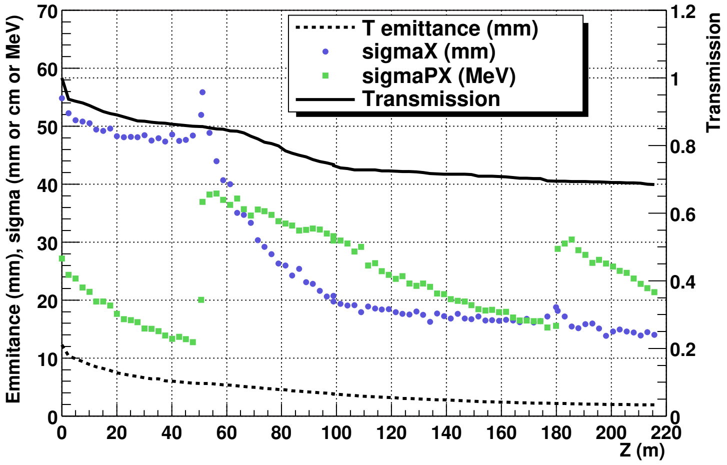

Figure B.21: Performance of the Double-Flip cooling channel with a Gaussian initial beam (“case a”).

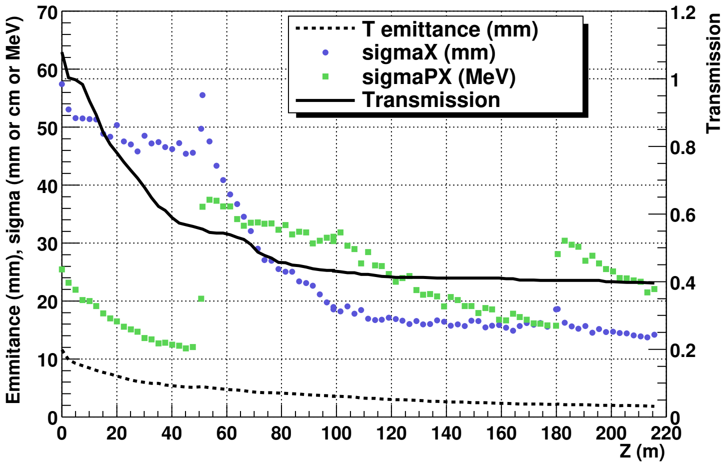

Figure B.22: Performance of the Double-Flip cooling channel with a “realistic” initial beam (“case b”), where the beam was generated from particle production at a carbon target and transported to the cooling channel.

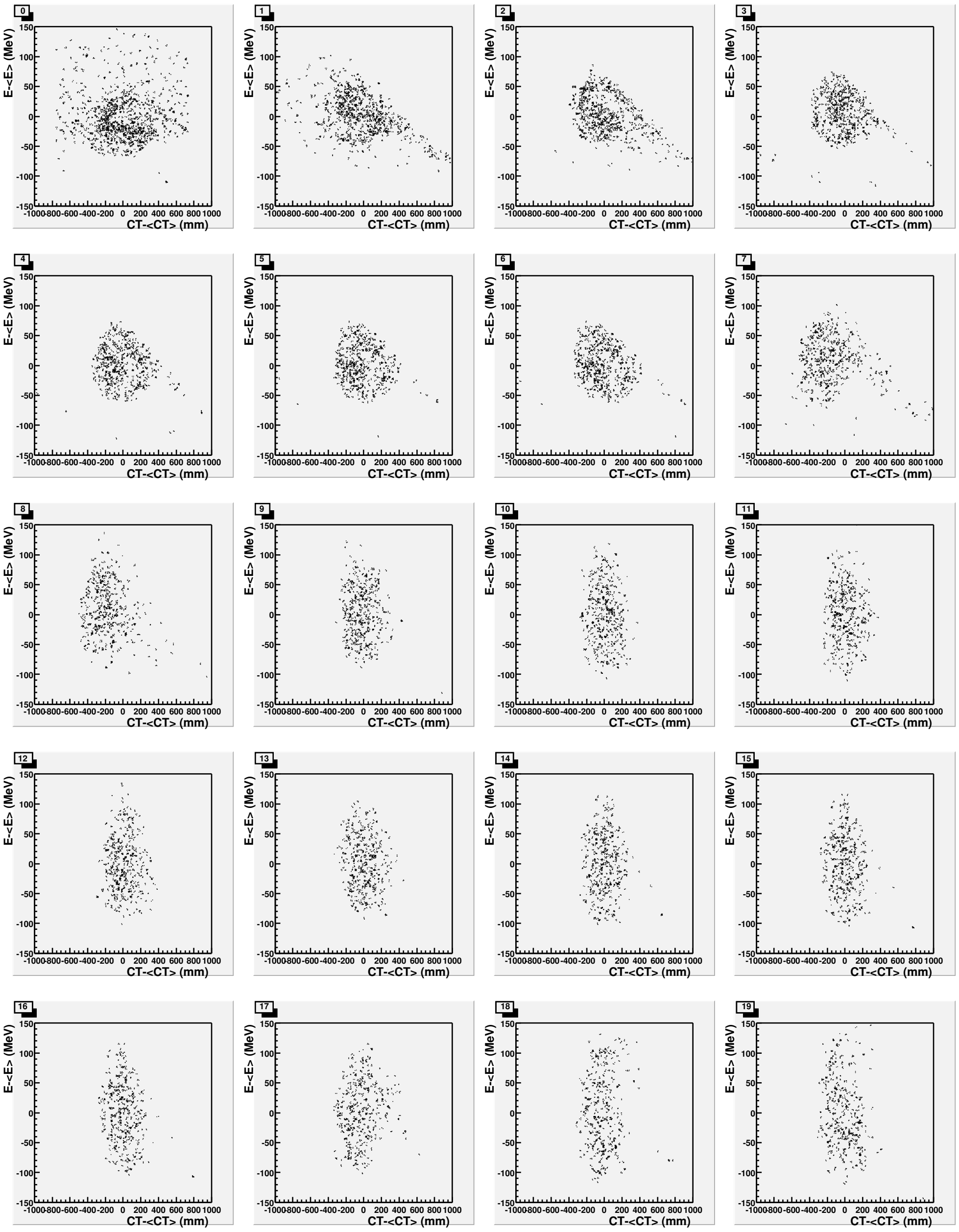

Figure B.23: Evolution of the longitudinal phase space. Plots 0 and 19 correspond to the initial and cooled beam, respectively. Plots 4, 5, and 6 (13, 14, 15) show the beam immediately before, in the middle, and after the first flip (second flip) region. The rest of the plots are snapshots of the beam taken approximately every five cooling cells.

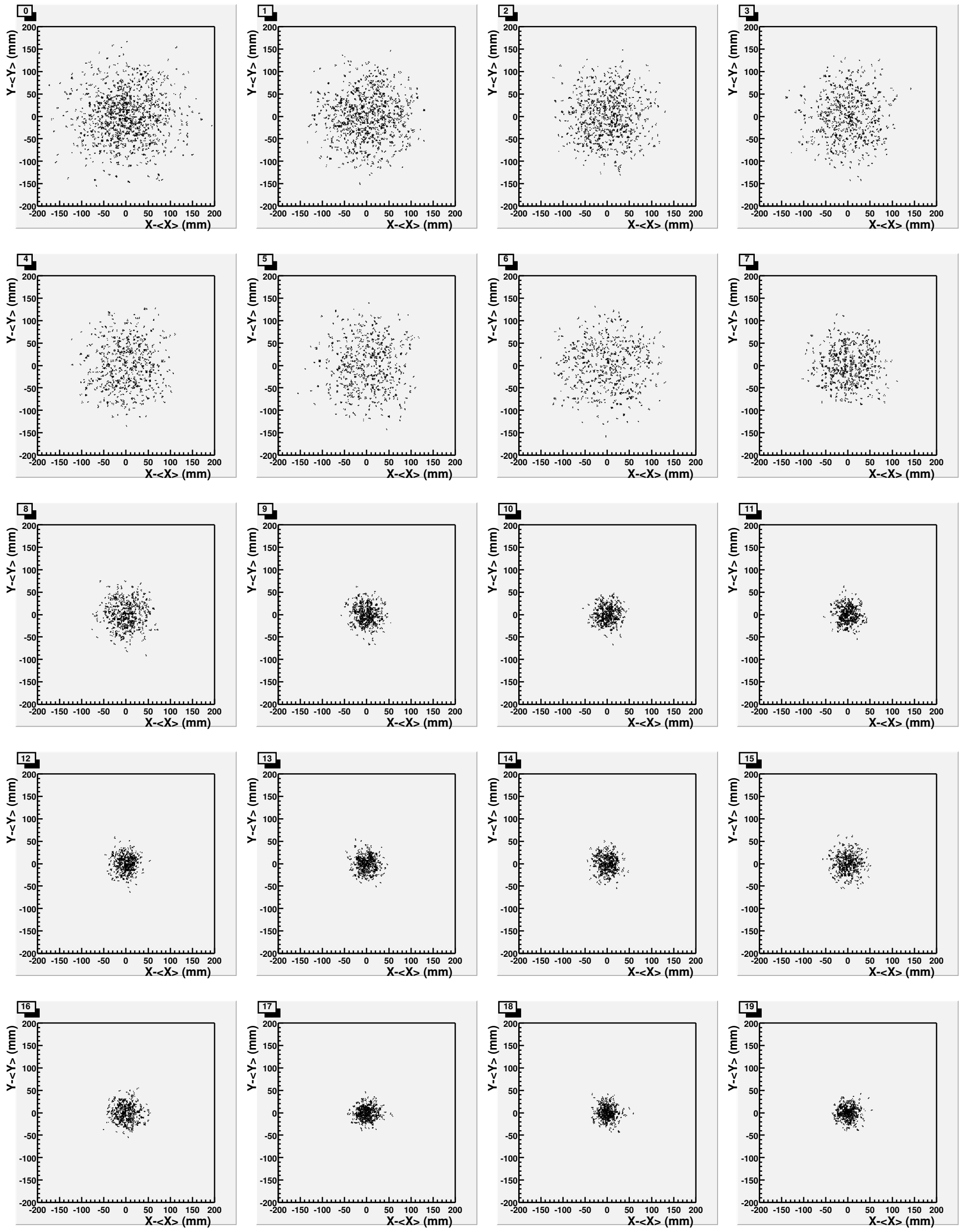

Figure B.24: Evolution of the beam size. Plots 0 and 19 correspond to the initial and cooled beam, respectively. Plots 4, 5, and 6 (13, 14, 15) show the beam immediately before, in the middle, and after the first flip (second flip) region. The rest of the plots are snapshots of the beam taken approximately every five cooling cells.

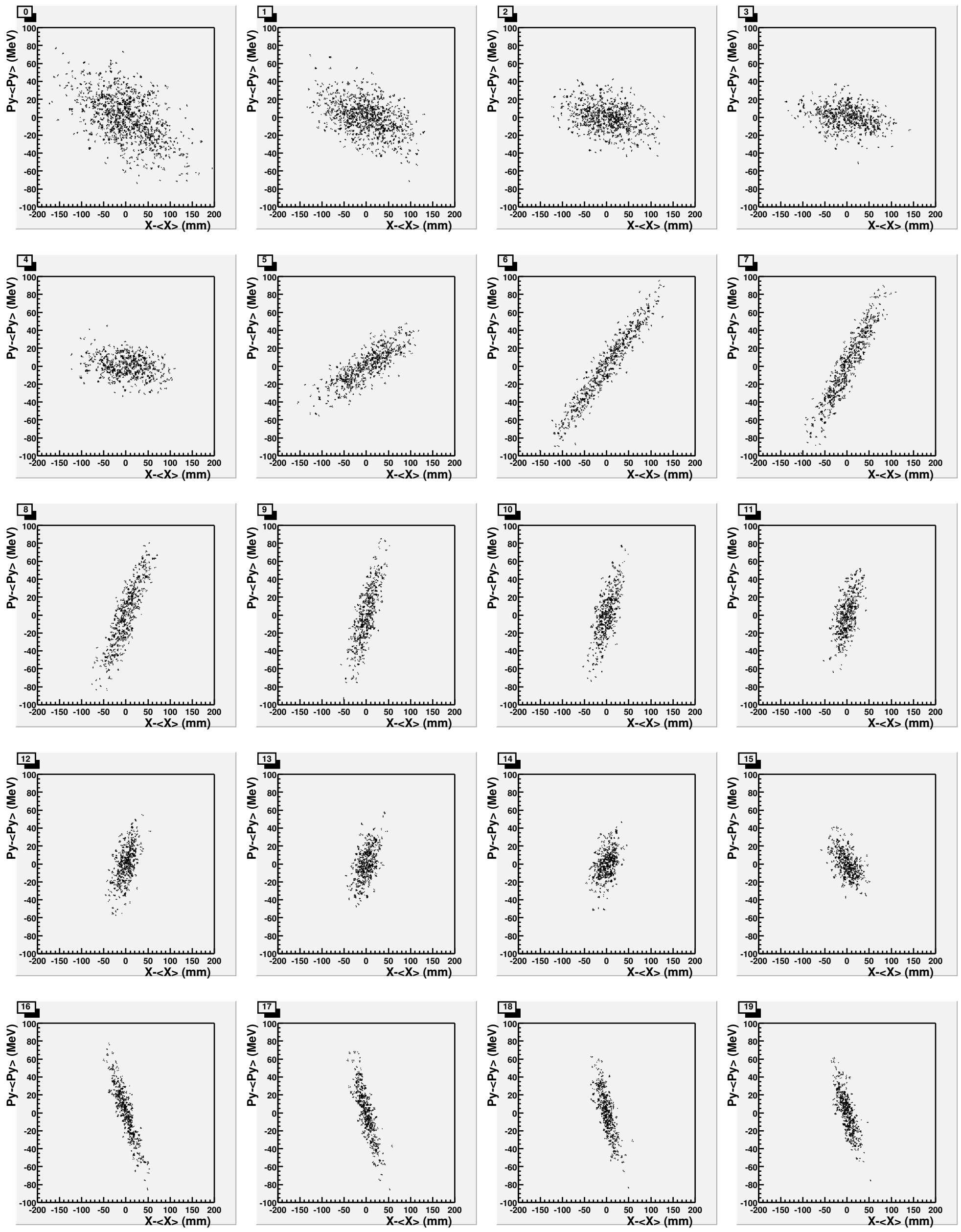

Figure B.25: Evolution of p_y versus x. Plots 0 and 19 correspond to the initial and cooled beam, respectively. Plots 4, 5, and 6 (13, 14, 15) show the beam immediately before, in the middle, and after the first flip (second flip) region. The rest of the plots are snapshots of the beam taken approximately every five cooling cells.

B.4.2.8 Muon/Proton (μ/p) Yield

The Muon/Proton Yield at the beginning of the cooling channel is 0.191, as listed in Table B.7. This means that at the end of the cooling channel, for the "realistic" beam with optimized window dimensions (b), the μ/p yield is 0.191 $\times$ transmission=0.076. If we upgraded the proton driver to 24 GeV, and the carbon target to a liquid mercury target (to match the baseline parameters set in the current feasibility study for a ν source), this yield should be scaled by a factor $24/16 \times 1.9$. The yield at the end of the DF cooling channel would therefore be $\simeq$0.22 muons per proton.

There are, however, constraints given by the acceptance associated with the accelerating system which follows the cooling channel: the linac, the recirculating linac, and the storage ring. A particle in a beam will be accepted by a succeeding accelerator if the following equations are satisfied:

$$\frac{\Delta z^2}{\beta_s \epsilon_z} + \frac{(\Delta p/p)^2 \beta_s}{\epsilon_z} < \frac{A_L}{\varepsilon_z}$$

$$\frac{\Delta r^2}{\beta_\perp \epsilon_x} + \frac{\Delta r'^2 \beta_\perp}{\epsilon_x} < \frac{A_\perp}{\varepsilon_x} ,$$

where $\Delta z = z - z_\circ$ and $\Delta p/p = (p - p_\circ)/p$, with z, p the particle z coordinate and total momentum, and $z_\circ$, $p_\circ$ the beam mean values for z and p. In the condition for the transverse direction, $\Delta r^2 = (x - x_\circ)^2 + (y - y_\circ)^2$ and $\Delta r' = \Delta p_T/p$, with p_T the particle transverse momentum; The longitudinal and transverse beta functions, β_s and $\beta_\perp$, are $\sigma_z/\sigma_{\Delta p/p}$ and $\sigma_x/\sigma_{x'}$, respectively. The normalized longitudinal and transverse emittance are invariant under Lorenz transformations. They are defined as:

$$\varepsilon_z = \beta\gamma\epsilon_z \ , \quad \epsilon_z = \sigma_z \sigma_{\Delta p/p}$$

$$\varepsilon_x = \beta\gamma\epsilon_x \ , \quad \epsilon_x = \sigma_x \sigma_{x'}$$

The longitudinal and transverse accelerator acceptances, A_L and $A_\perp$, depend on machine parameters. A_L also depends on the beam nominal energy which determines the vertical size of the r.f. bucket ($E - E_\circ$).

In the previous chapters, the acceptance of the accelerator system following the cooling channel was set to $A_L = 150$ mm and $A_\perp = 15$ mm. These values correspond to a beam nominal momentum of 200 MeV/c, which is constant through the channel for the baseline SFOFO. Since the DF channel accelerates the beam to 308 MeV/c, it would also replace the first section of the post-cooling linac, which would have a larger bucket and, therefore, accept a beam with larger longitudinal emittance. Since the longitudinal acceptance for a linac is $A_L \propto p^{3/2}$, the longitudinal acceptance cut for the DF channel would be

A_L=150 mm×(308/200)$^{3/2}$=286 mm. The issue of whether the large momentum spread associated with the DF channel could be accepted by the recirculating linac and the storage ring is currently under investigation. Fig. B.26 shows the μ/p yield at the end of the DF cooling channel as a function of the longitudinal acceptance of the downstream system for different values of the normalized transverse acceptance cut. For A_L=150 mm (286 mm) and $A_\perp$=15 mm, the μ/p yield is 0.118 (0.176).

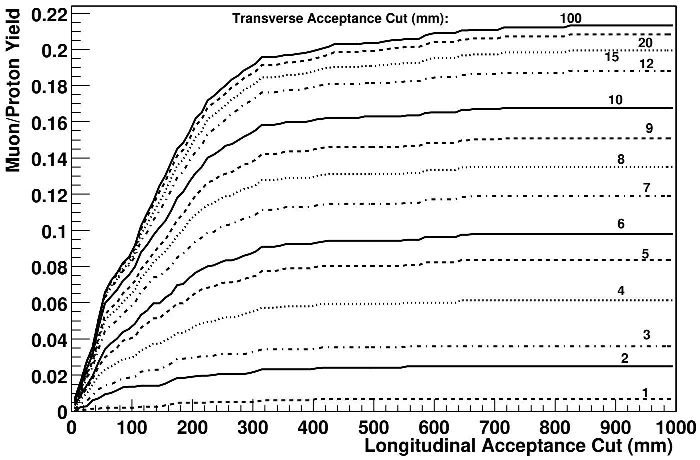

Figure B.26: μ/p yield at the end of the DF cooling channel as a function of the normalized longitudinal acceptance of the downstream system for different values of the normalized transverse acceptance cut. The optimum values of transverse and longitudinal acceptance are ~15 mm and ~300 mm, respectively. These acceptances are roughly consistent with those used for the baseline SFOFO cooling channel described in Chapter 5.

B.4.2.9 Summary

We have developed a conceptual and engineering design of a double flip cooling channel, and studied its performance tracking a "realistic" initial beam through a detailed GEANT4 simulation of the channel. The double flip channel offers greater mechanical simplicity than the baseline SFOFO, since it has only two field reversals. A final μ/p acceptance of 0.076 in the cooled beam is computed for a beam produced by a 16 GeV proton driver and a carbon target. If we upgraded the machine to a 24 GeV proton driver and a liquid mercury target, as in feasibility study II, the number of muons per proton would almost triple to 0.22. The acceptance cuts associated with the downstream accelerator further reduce this number following the curves in Fig B.26. The final transverse emittance of the beam before the acceptance cuts is 1.85 mm, which corresponds to a cooling factor of 6.8. The final longitudinal emittance before the acceptance cuts is 77.6 mm.

The current design can be further improved and optimized with modifications of the magnetic field strengths, r.f. parameters, section lengths, and window dimensions.

B.4.3 Emittance Exchange

In the baseline design, there is a large loss ($\approx 50\%$) of muons as they pass through the cooling channel. This is due mainly to the fact the lattice does not transport the increases in momentum spread that arise in the absorbers. This loss could be greatly reduced if the longitudinal acceptance of the lattice were increased, for instance by increasing the energy as the beam cools (as done in the double-flip alternative, see Section B.4). But this would not greatly improve the final result because the longitudinal acceptance is subsequently limited in the acceleration in particular, in the RLA. Increasing the acceptance there is expensive.

The preferred solution would be to cool the longitudinal emittance [14]. This can, in principle, be done by introducing dispersion (correlation of momentum with some transverse dimension) and placing a shaped absorber so that the higher momentum particles pass through more material than the lower momentum ones. In such a process, while the longitudinal emittance is reduced, the transverse emittance is increased, and thus we have emittance exchange, rather than cooling. When emittance exchange is combined with transverse cooling, however, all dimensions would be cooled.

This process, though simple in concept, has been found in full 6D simulations to be surprisingly hard to achieve efficiently. In unbunched beams, momentum spread can be efficiently exchanged with transverse emittance using bent solenoids or helical magnets. But in such systems, the dispersion introduces time-momentum correlations, that, for bunched beams in the presence of rf, greatly complicate the dynamics. Current designs do achieve some cooling in 6D, but with less than ideal efficiency. The problem will, we believe, be solved—it must be solved to realize a muon collider—and, when solved, could provide up to a factor of two improvement in performance. Further, if the cooled beam emittances could be further reduced, then the needed accelerator acceptances could be reduced, with concomitant cost savings.

B.4.4 NCRF: Grid of Tubes Alternative to Foil Windows.

Table B.11: Performance dependency on rf cavity apertures.

Maximum aperture (cm)	μ/p Be foil	μ/p Al tubes
21	.174	0.189
25	0.19	0.204
30	0.195	0.21

If the radii of the Be foil rf windows could be increased without increasing their thickness, then the performance can be improved. Table B.4.4 shows results for the baseline window thicknesses, and for 80μm Al windows that correspond in material thickness to a grid of tubes (see below). In both cases there appear to be significant gains. However, for edge-cooled Be foils, their thickness must be increased as the fourth power of radius to avoid excessive temperature rise. If this is done, the performance falls instead of rising. For a gas-cooled grid of thin-walled tubes, however, the pipe thickness is independent of aperture radius, and no degradation would be expected as the aperture increases.

Tracking with 5 cm diameter pipes has shown that the field non-uniformities lead to increases in emittance, but these problems can be avoided if the pipe diameter is reduced and the number of pipes is increased. A second advantage of many small tubes is that, for a given pressure, the wall thicknesses can be reduced.

For 1-cm diameter pipes, spaced on 2-cm centers, with wall thicknesses of 25 μm) the tension in the walls with 1 atmosphere of gas in the pipes would be only 3000 psi, which should be acceptable. For this diameter, the non-uniform field effects appear small. When a pair of such grids (at right angles to one another) is simulated by a plane foil with the same average material thickness (80 μm Al), then the performance gain with respect to the baseline, as seen in Table B.4.4, is 17% for a 25 cm aperture and approximately 20% for a 30 cm aperture (see Section 14.5 for a discussion of the grid tube approach).

B.5 Acceleration

B.5.1 Accelerator Acceptance.

The acceleration of the muons represents a major cost of the system. This cost could be reduced if the longitudinal and/or transverse acceptances could be reduced. And, conversely, the performance could be improved if these acceptances could be increased. The performance *vs.* acceptances are plotted in Fig. B.27. It is seen that a significant gain in performance could be achieved with greater transverse acceptance, but that the baseline longitudinal aperture already accepts almost all muons.

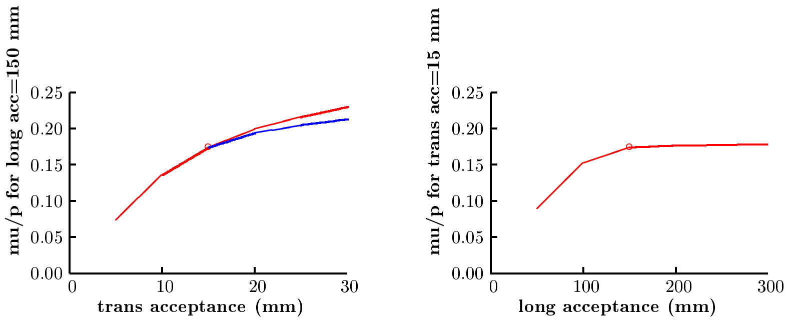

Figure B.27: Performance *vs.* accelerator acceptance: a) (left) transverse (upper line includes re-optimization of cooling length); b) (right) longitudinal. The baseline parameters are indicated by the circles.

B.5.2 Dogbone Configuration

A parametric study of costs [19] has been done on conventional racetrack and dogbone RLAs. The method used a semi-automatic longitudinal motion design, minimizing the energy spread. The costs were taken from the Feasibility Study-I: linac costs proportional to energy gain (C=35 ΔE per GeV) and arc costs proportional to length and energy spread (C=0.18 ΔE $\delta p/p$ per GeV and %.) The cost units are such that the two RLAs of Study-I cost 500 units.

For the conventional racetrack design (Fig. B.28,) the method shows that a cost minimum is achieved with 6 turns (Fig. B.30). However, four passes have been chosen for several practical reasons, including the difficulties of designing a switchyard with greater than 4 paths. If these problems could be overcome, then a cost saving of approximately 7% might be achieved.

An alternative geometry for the RLA is the dogbone (Fig. B.29). In this geometry there is only one linac, with the beam passing through it in alternate directions. Despite the larger number of passes, the number of paths on any one side of a switchyard is only

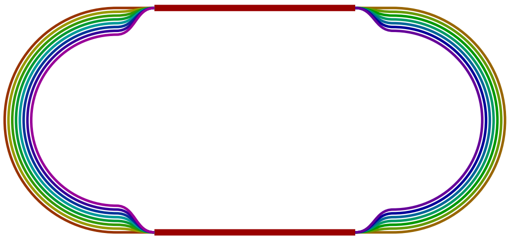

Figure B.28: Schematic of conventional racetrack RLA.

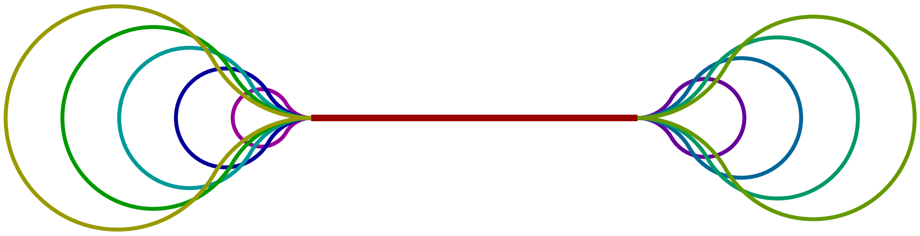

Figure B.29: Schematic of dogbone RLA.

four—no more than in the baseline. The savings in a dogbone arise primarily from the ability to reduce the length of the arcs when the momentum is lower. (If all the arcs were forced into a single tunnel, the gains would be lost.) A serious study based on actual costs will be needed to quantify the benefits of alternative accelerator approaches. This should include the use of FFAG (Fixed-Field Alternating Gradient) rings. However, the main motivation for an FFAG, its large longitudinal acceptance, seems moot based on Fig. B.27.

B.6 Detector

B.6.1 Introduction

An alternate to WIPP [20] for the location of the long-baseline neutrino detector is the Soudan Mine in northern Minnesota.

The Soudan Site is located in the Soudan Mine State Park, Minnesota; it has been the location of an underground neutrino facility since 1984 and is currently being prepared for the installation of the MINOS [21] experiment, which is scheduled to start taking data

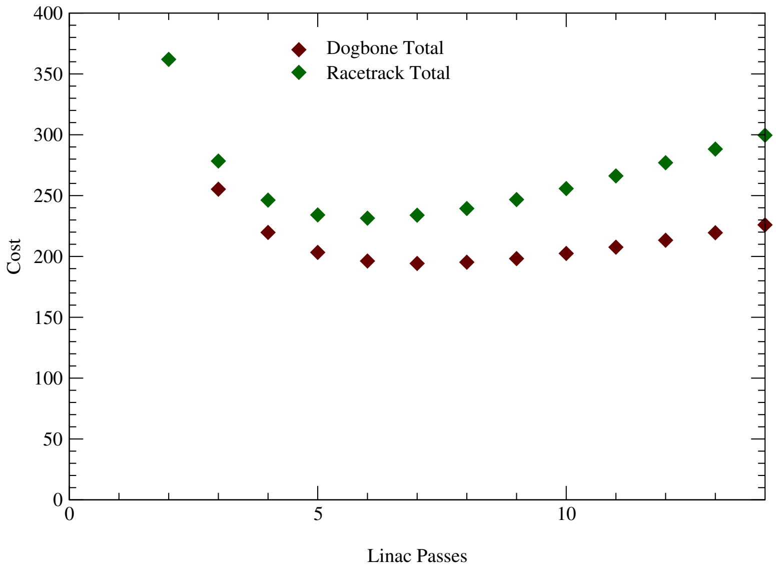

Figure B.30: Relative costs of RLA's *vs.* number of passes.

in 2004.

The Soudan site has both advantages and disadvantages compared with WIPP. The advantages include closer distance to BNL, higher event rate, existing infrastructure, and an operating underground neutrino detector. The closer distance means that the storage ring at the Neutrino Factory can have a smaller inclination angle (7.7° Soudan *vs.* 13.1° WIPP) which translates into easier and less expensive civil engineering. The 1700 km location also means a higher neutrino rate per kton at Soudan than at WIPP. A detector at Soudan could be 1/3 the size of one at WIPP and still have the same number of ν-interactions/year (see Table B.12.)

The site has infrastructure well matched to the requirements of a physics experiment, and offers the potential to use an existing detector (MINOS) upgraded for the Neutrino Factory program. The closer distance to BNL is also a disadvantage of the Soudan site. At 1700 km, both the matter oscillation and the CP violating term, δ, are harder to observe (See Fig. 15.1). However, the measurement of θ_{13} and the improvement in both $\Delta {m_{23}}^2$ and θ_{23} should not be significantly affected by the shorter distance.

Table B.12: Event rates at possible detectors at Soudan and WIPP.

E_μ Muon Ring (GeV)	Baseline (km)	E_{ν_μ}	E_{ν_e}	$N(\nu_\mu$ CC) (per kton-year)	$N(\nu_e$ CC) (per kton-year)
$10_{\text{BNL-SOU}}$	1700	7.5	6.5	260	120
$20_{\text{BNL-SOU}}$	1700	15	13	2150	960
$20_{\text{BNL-WIPP}}$	2900	15	13	740	330

B.6.2 Site

As noted the Soudan Site has two excavated halls available for physics experiments: the MINOS hall and a neighboring hall in which Soudan II was located. The halls are not optimally oriented with respect to BNL. MINOS is rotated 39° with respect to a ν-beam incident from Brookhaven. The second hall is also pointed away from BNL at a significant angle, but may be wide enough to allow for the installation of a detector rotated in an appropriate direction for the Neutrino Factory. Services such as elevator access, electricity, water and cranes, though available in both halls, would presumably need to be upgraded if a larger experiment were installed.

B.6.3 Detector

The MINOS detector could be upgraded to increase its mass for a future experiment at the Neutrino Factory. MINOS is a 5 kton detector composed of layers of 4-cm steel absorber plates interleaved with layers of scintillator slats (Fig. B.32). There is a field coil that runs through the center of each plate down the length of the detector. The coil magnetizes the plates, producing a toroidal field with a field of 1.5 T. The MINOS detector operates similarly to the Steel/Scintillator/PDT detector described in Chapter 15. The magnetic field enables the identification of the sign of the leading muon resulting from ν CC interactions. The momentum and energy of the muon can be determined by a combination of bending in the $\vec{B}$-field and range. Background events are rejected through momentum and isolation cuts, range-out and timing. The MINOS detector is approximately 40% steel by volume. The thin steel plates give the experiment the ability to identify muons down to 1 GeV/c and to possibly measure ν_e events. An upgrade to MINOS would add a front section to the detector that was 80% steel by volume, including 20-cm thick magnetized-steel absorber plates interleaved with standard MINOS scintillator slats. This could allow the detector to approach a total mass of 15 kton. Such an upgrade would totally fill the available space in the MINOS hall, and would not resolve the issue of

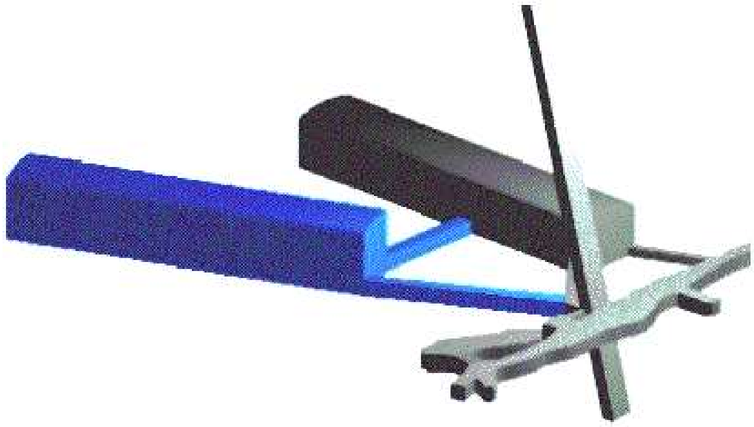

Figure B.31: The Soudan Site. The two underground experimental halls are located at 714 m below the surface. The MINOS hall is on the left and the Soudan II hall is on the right.

the detector angle relative to the incident beam angle. An alternate solution would be to build a 15 kton detector in the second hall available at Soudan. The second hall is wider than the MINOS hall, and could accommodate a detector installed at an angle rotated toward BNL. With this solution, the angle between the detector's major axis and the neutrino beam would be smaller, though not 0°. The choice between these alternate solutions requires additional study.

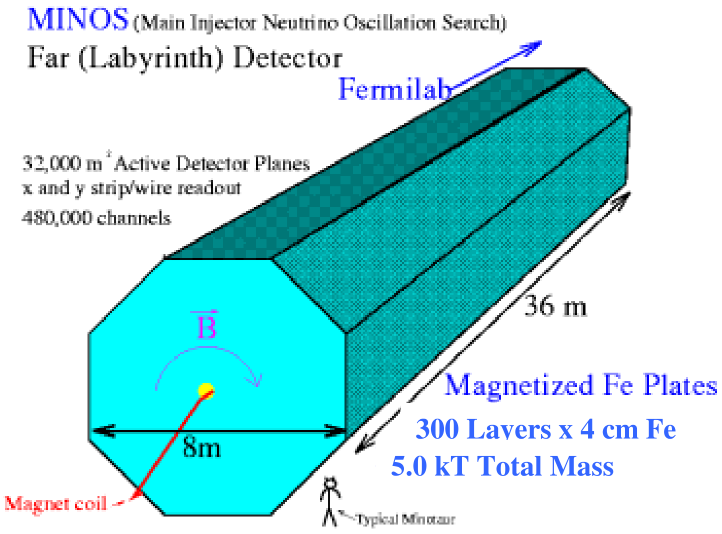

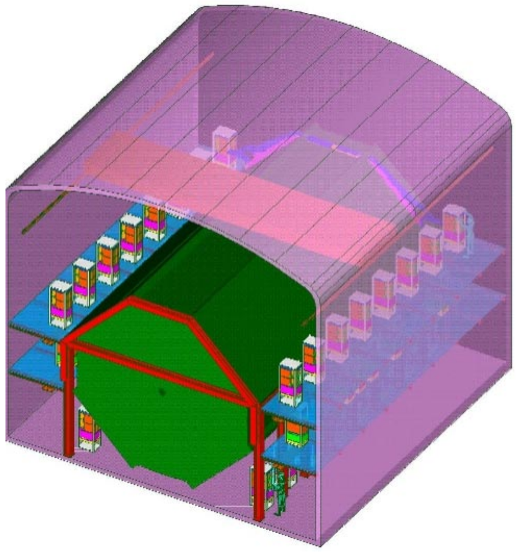

Figure B.32: Two views of the Minos detector showing both its general features and its configuration in the experiment hall.

B.6. Detector

Bibliography

[1] *A Cupronickel Rotating Band Pion Production Target for Muon Colliders*, B.J. King *et al.*, Proc. PAC'99, IEEE, pp. 3041-3.

[2] *Rotating Band Pion Production Targets for Muon Colliders and Neutrino Factories*, B.J. King, NIM A 451 (2000) pp. 335-343, Proc. ICFA/ECFA Workshop "Neutrino Factories based on Muon Storage Rings (nuFACT'99)", physics/0005007.

[3] *Some thoughts on a high-power, radiation cooled, rotating toroidal target for neutrino production*, J.R.J. Bennett, NIM A 451 (2000) pp. 344-348, Proc. ICFA/ECFA Workshop "Neutrino Factories based on Muon Storage Rings (nuFACT'99)".

[4] *A Rotating Band Target for Pion Production at a Neutrino Factory, using Study II Parameters*, B.J. King, N.V. Mokhov, N. Simos and R.J. Weggel, Muon Collider Note 199,
http://www-mucool.fnal.gov/notes/notes.html.

[5] BNL g-2 Collaboration, *The BNL Muon Storage Ring Beamline*, to be published.

[6] Graphalloys are manufactured from molded graphite impregnated with metal. Graphalloy is a registered trademark of the Graphite Metallizing Corporation.

[7] N.V. Mokhov, "The MARS Code System User's Guide", Fermilab-FN-628 (1995). N.V. Mokhov and O.E. Krivosheev, "MARS Code Status", Fermilab-Conf-00/181 (2000). http://www-ap.fnal.gov/MARS/ .

[8] N. Holtkamp, D. Finley, Editors, *A Feasibility Study of a Neutrino Factory Based on a Muon Storage Ring*, Aug., 2000 (http://www.fnal.gov/projects/muon_collider/nu-factory/fermi_study_after_april1st/)

[9] P. Sievers, *A Stationary Target for the CERN Neutrino Factory*, presented at NU-FACT01, Tsukuba, Japan

{http://www-prism.kek.jp/nufact01/May26/WG3/26wg3_sievers.pdf}

[10] R.B. Palmer, C. Johnson and E. Keil, *A Cost-Effective Design for a Neutrino Factory*, BNL-66971, CERN SL/99-070 AP, NEUTRINO FACTORY NOTE 09; published in the Proceedings of NuFact99, Lyon, (http://lyopsr.in2p3.fr/nufact99/.)

[11] N. Marseille and W. Pirkl, *Sparking Cavity Test Report*, {http://nicewww.cern.ch/~molat/neutrino/nf52.pdf}

[12] D. Neuffer "High Frequency Buncher and $\phi - \delta E$ Rotation for the $\mu^+ - \mu^-$ Source", MUCOOL Note 0181, Oct. 2000, (http://www-mucool.fnal.gov/notes/)

[13] V. Balbekov, P. Lebrun, J. Monroe, P. Spentzouris, *The Single Field Flip Cooling Channel for a Neutrino Factory*; MUC Note 0125, March 2000, (http://www-mucool.fnal.gov/notes/)

[14] G. Hanson, (http://needmore.physics.indiana.edu/~gail/emittance_exchange.html)

[15] V. Balbekov, *Double Field Flip Cooling Channel for Neutrino Factory (front-end simulation)*, MuCool #118, April 2000.

[16] *A Feasibility Study of a Neutrino Source Based on a Muon Storage Ring*. Edited by N. Holtkamp and D. Finley, March 2000.

[17] HTTP://WWWINFO.CERN.CH/ASD/GEANT4/GEANT4.HTML

[18] Open Inventor. Registered trademark of Silicon Graphics Inc.

[19] S.J. Berg, unpublished (http://pubweb.bnl.gov/people/jsberg/talks/010131/0101310all.pdf);
J.S. Berg, et al., *Acceleration Stages for a Muon Collider*, Proc. PAC99, New York (1999), pp. 3152.

[20] The WIPP Home Web Page, *http://www.wipp.carlsbad.nm.us/wipp.htm*

[21] The MINOS Experiment and the NuMI beam line, *http://www-numi.fnal.gov:8875/*